Carbonate precipitation during anoxic water-rock interaction, with implications for the formation of the Martian carbonates

Lucy Elizabeth Kissick

St Edmund Hall, Oxford



Submitted for the degree of

Doctor of Philosophy

Hilary 2021

Department of Earth Sciences

University of Oxford

UK

Contents Page

Table of Contents

ACKNOWLEDGEMENTS **8**

ABSTRACT **13**

EXTENDED ABSTRACT **15**

CHAPTER 1: AN INTRODUCTION TO THE MARTIAN ATMOSPHERE AND IRON CARBONATES **23**

1. THE MARTIAN ATMOSPHERE **23**

1.1. CONSTRAINTS ON ATMOSPHERIC PRESSURE THROUGH TIME 24
1.2. CONSTRAINTS ON ATMOSPHERIC COMPOSITION THROUGH TIME 28

2. CARBONATE MINERALS **29**

2.1. CARBONATES ON EARTH 29
2.2. CARBONATES ON MARS 34
2.3. HOW DID THE MARTIAN CARBONATES FORM? 37

3. AN EXPERIMENTAL APPROACH TO CARBONATE FORMATION ON MARS **46**

4. SUMMARY **51**

5. FIGURES **52**

6. REFERENCES **63**

CHAPTER 2: METHODS **103**

1. INTRODUCTION **103**

2. FAYALITE SYNTHESIS **103**

2.1. NATURAL FAYALITE SAMPLES 104
2.2. FAYALITE SYNTHESIS 104

3. EXPERIMENTAL METHODS **106**

3.1. THE ANOXIC GLOVE BOX 106
3.2. THE EXPERIMENTAL SET-UP 107
3.2.1. The aqueous solution *108*
3.2.2. Experimental variations: Rock:water ratio *108*
3.2.3. Experimental variations: CO_2 ..... *109*
3.3. THE EXPERIMENTS 110
3.3.1. Fayalite ± Forsterite Experiments *111*
3.3.2. Columbia River Basalt Experiments *113*
3.3.3. The 75 °C experiments *114*
3.4. THE SOLUTION SAMPLING PROCEDURE 115
3.5. THE SOLID SAMPLING PROCEDURE 116

4. ANALYTICAL METHODS **117**

4.1. SOLUTION SAMPLE ANALYSIS 117
4.1.1. Saturation state calculations *117*
4.1.2. ICP-MS measurements *118*
4.2. SOLID SAMPLE ANALYSES 118
4.2.1. X-Ray Diffractometry *119*
4.2.2. Scanning Electron Microscopy and Energy Dispersive X-Ray Spectroscopy *119*
4.2.3. Fourier Transform Infrared Spectroscopy *121*
4.2.4. Brunauer-Emmett-Teller theory *121*

5. KINETIC CALCULATIONS 121

5.1. RATE OF PRECIPITATION 122
5.2. THE DEBYE-HÜCKEL B-DOT EQUATION 123

6. POST-EXPERIMENT GEOCHEMICAL MODELLING 124

6.1. THE MODEL 125
6.2. DIC VS ALKALINITY PLOTS 127
6.3. THE GWB DATABASE 127

7. CONCLUSIONS 128

9. FIGURES 129

10. REFERENCES 145

CHAPTER 3 156

1. ABSTRACT 157

2. INTRODUCTION: UNRAVELLING SURFACE AND SUBSURFACE CARBON SINKS WITHIN THE EARLY MARTIAN CRUST 158

3. MATERIALS AND METHODS 161

3.1. EXPERIMENTS 161
3.2. GEOCHEMICAL MODELLING 165

4. RESULTS 166

4.1. TEMPORAL EVOLUTION OF SOLUTION CHEMISTRY 166
4.2. SIDERITE SATURATION 167
4.3. FE(II)-SILICATE AND AMORPHOUS SiO_2 FORMATION 168
4.4. SOLID PHASE CHARACTERISATION 169

5. DISCUSSION 170

5.1. SIDERITE PRECIPITATION KINETICS 170
5.2. UNRAVELLING SURFACE AND SUBSURFACE CARBON SINKS WITHIN THE EARLY MARTIAN CRUST 172
5.3. IMPLICATIONS FOR THE EARLY MARTIAN ATMOSPHERE 177

6. CONCLUSIONS 177

7. ACKNOWLEDGEMENTS 178

8. AUTHOR CONTRIBUTIONS 179

9. FIGURES 180

10. REFERENCES 186

11. SUPPLEMENTARY FIGURES 200

CHAPTER 4: COLUMBIA RIVER BASALT AS AN ANALOGUE FOR THE MARTIAN CRUST IN EXPERIMENTAL RECREATIONS OF SURFACE/NEAR-SURFACE CARBONATION 204

1. INTRODUCTION 204

1.1. COLUMBIA RIVER BASALT AS A MARTIAN ANALOGUE 204

2. MATERIALS AND METHODS 207

2.1. THE EXPERIMENTS 207
2.2. THE MODEL 210

3. RESULTS 212

3.1. SOLUTION CHEMISTRY RESULTS 212
3.1.1. pH 212
3.1.2. Oxidation-reduction potential 214
3.1.3. Iron 217
3.1.4. Silica 219
3.1.5. Magnesium 221
3.1.6. Summary 221

3.1.7. Siderite *222*
3.1.8. Amorphous silica *223*
3.1.9. Amorphous Fe-carbonate *224*
3.2. SOLID SAMPLE RESULTS 225
3.2.1. X-Ray diffraction *225*
3.2.2. Fourier transform infrared spectroscopy *226*
3.2.3. Scanning electron microscopy *226*

4. DISCUSSION 228

4.1. CONDITIONS CONDUCIVE TO FE(II)-CARBONATE PRECIPITATION 228
4.2. CONDITIONS CONDUCIVE TO THE FORMATION OF FE(II)-SILICATES 230
4.3. TWO HYPOTHESES FOR VARIATIONS IN DISSOLUTION RATE AS A FUNCTION OF MINERALOGY 232
4.4. MODELLED CONDITIONS CONDUCTIVE TO THE FORMATION OF FE(II)-CARBONATES AND -SILICATES 237
4.5. DISSOLVED INORGANIC CARBON AND TOTAL ALKALINITY AS CONSTRAINTS ON THE CO_2 SYSTEM 238
4.6. THE ROLE OF CALCIUM 240
4.7. MODELLING SUMMARY 241

5. CONCLUSIONS 243

6. FIGURES 247

7. REFERENCES 286

CHAPTER 5: CARBONATION IN HOT MARTIAN ENVIRONMENTS: EXPERIMENTAL PRECIPITATION OF FE(II)-CARBONATES AT 75 ºC 301

1. INTRODUCTION 301

1.1. CARBONATE FORMATION AT HYDROTHERMAL TEMPERATURES 304

2. MATERIALS AND METHODS 306

2.1. THE EXPERIMENTS 306
2.2. THE MODEL 308

3. RESULTS 309

3.1. SOLUTION CHEMISTRY RESULTS 309
3.1.1. pH *309*
3.1.2. Oxidation reduction potential (ORP) *310*
3.1.3. Fe, Si, and Mg *310*
3.1.4. Siderite *311*
3.1.5. Amorphous silica *311*
3.1.6. Magnesite *312*
3.1.7. Summary of saturation state calculations *312*
3.2. SOLID RESULTS 312
3.2.1. X-Ray diffraction *313*
3.2.2. Fourier transform infrared (FT-IR) spectroscopy *314*
3.2.3. Scanning electron microscopy (SEM) *315*

4. DISCUSSION 316

4.1. CARBONATE ACTIVITY 318
4.2. GREENALITE FORMATION 322
4.3. MODELLED REACTION PATHWAYS 325
4.3.1. Fayalite model *326*
4.3.2. Fayalite and forsterite model *326*
4.3.3. CRB model *327*
4.4. DISSOLVED INORGANIC CARBON VS TOTAL ALKALINITY 330
4.5. THE IMPLICATIONS FOR CARBONATE AND CLAY FORMATION ON THE MARTIAN SURFACE 331

5. CONCLUSIONS 334

6. FIGURES 338

7. REFERENCES 375

CHAPTER 6: CONCLUSIONS 390

1. OVERVIEW **390**
2. THE KINETICS OF FE(II)-CARBONATE FORMATION **392**
3. FE(II)-CARBONATE FORMATION CONDITIONS **394**
4. IMPLICATIONS FOR THE DISTRIBUTION OF CARBONATE MINERALS WITHIN THE MARTIAN CRUST **396**
5. SUMMARY AND FINAL WORDS **400**
6. FIGURES **404**
7. REFERENCES **405**
APPENDIX 1 ..... **413**
1. FAYALITE/FORSTERITE **413**
1.1. FAYALITE: NON-CO_2 413
1.1.1. 170906 ..... *413*
1.1.2. 180123 ..... *414*
1.1.3. 180203 ..... *414*
1.1.4. 180310 ..... *415*
1.2. FAYALITE ± FORSTERITE: CO_2, SHORT TERM 415
1.2.1. 180313 ..... *415*
1.2.2. 180406 ..... *415*
1.2.3. 180612 ..... *415*
1.2.4. 180829 ..... *416*
1.3. FAYALITE ± FORSTERITE: CO_2, LONG TERM 416
1.3.1. 180628 ..... *416*
1.3.2. 181029 Fa *416*
1.3.3. 181029 Fo *417*
1.3.4. 190423 Fa *417*
1.3.5. 190423 Fo *418*
1.4. FAYALITE ± FORSTERITE: CO_2, LOW ROCK:WATER RATIO 418
1.4.1. 181004 ..... *418*
1.4.2. 181205 ..... *419*
1.5. FAYALITE ± FORSTERITE: CO_2, HIGH FA-FO RATIO 419
1.5.1. 190121 ..... *419*
2. COLUMBIA RIVER BASALT **419**
2.1. CRB: CO_2, LONG TERM 419
2.1.1. 190414 ..... *420*
2.2. CRB: CO_2, LOW ROCK:WATER RATIO 420
2.3. CRB: CO_2, SHORT TERM 421
2.3.1. 190806 ..... *421*
2.3.2. 190807 ..... *421*
3. HEATED EXPERIMENTS AT 75 °C **422**
3.1. FAYALITE AT 75 °C 422
3.1.1. 191028 ..... *422*
3.2. FAYALITE + FORSTERITE AT 75 °C 423
3.2.1. 191107 ..... *423*
3.3. CRB AT 75 °C 423
3.3.1. 191118 ..... *423*
3.4. LOW WATER-ROCK AT 75 °C 423
3.4.1. 191128 ..... *424*
3.4.2. 191129 ..... *424*
4. CONCLUSIONS **424**
APPENDIX 2 ..... **425**
1. INTRODUCTION **425**
2. PH AND EH DURING EXPERIMENTATION **425**

2.1. pH 425
2.1.1. 180123 ..... *426*
2.1.2. 180203 ..... *427*
2.1.3. 180310 ..... *427*
2.1.4. 180313 ..... *429*
2.1.5. 180406 ..... *429*
2.1.6. 180612 ..... *430*
2.1.7. 180628 ..... *430*
2.1.8. 180829 ..... *431*
2.1.9. 181004 ..... *432*
2.1.10 181029 Fa *432*
2.1.11. 181029 Fo *433*
2.1.12. 191205 ..... *434*
2.1.13. 190121 ..... *434*
2.1.14. 190423 Fa *435*
2.1.15. 190423 Fo *435*
2.1.16. pH Conclusions *436*
2.2. Eh 438
2.2.1. 180123 ..... *439*
2.2.2. 180203 ..... *439*
2.2.3. 180310 ..... *439*
2.2.4. 180313 ..... *439*
2.2.5. 180406 ..... *440*
2.2.6. 180612 ..... *441*
2.2.7. 180628 ..... *442*
2.2.8. 180829 ..... *443*
2.2.9. 181004 ..... *443*
2.2.10. 181029 Fa *444*
2.2.11. 181029 Fo *444*
2.2.12. 181205 ..... *445*
2.2.13. 190121 ..... *446*
2.2.14. 190423 Fa *446*
2.2.15. 190423 Fo *447*
2.2.16. Eh conclusions *447*
2.3. pH and Eh comparison 448

3. SOLUTION CHEMISTRY: ICP-OES 451

3.1. Iron 451
3.1.1. 180123 ..... *452*
3.1.2. 180203 ..... *453*
3.1.3. 180313 ..... *453*
3.1.4. 180406 ..... *454*
3.1.5. 180612 ..... *454*
3.1.6. 180628 ..... *455*
3.1.7. 180829 ..... *456*
3.1.8. 181004 ..... *456*
3.1.9. 181029 Fa *457*
3.1.10. 181029 Fo *458*
3.1.11. 181205 ..... *458*
3.1.12. 190121 ..... *459*
3.1.13. 190423 Fa *459*
3.1.14. 190423 Fo *459*
3.1.15. Conclusions *460*
3.2. Silica 461
3.2.1. 180123 ..... *462*
3.2.2. 180123 ..... *463*
3.2.3. 180313 ..... *463*
3.2.4. 180406 ..... *464*
3.2.5. 180612 ..... *464*
3.2.6. 180628 ..... *465*
3.2.7. 180829 ..... *466*

3.2.8. 181004 ..... *467*
3.2.9. 181029 Fa *467*
3.2.10. 181029 Fo *468*
3.2.11. 181205 ..... *469*
3.2.12. 190121 ..... *469*
3.2.13. 190423 Fa *469*
3.2.14. 190423 Fo *470*
3.2.15. Conclusions *470*
3.3. MAGNESIUM 471
3.3.1. 180123 ..... *472*
3.3.2. 180203 ..... *472*
3.3.3. 180313 ..... *472*
3.3.4. 180406 ..... *472*
3.3.5. 180612 ..... *472*
3.3.6. 180628 ..... *473*
3.3.7. 180829 ..... *474*
3.3.8. 181004 ..... *474*
3.3.9. 181029 Fa *475*
3.3.10. 181029 Fo *475*
3.3.11. 181205 ..... *476*
3.3.12. 190121 ..... *476*
3.3.13. 190423 Fa *476*
3.3.14. 190423 Fo *476*
3.3.15. Conclusions *477*
3.4. SIDERITE 477
3.4.1. 180123 ..... *478*
3.4.2. 180203 ..... *478*
3.4.3. 180313 ..... *478*
3.4.4. 180406 ..... *479*
3.4.5. 180612 ..... *479*
3.4.6. 180628 ..... *480*
3.4.7. 180829 ..... *482*
3.4.8. 181004 ..... *482*
3.4.9. 181029 Fa *483*
3.4.10. 181029 Fo *483*
3.4.11. 181205 ..... *483*
3.4.12. 190121 ..... *484*
3.4.13. 190423 Fa *484*
3.4.14. 190423 Fo *484*
3.4.15. Conclusions *484*
3.5. AMORPHOUS SILICA 485
3.6. ICP-OES CONCLUSIONS 486

4. SOLID RESULTS 487

4.1. X-RAY DIFFRACTOMETRY 487
4.1.1. 180123 ..... *488*
4.1.2. 180203 ..... *488*
4.1.3. 180310 ..... *489*
4.1.4. 180313 ..... *489*
4.1.5. 180406 ..... *489*
4.1.6. 180612 ..... *490*
4.1.7. 180628 ..... *490*
4.1.8. 180829 ..... *491*
4.1.9. 181004 ..... *491*
4.1.10. 181029 Fa *491*
4.1.11. 181029 Fo *492*
4.1.12. 181205 ..... *493*
4.1.13. 190121 ..... *493*
4.1.14. 190423 Fa *494*
4.1.15. 190423 Fo *494*
4.1.16. Conclusions *494*

4.2. FOURIER TRANSFORM INFRA-RED SPECTROSCOPY 495
4.2.1. 180123 ..... *496*
4.2.2. 180203 ..... *496*
4.2.3. 180313 ..... *496*
4.2.4. 180406 ..... *496*
4.2.5. 180612 ..... *497*
4.2.6. 180628 ..... *497*
4.2.7. 180829 ..... *497*
4.2.8. 181004 ..... *497*
4.2.9. 181029 Fa *498*
4.2.10. 181029 Fo *498*
4.2.11. 181205 ..... *498*
4.2.12. 190121 ..... *498*
4.2.13. 190423 Fa *499*
4.2.14. 190423 Fo *499*
4.2.15. Conclusions *499*
4.3. SCANNING ELECTRON MICROSCOPY 500
4.3.1. Unreacted fayalite and forsterite *501*
4.3.2. 180123 ..... *501*
4.3.3. 180313 ..... *502*
4.3.4. 180406 ..... *502*
4.3.5. 180628 ..... *503*
4.3.6. 181004 ..... *503*
4.3.7. 181029 Fa and 181029 Fo *504*
4.3.8. 190121 ..... *504*
4.3.9. 190423 Fa and 190423 Fo *504*
4.3.10. Conclusions *507*
4.4. BRUNAUER-EMMETT-TELLER ANALYSIS 508

5. GEOCHEMICAL MODELLING 509

5.1. PH 509
5.2. ELEMENT CONCENTRATION IN SOLUTION 510
5.3. SPECIES SATURATION STATE 510
5.4. SUMMARY OF MODEL 511

6. CONCLUSIONS 511

7. FIGURES AND TABLES 512

APPENDIX 3 580

Acknowledgements

I would like firstly to thank my primary supervisor, **Nick Tosca**, who has been responsible for overseeing my entire DPhil, and who first devised the project of investigating carbonate formation on Mars. Nick has been continuously patient with me, coming from a non-chemistry background to a chemistry project, and I am indebted to him for taking that chance with me to begin with. While it must have been frustrating having a postgraduate student who at times struggled to grasp what must have seemed like basics, Nick always took the time to either explain or point me in the right direction, and thanks to his guidance I am now a far better scientist than I was when I first arrived in Oxford.

I thank **Tamsin Mather**, my secondary supervisor, who joined my project in third year but who has been key in honing my DPhil from the start. As my planned internal examiner, Tamsin kept up to date with my project from first year onwards and was always quick to offer valuable suggestions. When these suggestions became invaluable, it felt far wiser to have her on the team as the project progressed rather than waiting at the end to pick it apart, and it is not a decision I have ever regretted. Thank you, Tamsin, not just for your figure suggestions and thermodynamics assistance, but also for being the first person to say I should take pride in what I have learned compared to when I started, and not compare myself to where other students are now.

I cannot thank **Bernie Wood** and **Andrew Matzen** enough for their help at the very start of my research. Set with the task of synthesising my own fayalite and less than a year into my DPhil, I had no idea where to begin — Bernie Wood not only let me use his laboratory and facilities, but he took the time to run through the process with me step by step. The synthesis process took time to smooth out, with mystery impurities still forming after several weeks, and during this time Andrew Matzen worked with me on solving problem after problem as though he was my supervisor — running codes, talking me through calculations, letting me figure it out —

despite having his own work to do and no obligation to help me. Neither he nor Bernie wanted anything in return for their immeasurable support at this pivotal moment of my DPhil, and I am so grateful both for their expertise but also their kindness at a time when I could have easily become lost.

Before synthesising my own fayalite, I first contacted several museums around the world in search of natural specimens to use. While all the materials sourced ultimately contained too many impurities for use in my work, I nonetheless would like to thank **Stefan Nicolescu** (Yale Peabody Museum of Natural History, USA), **Kevin Czaja** (Harvard Museum of Natural History, USA), and **Robin Hansen** (London Museum of Natural History, UK). All sent me free samples of fayalite that were of the highest grade found naturally — a fine example of the cooperation between scientists both nationally and internationally.

Once my fayalite was pure and my research could begin, I was fortunate enough to have access to a suite of world-class analytical instruments on which to study the products of these experiments. In-house, I would like to thank **Kat Clayton** for operating the X-Ray diffractometer throughout my DPhil and **Phil Holdship** for running the inductively coupled plasma mass spectrometer in my fourth year. I would also like to thank **Gillian MacKinnon** of the Scottish Universities Environmental Research Centre for running the inductively coupled plasma optical emission spectrometer in my second and third year before I was unable to continue using her services. **Errin Johnson** in the University of Oxford's Pathology Department was kind enough to teach me how to use their scanning electron microscope (SEM) when the Earth Sciences equivalent was out of action.

Several other scientists have shown me great kindness over the course of my project. My lab-mate **Clancy Zhijian Jiang** has been an encyclopaedia of all things kinetics and was ever eager to share this knowledge over many helpful, coffee-mediated discussions. Without his tips in the lab, or interest in my findings, or time spent head-scratching over code, my thesis would be slightly less thorough. My officemate **Dan Spencer** was always a cheerful and patient teacher of MatLab

whenever I spun my computer chair around to ask yet another question on some coding issue. **Susanne Schwenzer** at the Open University became something of a mentor figure after we were stuck together in a tiny French airport: she was one of the first people to make me feel like my research was interesting and worthwhile, and her fascinating stories and advice made me set the bar higher for myself.

Jon Wade deserves his own paragraph. From Jon I had SEM lessons and advice; I had lengthy discussions on interesting new methods or useful new tips; I had encouragement and advice when applying for jobs. Again this was someone who was not a supervisor — not in my research group — not interested in being on any of my papers or receiving any recognition. I can't thank Jon enough for being a genuine mentor and for looking out for me throughout my DPhil.

Outside of my studies I was fortunate enough to do some incredible things during my time in Oxford, one of which was attend the European Space Agency's Alpbach Summer School in 2018. While unrelated to my research or to this thesis, my time in Alpbach, Austria, was formative in teaching me how to function under high pressure, to work as part of a team to a tight deadline, and to speak competently in front of large audiences where the stakes were high. For this I would like to thank my team's tutors **Günter Kargl** and **Cecilia Tubiana**, who kept us motivated and efficient, and **Michaela Gitch**, who organises the school each year.

I would not have been able to complete my DPhil in half as much comfort or tranquillity without the support of my college, **St Edmund Hall**. The Hall provided me with accommodation for all four of my years in Oxford, and it must have been some of the most beautiful in the city. There are three people I would like to specifically thank within the college. **Belinda Huse**, the accommodation officer, and **Alex Grant**, then-warden and now deputy estates manager, both consistently went out of their way to help me out when things occasionally needed it. They really didn't have to, and I was always taken aback by how patient and generous they were. Having a place to sleep and work that was clean and quiet was at times the difference between functioning and not functioning; both Belinda and Alex helped keep it the former.

The third person I would like to thank in association with St Edmund Hall is **Bill Miller**, college alumnus and generous benefactor of the William R. Miller scholarship. This I received in my second year and granted me one year's free accommodation, which essentially meant I did not have to worry about Oxford's somewhat steep rent prices for the rest of my time here. For removing that worry, and for offering this scholarship every year for students in similar positions, I cannot thank Bill Miller enough, and I was saddened to hear of his recent passing.

I thank **Victoria Forth**, who keeps my course the Doctoral Training Partnership (DTP) running smoothly and effectively year after year. Victoria's office was always open and her email responses always prompt — thank you for being a cheerful face. I would also like to thank **David Pyle** as my DTP supervisor at the very start of my project, as well as being a regular point of contact throughout the last four years. **Claire Rylatt** and **Ian Wright** of the Department of Earth Sciences were always my first point of call for any administrative or otherwise uncomfortable issues. Ian in particular felt like the departmental protector, always on standby to encourage us with haggis or defend us from the many odd and idiosyncratic arisings within an Oxford department. And no thesis would get by without IT support: with **May Chung** and **Stephen Usher** next door, I was kept quite free of major computer-related woes.

Most recently, I must sincerely thank the team I joined at my new place of employment, the National Nuclear Laboratory. With the departmental shutdown of summer 2020 came unanticipated laboratory delays that set my thesis back months: my new manager, **Matthew Barker**, always made it clear I could have as much time as needed to get this finished and was as accommodating as possible to my change in circumstance. I also could not be more fortunate having **David Hambley**, my technical lead, and **James Goode**, his deputy, for a teamlet, both of whom have been likewise understanding of my situation as well as excellent company these last few months.

I thank, with all the sincerity I have, **the gardeners of the University Parks**. The splendour of the Radcliffe Camera; the song of the bells of St. Giles; the secret door to the roof of St-Peter-in-the-East; the view beyond — the daffodils do it better every time.

Lastly, as with almost every thesis, my thanks go to my family. Thank you to **Mum** and **Dad**. Thank you to **Katie** and **Hannah**, my sisters. Thank you to **Tim Gregory**, my partner.

Abstract

Despite over a Martian decade (20 years) of surface-based observations, reconciling Mars' water-altered landscapes with a detailed reconstruction of its former atmosphere has remained problematic. Carbon dioxide is widely considered the main early atmospheric constituent based on expected outgassing behaviour and observed atmospheric isotope ratios, yet carbonate minerals — the expected sinks for this carbon — are only abundant in scarce isolated localities across the surface. While orbital spectroscopic investigations continue to yield an increasing inventory of these deposits, their relative rarity has prompted suggestions that the Noachian atmosphere was commonly characterised by low pCO_2. However, without a thorough investigation of how exactly carbonates form under Mars-like conditions, their absence cannot be definitively linked to the absence of an atmosphere. To supply this key information, and to answer the more fundamental issue of carbonate precipitation mechanisms under anoxic, aqueous conditions, this thesis examines the controls on Fe(II)-carbonate precipitation. Anoxic experiments were conducted that varied initial pH, rock:water ratio, and pCO_2. These were run with the minerals fayalite, a combination of fayalite/forsterite (Chapter 3), followed by rock common to Mars (basalt; Chapter 4). In these experiments no substantive Fe(II)-carbonate precipitation occurred despite significant supersaturation with respect to siderite. Reaction path models indicate Fe(II)-carbonate supersaturation thresholds would have been commonly met in low rock:water ratio systems within the subsurface as opposed to high-pCO_2, high water-rock systems exposed at the near-surface. This suggests that the rarity of Martian carbonates may be partly controlled by a lack of deep crustal exposures, rather than insufficient atmospheric pCO_2. Later, at hydrothermal temperatures of 75 °C (Chapter 5), siderite formed in appreciable quantities as rhombs and hexagonal platelets. This is consistent with carbonate formation in a warmer, sheltered subsurface. Together, the experiments within this thesis support wider orbital data by other researchers suggesting that

carbonates may comprise a large component of the deep crust, potentially representing a geologically significant carbon sink and offering a suggested fate for a once substantial (~1 bar) atmosphere.

Extended Abstract

Introduction: The formation of the Martian carbonates

Since William Hershel's first confident assurance of its existence in 1874, the atmosphere of the planet Mars has been a source of ceaseless and increasingly detailed speculation. Carbon dioxide was likely the main constituent of this atmosphere at its maximum in the Noachian era (~4.0-3.7 Ga), based on expected outgassing behaviour during crustal formation and atmospheric isotopic ratios. Despite this, the main proposed sink for such vast amounts of carbon — namely carbonate-bearing bedrock exposures — remain surprisingly rare at the surface. This is especially true for the Fe(II)-carbonate siderite ($FeCO_3$): Mars is a planet dominantly of mafic geology but this mineral is relatively and conspicuously absent, sighted far less than Mg(II)-carbonates. However, carbonates have been recognised from orbit, mostly either in Noachian-aged terrains or where subsurface lithologies are exposed, as well as within Martian meteorites, often associated with minerals that require neutral pH to form. This suggests that some environments on the early Martian surface produced carbonates, while others did not.

Three overarching possibilities may account for this relative scarcity: (1) surface carbonates formed under pCO_2 higher than present but were buried, or removed by dissolution; (2) atmospheric pCO_2 was significantly lower than current climate models predict, and thus carbonates did not form; or (3) carbonate formation was kinetically inhibited under aqueous conditions that characterised much of the early Martian surface.

In this thesis, possibility (3) is experimentally investigated. Anoxic water-rock interactions between acidified fluids and ferromagnesian minerals were designed in the laboratory with the aim of more closely examining the processes that control the precipitation of Martian carbonates, particularly Fe(II)-carbonates. Chapter 1 introduces the geologic, climatic, and geochemical background that motivates this study, followed by Chapter 2, which is a detailed methods

description recounting the 161 experiments that formed the basis of the thesis. Three data results chapters follow this (Chapters 3, 4, and 5), with a conclusions chapter (Chapter 6) that links these three together and summarises the key findings. Appendix I is a list describing all 161 experiments, while Appendix II is a supplement to Chapter 3, which is a short-format paper accepted for publication within the journal *Earth and Planetary Science Letters*, and due to length restrictions was heavily summarised. Lastly, Appendix III is an expansion upon the geochemical equations used to calculate several key thermodynamic properties that were important at several points within the thesis.

Methods: Experimental geochemistry

161 experiments were run within sealed vessels at varying temperature (25 or 75 ºC), rock:water ratio (1:1, 1:10, or 1:500), initial pH (2 or 4), and dissolved CO_2 content (0.1, 0.5, and 1.0 bars of equivalent pCO_2). These parameters reflect the typical surface and near-surface environment of the Noachian Mars as a planet where its atmosphere was increasingly thinning: from ~3.7-3.0 Ga, Mars is expected to have grown drier and more acidic through time, and this variety of parameters reflects both Mars' earlier, more clement conditions, as well as its transition to the present day's aridity. Strictly anoxic conditions were maintained to simulate Mars' lack of O_2 by conducting all experiments and analytical preparation techniques within N_2/H_2 glove boxes maintained at 0 ppm O_2. Experiments ran over intervals of 12 hours to 85 days, were each sampled regularly at 10 intervals (excepting those at rock:water ratio of 1:1 or 1:10), and the solutions were filtered for later analysis. Upon each experiment's termination, solids were filtered and dried.

Three categories of experiments were run. The first, discussed in Chapter 3 and Appendix II, concerned the use of the Fe-rich end member of olivine, fayalite and, later, a 1:1 mix of fayalite and forsterite (the Mg-rich end member). The solutions described above were added to either pure synthetic fayalite (Fa: Fe_2SiO_4), or a mixture of both fayalite and natural forsterite (Fo: Mg_2SiO_4; $Fo_{>90}$). Fe^{2+} and Mg^{2+} are two common cations derived from Mars' mafic crust, and so are readily available to react with both ground- and surface water. The second category of

experiments, discussed in Chapter 4, substituted the fayalite/forsterite combination for Columbia River Basalt (CRB) in powdered form and two particles sizes (<5 μm and 20 μm). CRB was selected as the next and more advanced proxy for the Martian surface owing to its mafic combination of minerals — predominantly the plagioclase feldspar albite, with quartz, hematite, diopside, and other minor phases — but additionally basalt's commonness across Mars. From vast Hesperian flood lava plains, e.g., the Thaumasia Plateau, Hesperia Planum, and Gusev Crater, to the mafic grains comprising the sandstones and mudstones of Gale Crater and Meridiani Planum, Mars is a planet dominated by basalt in various igneous and sedimentary stages. For these reasons CRB was selected as the next logical increase in complexity from the simpler olivine experiments. Lastly, Chapter 5 recreates the experiments of Chapters 3 and 4 but at hydrothermal temperatures of 75 ºC, using fayalite, the fayalite/forsterite mix, and the two CRB particle sizes as reactants. This is because Mars would have locally experienced hydrothermal conditions, for example in the wake of impact craters; related to volcanism; or deep within the crust (around >5 km) in relation to the planetary geotherm.

Results: Conditions for carbonate precipitation

Solution samples were analysed via both Inductively Coupled Plasma Optical Emission Spectrometry and Inductively Coupled Plasma Mass Spectrometry. For Chapter 3, 91 individual experiments were run. In many of these experiments, conducted at 25 ºC with fayalite/forsterite under the equivalent of 0.1-1.0 bar of atmospheric CO_2, it was found that the chemistry of multiple solution samples exceeded the saturation point of siderite. Thermodynamically, this predicts the formation of a precipitate. However, when the solids of the experiments were analysed via X-Ray Diffraction (XRD) and Fourier Transform Infrared Spectroscopy (FT-IR), the samples remained their initial mineralogy. This suggests that under a wide range of conditions, siderite saturation state failed to reach the point of spontaneous nucleation, and that some critical threshold must be exceeded prior to nucleation and subsequent precipitation occurring. While a possible precipitate did form for the experiments with the highest supersaturation states — nanometre-scale plates

were observed via Scanning Electron Microscopy (SEM), and Energy Dispersive X-Ray Spectrometry (EDS) determined elevated levels of carbon present in the phase — due to their size, the specific phase could not be determined with the analytical techniques employed thus far. The morphology of the plates, which were occasionally observed amassed together in clumps up to 10 μm across, was possibly consistent with amorphous Fe-carbonate (AFC), a recently characterised precursor phase to the metastable chukanovite and geologically stable siderite, both Fe(II)-carbonates. This was unable to be confirmed. An additional precipitate in the form of long, brittle, fibrous forms that apparently grew in interstitial zones between fayalite crystals was found commonly alongside the nanometre-scaled precipitate, and may have been a form of amorphous silica.

For the CRB experiments of Chapter 4, in comparison to Chapter 3 there was very little geochemical activity. Over 36 individual experiments, the saturation state for siderite in all solution samples remained well below 1, as well as for other minerals such as the serpentinite greenalite. Dissolved elemental levels also remained extremely low, with pH and Eh deviating only minorly from their starting positions, while under SEM, no observable changes had occurred to the morphology or structure of the CRB. Additionally, no precipitates were observed via XRD or FT-IR. Low rock:water ratio experiments displayed the most activity, with pH, elemental levels of Fe^{2+}, SiO_2, and Mg^{2+}, and siderite saturation state reaching their highest. However, the overall lack of significant chemical activity suggests that, under 25 ºC, CRB struggled to dissolve into solution, and that siderite and other carbonates were unable to form over the timescales observed. Reaction transport modelling reflected again a heightened propensity for low water-rock environments to yield higher siderite saturation states, reflecting the observed fayalite/forsterite experimental trends.

For the elevated temperatures of Chapter 5, 34 experiments were conducted that repeated those bearing fayalite, fayalite/forsterite, and CRB for 10 days, in comparison to up to 85 days as run in the previous chapters. However, even within those 10 days, new mineral growth was

observed in both the fayalite and fayalite/forsterite experiments in quantities sufficiently significant to be detected by XRD and FT-IR and observed as various morphologies in SEM. These morphologies included towers of smooth-surfaced, interlocking rhombs, each 2-5 μm across and collectively over 20 μm high; twin-faced, butterfly-crested minerals <1 μm in size scattered upon fayalite crystals; clean-cut, hexagonal plates ~5-10 μm across, partially embedded and growing out of the fayalite; and the previously observed nano-scale, aligned precipitates. These were identified as siderite. The fibrous, likely amorphous silica precipitate was also observed. No new growth was found in the high temperature CRB experiments.

Discussion: CO_2 in the Martian rock record

Set within a kinetic framework, the experimental data of this thesis indicates that anoxic water-rock systems on Mars evolved along a chemical pathway that only surpassed the threshold for spontaneous Fe(II)-carbonate nucleation under the combined conditions of: high Fe^{2+} activity; high alkalinity; and high dissolved CO_2, whereby pH and Fe^{2+} activity must reach higher levels in a 0.1 bar scenario than a 1.0 bar. In addition, that Fe(II)-carbonate precipitates occurred so rapidly over the course of the 75 ºC experiments, and in such volumes, suggests temperature is a key factor determining Fe(II)-carbonate formation, as these experiments were identical in all but temperature to those conducted in Chapter 3.

Fe(II)-carbonate distribution on Mars may be best explained by asking, where would these criteria best combine, and accordingly, where is siderite saturation likely to be the highest?

The main carbonate-forming environments on Mars, as determined by both meteoritic characterisation and orbital spectroscopy, include within brines, hydrothermal fluids, and by in-situ carbonation. These are commonly connected by occurring within the subsurface where deep, alkaline crustal fluids may migrate to the surface after sufficient residence time within a mafic substrate. Under such an environment, migrating fluids become buffered to highly alkaline pH from mafic wall-rock alteration, which may overwhelm the acidity contributed by a high pCO_2 atmosphere. Oxygen species are also lost, and Fe remains in the reduced state. Temperature is also

likely to be higher, whether as a result of residual heat from volcanic or impact activity, or from the planetary geotherm. Fe^{2+} in solution then precipitates in the presence of high alkalinity and CO_2, which may migrate into the system from the atmosphere to produce Fe(II)-carbonate. This is in contrast to surface waters which, in equilibrium with a CO_2-rich atmosphere, will be buffered to mild acidity and be less likely to cross requisite nucleation thresholds for Fe(II)-carbonate. Heat is also more readily dissipated in surface environments, rather than those sheltered within the crust where there is less air or water to act as poorer thermal conductors.

The above scenarios require liquid water, anoxia, warmer temperatures, and a source of CO_2, which are all met in the Noachian era of anticipated higher temperatures and a substantial CO_2-dominated atmosphere. This is consistent with Fe(II)-carbonate identification in some of the oldest terrains on Mars, and/or those exposed via impacts that pierce the deep crust. These exposures are windows into an ancient, aqueous, Fe^{2+}-rich, neutral-to-alkaline environment once in contact with CO_2-bearing fluids at elevated temperatures, which agrees with the criteria for Fe(II)-carbonate formation observed in this experimental research.

Additionally, an improved understanding of Fe(II)-carbonate mineralisation processes permits more robust atmospheric constraints derived from the rock record. The experimental observations documented here are consistent with geochemical studies of terrestrial aquatic environments and CO_2 sequestration/storage research that indicate significant supersaturation states are required for Fe(II)-carbonate formation. This must be taken into consideration when concerning how carbonate-bearing deposits do or do not constrain atmospheric pCO_2. The models in this thesis show Fe(II)-carbonate is unlikely to form in a high rock:waterrock:water ratio, open system even under high pCO_2, owing to how atmospherically controlled dissolved inorganic carbon contributions tend to outweigh the alkalinity generation from silicate mineral dissolution. This suggests it may not be fitting to extrapolate former pCO_2 levels from known surface-based carbonate volumes, as previous work has attempted, as such environments do not represent the most likely environment for carbonate precipitation.

Lastly, the geochemical scenario for subsurface carbonate formation is also consistent with recent observations of carbonates predominantly associated with the largest impact craters. This is alongside global groundwater models, oxygen escape rates, and hydrogen isotope ratios that appear to reflect a potentially significant subsurface carbon reservoir. Nevertheless, ancient subsurface environments preserved within the Martian crust remain poorly sampled, and accordingly, should feature as priority targets for orbital and in-situ exploration missions.

Conclusions: An archive of CO_2 in the Martian sedimentary record

The experiments within this thesis have demonstrated that Fe(II)-carbonate precipitation under conditions characteristic of Mars is subject to strong kinetic control, and that the conditions conducive to its formation best converge in subsurface environments. Here, high pH and high dissolved Fe^{2+} levels, alongside higher temperatures than those at the surface, enable the thresholds for Fe(II)-carbonate formation to be exceeded when under the presence of sufficient pCO_2, which may be transported from the atmosphere to the subsurface through percolating meteoric waters. Fe(II)-carbonates may subsequently precipitate under such an environment. This conclusion, supported by 161 individual experiments, is consistent with the currently mapped inventory of Fe(II)-carbonates on Mars: these are best located within ancient impact craters or across Noachian-aged terrain. Based on this research, it is here postulated that the apparent rarity of carbonates observed within the Martian crust is attributable to a rarity of both deep subsurface exposures, but also the high saturation state required for their precipitation. A problematic, opposing hypothesis for the scarcity of observable Martian carbonates — low atmospheric pCO_2 in the water-rich Noachian era — need not be invoked in light of this research: a reconciliation between a CO_2-rich atmosphere but few corresponding carbonates agrees with atmospheric isotopic ratios, widespread water-related morphology, and a variety of aqueously altered mineralogy that all necessitate a once more substantial CO_2 atmosphere than present. Furthermore, carbonates may represent a geologically significant, subsurface carbon sink that may account for missing levels of this element that cannot be accounted for by escape-to-space rates alone.

These data can be used to inform future investigations of the early Martian carbon cycle, which is most topical in anticipation of observations acquired by NASA's upcoming *Mars 2020* mission. Orbital investigations of Jezero Crater, the *Perseverance* rover's landing site, reveal regional geology that hosts the largest identified carbonate deposit on Mars, which recent spectroscopic research has suggested may be relatively Fe-rich. The presence of authigenic siderite preserved at Jezero, if observed by *Perseverance*, could offer broad constraints on maximum Fe(II)-carbonate saturation state that could be highly complementary to this research. More broadly, based on this research the presence of localised concentrations of siderite will be useful as evidence suggesting environments once rock-dominated and of high alkalinity, which may have efficiently buried and perhaps preserved carbon — both organic and inorganic — within the early Martian crust.

Chapter 1

An Introduction to the Martian Atmosphere and Iron Carbonates

1. The Martian atmosphere

The existence of an atmosphere around the planet Mars, tenuous and seasonally fluctuating, has been well known to its observers since the 18th century following its first confident assurance by Herschel (1784). Its composition — predominantly of carbon dioxide — was well-constrained before the close fly-bys of the 1960s that directly observed this atmosphere for the first time (Table 1). In winter, around 25 % of this atmospheric CO_2 condenses at the poles to form seasonal CO_2 ice caps, but its average pressure is extremely low at only around 6 mbar (Jakosky and Farmer, 1982) with an average temperature of around 200 K (Nier and McElroy, 1977). Despite this, water-carved features are evident across the planet (Figure 1): scarred scablands of catastrophic outflow channels excoriate the surface for hundreds of kilometres (e.g., Carr, 1979); sinuous valleys meet in deep crater basins where water once collected (e.g., Goudge et al., 2016); lacustrine sedimentary sequences have been observed by the *Curiosity* rover in Gale Crater (e.g., Grotzinger et al., 2014; Hurowitz et al., 2017). Signatures of liquid water accompany such features as observed both from orbit via the Compact Reconnaissance Imaging Spectrometer for Mars (CRISM, active 2005-present) and the Observatoire pour la Mineralogie, l'Eau, les Glaces et l'Activité (OMEGA, active 2003-present) orbital spectroscopes, or *in situ* via robotic exploration. This hydrated mineralogy commonly includes clays such as smectites, saponites, and phyllosilicates (Mustard et al., 2008; Murchie et al., 2009), oxides such as hematite and magnetite (Squyres et al., 2004), and carbonates

such as siderite, magnesite, and ankerite (Ehlmann et al., 2008; Morris et al., 2010; Wray et al., 2016).

Both these lines of evidence reveal a geologic history once involving abundant water. By inference, Mars was once a planet with surface pressures sufficient to support such water, with the requirement that these conditions persisted over geological timescales.

Despite decades of increasingly finely-scaled investigation into the surface and subsurface of Mars, detailed constraints on the atmospheric characteristics that enabled such water-rich conditions remain elusive: the words of Owen et al. (1977) from the Viking era are pertinent forty years on: "there is still no adequate model for climatic change on Mars that permits the planet's surface to be warm enough for this to occur."

Two fundamental pieces of information are lacking in the study of the former Martian atmosphere: what was its *pressure*, and what was its *composition*? As a planet's atmosphere may vary considerably on geologic timescales, the atmosphere relevant to this thesis is one that existed and persisted from the onset of the Noachian (~4.0-3.7 Ga) to its steady decline throughout the Hesperian (~3.7-3.0 Ga) into the tenuous ~6 mbar atmosphere of the Amazonian (3.0 Ga to present day) based on the Hartmann and Neukum (2001) dating system. Figure 2 helps to visualise these timescales.

1.1. Constraints on atmospheric pressure through time

Multiple lines of evidence suggest a formerly more substantial atmospheric pressure for Mars than presently observed.

Geomorphology across the planet's surface is one of the most striking: upon the southern highlands and along the north-south dichotomy boundary are vast valley networks (Figure 1 (a); e.g., Masursky, 1973; Fassett and Head, 2008; Hynek et al., 2010; Davis et al., 2016) that from their earliest study have been repeatedly demonstrated to be consistent with a water-carved formation (e.g., Baker and Milton, 1974; Carr and Clow, 1981; Baker and Partridge, 1986; Baker, 2001;

Harrison and Grimm, 2005) rather than ice (Lucchitta, 1982) or lava (Leverington, 2004). As high-resolution imaging has continued to improve for Mars, the observed density of these channels has only continued to increase, particularly with the discovery of inverted channels that represent the cementation and preservation of riverine sediments (Davis et al., 2016) and the identification of lake basins (Goudge et al., 2012, 2015a). Estimates for the duration of time to carve the Noachian-aged valley networks across the northern plains strongly imply the presence of a long-lived, stable atmosphere during their formation (Fassett and Head, 2008) because of the necessity for precipitation: whether these channels were formed by run-off or by aquifer springs, some source for the initial water is required. The valleys required an estimated global equivalent layer of ~5 m of water for their creation (Luo et al., 2017) over approximately between several 10^5 and several 10^6 of years, likely between 3.6 and 3.8 Ga (Hoke et al., 2011) but perhaps for as long as >1 Gyr (Kite et al., 2019). This is around the same period of time and duration — the Noachian-Hesperian boundary — as the lake or lacustrine system within Gale Crater observed by the *Curiosity* rover is expected to have existed (Grotzinger et al., 2014). While these valleys were found capable of forming over as short a period of time as 200 years, this would have required constant flows at 'hurricane-scale' (Hoke et al., 2011), which strongly implies formation over a lengthier time and requires a sufficiently warm and wet climate to support these liquid surface flows.

A widespread hydrological cycle has also been inferred from layered sedimentary deposits (e.g., Malin and Edgett, 2000; Lewis and Aharonson, 2014; Pondrelli et al., 2015; McLennan et al., 2019), modelled groundwater activity (e.g., Andrews-Hanna et al., 2010; Andrews-Hanna and Lewis, 2011; Kite and Melwani Daswani, 2019), and observed mineralogy (e.g., Ehlmann et al., 2009, 2008; Michalski et al., 2013; Salese et al., 2019). Layered sedimentary deposits in particular are of interest because sediment must first be produced by physical and chemical processes, then transported by additional, active means. Sediment-producing processes on Mars include freeze-thaw stresses, aeolian and fluvial abrasion, permafrost processes, salt weathering, impact cratering, volcanic processes including pyroclastic flows, and gravity-driven mass wasting (Grotzinger et al.,

2011; Melosh, 2011; Grotzinger and Milliken, 2012). These enable vast volumes of sediment to form deposits, from which their transportation pathways can be determined. Such deposits include alluvial fans, deltas, and lacustrine strata (Lucchitta et al., 1986; Malin and Edgett, 2000; Metz et al., 2009; Schon et al., 2012; Grotzinger et al., 2014; McLennan et al., 2014; Pondrelli et al., 2015).

Mineralogy is another hint towards a previously more hydrologically active Mars. Widespread hydrated minerals were first discovered on a global scale by the OMEGA instrument aboard the ESA Mars Express satellite (Bibring et al., 2006) and include phyllosilicates such as smectite, montmorillonite, and kaolinite (Bibring et al., 2006; Mustard et al., 2008). Modelling of the conditions required to form carbonates identified in Gusev Crater suggested CO_2 levels between 0.01 to 2.0 bar at the time of deposition (van Berk and Fu, 2011; van Berk et al., 2012).

An earlier, more substantial atmospheric pressure for Mars may also be inferred from the observation of fractionated isotopic ratios within the present-day exosphere. Carbon and oxygen isotopic ratios of atmospheric components were first measured from Earth by Kaplan et al. (1969) and later refined by the Viking (Owen et al., 1977) and Mars Science Laboratory missions (Mahaffy et al., 2013; Webster et al., 2013), and from trapped gas in shergottite, nakhlite, and chassignite (SNC) meteorites (Carr et al., 1985; Greenwood et al., 2008). All discovered significant enrichment in heavier isotopes relative to terrestrial for carbon, nitrogen, hydrogen, oxygen, and noble gases such as xenon. In the case of the Viking data, as much as twenty times the present CO_2 abundance was suggested as being released over geologic time by the planet (Owen et al., 1977). As there are no known mixing mechanisms between the volatile reservoirs and rocky interior of the planet, such as active plate tectonics (Connerney, 1999; Williams and Nimmo, 2004), these isotope ratios are a function of processes such as the impact of cometary material, atmospheric escape, or photochemical processes. Of these, escape to space alone is capable of selectively fractionating the atmosphere, and accordingly the massive loss of an early atmosphere through escape to space is inferred: as much as 1.0 bar of CO_2 may have been lost over the course of geological history

(Jakosky et al., 2017, 2018). This likely mostly occurred immediately following the loss of the planetary dynamo at around 4.0 Ga (Acuña, 1999).

Estimates for Mars' total inventory of CO_2 and H_2O, based on geochemical data and comparison with other terrestrial planets, indicate an initial total planetary reservoir of between 6-15.0 bars of CO_2 and a global equivalent layer of 150 km of water (Haberle et al., 2017, and references therein). A CO_2-rich early atmosphere of Mars is also indicated by the planet's lively volcanic history: the formation of the volcanic plateau Tharsis is estimated to have released >1.5 bar of CO_2 in its lifetime (Phillips et al., 2001), while at least 4.0 bars are estimated to be sourced from other Noachian-Hesperian sources (Greeley and Schneid, 1991; Phillips et al., 2001; Jakosky, 2019). Outgassing models estimate pressures of the CO_2-dominated Noachian atmosphere ranging from 200 mbar (Manga et al., 2012) or <400 mbar (Cassata et al., 2012), while an upper estimate of 1-2 bars has been indicated by secondary crater statistics (Kite et al., 2014; Warren et al., 2019), with Hu et al. (2015) estimating 1.0 bar according to surface-based $^{13}C/^{12}C$ isotopes. An additional lower pressure limit of >0.5 bar at ~4 Ga was inferred from N and Ar isotopes (Kurokawa et al., 2018). Most recently, data from the Mars Atmosphere and Volatile EvolutioN (MAVEN) mission provided constraints on the order of ~0.5-1.0 bar CO_2 in the Noachian (Jakosky et al., 2017, 2018). The demonstration of several Hesperian- or possibly Amazonian-aged outflow channels (e.g., Rodríguez et al., 2015; Kite et al., 2019) has called for a pressurised surface environment that extended later into the planet's history than expected, with perhaps as much as 600 mbar as late as 3.2 Ga (Bouley et al., 2009). CO_2 may also have been sourced from outgassed CH_4 to add as much as 2.0 bar to the atmosphere over Mars' lifetime (Chassefière and Leblanc, 2011).

Escape processes that are nonthermal in nature (i.e., not related to molecular velocity from thermal energy) were likely only capable of removing between ≳10 mbar (e.g., Barabash et al., 2007; Chassefière and Leblanc, 2011; Chassefière et al., 2013) to ~100 mbar CO_2 over the past 4.1 Gyr (Lammer et al., 2013). Such mechanisms include photochemical escape and sputtering.

This escape rate is low, and thus to account for the loss of any atmosphere capable of supporting above-zero temperatures, another sink for the early atmosphere is required on or within the planetary surface.

1.2. Constraints on atmospheric composition through time

The origin of the Martian atmosphere is intimately linked to the materials from which the planet itself formed, and the Noachian atmospheric composition has been inferred through various means. Beginning with chondritic accretion, the atmosphere must have formed from volatiles extracted from the asteroids and comets delivered during and after the planet formed. The standard model of solar system formation posits that planets formed by condensation and subsequent coalescence of solid dust motes from the solar nebula. However, there is significant depletion of noble gases on Mars compared to solar abundances (Owen et al., 1992), thus a solely nebular origin for the original Martian atmosphere is not likely. To account for this, the primary atmosphere instead may have formed from a process that either extracted volatiles from the accreted chondritic material, or else from volatiles within asteroids and comets that arrived after the planet formed, or a combination.

Given water is the most abundant chondritic volatile, it is likely the first atmosphere of Mars was of steam and was also hydrogen-rich due to photodissociation, which would have been accordingly susceptible to hydrodynamic escape (e.g., Lammer et al., 2013). It has been proposed that the primary atmosphere of Mars would have been totally lost following the colossal impact that has been hypothesised to have formed Mars' north-south dichotomy in crustal thickness (Wilhelms and Squyres, 1984; Andrews-Hanna et al., 2008; Catling and Kasting, 2017) at ~4.4 Ga (Debaille et al., 2007; Watters et al., 2007). A secondary atmosphere based on magmatic outgassing may be estimated from modelled or direct (meteoritic) estimates of mantle oxidation state, and hence the most likely compositions of outgassed products. Such products would have been highly

effective greenhouse gases whether oxidising (CO_2, H_2O, SO_2; Beaty et al., 2005) or reducing (CO, H_2, H_2S, CH_4; Wadhwa, 2008).

Carbon dioxide is widely considered to have been the main Noachian atmospheric constituent once these earlier, transient atmospheres stabilised (e.g., Pollack et al., 1987). This is assumed for several reasons: 1) CO_2 comprises >95 % of today's atmosphere (Mahaffy et al., 2013); 2) expected crustal outgassing behaviour during planetary accretion anticipates its widespread and long-lived release (e.g., Phillips et al., 2001); and 3) Mars has no known tectonic or biological mechanisms for the effective removal of CO_2 to the sub-surface (Ogawa and Manga, 2007). However, were this the case commensurately abundant carbonate minerals would be expected to constitute a significant proportion of the Martian crust (Pollack et al., 1987; Chevrier et al., 2007). Carbonates contain CO_2 incorporated into their crystallographic structure and represent a significant carbon sink on Earth. On Mars, however, where as much as 2 bars of CO_2 has been suggested within its former atmosphere (Kite et al., 2014), carbonates appear to comprise a relatively minor constituent of the surface crust. This paradox remains a major outstanding question in planetary research and forms the focus of this thesis.

2. Carbonate minerals

2.1. Carbonates on Earth

Carbonate minerals comprise a significant portion of the sedimentary rock record on Earth by mass and bear such elements as magnesium (e.g., magnesite, hydromagnesite, nesquehonite), calcium (e.g., calcite, aragonite, dolomite), manganese (e.g., rhodochrosite, ankerite), and iron (e.g., siderite, chukanovite). As well as revealing subtle information about their depositional environment in the deep past, carbonate rocks on Earth sequester significant deposits of carbon within the crust, making them a key controller of the planet's climate and with the ability to critically alter both the oceans and the atmosphere.

The vast majority of marine carbonates on Earth are produced biogenically, particularly calcium-based limestones: calcite and aragonite. A greater volume still (well over 90 %) can be attributed to formation within open bodies of water, both marine and lacustrine. Abiotic formation pathways also exist, a common pathway being the water-mediated direct replacement of rock-forming silicates with carbonates through the drawdown of aqueous CO_2. This process, called carbonation, involves the dissolution of atmospheric CO_2 within water to produce bicarbonate when CO_2-rich water reacts with basaltic materials to release various cations (Fe^{2+}, Mg^{2+}, Ca^{2+}, K^+, and Na^+). This reaction is shown in the equations below with the example of the iron silicate fayalite:

$$CO_{2(aq)} + H_2O \rightarrow HCO_3^- + H^+ \quad \text{(eq. 2.1.1.)}$$

$$Fe_2SiO_4 + 4H^+ \rightarrow 2Fe^{2+} + SiO_2 + 2H_2O \quad \text{(eq. 2.1.2.)}$$

$$Fe^{2+} + HCO_3^- \rightarrow FeCO_3 + H^+ \quad \text{(eq. 2.1.3.)}$$

In this example, the iron carbonate siderite ($FeCO_3$) has been formed with a proton as a biproduct following a two-step process: silicate dissolution (eq. 2.1.2) and carbonate precipitation (eq. 2.1.3; Daval et al., 2009, 2010). The bicarbonate ion deprotonates to release free H^+. This associated acidity further promotes mineral dissolution, driving hydrolysis and the dissolution of silicate minerals to release more Fe^{2+}, SiO_2, and HCO_3^- into solution (e.g., Eby, 2005). Crucially, the release of Fe^{2+} and its ability to react with and therefore consume O_2(aq), renders solutions reducing rather than oxidising, as has commonly been observed on Earth in mafic rocks (Minissale et al., 2000; Arnórsson et al., 2002), and Mars (Hurowitz et al., 2010), even where atmospheric oxygen abundance is around 10^{-5} times less than those currently on Earth (Mahaffy et al., 2013). These conditions, in the presence of dissolved CO_2, promote the formation of $FeCO_3$.

As an example, the Samail Ophiolite in Oman, the largest-known ophiolite sequence, draws down an estimated 4×10^7 kg/yr of CO_2 from the atmosphere (Kelemen and Matter, 2008) by the *in situ* carbonation of peridotite (Kelemen and Matter, 2008; Mervine et al., 2014). Other abiotic carbonate formation mechanisms include hydrothermalism: modern-day hydrothermal carbonate deposits in Iceland range from ~1-30 vol. % of its altered rock (Lonker et al., 1993), while in Archaean-aged Australian sediments, metasomatism under CO_2-bearing fluids resulted in their total carbonation (Donaldson, 1981). Carbonate precipitation within alkaline, low-temperature brines is also well-documented (e.g., Renaut, 1990; McCarthy et al., 1991), as well as at high temperatures and pressures (Druckenmiller and Maroto-Valer, 2005).

To summarise, these carbonate-forming environments are all linked by requiring aqueous conditions, high pH, and the presence of CO_2, forming under a wide range of temperatures. Across a range of pH, the varying ionic components of the carbonate system (HCO_3^-, CO_3^{2-}, CO_2) varies to produce differing dominant species, and this system is well-represented by the famous Bjerrum plot (Figure 3), devised by Bjerrum (1914). This plot is a good representation of the carbonate system in relation to pH, and forms an important means for exploring the interdependencies of the carbonate system on pH.

Another good means of representing two major components of the carbonate system — total dissolved inorganic carbon (DIC) and total alkalinity (TA) — is a diagram representing variation across the two during the occurrence of different processes within water, which is shown in Figure 4. Shown in Figure 5 is how these two parameters affect the omega of a mineral, in this case the iron carbonates siderite and amorphous Fe-carbonate (AFC). The *omega* of a mineral is its saturation state, where above 1 determines that a mineral is more likely to precipitate, and under 1 more likely to dissolve or remain in solution. It is expressed as:

$$\Omega = log\left(\frac{IAP}{K_{sp}}\right)$$

(eq. 2.1.4)

Where *IAP* is the ionic activity product, and K_{sp} is the solubility product.

Adding together the components of CO_2 in its various dissolved ionic states (HCO_3^-, CO_3^{2-}, CO_2) produces the measure of total dissolved inorganic carbon (DIC), which, when tracked alongside changes in the total alkalinity of a system, is a useful alternate means of estimating which conditions produce elevated supersaturation states for Fe(II)-carbonates. While many definitions exist, total alkalinity is perhaps best defined by Dickson (1981) as being the number of moles of hydrogen ion equivalent to the excess of proton acceptors (i.e. bases formed from weak acids with a dissociation constant of $K \leq 10^{-4.5}$ at 25 ºC and zero ionic strength) over proton donors (acids with $K > 10^{-4.5}$) per kilogram of solution. This is otherwise written as:

$$total\ alkalinity = [HCO_3^-] + 2[CO_3^{2-}] + [B(OH)_4^-] + [OH^-] - [H^+]$$

(eq. 2.1.5.)

TA is an important factor controlling carbonate precipitation because it is one of six (the others being CO_2, HCO_3^-, CO_3^{2-}, H^+, and DIC) that, when combined with the value of any of the other six factors, may be used to calculate all other variables (Deffeyes, 1965; Park, 1969; Zeebe and Wolf-Gladrow, 2001). Together with pH, DIC may be calculated by the following equations:

$$s = \frac{\left(TA - \frac{K_B\ B_T}{K_B\ + h} - \frac{K_W}{h} + h\right)}{\left(\frac{K_1}{h} + 2\frac{K_1\ K_2}{h^2}\right)}$$

(eq. 2.1.6.)

Where s is CO_2, K_1 is the first dissociation constant of carbonic acid given as $10^{-6.23}$ mol kg^{-1} (He and Morse, 1993), K_2 is the second dissociation constant of carbonic acid given as $10^{-10.12}$ mol kg^{-1} (He and Morse, 1993), h is 10^{-pH} divided by the ion activity coefficient for H^+ (0.8180 as calculated through the B-dot equation; Jiang and Tosca, 2019), and components with B refer to the boron content that is sometimes used in calculating the carbonate system. K_B is the Boltzmann constant (1.38×10^{-23} J K^{-1}), B_T is total boron content, and K_W is the ion product of water (mol^2 kg^{-2}). Inputting s into the following equation gives DIC:

$$DIC = s\left(1 + \frac{K_1}{h} + \frac{K_1\ K_2}{h^2}\right)$$

(eq. 2.1.7.)

In this sense, pH and TA together enable the carbonate system to be expanded to calculate the other variables in the system. This calculation of DIC can now be used to produce a diagram contrasting the evolution of TA against DIC, which together may be used to estimate the saturation state of a carbonate. In addition to this, to derive a saturation state relative to carbonates, a fixed cation concentration (e.g., Ca^{2+} or Fe^{2+}) is assumed.

Figure 4, adapted from Wetzel and Likens (1991) with principles discussed at length in Zeebe and Wolf-Gladrow (2001), illustrates how changes in different processes, such as photosynthesis, respiration, CO_2 uptake, or CO_2 release, affect the ability of carbonates to precipitate or dissolve. This diagram describes the dependency of carbonate formation upon subtle environmental conditions pertaining to available carbon and total alkalinity, alongside other factors including pH and the availability of the ions HCO_3^- and CO_3^{2-}. This is a co-dependency that becomes vital over the course of this thesis and is much discussed.

On Mars, environments where aqueous conditions, high pH, and CO_2 coincide are likely to have prevailed at some point in space and time upon its surface. Processes such as impact

gardening (widespread crustal disturbance through frequent meteor impact), volcanic activity, groundwater flow, and weathering are means by which CO_2-charged fluids may interact with host rocks, potentially producing carbonates that may be studied to understand past environmental conditions. Ancient carbonates on Mars are also a target for future lander investigations and eventual Mars sample return both for their isotopic composition, which could record atmospheric loss on Mars (e.g., Hu et al., 2015) and because carbonate precipitation in aqueous environments is an effective mechanism for biosignature preservation (e.g., Farmer and Des Marais, 1999).

Next discussed are the pathways for carbonate formation on Mars and the known environments that produced them.

2.2. Carbonates on Mars

Carbonates were also known to exist upon Mars by their presence within meteorites discovered on Earth. Bogard and Johnson (1983) were the first to confirm that the Shergottite, Nakhlite, and Chassignite (SNC) meteorite clan originated from Mars, after significant speculation (Stolper and McSween, 1979; Shih et al., 1982; Clayton and Mayeda, 1983). Carbonates were first identified within shergottites (Gooding et al., 1988) and later in others such as ALH 84001 (Mittlefehldt, 1994; Harvey and McSween, 1996; Figure 6), and nakhlites including Lafayette, Nakhla, and Governador Valadares (Treiman et al., 1993; Bridges, 2000; Bridges et al., 2001). ALH 84001 has been a particular focus within Martian meteoritics owing to its incredible age (4.50 ± 0.13 Ga; Nyquist et al., 1995), which unlike other Martian meteorites preserves the most ancient known crust on Mars, offering an insight into Mars as it existed 3 Gyr earlier than almost all other known Martian meteorites. In contrast, the nakhlite group are far younger in age at 1.3 Ga (Shih et al., 1999; Nyquist et al., 2001). The carbonates within these meteorites are mostly siderite within veins most likely produced by hydrothermal fluid intrusion (Bridges et al., 2001; Changela and Bridges, 2010; Bridges and Schwenzer, 2012; Hicks et al., 2014) and/or through *in situ* carbonation (Tomkinson et al., 2013). They are younger than their host rock, aged ≤670 Ma (Shih et al., 1999;

Swindle et al., 2000), and are of interest for the reverse reason to the carbonates of ALH 84001: those within the nakhlites may represent the youngest, not oldest, carbonate-producing activity on Mars.

Unlike Earth, where the upper continental crust is mostly felsic rocks containing minerals including quartz, K-feldspar, plagioclase, and micas (Taylor and McLennan, 1985), the Martian crust is more mafic, and is dominated by minerals including plagioclase, pyroxene, olivine, and Fe-oxides (Taylor and McLennan, 2009; Ehlmann and Edwards, 2014; McLennan et al., 2019). Accordingly, on Earth carbonates are dominated by Ca-rich phases from cations released by chemical weathering from this initial felsic mineralogy, whereas by the same process Martian carbonates are composed of more basic cations owing to the planet's differing geology. From its basaltic rocks a variety of cations are released into solution that may affect fluid chemistry, including Fe^{2+}, Mg^{2+}, Mn^{2+}, and Ca^{2+} (Milliken et al., 2009). The differing modes of carbonate formation also influence their record in the geologic setting: most notably, the absence of known biologic drivers and/or ocean environments reduces the percentage of Ca-based carbonates on Mars. While carbonates on Earth in the Precambrian period were prolific, and form a common mineralogy for this period prior to the evolution of $CaCO_3$ skeletons, the dominance of $CaCO_3$ in the Earth's oceans is also a function of the oceans acting as a sink for sediments of a more felsic nature than those on Mars, owing to more felsic primary mineralogy (e.g., Taylor and McLennan, 1985; Ehlmann and Edwards, 2014). Reacting with carbonate ions present in Earth's seawater, this Ca^{2+} is able to form carbonates *via* a means not confirmed to have ever operated on Mars, whereby the presence of a Noachian-aged ocean remains highly debated (e.g., (Clifford and Parker, 2001; Ivanov and Head, 2001; Carr and Head, 2003, 2015, 2019). A more critical explanation for the relative abundance of Ca^{2+} for carbonate formation on Earth compared to Mars is that the presence of O_2 on Earth sequesters Fe^{2+} out of seawater prior to its ability to precipitate. Fe^{2+} under seawater quickly forms either reduced clays such as Fe-saponite or green rust when anoxic,

or oxides and oxyhydroxides such as hematite when oxic (Harder, 1978; Rasmussen et al., 2014; Jiang and Tosca, 2019).

While carbonates on Mars itself were first identified in wind-blown dust using the Thermal Emission Spectrometer aboard the Mars Global Surveyor satellite (2-5 wt. %; Bandfield et al., 2003), the first confirmed identification of carbonates as rocks within regional-scale outcrops was in 2008 with CRISM (Ehlmann et al., 2008) as seen in Figure 7. Their presence had long been predicted from chemical modelling and experiments (Booth and Kieffer, 1978; Gooding, 1978; Catling, 1999; Orofino et al., 2000), inferred from ground- or Earth orbit-based telescopes (Warren, 1987; McKay and Nedell, 1988; Blaney and McCord, 1989; Pollack et al., 1990; Lellouch et al., 2000) or Mars-orbiting early spectrometers (Calvin et al., 1994). Pollack et al. (1987) predicted abundant surface carbonates as an indicator of a formerly dense CO_2 atmosphere, whereby rapid removal of CO_2 to the subsurface by carbonate formation, and its subsequent liberation by thermal decomposition, enabled the recycling of up to a 5.0 bar CO_2 atmosphere.

Since this first observation, carbonates have been identified in many locations across the planet (Figure 8). They were found *in situ* at 3-5 wt. % in polar soils by the *Phoenix* lander (Boynton et al., 2009) and at 1-2 wt. % in Gale Crater soils by the Mars Science Laboratory (MSL) *Curiosity* rover (Archer et al., 2014; Leshin et al., 2013), although <1 wt. % in the Yellowknife Bay (Gale Crater) rocks themselves (Ming et al., 2014). The only significantly carbonate-rich rocks that have been explored *in situ* are the Mg-Fe carbonates (16-34 wt. %) within the Comanche region in the Columbia Hills of Gusev crater (Morris et al. 2010; Figure 9), as seen by the Mars Exploration Rover (MER) *Spirit* during its traverse throughout the years 2004 to 2010.

From orbit, carbonate exposures tend to be found in the most ancient terrain on Mars from exhumed deep-crustal rocks. These often coincide with the walls and uplifted central peaks of craters such as Leighton (Michalski and Niles, 2010), McLaughlin (Michalski et al., 2013, 2019; see Figure 7 (c, d)), Stokes (Turner et al., 2016; Wray et al., 2016), and Robert Sharp near Gale (Carter et al., 2015), and in regions including Terra Tyrrhena (Carrozzo et al., 2017), Eridania

(Michalski et al., 2017), Capri Chasma to the eastern end of Valles Marineris (Viviano-Beck et al., 2014; Jain and Chauhan, 2015), and around Huygens Crater, Noachis Terra, and north of the Arygre Basin (Wray et al., 2016). The largest regional exposure by far is in the Nili Fossae region to the western rim of the Isidis Basin (Ehlmann et al., 2008, 2009; Brown et al., 2010; Gaudin et al., 2011; Bishop et al., 2013; Ehlmann and Edwards, 2014, 2014), where around ~20 wt. % Fe-Mg carbonates are found over 6800 km^2 of an olivine-rich outcrop. This outcrop includes Jezero Crater (Goudge et al., 2015b, 2017; Horgan et al., 2020), set to be the landing site for NASA's *Perseverance* rover in February 2021 (see Figure 8 for location). These carbonates probably sequestered 0.25-12 mbar CO_2 from the Noachian atmosphere during their formation, but this deposit is insufficient to account for the volume of carbonates predicted for atmospheric CO_2 levels above 500 mbar (Edwards and Ehlmann, 2015), which would require more than 35 Nili Fossae-sized deposits.

2.3. How did the Martian carbonates form?

Two problems exist with understanding how carbonates on Mars formed: (1) extremely detailed analyses of the carbonates exists in the form of meteorites — but these by definition exist without environmental context; and (2) conversely, with carbonates identified *in situ* on the Martian surface there is context to the mineralogy, but a lack of high-precision mineralogic analysis in the absence of laboratory techniques and instruments with which to study them.

For the meteorite-borne carbonates, while differing meteorites represent different environments, there is a common thread between those identified within the nakhlites as forming under hydrothermal temperatures, likely from interactions between volcanically- or impact-heated crustal fluids and host igneous rocks (Bridges et al., 2001). These igneous minerals were mildly-shocked during an impact event, which generated fractures through which heated fluids — liberated from H_2O-CO_2 ground ice — percolated through the top hundred metres of the crust (Bridges et al., 2001; Changela and Bridges, 2010). Carbonates, mostly siderite, were then formed

within an estimated temperature range 150-200 °C, at moderately alkaline pH (6-8), and moderate rock:water ratio conditions (<1:300; Bridges and Schwenzer, 2012). Other researchers have suggested such assemblages formed through *in situ* carbonation (Lee et al., 2015) or low-temperature evaporation (Bridges and Grady, 2000), which has been modelled as a plausible carbonate-forming mechanism for Mars (Marion et al., 2003). Bridges et al. (2019) continue to advocate this hydrothermal mechanism based on the agreement between modelled fluids in Bridges and Schwenzer (2012) and the observed mineralogy of Changela and Bridges (2010).

Meteorite ALH 84001 bears striking chemically zoned carbonates as rosettes, along fractures, and in interstitial zones (e.g., Mittlefehldt, 1994; Treiman, 1995; Harvey and McSween, 1996; McKay et al., 1996; Steele et al., 2007), but it experienced several extreme shock events (Treiman, 1995) that distort the legibility of its carbonate-forming process(es). Its carbonates likely formed ~3.9 Ga (Borg, 1999; Lapen et al., 2010) in a shallow subsurface water body (metres to tens of metres deep) at mild temperatures (Romanek et al., 1994) of 18 ± 4 °C (Halevy et al., 2011).

Of the two carbonate-bearing outcrops analysed *in situ* on the surface of Mars, one was within polar latitudes — the Phoenix lander — the other equatorial — the *Spirit* rover. For the Ca- and possibly Mg-Fe-carbonate-bearing soils analysed by *Phoenix* (Boynton et al., 2009), atmospheric CO_2 may have diffused into the uppermost layer of the basaltic regolith to interact with liquid water films on particle surfaces and precipitate as an icy cement. Nearby formations could also be due to impact-induced melting and excavation of CO_2-bearing ices (Boynton et al., 2009; Heet et al., 2009) as recently as the Amazonian (Turner et al., 2016). Sources of liquid water could even occur at temperatures of −68 °C with the presence of perchlorates, which significantly lower the eutectic point of near-surface brines (Hecht et al., 2009; Ojha et al., 2015). Alternatively, the carbonates could have arrived as windblown dust from the depositions of the Vastitas Borealis and Scandia formations (Niles et al., 2013).

The most carbonate-rich rocks explored *in situ* on Mars were the Comanche outcrops on the Haskin Ridge within the Columbia Hills of Gusev Crater, at up to 34 wt. % carbonate (62 % magnesite, 25 % siderite, 11 % calcite, and 2 % rhodochrosite; Morris et al., 2010). This composition is very similar to the carbonates of meteorite ALH 84001 (Mittlefehldt, 1994; Treiman, 1995). The Columbia Hills are an island of older rocks surrounded by Hesperian-aged, olivine-rich volcanics, which is a similar setting to the Nili Fossae carbonates and those of McLaughlin Crater. Accordingly, their carbonate formation pathways may be similar. The precipitation of C-, Mg-, and Fe-rich aqueous solutions under moderate temperatures (~150 °C) at near-neutral pH (~6-7) is known to produce carbonates in the quantities observed by *Spirit* (e.g., Steele et al., 2007; Treiman et al., 2002). The distance between the Columbia Hills and Nili Fossae carbonates, yet within a similar age range, suggests that such conditions may have been prevalent throughout the Noachian.

A shallow ephemeral lake or aquifer origin for the Comanche carbonates has also been considered (Ruff et al., 2014), which is an alternative hypothesis for the origins of carbonate globules in meteorite ALH 840001 (McSween and Harvey, 1998; Warren, 1998; Halevy et al., 2011). Ruff et al. (2014) argue that the components of the Comanche carbonates are better considered separate quantities of magnesite and siderite, rather than a single solid-solution mix. This compositional zoning could have formed in low-temperature brines produced from leaching of host volcanic rocks, which then infiltrated the Comanche outcrop and deposited the carbonates by evaporative precipitation. This agrees with modelling by van Berk et al. (2012) and van Berk and Fu (2011), whereby the use of a higher equilibration temperature (75 ºC) resulted in the formation of Ca-dominated Ca-Mg carbonate as opposed to Mg-rich Mg-Fe-Ca carbonate. The model at high temperature also displayed an inverse stratification with phyllosilicate-rich units that are commonly found overlying carbonate-rich units. This modelling work suggests temperatures as low as 5 °C may have been required for the Comanche carbonates' formation. Carbonates

occurring as aeolian deposits (Pollack et al., 1990; Bandfield et al., 2003), were perhaps extracted from such outcrops as the Comanche, and then windblown as dust.

Orbitally identified carbonates are more difficult to attribute a formation mechanism to. The Nili Fossae carbonates within the vicinity of Jezero Crater (see Figure 8), which form the only visible regional carbonate unit on Mars (Niles et al., 2013) may have formed in a variety of ways. Mg-rich carbonates associated with deltaic and lacustrine deposits in Jezero Crater may have formed through low-temperature hydrothermalism in impact-warmed lake-waters (Goudge et al., 2017; Horgan et al., 2020). Alternatively, widespread outcrops of siderite, dolomite, and magnesite (Brown et al., 2010) across Noachian-aged terrain in Nili Fossae interlaced with olivine suggest the direct replacement of olivine via *in situ* carbonation (Edwards and Ehlmann, 2015) or the intrusion of volcanically-heated fluids (Ehlmann et al., 2008; 2009; Brown et al., 2010). McLaughlin Crater (see Figure 8 for reference), which straddles the north-south dichotomy boundary, is similarly olivine-rich, but its layered carbonates have been attributed as forming from the upwelling of neutral-to-alkaline groundwater in a deep lake (Michalski et al., 2013, 2019). However, Gale Crater was also groundwater-fed (Grotzinger et al., 2014; Hurowitz et al., 2017), as indicated by two distinct mudstone strata representing oxidising versus reducing environments. This distinction appears to be a partial function of enhanced groundwater input to deeper zones of the Gale Crater lacustrine system (Hurowitz et al., 2017). Gale Crater, unlike the likewise-groundwater-fed McLaughlin Crater, does not contain appreciable carbonate deposits. The absence of carbonates in Gale, yet like McLaughlin an abundance of evidence in favour of groundwater influx, suggests that some alternative mechanism to groundwater ponding formed deposits such as those within McLaughlin. This is a mechanism that differentiates these two large, deep, groundwater-influenced, and otherwise similar crater-lakes. An alternative explanation for the carbonates at McLaughlin could be the *in situ* carbonation of olivine-rich bedrock: the mineralogy at McLaughlin is remarkably similar to that described in Nili Fossae by Edwards and Ehlmann (2015), which for both sites is unusually olivine- and serpentinite-rich, highly fractured, and rich in Fe-Mg

carbonates. Michalski and Niles (2010) note that interaction with ultramafic crust, particularly where olivine-rich, should neutralise aqueous fluids and accordingly prevent acidic weathering and the inhibition/dissolution of carbonates; this was substantiated by the modelling of van Berk et al. (2012), whose reconstruction of the fluids that formed the Comanche carbonates at Columbia Hills required an ultramafic host rock. A correlation between olivine- and carbonate-rich areas was also noted in the comprehensive survey of Wray et al. (2016).

Deposits across the planet in crater central peaks may have been uplifted from depth (Michalski and Niles, 2010; Bultel et al., 2015; Wray et al., 2016), although others represent post-impact hydrothermal system alteration (e.g., Turner et al., 2016; Carrozzo et al., 2017). These are especially interesting because they may represent a buried, massive carbonate layer Noachian in age. Figure 10 summarises these various means of forming carbonates on Mars into three categories: 1) low-temperature brines; 2) high-temperature hydrothermalism; and 3) *in situ* carbonation.

Despite these outcrops and meteorite observations, the question remains: if Mars is expected to have possessed a substantial CO_2-rich atmosphere in its past, why are carbonates not more abundant across its surface? In the 1980s vast fields of carbonates were predicted across the Martian surface (Toon et al., 1980; Kahn, 1985; Pollack et al., 1987; Warren, 1987), and several explanations have been proposed for their widespread absence. These include:

(1) their formation deep below the surface via circulating fluids (e.g., Ehlmann et al., 2008);

(2) formation increasingly removed from the surface with the downward migration of Hesperian aquifers (Griffith and Shock, 1995; Chassefière and Leblanc, 2011);

(3) formation and subsequent burial beneath younger rocks or dust (Glotch and Rogers, 2013);

(4) preferential preservation in acid-neutralising olivine-rich regions (Michalski and Niles, 2010);

(5) formation followed by weathering *via* subsequent acidic conditions (Bibring et al., 2006; Chevrier et al., 2007);

(6) formation of a sulphate coating, as observed in analogue experiments, obscuring the spectral signature of carbonates (Singer et al., 1979; Cloutis et al., 2010) or replacing them altogether; and

(7) inability of carbonates to form at levels detectable by remote sensing (Orofino et al., 2000).

Other suggestions include that carbonates never formed at all, whether:

(1) less kinetically favoured than oxide- and silicate-bearing clays (Ehlmann et al., 2012; Michalski et al., 2015);

(2) precluded by a sulphate- and iron-enriched acidic ocean (Fairén et al., 2004; Bullock and Moore, 2007)

(3) precluded by aquifer waters (Peretyazhko et al., 2018);

(4) precluded by insufficient levels of CO_2 (e.g., Chevrier et al., 2007) following earlier or more vigorous loss of CO_2 to space than anticipated (e.g., Christensen et al., 2001).

Recently, a thermodynamic argument was made by Bristow et al. (2017) that siderite ought to have formed in abundance, and that its absence within sedimentary rocks reflected low Noachian pCO_2. At such low pCO_2 levels (~70 mbar), they argued the young Mars would be unable to support liquid water at all and that the lake in Gale Crater formed by some undetermined mechanism under freezing conditions, perhaps by being perennially frozen.

Flaws with these hypotheses, however, have been identified: dissolution of carbonates by acids would only recycle the released CO_2 back into the atmosphere, creating a circular problem (Edwards and Ehlmann, 2015); evidence for an ocean is highly speculative (e.g., Carr and Head, 2015); escape to space rates would have to be orders of magnitude more substantial than their present estimates (Lammer et al., 2013); and the Bristow et al. (2017) study was modelled on the basis that siderite precipitates when its saturation state exceeds $\Omega = 1$, which, as a variety of experimental and analytical studies have shown, is not likely a realistic representation of $FeCO_3$

precipitation (Tosca et al., 2018). Other arguments that call for the dissolution or preclusion of carbonates by acidic conditions fail to address other pH-sensitive mineralogy that has been preserved (including localised carbonate outcrops), and how carbonate formation is unlikely to be suppressed by this mechanism everywhere at all times given the highly mafic mineralogy of the Martian crust, whereby the pH of circulating fluids within this medium are buffered through time to more basic conditions. It has also been noted (Edwards and Ehlmann, 2015) that sulphate mineralogy indicative of acidic conditions is not ubiquitous across Mars, thus that acidic conditions were in fact localised. Lastly, the hypothesis of an extremely low pCO_2 atmosphere altogether disagrees strongly with both widespread mineralogy of abundant water-rich clays (e.g., Bibring et al., 2006; Mustard et al., 2005; Murchie et al., 2009), geomorphology of long-lived rivers and lakes, and climate modelling that repeatedly necessitates the presence of carbon dioxide as the dominant component (Wordsworth et al., 2017; Ramirez et al., 2020). Additionally, the model of Bristow et al. (2017) relies on the assumption that levels of magnetite in Gale Crater place a lower limit on the amount of Fe^{2+} available to also produce siderite. However, Tosca et al. (2018) describe this magnetite as forming authigenically within CO_2-poor, neutral to alkaline waters produced at the interface between lake bottom waters and groundwater-infiltrated pore waters. These waters are thought to have been out of contact with the atmosphere, as determined by the highly reducing conditions required for magnetite authigenesis and the fact that this mineral was identified as forming within sediments syn- to post-depositionally. The argument by Bristow et al. (2017) for magnetite as a competing sink for Fe^{2+} at the time of Gale Crater's lake may require amendment to reflect this information.

The problem of reconciling a low-pressure atmosphere with Mars' water-carved features has been countered by hypotheses that do not invoke the presence of a long-lived or substantial atmosphere at all. Of these hypotheses, one that has gained traction over the past decade is the 'icy highlands' hypothesis (Fastook and Head, 2015; Wordsworth et al., 2015, 2017) whereby a massive ice sheet covered the southern highlands. Where this ice sheet reached sufficient thickness,

pressure-melting at the land-ice interface enabled sub-glacial channels, and these, according to the hypothesis, account for the vast highlands-based valley networks of Noachian age without requiring a sustained substantial atmosphere (<600 mbar; Palumbo and Head, 2019).

A separate hypothesis, which does not require a long-lived atmosphere and is sometimes viewed as a trigger for the icy highlands model above, invokes transient steam atmospheres (Segura et al., 2008, 2002, 2012) generated by impact events. In this scenario, the vaporised rock and water stirred high into the atmosphere, while short-lived, is sufficient to produce rainfall enough to account for the formation of the valley networks and to create other water-borne features such as mineralogy and crater-hosted lacustrine systems. Both of these hypotheses remain contentious, however: a purely transient steam atmosphere as the origin of the valley networks is not compelling given the discrepancy between estimated erosion rates (e.g., Hoke et al., 2011) and the amount of rainfall produced post-impact (Wordsworth et al., 2017). In the case of the icy highlands hypothesis, such erosion rates amongst other factors imply warmer, wetter conditions were at play, suggesting other models besides that of the icy highlands are useful to consider.

To thus summarise, there is at the time of writing no published, satisfactory explanation for the lack of widespread carbonates on Mars, nor how this issue relates to the ability of the atmospheric composition to be recorded as an archive within sedimentary rocks.

One explanation for the relative scarcity of carbonates, however, appears to gain further strength with the increasing inventory of high-resolution observations, namely that an increasing amount of carbonates have been observed within the most ancient terrain on Mars (Wray et al., 2016; Michalski et al., 2017), and exposed within uplifted crater central peaks (Michalski and Niles, 2010; Bultel et al., 2015). The carbonates in such central peaks as Leighton Crater's, which may have been uplifted by as much as 6 km (Michalski and Niles, 2010; see Figure 8 for location) strongly resemble the mineralogy predicted to form by deep circulating fluids as modelled by Griffith and Shock (1995) and Catling (1999). This includes siderite as well as non-carbonate-bearing aqueous minerals identified in peaks elsewhere (e.g., Bibring et al., 2006; Mustard et al.,

2008; Poulet et al., 2008; Murchie et al., 2009; Michalski et al., 2010). In fact, these central peaks on a global scale show the heaviest alteration for craters 50-100 km across, implying that the most intense alteration occurred at depths of >5 km (Michalski and Niles, 2010), and their widespread distribution suggests the conditions for Fe/Ca-carbonate formation were commensurately widespread (Wray et al., 2016). Such mineralogy was very likely present prior to impact and uplift (Michalski and Niles, 2010) given how secondary hydrothermal alteration in terrestrial impact craters typically only comprises a minority of host rock mineralogy (Naumov, 2005; Osinski et al., 2013).

This supports the presence of an aqueous geochemical setting where carbonate minerals could be formed across a widespread subsurface stratum in early Mars' history. With sufficient residence time within a fractured basaltic regolith, migrating fluids become reduced as oxygen species are lost, and buffer aquifers to alkaline pH at moderate temperatures following long transport pathways in the subsurface (Zolotov and Mironenko, 2007; McLennan et al., 2019). Such environments — anoxic, reducing, water-rich, CO_2-bearing, and of alkaline pH — are known and anticipated to enable efficient carbonate formation under Mars-like conditions (e.g., Ehlmann et al., 2008; Tosca et al., 2018). Shallower environments — those better exposed across the surface of Mars — would have been far less likely to produce the hydrothermal temperatures or alkaline pH sufficient to enable its alteration, except locally through magmatism. Dilute brines may have formed in these surface regions, but owing to interaction with a CO_2 and SO_2-rich atmosphere, these waters at the surface would be buffered to mildly acidic conditions (Hurowitz et al., 2017).

Such a continuum of environments — from acidic, oxidising, sulphate-rich surface to alkaline, reducing, clay- and carbonate-rich subsurface — is consistent with observed mineralogy, and could suggest that a vast reservoir of carbonates exists buried on Mars beyond the detection of surface-aimed spectroscopy. However, sequestration of CO_2 in deep basaltic crusts is a poorly understood process even on Earth (e.g., Gysi and Stefánsson, 2012; Gysi, 2017; Kumar et al., 2017) and requires further research. A case was recently advanced through oxygen escape calculations

and hydrogen isotopic ratios that CO_2 loss to space was significantly lower than expected, and that the gas instead remains on Mars as a large, as-yet-undiscovered sink of several equivalent bars of carbon in the form of carbonates, clathrates, or ices (Heard and Kite, 2020). Source-to-sink accounting that considers chondritic accretion and volcanic output against sedimentary basins and other sinks also estimates that carbonates buried 5-10 km below the surface are likely to be the main present-day source of Martian CO_2, holding as much as 1 bar (Jakosky, 2019). Groundwater modelling furthermore implies conditions that would promote the ready formation of subsurface carbonates (Andrews-Hanna et al., 2010; Kite and Melwani Daswani, 2019), while the basaltic chemistry and lack of tectonics or late-stage volcanism (Ogawa and Manga, 2007) removes mechanisms by which these deposits could be later decarbonated. Indeed, if as little as 1 wt. % of rocks in the topmost 10 km of the Martian crust were carbonates, this could sequester ~4.0 bars of CO_2 (Kite and Melwani Daswani, 2019). If a kinetic pathway for carbonate formation could be discovered that is anticipated in the deep Martian subsurface, such a reservoir could be reasonably inferred, and a means through which CO_2 could be effectively drawn down from the subsurface explained.

Conditions emulating such an environment have yet to be accurately reproduced in the laboratory, and the kinetics of carbonate formation under these conditions assessed. The purpose of this thesis is to investigate the gaps in our present understanding of carbonate formation, and in doing so to better understand the early climate and environment of young Mars.

3. An experimental approach to carbonate formation on Mars

The problem of carbonate formation under Mars-like conditions has not been examined from a kinetic perspective. Mars' broadly basaltic crust should generate mafic cations with commensurate proportions to basalt, resulting in carbonates bearing Fe, Mg, and, to a lesser extent, Ca. The formation of Mg-carbonates are kinetically-controlled such that their precipitation at low

temperature (25 °C) is confined to highly alkaline environments that generate metastable hydrous phases such as hydromagnesite and nesquehonite (Walter et al., 1973; Braithwate and Zedef, 1994), rather than its geologically stable form, magnesite, with most Mg-bearing carbonates on Mars expected to have formed at hydrothermal temperatures (Romanek et al., 2009). Given that NASA's Mars 2020 rover *Perseverance* will explore *in situ* carbonates that may be lacustrine (Horgan et al., 2020), this places the issue of Mg-carbonate identification in the realm of understanding localised hydrothermal conditions, rather than those relating to the wider atmosphere and climate. The study of hydrothermal conditions in respect to the formation of carbonates forms one facet of this thesis for this reason, but carbonate formation as a function of more ambient temperature, atmospheric involvement with water-rock interactions could offer a more regional perspective to carbonate formation globally. Low-temperature water-rock systems should more commonly have produced Fe(II)-carbonate, with the most stable representative, siderite, persisting over geological timescales. Accordingly, the problem of low-temperature carbonate formation on early Mars can be re-cast specifically as a problem of siderite formation, yet there is little empirical data to suggest how Fe(II)-carbonates behave under such conditions. Siderite is a common carbonate on Earth, and forms across a broad range of environments both terrestrial (e.g., Nagashima et al., 1973; Kelts and Hsü, 1978; Tucker and Wright, 1990; Riding, 1991; Morse and Arvidson, 2002; Ridgwell and Zeebe, 2005; Schrag et al., 2013) and extra-terrestrial (e.g., Romanek et al., 1994; McKay et al., 1996; Bridges et al., 2019) where O_2 is scarce, e.g., during marine sediment diagenesis, metal corrosion, CO_2 capture, or planetary surfaces without oxygen. Despite this abundance, little is known about its formation pathways. Understanding how Fe(II)-carbonates form under anoxic conditions, which may be readily applied within the context of Mars, is the focus of the work discussed herein.

This thesis consists of six chapters and three appendices. After Chapter 1 (Introduction) is Chapter 2 (Methods), which contains a complete description of all the processes involved in executing this thesis, including the synthesis of fayalite, the set-up of all the experiments, the set-

up of subsequent kinetic modelling, and the theory behind the kinetics that are vital to understanding the chemistry that drove the observed results.

Three results chapters then follow. The first of these is Chapter 3, which is the paper 'Unravelling surface and subsurface carbon sinks within the Martian crust', submitted for consideration by the journal *Earth and Planetary Science Letters*. In this research, the precipitation of Fe(II)-carbonates including siderite and its recently-discovered meta-stable precursor phases chukanovite (Azoulay et al., 2012; Pekov et al., 2007) and amorphous Fe-carbonate (AFC: Sel et al., 2012; Dideriksen et al., 2015; Jiang and Tosca, 2019) are investigated by reacting the iron-rich end member of olivine (fayalite; Fe_2SiO_4) with fluids containing varying levels of dissolved CO_2. Given research encouraging the need for longer-term experiments to permit the achievement of steady-state in low temperature reactions (Druckenmiller and Maroto-Valer, 2005; Dehouck et al., 2014, 2016; Gaudin et al., 2018), the 91 experiments discussed in this section were run for a maximum of 85 days under anoxic conditions within strictly-maintained glove boxes under low pH (2 and 4), whereby reaction rate is enhanced relative to higher pH values. This has been implemented by previous researchers (e.g., Tosca et al., 2004; Wajon et al., 1985; Dehouck et al., 2012). This research into the inorganic synthesis of Fe(II)-carbonates builds from similar work conducted at higher temperatures and pressures (e.g., 33 — 197 °C and 100 — 500 bars: Carothers et al., 1988; 100 °C and 19 bars: Wersin et al., 1989; Qafoku et al., 2012). Singer and Stumm (1970) were the first to precipitate inorganic siderite at <30 °C under 1 bar and low pCO_2 (<10 %). This was built upon by Jimenez-Lopez and Romanek (2004) and Romanek et al. (2009), who determined that precipitation rates for siderite are almost five orders of magnitude slower than for calcite.

In Chapter 4, 'Columbia River Basalt as an analogue for the Martian crust in experimental recreations of surface/near-surface carbonation', the focus is shifted from iron carbonates produced experimentally through simple separated minerals, and instead concerns the reaction of Columbia River Basalt (CRB) powder containing multiple minerals (albite, augite, anorthite, and

diopside). The focus of this chapter is to evaluate the role of host rock composition and mineralogy as a potentially important variable that controls the location and extent of carbonate formation *via* water-rock interaction. The use of CRB more realistically simulates the basalt-dominated crust of Mars: this contains a complex suite of minerals, including elements alongside Fe, SiO_2, and Mg such as Ca, Ti, Na, K, Mn, and Al, and has been used in other Martian analogue studies (e.g., Tosca et al., 2004; Michalski et al., 2006; Thomson et al., 2014) and for Earth (e.g., Stevens and McKinley, 2000). Additionally, previous modelling studies found siderite to be the first and commonest carbonate to precipitate under CO_2-bearing, basalt-based geochemical models, owing to it being the least soluble (Catling, 1999); no published follow-up experiments have sought to recreate such conditions experimentally and observe the results. Arguably, the largest motivation for this study is that there are very few anoxic, water-rock interaction experiments that examine carbonate formation from an initial basaltic substrate. This chapter runs 36 experiments, 28 of which yielded useful data, to observe the effect of reacting CRB to fluids of varying characteristics that simulate both the Martian surface and subsurface, recreating a range of environments including the surface and subsurface.

In Chapter 5, 'Carbonation upon a warm Mars: experimental precipitation of Fe(II)-carbonates at 75 ºC', experiments simulating both the mineral and rock substrates used in Chapters 3 and 4 were employed but at higher temperatures of 75 ºC to simulate the mechanism of hydrothermalism for carbonate formation, which is discussed within the literature as both a rival mechanism for carbonate formation (as opposed to carbonation) or as a means of enhancing the reaction rate (e.g., Peretyazhko et al., 2016). The main motivation behind this chapter is to understand whether carbonates were formed at elevated temperatures on Mars, and what the relevant geochemical pathways and mineralogical products are. Observing how these vary in comparison to the low temperature experiments permits a comparison of the two, and a subsequent study of which pathways — if any — best fit the observed mineralogy on the Martian surface. These questions are relevant to the surface and subsurface of Mars, which was once a

planet cultivated by volcanism (Phillips et al., 2001; Werner, 2009), resurfaced by impact cratering (Melosh, 2011), and with remnant subsurface heat from planetary formation (Parmentier and Zuber, 2007). Recent research suggests that the most carbonate-rich outcrop on Mars, the Nili Fossae region (Ehlmann et al., 2008; Edwards and Ehlmann, 2015), formed under such elevated temperatures. This is a region dominated by Mg-carbonates, which raises the question as to what effect the adjacent volcanism of Syrtis Major had on the Nili mineralogy. Fe/Ca-carbonates have also been identified in association with environments that likely experienced a former heat flux: the mineralogy of craters such as Leighton (Michalski and Niles, 2010), Holden (Wray et al., 2016), and possibly McLaughlin (Michalski et al., 2013) show non-Mg-dominated carbonates that appear to have formed at depths of up to 6 km and been uplifted during excavation. In these scenarios, heat has also played a role in the carbonate-forming process but related to the planetary geotherm, which may have been lower in temperature and longer-lived than the burst of volcanic activity that enabled the Mg-carbonates of the Nili Fossae region. 34 experiments were run for this section of the thesis, 26 of which yielded useful data.

Chapter 6 (Conclusions) concludes this thesis and summarises the results of the three methods chapters, synthesising the individual findings into a wider understanding of the processes that may have formed carbonates in the surface and/or near-surface of Mars in its deep past. This is followed by three appendices: Appendix 1 is a detailed list of all the experiments involved in this thesis, detailing the minutia of each set-up. Appendix 2 is an expanded discussion of the experimental results that were involved in the research of Chapter 3. This section was added because of the length limitations for the journal the paper of Chapter 3 was sent to, and may be used to expand upon the more concise findings outlined in Chapter 3. Appendix 3 follows a series of equations describing the kinetics behind Fe(II)-carbonate formation that become relevant across the three data chapters.

4. Summary

In summary, the goals of this thesis are as follows:

1. To experimentally investigate the formation pathways of siderite under anoxic, aqueous conditions and the presence of CO_2:
    1.1. using fayalite ± forsterite at low (25 °C) temperatures
    1.2. using powdered Columbia River Basalt at low (25 °C) temperatures
    1.3. using various substrates at high (75 °C) temperatures
2. To develop a thermodynamic and kinetic framework that synthesises these experiments within the context of the ancient Martian surface and/or subsurface
3. To understand the factors that control why and where carbonates formed on Mars, and to predict where best to search for undiscovered deposits within the context of the NASA *Perseverance* mission.

By this thesis' conclusion, these aims will have been addressed and the formation pathways of Fe(II)-carbonates on Mars discussed within the context of the experiments described here. These are the first experiments to use atmospherically realistic levels of CO_2 under anoxic conditions, and as such form an important foundation in the study of the warmer, wetter early history of Mars.

5. Figures

Atmospheric gas	Volume (units given)	Reference
CO_2	95.32 %	(Owen et al., 1977)
N_2	1.9 %	(Mahaffy et al., 2013)
Ar	1.6 %	(Owen et al., 1977)
O_2	0.145 %	(Hartogh et al., 2010)
CO	800 ppm	(Smith et al., 2009)
H_2O	15-1500 ppm	(Smith, 2004)
CH_4	0-40 ppb 0.7-7 ppb	(Mumma et al., 2009) (Webster et al., 2015)

Table 1: The relative abundances of gases that constitute the modern-day Martian atmosphere. Note the dominance of carbon dioxide, and the wide range for water vapour, which varies seasonally from an equivalent of 1-2 km^3 of ice (Jakosky and Farmer, 1982). Table after Mahaffy et al. (2013).

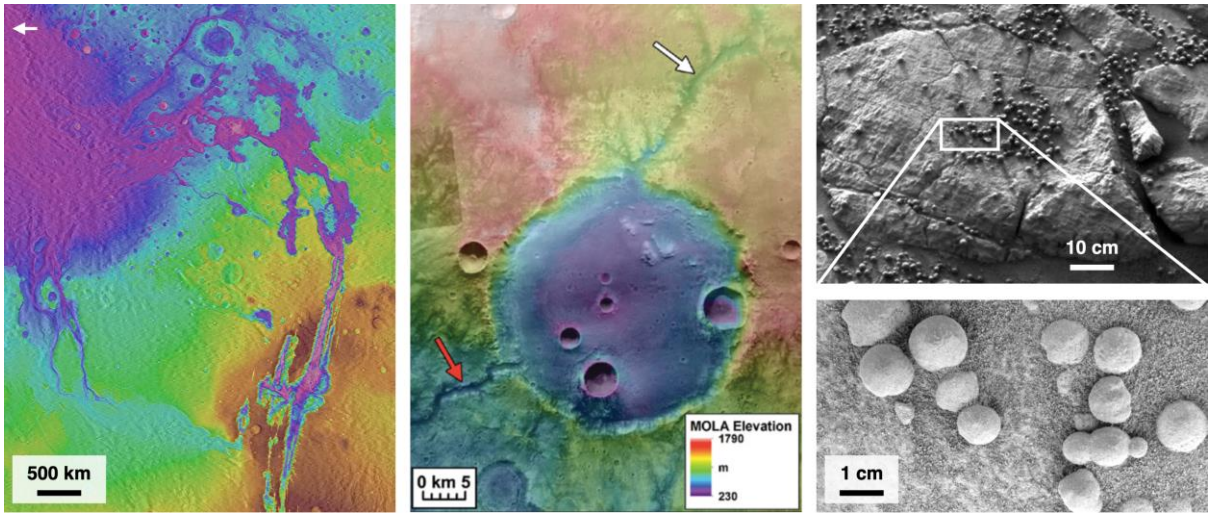


Figure 1: (a) Large-scale evidence of water on Mars: the great Valles Marineris outflow channels. Image by the author, Mars Orbital Laser Altimeter (MOLA) data atop Thermal Emission Imaging System (THEMIS). Arrow points north. (b) Moderate-scale evidence of water on Mars: open crater lakes where water has flowed in one channel (red arrow) and burst the crater wall to flow out (white arrow). Image from Goudge et al. (2016). (c) Fine-scale evidence of water on Mars: the so-called 'blueberries' of Meridiani Planum, spherical hematite concretions formed by the repeated cycling of groundwater. Images adapted from Squyres et al. (2004).

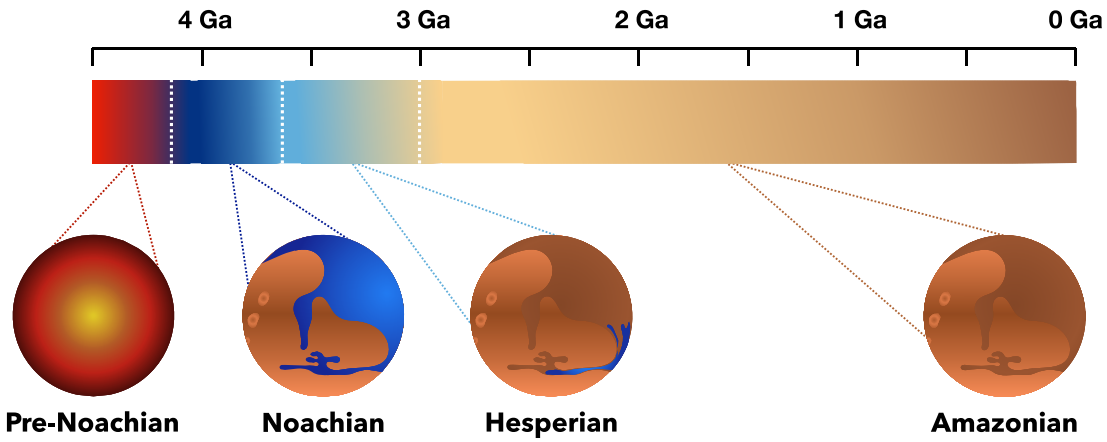


Figure 2: Mars' much-debated geological eras, whereby the boundary between each is frequently cited at varying ages. Dashed lines denote commonly cited literature era boundaries (Hartmann and Neukum, 2001), while the faded edges in colour represent the generally accepted nature of our poor understanding of the exact boundaries. 'Time zero' at 4.4 Ga is considered as occurring only 100 Myr prior the formation of the north-south crustal dichotomy (Debaille et al., 2007), which is considered to have been destructive on a scale comparable to the Moon-forming impact for Earth (Kleine et al., 2005).

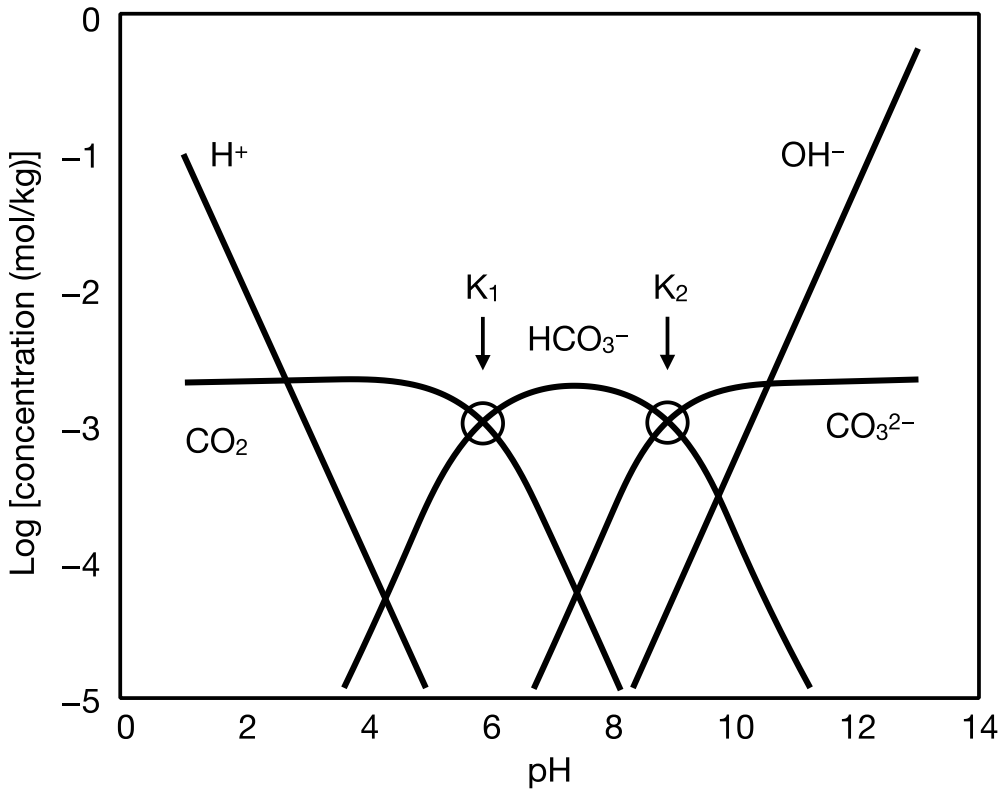


Figure 3: A Bjerrum plot at 25 ºC, adapted from Zeebe and Wolf-Gladrow (2001), which features the varying proportions of H^+, OH^-, and the three dissolved carbonate ions of CO_2, HCO_3^-, and CO_3^{2-} over varying pH. K_1 and K_2 are the points at which CO_2 and HCO_3^-, and HCO_3^- and CO_3^{2-} intersect, respectively.

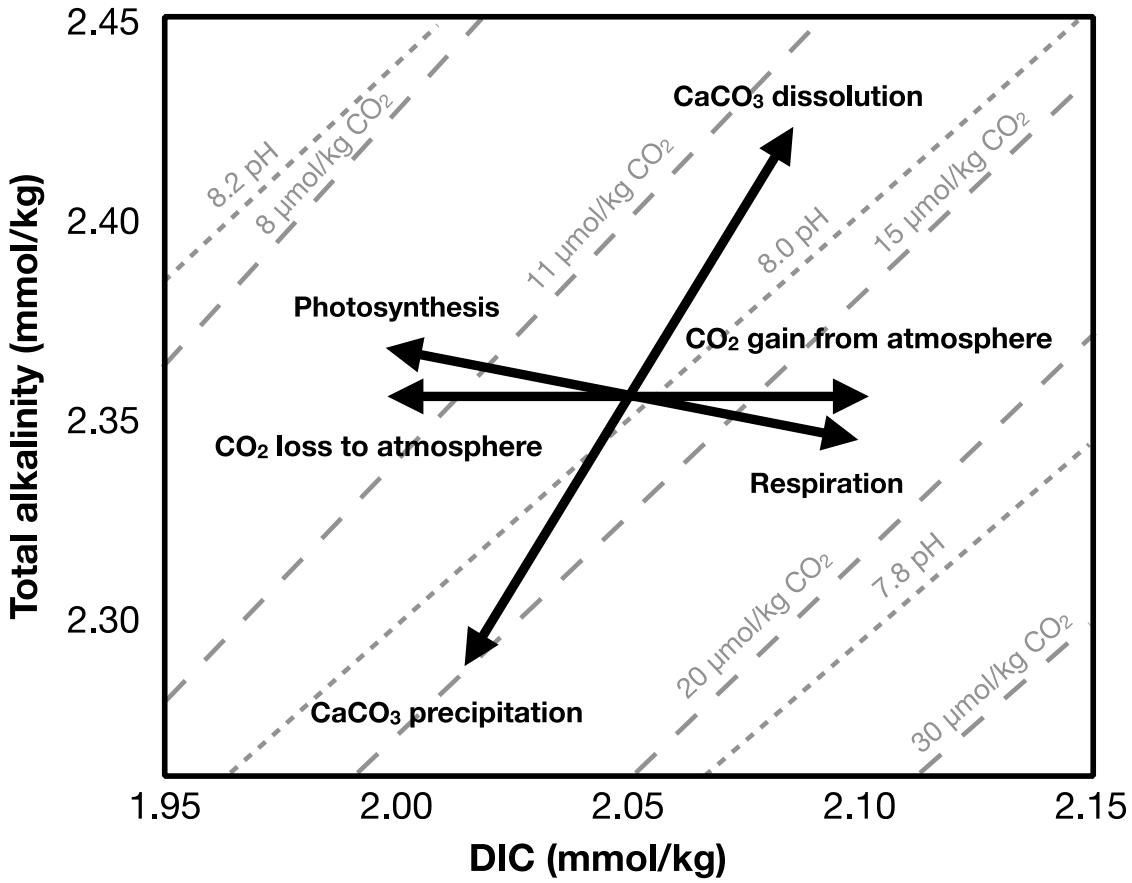


Figure 4: The relationship between DIC and TA variation for a variety of processes occurring within the ocean, with arrows indicating the effects upon the water. Thick-dashed lines indicate levels of constant dissolved CO_2 in µmol/kg, while short-dashed lines indicate constant pH. Adapted from Wetzel and Likens (1991) and Zeebe and Wolf-Gladrow (2001).

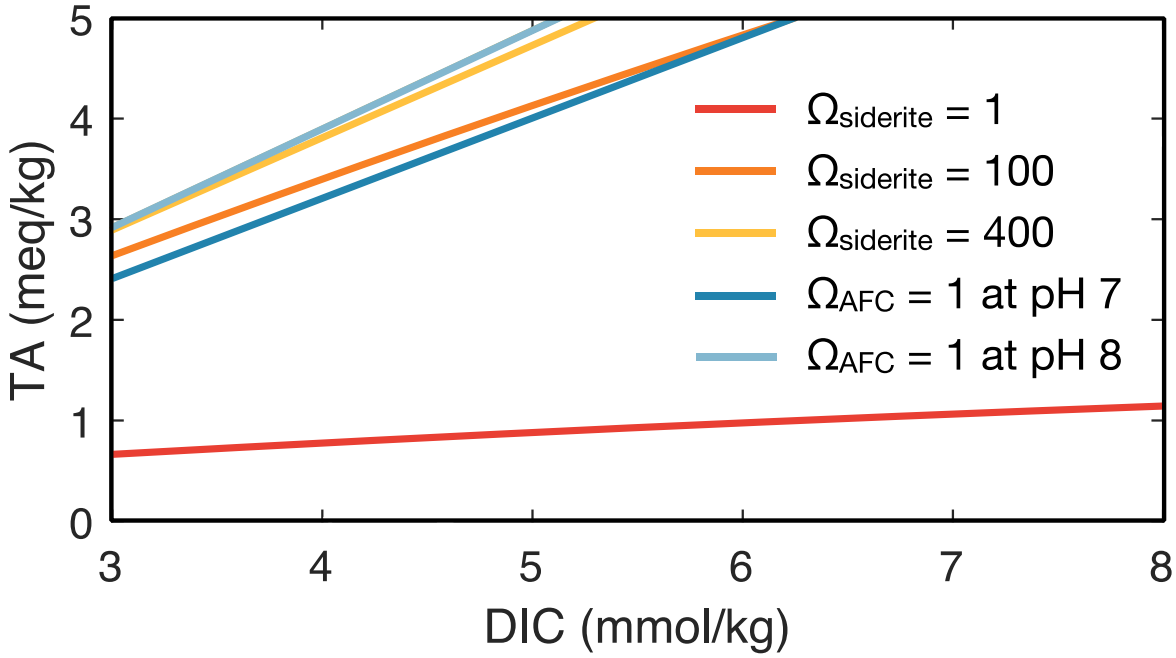


Figure 5: The effect of DIC and TA on the omega of two iron carbonates, siderite and amorphous Fe-carbonate.

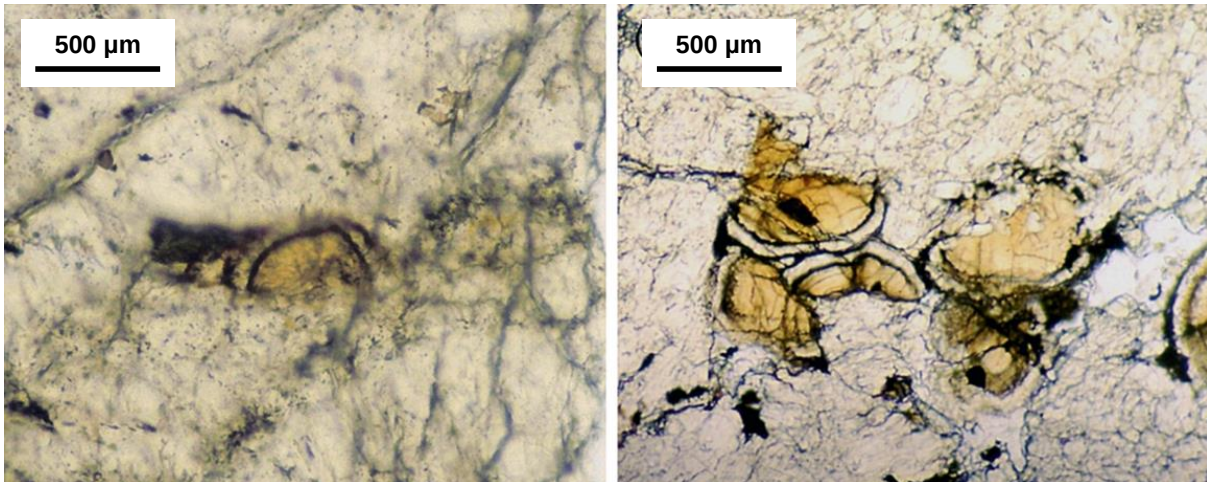


Figure 6: Carbonate globules (orange) in ALH 84001. Discs (left) and hemispheres (right) of the same compositional range with the same internal layering, surrounded by orthopyroxene crystals. Adapted from Treiman (1995).

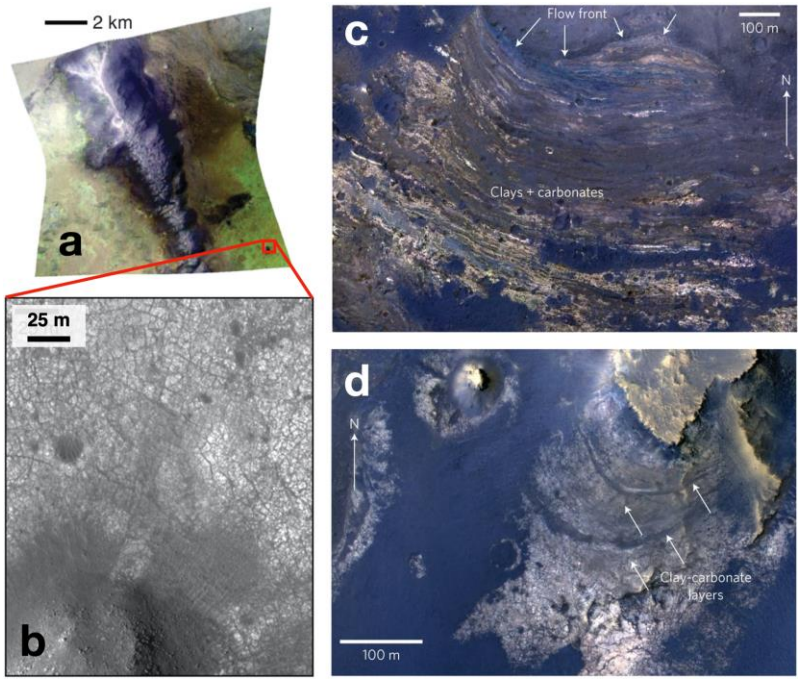


Figure 7: Several textures from orbit that characterise carbonate-bearing outcrops on Mars. (a) The CRISM context image showing mineralogy by colour: carbonate is green, olivine is yellow to brown, phyllosilicate is blue, and the mafic cap unit is purple. Image adapted from Ehlmann et al., 2008. (b) A High-Resolution Image Science Experiment (HiRISE) image of an Mg-carbonate-bearing outcrop in Nili Fossae, which is olivine-rich and highly fractured, overlain by a mafic knob to the bottom of the image. Image adapted from Ehlmann et al., 2008. (c) and (d) Coloured HiRISE image of layered carbonates in McLaughlin Crater, Arabia Terra, on the opposite side of the planet to Nili Fossae. Adapted from Michalski and Niles, 2013.

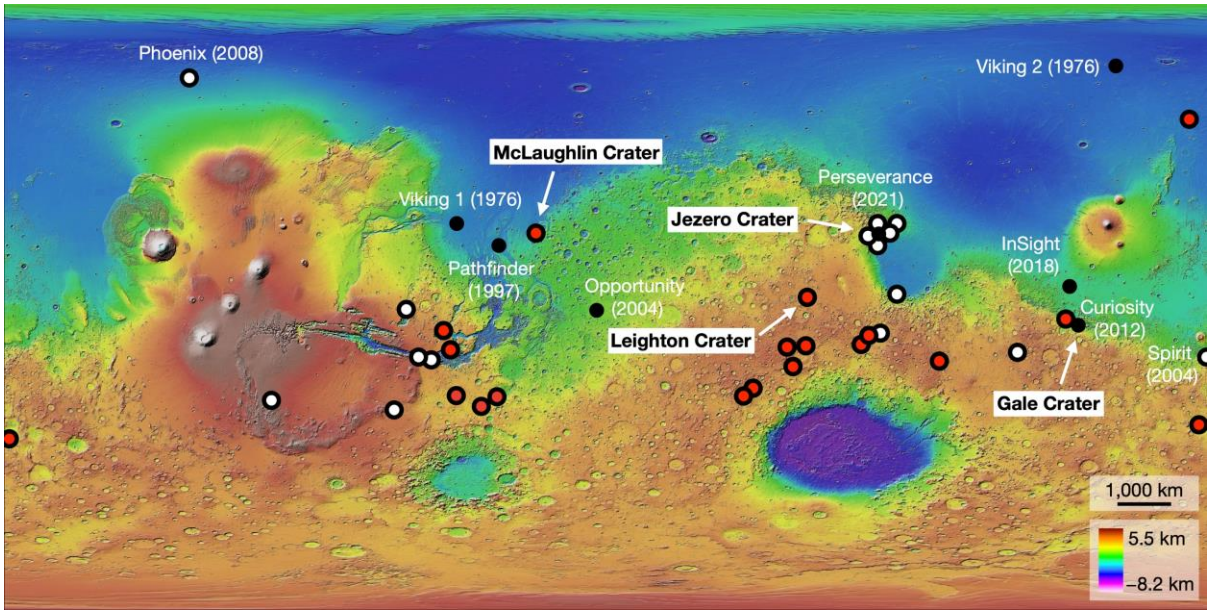


Figure 8: Mars Orbital Laser Altimeter (MOLA) map of Mars produced by the author, whereby colours correspond to topography. North is up. Circles correspond to the known sites bearing carbonates on Mars, including *in situ* from rovers and remotely from orbit-based spectroscopy. In red are Fe-bearing carbonates, while in white are carbonate signatures that do not bear Fe. Data compiled from Ehlmann et al., 2008; Boynton et al., 2009; Morris et al., 2010; Michalski and Niles, 2010; Carrozzo et al., 2013; Michalski et al., 2013; 2017; 2019; Gilmore et al., 2014; Carter et al., 2015; Edwards and Ehlmann, 2015; Jain and Chauhan, 2015; Wray et al., 2016; Turner et al., 2016; Viviano-Beck et al., 2017. Four oft-discussed impact craters in this thesis Jezero, Gale, Leighton, and McLaughlin, are noted for reference. Note also the dichotomy between blue (for lowland) and orange-red (for highland) between the north and south of this map of Mars.

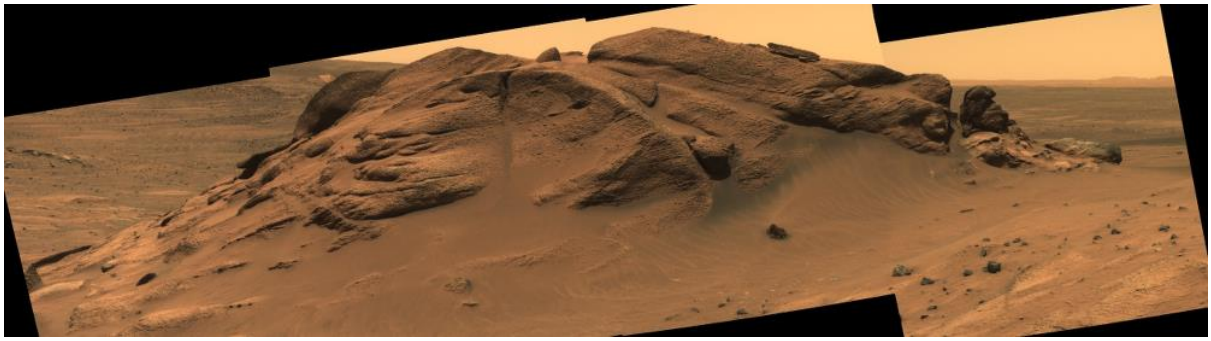


Figure 9: A Pancam true-colour mosaic of the carbonate-bearing Comanche outcrop on Gusev crater Mars, taken by the *Spirit* rover on sol 695, Pancam sequence P2422 (Credit: NASA/JPL/Pancam).

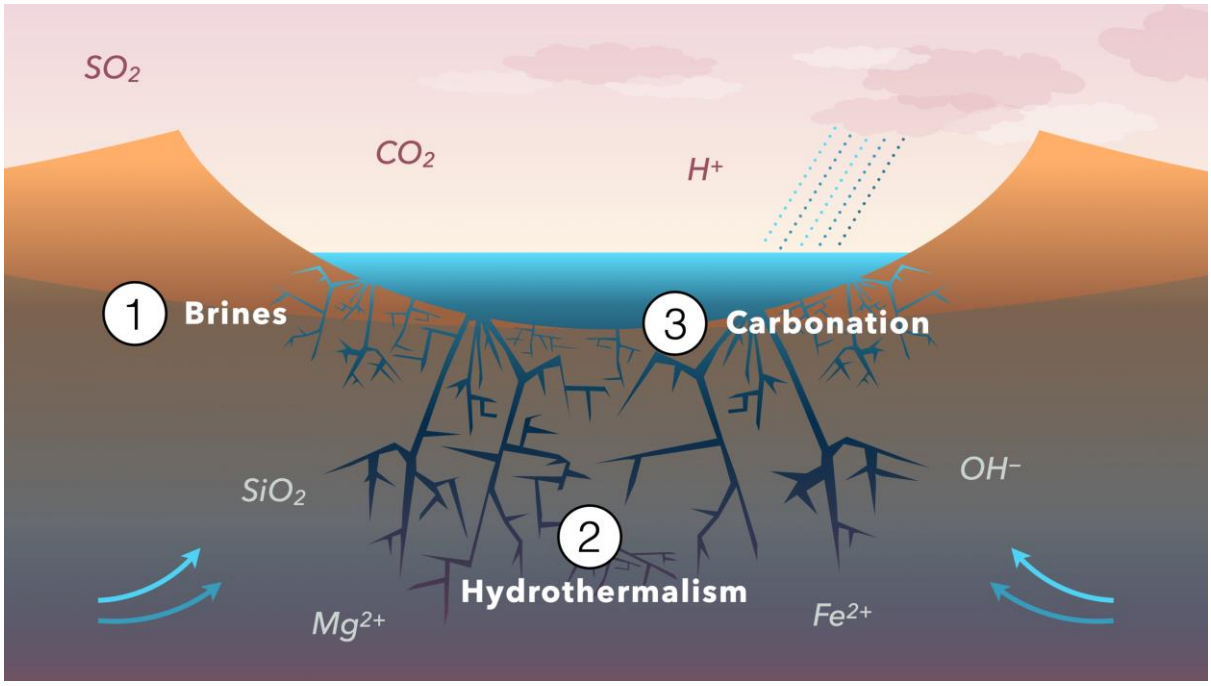


Figure 10: A schematic showing the three most common formation pathways for carbonates on Mars. The more acidic surface environment (shown with CO_2 and SO_2 in the atmosphere, is less favourable for the formation of carbonates owing to its enhanced acidity, while the subsurface is buffered to more alkaline pH by the release of reduced Fe and cations of OH^- and HCO_3^-. (1) Low-temperature (<150 °C) brines containing dissolved cations of Fe^{2+}, Mg^{2+}, OH^-, and HCO_3^-; (2) high-temperature (>150 °C) fluids associated with volcanism or impact; and (3) in situ carbonation, or the direct replacement of mafic minerals with carbonates.

6. References

Acuña, M.H., 1999. Global Distribution of Crustal Magnetization Discovered by the Mars Global Surveyor MAG/ER Experiment. Science 284, 790–793. https://doi.org/10.1126/science.284.5415.790

Andrews-Hanna, J.C., Lewis, K.W., 2011. Early Mars hydrology: 2. Hydrological evolution in the Noachian and Hesperian epochs. J. Geophys. Res. 116, E02007. https://doi.org/10.1029/2010JE003709

Andrews-Hanna, J.C., Zuber, M.T., Arvidson, R.E., Wiseman, S.M., 2010. Early Mars hydrology: Meridiani playa deposits and the sedimentary record of Arabia Terra. J. Geophys. Res. 115, E06002. https://doi.org/10.1029/2009JE003485

Andrews-Hanna, J.C., Zuber, M.T., Banerdt, W.B., 2008. The Borealis basin and the origin of the martian crustal dichotomy. Nature 453, 1212–1215. https://doi.org/10.1038/nature07011

Archer, P.D., Franz, H.B., Sutter, B., Arevalo, R.D., Coll, P., Eigenbrode, J.L., Glavin, D.P., Jones, J.J., Leshin, L.A., Mahaffy, P.R., McAdam, A.C., McKay, C.P., Ming, D.W., Morris, R.V., Navarro-González, R., Niles, P.B., Pavlov, A., Squyres, S.W., Stern, J.C., Steele, A., Wray, J.J., 2014. Abundances and implications of volatile-bearing species from evolved gas analysis of the Rocknest aeolian deposit, Gale Crater, Mars. J. Geophys. Res. Planets 119, 237—254. https://doi.org/10.1002/2013JE004493

Arnórsson, S., Gunnarsson, I., Stefánsson, A., Andrésdóttir, A., Sveinbjörnsdóttir, Á.E., 2002. Major element chemistry of surface- and ground waters in basaltic terrain, N-Iceland. Geochim. Cosmochim. Acta 66, 4015—4046. https://doi.org/10.1016/S0016-7037(02)00991-2

Azoulay, I., Rémazeilles, C., Refait, Ph., 2012. Determination of standard Gibbs free energy of formation of chukanovite and Pourbaix diagrams of iron in carbonated media. Corros. Sci. 58, 229—236. https://doi.org/10.1016/j.corsci.2012.01.033

Baker, V.R., 2001. Water and the martian landscape. Nature 412, 228—236. https://doi.org/10.1038/35084172

Baker, V.R., Milton, D.J., 1974. Erosion by catastrophic floods on Mars and Earth. Icarus 23, 27—41. https://doi.org/10.1016/0019-1035(74)90101-8

Baker, V.R., Partridge, J.B., 1986. Small Martian valleys: Pristine and degraded morphology. J. Geophys. Res. Solid Earth 91, 3561—3572. https://doi.org/10.1029/JB091iB03p03561

Bandfield, J.L., Glotch, T.D., Christensen, P.R., 2003. Spectroscopic Identification of Carbonate Minerals in the Martian Dust. Science 301, 1084—1087. https://doi.org/10.1126/science.1088054

Barabash, S., Fedorov, A., Lundin, R., Sauvaud, J.-A., 2007. Martian Atmospheric Erosion Rates. Science 315, 501—503. https://doi.org/10.1126/science.1134358

Beaty, D.W., Clifford, S.M., Borg, L.E., Catling, D.C., Craddock, R.A., Marais, D.J.D., Farmer, J.D., Frey, H.V., Haberle, R.M., Mckay, C.P., Newsom, H.E., Parker, T.J., Segura, T., Tanaka, K.L., 2005. Key Science Questions from the Second Conference on Early Mars: Geologic, Hydrologic, and Climatic Evolution and the Implications for Life. Astrobiology 5, 663—689. https://doi.org/10.1089/ast.2005.5.663

Bibring, J.-P., Langevin, Y., Mustard, J.F., Poulet, F., Arvidson, R., Gendrin, A., Gondet, B., Mangold, N., Pinet, P., Forget, F., the OMEGA team, Berthe, M., Bibring, J.-P., Gendrin, A., Gomez, C., Gondet, B., Jouglet, D., Poulet, F., Soufflot, A., Vincendon, M., Combes, M., Drossart, P., Encrenaz, T., Fouchet, T., Merchiorri, R., Belluci, G., Altieri, F., Formisano, V., Capaccioni, F., Cerroni, P., Coradini, A., Fonti, S., Korablev, O., Kottsov, V., Ignatiev, N., Moroz, V., Titov, D., Zasova, L., Loiseau, D., Mangold, N., Pinet, P., Doute, S., Schmitt, B., Sotin, C., Hauber, E., Hoffmann, H., Jaumann, R., Keller, U., Arvidson, R., Mustard, J.F., Duxbury, T., Forget, F., Neukum, G., 2006. Global Mineralogical and Aqueous Mars History Derived from OMEGA/Mars Express Data. Science 312, 400—404. https://doi.org/10.1126/science.1122659

Bishop, J.L., Perry, K.A., Darby Dyar, M., Bristow, T.F., Blake, D.F., Brown, A.J., Peel, S.E., 2013. Coordinated spectral and XRD analyses of magnesite-nontronite-forsterite mixtures and implications for carbonates on Mars: MAGNESITE-NONTRONITE-FORSTERITE MIXTURES. J. Geophys. Res. Planets 118, 635—650. https://doi.org/10.1002/jgre.20066

Bjerrum, N., 1914. Die theorie de alkalischen und azidemetrischen Titerieung. Summlung Chem. Chem-Tech. Vorträge 21, 1—128.

Blaney, D.L., McCord, T.B., 1989. An observational search for carbonates on Mars. J. Geophys. Res. Solid Earth 94, 10159—10166. https://doi.org/10.1029/JB094iB08p10159

Bogard, D.D., Johnson, P., 1983. Martian Gases in an Antarctic Meteorite? Science 221, 651—654. https://doi.org/10.1126/science.221.4611.651

Booth, M.C., Kieffer, H.H., 1978. Carbonate formation in Marslike environments. J. Geophys. Res. Solid Earth 83, 1809—1815. https://doi.org/10.1029/JB083iB04p01809

Borg, L.E., 1999. The Age of the Carbonates in Martian Meteorite ALH84001. Science 286, 90—94. https://doi.org/10.1126/science.286.5437.90

Bouley, S., Ansan, V., Mangold, N., Masson, Ph., Neukum, G., 2009. Fluvial morphology of Naktong Vallis, Mars: A late activity with multiple processes. Planet. Space Sci. 57, 982—999. https://doi.org/10.1016/j.pss.2009.01.015

Boynton, W.V., Ming, D.W., Kounaves, S.P., Young, S.M.M., Arvidson, R.E., Hecht, M.H., Hoffman, J., Niles, P.B., Hamara, D.K., Quinn, R.C., Smith, P.H., Sutter, B., Catling, D.C., Morris, R.V., 2009. Evidence for Calcium Carbonate at the Mars Phoenix Landing Site. Science 325, 61—64. https://doi.org/10.1126/science.1172768

Bridges, J., 2000. Evaporite mineral assemblages in the nakhlite (martian) meteorites. Earth Planet. Sci. Lett. 176, 267—279. https://doi.org/10.1016/S0012-821X(00)00019-4

Bridges, J.C., Catling, D.C., Saxton, J.M., Swindle, T.D., Lyon, I.C., Grady, M.M., 2001. Alteration Assemblages in Martian Meteorites: Implications for Near-Surface Processes. Space Sci. Rev. 96, 365—392. https://doi.org/10.1023/A:1011965826553

Bridges, J.C., Hicks, L.J., Treiman, A.H., 2019. Carbonates on Mars, in: Volatiles in the Martian Crust. Elsevier, pp. 89—118. https://doi.org/10.1016/B978-0-12-804191-8.00005-2

Bridges, J.C., Schwenzer, S.P., 2012. The nakhlite hydrothermal brine on Mars. Earth Planet. Sci. Lett. 359—360, 117—123. https://doi.org/10.1016/j.epsl.2012.09.044

Bristow, T.F., Haberle, R.M., Blake, D.F., Marais, D.J.D., Eigenbrode, J.L., Fairén, A.G., Grotzinger, J.P., Stack, K.M., Mischna, M.A., Rampe, E.B., Siebach, K.L., Sutter, B., Vaniman, D.T., Vasavada, A.R., 2017. Low Hesperian PCO2 constrained from in situ mineralogical analysis at Gale Crater, Mars. Proc. Natl. Acad. Sci. 201616649. https://doi.org/10.1073/pnas.1616649114

Brown, A.J., Hook, S.J., Baldridge, A.M., Crowley, J.K., Bridges, N.T., Thomson, B.J., Marion, G.M., de Souza Filho, C.R., Bishop, J.L., 2010. Hydrothermal formation of Clay-Carbonate alteration assemblages in the Nili Fossae region of Mars. Earth Planet. Sci. Lett. 297, 174—182. https://doi.org/10.1016/j.epsl.2010.06.018

Bullock, M.A., Moore, J.M., 2007. Atmospheric conditions on early Mars and the missing layered carbonates. Geophys. Res. Lett. 34, L19201. https://doi.org/10.1029/2007GL030688

Bultel, B., Quantin-Nataf, C., Andréani, M., Clénet, H., Lozac'h, L., 2015. Deep alteration between Hellas and Isidis Basins. Icarus 260, 141—160. https://doi.org/10.1016/j.icarus.2015.06.037

Calvin, W.M., King, T.V.V., Clark, R.N., 1994. Hydrous carbonates on Mars?: Evidence from Mariner 6/7 infrared spectrometer and ground-based telescopic spectra. J. Geophys. Res. 99, 14659. https://doi.org/10.1029/94JE01090

Carothers, W.W., Adami, L.H., Rosenbauer, R.J., 1988. Experimental oxygen isotope fractionation between siderite-water and phosphoric acid liberated CO2-siderite.

Geochim. Cosmochim. Acta 52, 2445—2450. https://doi.org/10.1016/0016-7037(88)90302-X

Carr, M., Head, J., 2019. Mars: Formation and fate of a frozen Hesperian ocean. Icarus 319, 433—443. https://doi.org/10.1016/j.icarus.2018.08.021

Carr, M.H., 1979. Formation of Martian flood features by release of water from confined aquifers. J. Geophys. Res. Solid Earth 84, 2995—3007. https://doi.org/10.1029/JB084iB06p02995

Carr, M.H., Clow, G.D., 1981. Martian channels and valleys: Their characteristics, distribution, and age. Icarus 48, 91—117. https://doi.org/10.1016/0019-1035(81)90156-1

Carr, M.H., Head, J.W., 2015. Martian surface/near-surface water inventory: Sources, sinks, and changes with time. Geophys. Res. Lett. 42, 2014GL062464. https://doi.org/10.1002/2014GL062464

Carr, M.H., Head, J.W., 2003. Oceans on Mars: An assessment of the observational evidence and possible fate. J. Geophys. Res. Planets 108.

Carr, R.H., Grady, M.M., Wright, I.P., Pillinger, C.T., 1985. Martian atmospheric carbon dioxide and weathering products in SNC meteorites. Nature 314, 248—250. https://doi.org/10.1038/314248a0

Carrozzo, F.G., Di Achille, G., Salese, F., Altieri, F., Bellucci, G., 2017. Geology and mineralogy of the Auki Crater, Tyrrhena Terra, Mars: A possible post impact-induced hydrothermal system. Icarus 281, 228—239. https://doi.org/10.1016/j.icarus.2016.09.001

Carter, J., Holmes, A., Dasgupta, R., Tumati, S., 2015. The Effects of Varying Crustal Carbonate Composition on Assimilation and CO2 Degassing at Arc Volcanoes. Presented at the American Geophysical Union Fall Meeting.

Cassata, W.S., Shuster, D.L., Renne, P.R., Weiss, B.P., 2012. Trapped Ar isotopes in meteorite ALH 84001 indicate Mars did not have a thick ancient atmosphere. Icarus 221, 461—465. https://doi.org/10.1016/j.icarus.2012.05.005

Catling, D.C., 1999. A chemical model for evaporites on early Mars: Possible sedimentary tracers of the early climate and implications for exploration. J. Geophys. Res. Planets 104, 16453—16469. https://doi.org/10.1029/1998JE001020

Catling, D.C., Kasting, J.F., 2017. Atmospheric Evolution on Inhabited and Lifeless Worlds. Cambridge University Press, Cambridge. https://doi.org/10.1017/9781139020558

Changela, H.G., Bridges, J.C., 2010. Alteration assemblages in the nakhlites: Variation with depth on Mars: Alteration assemblages in the nakhlites. Meteorit. Planet. Sci. 45, 1847—1867. https://doi.org/10.1111/j.1945-5100.2010.01123.x

Chassefière, E., Langlais, B., Quesnel, Y., Leblanc, F., 2013. The fate of early Mars' lost water: The role of serpentinization: WATER LOSS BY SERPENTINIZATION ON MARS. J. Geophys. Res. Planets 118, 1123—1134. https://doi.org/10.1002/jgre.20089

Chassefière, E., Leblanc, F., 2011. Methane release and the carbon cycle on Mars. Planet. Space Sci., Methane on Mars: Current Observations, Interpretation and Future Plans 59, 207—217. https://doi.org/10.1016/j.pss.2010.09.004

Christensen, P.R., Bandfield, J.L., Hamilton, V.E., Ruff, S.W., Kieffer, H.H., Titus, T.N., Malin, M.C., Morris, R.V., Lane, M.D., Clark, R.L., Jakosky, B.M., Mellon, M.T., Pearl, J.C., Conrath, B.J., Smith, M.D., Clancy, R.T., Kuzmin, R.O., Roush, T., Mehall, G.L., Gorelick, N., Bender, K., Murray, K., Dason, S., Greene, E., Silverman, S., Greenfield, M., 2001. Mars Global Surveyor Thermal Emission Spectrometer experiment: Investigation description and surface science results. J. Geophys. Res. Planets 106, 23823—23871. https://doi.org/10.1029/2000JE001370

Clayton, R.N., Mayeda, T.K., 1983. Oxygen isotopes in eucrites, shergottites, nakhlites, and chassignites. Earth Planet. Sci. Lett. 62, 1—6. https://doi.org/10.1016/0012-821X(83)90066-3

Clifford, S.M., Parker, T.J., 2001. The evolution of the Martian hydrosphere: Implications for the fate of a primordial ocean and the current state of the northern plains. Icarus 154, 40—79.

Cloutis, E.A., Grasby, S.E., Last, W.M., Léveillé, R., Osinski, G.R., Sherriff, B.L., 2010. Spectral reflectance properties of carbonates from terrestrial analogue environments: Implications for Mars. Planet. Space Sci. 58, 522—537. https://doi.org/10.1016/j.pss.2009.09.002

Connerney, J.E., 1999. Magnetic Lineations in the Ancient Crust of Mars. Science 284, 794—798. https://doi.org/10.1126/science.284.5415.794

Daval, D., Martinez, I., Corvisier, J., Findling, N., Goffé, B., Guyot, F., 2009. Carbonation of Ca-bearing silicates, the case of wollastonite: Experimental investigations and kinetic modeling. Chem. Geol. 265, 63—78. https://doi.org/10.1016/j.chemgeo.2009.01.022

Daval, D., Testemale, D., Recham, N., Tarascon, J.-M., Siebert, J., Martinez, I., Guyot, F., 2010. Fayalite (Fe2SiO4) dissolution kinetics determined by X-ray absorption spectroscopy. Chem. Geol. 275, 161—175. https://doi.org/10.1016/j.chemgeo.2010.05.005

Davis, J.M., Balme, M., Grindrod, P.M., Williams, R.M.E., Gupta, S., 2016. Extensive Noachian fluvial systems in Arabia Terra: Implications for early Martian climate. Geology 44, 847—850. https://doi.org/10.1130/G38247.1

Debaille, V., Brandon, A.D., Yin, Q.Z., Jacobsen, B., 2007. Coupled 142Nd—143Nd evidence for a protracted magma ocean in Mars. Nature 450, 525—528. https://doi.org/10.1038/nature06317

Deffeyes, K.S., 1965. CARBONATE EQUILIBRIA: A GRAPHIC AND ALGEBRAIC APPROACH1. Limnol. Oceanogr. 10, 412—426. https://doi.org/10.4319/lo.1965.10.3.0412

Dehouck, E., Chevrier, V., Gaudin, A., Mangold, N., Mathé, P.-E., Rochette, P., 2012. Evaluating the role of sulfide-weathering in the formation of sulfates or carbonates on

Mars. Geochim. Cosmochim. Acta 90, 47—63. https://doi.org/10.1016/j.gca.2012.04.057

Dehouck, E., Gaudin, A., Chevrier, V., Mangold, N., 2016. Mineralogical record of the redox conditions on early Mars. Icarus 271, 67—75. https://doi.org/10.1016/j.icarus.2016.01.030

Dehouck, E., Gaudin, A., Mangold, N., Lajaunie, L., Dauzères, A., Grauby, O., Le Menn, E., 2014. Weathering of olivine under CO2 atmosphere: A martian perspective. Geochim. Cosmochim. Acta 135, 170—189. https://doi.org/10.1016/j.gca.2014.03.032

Dickson, A.G., 1981. An exact definition of total alkalinity and a procedure for the estimation of alkalinity and total inorganic carbon from titration data. Deep Sea Res. Part Oceanogr. Res. Pap. 28, 609—623. https://doi.org/10.1016/0198-0149(81)90121-7

Dideriksen, K., Frandsen, C., Bovet, N., Wallace, A.F., Sel, O., Arbour, T., Navrotsky, A., De Yoreo, J.J., Banfield, J.F., 2015. Formation and transformation of a short range ordered iron carbonate precursor. Geochim. Cosmochim. Acta 164, 94—109. https://doi.org/10.1016/j.gca.2015.05.005

Donaldson, M.J., 1981. Redistribution of ore elements during serpentinization and talc-carbonate alteration of some Archean dunites, Western Australia. Econ. Geol. 76, 1698—1713. https://doi.org/10.2113/gsecongeo.76.6.1698

Druckenmiller, M.L., Maroto-Valer, M.M., 2005. Carbon sequestration using brine of adjusted pH to form mineral carbonates. Fuel Process. Technol. 86, 1599—1614. https://doi.org/10.1016/j.fuproc.2005.01.007

Eby, N.G., 2005. Principles of environmental geochemistry, 3. printing. ed. Thomson-Brooks/Cole, Pacific Grove, Calif.

Ehlmann, B.L., Bish, D.L., Ruff, S.W., Mustard, J.F., 2012. Mineralogy and chemistry of altered Icelandic basalts: Application to clay mineral detection and understanding aqueous

environments on Mars: CLAY MINERAL DETECTION, ICELANDIC BASALT. J. Geophys. Res. Planets 117, n/a-n/a. https://doi.org/10.1029/2012JE004156

Ehlmann, B.L., Edwards, C.S., 2014. Mineralogy of the Martian Surface. Annu. Rev. Earth Planet. Sci. 42, 291—315. https://doi.org/10.1146/annurev-earth-060313-055024

Ehlmann, B.L., Mustard, J.F., Murchie, S.L., Poulet, F., Bishop, J.L., Brown, A.J., Calvin, W.M., Clark, R.N., Marais, D.J.D., Milliken, R.E., Roach, L.H., Roush, T.L., Swayze, G.A., Wray, J.J., 2008. Orbital Identification of Carbonate-Bearing Rocks on Mars. Science 322, 1828—1832. https://doi.org/10.1126/science.1164759

Ehlmann, B.L., Mustard, J.F., Swayze, G.A., Clark, R.N., Bishop, J.L., Poulet, F., Des Marais, D.J., Roach, L.H., Milliken, R.E., Wray, J.J., Barnouin-Jha, O., Murchie, S.L., 2009. Identification of hydrated silicate minerals on Mars using MRO-CRISM: Geologic context near Nili Fossae and implications for aqueous alteration. J. Geophys. Res. 114, E00D08. https://doi.org/10.1029/2009JE003339

Fairén, A.G., Fernández-Remolar, D., Dohm, J.M., Baker, V.R., Amils, R., 2004. Inhibition of carbonate synthesis in acidic oceans on early Mars. Nature 431, 423—426. https://doi.org/10.1038/nature02911

Farmer, J.D., Des Marais, D.J., 1999. Exploring for a record of ancient Martian life. J. Geophys. Res. Planets 104, 26977—26995. https://doi.org/10.1029/1998JE000540

Fassett, C.I., Head III, J.W., 2008. Valley network-fed, open-basin lakes on Mars: Distribution and implications for Noachian surface and subsurface hydrology. Icarus 198, 37—56. https://doi.org/10.1016/j.icarus.2008.06.016

Fastook, J.L., Head, J.W., 2015. Glaciation in the Late Noachian Icy Highlands: Ice accumulation, distribution, flow rates, basal melting, and top-down melting rates and patterns. Planet. Space Sci. 106, 82—98. https://doi.org/10.1016/j.pss.2014.11.028

Gaudin, A., Dehouck, E., Grauby, O., Mangold, N., 2018. Formation of clay minerals on Mars: Insights from long-term experimental weathering of olivine. Icarus 311, 210—223. https://doi.org/10.1016/j.icarus.2018.01.029

Gaudin, A., Dehouck, E., Mangold, N., 2011. Evidence for weathering on early Mars from a comparison with terrestrial weathering profiles. Icarus 216, 257—268. https://doi.org/10.1016/j.icarus.2011.09.004

Glotch, T.D., Rogers, A.D., 2013. Evidence for magma-carbonate interaction beneath Syrtis Major, Mars. J. Geophys. Res. Planets 118, 126—137. https://doi.org/10.1029/2012JE004230

Gooding, J.L., 1978. Chemical weathering on Mars thermodynamic stabilities of primary minerals (and their alteration products) from mafic igneous rocks. Icarus 33, 483—513. https://doi.org/10.1016/0019-1035(78)90186-0

Gooding, J.L., Wentworth, S.J., Zolensky, M.E., 1988. Calcium carbonate and sulfate of possible extraterrestrial origin in the EETA 79001 meteorite. Geochim. Cosmochim. Acta 52, 909—915. https://doi.org/10.1016/0016-7037(88)90361-4

Goudge, T.A., Aureli, K.L., Head, J.W., Fassett, C.I., Mustard, J.F., 2015a. Classification and analysis of candidate impact crater-hosted closed-basin lakes on Mars. Icarus 260, 346—367. https://doi.org/10.1016/j.icarus.2015.07.026

Goudge, T.A., Fassett, C.I., Head, J.W., Mustard, J.F., Aureli, K.L., 2016. Insights into surface runoff on early Mars from paleolake basin morphology and stratigraphy. Geology 44, 419—422. https://doi.org/10.1130/G37734.1

Goudge, T.A., Head, J.W., Mustard, J.F., Fassett, C.I., 2012. An analysis of open-basin lake deposits on Mars: Evidence for the nature of associated lacustrine deposits and post-lacustrine modification processes. Icarus 219, 211—229. https://doi.org/10.1016/j.icarus.2012.02.027

Goudge, T.A., Milliken, R.E., Head, J.W., Mustard, J.F., Fassett, C.I., 2017. Sedimentological evidence for a deltaic origin of the western fan deposit in Jezero crater, Mars and implications for future exploration. Earth Planet. Sci. Lett. 458, 357—365. https://doi.org/10.1016/j.epsl.2016.10.056

Goudge, T.A., Mustard, J.F., Head, J.W., Fassett, C.I., Wiseman, S.M., 2015b. Assessing the mineralogy of the watershed and fan deposits of the Jezero crater paleolake system, Mars: Jezero Paleolake System Mineralogy. J. Geophys. Res. Planets 120, 775—808. https://doi.org/10.1002/2014JE004782

Greeley, R., Schneid, B.D., 1991. Magma Generation on Mars: Amounts, Rates, and Comparisons with Earth, Moon, and Venus. Science 254, 996—998. https://doi.org/10.1126/science.254.5034.996

Greenwood, J.P., Itoh, S., Sakamoto, N., Vicenzi, E.P., Yurimoto, H., 2008. Hydrogen isotope evidence for loss of water from Mars through time. Geophys. Res. Lett. 35, L05203. https://doi.org/10.1029/2007GL032721

Griffith, L.L., Shock, E.L., 1995. A geochemical model for the formation of hydrothermal carbonates on Mars. Nature 377, 406—408. https://doi.org/10.1038/377406a0

Grotzinger, J., Beaty, D., Dromart, G., Gupta, S., Harris, M., Hurowitz, J., Kocurek, G., McLennan, S., Milliken, R., Ori, G.G., Sumner, D., 2011. Mars Sedimentary Geology: Key Concepts and Outstanding Questions. Astrobiology 11, 77—87. https://doi.org/10.1089/ast.2010.0571

Grotzinger, J.P., Milliken, R.E. (Eds.), 2012. Sedimentary geology of Mars, SEPM special publication. SEPM (Society for Sedimentary Geology), Tulsa, Okla.

Grotzinger, J.P., Sumner, D.Y., Kah, L.C., Stack, K., Gupta, S., Edgar, L., Rubin, D., Lewis, K., Schieber, J., Mangold, N., Milliken, R., Conrad, P.G., DesMarais, D., Farmer, J., Siebach, K., Calef, F., Hurowitz, J., McLennan, S.M., Ming, D., Vaniman, D., Crisp, J., Vasavada, A., Edgett, K.S., Malin, M., Blake, D., Gellert, R., Mahaffy, P., Wiens, R.C., Maurice, S.,

Grant, J.A., Wilson, S., Anderson, R.C., Beegle, L., Arvidson, R., Hallet, B., Sletten, R.S., Rice, M., Bell, J., Griffes, J., Ehlmann, B., Anderson, R.B., Bristow, T.F., Dietrich, W.E., Dromart, G., Eigenbrode, J., Fraeman, A., Hardgrove, C., Herkenhoff, K., Jandura, L., Kocurek, G., Lee, S., Leshin, L.A., Leveille, R., Limonadi, D., Maki, J., McCloskey, S., Meyer, M., Minitti, M., Newsom, H., Oehler, D., Okon, A., Palucis, M., Parker, T., Rowland, S., Schmidt, M., Squyres, S., Steele, A., Stolper, E., Summons, R., Treiman, A., Williams, R., Yingst, A., Team, M.S., 2014. A Habitable Fluvio-Lacustrine Environment at Yellowknife Bay, Gale Crater, Mars. Science 343, 1242777. https://doi.org/10.1126/science.1242777

Gysi, A.P., 2017. Numerical simulations of CO2 sequestration in basaltic rock formations: challenges for optimizing mineral-fluid reactions. Pure Appl. Chem. 89, 581—596. https://doi.org/10.1515/pac-2016-1016

Gysi, A.P., Stefánsson, A., 2012. CO2-water—basalt interaction. Low temperature experiments and implications for CO2 sequestration into basalts. Geochim. Cosmochim. Acta 81, 129—152. https://doi.org/10.1016/j.gca.2011.12.012

Haberle, R.M., Clancy, R.T., Forget, F., Smith, M.D., Zurek, R.W., 2017. The atmosphere and climate of Mars. Cambridge University Press.

Halevy, I., Fischer, W.W., Eiler, J.M., 2011. Carbonates in the Martian meteorite Allan Hills 84001 formed at 18 4 C in a near-surface aqueous environment. Proc. Natl. Acad. Sci. 108, 16895—16899. https://doi.org/10.1073/pnas.1109444108

Harder, H., 1978. Synthesis of Iron Layer Silicate Minerals under Natural Conditions. Clays Clay Miner. 26, 65—72. https://doi.org/10.1346/CCMN.1978.0260108

Harrison, K., Grimm, R., 2005. Groundwater-controlled valley networks and the decline of surface runoff on early Mars. J. Geophys. Res. Planets 110. https://doi.org/10.1029/2005JE002455

Hartmann, W.K., Neukum, G., 2001. Cratering Chronology and the Evolution of Mars, in: Chronology and Evolution of Mars, Space Sciences Series of ISSI. Springer, Dordrecht, pp. 165—194. https://doi.org/10.1007/978-94-017-1035-0_6

Harvey, R.P., McSween, H.Y., 1996. A possible high-temperature origin for the carbonates in the martian meteorite ALH84001. Nature 382, 49—51. https://doi.org/10.1038/382049a0

He, S., Morse, J.W., 1993. The carbonic acid system and calcite solubility in aqueous Na-K-Ca-Mg-Cl-SO4 solutions from 0 to 90°C. Geochim. Cosmochim. Acta 57, 3533—3554. https://doi.org/10.1016/0016-7037(93)90137-L

Heard, A.W., Kite, E.S., 2020. A probabilistic case for a large missing carbon sink on Mars after 3.5 billion years ago. Earth Planet. Sci. Lett. 531, 116001. https://doi.org/10.1016/j.epsl.2019.116001

Hecht, M.H., Kounaves, S.P., Quinn, R.C., West, S.J., Young, S.M.M., Ming, D.W., Catling, D.C., Clark, B.C., Boynton, W.V., Hoffman, J., DeFlores, L.P., Gospodinova, K., Kapit, J., Smith, P.H., 2009. Detection of Perchlorate and the Soluble Chemistry of Martian Soil at the Phoenix Lander Site. Science 325, 64—67. https://doi.org/10.1126/science.1172466

Heet, T.L., Arvidson, R.E., Cull, S.C., Mellon, M.T., Seelos, K.D., 2009. Geomorphic and geologic settings of the Phoenix Lander mission landing site. J. Geophys. Res. 114, E00E04. https://doi.org/10.1029/2009JE003416

Herschel, W., 1784. XIX. On the remarkable appearances at the polar regions of the planet Mars, and its spheroidical figure; with a few hints relating to its real diameter and atmosphere. Philos. Trans. R. Soc. Lond. 74, 233—273. https://doi.org/10.1098/rstl.1784.0020

Hicks, L.J., Bridges, J.C., Gurman, S.J., 2014. Ferric saponite and serpentine in the nakhlite martian meteorites. Geochim. Cosmochim. Acta 136, 194—210. https://doi.org/10.1016/j.gca.2014.04.010

Hoke, M.R.T., Hynek, B.M., Tucker, G.E., 2011. Formation timescales of large Martian valley networks. Earth Planet. Sci. Lett. 312, 1—12. https://doi.org/10.1016/j.epsl.2011.09.053

Horgan, B.H.N., Anderson, R.B., Dromart, G., Amador, E.S., Rice, M.S., 2020. The mineral diversity of Jezero crater: Evidence for possible lacustrine carbonates on Mars. Icarus 339, 113526. https://doi.org/10.1016/j.icarus.2019.113526

Hu, R., Kass, D.M., Ehlmann, B.L., Yung, Y.L., 2015. Tracing the fate of carbon and the atmospheric evolution of Mars. Nat. Commun. 6. https://doi.org/10.1038/ncomms10003

Hurowitz, J.A., Fischer, W.W., Tosca, N.J., Milliken, R.E., 2010. Origin of acidic surface waters and the evolution of atmospheric chemistry on early Mars. Nat. Geosci. 3, 323—326. https://doi.org/10.1038/ngeo831

Hurowitz, J.A., Grotzinger, J.P., Fischer, W.W., McLennan, S.M., Milliken, R.E., Stein, N., Vasavada, A.R., Blake, D.F., Dehouck, E., Eigenbrode, J.L., Fairén, A.G., Frydenvang, J., Gellert, R., Grant, J.A., Gupta, S., Herkenhoff, K.E., Ming, D.W., Rampe, E.B., Schmidt, M.E., Siebach, K.L., Stack-Morgan, K., Sumner, D.Y., Wiens, R.C., 2017. Redox stratification of an ancient lake in Gale crater, Mars. Science 356, eaah6849. https://doi.org/10.1126/science.aah6849

Hynek, B.M., Beach, M., Hoke, M.R.T., 2010. Updated global map of Martian valley networks and implications for climate and hydrologic processes. J. Geophys. Res. 115, E09008. https://doi.org/10.1029/2009JE003548

Ivanov, M.A., Head, J.W., 2001. Chryse Planitia, Mars: Topographic configuration, outflow channel continuity and sequence, and tests for hypothesized ancient bodies of water using Mars Orbiter Laser Altimeter (MOLA) data. J. Geophys. Res. Planets 106, 3275—3295. https://doi.org/10.1029/2000JE001257

Jain, N., Chauhan, P., 2015. Study of phyllosilicates and carbonates from the Capri Chasma region of Valles Marineris on Mars based on Mars Reconnaissance Orbiter-Compact

Reconnaissance Imaging Spectrometer for Mars (MRO-CRISM) observations. Icarus 250, 7—17. https://doi.org/10.1016/j.icarus.2014.11.018

Jakosky, B.M., 2019. The CO2 inventory on Mars. Planet. Space Sci. 175, 52—59. https://doi.org/10.1016/j.pss.2019.06.002

Jakosky, B.M., Brain, D., Chaffin, M., Curry, S., Deighan, J., Grebowsky, J., Halekas, J., Leblanc, F., Lillis, R., Luhmann, J.G., Andersson, L., Andre, N., Andrews, D., Baird, D., Baker, D., Bell, J., Benna, M., Bhattacharyya, D., Bougher, S., Bowers, C., Chamberlin, P., Chaufray, J.-Y., Clarke, J., Collinson, G., Combi, M., Connerney, J., Connour, K., Correira, J., Crabb, K., Crary, F., Cravens, T., Crismani, M., Delory, G., Dewey, R., DiBraccio, G., Dong, C., Dong, Y., Dunn, P., Egan, H., Elrod, M., England, S., Eparvier, F., Ergun, R., Eriksson, A., Esman, T., Espley, J., Evans, S., Fallows, K., Fang, X., Fillingim, M., Flynn, C., Fogle, A., Fowler, C., Fox, J., Fujimoto, M., Garnier, P., Girazian, Z., Groeller, H., Gruesbeck, J., Hamil, O., Hanley, K.G., Hara, T., Harada, Y., Hermann, J., Holmberg, M., Holsclaw, G., Houston, S., Inui, S., Jain, S., Jolitz, R., Kotova, A., Kuroda, T., Larson, D., Lee, Y., Lee, C., Lefevre, F., Lentz, C., Lo, D., Lugo, R., Ma, Y.-J., Mahaffy, P., Marquette, M.L., Matsumoto, Y., Mayyasi, M., Mazelle, C., McClintock, W., McFadden, J., Medvedev, A., Mendillo, M., Meziane, K., Milby, Z., Mitchell, D., Modolo, R., Montmessin, F., Nagy, A., Nakagawa, H., Narvaez, C., Olsen, K., Pawlowski, D., Peterson, W., Rahmati, A., Roeten, K., Romanelli, N., Ruhunusiri, S., Russell, C., Sakai, S., Schneider, N., Seki, K., Sharrar, R., Shaver, S., Siskind, D.E., Slipski, M., Soobiah, Y., Steckiewicz, M., Stevens, M.H., Stewart, I., Stiepen, A., Stone, S., Tenishev, V., Terada, N., Terada, K., Thiemann, E., Tolson, R., Toth, G., Trovato, J., Vogt, M., Weber, T., Withers, P., Xu, S., Yelle, R., Yiğit, E., Zurek, R., 2018. Loss of the Martian atmosphere to space: Present-day loss rates determined from MAVEN observations and integrated loss through time. Icarus 315, 146—157. https://doi.org/10.1016/j.icarus.2018.05.030

Jakosky, B.M., Farmer, C.B., 1982. The seasonal and global behavior of water vapor in the Mars atmosphere: Complete global results of the Viking Atmospheric Water Detector Experiment. J. Geophys. Res. 87, 2999. https://doi.org/10.1029/JB087iB04p02999

Jakosky, B.M., Slipski, M., Benna, M., Mahaffy, P., Elrod, M., Yelle, R., Stone, S., Alsaeed, N., 2017. Mars' atmospheric history derived from upper-atmosphere measurements of ^{38}Ar/^{36}Ar. Science 355, 1408—1410. https://doi.org/10.1126/science.aai7721

Jiang, C.Z., Tosca, N.J., 2019. Fe(II)-carbonate precipitation kinetics and the chemistry of anoxic ferruginous seawater. Earth Planet. Sci. Lett. 506, 231—242. https://doi.org/10.1016/j.epsl.2018.11.010

Jimenez-Lopez, C., Romanek, C.S., 2004. Precipitation kinetics and carbon isotope partitioning of inorganic siderite at 25°C and 1 atm. Geochim. Cosmochim. Acta 68, 557—571. https://doi.org/10.1016/S0016-7037(03)00460-5

Kahn, R., 1985. The evolution of CO2 on Mars. Icarus 62, 175—190. https://doi.org/10.1016/0019-1035(85)90116-2

Kelemen, P.B., Matter, J., 2008. In situ carbonation of peridotite for CO2 storage. Proc. Natl. Acad. Sci. 105, 17295—17300. https://doi.org/10.1073/pnas.0805794105

Kelts, K., Hsü, K.J., 1978. Freshwater Carbonate Sedimentation, in: Lerman, A. (Ed.), Lakes. Springer New York, New York, NY, pp. 295—323. https://doi.org/10.1007/978-1-4757-1152-3_9

Kite, E.S., Mayer, D.P., Wilson, S.A., Davis, J.M., Lucas, A.S., Stucky de Quay, G., 2019. Persistence of intense, climate-driven runoff late in Mars history. Sci. Adv. 5, eaav7710. https://doi.org/10.1126/sciadv.aav7710

Kite, E.S., Melwani Daswani, M., 2019. Geochemistry constrains global hydrology on Early Mars. Earth Planet. Sci. Lett. 524, 115718. https://doi.org/10.1016/j.epsl.2019.115718

Kite, E.S., Williams, J.-P., Lucas, A., Aharonson, O., 2014. Low palaeopressure of the martian atmosphere estimated from the size distribution of ancient craters. Nat. Geosci. 7, 335—339. https://doi.org/10.1038/ngeo2137

Kumar, S., Soukup, M., Elbaum, R., 2017. Silicification in Grasses: Variation between Different Cell Types. Front. Plant Sci. 8. https://doi.org/10.3389/fpls.2017.00438

Kurokawa, H., Kurosawa, K., Usui, T., 2018. A lower limit of atmospheric pressure on early Mars inferred from nitrogen and argon isotopic compositions. Icarus 299, 443—459. https://doi.org/10.1016/j.icarus.2017.08.020

Lammer, H., Chassefière, E., Karatekin, Ö., Morschhauser, A., Niles, P.B., Mousis, O., Odert, P., Möstl, U.V., Breuer, D., Dehant, V., Grott, M., Gröller, H., Hauber, E., Pham, L.B.S., 2013. Outgassing History and Escape of the Martian Atmosphere and Water Inventory. Space Sci. Rev. 174, 113—154. https://doi.org/10.1007/s11214-012-9943-8

Lapen, T.J., Righter, M., Brandon, A.D., Debaille, V., Beard, B.L., Shafer, J.T., Peslier, A.H., 2010. A Younger Age for ALH84001 and Its Geochemical Link to Shergottite Sources in Mars. Science 328, 347—351. https://doi.org/10.1126/science.1185395

Lee, M.R., MacLaren, I., Andersson, S.M.L., Kovács, A., Tomkinson, T., Mark, D.F., Smith, C.L., 2015. Opal-A in the Nakhla meteorite: A tracer of ephemeral liquid water in the Amazonian crust of Mars. Meteorit. Planet. Sci. 50, 1362—1377. https://doi.org/10.1111/maps.12471

Lellouch, E., Encrenaz, T., de Graauw, T., Erard, S., Morris, P., Crovisier, J., Feuchtgruber, H., Girard, T., Burgdorf, M., 2000. The 2.4— spectrum of Mars observed with the infrared space observatory. Planet. Space Sci. 48, 1393—1405. https://doi.org/10.1016/S0032-0633(00)00118-5

Leshin, L.A., Mahaffy, P.R., Webster, C.R., Cabane, M., Coll, P., Conrad, P.G., Archer, P.D., Atreya, S.K., Brunner, A.E., Buch, A., Eigenbrode, J.L., Flesch, G.J., Franz, H.B., Freissinet, C., Glavin, D.P., McAdam, A.C., Miller, K.E., Ming, D.W., Morris, R.V.,

Navarro-González, R., Niles, P.B., Owen, T., Pepin, R.O., Squyres, S., Steele, A., Stern, J.C., Summons, R.E., Sumner, D.Y., Sutter, B., Szopa, C., Teinturier, S., Trainer, M.G., Wray, J.J., Grotzinger, J.P., Team, M.S., 2013. Volatile, Isotope, and Organic Analysis of Martian Fines with the Mars Curiosity Rover. Science 341, 1238937. https://doi.org/10.1126/science.1238937

Leverington, D.W., 2004. Volcanic rilles, streamlined islands, and the origin of outflow channels on Mars. J. Geophys. Res. 109, E10011. https://doi.org/10.1029/2004JE002311

Lewis, K.W., Aharonson, O., 2014. Occurrence and origin of rhythmic sedimentary rocks on Mars. J. Geophys. Res. Planets 119, 1432—1457. https://doi.org/10.1002/2013JE004404

Lonker, S.W., Franzson, H., Kristmannsdottir, H., 1993. Mineral-fluid interactions in the Reykjanes and Svartsengi geothermal systems, Iceland. Am. J. Sci. 293, 605—670. https://doi.org/10.2475/ajs.293.7.605

Lucchitta, B.K., 1982. Ice sculpture in the Martian outflow channels. J. Geophys. Res. 87, 9951. https://doi.org/10.1029/JB087iB12p09951

Lucchitta, B.K., Ferguson, H.M., Summers, C., 1986. Sedimentary deposits in the Northern Lowland Plains, Mars. J. Geophys. Res. 91, E166. https://doi.org/10.1029/JB091iB13p0E166

Luo, W., Cang, X., Howard, A.D., 2017. New Martian valley network volume estimate consistent with ancient ocean and warm and wet climate. Nat. Commun. 8, 15766. https://doi.org/10.1038/ncomms15766

Mahaffy, P.R., Webster, C.R., Atreya, S.K., Franz, H., Wong, M., Conrad, P.G., Harpold, D., Jones, J.J., Leshin, L.A., Manning, H., Owen, T., Pepin, R.O., Squyres, S., Trainer, M., MSL Science Team, Kemppinen, O., Bridges, N., Johnson, J.R., Minitti, M., Cremers, D., Bell, J.F., Edgar, L., Farmer, J., Godber, A., Wadhwa, M., Wellington, D., McEwan, I., Newman, C., Richardson, M., Charpentier, A., Peret, L., King, P., Blank, J., Weigle, G.,

Schmidt, M., Li, S., Milliken, R., Robertson, K., Sun, V., Baker, M., Edwards, C., Ehlmann, B., Farley, K., Griffes, J., Grotzinger, J., Miller, H., Newcombe, M., Pilorget, C., Rice, M., Siebach, K., Stack, K., Stolper, E., Brunet, C., Hipkin, V., Leveille, R., Marchand, G., Sanchez, P.S., Favot, L., Cody, G., Steele, A., Fluckiger, L., Lees, D., Nefian, A., Martin, M., Gailhanou, M., Westall, F., Israel, G., Agard, C., Baroukh, J., Donny, C., Gaboriaud, A., Guillemot, P., Lafaille, V., Lorigny, E., Paillet, A., Perez, R., Saccoccio, M., Yana, C., Armiens-Aparicio, C., Rodriguez, J.C., Blazquez, I.C., Gomez, F.G., Gomez-Elvira, J., Hettrich, S., Malvitte, A.L., Jimenez, M.M., Martinez-Frias, J., Martin-Soler, J., Martin-Torres, F.J., Jurado, A.M., Mora-Sotomayor, L., Caro, G.M., Lopez, S.N., Peinado-Gonzalez, V., Pla-Garcia, J., Manfredi, J.A.R., Romeral-Planello, J.J., Fuentes, S.A.S., Martinez, E.S., Redondo, J.T., Urqui-O'Callaghan, R., Mier, M.-P.Z., Chipera, S., Lacour, J.-L., Mauchien, P., Sirven, J.-B., Fairen, A., Hayes, A., Joseph, J., Sullivan, R., Thomas, P., Dupont, A., Lundberg, A., Melikechi, N., Mezzacappa, A., DeMarines, J., Grinspoon, D., Reitz, G., Prats, B., Atlaskin, E., Genzer, M., Harri, A.-M., Haukka, H., Kahanpaa, H., Kauhanen, J., Kemppinen, O., Paton, M., Polkko, J., Schmidt, W., Siili, T., Fabre, C., Wray, J., Wilhelm, M.B., Poitrasson, F., Patel, K., Gorevan, S., Indyk, S., Paulsen, G., Gupta, S., Bish, D., Schieber, J., Gondet, B., Langevin, Y., Geffroy, C., Baratoux, D., Berger, G., Cros, A., d'Uston, C., Forni, O., Gasnault, O., Lasue, J., Lee, Q.-M., Maurice, S., Meslin, P.-Y., Pallier, E., Parot, Y., Pinet, P., Schroder, S., Toplis, M., Lewin, E., Brunner, W., Heydari, E., Achilles, C., Oehler, D., Sutter, B., Cabane, M., Coscia, D., Israel, G., Szopa, C., Dromart, G., Robert, F., Sautter, V., Le Mouelic, S., Mangold, N., Nachon, M., Buch, A., Stalport, F., Coll, P., Francois, P., Raulin, F., Teinturier, S., Cameron, J., Clegg, S., Cousin, A., DeLapp, D., Dingler, R., Jackson, R.S., Johnstone, S., Lanza, N., Little, C., Nelson, T., Wiens, R.C., Williams, R.B., Jones, A., Kirkland, L., Treiman, A., Baker, B., Cantor, B., Caplinger, M., Davis, S., Duston, B., Edgett, K., Fay, D., Hardgrove, C., Harker, D., Herrera, P., Jensen, E.,

Kennedy, M.R., Krezoski, G., Krysak, D., Lipkaman, L., Malin, M., McCartney, E., McNair, S., Nixon, B., Posiolova, L., Ravine, M., Salamon, A., Saper, L., Stoiber, K., Supulver, K., Van Beek, J., Van Beek, T., Zimdar, R., French, K.L., Iagnemma, K., Miller, K., Summons, R., Goesmann, F., Goetz, W., Hviid, S., Johnson, M., Lefavor, M., Lyness, E., Breves, E., Dyar, M.D., Fassett, C., Blake, D.F., Bristow, T., DesMarais, D., Edwards, L., Haberle, R., Hoehler, T., Hollingsworth, J., Kahre, M., Keely, L., McKay, C., Wilhelm, M.B., Bleacher, L., Brinckerhoff, W., Choi, D., Dworkin, J.P., Eigenbrode, J., Floyd, M., Freissinet, C., Garvin, J., Glavin, D., Jones, A., Martin, D.K., McAdam, A., Pavlov, A., Raaen, E., Smith, M.D., Stern, J., Tan, F., Meyer, M., Posner, A., Voytek, M., Anderson, R.C., Aubrey, A., Beegle, L.W., Behar, A., Blaney, D., Brinza, D., Calef, F., Christensen, L., Crisp, J.A., DeFlores, L., Ehlmann, B., Feldman, J., Feldman, S., Flesch, G., Hurowitz, J., Jun, I., Keymeulen, D., Maki, J., Mischna, M., Morookian, J.M., Parker, T., Pavri, B., Schoppers, M., Sengstacken, A., Simmonds, J.J., Spanovich, N., Juarez, M. d. l. T., Vasavada, A.R., Yen, A., Archer, P.D., Cucinotta, F., Ming, D., Morris, R.V., Niles, P., Rampe, E., Nolan, T., Fisk, M., Radziemski, L., Barraclough, B., Bender, S., Berman, D., Dobrea, E.N., Tokar, R., Vaniman, D., Williams, R.M.E., Yingst, A., Lewis, K., Cleghorn, T., Huntress, W., Manhes, G., Hudgins, J., Olson, T., Stewart, N., Sarrazin, P., Grant, J., Vicenzi, E., Wilson, S.A., Bullock, M., Ehresmann, B., Hamilton, V., Hassler, D., Peterson, J., Rafkin, S., Zeitlin, C., Fedosov, F., Golovin, D., Karpushkina, N., Kozyrev, A., Litvak, M., Malakhov, A., Mitrofanov, I., Mokrousov, M., Nikiforov, S., Prokhorov, V., Sanin, A., Tretyakov, V., Varenikov, A., Vostrukhin, A., Kuzmin, R., Clark, B., Wolff, M., McLennan, S., Botta, O., Drake, D., Bean, K., Lemmon, M., Schwenzer, S.P., Anderson, R.B., Herkenhoff, K., Lee, E.M., Sucharski, R., Hernandez, M.A. d. P., Avalos, J.J.B., Ramos, M., Kim, M.-H., Malespin, C., Plante, I., Muller, J.-P., Navarro-Gonzalez, R., Ewing, R., Boynton, W., Downs, R., Fitzgibbon, M., Harshman, K., Morrison, S., Dietrich, W., Kortmann, O., Palucis, M., Sumner, D.Y., Williams, A.,

Lugmair, G., Wilson, M.A., Rubin, D., Jakosky, B., Balic-Zunic, T., Frydenvang, J., Jensen, J.K., Kinch, K., Koefoed, A., Madsen, M.B., Stipp, S.L.S., Boyd, N., Campbell, J.L., Gellert, R., Perrett, G., Pradler, I., VanBommel, S., Jacob, S., Rowland, S., Atlaskin, E., Savijarvi, H., Boehm, E., Bottcher, S., Burmeister, S., Guo, J., Kohler, J., Garcia, C.M., Mueller-Mellin, R., Wimmer-Schweingruber, R., Bridges, J.C., McConnochie, T., Benna, M., Bower, H., Brunner, A., Blau, H., Boucher, T., Carmosino, M., Elliott, H., Halleaux, D., Renno, N., Elliott, B., Spray, J., Thompson, L., Gordon, S., Newsom, H., Ollila, A., Williams, J., Vasconcelos, P., Bentz, J., Nealson, K., Popa, R., Kah, L.C., Moersch, J., Tate, C., Day, M., Kocurek, G., Hallet, B., Sletten, R., Francis, R., McCullough, E., Cloutis, E., ten Kate, I.L., Kuzmin, R., Arvidson, R., Fraeman, A., Scholes, D., Slavney, S., Stein, T., Ward, J., Berger, J., Moores, J.E., 2013. Abundance and Isotopic Composition of Gases in the Martian Atmosphere from the Curiosity Rover. Science 341, 263—266. https://doi.org/10.1126/science.1237966

Malin, M.C., Edgett, K.S., 2000. Sedimentary Rocks of Early Mars. Science 290, 1927—1937. https://doi.org/10.1126/science.290.5498.1927

Manga, M., Patel, A., Dufek, J., Kite, E.S., 2012. Wet surface and dense atmosphere on early Mars suggested by the bomb sag at Home Plate, Mars: MARS: WET SURFACE, DENSE ATMOSPHERE. Geophys. Res. Lett. 39, n/a-n/a. https://doi.org/10.1029/2011GL050192

Marion, G.M., Catling, D.C., Kargel, J.S., 2003. Modeling aqueous ferrous iron chemistry at low temperatures with application to Mars. Geochim. Cosmochim. Acta 67, 4251—4266. https://doi.org/10.1016/S0016-7037(03)00372-7

Masursky, H., 1973. An overview of geological results from Mariner 9. J. Geophys. Res. 78, 4009—4030. https://doi.org/10.1029/JB078i020p04009

McCarthy, T.S., McIver, J.R., Verhagen, B.Th., 1991. Groundwater evolution, chemical sedimentation and carbonate brine formation on an island in the Okavango Delta

swamp, Botswana. Appl. Geochem. 6, 577—595. https://doi.org/10.1016/0883-2927(91)90071-V

McKay, C.P., Nedell, S.S., 1988. Are there carbonate deposits in the Valles Marineris, Mars? Icarus 73, 142—148. https://doi.org/10.1016/0019-1035(88)90088-7

McKay, D.S., Gibson, E.K., Thomas-Keprta, K.L., Vali, H., Romanek, C.S., Clemett, S.J., Chillier, X.D.F., Maechling, C.R., Zare, R.N., 1996. Search for Past Life on Mars: Possible Relic Biogenic Activity in Martian Meteorite ALH84001. Science 273, 924—930. https://doi.org/10.1126/science.273.5277.924

McLennan, S.M., Anderson, R.B., Bell, J.F., Bridges, J.C., Calef, F., Campbell, J.L., Clark, B.C., Clegg, S., Conrad, P., Cousin, A., Des Marais, D.J., Dromart, G., Dyar, M.D., Edgar, L.A., Ehlmann, B.L., Fabre, C., Forni, O., Gasnault, O., Gellert, R., Gordon, S., Grant, J.A., Grotzinger, J.P., Gupta, S., Herkenhoff, K.E., Hurowitz, J.A., King, P.L., Le Mouelic, S., Leshin, L.A., Leveille, R., Lewis, K.W., Mangold, N., Maurice, S., Ming, D.W., Morris, R.V., Nachon, M., Newsom, H.E., Ollila, A.M., Perrett, G.M., Rice, M.S., Schmidt, M.E., Schwenzer, S.P., Stack, K., Stolper, E.M., Sumner, D.Y., Treiman, A.H., VanBommel, S., Vaniman, D.T., Vasavada, A., Wiens, R.C., Yingst, R.A., MSL Science Team, Kemppinen, O., Bridges, N., Johnson, J.R., Minitti, M., Cremers, D., Farmer, J., Godber, A., Wadhwa, M., Wellington, D., McEwan, I., Newman, C., Richardson, M., Charpentier, A., Peret, L., Blank, J., Weigle, G., Li, S., Milliken, R., Robertson, K., Sun, V., Baker, M., Edwards, C., Farley, K., Griffes, J., Miller, H., Newcombe, M., Pilorget, C., Siebach, K., Brunet, C., Hipkin, V., Marchand, G., Sanchez, P.S., Favot, L., Cody, G., Steele, A., Fluckiger, L., Lees, D., Nefian, A., Martin, M., Gailhanou, M., Westall, F., Israel, G., Agard, C., Baroukh, J., Donny, C., Gaboriaud, A., Guillemot, P., Lafaille, V., Lorigny, E., Paillet, A., Perez, R., Saccoccio, M., Yana, C., Armiens-Aparicio, C., Rodriguez, J.C., Blazquez, I.C., Gomez, F.G., Gomez-Elvira, J., Hettrich, S., Malvitte, A.L., Jimenez, M.M., Martinez-Frias, J., Martin-Soler, J., Martin-Torres, F.J., Jurado,

A.M., Mora-Sotomayor, L., Caro, G.M., Lopez, S.N., Peinado-Gonzalez, V., Pla-Garcia, J., Manfredi, J.A.R., Romeral-Planello, J.J., Fuentes, S.A.S., Martinez, E.S., Redondo, J.T., Urqui-O'Callaghan, R., Mier, M.-P.Z., Chipera, S., Lacour, J.-L., Mauchien, P., Sirven, J.-B., Manning, H., Fairen, A., Hayes, A., Joseph, J., Squyres, S., Sullivan, R., Thomas, P., Dupont, A., Lundberg, A., Melikechi, N., Mezzacappa, A., DeMarines, J., Grinspoon, D., Reitz, G., Prats, B., Atlaskin, E., Genzer, M., Harri, A.-M., Haukka, H., Kahanpaa, H., Kauhanen, J., Kemppinen, O., Paton, M., Polkko, J., Schmidt, W., Siili, T., Wray, J., Wilhelm, M.B., Poitrasson, F., Patel, K., Gorevan, S., Indyk, S., Paulsen, G., Bish, D., Schieber, J., Gondet, B., Langevin, Y., Geffroy, C., Baratoux, D., Berger, G., Cros, A., d'Uston, C., Lasue, J., Lee, Q.-M., Meslin, P.-Y., Pallier, E., Parot, Y., Pinet, P., Schroder, S., Toplis, M., Lewin, E., Brunner, W., Heydari, E., Achilles, C., Oehler, D., Sutter, B., Cabane, M., Coscia, D., Israel, G., Szopa, C., Robert, F., Sautter, V., Buch, A., Stalport, F., Coll, P., Francois, P., Raulin, F., Teinturier, S., Cameron, J., DeLapp, D., Dingler, R., Jackson, R.S., Johnstone, S., Lanza, N., Little, C., Nelson, T., Williams, R.B., Jones, A., Kirkland, L., Baker, B., Cantor, B., Caplinger, M., Davis, S., Duston, B., Edgett, K., Fay, D., Hardgrove, C., Harker, D., Herrera, P., Jensen, E., Kennedy, M.R., Krezoski, G., Krysak, D., Lipkaman, L., Malin, M., McCartney, E., McNair, S., Nixon, B., Posiolova, L., Ravine, M., Salamon, A., Saper, L., Stoiber, K., Supulver, K., Van Beek, J., Van Beek, T., Zimdar, R., French, K.L., Iagnemma, K., Miller, K., Summons, R., Goesmann, F., Goetz, W., Hviid, S., Johnson, M., Lefavor, M., Lyness, E., Breves, E., Fassett, C., Blake, D.F., Bristow, T., Edwards, L., Haberle, R., Hoehler, T., Hollingsworth, J., Kahre, M., Keely, L., McKay, C., Wilhelm, M.B., Bleacher, L., Brinckerhoff, W., Choi, D., Dworkin, J.P., Eigenbrode, J., Floyd, M., Freissinet, C., Garvin, J., Glavin, D., Harpold, D., Jones, A., Mahaffy, P., Martin, D.K., McAdam, A., Pavlov, A., Raaen, E., Smith, M.D., Stern, J., Tan, F., Trainer, M., Meyer, M., Posner, A., Voytek, M., Anderson, R.C., Aubrey, A., Beegle, L.W., Behar, A., Blaney, D., Brinza, D., Christensen, L., Crisp, J.A., DeFlores, L.,

Ehlmann, B., Feldman, J., Feldman, S., Flesch, G., Jun, I., Keymeulen, D., Maki, J., Mischna, M., Morookian, J.M., Parker, T., Pavri, B., Schoppers, M., Sengstacken, A., Simmonds, J.J., Spanovich, N., Juarez, M. d. l. T., Webster, C.R., Yen, A., Archer, P.D., Cucinotta, F., Jones, J.H., Niles, P., Rampe, E., Nolan, T., Fisk, M., Radziemski, L., Barraclough, B., Bender, S., Berman, D., Dobrea, E.N., Tokar, R., Williams, R.M.E., Cleghorn, T., Huntress, W., Manhes, G., Hudgins, J., Olson, T., Stewart, N., Sarrazin, P., Vicenzi, E., Wilson, S.A., Bullock, M., Ehresmann, B., Hamilton, V., Hassler, D., Peterson, J., Rafkin, S., Zeitlin, C., Fedosov, F., Golovin, D., Karpushkina, N., Kozyrev, A., Litvak, M., Malakhov, A., Mitrofanov, I., Mokrousov, M., Nikiforov, S., Prokhorov, V., Sanin, A., Tretyakov, V., Varenikov, A., Vostrukhin, A., Kuzmin, R., Wolff, M., Botta, O., Drake, D., Bean, K., Lemmon, M., Lee, E.M., Sucharski, R., Hernandez, M.A. d. P., Avalos, J.J.B., Ramos, M., Kim, M.-H., Malespin, C., Plante, I., Muller, J.-P., Navarro-Gonzalez, R., Ewing, R., Boynton, W., Downs, R., Fitzgibbon, M., Harshman, K., Morrison, S., Dietrich, W., Kortmann, O., Palucis, M., Williams, A., Lugmair, G., Wilson, M.A., Rubin, D., Jakosky, B., Balic-Zunic, T., Frydenvang, J., Jensen, J.K., Kinch, K., Koefoed, A., Madsen, M.B., Stipp, S.L.S., Boyd, N., Pradler, I., Jacob, S., Owen, T., Rowland, S., Atlaskin, E., Savijarvi, H., Boehm, E., Bottcher, S., Burmeister, S., Guo, J., Kohler, J., Garcia, C.M., Mueller-Mellin, R., Wimmer-Schweingruber, R., McConnochie, T., Benna, M., Franz, H., Bower, H., Brunner, A., Blau, H., Boucher, T., Carmosino, M., Atreya, S., Elliott, H., Halleaux, D., Renno, N., Wong, M., Pepin, R., Elliott, B., Spray, J., Thompson, L., Williams, J., Vasconcelos, P., Bentz, J., Nealson, K., Popa, R., Kah, L.C., Moersch, J., Tate, C., Day, M., Kocurek, G., Hallet, B., Sletten, R., Francis, R., McCullough, E., Cloutis, E., ten Kate, I.L., Kuzmin, R., Arvidson, R., Fraeman, A., Scholes, D., Slavney, S., Stein, T., Ward, J., Berger, J., Moores, J.E., 2014. Elemental Geochemistry of Sedimentary Rocks at Yellowknife Bay, Gale Crater, Mars. Science 343, 1244734—1244734. https://doi.org/10.1126/science.1244734

McLennan, S.M., Grotzinger, J.P., Hurowitz, J.A., Tosca, N.J., 2019. The Sedimentary Cycle on Early Mars. Annu. Rev. Earth Planet. Sci. 47, 91—118. https://doi.org/10.1146/annurev-earth-053018-060332

McSween, H.Y., Harvey, R.P., 1998. An Evaporation Model for Formation of Carbonates in the ALH84001 Martian Meteorite. Int. Geol. Rev. 40, 774—783. https://doi.org/10.1080/00206819809465238

Melosh, H.J., 2011. Planetary Surface Processes. Cambridge University Press, Cambridge. https://doi.org/10.1017/CBO9780511977848

Mervine, E.M., Humphris, S.E., Sims, K.W.W., Kelemen, P.B., Jenkins, W.J., 2014. Carbonation rates of peridotite in the Samail Ophiolite, Sultanate of Oman, constrained through 14C dating and stable isotopes. Geochim. Cosmochim. Acta 126, 371—397. https://doi.org/10.1016/j.gca.2013.11.007

Metz, J.M., Grotzinger, J.P., Mohrig, D., Milliken, R., Prather, B., Pirmez, C., McEwen, A.S., Weitz, C.M., 2009. Sublacustrine depositional fans in southwest Melas Chasma. J. Geophys. Res. Planets 114, E10002. https://doi.org/10.1029/2009JE003365

Michalski, J., Kraft, M., Sharp, T., Christensen, P., 2006. Effects of chemical weathering on infrared spectra of Columbia River Basalt and spectral interpretations of martian alteration. Earth Planet. Sci. Lett. 248, 822—829. https://doi.org/10.1016/j.epsl.2006.06.034

Michalski, J., Poulet, F., Bibring, J.-P., Mangold, N., 2010. Analysis of phyllosilicate deposits in the Nili Fossae region of Mars: Comparison of TES and OMEGA data. Icarus 206, 269—289. https://doi.org/10.1016/j.icarus.2009.09.006

Michalski, J.R., Cuadros, J., Bishop, J.L., Darby Dyar, M., Dekov, V., Fiore, S., 2015. Constraints on the crystal-chemistry of Fe/Mg-rich smectitic clays on Mars and links to global alteration trends. Earth Planet. Sci. Lett. 427, 215—225. https://doi.org/10.1016/j.epsl.2015.06.020

Michalski, J.R., Cuadros, J., Niles, P.B., Parnell, J., Deanne Rogers, A., Wright, S.P., 2013. Groundwater activity on Mars and implications for a deep biosphere. Nat. Geosci. 6, 133—138. https://doi.org/10.1038/ngeo1706

Michalski, J.R., Dobrea, E.Z.N., Niles, P.B., Cuadros, J., 2017. Ancient hydrothermal seafloor deposits in Eridania basin on Mars. Nat. Commun. 8, 15978. https://doi.org/10.1038/ncomms15978

Michalski, J.R., Glotch, T.D., Rogers, A.D., Niles, P.B., Cuadros, J., Ashley, J.W., Johnson, S.S., 2019. The Geology and Astrobiology of McLaughlin Crater, Mars: An Ancient Lacustrine Basin Containing Turbidites, Mudstones, and Serpentinites. J. Geophys. Res. Planets 124, 910—940. https://doi.org/10.1029/2018JE005796

Michalski, J.R., Niles, P.B., 2010. Deep crustal carbonate rocks exposed by meteor impact on Mars. Nat. Geosci. 3, 751—755. https://doi.org/10.1038/ngeo971

Milliken, R.E., Fischer, W.W., Hurowitz, J.A., 2009. Missing salts on early Mars. Geophys. Res. Lett. 36, L11202. https://doi.org/10.1029/2009GL038558

Ming, D.W., Archer, P.D., Glavin, D.P., Eigenbrode, J.L., Franz, H.B., Sutter, B., Brunner, A.E., Stern, J.C., Freissinet, C., McAdam, A.C., Mahaffy, P.R., Cabane, M., Coll, P., Campbell, J.L., Atreya, S.K., Niles, P.B., Bell, J.F., Bish, D.L., Brinckerhoff, W.B., Buch, A., Conrad, P.G., Des Marais, D.J., Ehlmann, B.L., Fairen, A.G., Farley, K., Flesch, G.J., Francois, P., Gellert, R., Grant, J.A., Grotzinger, J.P., Gupta, S., Herkenhoff, K.E., Hurowitz, J.A., Leshin, L.A., Lewis, K.W., McLennan, S.M., Miller, K.E., Moersch, J., Morris, R.V., Navarro-Gonzalez, R., Pavlov, A.A., Perrett, G.M., Pradler, I., Squyres, S.W., Summons, R.E., Steele, A., Stolper, E.M., Sumner, D.Y., Szopa, C., Teinturier, S., Trainer, M.G., Treiman, A.H., Vaniman, D.T., Vasavada, A.R., Webster, C.R., Wray, J.J., Yingst, R.A., MSL Science Team, Kemppinen, O., Bridges, N., Johnson, J.R., Minitti, M., Cremers, D., Edgar, L., Farmer, J., Godber, A., Wadhwa, M., Wellington, D., McEwan, I., Newman, C., Richardson, M., Charpentier, A., Peret, L., King, P., Blank, J., Weigle, G., Schmidt,

M., Li, S., Milliken, R., Robertson, K., Sun, V., Baker, M., Edwards, C., Ehlmann, B., Griffes, J., Newcombe, M., Pilorget, C., Rice, M., Siebach, K., Stack, K., Brunet, C., Hipkin, V., Leveille, R., Marchand, G., Sanchez, P.S., Favot, L., Cody, G., Fluckiger, L., Lees, D., Nefian, A., Martin, M., Gailhanou, M., Westall, F., Israel, G., Agard, C., Baroukh, J., Donny, C., Gaboriaud, A., Guillemot, P., Lafaille, V., Lorigny, E., Paillet, A., Perez, R., Saccoccio, M., Yana, C., Armiens-Aparicio, C., Rodriguez, J.C., Blazquez, I.C., Gomez, F.G., Gomez-Elvira, J., Hettrich, S., Malvitte, A.L., Jimenez, M.M., Martinez-Frias, J., Martin-Soler, J., Martin-Torres, F.J., Jurado, A.M., Mora-Sotomayor, L., Caro, G.M., Lopez, S.N., Peinado-Gonzalez, V., Pla-Garcia, J., Manfredi, J.A.R., Romeral-Planello, J.J., Fuentes, S.A.S., Martinez, E.S., Redondo, J.T., Urqui-O'Callaghan, R., Mier, M.-P.Z., Chipera, S., Lacour, J.-L., Mauchien, P., Sirven, J.-B., Manning, H., Hayes, A., Joseph, J., Sullivan, R., Thomas, P., Dupont, A., Lundberg, A., Melikechi, N., Mezzacappa, A., DeMarines, J., Grinspoon, D., Reitz, G., Prats, B., Atlaskin, E., Genzer, M., Harri, A.-M., Haukka, H., Kahanpaa, H., Kauhanen, J., Kemppinen, O., Paton, M., Polkko, J., Schmidt, W., Siili, T., Fabre, C., Wilhelm, M.B., Poitrasson, F., Patel, K., Gorevan, S., Indyk, S., Paulsen, G., Schieber, J., Gondet, B., Langevin, Y., Geffroy, C., Baratoux, D., Berger, G., Cros, A., d'Uston, C., Forni, O., Gasnault, O., Lasue, J., Lee, Q.-M., Maurice, S., Meslin, P.-Y., Pallier, E., Parot, Y., Pinet, P., Schroder, S., Toplis, M., Lewin, E., Brunner, W., Heydari, E., Achilles, C., Oehler, D., Coscia, D., Israel, G., Dromart, G., Robert, F., Sautter, V., Le Mouelic, S., Mangold, N., Nachon, M., Stalport, F., Raulin, F., Cameron, J., Clegg, S., Cousin, A., DeLapp, D., Dingler, R., Jackson, R.S., Johnstone, S., Lanza, N., Little, C., Nelson, T., Wiens, R.C., Williams, R.B., Jones, A., Kirkland, L., Baker, B., Cantor, B., Caplinger, M., Davis, S., Duston, B., Edgett, K., Fay, D., Hardgrove, C., Harker, D., Herrera, P., Jensen, E., Kennedy, M.R., Krezoski, G., Krysak, D., Lipkaman, L., Malin, M., McCartney, E., McNair, S., Nixon, B., Posiolova, L., Ravine, M., Salamon, A., Saper, L., Stoiber, K., Supulver, K., Van Beek, J., Van Beek,

T., Zimdar, R., French, K.L., Iagnemma, K., Miller, K., Goesmann, F., Goetz, W., Hviid, S., Johnson, M., Lefavor, M., Lyness, E., Breves, E., Dyar, M.D., Fassett, C., Blake, D.F., Bristow, T., Edwards, L., Haberle, R., Hoehler, T., Hollingsworth, J., Kahre, M., Keely, L., McKay, C., Wilhelm, M.B., Bleacher, L., Choi, D., Dworkin, J.P., Floyd, M., Garvin, J., Harpold, D., Jones, A., Martin, D.K., Raaen, E., Smith, M.D., Tan, F., Meyer, M., Posner, A., Voytek, M., Anderson, R.C., Aubrey, A., Beegle, L.W., Behar, A., Blaney, D., Brinza, D., Calef, F., Christensen, L., Crisp, J.A., DeFlores, L., Feldman, J., Feldman, S., Jun, I., Keymeulen, D., Maki, J., Mischna, M., Morookian, J.M., Parker, T., Pavri, B., Schoppers, M., Sengstacken, A., Simmonds, J.J., Spanovich, N., Juarez, M. d. l. T., Yen, A., Cucinotta, F., Jones, J.H., Rampe, E., Nolan, T., Fisk, M., Radziemski, L., Barraclough, B., Bender, S., Berman, D., Dobrea, E.N., Tokar, R., Williams, R.M.E., Cleghorn, T., Huntress, W., Manhes, G., Hudgins, J., Olson, T., Stewart, N., Sarrazin, P., Vicenzi, E., Wilson, S.A., Bullock, M., Ehresmann, B., Hamilton, V., Hassler, D., Peterson, J., Rafkin, S., Zeitlin, C., Fedosov, F., Golovin, D., Karpushkina, N., Kozyrev, A., Litvak, M., Malakhov, A., Mitrofanov, I., Mokrousov, M., Nikiforov, S., Prokhorov, V., Sanin, A., Tretyakov, V., Varenikov, A., Vostrukhin, A., Kuzmin, R., Clark, B., Wolff, M., Botta, O., Drake, D., Bean, K., Lemmon, M., Schwenzer, S.P., Anderson, R.B., Lee, E.M., Sucharski, R., Hernandez, M.A. d. P., Avalos, J.J.B., Ramos, M., Kim, M.-H., Malespin, C., Plante, I., Muller, J.-P., Ewing, R., Boynton, W., Downs, R., Fitzgibbon, M., Harshman, K., Morrison, S., Dietrich, W., Kortmann, O., Palucis, M., Williams, A., Lugmair, G., Wilson, M.A., Rubin, D., Jakosky, B., Balic-Zunic, T., Frydenvang, J., Jensen, J.K., Kinch, K., Koefoed, A., Madsen, M.B., Stipp, S.L.S., Boyd, N., VanBommel, S., Jacob, S., Owen, T., Rowland, S., Atlaskin, E., Savijarvi, H., Boehm, E., Bottcher, S., Burmeister, S., Guo, J., Kohler, J., Garcia, C.M., Mueller-Mellin, R., Wimmer-Schweingruber, R., Bridges, J.C., McConnochie, T., Benna, M., Bower, H., Blau, H., Boucher, T., Carmosino, M., Elliott, H., Halleaux, D., Renno, N., Wong, M.,

Pepin, R., Elliott, B., Spray, J., Thompson, L., Gordon, S., Newsom, H., Ollila, A., Williams, J., Vasconcelos, P., Bentz, J., Nealson, K., Popa, R., Kah, L.C., Tate, C., Day, M., Kocurek, G., Hallet, B., Sletten, R., Francis, R., McCullough, E., Cloutis, E., ten Kate, I.L., Kuzmin, R., Arvidson, R., Fraeman, A., Scholes, D., Slavney, S., Stein, T., Ward, J., Berger, J., Moores, J.E., 2014. Volatile and Organic Compositions of Sedimentary Rocks in Yellowknife Bay, Gale Crater, Mars. Science 343, 1245267—1245267. https://doi.org/10.1126/science.1245267

Minissale, A., Vaselli, O., Chandrasekharam, D., Magro, G., Tassi, F., Casiglia, A., 2000. Origin and evolution of 'intracratonic' thermal fluids from central-western peninsular India. Earth Planet. Sci. Lett. 181, 377—394. https://doi.org/10.1016/S0012-821X(00)00200-4

Mittlefehldt, D.W., 1994. ALH84001, a cumulate orthopyroxenite member of the martian meteorite clan. Meteoritics 29, 214—221. https://doi.org/10.1111/j.1945-5100.1994.tb00673.x

Morris, R.V., Ruff, S.W., Gellert, R., Ming, D.W., Arvidson, R.E., Clark, B.C., Golden, D.C., Siebach, K., Klingelhofer, G., Schroder, C., Fleischer, I., Yen, A.S., Squyres, S.W., 2010. Identification of Carbonate-Rich Outcrops on Mars by the Spirit Rover. Science 329, 421—424. https://doi.org/10.1126/science.1189667

Morse, J.W., Arvidson, R.S., 2002. The dissolution kinetics of major sedimentary carbonate minerals. Earth-Sci. Rev. 58, 51—84. https://doi.org/10.1016/S0012-8252(01)00083-6

Murchie, S.L., Mustard, J.F., Ehlmann, B.L., Milliken, R.E., Bishop, J.L., McKeown, N.K., Noe Dobrea, E.Z., Seelos, F.P., Buczkowski, D.L., Wiseman, S.M., Arvidson, R.E., Wray, J.J., Swayze, G., Clark, R.N., Des Marais, D.J., McEwen, A.S., Bibring, J.-P., 2009. A synthesis of Martian aqueous mineralogy after 1 Mars year of observations from the Mars Reconnaissance Orbiter. J. Geophys. Res. 114, E00D06. https://doi.org/10.1029/2009JE003342

Mustard, J.F., Murchie, S.L., Pelkey, S.M., Ehlmann, B.L., Milliken, R.E., Grant, J.A., Bibring, J.-P., Poulet, F., Bishop, J., Dobrea, E.N., Roach, L., Seelos, F., Arvidson, R.E., Wiseman, S., Green, R., Hash, C., Humm, D., Malaret, E., McGovern, J.A., Seelos, K., Clancy, T., Clark, R., Marais, D.D., Izenberg, N., Knudson, A., Langevin, Y., Martin, T., McGuire, P., Morris, R., Robinson, M., Roush, T., Smith, M., Swayze, G., Taylor, H., Titus, T., Wolff, M., 2008. Hydrated silicate minerals on Mars observed by the Mars Reconnaissance Orbiter CRISM instrument. Nature 454, 305—309. https://doi.org/10.1038/nature07097

Nagashima, K., Wakita, H., Mochizuki, A., 1973. The Synthesis of Crystalline Rare Earth Carbonates. Bull. Chem. Soc. Jpn. 46, 152—156. https://doi.org/10.1246/bcsj.46.152

Naumov, M.V., 2005. Principal features of impact-generated hydrothermal circulation systems: mineralogical and geochemical evidence. Geofluids 5, 165—184. https://doi.org/10.1111/j.1468-8123.2005.00092.x

Nier, A.O., McElroy, M.B., 1977. Composition and structure of Mars' Upper atmosphere: Results from the neutral mass spectrometers on Viking 1 and 2. J. Geophys. Res. 82, 4341—4349. https://doi.org/10.1029/JS082i028p04341

Niles, P.B., Catling, D.C., Berger, G., Chassefière, E., Ehlmann, B.L., Michalski, J.R., Morris, R., Ruff, S.W., Sutter, B., 2013. Geochemistry of Carbonates on Mars: Implications for Climate History and Nature of Aqueous Environments. Space Sci. Rev. 174, 301—328. https://doi.org/10.1007/s11214-012-9940-y

Nyquist, L.E., Bogard, D.D., Shih, C.-Y., Greshake, A., Stöffler, D., Eugster, O., 2001. Ages and Geologic Histories of Martian Meteorites, in: Kallenbach, R., Geiss, J., Hartmann, W.K. (Eds.), Chronology and Evolution of Mars, Space Sciences Series of ISSI. Springer Netherlands, Dordrecht, pp. 105—164. https://doi.org/10.1007/978-94-017-1035-0_5

Ogawa, Y., Manga, M., 2007. Thermal demagnetization of Martian upper crust by magma intrusion: HYDROTHERMAL DEMAGNETIZATION. Geophys. Res. Lett. 34. https://doi.org/10.1029/2007GL030565

Ojha, L., Wilhelm, M.B., Murchie, S.L., McEwen, A.S., Wray, J.J., Hanley, J., Massé, M., Chojnacki, M., 2015. Spectral evidence for hydrated salts in recurring slope lineae on Mars. Nat. Geosci. 8, 829—832. https://doi.org/10.1038/ngeo2546

Orofino, V., Blanco, A., Blecka, M.I., Fonti, S., Jurewicz, A., 2000. Carbonates and coated particles on Mars. Planet. Space Sci. 48, 1341—1347. https://doi.org/10.1016/S0032-0633(00)00114-8

Osinski, G.R., Tornabene, L.L., Banerjee, N.R., Cockell, C.S., Flemming, R., Izawa, M.R.M., McCutcheon, J., Parnell, J., Preston, L.J., Pickersgill, A.E., Pontefract, A., Sapers, H.M., Southam, G., 2013. Impact-generated hydrothermal systems on Earth and Mars. Icarus, Terrestrial Analogs for Mars: Mars Science Laboratory and Beyond 224, 347—363. https://doi.org/10.1016/j.icarus.2012.08.030

Owen, T., Bar-Nun, A., Kleinfeld, I., 1992. Possible cometary origin of heavy noble gases in the atmospheres of Venus, Earth and Mars. Nature 358, 43—46. https://doi.org/10.1038/358043a0

Owen, T., Biemann, K., Rushneck, D.R., Biller, J.E., Howarth, D.W., Lafleur, A.L., 1977. The composition of the atmosphere at the surface of Mars. J. Geophys. Res. 82, 4635—4639. https://doi.org/10.1029/JS082i028p04635

Palumbo, A.M., Head, J.W., 2019. Oceans on Mars: The possibility of a Noachian groundwater-fed ocean in a sub-freezing martian climate. Icarus 331, 209—225. https://doi.org/10.1016/j.icarus.2019.04.022

Park, P.K., 1969. OCEANIC CO $_2$ SYSTEM: AN EVALUATION OF TEN METHODS OF INVESTIGATION1: OCEANIC CO $_2$ SYSTEM. Limnol. Oceanogr. 14, 179—186. https://doi.org/10.4319/lo.1969.14.2.0179

Parmentier, E.M., Zuber, M.T., 2007. Early evolution of Mars with mantle compositional stratification or hydrothermal crustal cooling. J. Geophys. Res. 112, E02007. https://doi.org/10.1029/2005JE002626

Pekov, I.V., Perchiazzi, N., Merlino, S., Kalachev, V.N., Merlini, M., Zadov, A.E., 2007. Chukanovite, Fe2(CO3)(OH)2, a new mineral from the weathered iron meteorite Dronino. Eur. J. Mineral. 19, 891—898. https://doi.org/10.1127/0935-1221/2007/0019-1767

Peretyazhko, T.S., Niles, P.B., Sutter, B., Morris, R.V., Agresti, D.G., Le, L., Ming, D.W., 2018. Smectite formation in the presence of sulfuric acid: Implications for acidic smectite formation on early Mars. Geochim. Cosmochim. Acta 220, 248—260. https://doi.org/10.1016/j.gca.2017.10.004

Peretyazhko, T.S., Sutter, B., Morris, R.V., Agresti, D.G., Le, L., Ming, D.W., 2016. Fe/Mg smectite formation under acidic conditions on early Mars. Geochim. Cosmochim. Acta 173, 37—49. https://doi.org/10.1016/j.gca.2015.10.012

Phillips, R.J., Zuber, M., Solomon, S.C., Golombek, M.P., Jakosky, B.M., Banerdt, W.B., Smith, D.E., Williams, R.B., Hynek, B.M., Aharonson, O., Hauck, S.A., 2001. Ancient Geodynamics and Global-Scale Hydrology on Mars. Science 291, 2587—2591. https://doi.org/10.1126/science.1058701

Pollack, J.B., Kasting, J.F., Richardson, S.M., Poliakoff, K., 1987. The case for a wet, warm climate on early Mars. Icarus 71, 203—224. https://doi.org/10.1016/0019-1035(87)90147-3

Pollack, J.B., Roush, T., Witteborn, F., Bregman, J., Wooden, D., Stoker, C., Toon, O.B., Rank, D., Dalton, B., Freedman, R., 1990. Thermal emission spectra of Mars (5.4—10.5 μm): Evidence for sulfates, carbonates, and hydrates. J. Geophys. Res. Solid Earth 95, 14595—14627. https://doi.org/10.1029/JB095iB09p14595

Pondrelli, M., Rossi, A.P., Le Deit, L., Fueten, F., van Gasselt, S., Glamoclija, M., Cavalazzi, B., Hauber, E., Franchi, F., Pozzobon, R., 2015. Equatorial layered deposits in Arabia Terra, Mars: Facies and process variability. Geol. Soc. Am. Bull. B31225.1. https://doi.org/10.1130/B31225.1

Poulet, F., Mangold, N., Loizeau, D., Bibring, J.-P., Langevin, Y., Michalski, J., Gondet, B., 2008. Abundance of minerals in the phyllosilicate-rich units on Mars. Astron. Astrophys. 487, L41—L44. https://doi.org/10.1051/0004-6361:200810150

Qafoku, O., Kovarik, L., Kukkadapu, R.K., Ilton, E.S., Arey, B.W., Tucek, J., Felmy, A.R., 2012. Fayalite dissolution and siderite formation in water-saturated supercritical CO2. Chem. Geol. 332—333, 124—135. https://doi.org/10.1016/j.chemgeo.2012.09.028

Ramirez, R.M., Craddock, R.A., Usui, T., 2020. Climate Simulations of Early Mars With Estimated Precipitation, Runoff, and Erosion Rates. J. Geophys. Res. Planets 125. https://doi.org/10.1029/2019JE006160

Rasmussen, B., Krapez, B., Meier, D.B., 2014. Replacement origin for hematite in 2.5 Ga banded iron formation: Evidence for postdepositional oxidation of iron-bearing minerals. Geol. Soc. Am. Bull. 126, 438—446. https://doi.org/10.1130/B30944.1

Renaut, R.W., 1990. Recent carbonate sedimentation and brine evolution in the saline lake basins of the Cariboo Plateau, British Columbia, Canada, in: Comín, F.A., Northcote, T.G. (Eds.), Saline Lakes. Springer Netherlands, Dordrecht, pp. 67—81. https://doi.org/10.1007/978-94-009-0603-7_6

Ridgwell, A., Zeebe, R., 2005. The role of the global carbonate cycle in the regulation and evolution of the Earth system. Earth Planet. Sci. Lett. 234, 299—315. https://doi.org/10.1016/j.epsl.2005.03.006

Riding, R., 1991. Classification of Microbial Carbonates, in: Riding, Robert (Ed.), Calcareous Algae and Stromatolites. Springer Berlin Heidelberg, Berlin, Heidelberg, pp. 21—51. https://doi.org/10.1007/978-3-642-52335-9_2

Rodríguez, J.A.P., Kargel, J.S., Baker, V.R., Gulick, V.C., Berman, D.C., Fairén, A.G., Linares, R., Zarroca, M., Yan, J., Miyamoto, H., Glines, N., 2015. Martian outflow channels: How did their source aquifers form, and why did they drain so rapidly? Sci. Rep. 5, 13404. https://doi.org/10.1038/srep13404

Romanek, C.S., Grady, M.M., Wright, I.P., Mittlefehldt, D.W., Socki, R.A., Pillinger, C.T., Gibson, E.K., 1994. Record of fluid—rock interactions on Mars from the meteorite ALH84001. Nature 372, 655—657. https://doi.org/10.1038/372655a0

Romanek, C.S., Jiménez-López, C., Navarro, A.R., Sánchez-Román, M., Sahai, N., Coleman, M., 2009. Inorganic synthesis of Fe—Ca—Mg carbonates at low temperature. Geochim. Cosmochim. Acta 73, 5361—5376. https://doi.org/10.1016/j.gca.2009.05.065

Ruff, S.W., Niles, P.B., Alfano, F., Clarke, A.B., 2014. Evidence for a Noachian-aged ephemeral lake in Gusev crater, Mars. Geology 42, 359—362. https://doi.org/10.1130/G35508.1

Salese, F., Pondrelli, M., Neeseman, A., Schmidt, G., Ori, G.G., 2019. Geological Evidence of Planet-Wide Groundwater System on Mars. J. Geophys. Res. Planets 124, 374—395. https://doi.org/10.1029/2018JE005802

Schon, S.C., Head, J.W., Fassett, C.I., 2012. An overfilled lacustrine system and progradational delta in Jezero crater, Mars: Implications for Noachian climate. Planet. Space Sci. 67, 28—45. https://doi.org/10.1016/j.pss.2012.02.003

Schrag, D.P., Higgins, John.A., Macdonald, F.A., Johnston, D.T., 2013. Authigenic Carbonate and the History of the Global Carbon Cycle. Science 339, 540—543. https://doi.org/10.1126/science.1229578

Segura, T.L., McKay, C.P., Toon, O.B., 2012. An impact-induced, stable, runaway climate on Mars. Icarus 220, 144—148. https://doi.org/10.1016/j.icarus.2012.04.013

Segura, T.L., Toon, O., Colaprete, A., Zahnle, K., 2002. Environmental Effects of Large Impacts on Mars. Science 298, 1977—1980. https://doi.org/10.1126/science.1073586

Segura, T.L., Toon, O.B., Colaprete, A., 2008. Modeling the environmental effects of moderate-sized impacts on Mars. J. Geophys. Res. 113, E11007. https://doi.org/10.1029/2008JE003147

Sel, O., Radha, A.V., Dideriksen, K., Navrotsky, A., 2012. Amorphous iron (II) carbonate: Crystallization energetics and comparison to other carbonate minerals related to CO2 sequestration. Geochim. Cosmochim. Acta 87, 61—68. https://doi.org/10.1016/j.gca.2012.03.011

Shih, C.-Y., Nyquist, L.E., Bogard, D.D., McKay, G.A., Wooden, J.L., Bansal, B.M., Wiesmann, H., 1982. Chronology and petrogenesis of young achondrites, Shergotty, Zagami, and ALHA77005: late magmatism on a geologically active planet. Geochim. Cosmochim. Acta 46, 2323—2344. https://doi.org/10.1016/0016-7037(82)90205-8

Shih, C.-Y., Nyquist, L.E., Wiesmann, H., 1999. Samarium-neodymium and rubidium-strontium systematics of nakhlite Governador Valadares. Meteorit. Planet. Sci. 34, 647—655. https://doi.org/10.1111/j.1945-5100.1999.tb01370.x

Singer, P.C., Stumm, W., 1970. The Solubility of Ferrous Iron in Carbonate-Bearing Waters. J. - Am. Water Works Assoc. 62, 198—202. https://doi.org/10.1002/j.1551-8833.1970.tb03888.x

Singer, R.B., McCord, T.B., Clark, R.N., Adams, J.B., Huguenin, R.L., 1979. Mars surface composition from reflectance spectroscopy: A summary. J. Geophys. Res. 84, 8415. https://doi.org/10.1029/JB084iB14p08415

Squyres, S.W., Grotzinger, J.P., Arvidson, R.E., Bell, J.F., Calvin, W., Christensen, P.R., Clark, B.C., Crisp, J.A., Farrand, W.H., Herkenhoff, K.E., Johnson, J.R., Klingelhöfer, G., Knoll, A.H., McLennan, S.M., McSween, H.Y., Morris, R.V., Rice, J.W., Rieder, R., Soderblom, L.A., 2004. In Situ Evidence for an Ancient Aqueous Environment at Meridiani Planum, Mars. Science 306, 1709—1714. https://doi.org/10.1126/science.1104559

Steele, A., Fries, M.D., Amundsen, H.E.F., Mysen, B.O., Fogel, M.L., Schweizer, M., Boctor, N.Z., 2007. Comprehensive imaging and Raman spectroscopy of carbonate globules from Martian meteorite ALH 84001 and a terrestrial analogue from Svalbard. Meteorit. Planet. Sci. 42, 1549—1566. https://doi.org/10.1111/j.1945-5100.2007.tb00590.x

Stevens, T.O., McKinley, J.P., 2000. Abiotic Controls on H2 Production from Basalt−Water Reactions and Implications for Aquifer Biogeochemistry. Environ. Sci. Technol. 34, 826—831. https://doi.org/10.1021/es990583g

Stolper, E., McSween, H.Y., 1979. Petrology and origin of the shergottite meteorites. Geochim. Cosmochim. Acta 43, 1475—1498. https://doi.org/10.1016/0016-7037(79)90142-X

Swindle, T.D., Treiman, A.H., Lindstrom, D.J., Burkland, M.K., Cohen, B.A., Grier, J.A., Li, B., Olson, E.K., 2000. Noble gases in iddingsite from the Lafayette meteorite: Evidence for liquid water on Mars in the last few hundred million years. Meteorit. Planet. Sci. 35, 107—115. https://doi.org/10.1111/j.1945-5100.2000.tb01978.x

Taylor, S.R., McLennan, S.M., 2009. Planetary crusts: their composition, origin and evolution, Cambridge planetary science. Cambridge University Press, Cambridge, UK ; New York.

Taylor, S.R., McLennan, S.M., 1985. The continental crust: its composition and evolution: an examination of the geochem. record preserved in sedimentary rocks, Geoscience texts. Blackwell, Oxford.

Thomson, B.J., Hurowitz, J.A., Baker, L.L., Bridges, N.T., Lennon, A.M., Paulsen, G., Zacny, K., 2014. The effects of weathering on the strength and chemistry of Columbia River Basalts and their implications for Mars Exploration Rover Rock Abrasion Tool (RAT) results. Earth Planet. Sci. Lett. 400, 130—144. https://doi.org/10.1016/j.epsl.2014.05.012

Tomkinson, T., Lee, M.R., Mark, D.F., Smith, C.L., 2013. Sequestration of Martian CO2 by mineral carbonation. Nat. Commun. 4, 2662. https://doi.org/10.1038/ncomms3662

Toon, O.B., Pollack, J.B., Ward, W., Burns, J.A., Bilski, K., 1980. The astronomical theory of climatic change on Mars. Icarus 44, 552—607. https://doi.org/10.1016/0019-1035(80)90130-X

Tosca, N.J., Ahmed, I.A.M., Tutolo, B.M., Ashpitel, A., Hurowitz, J.A., 2018. Magnetite authigenesis and the warming of early Mars. Nat. Geosci. 11, 635—639. https://doi.org/10.1038/s41561-018-0203-8

Tosca, N.J., McLennan, S.M., Lindsley, D.H., Schoonen, M.A.A., 2004. Acid-sulfate weathering of synthetic Martian basalt: The acid fog model revisited. J. Geophys. Res. Planets 109. https://doi.org/10.1029/2003JE002218

Treiman, A.H., 1995. A petrographic history of martian meteorite ALH84001: Two shocks and an ancient age. Meteoritics 30, 294—302. https://doi.org/10.1111/j.1945-5100.1995.tb01127.x

Treiman, A.H., Amundsen, H.E.F., Blake, D.F., Bunch, T., 2002. Hydrothermal origin for carbonate globules in Martian meteorite ALH84001: a terrestrial analogue from Spitsbergen (Norway). Earth Planet. Sci. Lett. 204, 323—332. https://doi.org/10.1016/S0012-821X(02)00998-6

Treiman, A.H., Barrett, R.A., Gooding, J.L., 1993. Preterrestrial aqueous alteration of the Lafayette (SNC) meteorite. Meteoritics 28, 86—97. https://doi.org/10.1111/j.1945-5100.1993.tb00251.x

Tucker, M.E., Wright, V.P., 1990. Carbonate Sedimentology. Blackwell Publishing Ltd., Oxford, UK. https://doi.org/10.1002/9781444314175

Turner, S.M.R., Bridges, J.C., Grebby, S., Ehlmann, B.L., 2016. Hydrothermal activity recorded in post Noachian-aged impact craters on Mars. J. Geophys. Res. Planets 121, 608—625. https://doi.org/10.1002/2015JE004989

van Berk, W., Fu, Y., 2011. Reproducing hydrogeochemical conditions triggering the formation of carbonate and phyllosilicate alteration mineral assemblages on Mars (Nili Fossae region). J. Geophys. Res. 116, E10006. https://doi.org/10.1029/2011JE003886

van Berk, W., Fu, Y., Ilger, J.-M., 2012. Reproducing early Martian atmospheric carbon dioxide partial pressure by modeling the formation of Mg-Fe-Ca carbonate identified in the Comanche rock outcrops on Mars: REPRODUCING EARLY MARTIAN pCO2. J. Geophys. Res. Planets 117. https://doi.org/10.1029/2012JE004173

Viviano-Beck, C.E., Seelos, F.P., Murchie, S.L., Kahn, E.G., Seelos, K.D., Taylor, H.W., Taylor, K., Ehlmann, B.L., Wiseman, S.M., Mustard, J.F., Morgan, M.F., 2014. Revised CRISM spectral parameters and summary products based on the currently detected mineral diversity on Mars: REVISED CRISM SUMMARY PRODUCTS. J. Geophys. Res. Planets 119, 1403—1431. https://doi.org/10.1002/2014JE004627

Wadhwa, M., 2008. Redox Conditions on Small Bodies, the Moon and Mars. Rev. Mineral. Geochem. 68, 493—510. https://doi.org/10.2138/rmg.2008.68.17

Wajon, J.E., Ho, G.-E., Murphy, P.J., 1985. Rate of precipitation of ferrous iron and formation of mixed iron-calcium carbonates by naturally occurring carbonate materials. Water Res. 19, 831—837. https://doi.org/10.1016/0043-1354(85)90140-X

Warren, A.O., Kite, E.S., Williams, J. -P., Horgan, B., 2019. Through the Thick and Thin: New Constraints on Mars Paleopressure History 3.8 — 4 Ga from Small Exhumed Craters. J. Geophys. Res. Planets 124, 2793—2818. https://doi.org/10.1029/2019JE006178

Warren, P.H., 1998. Petrologic evidence for low-temperature, possibly flood evaporitic origin of carbonates in the ALH84001 meteorite. J. Geophys. Res. Planets 103, 16759—16773. https://doi.org/10.1029/98JE01544

Warren, P.H., 1987. Mars regolith versus SNC meteorites: Possible evidence for abundant crustal carbonates. Icarus 70, 153—161. https://doi.org/10.1016/0019-1035(87)90082-0

Watters, T.R., McGovern, P.J., Irwin III, R.P., 2007. Hemispheres Apart: The Crustal Dichotomy on Mars. Annu. Rev. Earth Planet. Sci. 35, 621—652. https://doi.org/10.1146/annurev.earth.35.031306.140220

Webster, C.R., Mahaffy, P.R., Flesch, G.J., Niles, P.B., Jones, J.H., Leshin, L.A., Atreya, S.K., Stern, J.C., Christensen, L.E., Owen, T., Franz, H., Pepin, R.O., Steele, A., Team, the M.S., 2013. Isotope Ratios of H, C, and O in CO2 and H2O of the Martian Atmosphere. Science 341, 260—263. https://doi.org/10.1126/science.1237961

Werner, S.C., 2009. The global martian volcanic evolutionary history. Icarus 201, 44—68. https://doi.org/10.1016/j.icarus.2008.12.019

Wersin, P., Charlet, L., Karthein, R., Stumm, W., 1989. From adsorption to precipitation: Sorption of Mn2+ on FeCO3(s). Geochim. Cosmochim. Acta 53, 2787—2796. https://doi.org/10.1016/0016-7037(89)90156-7

Wetzel, R.G., Likens, G.E., 1991. Inorganic Nutrients: Nitrogen, Phosphorus, and Other Nutrients, in: Limnological Analyses. Springer New York, New York, NY, pp. 81—105. https://doi.org/10.1007/978-1-4757-4098-1_7

Wilhelms, D.E., Squyres, S.W., 1984. The martian hemispheric dichotomy may be due to a giant impact. Nature 309, 138—140. https://doi.org/10.1038/309138a0

Williams, J.-P., Nimmo, F., 2004. Thermal evolution of the Martian core: Implications for an early dynamo. Geology 32, 97. https://doi.org/10.1130/G19975.1

Wordsworth, R., Kalugina, Y., Lokshtanov, S., Vigasin, A., Ehlmann, B., Head, J., Sanders, C., Wang, H., 2017. Transient reducing greenhouse warming on early Mars. Geophys. Res. Lett. 44, 2016GL071766. https://doi.org/10.1002/2016GL071766

Wordsworth, R.D., Kerber, L., Pierrehumbert, R.T., Forget, F., Head, J.W., 2015. Comparison of "warm and wet" and "cold and icy" scenarios for early Mars in a 3-D climate model. J. Geophys. Res. Planets 120, 2015JE004787. https://doi.org/10.1002/2015JE004787

Wray, J.J., Murchie, S.L., Bishop, J.L., Ehlmann, B.L., Milliken, R.E., Wilhelm, M.B., Seelos, K.D., Chojnacki, M., 2016. Orbital evidence for more widespread carbonate-bearing rocks on Mars. J. Geophys. Res. Planets 121, 652—677. https://doi.org/10.1002/2015JE004972

Zeebe, R., Wolf-Gladrow, D., 2001. CO2 in Sewater: Equilibrium, Kinetics, Isotopes. Gulf Professional Publishing.

Zolotov, M.Y., Mironenko, M.V., 2007. Timing of acid weathering on Mars: A kinetic-thermodynamic assessment. J. Geophys. Res. 112, E07006. https://doi.org/10.1029/2006JE002882

Chapter 2

Methods

1. Introduction

This chapter follows in their entirety the methods employed to execute the experimental aspects of this project.

In section 2, a Martian rock proxy was devised for the experimental substrate. I will discuss what comprises 'Mars-like' before describing the experimental conditions in full to explain how such conditions are met; this will be covered in section 3, which will describe all the experiments conducted for this part of the research.

The variety of analytical techniques employed will be discussed in section 4, which will cover techniques used for both liquid and solid samples. In section 5, the kinetic calculations used to understand the chemistry behind the experimental results will be described in detail, as these are vital to understanding the conclusions of this work. Lastly, section 6 discusses the set-up and parameters of post-experimental kinetic modelling run in GWB. Section 7 then concludes this chapter.

The results of these experiments are contained within Chapters 3, 4, and 5. The justifications for the study is contained within Chapter 1. The experimental set-up will now be described in detail.

2. Fayalite synthesis

In this section the process of finding and ultimately synthesising the most efficacious mineral to act as a Mars proxy for the experiments is detailed. First described are the acquirement and purity

testing of several samples of naturally occurring fayalite from generous museums around the world. The following section details the process of fayalite synthesis in-house in the Department of Earth Sciences Experimental Petrology lab.

2.1. Natural fayalite samples

Several specimens of natural fayalite, mostly Rockport fayalite prized for its purity, were obtained from around the world by generous curators at the Natural History Museum of London (NHM, sample BM.1985); the Peabody Museum, Yale University (sample MIN.040678), USA; and the Mineralogical & Geological Museum, Harvard University (sample M6MH #136633). When crushed and run on a PANalytical Empyrean Series 2 powder X-Ray diffractometer (XRD) using a Co Kα source, operated at 40 kV and 40 mA, and scanned between 5-65 2Ø, most samples revealed significant impurities rendering them unsuitable for experiments. The facilities to synthesise pure fayalite exist at the University of Oxford within Professor Bernie Wood's Experimental Petrology lab, who kindly allowed use of their equipment.

2.2. Fayalite synthesis

To simulate the Martian crust in contact with varying amounts of water, 100 % pure iron olivine was synthesised (fayalite, Fe_2SiO_4, F_0 = 0 % Mg present) to isolate reactions associated with dissolved Fe^{2+}. Fe-bearing olivine was selected as the substrate as it is the most reactive component of all primary silicates found on Mars: this is thought to be due to unpolymerised tetrahedra within the olivine structure, along with their weak metal–oxygen bonds (Velbel, 1999) and it is a good proxy for the Martian crust given the ubiquity of basalt, of which olivine is a primary constituent mineral. Additionally, fayalite is a very simple mineral, comprising only Fe (the element of interest), Si (which seldom forms relevant reactions to carbonate formation at low temperatures), and O, and such purity of initial substrate has not been implemented before in similar Fe(II)-carbonate formation studies (e.g., Daval et al., 2010; Neubeck et al., 2011; Qafoku et al., 2012).

Figure 1 illustrates the fayalite synthesis process. To synthesise 10 g fayalite, 2.9485 g of silicon (IV) oxide (SiO_2) and 7.8365 g of Fe(III)-oxide (Fe_2O_3), both manufactured by Alfa Aesar at 99.5 % purity, were weighed then heated to 800 ºC to remove unwanted volatiles (note that these values add to 10.785 g; this factors in loss of gaseous oxygen to leave 10 g of solid). The materials were thoroughly homogenised in an agate pestle and mortar, pelletised under 4 tonnes for one minute into 2-3 g individual pellets, then placed in an alumina crucible and heated in a furnace at 1080 ºC for 3 hours. Temperatures at 1080 ºC were selected to be as high as possible to enhance reaction kinetics, but no more than ~1200 ºC where fayalite melts. To prevent the formation of impurities such as wüstite or magnetite, the chosen oxygen fugacity at this temperature is directly in between the iron-wüstite and wüstite-magnetite stability fields (Figure 2). This translates to using a gas mixture of 84 mL/s CO and 114 mL/s CO_2 to reduce Fe(III) and enable the full reaction of SiO_2 and Fe_2O_3 into fayalite, Fe_2SiO_4.

The resulting material was crushed again, and the process repeated 3 times before analysis with an XRD was undertaken to check the purity. The resulting graph displays a perfect overlay of the synthesised fayalite with the XRD's computed pure fayalite signature. The PANalytical XRD used (as described in Chapter 1, section 2.1) has a <1 % detection limit; hence the fayalite produced is >99 % pure, which is more than satisfactory for the experiments that will shortly be described.

For later experiments the mineral forsterite was required. Forsterite is the magnesium-rich end member of olivine (F_{100} = 100 % Mg-rich olivine), and its addition alongside its Fe-rich counterpart during reactions was anticipated to release anions to uptake available H^+, hence raising the pH to Fe(II)-carbonate-relevant levels. Forsterite was in the form of natural gem-grade peridot (Figure 3; a), which was hand-separated from impurities (Figure 3; b) then powdered (Figure 3; c) and consisted of olive-green, centimetre-sized monocrystals (De Hoog et al., 2010). The grains most free of dark impurities (likely spinels) were selected from the original batch and hand-crushed within an agate pestle and mortar. To monitor the purity of the white powder before the experiment, we performed a precise mineralogical and chemical characterisation using powder X-

ray diffraction. The XRD pattern showed the powder was shown to be ferroan forsterite with one unidentified peak (1.6187). Iron content when analysed with EDS (for more details see Section on SEM/EDS was minor ($Fo_{\sim 95}$). Increasing the complexity of the system through the addition of another mineral increases the realism the experiments while agreeing with known Martian mineralogy, where olivine is found in both its forsteritic and fayalitic members (Bridges et al., 2015).

With the fayalite successfully synthesised, which was achieved in November 2017 after several months' work, and the forsterite obtained to satisfactory purity, the experimental phase of the DPhil could begin, as will now be detailed. 'Satisfactory purity' in this instance was considered when no XRD peaks besides forsterite were obtained.

3. Experimental methods

Experimental geochemistry comprises the bulk of this thesis. The experimental set-up will now be described.

3.1. The anoxic glove box

Mars has a chemically insignificant amount of O_2 in its atmosphere both presently (Lillis et al., 2017) and likely in its deep past (Haberle et al., 2017). This is due to the gas' low escape velocity commensurate with Mars' low mass (Lammer et al., 2003) as well as the lack of known O_2-producing biological processes. While oxygen is found in Mars in the form of oxidised minerals, particularly at its surface, this is owing to photo-oxidation of H_2O or, more minorly, CO_2 (Heard and Kite, 2020), and is not due to the presence of large amounts of free oxygen. Hence, to fully simulate the interaction between water and rock in contact with such an atmosphere, a sealed box with a manipulatable atmosphere is vital that may ensure strictly anoxic conditions during experimentation.

All experiments were conducted within a Coy polymer anoxic glovebox where a mix of 4 % H_2/96 % N_2 gas is maintained via a Pd catalyst. O_2 is scrubbed from the system by the Pd continuously reacting trace O_2 with available H_2 in the chamber to produce H_2O, which is removed from the system via adsorption onto an anhydrous $CaSO_4$ desiccant. Figure 3 shows the glove box set-up featuring the features described in this section. Ambient atmosphere was kept at a low relative humidity (<20 %). The gas composition of the anoxic chamber is continuously monitored with a Coy gas analyser and the atmosphere maintained at <1 ppm $O_{2(g)}$ for the duration of all experiments, sample preparation, and analysis. An airlock to one end of the chamber is used for bringing in/taking out any items without compromising the atmospheric integrity of the glove box, therefore enabling contents to be exchanged during experiments without jeopardising the anoxic conditions.

3.2. The experimental set-up

All experiments were conducted at 25 ºC (± 1.5 ºC) within 0.172 L Nalgene reaction vessels sealed with 1 cm butyl-rubber septum caps, triple-wrapped in Al-foil to prevent photo-oxidation (Braterman et al., 1984). During experiments, these vessels were continuously shaken at 260 revs per minute upon an orbital shaker to expose the maximum surface area of fayalite powder within the vessels to reaction fluids, and to enable an overturn of fresh surfaces, catalysing any reaction. pH and Eh were data-logged using a VWR epoxy/gel pH electrode (model no. SJ 113), and an Oakton Instruments platinum band platinum oxidation-reduction potential (ORP) electrode (model no. WD-35805-13). The pH electrode was calibrated with standard buffer solutions for slope correction (pH 4 and 7) and the ORP electrode using ZoBell's solution, which is an equi-molar solution of Fe^{2+} and Fe^{3+} stabilised in 0.1 molal KCl, where Fe is stabilised by aqueous complexing with dissolved cyanide (Nordstrom, 1977). Based on the periodic measurement of calibrant standards, accuracy for pH was ± 0.05 mV (1σ) while for Eh this remained constant.

3.2.1. The aqueous solution

The basis for all aqueous solutions used during experimentation was deionised water (resistivity 18.2 MΩ·cm) first purged of dissolved O_2 by bubbling O_2-free N_2 gas through the solution for at least 45 minutes (Butler et al., 1994) before transfer to the glovebox. The water was then stirred for 1 hour in the anoxic atmosphere and left for at least 24 hours to allow any residual O_2 to escape and be removed by catalysts and desiccants.

To alter the starting pH, sulphuric acid (H_2SO_4) was introduced. This acid was selected based on the abundance of sulphuric compounds and derivatives across Mars resulting from its volcanic history. The exact amounts of the acid to add were calculated to precision on the basis of using 50 % H_2SO_4, which has a density of 1.3911 g/mL, which would then be added to the deionised, deoxygenated water to produce the intended pH for each experiment. Several stock solutions were made by the following method to produce quantities of solutions with pHs of exactly 2, 3, 4, 5, and 6. Table 1 shows the resulting amount of H_2SO_4 to add to produce each desired pH. The low pHs were chosen following computer modelling via *The Geochemist's Workbench* (GWB; Bethke, 2017) that estimated significantly faster rates of rock dissolution under such conditions (not shown in figures), but also because meteoric water on Mars is expected to be low pH due to contact with high CO_2 levels and/or the input of volcanic volatiles such as H_2SO_4 or HCl (e.g., Tosca et al., 2008).

3.2.2. Experimental variations: Rock:water ratio

Rock:water ratio is an additional parameter explored in these experiments. This is because the concentration of available reactant ions in solution to interact with substrate surface area affects the probability of a reaction occurring, and has been explored for related Mars analogue research (e.g., Baker et al., 2000; Hurowitz et al., 2006; Sætre et al., 2019). Documented instances of Fe(II)-carbonate either within Martian meteorites (e.g., Bridges et al., 2001; Halevy et al., 2011; Bridges et al., 2019) or from space (e.g., Ehlmann et al., 2008; Michalski and Niles, 2010; Wray et al., 2016) group carbonate formation as within or by one of three categories: 1) low-temperature

hydrothermalism; 2) subsurface brines, or 3) in-situ carbonation. These all occur within rock pore space, as opposed to subaerially such as within open expanses of water such as lakes. Whether the low water-rock observation is due to the low rock:water ratio consistent across such environments or some additional linking factor is uncertain, and is worth investigation.

Rock:water ratio in the experiments varied from 1:1 to 1:500. This range was chosen to reflect aquifer-type environments where there is little water in relation to host rock, and lacustrine-type environments where there is a large amount of water per host rock. The effect of rock:water ratio was studied first in a non-CO_2 environment in experiments 180123, 180203, and 180303 at ratios of 1:100 and 1:500. Subsequent experiments, unless otherwise specified, were conducted at the 1:500 ratio after little variation in pH and Eh was observed between the 1:100 and 1:500 experiments. Specifically low rock:water ratio experiments at far-lower ratios of 1:1 and 1:10 were conducted in the cases of 181004, 181205, and 180418.

3.2.3. Experimental variations: CO_2

Experiments were run initially without dissolved CO_2 present to understand the basic chemistry of waters out of equilibrium with the atmosphere. However, for experiments that were to simulate contact with varying levels of atmospheric CO_2, the gas was dissolved within the H_2SO_4 and water solutions through the addition of sodium bicarbonate ($NaHCO_3$) to produce the equivalent of 0.1, 0.5, and 1.0 bars of a CO_2 atmosphere. The calculations involved with this process will now be discussed.

First, a 0.1 mol/kg of $NaHCO_3$ stock solution was prepared by adding 2.52 g $NaHCO_3$ to 300 mL of deionised, deoxygenated water. Unlike non-CO_2 experiments, which used 125 mL of solution, for experiments containing CO_2 no head space at the top of the beakers was necessary to minimise outgassing, thus the exact volume of the beakers — 0.172 mL — was used. For beakers of this volume, Table 2 contains the exact amounts of the stock solution that were pipetted into each beaker to produce equivalent CO_2 fugacities of 0.1, 0.5, and 1.0. These were calculated in the GWB programme React using the premise that the carbonate system can be solved if two

of any six fundamental parameters of the carbonate system are determined (Deffeyes, 1965; Park, 1969). In this case, these are pH and pCO_2. The equations required for calculating the other four factors for use in GWB are found in Appendix 3 and are derived from Zeebe and Wolf-Gladrow (2001).

Once the total HCO_3^- required had been calculated, the exact amount of 0.1 bar stock solution to add to each experiment to produce the desired fugacity per set pH was calculated by multiplying the HCO_3^- by the total beaker volume (0.172 L, used in μL as 1,720 in this calculation) to produce the results in the far-right column (Table 2). The sulphur column, while not immediately relevant to the experiments' beginning, comes in later during solution analysis.

Once the exact amount of stock solution was added, the beakers were topped up to their brims with deionised water. As CO_2 outgassing was visible already as the growth of air bubbles on the beakers' sides, especially with 1.0 bar experiments, the correctly-weighed fayalite (and, for certain experiments, forsterite) was at this point added immediately, the beakers sealed, and the orbital shaker upon which they were set begun its cycle. The experiments themselves, their various parameters, and their purpose will now be described in detail.

3.3. The experiments

For the first section of the project, involving fayalite ± forsterite substrates, 91 experiments (including the terminated 170903) were conducted. A table summarising these experiments into 16 groups, complete with the duration, pHs, rock:water ratio, CO_2 levels, and any other notable parameters used in each experiment, is shown in Table 3. For the second part of the project, powdered Columbia River Basalt sediment was used across of 36 experiments (including the failed 190418). A complete table complete with the duration, pHs, rock:water ratio, CO_2 levels, and any other notable parameters used in each experiment is shown in Table 4. Fewer experiments were conducted for the CRB series because the exact parameters to be explored had been better

constrained by this stage of the project, and fewer repeats needed to be conducted as skills in experimental technique improved.

Lastly, 34 experiments (including the failed 191128 and 191129) at 75 °C within a furnace enclosed within the glove box were conducted to investigate the effect of higher temperatures upon both the fayalite/forsterite and CRB sets of experiments. In this category, experiments that yielded the most important results at room temperature (25 °C) were repeated at 75 °C. Table 5 lists the experiments conducted in this category and their notable parameters.

All of the experiments henceforth discussed are also described in detail individually in Appendix 1.

3.3.1. Fayalite ± Forsterite Experiments

Five groups of experiments were conducted for the fayalite ± forsterite sub-set of experiments:

1) No CO_2 + fayalite experiments. 0.25 g of synthetic fayalite was reacted with 50 mL (ratio: 1:200) and 125 mL (ratio: 1:500) at starter pHs of 2, 4, and 6. These are experiments where no CO_2 was added as a control to understand the chemistry under zero-CO_2 conditions. The effect of rock:water ratio on mineral dissolution was also explored here. As previously mentioned, experiments begun at pH 6 experienced no notable results and so its use was discontinued. 180123 was the longest experiment run in this category at 8 days, which experienced the bulk of its activity within the first day. Experiment 180203 was devised to sample on the hour every hour for the first ten hours of the experiment under identical conditions to observe how the reaction changed over this active period. 180310 was a repeat of 180203.

2) CO_2 + fayalite experiments under high water-rock conditions. 0.344 g of synthetic fayalite was reacted with 0.172 L (ratio of 1:500) of H_2SO_4 from starter pHs of 2 and 4 for up to 80 days. For each starter pH was a CO_2 fugacity of 0.1, 0.5, and 1.0 bars. 180313 and 180406 were identical runs designed to test the reproducibility of their results, as were 181029 Fa and 190423 Fa.

3) CO_2 + fayalite + forsterite experiments. Identical to (2), but with 0.172 g of fayalite and 0.172 g of forsterite employed (rock:water ratio of 1:500). Experiment 180612 lasted for 15 days, but as pH for several sub-experiments dropped in a manner unpredicted and unusual compared to past experiments, this was repeated as 180829 over 12 days, which behaved more akin to these previous experiments and suggested a still-unknown anomaly in the 180612 set. 180628 was the first experiment run for 60 days and revealed a remarkable range of results that will be discussed in subsequent chapters, but which included significantly elevated pH, dissolved Fe^{2+} content, and — accordingly — Fe(II)-carbonate saturation states. As a result, experiments subsequent to 180628 were run for at least 60 days. 180628 was itself repeated, as its results so interesting, to test the reproducibility of these results, in experiment 181029 Fo, which ran for 80 days, and 190423 Fo, which ran for 85 days.

4) CO_2 + fayalite ± forsterite experiments under low water-rock conditions. 2 g of synthetic fayalite (also 50:50 Fa-Fo, 1 g Fa, 1 g Fo) was reacted with 2 mL (ratio of 1:1) and 20 mL (ratio of 1:10) of H_2SO_4 from starter pHs of 2 and 4. All experiments had the equivalent of 1 bar of CO_2 dissolved within the fluids. Due to the minute amounts of fluids involved, and the need to eliminate beaker head space to discourage outgassing, a new experimental set-up for these sets of experiments was devised. Rather than beakers, large gas-tight syringes were employed that were sealed at their ends with adjustable valves. Once the solutions and their solid substrates were added to the open syringe, it was sealed shut by holding the syringe nozzle-end upwards with the valve open, so that air could escape as the syringe was slowly closed, while enabling that no fluid or substrate was lost, as this remained on the floor of the closing syringe. When the last air bubble was removed the valves were sealed, the syringe thoroughly shaken to homogenise the material within, and left for 60 days. 181004 was conducted with pure fayalite, while 181205 was both fayalite and forsterite.

5) High Fa-Fo ratio experiments. For experiment 190121 the high Fa-Fo ratio of 20:80 was used to produce more free ions in solution, modelled via GWB to increase the pH and induce

conditions more favourable for the formation of Fe(II)-carbonate. As previously discussed, the additional of forsterite also increases the complexity of the system through the addition of another mineral while also increasing the realism the experiments by agreeing known Martian mineralogy, where olivine is found in both its forsteritic and fayalitic members (e.g., Bridges et al., 2015).

Solution samples (each 1 % of the solution) were withdrawn via 0.1 μm syringes through the gas-tight septum caps of the reaction vessels, with the exception being the low rock:water ratio experiments, which contained too little fluid to sample and so were left untouched until the experiments' ends.

3.3.2. Columbia River Basalt Experiments

Experiments were run using powdered Columbia River Basalt in two particle sizes: fine and coarse. Two categories of experiments were conducted for the CRB experiments:

1) CRB experiments run with both fine and coarse CRB at high rock:water ratio. These were run either for 85 days, as with 190414: 0.344 g of fine or coarse CRB was reacted with 0.172 L (ratio of 1:500) of H_2SO_4 from starter pHs of 2 and 4 for up to 80 days. For each starter pH was a CO_2 fugacity of 0.5 or 1.0 bars. 0.1 bar experiments were neglected in the CRB experiments due to only minor differences in results between 0.1 and 0.5 when analysed. Like the fayalite ± forsterite experiments, the experimental set-up involved lining square beakers of 0.172 L capacity atop an orbital shaker. The beakers had septum caps for the extraction of fluids via syringe. These experiments were also run short-term. These were experiments sampled daily over ten days to capture the more rapid kinetics that occur during an experiment's immediate onset. Like the long-term CRB experiments, these used a rock:water ratio of 1:500 in an identical set-up atop an orbital shaker with a septum cap for solution extraction.

2) CRB experiments under low rock:water ratio. This includes experiments 190418, and 190812. 2 g of CRB was reacted with 2 mL (ratio of 1:1) and 20 mL (ratio of 1:10) of H_2SO_4 from starter pHs of 2 and 4. All experiments had the equivalent of 1.0 bar of CO_2 dissolved within

the fluids. These experiments were also run in 50 mL syringes as with the fayalite ± forsterite low water-rock equivalents.

These experiments contained too little fluid for regular sampling and were left untouched until the experiments' ends. For 1:1 experiments, insufficient fluids could be obtained for sampling, but for 1:10 these were obtained.

3.3.3. The 75 °C experiments

Lastly, experiments were run that repeated those of the fayalite/forsterite and CRB classes, but at 75 °C rather than the room temperature used previously (~25 °C). This was obtained by situating a small furnace inside the glove boxes and repeating the same experimental set-up as was employed previously for selected experiments. Four categories of experiment were conducted for this section:

1) Fayalite-bearing experiments as a repeat of 180313, 180406, 181029 Fa, and 190423 Fa but at elevated temperatures. This includes 191028, which ran for 10 days. As with low temperature fayalite-bearing experiments, 0.344 g of fayalite was reacted with 0.172 L (ratio of 1:500) of H_2SO_4 from starter pHs of 2 and 4. For each starter pH was a CO_2 fugacity of 0.1, 0.5, or 1.0 bars. For 191028, two experiments, one begun at pH 2, the other at pH 4, ran without any CO_2 present to simulate 180123.

2) Fayalite- and forsterite-bearing experiments as a repeat of 180612, 180628, 180829, 181029 Fo, and 190423 Fo but at elevated temperatures. This includes 191107, which ran for 10 days. 0.172 g of fayalite and 0.172 g of forsterite was reacted with 0.172 L (ratio of 1:500) of H_2SO_4 from starter pHs of 2 and 4. For each starter pH was a CO_2 fugacity of 0.1, 0.5, or 1.0 bars.

3) Low rock:water ratio experiments using fayalite, and fayalite/forsterite. This includes experiments 191128 and 191129, which both failed due to heat-related rupturing. 2 g of fayalite, fine CRB, coarse CRB, or 1 g fayalite and 1 g forsterite was reacted with 2 mL (ratio of

1:1) and 20 mL (ratio of 1:10) of H_2SO_4 from starter pHs of 2 and 4. All experiments had the equivalent of 1 bar of CO_2 dissolved within the fluids.

4) CRB-bearing experiments at 1:500 rock:water ratio. This includes 191118. 0.344 g of fine or coarse CRB was reacted with 0.172 L (ratio of 1:500) of H_2SO_4 from starter pHs of 2 and 4 for 10 days. For each starter pH was a CO_2 fugacity of 0.5 or 1.0 bars.

All experiments are described in detail in Appendix 1.

3.4. The solution sampling procedure

The sampling procedure was as follows: a 0.1 μm MicroLance needle was attached to a syringe and penetrated into the septum cap of the desired experiment. No more than 1.72 mL was withdrawn (1 % of the solution). The needle was removed, sealed in a plastic cap, and safely disposed of in a waste bin awaiting incineration. A syringe-filter at 0.22 μm thickness was attached to the nozzle of the syringe and the solution pressed through the filter into a 15 mL polypropylene sample tube (used in all experiments unless otherwise stated), into which a pH and Eh probe were placed to gauge fluid properties immediately upon its removal from the experiment. A 0.45 μm filter fails to remove any iron colloids (Kennedy et al., 1974), but a 0.22 μm filter is usually sufficient.

The results — including the date and time of the sample — were recorded in a spreadsheet.

Once analysed via pH and Eh probes, the solution samples were then added to a waiting sample tube already holding 14 mL 5 % HNO_3 and sealed off at the same time. This acid prevents oxidation or other reactions that are rapid at neutral pH that could cause precipitates to adhere to the vials if not acidified. The samples were each given a unique name. The tube into which the sample was placed was already labelled with this unique name and was, prior to having nitric acid added, weighed. After weighing when empty, the 14 mL 5 % HNO_3 was pipetted into the tubes, which were then re-weighed. Vials were then re-weighed following the addition of the <1.72 mL sample. By adding the experiment sample immediately to weak acid, the precipitation of any

mineral out of solution could be precluded by keeping the solution in a heightened state of oxidation and pH. Upon the addition of the sample to the acid, the vials were sealed within the glove box, weighed outside without being opened, and stored within sealed sandwich bags within a refrigerator maintained at 2 ºC.

In total, 10 solution samples (10 % of the total solution) were collected from each experiment to monitor solution changes occurring during mineral nucleation and growth stages. These samples were sent for inductively coupled plasma optical emission spectrometry (ICP-OES) and inductively coupled plasma mass spectrometry (ICP-MS) analysis, which is described in full in section 4.1.1.

This same process was also run for the low rock:water ratio experiments, though only at the experiments' terminations when the gas-tight syringes containing these experiments were opened. While no solution was able to be extracted from the 1:1 ratio experiments due to the mud-like nature of the solid-water mixture, it was possible to perform the usual extraction technique of obtaining 1.72 mL from the 1:10 ratio experiments and thus obtain ICP-OES/MS data for one datapoint in these experiments.

3.5. The solid sampling procedure

Only at an experiment's termination could solids be extracted from the solution. The means by which this was done will now be discussed. Unless otherwise stated, all procedures took place within the anoxic environment of the glove box.

Following the extraction of the last solution sample, the beakers were each opened for the first time since the inception of the experiments. The contents were drained into a cone that directed the fluids to a 0.22 μm filter atop a vacuum pump, where the fluids were drawn through the membrane, leaving a solid residue behind. The filter paper was peeled off the top of the holder when all the fluid had been disposed of, and the paper placed into a petri dish on a dark shelf within the glove box. The lid of the petri dish was placed almost entirely over the paper but was

not sealed entirely to permit dehydration of the paper for several days; the lid's coverage and the close proximity of the shelf's roof, however, would permit only minute airborne contaminants to enter the dish.

Once the paper was dry, the solid residue upon it was carefully scraped into labelled glass vials and stored within the glove box, where they remained free from oxygen, water, or other substances that might alter their mineralogy in any way.

4. Analytical methods

In this section, the analytical methods employed following or during the course of the experiments described in the previous section will be discussed in detail. Solution samples and solid samples will be discussed separately; the former shall be described first.

4.1. Solution sample analysis

Following the careful storage of extracted solution samples, these samples, from experiments 180123 to 191029 Fo were packaged and sent to the Scottish University Environmental Research Centre at the University of Glasgow for elemental analysis via solution-phase inductively coupled optical emission spectrometry (ICP-OES). The elements of interest for analysis were Fe, Si, and, where available, Mg. The analysis was conducted by Gillian McKinnon and was returned in a spreadsheet as raw mg/L. From this mmol/kg could be extracted following some calculations, which were calculated for each element in its own individual spreadsheet. The limit of detection for Fe and Si was 0.01 mg/L; this was 1 mg/L for Mg. Analytical uncertainty for ICP-OES was on average ± 0.05 mg/L (1σ) for all data.

4.1.1. Saturation state calculations

In GWB, in the React programme, two factors were configured before beginning. Precipitation was inhibited, as this calculation is interested in solution chemistry; and the Ksp for

greenalite under 25 ºC was changed to 27.6 to reflect the experimental data of Tosca et al. (2016). Experimental elemental solution data, as obtained from ICP-OES/MS, was added to the model at 25 ºC alongside the pH measurement at the time of the sample's extraction. In experiments involving CO_2, CO_2(g) was added and switched to the soluble ion HCO_3^-, with the experiment's fugacity (0.1-1.0) used.

Once run, only minerals relevant to the study were noted. These included: fayalite and forsterite, the two initial substrates; the Fe-silicate greenalite and the oxide $Fe(OH)_2$; amorphous silica, a common by-product of silicate reactions; and siderite and magnesite, Fe- and Mg-carbonates respectively. For non-Fo-bearing experiments, forsterite and magnesite were excluded.

4.1.2. ICP-MS measurements

Owing to an inability of the Glasgow research centre to continue handling solution samples, ICP-MS was conducted in-house for experiments from 181205 onwards, including all CRB and high temperature experiments. Samples stored within 4 % HNO_3 acid in a ~1:15 ratio were further diluted in ultra-clean 2 % HNO_3 acid within the clean laboratories of the Department of Earth Sciences, University of Oxford, at a 1:100 ratio. These samples were obtained with the assistance of Phil Holdship. With each dilution the samples were weighed to keep track of the volume of sample within solution. A PerkinElmer NexION 350D spectrometer was used and produced results that appeared to be in good agreement with the ICP-OES data. This unfortunately could only be qualitatively gauged, and was deemed satisfactory based on the data being within the same order of magnitude at roughly similar amounts.

4.2. Solid sample analyses

Solids that remained at the end of experiments were placed into careful storage. Several high resolution, destructive analytical techniques were used to understand their mineralogy, including XRD, SEM/EDS, and FTIR.

4.2.1. X-Ray Diffractometry

The Department of Earth Sciences at the University of Oxford has its own powder X-Ray Diffractometer (XRD), a PANalytical Empyrean Series 2 with a Co $K_{\alpha 1}$ source operated at 40 kV and 40 mA, within which samples were scanned between 5 and 80 degrees 2Θ. All samples were processed with the PANalytical analytical software, which has a detection limit of broadly 1 wt. % of the crystalline sample. This is known to vary depending on the mineral type under investigation: for example, the detection limits of clays compared to oxides are known to differ. Additionally, the signal to noise ratio is known to be affected by clay type in particular, with difficulties arising in distinguishing these from similar clay types (Warren and Ransom, 1992). Figure 5 visualises the preparation from sample to X-ray diffractogram.

Using the equipment outlined in Figure 5 (a), ~0.005 g of sample powder was loaded onto a single crystal silicon sample holder (b) and wrapped with Kapton film (c) within the glovebox to minimise oxidation during analysis. The prepared samples were only removed from the glove box in time for the analysis to occur; accordingly, the powders were only exposed to oxygen for ~30 minutes. In (e) the sample can be seen awaiting analysis within the XRD (f). Ms. Katherine Clayton, the XRD technician, ran the samples in batches of two so that no samples were left waiting exposed to oxygen any longer than necessary. The XRD has a sensitivity of <1 % of the sample, therefore such isolated unidentified peaks represent only the slightest fraction of the sample.

The produced X-ray diffractograms had their background patterns subtracted after removing several analyses performed on blank sample holders covered with Kapton film.

4.2.2. Scanning Electron Microscopy and Energy Dispersive X-Ray Spectroscopy

Scanning electron microscopy (SEM) was performed in-house using a FEI Quanta 650 FEG to characterise the morphology of solid materials both before and after experimentation, and to identify any minor phases below XRD detection levels. A small amount of the powered solid was mounted on a sticky pure-carbon pad attached to a steel stub. This was completed within the glovebox, then transferred immediately into the evacuated SEM chamber to ensure minimal

contact with oxygen (~10 mins). The material was neither carbon- nor gold-coated with the intention of performing Electron Dispersal Spectroscopy (EDS) to identify the location of particular elements, but this proved ineffective due to: backscattering from carbon stub and the inability to distinguish C as a residue from the $NaHCO_3$ solution or as within the mineral structure. Samples were initially run at high vacuum, ~$1e^{-4}$ to ~$6e^{-4}$ Pa, with the beam was switched on to 15 kV with an Everhart-Thornley Detector (ETD), which is a secondary electron and back-scattered electron detector commonly employed in SEMs (Everhart and Thornley, 1960). However, as this eventually proved to produce too much charging due to the lack of coating, the SEM was for later samples switched to low-vacuum mode (60 Pa), lower voltage (10 mV), and a Large Field low-vacuum secondary electron Detector (LFD) was used. The emission current used was 294 μA; chamber pressure was $1.32e^{-3}$ Pa; gun pressure was $1.40e^{7}$ Pa; voltage was 10 mV; and this was performed under high vacuum.

For EDS, Figure 6 shows the typical images returned. While interesting in themselves, they cannot be used to accurately detect the presence of carbonate minerals because, as visible in (c), carbon is clearly visible homogeneously permeating the image, meaning this is likely background-induced scattering and cannot be certain to represent the presence of C within the mineral structure. For samples as basic as those employed in this section of research, namely involving only Fe, Si, O, and sometimes Mg, EDS only offer limited information because in this research no new minerals were produced, and so fayalite (and, if present, forsterite) are the only minerals present. In Figure 6 this typical example shows that the only distinctive features shown in EDS are due to topography, particularly prevalent in (f) for Fe. Therefore, while EDS was conducted for several samples of interest, this method does not form a crucial aspect of the DPhil research.

For later analyses, where nanoscale precipitates appeared to have formed upon host minerals, point EDS was employed. This proved of limited use, given the minute scale of the particles, as the point analysed was larger than the precipitates. In the absence of alternative

techniques to better elucidate its composition, however, EDS was useful in identifying basic composition to a limited degree.

4.2.3. Fourier Transform Infrared Spectroscopy

Fourier transform infrared spectroscopy (FT-IR) was the highest-resolution technique used and was deployed as a means of searching for nano-particulates of products below the detection limits of both XRD and SEM. Analyses were performed using a PerkinElmer Frontier mid-IR spectrometer on powdered solid samples mixed with KBr powder at a KBr-sample ratio of ~1:200, which were ground together and pelletised at 7 tonnes and analysed within 20 minutes of exposure to air to prevent oxidation. Measurements were collected from 400 to 4800 cm^{-1} at 1 cm^{-1}. Pellets were reanalysed after heating for 24 hours at 150 °C to remove any adsorbed H_2O.

4.2.4. Brunauer-Emmett-Teller theory

To obtain a precise average grain size for the powdered fayalite, forsterite, and fine/coarse-grained CRB used in the experiments, Brunauer-Emmett-Teller theory (BET) was applied for analysis of gas adsorption-desorption (Brunauer et al., 1938; Lowell and Shields, 1991). This was run using the Micromeritics 3flex facilities at the Chemistry Research Laboratory, University of Oxford. BET is a method where the physical adsorption of gas molecules on a solid surface is used to measure the surface area of materials, whereby the decrease in chamber gaseous pressure corresponds to surface area. For this thesis, nitrogen was the gaseous adsorbate.

5. Kinetic calculations

Understanding the kinetics that drive chemical changes allows for discrepancies between expected and observed results to be quantified and explained. Chapter 3, 4, and 5, and Appendix 2 outline the experimental results derived from the methods described in this chapter, and these deviated significantly from expected based on similar experiments conducted by other researchers. Either

our understanding of the kinetic system was flawed and something previously unrecorded was occurring within the experiments, or something had gone awry within the experiments themselves.

Within this research several experiments under very similar conditions were conducted, several even being identical repeats, and all showed this unexpected behaviour. A flaw in the experimental set-up seems unlikely to persevere over months and in different equipment. This section is a study of the kinetics behind the reactions that took place during the experiments to understand what drove the observed results.

5.1. Rate of precipitation

A kinetic rate equation calculates the rate of precipitation that should in theory have occurred over a length of time under certain conditions. It is written as:

$$R_{sidprec} = K_{sidprec}(\Omega_{siderite} - 1)^n \qquad \text{(eq. 5.1.1.)}$$

where $R_{sidprec}$ is the rate of precipitation of the mineral in question, in this case Fe(II)-carbonate ($FeCO_3$). $K_{sidprec}$ is the reaction rate coefficient (or reaction rate constant) for Fe(II)-carbonate, which quantifies the rate of the reaction; the value inputted here is 0.05 $year^{-1}$ (mmol per kilogram of solution per year), which is the slowest kinetic rate of Fe(II)-carbonate precipitation published in the literature, by Hunter et al. (1998), and therefore represents an absolute minimum Fe(II)-carbonate precipitation rate. There are drawbacks to using this value rather than others given in Table 6: the number is computed via a reactive transport model that was conducted under oxygenated conditions mediated by bacteria — conditions that do not represent Mars. Two alternative rate constants were considered (see Table 6) but ultimately not used as they, too, are also unsuited to application to Mars: both involve bacterial mediation, and one (Liu et al., 2001) is based off the oxygenated model of Hunter et al. (1998), while the other (Matsunaga et al., 1991)

conducts its experiments aerobically. As we did not produce solid precipitates in our experiments, therefore cannot calculate our own rate of precipitation, the Hunter et al. (1998) rates were used regardless of the aforementioned flaws because all these rate constants were flawed; the positive to using the Hunter value is that it offers a lower rate by an order of magnitude than the Matsunaga et al. (1991) value, and the Liu et al. (2001) value is itself based upon the work of Hunter et al. (1998).

$\Omega_{siderite}$ is the Fe(II)-carbonate saturation state. It is represented by:

$$\Omega_{siderite} = \frac{Fe^{2+} \times CO_3^{2-}}{K_{sp}} \qquad \text{(eq. 5.1.)}$$

where Fe^{2+} is obtained from ICP-OES results; CO_3^{2-} is derived from the calculations in Appendix 3; and K_{sp} is the solubility product of Fe(II)-carbonate, which is defined, in the case of dissolution of a solid by dissociation, as when equilibrium between a solid and its ions in solution is reached.

5.2. The Debye-Hückel B-dot Equation

Activity is a thermodynamic quantity and dimensionless measure of the effective concentration of a species within a solution. Ions in solution interact with other molecules and behave chemically as though they are at a lower concentration than they are, or are measured, and this effective concentration, or the concentration that is available for a reaction, is called activity. Activity is calculated by:

$$activity = \gamma_i c_i$$

(eq. 5.2.1.)

whereby γ_i is activity coefficient (which is dependent on ionic strength and the ionic properties of the component under consideration), and and c_i is concentration in moles/kg. Alongside activity, solution pH is also key in calculating the saturation state of silicate minerals where H^+ occurs in the precipitation reaction, or for minerals that are pH-dependent. These together are used to calculate the thermodynamic tendency of a mineral remaining in dissolved form in solution or precipitating from it.

An appropriate ion activity coefficient model must be used to calculate activity, and the Debye-Hückel model (Debye and Hückel, 1923) was here used owing to this being a widely adopted model appropriate for the ionic strength of the solutions seen in these experiments. The Debye-Hückel model uses the B-dot equation, derived from the Helgeson-Kirkham-Flower model (Helgeson et al., 1981; Helgeson and Kirkham, 1974), which describes the activity coefficient as calculated by:

$$log\gamma_i = -\frac{Az_i^2\sqrt{\bar{I}}}{1 + B\mathring{a}_i\sqrt{\bar{I}}} + B_{dot}\bar{I}$$

(eq 5.2.2.)

where A and B are the molal Debye-Hückel coefficients, z_i is the ith ion's valency, $\mathring{a}_i$ is mean distance of the closest approach of the ith ion (the ion size parameter), *B-dot* is a fitting parameter that is temperature-dependent, and $\bar{I}$ is the measured ionic strength of the solution.

6. Post-experiment geochemical modelling

The experiments conducted in this thesis suggested environmental parameters best conductive to the formation of Fe(II)-carbonates, but they were run for a maximum of 85 days. To test the merit of these results under conditions better simulating a more complex environment of competing

minerals and longer timescales, the experimental conditions and others were modelled in the software *The Geochemist's Workbench* (GWB; Bethke, 2017) with the aim of exploring the factors that affect Fe(II)-carbonate precipitation. This section describes the model set-up.

6.1. The model

In the model, Table 7 outlines the default parameters set up and their dimensions/units, which comprises: H_2O, H^+, Fe^{2+}, SiO_2, Mg^{2+}, Cl^-, SO_4^{2-}, $CO_{2(g)} \leftrightarrows HCO_3^-$, time, temperature, reactant time (proportional to rock:water ratio), surface area, rate constant, fayalite, forsterite, and the 'fixed' or 'unfixed' nature of the CO_2 present, whereby CO_2 may leave the system in an unfixed scenario. The model was run with these dimensions and was considered the *default*, or standard base-level, by which selected parameters could then be changed to simulate how this environment would respond to differing conditions. One parameter would then be changed at a time to investigate its effects upon the system.

Five key parameters were explored: varying rock:water ratio, particulate surface area, dissolved CO_2 levels, CO_2 level stability, and time. Table 8 outlines the default and the change that was made to this parameter.

For rock:water ratio, a default value of 1:500 was used to simulate high rock:water ratio environments where there is plentiful throughflow of water. This also best simulated the majority of the experiments in this thesis. A low rock:water ratio of 1:1 was chosen to simulate water-scarce environments. Changes to rock:water ratio were achieved by altering the parameter 'reactant times' in the 'reactant' tab.

Varying particulate surface area was achieved by altering the surface area section in the reactant tab. This was 1000 cm^2/g in the default position, as used in the model of Tosca et al. (2018) based on observations from the MSL *Curiosity* rover, which specifically simulated the surface area of Rocknest Basalt (Bish et al., 2013; Blake et al., 2013). The other value for this parameter

used was 100 cm^2/g based on the data of (Brantley and Mellott, 2000) for the lowest surface area identified for San Carlos olivine (223-3550 cm^2/g).

Simulating dissolved CO_2 levels was achieved by modelling an exchange mechanism between CO_2 gas and CO_2 dissolved within an aqueous solution (HCO_3^-) in the basis tab. 1.0 bar was used as default, simulating the maximum value used in this thesis' experiments, while 0.1 bar was used as the lowest value because this was the lowest value used in the experiments. No CO_2 present at all was not explored because this would lead to no possibility of the production of carbonates.

Making CO_2 levels 'fixed' or 'unfixed' was achieved by adding CO_2 to the reactant tab. Once added, CO_2 will not leave the system and is said to be in a 'closed system'. This better simulates open-air waters where the atmosphere maintains a constant supply of gas to the water body, whereas non-fixed CO_2 levels better represent the subsurface where meteoric water containing atmospheric CO_2 may trickle through pore spaces as a finite level that can be slowly lost.

The model was capable of tracking many qualities of the solution, and of all minerals capable of forming under its set-up. Only the minerals siderite, amorphous Fe-carbonate (AFC), $Fe(OH)_2$ (a precursor to magnetite; Tosca et al., 2018), and the clay greenalite were tracked. $Fe(OH)_2$ is of interest because magnetite may be a competing mineral for the formation of siderite (Tosca et al., 2018), while greenalite is of interest because this too is in competition with siderite (Tosca et al., 2016). All minerals were suppressed from participating in the model except for: AFC, amorphous silica, $CO_{2(aq)}$, $CO_{2(g)}$, CO_3^{2-}, fayalite, $FeCO_3$, forsterite, greenalite, hydromagnesite, magnesite, $MgCO_3$, nesquehonite, OH^-, siderite, smectite (high Fe-Mg), smectite (low Fe/Mg). This is because the behaviour of these specific species was of interest in this model.

6.2. DIC vs alkalinity plots

An important component of the modelling, which is difficult to achieve solely with GWB, is modelling of the change in total dissolved inorganic carbon (DIC) against total alkalinity. The DIC/alkalinity plot is an effective means of displaying processes that affect carbonate equilibria because DIC and alkalinity can be used together to constrain the carbonate system. DIC will be unaffected by silicate dissolution over the course of an experiment, but alkalinity will increase. When comparing closed vs open systems, DIC remains constant for closed systems (no more CO_2 may enter the system) but evolves higher for open systems, where CO_2 from the atmosphere may enter the system. Involving both DIC from atmospheric interaction, or lack thereof, alongside alkalinity increase from silicate dissolution is a highly useful way to understand the impact of open vs closed systems upon the chemistry of an environment.

The DIC-alkalinity plots used in Chapters 3, 4, and 5 were constructed by exporting the GWB models described above into MatLab, and selecting from the model script the concentration of varying solution components relevant to calculating DIC and alkalinity. These included: H^+, OH^-, HCO_3^-, and CO_3^{2-}. DIC is calculated by adding together the concentrations of HCO_3^-, CO_2, and CO_3^{2-}, while total alkalinity is calculated from:

$$alkalinity = HCO_3^- conc + (2 \times CO_3^{2-} conc) + OH^- conc - H^+ conc \quad \text{(eq. 6.2.1.)}$$

Fe concentration is fixed, as this may be taken up by multiple minerals and thus its geochemical pathways are uncertain.

6.3. The GWB database

The thermodynamic database for GWB did not include AFC within it, owing to its novelty as a recently discovered phase with limited studies conducted on its thermodynamic and kinetic

properties (e.g., Sel et al., 2012; Dideriksen et al., 2015; Jiang and Tosca, 2019). To include AFC in the modelling, this phase had to be manually added to the GWB database. The reaction of AFC may be written by the following equation (Jiang and Tosca, 2019):

$$Fe^{2+} + H_2O + 0.5HCO_3^- = AFC + 1.5H^+ \quad \text{(eq. 6.2.1.)}$$

From this equation, the necessary species for reaction can be calculated in their relative stoichiometry for addition to a new database for GWB that incorporates AFC at 25 °C. The log K for 25 °C was calculated as 7.372. This is distinct from the solubility estimate calculated in Jiang and Tosca (2019), and was calculated here by calculating the molar weights of the elements involved based on the amount they are present within as species involved in the AFC reaction. When calculated, this was a log K of 7.372.

The results of this modelling are detailed in Appendix 2.

7. Conclusions

In this chapter, the in-depth methods employed to produce this thesis were reproduced to exacting detail. From the thermodynamic models that allowed experiment designs to be simulated and tested before their set-up; through to the synthesis of pure minerals for use in experiments; to the set-up of the experiments themselves and their individual descriptions; to the analytical methods following experimental termination; and lastly to the kinetic equations used to understand their events, the means of producing the data in the following results chapters of this thesis have been as thoroughly described as possible.

While each subsequent results chapter will briefly cover its methods before describing its findings, the reader will be returned here for their in-depth description. This thesis now turns to describe the experimental and analytical results themselves.

9. Figures

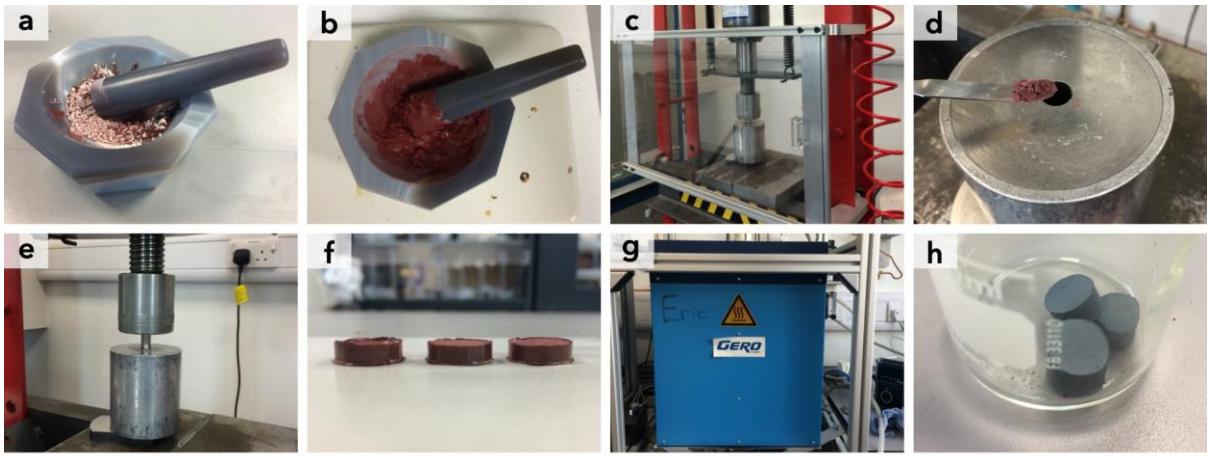


Figure 1: (a) Fe_2O_3 and SiO_2 are thoroughly homogenised in an agate pestle and mortar, with ethanol used to add slight adhesion to the powder and therefore prevent spillage, as maintaining precise stoichiometric ratio of material is vital at this stage; (b) The homogenised material is left to dry; (c) The powder is then pelletised in increments of 2-3 g using a compact pelletiser; (d) The dried powder may be seen being spooned carefully into a strengthened holder; (e) A steel rod is then inserted into the holder and increasing pressure mounted to drive it inside the holder, which compacts the powder into loosely-maintained pellets; (f) The pellets post-pelletisation; (g) The pellets are placed in an alumina crucible and fired in a furnace at 1080 °C for at least 3 hours; (h) The end result of pigeon-grey pellets that are now mechanically strong, which will shortly be powdered and their purity checked via XRD. When powdered, pure fayalite assumed a uniform beige colour.

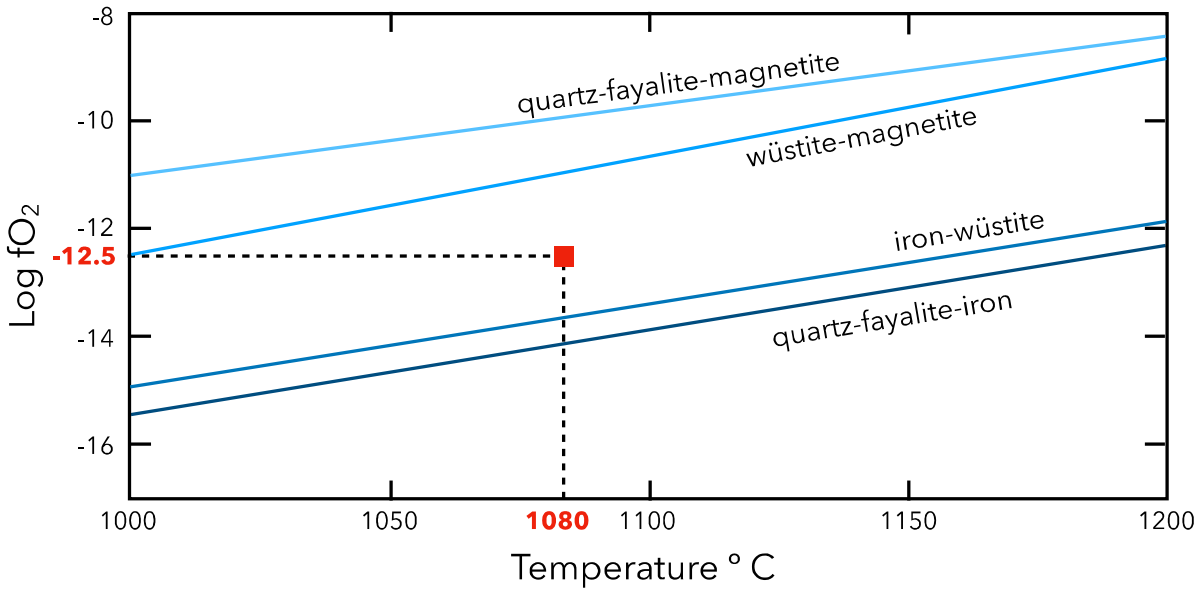


Figure 2: Fayalite forms above the iron-wüstite and below the wüstite-magnetite lines. As fayalite melts at 1200 ºC, 1080 ºC was chosen as the furnace temperature to produce the fastest results; reading off the graph to directly between these two lines produced the optimal oxygen fugacity to use.

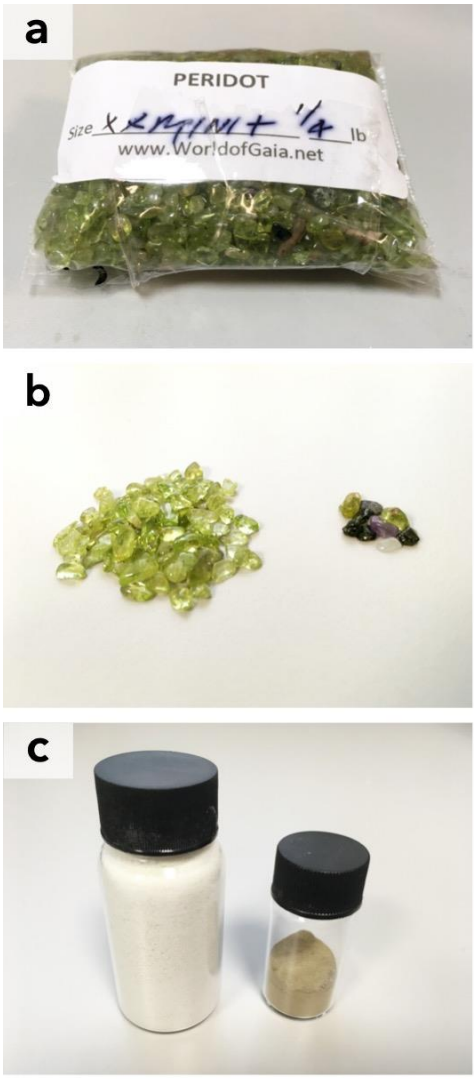


Figure 3: The preparation process from raw peridot crystals to powdered forsterite. (a) Peridot gems bought in bulk; (b) The gems are hand-separated to remove impurities (right-hand pile); (c) The gems are powdered in an agate pestle and mortar to produce <63 μm white powder, shown left besides powdered fayalite to the right.

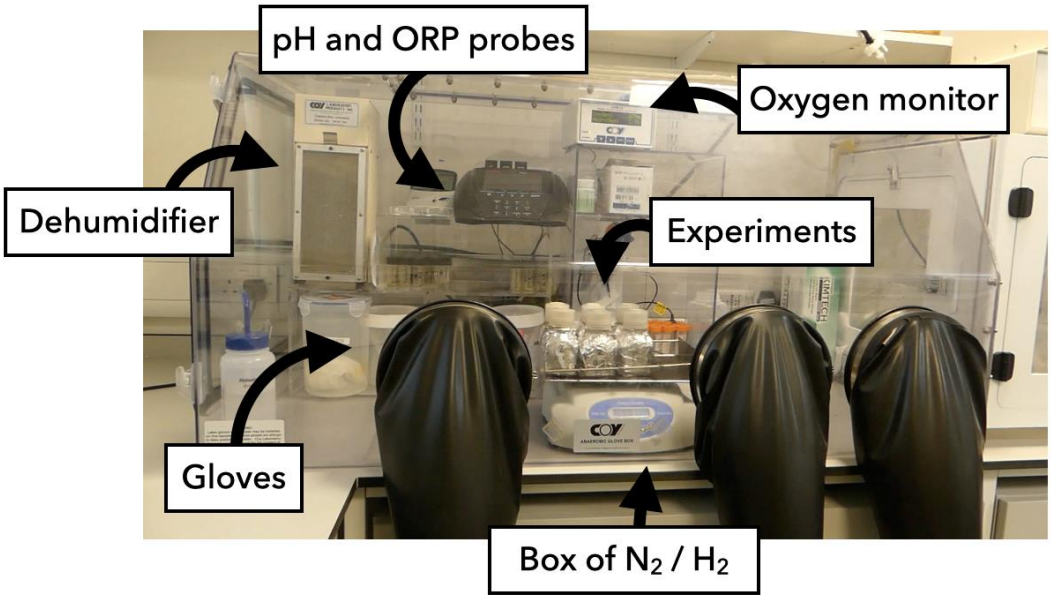


Figure 4: The experimental setup.

Desired pH	**Amount of 50 % H_2SO_4 added (mL)**	**Amount added to deionised H_2O**
2	0.2441	0.2441 mL 50 % H_2SO_4 to 249.75599 g H_2O
3	0.0191	19.5809 mL of pH 2 to 230.4191 g H_2O
4	1.8389	1.8389 mL of pH 2 to 248.1611 g H_2O
5	2.3155	2.3255 mL of pH 3 to 247.6845 g H_2O
6	2.4365	2.4365 mL of pH 4 to 247.5635 g H_2O

Table 1: Additions of H_2SO_4 to produce stock solutions of exact pH that could then be added to deionised H_2O to produce larger quantities of the desired starting pH for experiments.

Experiment's pH and CO_2	**SO_4^{2-} (mol/kg) to balance**	**Total HCO_3^- (as $NaHCO_3$) required, in mol/kg**	**Amount of $NaHCO_3$ stock solution to be added in mL**
pH 2 0.1 bar	0.00696	0.00353	6.072
pH 2 0.5 bar	0.00696	0.01760	30.272
pH 2 1.0 bar	0.00696	0.03530	60.716
pH 4 0.1 bar	0.0000778	0.00354	6.0888
pH 4 0.5 bar	0.0000577	0.01770	30.0444
pH 4 1.0 bar	0.0000326	0.03540	60.888

Table 2: Far right: Additions of the $NaHCO_3$ stock solution to 0.172 mL deionised water to reach certain levels of CO_2 fugacity per set pH levels. The calculated figures from GWB are also shown: SO_4^{2-} required to balance the reaction, and the total HCO_3^- required, which was translated into the far-right column as the amount of stock solution to add.

Experiment name (date of inception)	Duration in days (if hours, given)	pH used	Rock:water ratio	Levels of CO_2 (bar)	Fayalite-forsterite ratio	Comments
170903	(failed)	2, 3, 4, 5, 6	1:100, 1:500	0	Fa	Prematurely terminated with the leak of oxygen into the glove box
180123	8	2, 4, 6	1:200, 1:500	0	Fa	Explores rock:water ratio
180203	10 hrs	2, 4, 6	1:200, 1:500	0	Fa	Repeat of 180123 sampling hourly
180310	10 hrs	2, 4, 6	1:200, 1:500	0	Fa	Repeat of 180203
180313	13	2, 4	1:500	0.1, 0.5, 1.0	Fa	First addition of CO_2
180406	17	2, 4	1:500	0.1, 0.5, 1.0	Fa	Repeat of 180313
180612	15	2, 4	1:500	0.1, 0.5, 1.0	50:50 Fa-Fo	First addition of Fo
180628	61	2, 4	1:500	0.1, 0.5, 1.0	50:50 Fa-Fo	Repeat of 180612 to 60 days
180829	12	2, 4	1:500	0.1, 0.5, 1.0	50:50 Fa-Fo	Repeat of 180812

181004	60	2, 4	1:1, 1:10	1.0	Fa	Explores low rock:water ratio
181029 Fa	80	2, 4	1:500	0.1, 0.5, 1.0	Fa	Pure Fa equivalent of 180628
181029 Fo	80	2, 4	1:500	0.1, 0.5, 1.0	50:50 Fa-Fo	Repeat of 180628
181205	60	2, 4	1:1, 1:10	1.0	50:50 Fa-Fo	Explores low rock:water ratio
190121	80	2, 4	1:500	0.1, 0.5, 1.0	10:90	Explores Fa-Fo ratio
190423 Fa	85	2, 4	1:500	0.1, 0.5, 1.0	Fa	Repeat of 181029 Fa
190423 Fo	85	2, 4	1:500	0.1, 0.5, 1.0	50:50 Fa-Fo	Repeat of 180628, 181029 Fa

Table 3: All experiments, arranged in date order, conducted in the first part of the project towards the kinetics of siderite investigation chapter. In blue: non-CO_2-bearing experiments investigating the effects of rock:water ratio. Yellow: CO_2- and fayalite-bearing experiments. Green: Fa-Fo-bearing experiments with CO_2. Red: Low-water rock experiments. Purple: High Fa-Fo ratio experiments.

Experiment name (date of inception)	Duration in days (if hours, given)	pH used	Rock:water ratio	Levels of CO_2 (bar)	Substrate used	Comments
190414	85	2, 4	1:500	0, 0.5, 1.0	Fine CRB, coarse CRB	Explores high rock:water ratio
190418	(failed)	2, 4	1:1, 1:10	1.0	Fine CRB, coarse CRB	Explores low rock:water ratios
190812	72	2, 4	1:1, 1:10	1.0	Fine CRB, coarse CRB	Repeat of 190418 after loss of sample solutions
190806	10	2, 4	1:500	0	Fine CRB, coarse CRB	Repeat of 0 bar experiments of 190414 but short run
190807	10	2, 4	1:500	0.5	Fine CRB, coarse CRB	Repeat of 0.5 bar experiments of 190414 but short run
190808	10	2, 4	1:500	1.0	Fine CRB, coarse CRB	Repeat of 1.0 bar experiments of 190414 but short run

Table 4: All experiments, arranged in date order, conducted in the CRB part of the project towards the kinetics of siderite investigation chapter. In pink: CRB-bearing experiments at high rock:water ratio (1 part rock to 500 part fluid). Lime-green: Low-water rock experiments at 1 to 1 or 1 to 10 rock:water ratios.

Experiment name (date of inception)	Duration in days (if hours, given)	pH used	Rock:water ratio	Levels of CO_2 (bar)	Substrate used	Comments
191028	10	2, 4	1:500	0, 0.1, 0.5, 1.0	Fa	Repeat of 180313 and 180406 but at 75 °C
191107	10	2, 4	1:500	0.1, 0.5, 1.0	Fa/Fo 50:50	Repeat of 180829 but at 75 °C
191118	10	2, 4	1:500	0.1, 0.5, 1.0	CRB, fine, coarse	Repeat of 190414 but at 75 °C
191128	(failed)	2, 4	1:1, 1:10	1.0	Fa	Repeat of 181004 but at 75 °C
191129	(failed)	2, 4	1:1, 1:10	1.0	Fa/Fo	Repeat of 181205 but at 75 °C

Table 5: All experiments, arranged in date order, conducted in the 'hot' (75 °C) part of the project towards the kinetics of siderite investigation chapter. In yellow: fayalite-bearing experiments at high rock:water ratio (1 part rock to 500 part fluid). Green: forsterite-bearing experiments at high rock:water ratio (1 part rock to 500 part fluid). Red: Low-water rock Fa/Fo experiments at 1 to 1 or 1 to 10 rock:water ratios. Blue: CRB-bearing experiments at high rock:water ratio (1 part rock to 500 part fluid).

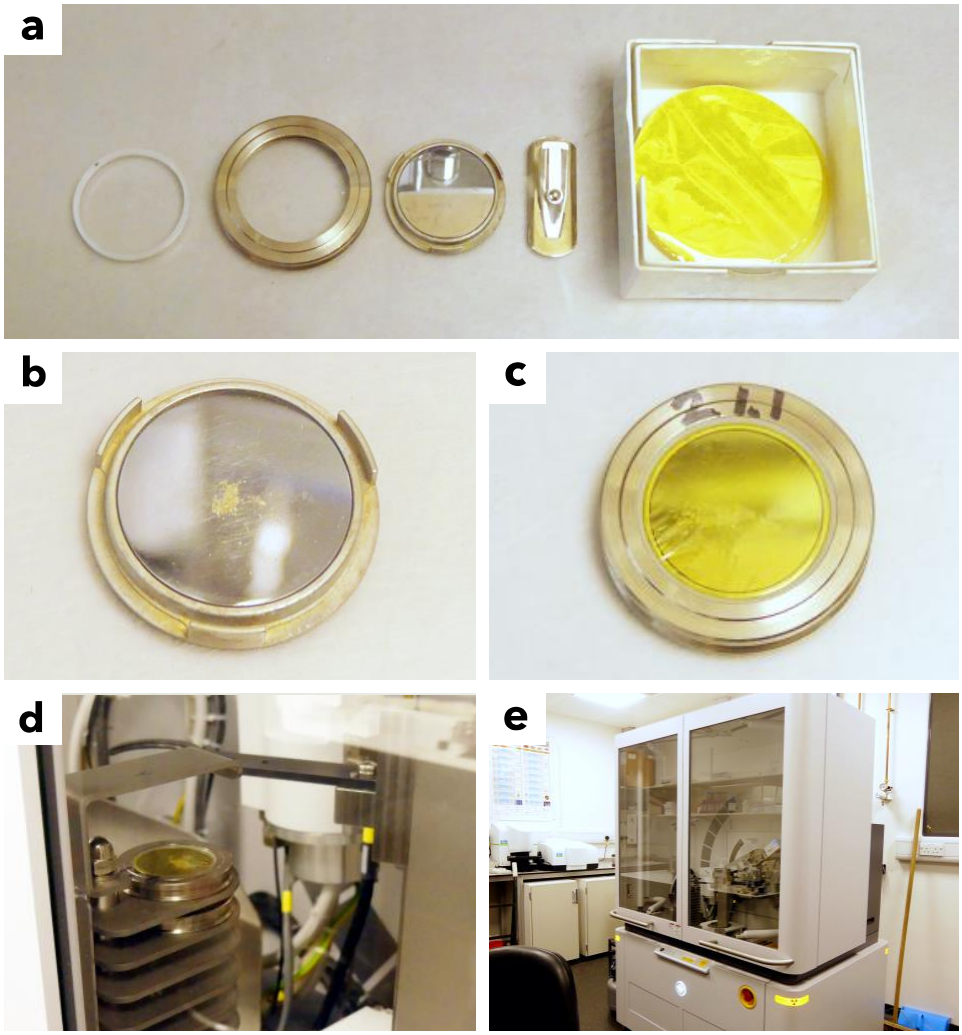


Figure 5: The process of preparing a sample for XRD analysis under anoxic conditions. (a) The equipment required, including (left to right) a flexible plastic ring, an XRD cover, a crystal silicon disc, a clip, and Kapton film; (b) The crystal disc with ~0.005 g of powder in its centre; (c) The Kapton-covered disc with sample name written in removable ink; (d) The sample waiting to be run within the XRD; (e) The XRD in Oxford.

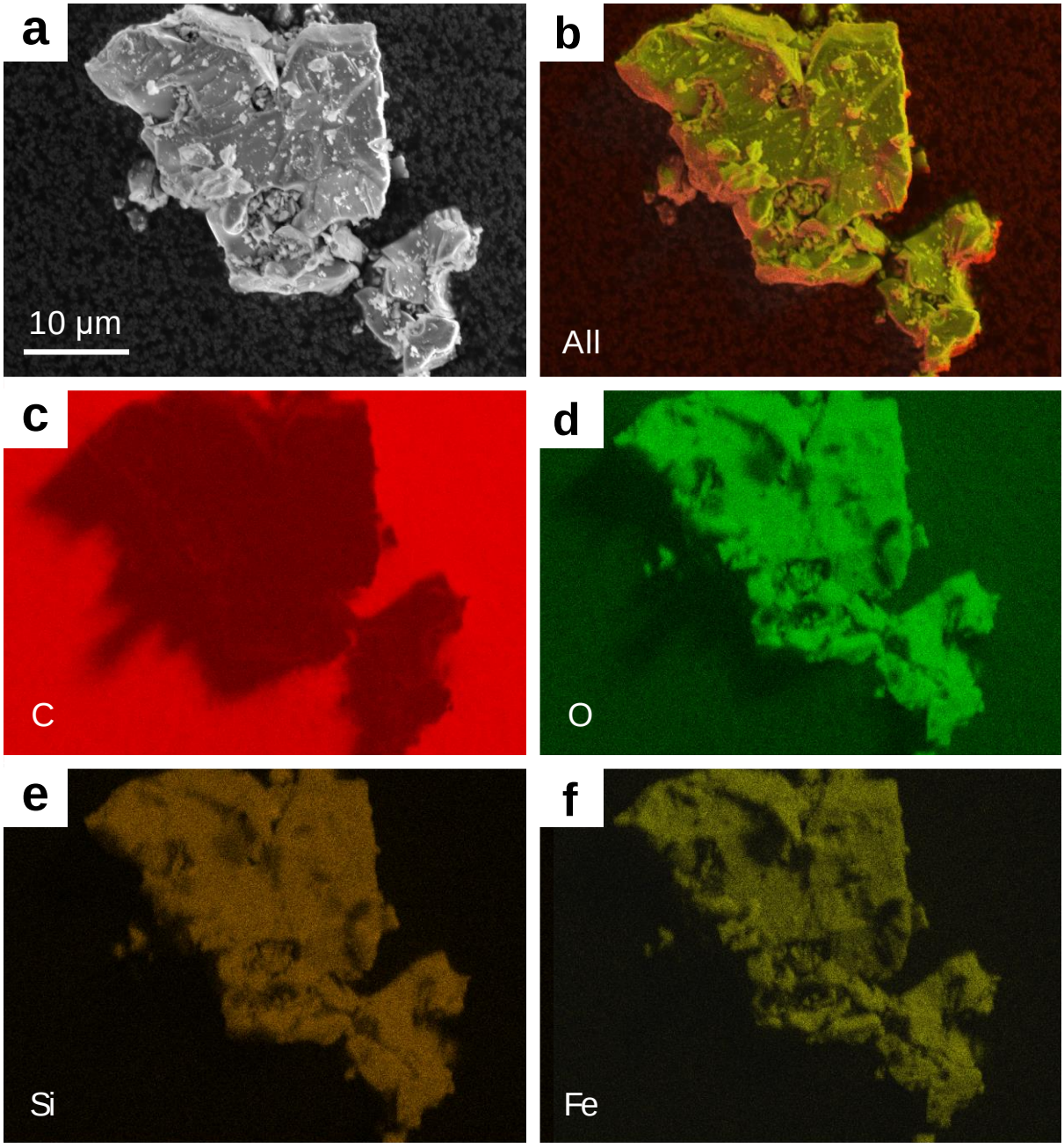


Figure 6: Energy Dispersive Spectroscopy images of a sample from experiment 181004, conducted under a rock:water ratio of 1:10 and a starting pH of 2. (a) LFD SEM image of a ~10 µm piece of rock; (b) All EDS images overlain on top of each other. Note the shadowing effect as a result of the beam's location from the northwest of the image; (c) Carbon; (d) Oxygen; (e) Silica; (f) Iron.

Reference	**Reaction rate constant ($mmol \cdot kg^{-1} \cdot year^{-1}$)**	**Flaws**
Hunter et al. (1998)	0.050	Mediated by bacteria; oxygenated conditions; run as a model, not based on experimental evidence
Liu et al. (2001)	0.053	Based off the oxygenated model of Hunter et al. (1998); produces siderite by the bio-reduction of goethite
Matsunaga et al. (1992)	12.623	Mediated by bacteria; 'oxygen-saturated' water

Table 6: The choice of rate constants in the literature that could have been employed in equation 1. The value of Hunter et al. (1998) was ultimately selected.

Parameter	Unit
H_2O	1 kg
H^+	Charge balance
Fe^{2+}	0.1 mmol/kg
SiO_2	0.1 mmol/kg
Mg^{2+}	0.1 mmol/kg
Cl^-	1.0 mmol/kg
SO_4^{2-}	1.0 mmol/kg
$CO_{2(g)} \leftrightarrows HCO_3^-$	1 fugacity
Time	30 years (all systems reach equilibrium)
Temp	25 °C
Reactant time	2 (1:500)
Fayalite	5 g
Forsterite	5 g
Surface area	1000 cm/g
Rate constant	$2.34e^{-11}$
$CO_{2(g)}$	Fixed

Table 7: The default conditions that began the model used to expand the results obtained in Chapter 3 of this thesis.

Parameter	Default value	Changed value
Water/rock	1:500 (2)	1:1 (100)
CO_2 un/fixed	Fixed	Unfixed
Surface area	1000 cm^2/g	100 cm^2/g
CO2 fugacity	1.0 bar	0.1 bar

Figure 8: The five parameters investigated in the model, with their default values and the changed values shown.

10. References

Baker, L.L., Agenbroad, D.J., Wood, S.A., 2000. Experimental hydrothermal alteration of a martian analog basalt: Implications for martian meteorites. Meteorit. Planet. Sci. 35, 31–38. https://doi.org/10.1111/j.1945-5100.2000.tb01971.x

Bethke, C.M., 2017. The Geochemist's Workbench, Version 12.0: GWB Essentials Guide. Champaign, Illinois, US.

Bish, D.L., Blake, D.F., Vaniman, D.T., Chipera, S.J., Morris, R.V., Ming, D.W., Treiman, A.H., Sarrazin, P., Morrison, S.M., Downs, R.T., Achilles, C.N., Yen, A.S., Bristow, T.F., Crisp, J.A., Morookian, J.M., Farmer, J.D., Rampe, E.B., Stolper, E.M., Spanovich, N., MSL Science Team, Achilles, C., Agard, C., Verdasca, J.A.A., Anderson, R., Anderson, R., Archer, D., Armiens-Aparicio, C., Arvidson, R., Atlaskin, E., Atreya, S., Aubrey, A., Baker, B., Baker, M., Balic-Zunic, T., Baratoux, D., Baroukh, J., Barraclough, B., Bean, K., Beegle, L., Behar, A., Bell, J., Bender, S., Benna, M., Bentz, J., Berger, G., Berger, J., Berman, D., Bish, D., Blake, D.F., Avalos, J.J.B., Blaney, D., Blank, J., Blau, H., Bleacher, L., Boehm, E., Botta, O., Bottcher, S., Boucher, T., Bower, H., Boyd, N., Boynton, B., Breves, E., Bridges, J., Bridges, N., Brinckerhoff, W., Brinza, D., Bristow, T., Brunet, C., Brunner, A., Brunner, W., Buch, A., Bullock, M., Burmeister, S., Cabane, M., Calef, F., Cameron, J., Campbell, J.I., Cantor, B., Caplinger, M., Rodriguez, J.C., Carmosino, M., Blazquez, I.C., Charpentier, A., Chipera, S., Choi, D., Clark, B., Clegg, S., Cleghorn, T., Cloutis, E., Cody, G., Coll, P., Conrad, P., Coscia, D., Cousin, A., Cremers, D., Crisp, J., Cros, A., Cucinotta, F., d'Uston, C., Davis, S., Day, M.K., Juarez, M. d. l. T., DeFlores, L., DeLapp, D., DeMarines, J., DesMarais, D., Dietrich, W., Dingler, R., Donny, C., Downs, B., Drake, D., Dromart, G., Dupont, A., Duston, B., Dworkin, J., Dyar, M.D., Edgar, L., Edgett, K., Edwards, C., Edwards, L., Ehlmann, B., Ehresmann, B., Eigenbrode, J., Elliott, B., Elliott, H., Ewing, R., Fabre, C., Fairen, A., Farley, K., Farmer, J., Fassett, C., Favot, L., Fay, D., Fedosov, F., Feldman, J., Feldman, S., Fisk, M.,

Fitzgibbon, M., Flesch, G., Floyd, M., Fluckiger, L., Forni, O., Fraeman, A., Francis, R., Francois, P., Franz, H., Freissinet, C., French, K.L., Frydenvang, J., Gaboriaud, A., Gailhanou, M., Garvin, J., Gasnault, O., Geffroy, C., Gellert, R., Genzer, M., Glavin, D., Godber, A., Goesmann, F., Goetz, W., Golovin, D., Gomez, F.G., Gomez-Elvira, J., Gondet, B., Gordon, S., Gorevan, S., Grant, J., Griffes, J., Grinspoon, D., Grotzinger, J., Guillemot, P., Guo, J., Gupta, S., Guzewich, S., Haberle, R., Halleaux, D., Hallet, B., Hamilton, V., Hardgrove, C., Harker, D., Harpold, D., Harri, A.-M., Harshman, K., Hassler, D., Haukka, H., Hayes, A., Herkenhoff, K., Herrera, P., Hettrich, S., Heydari, E., Hipkin, V., Hoehler, T., Hollingsworth, J., Hudgins, J., Huntress, W., Hurowitz, J., Hviid, S., Iagnemma, K., Indyk, S., Israel, G., Jackson, R., Jacob, S., Jakosky, B., Jensen, E., Jensen, J.K., Johnson, J., Johnson, M., Johnstone, S., Jones, A., Jones, J., Joseph, J., Jun, I., Kah, L., Kahanpaa, H., Kahre, M., Karpushkina, N., Kasprzak, W., Kauhanen, J., Keely, L., Kemppinen, O., Keymeulen, D., Kim, M.-H., Kinch, K., King, P., Kirkland, L., Kocurek, G., Koefoed, A., Kohler, J., Kortmann, O., Kozyrev, A., Krezoski, J., Krysak, D., Kuzmin, R., Lacour, J.L., Lafaille, V., Langevin, Y., Lanza, N., Lasue, J., Le Mouelic, S., Lee, E.M., Lee, Q.-M., Lees, D., Lefavor, M., Lemmon, M., Malvitte, A.L., Leshin, L., Leveille, R., Lewin-Carpintier, E., Lewis, K., Li, S., Lipkaman, L., Little, C., Litvak, M., Lorigny, E., Lugmair, G., Lundberg, A., Lyness, E., Madsen, M., Mahaffy, P., Maki, J., Malakhov, A., Malespin, C., Malin, M., Mangold, N., Manhes, G., Manning, H., Marchand, G., Jimenez, M.M., Garcia, C.M., Martin, D., Martin, M., Martinez-Frias, J., Martin-Soler, J., Martin-Torres, F.J., Mauchien, P., Maurice, S., McAdam, A., McCartney, E., McConnochie, T., McCullough, E., McEwan, I., McKay, C., McLennan, S., McNair, S., Melikechi, N., Meslin, P.-Y., Meyer, M., Mezzacappa, A., Miller, H., Miller, K., Milliken, R., Ming, D., Minitti, M., Mischna, M., Mitrofanov, I., Moersch, J., Mokrousov, M., Jurado, A.M., Moores, J., Mora-Sotomayor, L., Morookian, J.M., Morris, R., Morrison, S., Mueller-Mellin, R., Muller, J.-P., Caro, G.M., Nachon, M., Lopez, S.N.,

Navarro-Gonzalez, R., Nealson, K., Nefian, A., Nelson, T., Newcombe, M., Newman, C., Newsom, H., Nikiforov, S., Niles, P., Nixon, B., Dobrea, E.N., Nolan, T., Oehler, D., Ollila, A., Olson, T., Owen, T., Hernandez, M.A. d. P., Paillet, A., Pallier, E., Palucis, M., Parker, T., Parot, Y., Patel, K., Paton, M., Paulsen, G., Pavlov, A., Pavri, B., Peinado-Gonzalez, V., Pepin, R., Peret, L., Perez, R., Perrett, G., Peterson, J., Pilorget, C., Pinet, P., Pla-Garcia, J., Plante, I., Poitrasson, F., Polkko, J., Popa, R., Posiolova, L., Posner, A., Pradler, I., Prats, B., Prokhorov, V., Purdy, S.W., Raaen, E., Radziemski, L., Rafkin, S., Ramos, M., Rampe, E., Raulin, F., Ravine, M., Reitz, G., Renno, N., Rice, M., Richardson, M., Robert, F., Robertson, K., Manfredi, J.A.R., Romeral-Planello, J.J., Rowland, S., Rubin, D., Saccoccio, M., Salamon, A., Sandoval, J., Sanin, A., Fuentes, S.A.S., Saper, L., Sarrazin, P., Sautter, V., Savijarvi, H., Schieber, J., Schmidt, M., Schmidt, W., Scholes, D.D., Schoppers, M., Schroder, S., Schwenzer, S., Martinez, E.S., Sengstacken, A., Shterts, R., Siebach, K., Siili, T., Simmonds, J., Sirven, J.-B., Slavney, S., Sletten, R., Smith, M., Sanchez, P.S., Spanovich, N., Spray, J., Squyres, S., Stack, K., Stalport, F., Steele, A., Stein, T., Stern, J., Stewart, N., Stipp, S.L.S., Stoiber, K., Stolper, E., Sucharski, B., Sullivan, R., Summons, R., Sumner, D., Sun, V., Supulver, K., Sutter, B., Szopa, C., Tan, F., Tate, C., Teinturier, S., ten Kate, I., Thomas, P., Thompson, L., Tokar, R., Toplis, M., Redondo, J.T., Trainer, M., Treiman, A., Tretyakov, V., Urqui-O'Callaghan, R., Van Beek, J., Van Beek, T., VanBommel, S., Vaniman, D., Varenikov, A., Vasavada, A., Vasconcelos, P., Vicenzi, E., Vostrukhin, A., Voytek, M., Wadhwa, M., Ward, J., Webster, C., Weigle, E., Wellington, D., Westall, F., Wiens, R.C., Wilhelm, M.B., Williams, A., Williams, J., Williams, R., Williams, R.B.M., Wilson, M., Wimmer-Schweingruber, R., Wolff, M., Wong, M., Wray, J., Wu, M., Yana, C., Yen, A., Yingst, A., Zeitlin, C., Zimdar, R., Mier, M.-P.Z., 2013. X-ray Diffraction Results from Mars Science Laboratory: Mineralogy of Rocknest at Gale Crater. Science 341, 1238932–1238932. https://doi.org/10.1126/science.1238932

Blake, D.F., Morris, R.V., Kocurek, G., Morrison, S.M., Downs, R.T., Bish, D., Ming, D.W., Edgett, K.S., Rubin, D., Goetz, W., Madsen, M.B., Sullivan, R., Gellert, R., Campbell, I., Treiman, A.H., McLennan, S.M., Yen, A.S., Grotzinger, J., Vaniman, D.T., Chipera, S.J., Achilles, C.N., Rampe, E.B., Sumner, D., Meslin, P.-Y., Maurice, S., Forni, O., Gasnault, O., Fisk, M., Schmidt, M., Mahaffy, P., Leshin, L.A., Glavin, D., Steele, A., Freissinet, C., Navarro-Gonzalez, R., Yingst, R.A., Kah, L.C., Bridges, N., Lewis, K.W., Bristow, T.F., Farmer, J.D., Crisp, J.A., Stolper, E.M., Des Marais, D.J., Sarrazin, P., MSL Science Team, Agard, C., Alves Verdasca, J.A., Anderson, R., Anderson, R., Archer, D., Armiens-Aparicio, C., Arvidson, R., Atlaskin, E., Atreya, S., Aubrey, A., Baker, B., Baker, M., Balic-Zunic, T., Baratoux, D., Baroukh, J., Barraclough, B., Bean, K., Beegle, L., Behar, A., Bell, J., Bender, S., Benna, M., Bentz, J., Berger, G., Berger, J., Berman, D., Blanco Avalos, J.J., Blaney, D., Blank, J., Blau, H., Bleacher, L., Boehm, E., Botta, O., Bottcher, S., Boucher, T., Bower, H., Boyd, N., Boynton, B., Breves, E., Bridges, J., Brinckerhoff, W., Brinza, D., Brunet, C., Brunner, A., Brunner, W., Buch, A., Bullock, M., Burmeister, S., Cabane, M., Calef, F., Cameron, J., Cantor, B., Caplinger, M., Rodriguez, J.C., Carmosino, M., Blazquez, I.C., Charpentier, A., Choi, D., Clark, B., Clegg, S., Cleghorn, T., Cloutis, E., Cody, G., Coll, P., Conrad, P., Coscia, D., Cousin, A., Cremers, D., Cros, A., Cucinotta, F., d'Uston, C., Davis, S., Day, M., Juarez, M. d. l. T., DeFlores, L., DeLapp, D., DeMarines, J., Dietrich, W., Dingler, R., Donny, C., Drake, D., Dromart, G., Dupont, A., Duston, B., Dworkin, J., Dyar, M.D., Edgar, L., Edwards, C., Edwards, L., Ehlmann, B., Ehresmann, B., Eigenbrode, J., Elliott, B., Elliott, H., Ewing, R., Fabre, C., Fairen, A., Farley, K., Fassett, C., Favot, L., Fay, D., Fedosov, F., Feldman, J., Feldman, S., Fitzgibbon, M., Flesch, G., Floyd, M., Fluckiger, L., Fraeman, A., Francis, R., Francois, P., Franz, H., French, K.L., Frydenvang, J., Gaboriaud, A., Gailhanou, M., Garvin, J., Geffroy, C., Genzer, M., Godber, A., Goesmann, F., Golovin, D., Gomez, F.G., Gomez-Elvira, J., Gondet, B., Gordon, S., Gorevan, S., Grant, J.,

Griffes, J., Grinspoon, D., Guillemot, P., Guo, J., Gupta, S., Guzewich, S., Haberle, R., Halleaux, D., Hallet, B., Hamilton, V., Hardgrove, C., Harker, D., Harpold, D., Harri, A.-M., Harshman, K., Hassler, D., Haukka, H., Hayes, A., Herkenhoff, K., Herrera, P., Hettrich, S., Heydari, E., Hipkin, V., Hoehler, T., Hollingsworth, J., Hudgins, J., Huntress, W., Hurowitz, J., Hviid, S., Iagnemma, K., Indyk, S., Israel, G., Jackson, R., Jacob, S., Jakosky, B., Jensen, E., Jensen, J.K., Johnson, J., Johnson, M., Johnstone, S., Jones, A., Jones, J., Joseph, J., Jun, I., Kahanpaa, H., Kahre, M., Karpushkina, N., Kasprzak, W., Kauhanen, J., Keely, L., Kemppinen, O., Keymeulen, D., Kim, M.-H., Kinch, K., King, P., Kirkland, L., Koefoed, A., Kohler, J., Kortmann, O., Kozyrev, A., Krezoski, J., Krysak, D., Kuzmin, R., Lacour, J.L., Lafaille, V., Langevin, Y., Lanza, N., Lasue, J., Le Mouelic, S., Lee, E.M., Lee, Q.-M., Lees, D., Lefavor, M., Lemmon, M., Lepinette Malvitte, A., Leveille, R., Lewin-Carpintier, E., Li, S., Lipkaman, L., Little, C., Litvak, M., Lorigny, E., Lugmair, G., Lundberg, A., Lyness, E., Maki, J., Malakhov, A., Malespin, C., Malin, M., Mangold, N., Manning, H., Marchand, G., Marin Jimenez, M., Martin Garcia, C., Martin, D., Martin, M., Martinez-Frias, J., Martin-Soler, J., Martin-Torres, F.J., Mauchien, P., McAdam, A., McCartney, E., McConnochie, T., McCullough, E., McEwan, I., McKay, C., McNair, S., Melikechi, N., Meyer, M., Mezzacappa, A., Miller, H., Miller, K., Milliken, R., Minitti, M., Mischna, M., Mitrofanov, I., Moersch, J., Mokrousov, M., Molina Jurado, A., Moores, J., Mora-Sotomayor, L., Morookian, J.M., Mueller-Mellin, R., Muller, J.-P., Munoz Caro, G., Nachon, M., Navarro Lopez, S., Nealson, K., Nefian, A., Nelson, T., Newcombe, M., Newman, C., Newsom, H., Nikiforov, S., Niles, P., Nixon, B., Dobrea, E.N., Nolan, T., Oehler, D., Ollila, A., Olson, T., Owen, T., Pablo, H., Paillet, A., Pallier, E., Palucis, M., Parker, T., Parot, Y., Patel, K., Paton, M., Paulsen, G., Pavlov, A., Pavri, B., Peinado-Gonzalez, V., Pepin, R., Peret, L., Perez, R., Perrett, G., Peterson, J., Pilorget, C., Pinet, P., Pla-Garcia, J., Plante, I., Poitrasson, F., Polkko, J., Popa, R., Posiolova, L., Pradler, I., Prats, B., Prokhorov, V.,

Purdy, S.W., Raaen, E., Radziemski, L., Rafkin, S., Ramos, M., Raulin, F., Ravine, M., Reitz, G., Renno, N., Rice, M., Richardson, M., Robert, F., Rodriguez Manfredi, J.A., Romeral-Planello, J.J., Rowland, S., Saccoccio, M., Salamon, A., Sandoval, J., Sanin, A., Sans Fuentes, S.A., Saper, L., Sautter, V., Savijarvi, H., Schieber, J., Schmidt, W., Scholes, D., Schoppers, M., Schroder, S., Sebastian Martinez, E., Sengstacken, A., Shterts, R., Siebach, K., Siili, T., Simmonds, J., Sirven, J.-B., Slavney, S., Sletten, R., Smith, M., Sobron Sanchez, P., Spanovich, N., Spray, J., Squyres, S., Stack, K., Stalport, F., Stein, T., Stern, J., Stewart, N., Stipp, S.L.S., Stoiber, K., Sucharski, B., Summons, R., Sun, V., Supulver, K., Sutter, B., Szopa, C., Tate, C., Teinturier, S., ten Kate, I.L., Thomas, P., Thompson, L., Tokar, R., Toplis, M., Torres Redondo, J., Trainer, M., Tretyakov, V., Urqui-O'Callaghan, R., Van Beek, J., Van Beek, T., VanBommel, S., Varenikov, A., Vasavada, A., Vasconcelos, P., Vicenzi, E., Vostrukhin, A., Voytek, M., Wadhwa, M., Ward, J., Webster, C., Weigle, E., Wellington, D., Westall, F., Wiens, R.C., Wilhelm, M.B., Williams, A., Williams, J., Williams, R., Williams, R.B., Wilson, M., Wimmer-Schweingruber, R., Wolff, M., Wong, M., Wray, J., Wu, M., Yana, C., Zeitlin, C., Zimdar, R., Zorzano Mier, M.-P., 2013. Curiosity at Gale Crater, Mars: Characterization and Analysis of the Rocknest Sand Shadow. Science 341, 1239505–1239505. https://doi.org/10.1126/science.1239505

Brantley, S.L., Mellott, N.P., 2000. Surface area and porosity of primary silicate minerals. Am. Mineral. 85, 1767–1783. https://doi.org/10.2138/am-2000-11-1220

Braterman, P.S., Graham Cairns-Smith, A., W. Sloper, R., George Truscott, T., Craw, M., 1984. Photo-oxidation of iron(II) in water between pH 7.5 and 4.0. J. Chem. Soc. Dalton Trans. 0, 1441–1445. https://doi.org/10.1039/DT9840001441

Bridges, J.C., Catling, D.C., Saxton, J.M., Swindle, T.D., Lyon, I.C., Grady, M.M., 2001. Alteration Assemblages in Martian Meteorites: Implications for Near-Surface Processes. Space Sci. Rev. 96, 365–392. https://doi.org/10.1023/A:1011965826553

Bridges, J.C., Hicks, L.J., Treiman, A.H., 2019. Carbonates on Mars, in: Volatiles in the Martian Crust. Elsevier, pp. 89–118. https://doi.org/10.1016/B978-0-12-804191-8.00005-2

Bridges, J.C., Schwenzer, S.P., Leveille, R., Westall, F., Wiens, R.C., Mangold, N., Bristow, T., Edwards, P., Berger, G., 2015. Diagenesis and clay mineral formation at Gale Crater, Mars. J. Geophys. Res. Planets 120, 1–19. https://doi.org/10.1002/2014JE004757

Brunauer, S., Emmett, P.H., Teller, E., 1938. Adsorption of Gases in Multimolecular Layers. J. Am. Chem. Soc. 60, 309–319. https://doi.org/10.1021/ja01269a023

Butler, I.B., Schoonen, M.A.A., Rickard, D.T., 1994. Removal of dissolved oxygen from water: A comparison of four common techniques. Talanta 41, 211–215. https://doi.org/10.1016/0039-9140(94)80110-X

Daval, D., Testemale, D., Recham, N., Tarascon, J.-M., Siebert, J., Martinez, I., Guyot, F., 2010. Fayalite (Fe2SiO4) dissolution kinetics determined by X-ray absorption spectroscopy. Chem. Geol. 275, 161–175. https://doi.org/10.1016/j.chemgeo.2010.05.005

De Hoog, J.C.M., Gall, L., Cornell, D.H., 2010. Trace-element geochemistry of mantle olivine and application to mantle petrogenesis and geothermobarometry. Chem. Geol. 270, 196–215. https://doi.org/10.1016/j.chemgeo.2009.11.017

Deffeyes, K.S., 1965. CARBONATE EQUILIBRIA: A GRAPHIC AND ALGEBRAIC APPROACH1. Limnol. Oceanogr. 10, 412–426. https://doi.org/10.4319/lo.1965.10.3.0412

Dideriksen, K., Frandsen, C., Bovet, N., Wallace, A.F., Sel, O., Arbour, T., Navrotsky, A., De Yoreo, J.J., Banfield, J.F., 2015. Formation and transformation of a short range ordered iron carbonate precursor. Geochim. Cosmochim. Acta 164, 94–109. https://doi.org/10.1016/j.gca.2015.05.005

Ehlmann, B.L., Mustard, J.F., Murchie, S.L., Poulet, F., Bishop, J.L., Brown, A.J., Calvin, W.M., Clark, R.N., Marais, D.J.D., Milliken, R.E., Roach, L.H., Roush, T.L., Swayze, G.A.,

Wray, J.J., 2008. Orbital Identification of Carbonate-Bearing Rocks on Mars. Science 322, 1828–1832. https://doi.org/10.1126/science.1164759

Everhart, T.E., Thornley, R.F.M., 1960. Wide-band detector for micro-microampere low-energy electron currents. J. Sci. Instrum. 37, 246–248. https://doi.org/10.1088/0950-7671/37/7/307

Haberle, R.M., Clancy, R.T., Forget, F., Smith, M.D., Zurek, R.W., 2017. The atmosphere and climate of Mars. Cambridge University Press.

Halevy, I., Fischer, W.W., Eiler, J.M., 2011. Carbonates in the Martian meteorite Allan Hills 84001 formed at 18 4 C in a near-surface aqueous environment. Proc. Natl. Acad. Sci. 108, 16895–16899. https://doi.org/10.1073/pnas.1109444108

Heard, A.W., Kite, E.S., 2020. A probabilistic case for a large missing carbon sink on Mars after 3.5 billion years ago. Earth Planet. Sci. Lett. 531, 116001. https://doi.org/10.1016/j.epsl.2019.116001

Hunter, K.S., Wang, Y., Van Cappellen, P., 1998. Kinetic modeling of microbially-driven redox chemistry of subsurface environments: coupling transport, microbial metabolism and geochemistry. J. Hydrol. 209, 53–80. https://doi.org/10.1016/S0022-1694(98)00157-7

Hurowitz, J.A., McLennan, S.M., Tosca, N.J., Arvidson, R.E., Michalski, J.R., Ming, D.W., Schröder, C., Squyres, S.W., 2006. In situ and experimental evidence for acidic weathering of rocks and soils on Mars: EVIDENCE FOR ACIDIC WEATHERING ON MARS. J. Geophys. Res. Planets 111, n/a-n/a. https://doi.org/10.1029/2005JE002515

Jiang, C.Z., Tosca, N.J., 2019. Fe(II)-carbonate precipitation kinetics and the chemistry of anoxic ferruginous seawater. Earth Planet. Sci. Lett. 506, 231–242. https://doi.org/10.1016/j.epsl.2018.11.010

Kennedy, V.C., Zellweger, G.W., Jones, B.F., 1974. Filter pore-size effects on the analysis of Al, Fe, Mn, and Ti in water. Water Resour. Res. 10, 785–790. https://doi.org/10.1029/WR010i004p00785

Lammer, H., Lichtenegger, H.I.M., Kolb, C., Ribas, I., Guinan, E.F., Abart, R., Bauer, S.J., 2003. Loss of water from Mars: Icarus 165, 9–25. https://doi.org/10.1016/S0019-1035(03)00170-2

Lillis, R.J., Deighan, J., Fox, J.L., Bougher, S.W., Lee, Y., Combi, M.R., Cravens, T.E., Rahmati, A., Mahaffy, P.R., Benna, M., Elrod, M.K., McFadden, J.P., Ergun, Robert.E., Andersson, L., Fowler, C.M., Jakosky, B.M., Thiemann, E., Eparvier, F., Halekas, J.S., Leblanc, F., Chaufray, J., 2017. Photochemical escape of oxygen from Mars: First results from MAVEN in situ data. J. Geophys. Res. Space Phys. 122, 3815–3836. https://doi.org/10.1002/2016JA023525

Liu, C., Kota, S., Zachara, J.M., Fredrickson, J.K., Brinkman, C.K., 2001. Kinetic Analysis of the Bacterial Reduction of Goethite. Environ. Sci. Technol. 35, 2482–2490. https://doi.org/10.1021/es001956c

Lowell, S., Shields, J.E., 1991. Langmuir and BET theories (kinetic isotherms), in: Powder Surface Area and Porosity. Springer Netherlands, Dordrecht, pp. 14–29. https://doi.org/10.1007/978-94-015-7955-1_4

Matsunaga, T., Sakaguchi, T., Tadakoro, F., 1991. Magnetite formation by a magnetic bacterium capable of growing aerobically. Appl. Microbiol. Biotechnol. 35. https://doi.org/10.1007/BF00169632

Michalski, J.R., Niles, P.B., 2010. Deep crustal carbonate rocks exposed by meteor impact on Mars. Nat. Geosci. 3, 751–755. https://doi.org/10.1038/ngeo971

Neubeck, A., Duc, N.T., Bastviken, D., Crill, P., Holm, N.G., 2011. Formation of H2 and CH4by weathering of olivine at temperatures between 30 and 70°C. Geochem. Trans. 12, 6. https://doi.org/10.1186/1467-4866-12-6

Nordstrom, D.K., 1977. Thermochemical redox equilibria of ZoBell's solution. Geochim. Cosmochim. Acta 41, 1835–1841. https://doi.org/10.1016/0016-7037(77)90215-0

Park, P.K., 1969. OCEANIC CO $_2$ SYSTEM: AN EVALUATION OF TEN METHODS OF INVESTIGATION1: OCEANIC CO $_2$ SYSTEM. Limnol. Oceanogr. 14, 179–186. https://doi.org/10.4319/lo.1969.14.2.0179

Qafoku, O., Kovarik, L., Kukkadapu, R.K., Ilton, E.S., Arey, B.W., Tucek, J., Felmy, A.R., 2012. Fayalite dissolution and siderite formation in water-saturated supercritical CO2. Chem. Geol. 332–333, 124–135. https://doi.org/10.1016/j.chemgeo.2012.09.028

Sætre, C., Hellevang, H., Riu, L., Dypvik, H., Pilorget, C., Poulet, F., Werner, S.C., 2019. Experimental hydrothermal alteration of basaltic glass with relevance to Mars. Meteorit. Planet. Sci. 54, 357–378. https://doi.org/10.1111/maps.13214

Sel, O., Radha, A.V., Dideriksen, K., Navrotsky, A., 2012. Amorphous iron (II) carbonate: Crystallization energetics and comparison to other carbonate minerals related to CO2 sequestration. Geochim. Cosmochim. Acta 87, 61–68. https://doi.org/10.1016/j.gca.2012.03.011

Tosca, N.J., Ahmed, I.A.M., Tutolo, B.M., Ashpitel, A., Hurowitz, J.A., 2018. Magnetite authigenesis and the warming of early Mars. Nat. Geosci. 11, 635–639. https://doi.org/10.1038/s41561-018-0203-8

Tosca, N.J., Guggenheim, S., Pufahl, P.K., 2016. An authigenic origin for Precambrian greenalite: Implications for iron formation and the chemistry of ancient seawater. Geol. Soc. Am. Bull. 128, 511–530. https://doi.org/10.1130/B31339.1

Tosca, N.J., Knoll, A.H., McLennan, S.M., 2008. Water Activity and the Challenge for Life on Early Mars. Science 320, 1204–1207. https://doi.org/10.1126/science.1155432

Velbel, M.A., 1999. Bond strength and the relative weathering rates of simple orthosilicates. Am. J. Sci. 299, 679–696. https://doi.org/10.2475/ajs.299.7-9.679

Warren, E.A. and Ransom, B., 1992. The influence of analytical error upon the interpretation of

chemical variations in clay minerals. *Clay Minerals*, *27*(2), pp.193-209.

Wray, J.J., Murchie, S.L., Bishop, J.L., Ehlmann, B.L., Milliken, R.E., Wilhelm, M.B., Seelos, K.D., Chojnacki, M., 2016. Orbital evidence for more widespread carbonate-bearing rocks on Mars. J. Geophys. Res. Planets 121, 652–677. https://doi.org/10.1002/2015JE004972

Zeebe, R., Wolf-Gladrow, D., 2001. CO2 in Sewater: Equilibrium, Kinetics, Isotopes. Gulf Professional Publishing.

Chapter 3

Unravelling Surface and Subsurface Carbon Sinks Within the Early Martian Crust

Author's note: This chapter is the document submitted to and subsequently published within the journal *Earth and Planetary Science Letters* (Kissick et al., (2021), Unravelling surface and subsurface carbon sinks within the early Martian crust, Earth and Planetary Science Letters, 557, 116663, doi: 10.1016/j.epsl.2020.116663). Owing to copyright, the original paper cannot be displayed within this thesis. The text below is what was accepted as the final paper proofs and includes author contributions, all figures, and all supplementary information excepting the Excel spreadsheet published with all data, which is available upon request or here online: https://www.sciencedirect.com/science/article/pii/S0012821X20306075?dgcid=rss_sd_all.

Unravelling surface and subsurface carbon sinks within the early Martian crust

Lucy E. Kissick[a,b]*, Tamsin A. Mather[a], and Nicholas J. Tosca[a,c]

[a] *Department of Earth Sciences, University of Oxford, Oxford, UK*

[b] *Present address: National Nuclear Laboratory, Cumbria, UK*

[c] *Present address: Department of Earth Sciences, University of Cambridge, Cambridge, UK.*

**lucy.kissick@uknnl.com*

1. Abstract

Understanding the climate history of Mars, one of our closest planetary neighbours, has important implications for understanding the environmental evolution of Earth and other rocky planets in general. The widespread recognition of an extensive sedimentary record modified, at least in part, by liquid water, holds much promise to provide evidence about Mars' past. However, unravelling the pressure and compositional history of Mars' Noachian atmosphere has remained problematic. Based on expected outgassing behaviour, observed atmospheric isotope ratios, and climate models, carbon dioxide is widely considered a main constituent of the early Martian atmosphere. If this was indeed the case, it is surprising that carbonate minerals, the expected sinks for this carbon, are only abundant in a few isolated localities across the Martian surface. Three broad possibilities may account for this apparent inconsistency: (1) carbonates formed under pCO_2 higher than present but were buried, or subsequently destroyed; (2) Noachian atmospheric pCO_2 was significantly lower than current estimates; or (3) low-temperature carbonate formation was kinetically controlled under the aqueous conditions that characterised much of the early Martian surface. While orbital spectroscopic investigations have yielded an increasing inventory of isolated carbonate-bearing deposits, their relative rarity at the near-surface has prompted suggestions that the Noachian atmosphere was commonly characterised by low pCO_2. Without a more complete investigation of the carbonate-forming processes occurring within the ancient crust, no hypothesis can be tested robustly. Here, we examine the controls on Fe(II)-carbonate precipitation in low-temperature, anoxic water-rock systems as a function of pCO_2. In experiments lasting up to 85 days, no measurable Fe(II)-carbonate precipitation occurred within the limits of analytical detection, despite significant and sustained supersaturation with respect to siderite. These observations are quantitatively consistent with recent investigations highlighting a significant supersaturation threshold for Fe(II)-carbonate nucleation. Reaction path models that incorporate these constraints indicate that Fe(II)-carbonate supersaturation thresholds would have been commonly met in low rock:water ratio systems isolated from the Noachian atmosphere as opposed

to high rock:water ratio, open-systems exposed at the near surface. These results suggest the rarity of carbonates exposed at or near the surface of Mars may be controlled, at least in part, by a lack of deep crustal exposures and lack of the geochemical conditions conducive to carbonate formation, rather than insufficient atmospheric pCO_2. Such geochemical constraints are in turn consistent with available orbital geological data indicating that carbonates may be more abundant within the deep crust, potentially representing a significant subsurface carbon sink.

Keywords

Noachian Mars, siderite, carbonate, Martian atmosphere, experimental geochemistry.

2. Introduction

The early evolution of rocky planetary bodies is archived by the minerals deposited within their crusts. Plate tectonics has obliterated the geological record of the first ~1 billion years of Earth's history. Mars has not experienced crustal destruction in the same manner as Earth, and the recent discovery of an extensive and ancient sedimentary record on Mars offers a unique opportunity to understand Earth's earliest evolution in the context of other rocky planetary bodies (Malin and Edgett, 2000; McLennan et al., 2019). Yet, although the last two decades of Mars exploration have shown that liquid water shaped much of the planet's ancient sedimentary record, the early evolution of the Martian climate has endured as a major problem in modern planetary science. It is generally assumed that CO_2 has always remained the dominant constituent of the Martian atmosphere, as observed today (Owen et al., 1977; Wordsworth et al., 2017), but climate models have shown that a thick CO_2 atmosphere alone could not have produced a greenhouse effect sufficient to stabilise liquid water in the context of a faint young sun (Sagan and Chyba, 1997). Accordingly, a lack of constraints on both the total atmospheric pressure as well as the identity of

both major and minor atmospheric constituents have fuelled active debate as to how liquid water was stabilised over geologically significant timescales (Pollack et al., 1987; Wordsworth et al., 2017).

More information about the Martian sedimentary record also leads to further unknowns in terms of how to interpret it in relation to past atmospheric composition. As geochemical considerations indicate that liquid water and a CO_2-rich atmosphere should produce carbonate minerals, their apparent scarcity on both the ancient and extant Martian surface has persisted as a conundrum (Fairén et al., 2004; Ehlmann et al., 2008; Michalski et al., 2013). Carbonate minerals have long been recognised as minor pre-terrestrial alteration phases within Martian meteorites (see Bridges et al., 2019, for summary), and as minor or trace components of surficial dust (Bandfield et al., 2003) and soils (Boynton et al., 2009) but they are rarely exposed in significant quantities at the surface. Numerous hypotheses have sought to explain this rarity, including formation and subsequent burial or destruction (Ehlmann et al., 2008; Michalski and Niles, 2010), kinetic competition with clay minerals (Michalski et al., 2015), insufficient pCO_2 (Bristow et al., 2017), loss of CO_2 to space (Jakosky, 2019), or suppression by widespread acidic fluids (Fairén et al., 2004), but these hypotheses have proven difficult to test against the geological record. Alternatively, oxalates have been recently suggested as a possible terminal C-sink within the Martian crust (Franz et al., 2020), but the global importance of this potential sink is unknown at present.

The problem of carbonate formation on ancient Mars was further intensified when NASA's Mars Science Laboratory (MSL) mission obtained evidence for a redox-stratified lacustrine environment preserved within the sedimentary rocks at Gale Crater (Hurowitz et al., 2017). This depositional system commonly featured Fe^{2+} and geochemical/mineralogical characteristics consistent with circum-neutral pH — favourable conditions for carbonate production in the presence of a CO_2-rich atmosphere (Pollack et al., 1987). Yet, carbonate minerals remain well below 1 wt. % within these rocks, although reach a maximum of ~1-2 wt. % in some aeolian materials (Ming et al., 2014; Franz et al., 2020). On the basis of kinetic and thermodynamic relationships, these results were taken to reflect an ancient atmosphere featuring low pCO_2 — a

problematic result for all current models of atmospheric and climatic evolution (Bristow et al., 2017). However, experimental and theoretical data raised the possibility that Fe(II)-carbonate production within Gale Crater sedimentary rocks was instead subject to strong kinetic controls, which may have in turn influenced the distribution of carbonates within the ancient crust (Tosca et al., 2018).

In apparent contrast with data obtained from sedimentary rocks, some investigations have identified regionally significant accumulations of carbonate within exhumed deep-crustal rocks (Michalski and Niles, 2010; Wray et al., 2016), and isolated surface or near-surface deposits (Ehlmann et al., 2008; Morris et al., 2010; Edwards and Ehlmann, 2015). Together, these observations indicate that while carbonate formation was favoured in some geochemical systems, the mechanisms controlling carbonate formation, and therefore the cycling of carbon between the early Martian crust and atmosphere, are poorly constrained (Tosca et al., 2018; Franz et al., 2020). This precludes attempts to reconstruct palaeo-climatic conditions from the geological record, a particularly urgent problem given that NASA's *Perseverance* rover will soon investigate carbonate-rich sedimentary strata hosted at Jezero Crater (e.g., Ehlmann et al., 2008; Horgan et al., 2020).

Upon aqueous alteration under mildly acidic conditions at relatively low temperature (<50 °C), cations should be released in proportions controlled by a largely basaltic Martian crust (Milliken et al., 2009). Thus, under a CO_2-bearing atmosphere, Fe- and Mg-carbonates, and to a lesser extent Ca-carbonates, should be produced. Mg-rich carbonates are kinetically controlled such that their precipitation at low temperature is typically confined to highly alkaline environments that initially generate metastable hydrous phases such as hydromagnesite and nesquehonite, rather than its geologically stable form, magnesite (Königsberger et al., 1999; Power et al., 2019). $CaCO_3$, on the other hand, readily forms in some arid basaltic soils on Earth, although these environments reflect largely oxic conditions with cation budgets that can be influenced by sea-spray aerosols (Whipkey et al., 2000, 2002). How this picture might change in completely anoxic systems, however, is more difficult to evaluate. For example, experiments and numerical

modelling of low-temperature basalt-water interactions under Earth's currently oxic atmosphere show that the kinetics of Fe(II)-oxidation outpace Fe(II)-carbonate precipitation as pH (and therefore carbonate saturation states) increases (i.e., Gysi and Stefansson, 2012). Thus, although Ca- and Mg-carbonate formation cannot be discounted, by molar proportion, Fe(II)-carbonate precipitation should represent a quantitatively important carbon sink within the Martian crust, especially given that, on average, Martian basalts feature FeO concentrations two times higher than most terrestrial basalts (Wade et al., 2017). Consistent with this expectation, pre-terrestrial carbonates in Martian meteorites are overwhelmingly dominated by Fe(II), and siderite appears more common than previously thought in outcrops that sample deeper portions of the ancient Martian crust (Wray et al., 2016; Bridges et al., 2019). Nevertheless, there is little empirical data to predict the extent of Fe(II)-carbonate formation under anoxic conditions at low temperatures — a key component in developing a more complete understanding of carbonate deposition within the Martian crust.

To address these problems, we experimentally investigate anoxic water-rock interactions to examine the processes that control the precipitation of Fe(II)-carbonate minerals from a largely basaltic surface at 25 °C. We place these results in a broader geochemical context by examining kinetic controls on Fe(II)-carbonate formation, identified from our experiments, with reaction path models of water-rock interaction. We then contextualise our observations within the current inventory of surface carbonates on Mars to understand the factors controlling their formation and distribution.

3. Materials and Methods

3.1. Experiments

The focus of our experimental approach is to examine and constrain the parameters that promote Fe(II)-carbonate formation from the dissolution of rock-forming ferromagnesian minerals. To

isolate the Fe(II)-carbonate system and simplify the experimental approach, we first examined interactions between water and Fe-bearing olivine (fayalite: Fe_2SiO_4, Fo_0), which is the most reactive of rock-forming silicates found within the Martian crust (Velbel, 1999). As aqueous Fe chemistry may be influenced by the catalytic activity of minerals that commonly occur with natural fayalite, we chose to synthesise pure fayalite to be sure what reactions we were studying. Although the chemical composition of olivine in many igneous and sedimentary rocks on Mars is known to contain appreciable Mg (Vaniman et al., 2014), our experiments featured pure synthetic fayalite or physical mixtures of synthetic fayalite and natural forsterite. Large, optically pure individual crystals of forsterite were hand-picked from a natural specimen, crushed, then sieved to the desired particle size (average 0.0554 m^2/g). Mineralogical purity was confirmed via powder X-ray diffraction.

To synthesise 10 g fayalite, 2.9485 g of SiO_2 and 7.8365 g of Fe_2O_3, (Alfa Aesar; 99.5 % purity), were heated to 800 °C to remove volatiles. The materials were thoroughly homogenised in an agate pestle and mortar, pelletised under 4 metric tonnes of pressure into 2-3 g individual pellets, placed in an alumina crucible, and heated in a furnace for 3 hours. Temperatures were 1080 °C: as high as possible to accelerate reaction kinetics, but below the fayalite melting point of ~1200 °C. To prevent the formation of more oxidised Fe-phases such as wüstite or magnetite, we fixed oxygen fugacity (f_{O2}) at this temperature between the iron-wüstite and wüstite-magnetite buffers ($\log f_{O2} = -12.5$) by utilising a gas flow mixture of 84 mL/s CO and 114 mL/s CO_2 to reduce Fe(III). When analysed via BET (Brunauer-Emmett-Teller) surface area analysis using the Micromeritics 3flex facilities at the Chemistry Research Laboratory, University of Oxford, the average specific surface area for fayalite was 0.3 m^2/g, with an estimated precision of ~10 relative percent.

All water-rock interaction experiments were conducted within a Coy polymer anoxic glovebox with an atmosphere of 4 % H_2/96 % N_2. Trace O_2 was scrubbed from the system by a Pd catalyst, which produces H_2O as a by-product, which is then removed via adsorption onto an

anhydrous $CaSO_4$ desiccant. The gas composition of the anoxic chamber was continuously monitored with a Coy gas analyser and the atmosphere maintained at <1 ppm $O_{2(g)}$ for the duration of all experiments, sample preparation, and analysis. All experiments were conducted at 25 °C (± 1.5 °C) within 0.172 L Nalgene serum bottles sealed with 1 cm butyl-rubber caps, wrapped in Al-foil to prevent photo-oxidation (Braterman et al., 1984), and continuously stirred on an orbital shaker. pH and oxidation-reduction potential (ORP) were data-logged using Ag/AgCl combination pH and platinum ORP electrodes. The pH electrode was calibrated with NIST standard buffer solutions (pH 4 and 7) and the ORP electrode with ZoBell's solution (Nordstrom, 1977). Based on the periodic measurement of calibrant standards, precision for pH was ± 0.05 (1σ).

All aqueous solutions were made with deionised Milli-Q first purged of dissolved O_2 by bubbling O_2-free N_2 gas through the solution for at least 45 minutes (Butler et al., 1994) before transfer to the glovebox. The water was then stirred for 1 hour in the anoxic atmosphere and left for at least 24 hours to allow any residual O_2 to escape. We used dilute sulphuric acid (H_2SO_4) to fix the starting pH of each experiment to either 2 or 4. This is because Martian meteoric water may have commonly featured low pH due to the input of volcanic volatiles such as H_2SO_4 or HCl (Hurowitz et al., 2010). This may have been continuously provided to Martian soils as meteoric water, enabling through-flow systems and transport phenomena relevant under specific circumstances.

Total dissolved inorganic carbon (DIC) concentrations for each experiment were chosen to equate to saturation with either a 0.1, 0.5, or 1.0 bar CO_2 atmosphere under the desired initial pH. DIC was initially set with freshly prepared sodium bicarbonate ($NaHCO_3$) stock solutions.

To minimise degassing of CO_2 over the course of experiments, headspace in reaction vessels was eliminated by completely filling each vessel with solution and sealing with gas-tight septum caps. Solution samples (each 1 % of solution volume) were withdrawn via 0.1 μm syringes through the septum caps. The samples were then syringe-filtered to 0.22 μm. In total, 10 solution

samples were collected from each experiment, except from low rock:water ratio experiments, where solution volume did not allow repeated sampling; in these cases, one sample was extracted at experiment termination. Experiments lasted between 12 hours and 85 days. 86 individual experiments form the basis of the discussion in this paper.

Four groups of experiments were conducted, detailed in Table 1. These experiments vary in dissolved CO_2 concentration, rock:water ratio, and initial pH of the solution to examine a variety of conditions conducive to the saturation and precipitation of Fe(II)-carbonate.

Elemental analysis of solution samples was performed via inductively coupled optical emission spectrometry (ICP-OES) at the Scottish University Environmental Research Centre, University of Glasgow, and also via mass spectrometry (ICP-MS) in-house at the Department of Earth Sciences, University of Oxford. 0.15 mL samples of solution were acidified with 14.75 mL of O_2-free 5 % HNO_3 to prevent the formation of solid phases before analysis.

Upon experiment termination, solutions were vacuum-filtered through a 0.22 μm nylon membrane and solids left to dry within the glovebox. Solids were analysed in-house via powder X-ray diffraction (XRD) using a PANalytical Empyrean Series 2 X-ray diffractometer with a Co $K\alpha_1$ source operated at 40 kV and at 40 mA, scanned between 5 and 80 degrees 2Θ. Powders were loaded onto single crystal silicon sample holders and wrapped with Kapton film within the glovebox to minimise oxidation during analysis.

Scanning electron microscopy (SEM) was performed using a FEI Quanta 650 FEG on selected, uncoated samples to characterise the morphology of solid materials and identify any minor phases below XRD detection levels (estimated at 1-5 wt. % depending on the nature of the crystalline phase). A small amount of solid was mounted on a carbon stub within the glovebox, then transferred into the evacuated SEM chamber. Energy dispersive X-ray spectrometry (EDS) was also performed using this SEM for *in situ*, semi-quantitative, compositional analysis.

To additionally identify and characterise the presence of secondary minerals, transmission Fourier transform infrared spectroscopy (FT-IR) was performed using a PerkinElmer Frontier

mid-IR spectrometer on powdered solid samples mixed with KBr powder at a KBr-sample ratio of ~1:200. These samples were ground together, pelletised at 7 metric tonnes, and analysed within 20 minutes of exposure to air. Measurements were collected from between 400 to 4000 cm^{-1} at 1 cm^{-1} resolution. We estimate the minimum detection limits for carbonate phases within our samples at ~0.8 wt. % following standardisation procedures outlined in Vagenas et al. (2003).

3.2. Geochemical Modelling

To more broadly investigate a range of environmental parameters on the evolution of solution chemistry during water-rock interaction, we adapted the kinetic model used in Tosca et al. (2018) in the software *The Geochemist's Workbench* (version 12, Bethke, 2017), which uses thermodynamic data from the Lawrence Livermore National Laboratory (LLNL) database (Delany and Lundeen, 1991). The model computes mineral dissolution rates according to the following equation:

$$\boldsymbol{r = A_S k_+ a_{H+}^n \left(1 - \frac{Q}{K}\right)} \quad \text{(eq. 1)}$$

where r is the rate of dissolution, A_S is the surface area (cm^2), k_+ is the rate constant (2.34×10^{-11} mol cm^{-2} sec^{-1} for both fayalite and forsterite; Bandstra and Brantley, 2008), a_{H+} is the dissolution reaction's dependence upon the concentration of protons to the power of n (where n was determined to be 0.372 by Bandstra and Brantley, 2008), Q is the activity product and K the equilibrium constant for the dissolution reaction.

The reaction path model introduces free quantities of fayalite and/or forsterite to a dilute 1 kg solution and iteratively solves the equilibrium state of the system as a function of the reaction progress variable. pH was allowed to evolve until steady state conditions were reached. Four key parameters were varied in each model: (1) rock:water ratio (1:1 or 1:500, approximating subsurface/surface waters respectively); (2) particulate specific surface area with values (100 or

1000 cm^2/g) reflecting varying estimates for San Carlos olivine (~40-840 cm^2/g from the study of Brantley and Mellott, 2000, and our own BET analyses, which together represent realistic estimates of minimum and maximum olivine particle surface areas typical of this mineral, and thus the surface available for reaction); (3) dissolved CO_2 content (equating to 0.1 or 1.0 bar CO_2); and (4) open versus closed system conditions with respect to CO_2 (simulating a water in constant contact with the atmosphere, or a subsurface aqueous system isolated from the atmosphere, respectively).

4. Results

4.1. Temporal evolution of solution chemistry

The temporal evolution of solution chemistry during water-rock interaction is controlled by mineral dissolution and, once secondary mineral phases become supersaturated, mineral precipitation. The fayalite dissolution rate, as for many other rock-forming silicate minerals, is controlled by a number of factors, but principally pH, particle surface area, temperature, and the degree of undersaturation (which is typically a function of the Gibbs free energy change of the dissolution reaction; (Aagaard and Helgeson, 1982; Lasaga, 1998). As H^+ is consumed and cations are released to solution during the dissolution reaction, pH increases, which decreases dissolution rate accordingly. As a consequence, closed-system water-rock experiments typically exhibit an initial rapid phase of chemical change, followed by a gradual change to steady state (e.g., Qafoku et al., 2012). This relationship is directly observed in Figure 1, which illustrates the pH pathway (a), dissolved Fe (b), dissolved SiO_2 (c), and Fe/Si ratio (d) over time for a typical fayalite-bearing experiment. As this particular experiment was run for over two months, the time intervals between each extraction do not permit visualisation of the rapid initial dissolution kinetics that were observed for other experiments sampled more frequently across the first days (for the full set of experimental data, see Supplementary Data). The Fe/Si ratio in Figure 1d indicates that dissolution is, in some cases, non-stoichiometric with respect to Fe and Si, with Fe/Si ratio reaching 1.7-2.2.

Figure 1d shows the preferential release of Fe in solutions begun at an acidic pH, while for experiments begun at pH 4 this is slightly closer to stoichiometric. The precipitation of Si from solution as amorphous Si (discussed below) is likely to have removed Si from solution, increasing the Fe/Si ratio over the course of these experiments.

4.2. Siderite saturation

To assess the evolution of our experiments with respect to siderite saturation state, Figure 2 shows all solution data as a function of Fe^{2+} activity and pH at three different DIC concentrations (which are proportional to the three pCO_2 conditions explored at fixed initial pH of 2 or 4; Table 1). Fe^{2+} activities were obtained from solution concentrations by iteratively calculating the ion activity coefficients and ionic strength for all dissolved aqueous species using the B-dot equation (Helgeson and Kirkham, 1974), and dissociation constants for carbonic acid (K_1 and K_2; (He and Morse, 1993). Here saturation state with respect to siderite is defined as:

$$\boldsymbol{\Omega(siderite) = \frac{a_{Fe^{2+}} \times a_{CO_3^{2-}}}{K_{sp}}} \qquad \text{(eq. 2)}$$

where Ω is the ratio between K_{sp} and the Ion Activity Product (IAP, which equals the activities of Fe^{2+} and CO_3^{2-} multiplied together), K_{sp} is the solubility product for siderite ($10^{-10.24}$; Singer and Stumm, 1970), and $\boldsymbol{a_{CO_3^{2-}}}$ is the activity of CO_3^{2-}. For reference, the equilibrium solubility line for siderite is plotted on Figure 2. We have opted to use this simple approach, rather than adopt a speciation model for aqueous Fe(II) chemistry, because speciation models are poorly constrained and not supported by available data (Jiang and Tosca, 2020). An important assumption behind this figure is that solution DIC is fixed (i.e., there is no significant exchange between headspace and solution) and that carbonate mineral precipitation is effectively none over the course of the experiment, thus leaving the solution DIC pool largely unaltered. As pH and dissolved Fe^{2+}

concentration (and therefore Fe^{2+} activity) generally increase throughout the course of an experiment, experimental solutions progressively evolve toward higher supersaturation with respect to siderite (Figure 2). Experiments begun at pH 2 (in red) consistently display the highest Fe^{2+} activities, reflecting greater amounts of fayalite dissolution in acidic solutions, but experiments begun at pH 4 (in blue) consistently reach the highest pH levels owing to their higher initial pH and thus lower buffer capacity against alkalinity generated by silicate dissolution.

The three graphs in Figure 2 suggest that all experiments evolve to varying levels of supersaturation with respect to siderite, and that some experiments evolve to exceedingly high supersaturation levels. As expected from equilibrium carbonate chemistry, siderite saturation state is maximised with high pH and, to a lesser extent, high Fe^{2+} activity, for a given fixed DIC pool.

4.3. Fe(II)-silicate and amorphous SiO_2 formation

An additional factor that may influence the nucleation and subsequent precipitation of siderite is the precipitation of other Fe-bearing phases. In the fayalite-water system investigated here, Fe(II)-silicate precipitation constitutes one such process. The Fe(II)-silicate greenalite ($Fe^{II}_3Si_2O_5OH_4$), like siderite, precipitates under anoxic conditions at circum-neutral pH (Tosca et al., 2016) and this kinetic competition may have influenced biogeochemical cycles on the Archaean Earth (Jiang and Tosca, 2019).

Figure 3, a solubility diagram for the Fe^{2+}-SiO_2-H_2O system, encompasses the dominant controls on greenalite, which are pH, the activity of SiO_2, and the activity of Fe^{2+}. In Figure 3, the apparent solubility of greenalite, as estimated by Tosca et al. (2016) ($\log K_{sp} = 27.6$), provides a reference for chemical conditions likely to trigger Fe(II)-silicate nucleation, with the supersaturation of amorphous Si estimated by the exceeding of the dashed line (Siever, 1992). In Figure 3, datapoints from experiments begun at both pH 2 and 4 (red and blue) exceed the apparent solubility of greenalite across all DIC concentrations. The figure also indicates that all experiments conducted under lower initial pH are supersaturated with respect to amorphous silica.

Amorphous silica precipitation in these experiments is consistent with the earlier observation of non-stoichiometric Fe/Si release (Figure 1). From these constraints on the stoichiometry of dissolution, we can quantify the amount of amorphous silica by assuming that the $SiO_{2(aq)}$ not released into solution (therefore resulting in non-stoichiometric solution Fe/Si levels) has all precipitated as amorphous silica. From this, we estimate that a total of 6×10^{-4} moles of amorphous silica precipitated over the course of the experiment.

4.4. Solid phase characterisation

XRD, FT-IR, and SEM were all employed to examine whether secondary minerals precipitated over the course of the experiments. XRD analysis did not identify any new mineral phases: no new diffraction peaks were observed relative to unaltered fayalite or forsterite-fayalite mixtures (Supplementary Figure 1). This indicates that no additional crystalline phases are present above the detection limits of the instrument, which, under the analysis conditions used here, corresponds to approximately 5 wt %.

FT-IR analysis offers a more sensitive evaluation of both crystalline and non-crystalline phases present. FT-IR transmission spectra show no indication of the presence of carbonates. For example, the most intense absorption for carbonates arises from CO_3^{2-} stretching within the mineral lattice (Farmer, 1974); this is located at ~1350-1500 cm^{-1} for rhombohedral carbonate minerals, but is absent from all spectra (Supplementary Figure 2).

In addition to XRD and FT-IR, SEM was employed to examine morphological changes between reacted and unreacted solids. This analysis revealed no clear evidence of secondary Fe-carbonate phases, including characteristic morphologies observed in other synthetic studies (e.g., (Jimenez-Lopez and Romanek, 2004; Qafoku et al., 2012; Jiang and Tosca, 2019). However, in several experiments conducted for 85 days (the longest period run), with both fayalite and forsterite present, evidence for secondary mineral formation was observed upon the fayalite grains under all CO_2 levels and begun at both pH 2 and 4. The secondary precipitates displayed a

morphology that replicated grain boundaries and interstices (Figure 4a, b). Given the relatively fine scale at which the precipitates occur, EDS spectra do not allow unambiguous chemical differentiation from the underlying olivine substrate, but a clear lack of euhedral morphology is consistent with the presence of amorphous silica, consistent with solution chemistry analyses discussed above.

SEM evidence also indicates a distinct secondary phase in addition to tentative amorphous silica. This phase occurred in four of the same experiments where amorphous silica was identified, and one where no silica was identified. This phase occurs as aligned, uniformly dispersed, nanometre-scale plates (Figure 4c and d) and was identified only either upon fayalite grains Figure 4c or possibly either as coalesced nuclei sometimes as large as 10 μm across or upon an aggregate material Figure 4d. When analysed via EDS without carbon/gold coating and at low vacuum, Fe, Si, O, and C are present; however, contribution from the fayalite and surrounding carbon adhesive cannot be discounted. While C was also identified via EDS on non-precipitate-bearing fayalite grains, as well as unreacted fayalite, this was consistently ~4 wt % lower than the precipitate-bearing grains, and likely reflects contribution from the surrounding carbon adhesive upon which the samples were set. If this C-bearing phase is a Fe(II)-carbonate, its negligible overall abundance and/or a potentially non/poorly-crystalline nature may render it undetectable by FT-IR and XRD.

5. Discussion

5.1. Siderite precipitation kinetics

Solution-phase analyses indicate that the anoxic water-rock systems investigated here commonly feature excessive supersaturation with respect to siderite (i.e., $\Omega_{siderite}$ up to 3,610). However, despite such high supersaturation, XRD, FT-IR and SEM all indicate that the formation of secondary Fe(II)-carbonate is negligible. Taken together, these data indicate that the precipitation of Fe(II)-carbonate at 25 °C is strongly controlled by kinetics.

Mineral precipitation must be preceded first by nucleation, where constituent ions form a nucleus or cluster that is sufficiently large to be thermodynamically stable (Volmer and Weber, 1926; Lasaga, 1998). Nucleation thus occurs when this stability threshold is exceeded, which in turn corresponds to a critical threshold in solution supersaturation state. Once stable nuclei are produced and the solution remains supersaturated, crystal growth may occur. In many low-temperature aqueous systems, the homogeneous (or spontaneous) nucleation of secondary minerals from solution requires significant levels of supersaturation (Turnbull and Fisher, 1949). This varies depending on the solid phase, and is sensitive to factors such as mineral chemistry and structure, and, most importantly, mineral-solution interfacial energy (Lasaga, 1998).

For Fe(II)-carbonate, it has been long known that the effective critical supersaturation threshold at 25 °C is far higher than for other carbonates such as calcite (e.g., Jimenez-Lopez and Romanek, 2004). Two recent experimental datasets clarify where the effective saturation threshold might lie for the homogenous nucleation of Fe(II)-carbonate. The first is outlined in Tosca et al. (2018) where the critical threshold for Fe(II)-carbonate nucleation was estimated at $\Omega_{siderite}$ values of ~400. This $\Omega_{siderite}$ was exceeded in many of our experiments (Figure 2), including three with nano-particle precipitation observed via SEM. Jiang and Tosca (2019) also constrained the critical supersaturation associated with Fe(II)-carbonate nucleation. These authors hypothesised that under highly supersaturated conditions Fe(II)-carbonate nucleation proceeds via amorphous iron carbonate (AFC), a metastable precursor to siderite. In their study, Jiang and Tosca (2019) suggested that the AFC precursor is characterised by a different chemical composition than siderite, and that the apparent solubility of AFC effectively defines the maximum supersaturation of the Fe(II)-carbonate system at 25 °C. Plotting Jiang & Tosca (2019)'s AFC apparent solubility (the *AFC supersaturation line*) delineates conditions where AFC and thus Fe(II)-carbonate, may nucleate and precipitate. The AFC supersaturation line is plotted on three graphs in Figure 2, where each plot represents experiments conducted under three DIC concentrations that equate to either 0.1, 0.5, or 1.0 bars of dissolved CO_2 at initial pH of 2 or 4. Plotted upon each are the pH

and dissolved Fe^{2+} content for each extracted sample (10 × samples per one experiment), which, in addition to DIC, comprise the three factors controlling Fe(II)-carbonate saturation state. Out of the data shown in Figure 2, only a relatively small number of individual datapoints exceed this line. This analysis provides a possible explanation for why Fe(II)-carbonate formation is apparently negligible in our system despite significant supersaturation: in light of available constraints on Fe(II)-carbonate nucleation, the conditions explored here only surpassed the nucleation threshold infrequently. For the experiments that did exceed the AFC line, solution-phase analyses and solid-phase characterisation indicate that precipitation of Fe(II)-carbonate was negligible; even though some nanometre-scale precipitates were identified across the most saturated experiments, their formation did not control Fe and/or CO_2 concentrations in these experiments (Figure 2). This result can be understood in the context of 'induction time,' or the time elapsed between the moment supersaturation is reached and the moment nucleation occurs (Kashchiev et al., 1991). The induction time typically carries a strong exponential dependence on supersaturation state (Lasaga, 1998), and so these experiments may have been terminated before significant nucleation occurred. Consistent with this, Jiang and Tosca (2019) noted that even when AFC solubility is crossed, nucleation and apparent solubility control is relatively slow, occurring over a period of several days.

5.2. Unravelling surface and subsurface carbon sinks within the early Martian crust

Our experimental results indicate that Fe(II)-carbonate precipitation from supersaturated solutions is unlikely to occur unless a critical nucleation threshold is crossed, and that this only rarely occurred across a broad range of conditions explored in our experiments. From these results, we can best understand the distribution of these phases on Mars by posing the question: which environments hosting water-rock interaction were most likely to surpass the nucleation threshold for Fe(II)-carbonate precipitation? In other words, how would carbon burial have been distributed within the Martian crust?

To explore this in a more quantitative manner, we used reaction path models of rock:water interaction to examine how rock:water ratio, particulate surface area, dissolved CO_2 levels, and open versus closed systems with respect to CO_2 influence solution chemistry and Fe(II)-carbonate saturation states (Figure 5). Specifically, we examined which conditions promote Fe(II)-carbonate supersaturation levels that exceed AFC solubility estimates derived from Jiang and Tosca (2019). These results are consistent with the general expectation that changes in alkalinity and/or DIC concentration will fundamentally control carbonate mineral saturation state (Zeebe and Wolf-Gladrow, 2001). Among the most important processes that influence alkalinity during rock:water interaction are the rock:water ratio and initial pH. Both of these parameters control how rapidly silicate mineral dissolution provides alkalinity to the solution (the rate of which is maximised by low rock:water ratios and relatively high initial pH; Figure 5c and d). However, pCO_2 is the most significant parameter controlling Fe-carbonate saturation, in that it controls how DIC concentrations evolve during water-rock interaction (left-hand column: 0.1 bar CO_2; right-hand column: 1.0 bar CO_2).

If pCO_2 is increased and the system remains open with respect to the atmosphere, Fe(II)-carbonate supersaturation remains relatively low, and requisite supersaturation thresholds are not crossed. These conditions would be satisfied in rock:water interaction systems which are open to the atmosphere where alkalinity contributions from silicate weathering cannot compete with acid-base CO_2 buffering from the atmosphere. Under these conditions, increased alkalinity resulting from water-rock interaction in turn results in CO_2 absorption from the atmosphere which also increases DIC concentrations. This results in reaction path trajectories in DIC-alkalinity space that evolve sub-parallel to the Fe-carbonate saturation threshold (Figure 5a and b), sustaining undersaturated conditions in atmospherically buffered systems.

Conversely, our reaction path models show that AFC solubility is commonly exceeded in systems that are closed with respect to CO_2, such as sub-surface aquifers or ice-covered lakes (Kling et al., 2020). This is because the DIC pool is fixed, but alkalinity increases due to silicate dissolution,

which drives rapid changes in Fe(II)-carbonate saturation state (i.e., vertical trajectories on Figure 5a and b). This effect has been observed in Icelandic basaltic catchments, where the rapid consumption of CO_2 with basaltic materials drove pH to relatively high levels (Gislason et al., 1996; Perez-Fodich and Derry, 2019). This effect is further magnified at low rock:water ratio. It is worth noting here that the maximum pH levels reached in our reaction path models are limited by thermodynamic saturation with respect to olivine, which causes the dissolution rate to collapse to zero. The difference in pH between this threshold and observations in natural systems where pH may reach 9 or even 10 (i.e., Gislason et al., 1996; Perez-Fodich and Derry, 2019) may be due in part to the surface chemistry of silicate minerals and exchange reactions that consume additional protons. These reactions are thought to account for the observation that the "immersion pH" of Ca/Mg-rock forming silicates in pure or dilute water ranges from ~9-11 (Oelkers et al., 2009; Pokrovsky and Schott, 2000). These surface proton exchange reactions are not accommodated in our model. Nevertheless, by extension, our results indicate that environments most likely to favour Fe(II)-carbonate formation at low temperature involve low rock:water ratio and a closed system with respect to CO_2 (but relatively high initial pCO_2 or DIC concentrations). This includes, for example, subsurface environments which feature infiltration by CO_2-charged meteoric water. Carbonate formation has also been advocated within lacustrine systems (i.e., open system conditions), though constraints on the temperature of carbonate precipitation are lacking for these examples and geological evidence indicates that contribution from magmatic- or impact-hosted hydrothermal waters cannot be ruled out (e.g., Ruff et al., 2014; Brown et al., 2020; Horgan et al., 2020). *In-situ* constraints on open system lacustrine systems on early Mars show that siderite was absent from the primary mineral assemblage even though such environments were characterised by intermittent subaerial exposure and potential evaporative concentration (Ming et al., 2014; Stein et al., 2018).

Although constraints from reaction path modelling illuminate the controls on Fe(II)-carbonate supersaturation in water-rock systems on early Mars, kinetic controls on the precipitation of non-

carbonate Fe-phases (i.e., Fe-oxides, Fe-silicates, etc.) undoubtedly also played an important role in the distribution of Fe-carbonates. These were not considered explicitly in the reaction path models explored here because of a general lack of robust kinetic data for these phases. In anoxic systems, pH levels at circum-neutral or higher favour the precipitation of Fe(II)-oxides and Fe(II)-silicates in addition to Fe(II)-carbonate (Ruff et al., 2014; Horgan et al., 2020; Brown et al., 2020). Although available data do not permit quantitative assessments of Fe(II)-silicate formation from a kinetic standpoint, experiments show that Fe(II)-silicate formation rates are relatively slow under supersaturated conditions, similar to Fe(II)-carbonates. However, clay formation on Mars appears to have been relatively efficient over geological timescales — over 70 % of Martian smectites, the most common clay identified, are classed as Fe-rich (Michalski et al., 2015). Similarly, clays and carbonates are rarely found contemporaneously on Mars (Ehlmann et al., 2012), and where they are, they are Mg-rich (e.g., Ehlmann et al., 2008). This may indicate that clay formation proceeded under conditions not typically conducive to Fe(II)-carbonate formation, that Fe-bearing clays efficiently outcompeted carbonate phases for Fe, or that Fe-carbonates were poorly preserved over geological timescales relative to clay minerals.

In addition, magnetite, as on the early Earth, competed with siderite for Fe on early Mars. Tosca et al. (2018) presented experimental data showing that, under some conditions, Fe(II)-oxide formation (and subsequent transformation to green rust and magnetite) outpaces Fe(II)-carbonate nucleation. None of our experiments reached $Fe(OH)_2$ saturation, which would be surpassed by exceeding a log $\left(a_{Fe^{2+}}/a_{H^+}^2\right)$ value of 14.0 (Feitknecht and Schindler, 1963) on Figure 3. However, the reactive transport models of Tosca et al. (2018) showed these conditions were maximised at the interface between lake bottom water and groundwater in the Gale Crater lacustrine system, and may not reflect water-rock interaction within the basaltic crust more generally.

Taken together, our experimental results and reaction path modelling provide kinetic insight on the known distribution of carbonates within the Martian crust. Although Mg-bearing carbonates

have been recognised from *in-situ* rover data and orbital spectroscopy, data indicate that hydrothermal processes may have played an important role in their formation (e.g., Ehlmann et al., 2008; Morris et al., 2010). Fe-bearing carbonates, however, appear to be mostly focused in exhumed crustal rocks potentially sampling the deep subsurface (e.g., Michalski and Niles, 2010; Michalski et al, 2013). For instance, siderite has been identified within excavated crustal exposures from up to 6 km deep (Michalski and Niles, 2010). Such exposures from the deep subsurface are rare, but increasingly detailed surveys continue to yield evidence for further siderite-bearing outcrops (e.g., Wray et al., 2016). Siderite has also long been recognised as a component of pre-terrestrial alteration assemblages in Martian meteorites thought to have been formed predominantly by sub-surface fluids (e.g., Bridges et al., 2019). Siderite hosted in Martian meteorites suggests these samples were once part of such a favourable geochemical environment: many of them appear to record low rock:water ratio, closed system conditions most favourable to overcoming kinetic influences on Fe(II)-carbonate nucleation discussed above (e.g., Halevy et al., 2011). Together, this pattern is consistent with the experimental and theoretical constraints on Fe(II)-carbonate formation presented here.

Deep crustal exposures into the Noachian crust may also represent preservational windows into warm, Fe^{2+}-rich, neutral-to-alkaline environments once in contact with CO_2-bearing fluids; however, the geochemical characteristics of these environments are comparatively less constrained. Nevertheless, experimental and theoretical constraints provide a framework for understanding why carbonate formation should have apparently been favoured within the subsurface, and this reservoir has yet to be exhaustively characterised. New constraints are likely to emerge as the *Perseverance* rover investigates sedimentary rocks that were at least partly derived from such a carbonate-rich crustal environment (e.g., Ehlmann et al., 2008), with orbital spectroscopy suggesting a detrital/deltaic origin for the carbonates at Jezero Crater, including evidence for carbonate-cemented point bar deposits (e.g., Goudge et al., 2017; Horgan et al., 2020).

5.3. Implications for the early Martian atmosphere

Finally, an improved understanding of Fe(II)-carbonate mineralisation processes permits more robust atmospheric constraints derived from the rock record. Our experimental observations are consistent with geochemical studies of terrestrial aquatic environments (e.g., Postma, 1982) and CO_2 sequestration and storage (Gysi and Stefánsson, 2012) that indicate significant supersaturation states required for Fe(II)-carbonate formation, and this must be folded into future considerations of how carbonate-bearing deposits do or do not constrain atmospheric pCO_2. Our models show Fe(II)-carbonate is unlikely to form in a high rock:water ratio, open system even under high pCO_2, owing to how atmospherically controlled DIC contributions tend to outweigh the alkalinity generation from silicate mineral dissolution. This suggests that accurate palaeo-pCO_2 constraints may be difficult to derive from estimates of carbonate exposed at the surface (Edwards and Ehlmann, 2015), or from strictly thermodynamic constraints on carbonate precipitation (e.g., Bristow et al., 2017).

This geochemical scenario for subsurface carbonate formation is consistent with recent observations of carbonates dominantly associated with the largest impact craters (Wray et al., 2016; Michalski and Niles, 2010; Michalski et al., 2013). In addition, global groundwater models (Kite and Melwani Daswani, 2019) and oxygen escape rates and hydrogen isotope ratios (Heard and Kite, 2020) have been interpreted to reflect a potentially significant subsurface carbon reservoir. Nevertheless, ancient subsurface environments preserved within the Martian crust remain poorly sampled, and accordingly, should feature as priority targets for orbital and *in-situ* exploration missions.

6. Conclusions

Our experiments demonstrate that Fe(II)-carbonate precipitation is subject to strong kinetic control, which is consistent with the current data constraining the distribution of Fe(II)-carbonates

within the Martian crusts. This is also quantitatively consistent with our geochemical modelling of different anoxic, aqueous systems. We consider, based on this research, that the apparent rarity of Fe(II)-carbonates preserved at the modern Martian surface, and perhaps carbonates in general, may be attributed to the following: a rarity of both deep subsurface exposures and the high saturation state required for their precipitation in low temperature water-rock systems, as opposed to low atmospheric pCO_2 during Mars' deep past. This data, in turn, informs future investigations of the early Martian C-cycle, which is likely to be further constrained by observations acquired by NASA's *Mars 2020* mission. For example, orbital investigations of the *Perseverance* landing site, Jezero Crater, reveal that regional geology may host carbonates that are relatively Fe-rich (e.g., Horgan et al., 2020). The presence of authigenic siderite preserved at Jezero, for example, may in turn offer broad constraints on maximum Fe(II)-carbonate saturation state that could be refined through inverse modelling approaches of water-rock interaction and sedimentation. More broadly, localised concentrations of siderite could best express relatively high alkalinity, rock-dominated environments responsible for efficiently burying inorganic carbon within the early Martian subsurface.

7. Acknowledgements

This study was funded by the UK Research and Innovation's Natural Environmental Research Council as part of the Doctoral Training Partnership in Environmental Research at the University of Oxford (grant number NE/L002612/1). The authors wish to thank the insightful comments of Louis Derry, Edwin Kite, and an anonymous reviewer, which significantly improved the science of this manuscript. The authors also wish to thank Louis Derry for his editorial handling and interest in the research. LEK wishes to thank Andrew Matzen and Bernie Wood for generous assistance and use of laboratory facilities for fayalite synthesis; Kat Clayton for assistance with XRD; Robert Jacobs for assistance with BET; Gillian MacKinnon for assistance with ICP-OES;

Phil Holdship for assistance with ICP-MS; and Jon Wade for assistance with SEM as well as many helpful discussions. This study also benefited from helpful discussions with Clancy Zhijian Jiang.

8. Author Contributions

Lucy E. Kissick: Data curation, Formal analysis, Investigation, Methodology, Project administration, Software, Visualization, Writing – original draft, Writing – review & editing. Tamsin A. Mather: Supervision, Validation, Writing – review & editing. Nicholas J. Tosca: Conceptualization, Funding acquisition, Methodology, Project administration, Resources, Supervision, Validation, Visualisation, Writing – review & editing.

9. Figures

Experiment group name	Initial pH	Maximum duration	DIC concentrations	Initial pCO_2 at initial pH of 2 or 4	Rock:water ratio(s)	Fayalite-forsterite ratio(s)
Low water-rock	2 and 4	60 days	33.51 mmol/kg	1.0 bar	1:1, 1:10	Fa, 1:1 Fa/Fo
Fayalite-bearing	2 and 4	85 days	3.356, 16.79, and 33.51 mmol/kg	0.1, 0.5, 1.0 bar	1:500	Fa
Fayalite- and forsterite-bearing	2 and 4	85 days	3.356, 16.79, and 33.51 mmol/kg	0.1, 0.5, 1.0 bar	1:500	1:1 Fa/Fo, 1:9 Fa/Fo
Non-CO_2	2 and 4	8 days	Non	Non	1:200, 1:500	Fa

Table 1: Table detailing the categories of the 86 experiments conducted in this research.

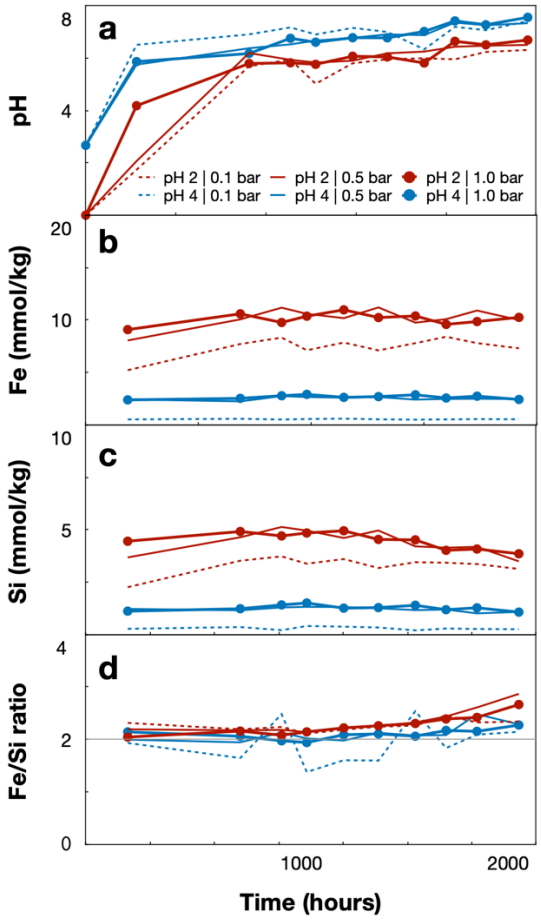


Figure 1: The pH, dissolved Fe and Si, and Fe/Si ratio over time through a typical fayalite-bearing experiment. Note the differing axes. (a) pH for experiments begun at pH 2 or 4, corresponding to equilibration with 0.1 to 1.0 bars of dissolved CO_2 at these initial pHs; (b) Fe concentration over time; (c) Si concentration over time; and (d) the ratio of Fe/Si over time, the stoichiometric ratio in pure fayalite marked as a grey line. Uncertainty for Fe and Si measurements is at 1.2 %; the uncertainty bars for this fall within the thickness of the lines. It is worth noting that pCO_2 depends on pH under a closed system and so will have fluctuated over the course of the experiments. Lines between datapoints are included for ease of following each dataset, and should not be construed as representing exact reaction pathway between datapoints.

[Single column image]

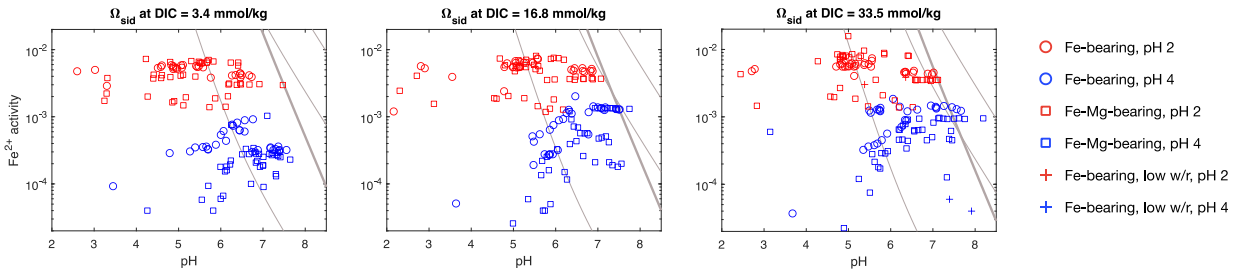


Figure 2: Fe^{2+} activity and pH from solution samples extracted at 10 intervals across 68 experiments, in separate graphs for $\Omega_{siderite}$ at DICs of 3.4, 16.8, and 33.5 mmol/kg. Datapoints in red correspond to experiments begun at pH 2; blue for pH 4. Circular datapoints correspond to fayalite-bearing experiments, while squares denote those bearing fayalite and forsterite, and plus-symbols for low rock:water ratio (1:10). pH and Fe^{2+} activity generally increased over the course of an experiment, thus datapoints towards the upper-right generally correspond to increasing reaction times. From left to right, the thin grey lines denote contours of $\Omega_{siderite}$: 1, 400, and 5000. The heavy grey line is the AFC saturation line of Jiang and Tosca (2019).

[Double column image]

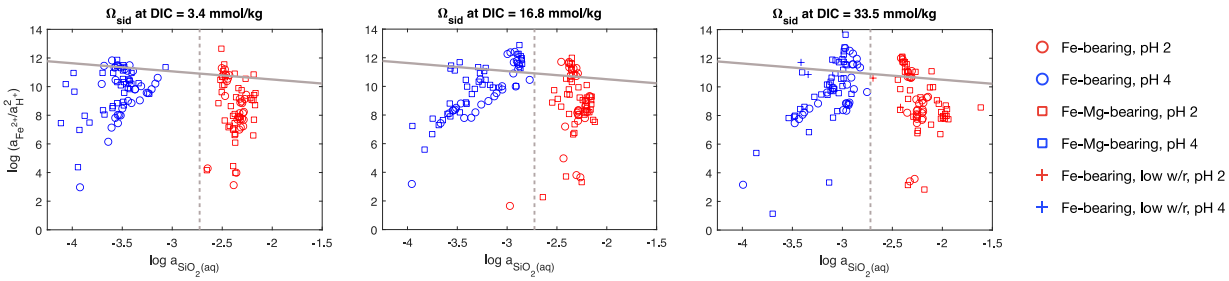


Figure 3: Solubility diagrams for the Fe(II)-silicate system involving the three principal factors controlling greenalite stability. All data are from solution samples extracted at 10 intervals across 68 experiments. Datapoints in red correspond to experiments begun at pH 2; blue for pH 4. Circular datapoints correspond to fayalite-bearing experiments, while squares denote those bearing fayalite and forsterite, and plus-symbols for low rock:water ratio (1:10). Datapoints towards the upper-right generally correspond to increasing reaction times. The heavy grey corresponds to the greenalite saturation (Tosca et al., 2016). The dashed grey line corresponds to amorphous silica saturation (Siever 1992).

[Double column image]

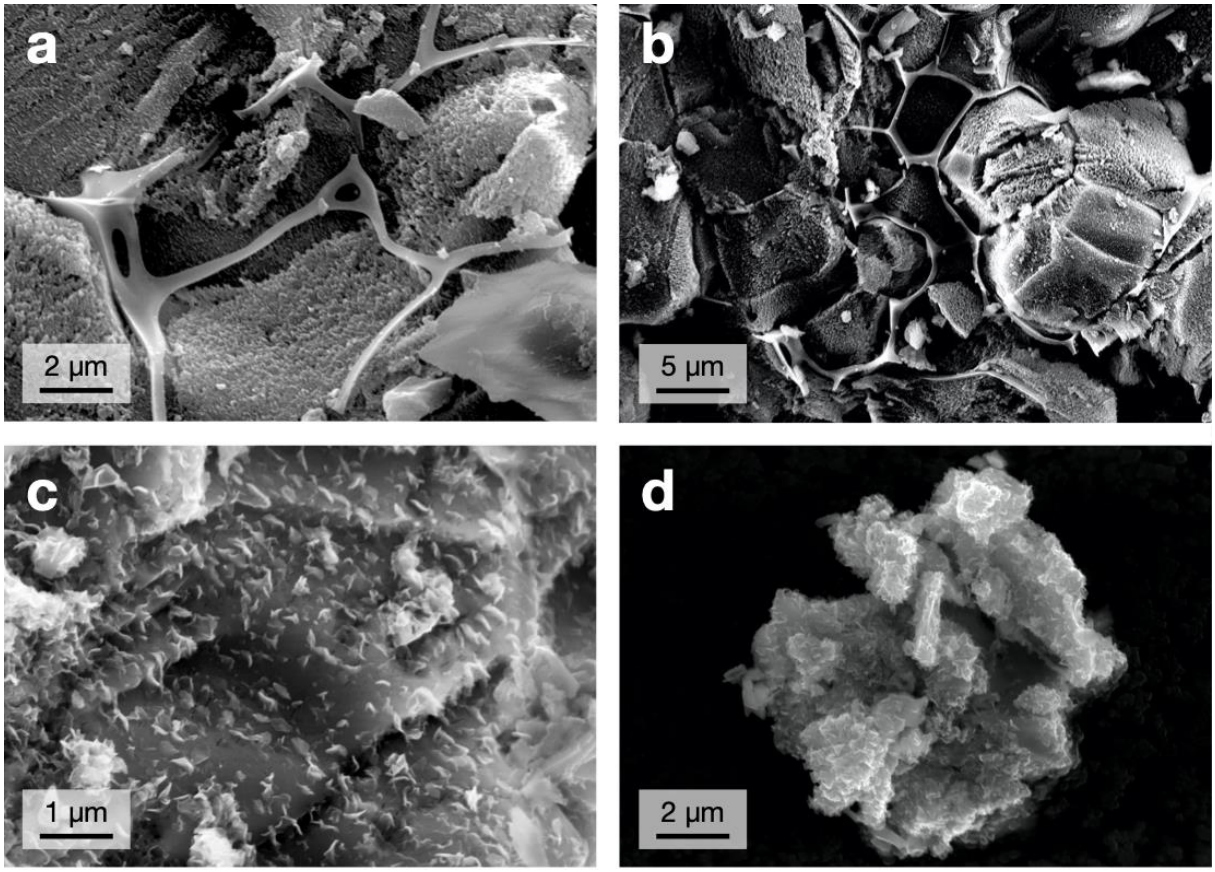


Figure 4: (a) Long, thin, fibrous structures found only upon or between (b) fayalite grains, apparently growing in interstitial spaces and breaking loose when disturbed, as in (a). (c) Aligned, nanometre-scaled precipitates found only upon fayalite grains, or (d) either as individual nuclei apparently formed of the precipitates' coalescence and growth upon each other, or growth upon a separate aggregate.

[Double column image]

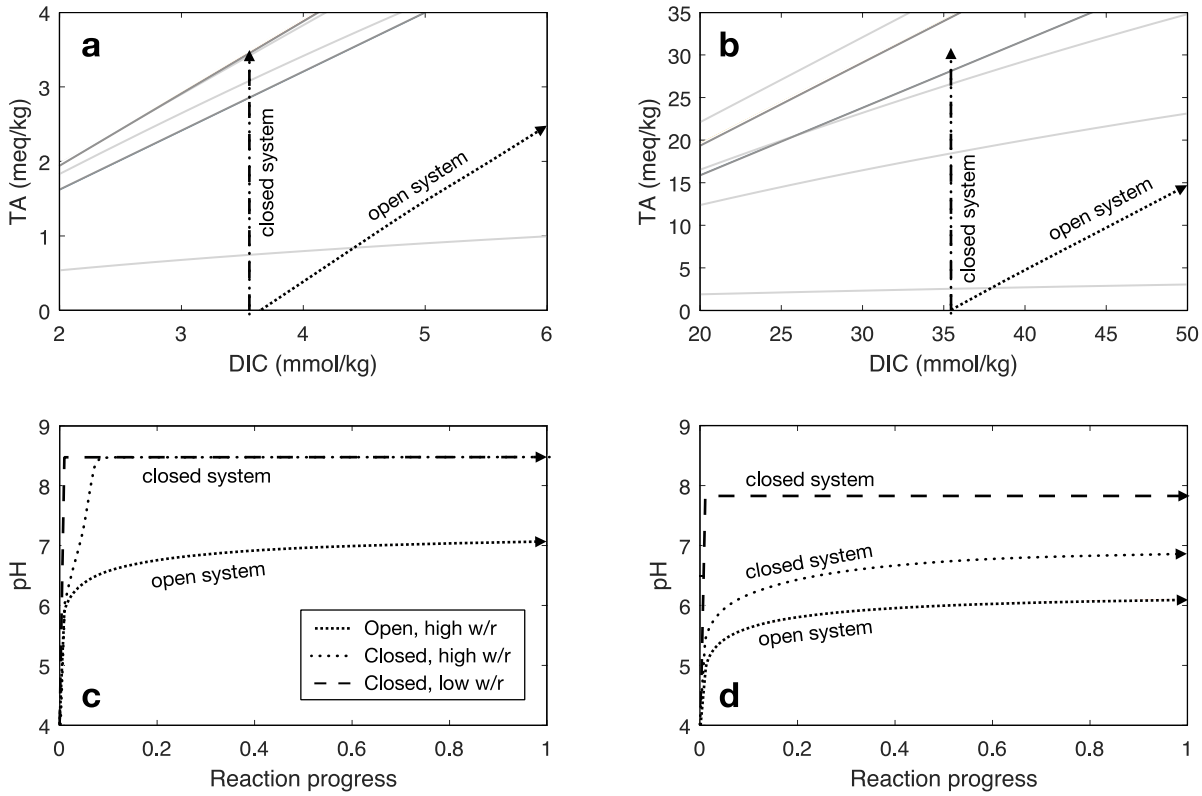


Figure 5: Results from three reaction path models of water-rock interaction at 25 °C: open-system with respect to CO_2 at high rock:water ratio (tightly-dotted lines), closed-system with respect to CO_2 at high rock:water ratio (circular-dotted lines), and closed-system with respect to CO_2 at low rock:water ratio (dashed lines). Left column: models run with 0.1 bar CO_2; right column: models run with 1.0 bar CO_2. (a) and (b): siderite and AFC saturation state as a function of DIC and total alkalinity (TA). From bottom-up, pale-grey lines represent $\Omega_{siderite}$ of 1, 100, 400, and 100,000; from bottom-up, dark-grey lines represent an Ω_{AFC} saturation at pH 7 (lower) or 8 (higher). (c) and (d): pH variation over the course of the experiment (which corresponds closely to total alkalinity in this system). In order to illustrate the influence of water-rock interaction on the Fe(II)-carbonate system in DIC-TA space, these models were run under fixed Fe^{2+} concentration of 10 mmol/kg with forsterite as the sole reactant.

[Double column image]

10. References

Aagaard, P., Helgeson, H.C., 1982. Thermodynamic and kinetic constraints on reaction rates among minerals and aqueous solutions; I, Theoretical considerations. Am. J. Sci. 282, 237–285. https://doi.org/10.2475/ajs.282.3.237

Bandfield, J.L., Glotch, T.D., Christensen, P.R., 2003. Spectroscopic Identification of Carbonate Minerals in the Martian Dust. Science 301, 1084–1087. https://doi.org/10.1126/science.1088054

Bandstra, J.Z., Brantley, S.L., 2008. Data Fitting Techniques with Applications to Mineral Dissolution Kinetics, in: Brantley, S.L., Kubicki, J.D., White, A.F. (Eds.), Kinetics of Water-Rock Interaction. Springer New York, New York, NY, pp. 211–257. https://doi.org/10.1007/978-0-387-73563-4_6

Bethke, C.M., 2017. The Geochemist's Workbench, Version 12.0: GWB Essentials Guide. Champaign, Illinois, US.

Boynton, W.V., Ming, D.W., Kounaves, S.P., Young, S.M.M., Arvidson, R.E., Hecht, M.H., Hoffman, J., Niles, P.B., Hamara, D.K., Quinn, R.C., Smith, P.H., Sutter, B., Catling, D.C., Morris, R.V., 2009. Evidence for Calcium Carbonate at the Mars Phoenix Landing Site. Science 325, 61–64. https://doi.org/10.1126/science.1172768

Brantley, S.L., Mellott, N.P., 2000. Surface area and porosity of primary silicate minerals. Am. Mineral. 85, 1767–1783. https://doi.org/10.2138/am-2000-11-1220

Braterman, P.S., Graham Cairns-Smith, A., W. Sloper, R., George Truscott, T., Craw, M., 1984. Photo-oxidation of iron(II) in water between pH 7.5 and 4.0. J. Chem. Soc. Dalton Trans. 0, 1441–1445. https://doi.org/10.1039/DT9840001441

Bridges, J.C., Catling, D.C., Saxton, J.M., Swindle, T.D., Lyon, I.C., Grady, M.M., 2001. Alteration Assemblages in Martian Meteorites: Implications for Near-Surface Processes. Space Sci. Rev. 96, 365–392. https://doi.org/10.1023/A:1011965826553

Bridges, J.C., Hicks, L.J., Treiman, A.H., 2019. Carbonates on Mars, in: Volatiles in the Martian Crust. Elsevier, pp. 89–118. https://doi.org/10.1016/B978-0-12-804191-8.00005-2

Bristow, T.F., Haberle, R.M., Blake, D.F., Marais, D.J.D., Eigenbrode, J.L., Fairén, A.G., Grotzinger, J.P., Stack, K.M., Mischna, M.A., Rampe, E.B., Siebach, K.L., Sutter, B., Vaniman, D.T., Vasavada, A.R., 2017. Low Hesperian PCO2 constrained from in situ mineralogical analysis at Gale Crater, Mars. Proc. Natl. Acad. Sci. 201616649. https://doi.org/10.1073/pnas.1616649114

Brown, A.J., Viviano, C.E., Goudge, T.A., 2020. Olivine-Carbonate Mineralogy of the Jezero Crater Region. J. Geophys. Res. Planets 125. https://doi.org/10.1029/2019JE006011

Butler, I.B., Schoonen, M.A.A., Rickard, D.T., 1994. Removal of dissolved oxygen from water: A comparison of four common techniques. Talanta 41, 211–215. https://doi.org/10.1016/0039-9140(94)80110-X

Delany, J.M., Lundeen, S.R., 1991. The LLNL thermochemical data base--revised data and file format for the EQ3/6 package. Lawrence Livermore National Lab., CA (United States). Vancouver.

Edwards, C.S., Ehlmann, B.L., 2015. Carbon sequestration on Mars. Geology 43, 863–866. https://doi.org/10.1130/G36983.1

Ehlmann, B.L., Bish, D.L., Ruff, S.W., Mustard, J.F., 2012. Mineralogy and chemistry of altered Icelandic basalts: Application to clay mineral detection and understanding aqueous environments on Mars: CLAY MINERAL DETECTION, ICELANDIC BASALT. J. Geophys. Res. Planets 117, n/a-n/a. https://doi.org/10.1029/2012JE004156

Ehlmann, B.L., Mustard, J.F., Murchie, S.L., Poulet, F., Bishop, J.L., Brown, A.J., Calvin, W.M., Clark, R.N., Marais, D.J.D., Milliken, R.E., Roach, L.H., Roush, T.L., Swayze, G.A., Wray, J.J., 2008. Orbital Identification of Carbonate-Bearing Rocks on Mars. Science 322, 1828–1832. https://doi.org/10.1126/science.1164759

Fairén, A.G., Fernández-Remolar, D., Dohm, J.M., Baker, V.R., Amils, R., 2004. Inhibition of carbonate synthesis in acidic oceans on early Mars. Nature 431, 423–426. https://doi.org/10.1038/nature02911

Farmer, V.C. (Ed.), 1974. The Infrared Spectra of Minerals. Mineralogical Society of Great Britain and Ireland, Londan. https://doi.org/10.1180/mono-4

Feitknecht, W., Schindler, P., 1963. Solubility constants of metal oxides, metal hydroxides and metal hydroxide salts in aqueous solution. Pure Appl. Chem. 6, 125–206. https://doi.org/10.1351/pac196306020125

Gislason, S.R., Arnorsson, S., Armannsson, H., 1996. Chemical weathering of basalt in Southwest Iceland; effects of runoff, age of rocks and vegetative/glacial cover. Am. J. Sci. 296, 837–907. https://doi.org/10.2475/ajs.296.8.837

Gysi, A.P., Stefánsson, A., 2012. CO2-water–basalt interaction. Low temperature experiments and implications for CO2 sequestration into basalts. Geochim. Cosmochim. Acta 81, 129–152. https://doi.org/10.1016/j.gca.2011.12.012

Halevy, I., Fischer, W.W., Eiler, J.M., 2011. Carbonates in the Martian meteorite Allan Hills 84001 formed at 18 4 C in a near-surface aqueous environment. Proc. Natl. Acad. Sci. 108, 16895–16899. https://doi.org/10.1073/pnas.1109444108

He, S., Morse, J.W., 1993. The carbonic acid system and calcite solubility in aqueous Na-K-Ca-Mg-Cl-SO4 solutions from 0 to 90°C. Geochim. Cosmochim. Acta 57, 3533–3554. https://doi.org/10.1016/0016-7037(93)90137-L

Heard, A.W., Kite, E.S., 2020. A probabilistic case for a large missing carbon sink on Mars after 3.5 billion years ago. Earth Planet. Sci. Lett. 531, 116001. https://doi.org/10.1016/j.epsl.2019.116001

Helgeson, H.C., Kirkham, D.H., 1974. Theoretical prediction of the thermodynamic behavior of aqueous electrolytes at high pressures and temperatures; II, Debye-Huckel parameters for

activity coefficients and relative partial molal properties. Am. J. Sci. 274, 1199–1261. https://doi.org/10.2475/ajs.274.10.1199

Horgan, B.H.N., Anderson, R.B., Dromart, G., Amador, E.S., Rice, M.S., 2020. The mineral diversity of Jezero crater: Evidence for possible lacustrine carbonates on Mars. Icarus 339, 113526. https://doi.org/10.1016/j.icarus.2019.113526

Hurowitz, J.A., Fischer, W.W., Tosca, N.J., Milliken, R.E., 2010. Origin of acidic surface waters and the evolution of atmospheric chemistry on early Mars. Nat. Geosci. 3, 323–326. https://doi.org/10.1038/ngeo831

Hurowitz, J.A., Grotzinger, J.P., Fischer, W.W., McLennan, S.M., Milliken, R.E., Stein, N., Vasavada, A.R., Blake, D.F., Dehouck, E., Eigenbrode, J.L., Fairén, A.G., Frydenvang, J., Gellert, R., Grant, J.A., Gupta, S., Herkenhoff, K.E., Ming, D.W., Rampe, E.B., Schmidt, M.E., Siebach, K.L., Stack-Morgan, K., Sumner, D.Y., Wiens, R.C., 2017. Redox stratification of an ancient lake in Gale crater, Mars. Science 356, eaah6849. https://doi.org/10.1126/science.aah6849

Jakosky, B.M., 2019. The CO2 inventory on Mars. Planet. Space Sci. 175, 52–59. https://doi.org/10.1016/j.pss.2019.06.002

Jiang, C.Z., Tosca, N.J., 2020. Growth kinetics of siderite at 298.15 K and 1 bar. Geochim. Cosmochim. Acta 274, 97–117. https://doi.org/10.1016/j.gca.2020.01.047

Jiang, C.Z., Tosca, N.J., 2019. Fe(II)-carbonate precipitation kinetics and the chemistry of anoxic ferruginous seawater. Earth Planet. Sci. Lett. 506, 231–242. https://doi.org/10.1016/j.epsl.2018.11.010

Jimenez-Lopez, C., Romanek, C.S., 2004. Precipitation kinetics and carbon isotope partitioning of inorganic siderite at 25°C and 1 atm. Geochim. Cosmochim. Acta 68, 557–571. https://doi.org/10.1016/S0016-7037(03)00460-5

Kashchiev, D., Verdoes, D., van Rosmalen, G.M., 1991. Induction time and metastability limit in new phase formation. J. Cryst. Growth 110, 373–380. https://doi.org/10.1016/0022-0248(91)90273-8

Kite, E.S., Melwani Daswani, M., 2019. Geochemistry constrains global hydrology on Early Mars. Earth Planet. Sci. Lett. 524, 115718. https://doi.org/10.1016/j.epsl.2019.115718

Kling, A.M., Haberle, R.M., McKay, C.P., Bristow, T.F., Rivera-Hernández, F., 2020. Subsistence of ice-covered lakes during the Hesperian at Gale crater, Mars. Icarus 338, 113495. https://doi.org/10.1016/j.icarus.2019.113495

Königsberger, E., Königsberger, L.-C., Gamsjäger, H., 1999. Low-temperature thermodynamic model for the system Na2CO3−MgCO3−CaCO3−H2O. Geochim. Cosmochim. Acta 63, 3105–3119. https://doi.org/10.1016/S0016-7037(99)00238-0

Lasaga, A.C., 1998. Kinetic Theory in the Earth Sciences: Princeton University Press, Princeton. https://doi.org/10.1515/9781400864874

Malin, M.C., Edgett, K.S., 2000. Sedimentary Rocks of Early Mars. Science 290, 1927–1937. https://doi.org/10.1126/science.290.5498.1927

McLennan, S.M., Grotzinger, J.P., Hurowitz, J.A., Tosca, N.J., 2019. The Sedimentary Cycle on Early Mars. Annu. Rev. Earth Planet. Sci. 47, 91–118. https://doi.org/10.1146/annurev-earth-053018-060332

Michalski, J.R., Cuadros, J., Bishop, J.L., Darby Dyar, M., Dekov, V., Fiore, S., 2015. Constraints on the crystal-chemistry of Fe/Mg-rich smectitic clays on Mars and links to global alteration trends. Earth Planet. Sci. Lett. 427, 215–225. https://doi.org/10.1016/j.epsl.2015.06.020

Michalski, J.R., Cuadros, J., Niles, P.B., Parnell, J., Deanne Rogers, A., Wright, S.P., 2013. Groundwater activity on Mars and implications for a deep biosphere. Nat. Geosci. 6, 133–138. https://doi.org/10.1038/ngeo1706

Michalski, J.R., Niles, P.B., 2010. Deep crustal carbonate rocks exposed by meteor impact on Mars. Nat. Geosci. 3, 751–755. https://doi.org/10.1038/ngeo971

Milliken, R.E., Fischer, W.W., Hurowitz, J.A., 2009. Missing salts on early Mars. Geophys. Res. Lett. 36, L11202. https://doi.org/10.1029/2009GL038558

Ming, D.W., Archer, P.D., Glavin, D.P., Eigenbrode, J.L., Franz, H.B., Sutter, B., Brunner, A.E., Stern, J.C., Freissinet, C., McAdam, A.C., Mahaffy, P.R., Cabane, M., Coll, P., Campbell, J.L., Atreya, S.K., Niles, P.B., Bell, J.F., Bish, D.L., Brinckerhoff, W.B., Buch, A., Conrad, P.G., Des Marais, D.J., Ehlmann, B.L., Fairen, A.G., Farley, K., Flesch, G.J., Francois, P., Gellert, R., Grant, J.A., Grotzinger, J.P., Gupta, S., Herkenhoff, K.E., Hurowitz, J.A., Leshin, L.A., Lewis, K.W., McLennan, S.M., Miller, K.E., Moersch, J., Morris, R.V., Navarro-Gonzalez, R., Pavlov, A.A., Perrett, G.M., Pradler, I., Squyres, S.W., Summons, R.E., Steele, A., Stolper, E.M., Sumner, D.Y., Szopa, C., Teinturier, S., Trainer, M.G., Treiman, A.H., Vaniman, D.T., Vasavada, A.R., Webster, C.R., Wray, J.J., Yingst, R.A., MSL Science Team, Kemppinen, O., Bridges, N., Johnson, J.R., Minitti, M., Cremers, D., Edgar, L., Farmer, J., Godber, A., Wadhwa, M., Wellington, D., McEwan, I., Newman, C., Richardson, M., Charpentier, A., Peret, L., King, P., Blank, J., Weigle, G., Schmidt, M., Li, S., Milliken, R., Robertson, K., Sun, V., Baker, M., Edwards, C., Ehlmann, B., Griffes, J., Newcombe, M., Pilorget, C., Rice, M., Siebach, K., Stack, K., Brunet, C., Hipkin, V., Leveille, R., Marchand, G., Sanchez, P.S., Favot, L., Cody, G., Fluckiger, L., Lees, D., Nefian, A., Martin, M., Gailhanou, M., Westall, F., Israel, G., Agard, C., Baroukh, J., Donny, C., Gaboriaud, A., Guillemot, P., Lafaille, V., Lorigny, E., Paillet, A., Perez, R., Saccoccio, M., Yana, C., Armiens-Aparicio, C., Rodriguez, J.C., Blazquez, I.C., Gomez, F.G., Gomez-Elvira, J., Hettrich, S., Malvitte, A.L., Jimenez, M.M., Martinez-Frias, J., Martin-Soler, J., Martin-Torres, F.J., Jurado, A.M., Mora-Sotomayor, L., Caro, G.M., Lopez, S.N., Peinado-Gonzalez, V., Pla-Garcia, J., Manfredi, J.A.R., Romeral-Planello, J.J., Fuentes, S.A.S., Martinez, E.S., Redondo, J.T., Urqui-O'Callaghan, R., Mier, M.-P.Z.,

Chipera, S., Lacour, J.-L., Mauchien, P., Sirven, J.-B., Manning, H., Hayes, A., Joseph, J., Sullivan, R., Thomas, P., Dupont, A., Lundberg, A., Melikechi, N., Mezzacappa, A., DeMarines, J., Grinspoon, D., Reitz, G., Prats, B., Atlaskin, E., Genzer, M., Harri, A.-M., Haukka, H., Kahanpaa, H., Kauhanen, J., Kemppinen, O., Paton, M., Polkko, J., Schmidt, W., Siili, T., Fabre, C., Wilhelm, M.B., Poitrasson, F., Patel, K., Gorevan, S., Indyk, S., Paulsen, G., Schieber, J., Gondet, B., Langevin, Y., Geffroy, C., Baratoux, D., Berger, G., Cros, A., d'Uston, C., Forni, O., Gasnault, O., Lasue, J., Lee, Q.-M., Maurice, S., Meslin, P.-Y., Pallier, E., Parot, Y., Pinet, P., Schroder, S., Toplis, M., Lewin, E., Brunner, W., Heydari, E., Achilles, C., Oehler, D., Coscia, D., Israel, G., Dromart, G., Robert, F., Sautter, V., Le Mouelic, S., Mangold, N., Nachon, M., Stalport, F., Raulin, F., Cameron, J., Clegg, S., Cousin, A., DeLapp, D., Dingler, R., Jackson, R.S., Johnstone, S., Lanza, N., Little, C., Nelson, T., Wiens, R.C., Williams, R.B., Jones, A., Kirkland, L., Baker, B., Cantor, B., Caplinger, M., Davis, S., Duston, B., Edgett, K., Fay, D., Hardgrove, C., Harker, D., Herrera, P., Jensen, E., Kennedy, M.R., Krezoski, G., Krysak, D., Lipkaman, L., Malin, M., McCartney, E., McNair, S., Nixon, B., Posiolova, L., Ravine, M., Salamon, A., Saper, L., Stoiber, K., Supulver, K., Van Beek, J., Van Beek, T., Zimdar, R., French, K.L., Iagnemma, K., Miller, K., Goesmann, F., Goetz, W., Hviid, S., Johnson, M., Lefavor, M., Lyness, E., Breves, E., Dyar, M.D., Fassett, C., Blake, D.F., Bristow, T., Edwards, L., Haberle, R., Hoehler, T., Hollingsworth, J., Kahre, M., Keely, L., McKay, C., Wilhelm, M.B., Bleacher, L., Choi, D., Dworkin, J.P., Floyd, M., Garvin, J., Harpold, D., Jones, A., Martin, D.K., Raaen, E., Smith, M.D., Tan, F., Meyer, M., Posner, A., Voytek, M., Anderson, R.C., Aubrey, A., Beegle, L.W., Behar, A., Blaney, D., Brinza, D., Calef, F., Christensen, L., Crisp, J.A., DeFlores, L., Feldman, J., Feldman, S., Jun, I., Keymeulen, D., Maki, J., Mischna, M., Morookian, J.M., Parker, T., Pavri, B., Schoppers, M., Sengstacken, A., Simmonds, J.J., Spanovich, N., Juarez, M. d. l. T., Yen, A., Cucinotta, F., Jones, J.H., Rampe, E., Nolan, T., Fisk, M., Radziemski, L., Barraclough, B., Bender, S., Berman, D.,

Dobrea, E.N., Tokar, R., Williams, R.M.E., Cleghorn, T., Huntress, W., Manhes, G., Hudgins, J., Olson, T., Stewart, N., Sarrazin, P., Vicenzi, E., Wilson, S.A., Bullock, M., Ehresmann, B., Hamilton, V., Hassler, D., Peterson, J., Rafkin, S., Zeitlin, C., Fedosov, F., Golovin, D., Karpushkina, N., Kozyrev, A., Litvak, M., Malakhov, A., Mitrofanov, I., Mokrousov, M., Nikiforov, S., Prokhorov, V., Sanin, A., Tretyakov, V., Varenikov, A., Vostrukhin, A., Kuzmin, R., Clark, B., Wolff, M., Botta, O., Drake, D., Bean, K., Lemmon, M., Schwenzer, S.P., Anderson, R.B., Lee, E.M., Sucharski, R., Hernandez, M.A. d. P., Avalos, J.J.B., Ramos, M., Kim, M.-H., Malespin, C., Plante, I., Muller, J.-P., Ewing, R., Boynton, W., Downs, R., Fitzgibbon, M., Harshman, K., Morrison, S., Dietrich, W., Kortmann, O., Palucis, M., Williams, A., Lugmair, G., Wilson, M.A., Rubin, D., Jakosky, B., Balic-Zunic, T., Frydenvang, J., Jensen, J.K., Kinch, K., Koefoed, A., Madsen, M.B., Stipp, S.L.S., Boyd, N., VanBommel, S., Jacob, S., Owen, T., Rowland, S., Atlaskin, E., Savijarvi, H., Boehm, E., Bottcher, S., Burmeister, S., Guo, J., Kohler, J., Garcia, C.M., Mueller-Mellin, R., Wimmer-Schweingruber, R., Bridges, J.C., McConnochie, T., Benna, M., Bower, H., Blau, H., Boucher, T., Carmosino, M., Elliott, H., Halleaux, D., Renno, N., Wong, M., Pepin, R., Elliott, B., Spray, J., Thompson, L., Gordon, S., Newsom, H., Ollila, A., Williams, J., Vasconcelos, P., Bentz, J., Nealson, K., Popa, R., Kah, L.C., Tate, C., Day, M., Kocurek, G., Hallet, B., Sletten, R., Francis, R., McCullough, E., Cloutis, E., ten Kate, I.L., Kuzmin, R., Arvidson, R., Fraeman, A., Scholes, D., Slavney, S., Stein, T., Ward, J., Berger, J., Moores, J.E., 2014. Volatile and Organic Compositions of Sedimentary Rocks in Yellowknife Bay, Gale Crater, Mars. Science 343, 1245267–1245267. https://doi.org/10.1126/science.1245267

Morris, R.V., Ruff, S.W., Gellert, R., Ming, D.W., Arvidson, R.E., Clark, B.C., Golden, D.C., Siebach, K., Klingelhofer, G., Schroder, C., Fleischer, I., Yen, A.S., Squyres, S.W., 2010. Identification of Carbonate-Rich Outcrops on Mars by the Spirit Rover. Science 329, 421–424. https://doi.org/10.1126/science.1189667

Nordstrom, D.K., 1977. Thermochemical redox equilibria of ZoBell's solution. Geochim. Cosmochim. Acta 41, 1835–1841. https://doi.org/10.1016/0016-7037(77)90215-0

Oelkers, E.H., Golubev, S.V., Chairat, C., Pokrovsky, O.S., Schott, J., 2009. The surface chemistry of multi-oxide silicates. Geochim. Cosmochim. Acta 73, 4617–4634. https://doi.org/10.1016/j.gca.2009.05.028

Owen, T., Biemann, K., Rushneck, D.R., Biller, J.E., Howarth, D.W., Lafleur, A.L., 1977. The composition of the atmosphere at the surface of Mars. J. Geophys. Res. 82, 4635–4639. https://doi.org/10.1029/JS082i028p04635

Perez-Fodich, A., Derry, L.A., 2019. Organic acids and high soil CO2 drive intense chemical weathering of Hawaiian basalts: Insights from reactive transport models. Geochim. Cosmochim. Acta 249, 173–198. https://doi.org/10.1016/j.gca.2019.01.027

Pokrovsky, O.S., Schott, J., 2000. Forsterite surface composition in aqueous solutions: a combined potentiometric, electrokinetic, and spectroscopic approach. Geochim. Cosmochim. Acta 64, 3299–3312. https://doi.org/10.1016/S0016-7037(00)00435-X

Pollack, J.B., Kasting, J.F., Richardson, S.M., Poliakoff, K., 1987. The case for a wet, warm climate on early Mars. Icarus 71, 203–224. https://doi.org/10.1016/0019-1035(87)90147-3

Postma, D., 1982. Pyrite and siderite formation in brackish and freshwater swamp sediments. Am. J. Sci. 282, 1151–1183. https://doi.org/10.2475/ajs.282.8.1151

Power, I.M., Harrison, A.L., Dipple, G.M., Wilson, S.A., Barker, S.L.L., Fallon, S.J., 2019. Magnesite formation in playa environments near Atlin, British Columbia, Canada. Geochim. Cosmochim. Acta 255, 1–24. https://doi.org/10.1016/j.gca.2019.04.008

Qafoku, O., Kovarik, L., Kukkadapu, R.K., Ilton, E.S., Arey, B.W., Tucek, J., Felmy, A.R., 2012. Fayalite dissolution and siderite formation in water-saturated supercritical CO2. Chem. Geol. 332–333, 124–135. https://doi.org/10.1016/j.chemgeo.2012.09.028

Ruff, S.W., Niles, P.B., Alfano, F., Clarke, A.B., 2014. Evidence for a Noachian-aged ephemeral lake in Gusev crater, Mars. Geology 42, 359–362. https://doi.org/10.1130/G35508.1

Siever, R., 1992. The silica cycle in the Precambrian. Geochim. Cosmochim. Acta 56, 3265–3272. https://doi.org/10.1016/0016-7037(92)90303-Z

Singer, P.C., Stumm, W., 1970. The Solubility of Ferrous Iron in Carbonate-Bearing Waters. J. - Am. Water Works Assoc. 62, 198–202. https://doi.org/10.1002/j.1551-8833.1970.tb03888.x

Stein, N., Grotzinger, J.P., Schieber, J., Mangold, N., Hallet, B., Newsom, H., Stack, K.M., Berger, J.A., Thompson, L., Siebach, K.L., Cousin, A., Le Mouélic, S., Minitti, M., Sumner, D.Y., Fedo, C., House, C.H., Gupta, S., Vasavada, A.R., Gellert, R., Wiens, R.C., Frydenvang, J., Forni, O., Meslin, P.Y., Payré, V., Dehouck, E., 2018. Desiccation cracks provide evidence of lake drying on Mars, Sutton Island member, Murray formation, Gale Crater. Geology 46, 515–518. https://doi.org/10.1130/G40005.1

Tosca, N.J., Ahmed, I.A.M., Tutolo, B.M., Ashpitel, A., Hurowitz, J.A., 2018. Magnetite authigenesis and the warming of early Mars. Nat. Geosci. 11, 635–639. https://doi.org/10.1038/s41561-018-0203-8

Tosca, N.J., Guggenheim, S., Pufahl, P.K., 2016. An authigenic origin for Precambrian greenalite: Implications for iron formation and the chemistry of ancient seawater. Geol. Soc. Am. Bull. 128, 511–530. https://doi.org/10.1130/B31339.1

Turnbull, D., Fisher, J.C., 1949. Rate of Nucleation in Condensed Systems. J. Chem. Phys. 17, 71–73. https://doi.org/10.1063/1.1747055

Vagenas, N., Gatsouli, A., Kontoyannis, C.G., 2003. Quantitative analysis of synthetic calcium carbonate polymorphs using FT-IR spectroscopy. Talanta 59, 831–836. https://doi.org/10.1016/S0039-9140(02)00638-0

van Berk, W., Fu, Y., 2011. Reproducing hydrogeochemical conditions triggering the formation of carbonate and phyllosilicate alteration mineral assemblages on Mars (Nili Fossae region). J. Geophys. Res. 116, E10006. https://doi.org/10.1029/2011JE003886

Vaniman, D.T., Bish, D.L., Ming, D.W., Bristow, T.F., Morris, R.V., Blake, D.F., Chipera, S.J., Morrison, S.M., Treiman, A.H., Rampe, E.B., Rice, M., Achilles, C.N., Grotzinger, J.P., McLennan, S.M., Williams, J., Bell, J.F., Newsom, H.E., Downs, R.T., Maurice, S., Sarrazin, P., Yen, A.S., Morookian, J.M., Farmer, J.D., Stack, K., Milliken, R.E., Ehlmann, B.L., Sumner, D.Y., Berger, G., Crisp, J.A., Hurowitz, J.A., Anderson, R., Des Marais, D.J., Stolper, E.M., Edgett, K.S., Gupta, S., Spanovich, N., MSL Science Team, Agard, C., Alves Verdasca, J.A., Anderson, R., Archer, D., Armiens-Aparicio, C., Arvidson, R., Atlaskin, E., Atreya, S., Aubrey, A., Baker, B., Baker, M., Balic-Zunic, T., Baratoux, D., Baroukh, J., Barraclough, B., Bean, K., Beegle, L., Behar, A., Bender, S., Benna, M., Bentz, J., Berger, J., Berman, D., Blanco Avalos, J.J., Blaney, D., Blank, J., Blau, H., Bleacher, L., Boehm, E., Botta, O., Bottcher, S., Boucher, T., Bower, H., Boyd, N., Boynton, B., Breves, E., Bridges, J., Bridges, N., Brinckerhoff, W., Brinza, D., Brunet, C., Brunner, A., Brunner, W., Buch, A., Bullock, M., Burmeister, S., Cabane, M., Calef, F., Cameron, J., Campbell, J.I., Cantor, B., Caplinger, M., Caride Rodriguez, J., Carmosino, M., Carrasco Blazquez, I., Charpentier, A., Choi, D., Clark, B., Clegg, S., Cleghorn, T., Cloutis, E., Cody, G., Coll, P., Conrad, P., Coscia, D., Cousin, A., Cremers, D., Cros, A., Cucinotta, F., d'Uston, C., Davis, S., Day, M.K., de la Torre Juarez, M., DeFlores, L., DeLapp, D., DeMarines, J., Dietrich, W., Dingler, R., Donny, C., Drake, D., Dromart, G., Dupont, A., Duston, B., Dworkin, J., Dyar, M.D., Edgar, L., Edwards, C., Edwards, L., Ehresmann, B., Eigenbrode, J., Elliott, B., Elliott, H., Ewing, R., Fabre, C., Fairen, A., Farley, K., Fassett, C., Favot, L., Fay, D., Fedosov, F., Feldman, J., Feldman, S., Fisk, M., Fitzgibbon, M., Flesch, G., Floyd, M., Fluckiger, L., Forni, O., Fraeman, A., Francis, R., Francois, P., Franz, H., Freissinet, C., French, K.L., Frydenvang, J., Gaboriaud, A., Gailhanou, M., Garvin, J., Gasnault, O., Geffroy, C., Gellert, R., Genzer, M., Glavin, D., Godber, A., Goesmann, F., Goetz, W., Golovin, D., Gomez Gomez, F., Gomez-Elvira, J., Gondet, B., Gordon, S., Gorevan, S., Grant, J., Griffes, J., Grinspoon, D., Guillemot, P., Guo, J., Guzewich, S., Haberle, R.,

Halleaux, D., Hallet, B., Hamilton, V., Hardgrove, C., Harker, D., Harpold, D., Harri, A.-M., Harshman, K., Hassler, D., Haukka, H., Hayes, A., Herkenhoff, K., Herrera, P., Hettrich, S., Heydari, E., Hipkin, V., Hoehler, T., Hollingsworth, J., Hudgins, J., Huntress, W., Hviid, S., Iagnemma, K., Indyk, S., Israel, G., Jackson, R., Jacob, S., Jakosky, B., Jensen, E., Jensen, J.K., Johnson, J., Johnson, M., Johnstone, S., Jones, A., Jones, J., Joseph, J., Jun, I., Kah, L., Kahanpaa, H., Kahre, M., Karpushkina, N., Kasprzak, W., Kauhanen, J., Keely, L., Kemppinen, O., Keymeulen, D., Kim, M.-H., Kinch, K., King, P., Kirkland, L., Kocurek, G., Koefoed, A., Kohler, J., Kortmann, O., Kozyrev, A., Krezoski, J., Krysak, D., Kuzmin, R., Lacour, J.L., Lafaille, V., Langevin, Y., Lanza, N., Lasue, J., Le Mouelic, S., Lee, E.M., Lee, Q.-M., Lees, D., Lefavor, M., Lemmon, M., Malvitte, A.L., Leshin, L., Leveille, R., Lewin-Carpintier, E., Lewis, K., Li, S., Lipkaman, L., Little, C., Litvak, M., Lorigny, E., Lugmair, G., Lundberg, A., Lyness, E., Madsen, M., Mahaffy, P., Maki, J., Malakhov, A., Malespin, C., Malin, M., Mangold, N., Manhes, G., Manning, H., Marchand, G., Marin Jimenez, M., Martin Garcia, C., Martin, D., Martin, M., Martinez-Frias, J., Martin-Soler, J., Martin-Torres, F.J., Mauchien, P., McAdam, A., McCartney, E., McConnochie, T., McCullough, E., McEwan, I., McKay, C., McNair, S., Melikechi, N., Meslin, P.-Y., Meyer, M., Mezzacappa, A., Miller, H., Miller, K., Minitti, M., Mischna, M., Mitrofanov, I., Moersch, J., Mokrousov, M., Molina Jurado, A., Moores, J., Mora-Sotomayor, L., Mueller-Mellin, R., Muller, J.-P., Munoz Caro, G., Nachon, M., Navarro Lopez, S., Navarro-Gonzalez, R., Nealson, K., Nefian, A., Nelson, T., Newcombe, M., Newman, C., Nikiforov, S., Niles, P., Nixon, B., Noe Dobrea, E., Nolan, T., Oehler, D., Ollila, A., Olson, T., Owen, T., de Pablo Hernandez, M.A., Paillet, A., Pallier, E., Palucis, M., Parker, T., Parot, Y., Patel, K., Paton, M., Paulsen, G., Pavlov, A., Pavri, B., Peinado-Gonzalez, V., Pepin, R., Peret, L., Perez, R., Perrett, G., Peterson, J., Pilorget, C., Pinet, P., Pla-Garcia, J., Plante, I., Poitrasson, F., Polkko, J., Popa, R., Posiolova, L., Posner, A., Pradler, I., Prats, B., Prokhorov, V., Purdy, S.W., Raaen, E., Radziemski, L., Rafkin, S.,

Ramos, M., Raulin, F., Ravine, M., Reitz, G., Renno, N., Richardson, M., Robert, F., Robertson, K., Rodriguez Manfredi, J.A., Romeral-Planello, J.J., Rowland, S., Rubin, D., Saccoccio, M., Salamon, A., Sandoval, J., Sanin, A., Sans Fuentes, S.A., Saper, L., Sautter, V., Savijarvi, H., Schieber, J., Schmidt, M., Schmidt, W., Scholes, D.D., Schoppers, M., Schroder, S., Schwenzer, S., Sebastian Martinez, E., Sengstacken, A., Shterts, R., Siebach, K., Siili, T., Simmonds, J., Sirven, J.-B., Slavney, S., Sletten, R., Smith, M., Sobron Sanchez, P., Spray, J., Squyres, S., Stalport, F., Steele, A., Stein, T., Stern, J., Stewart, N., Stipp, S.L.S., Stoiber, K., Sucharski, B., Sullivan, R., Summons, R., Sun, V., Supulver, K., Sutter, B., Szopa, C., Tan, F., Tate, C., Teinturier, S., ten Kate, I., Thomas, P., Thompson, L., Tokar, R., Toplis, M., Torres Redondo, J., Trainer, M., Tretyakov, V., Urqui-O'Callaghan, R., Van Beek, J., Van Beek, T., VanBommel, S., Varenikov, A., Vasavada, A., Vasconcelos, P., Vicenzi, E., Vostrukhin, A., Voytek, M., Wadhwa, M., Ward, J., Webster, C., Weigle, E., Wellington, D., Westall, F., Wiens, R.C., Wilhelm, M.B., Williams, A., Williams, R., Williams, R.B.M., Wilson, M., Wimmer-Schweingruber, R., Wolff, M., Wong, M., Wray, J., Wu, M., Yana, C., Yingst, A., Zeitlin, C., Zimdar, R., Zorzano Mier, M.-P., 2014. Mineralogy of a Mudstone at Yellowknife Bay, Gale Crater, Mars. Science 343, 1243480–1243480. https://doi.org/10.1126/science.1243480

Velbel, M.A., 1999. Bond strength and the relative weathering rates of simple orthosilicates. Am. J. Sci. 299, 679–696. https://doi.org/10.2475/ajs.299.7-9.679

Volmer, M., Weber, A.Z., 1926. Nucleus Formation in Supersaturated Systems. Z. Für Phys. Chem. 119, 277–301.

Wade, J., Dyck, B., Palin, R.M., Moore, J.D.P., Smye, A.J., 2017. The divergent fates of primitive hydrospheric water on Earth and Mars. Nature 552, 391–394. https://doi.org/10.1038/nature25031

Whipkey, C.E., Capo, R.C., Chadwick, O.A., Stewart, B.W., 2000. The importance of sea spray to the cation budget of a coastal Hawaiian soil: a strontium isotope approach. Chem. Geol. 168, 37–48. https://doi.org/10.1016/S0009-2541(00)00187-X

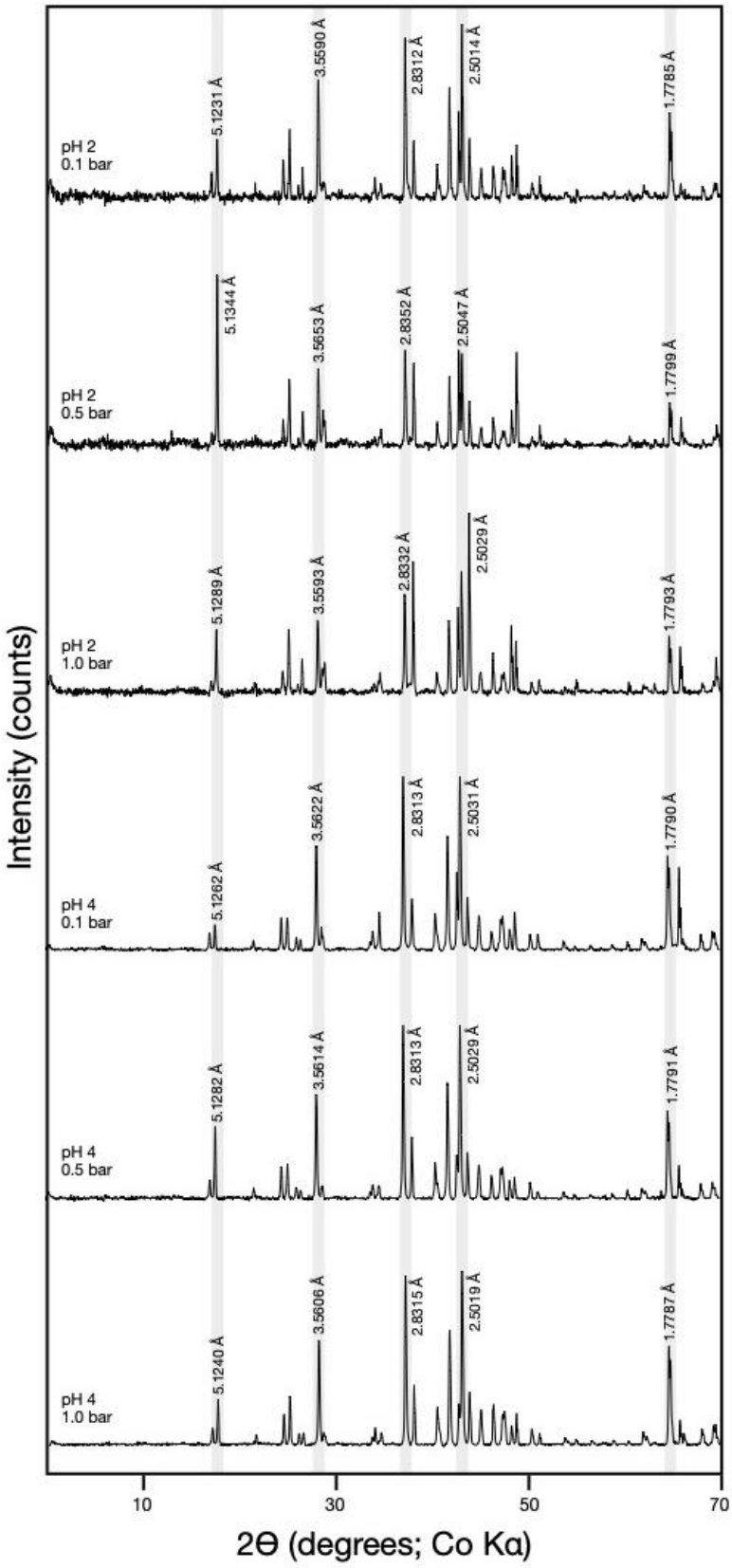
Whipkey, C.E., Capo, R.C., Hsieh, J.C.C., Chadwick, O.A., 2002. Development of Magnesian Carbonates in Quaternary Soils on the Island of Hawaii. J. Sediment. Res. 72, 158–165. https://doi.org/10.1306/050801720158

Wordsworth, R., Kalugina, Y., Lokshtanov, S., Vigasin, A., Ehlmann, B., Head, J., Sanders, C., Wang, H., 2017. Transient reducing greenhouse warming on early Mars. Geophys. Res. Lett. 44, 2016GL071766. https://doi.org/10.1002/2016GL071766

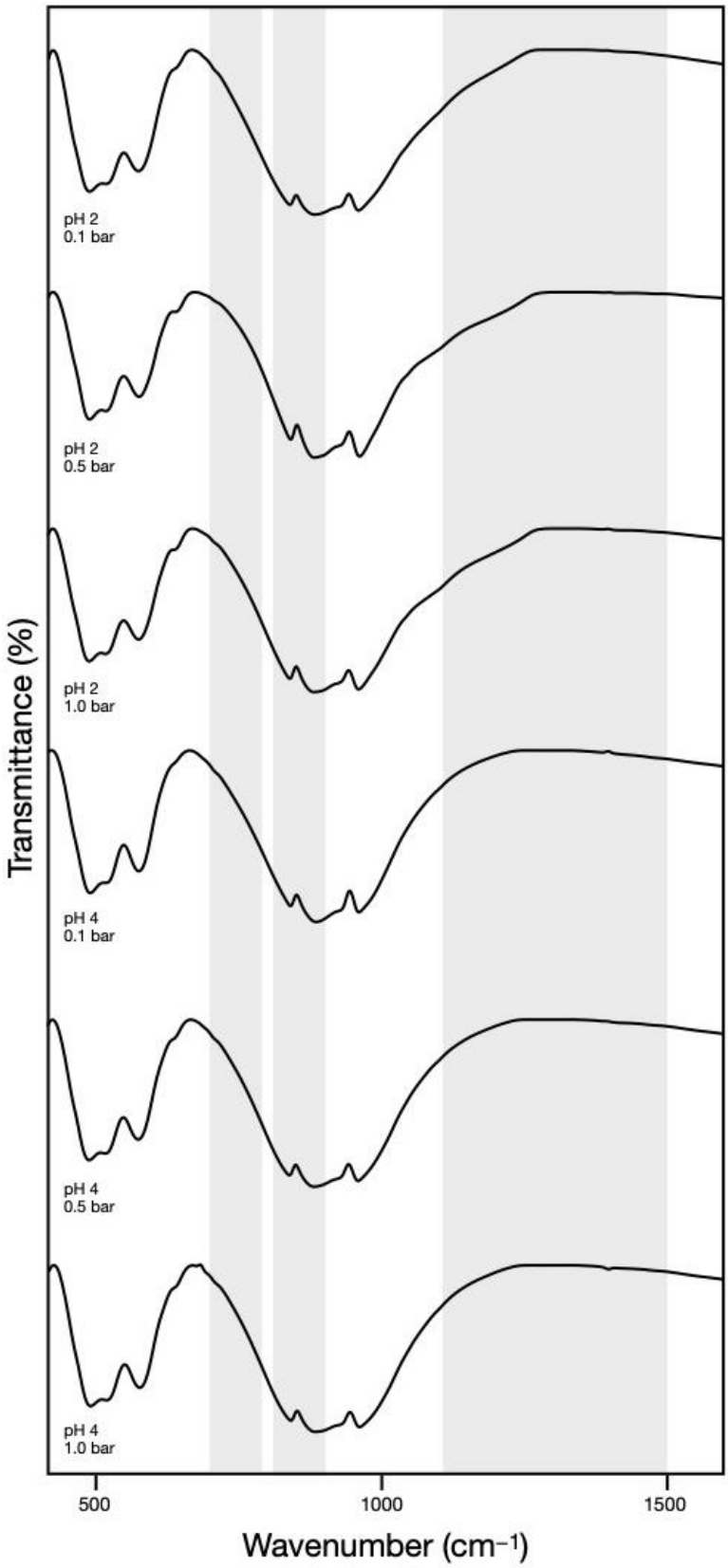
Wray, J.J., Murchie, S.L., Bishop, J.L., Ehlmann, B.L., Milliken, R.E., Wilhelm, M.B., Seelos, K.D., Chojnacki, M., 2016. Orbital evidence for more widespread carbonate-bearing rocks on Mars. J. Geophys. Res. Planets 121, 652–677. https://doi.org/10.1002/2015JE004972

Zeebe, R., Wolf-Gladrow, D., 2001. CO2 in Sewater: Equilibrium, Kinetics, Isotopes. Gulf Professional Publishing.

11. Supplementary Figures



Supplementary Figure 1: The typical signatures returned from X-Ray diffraction (XRD) analysis of solid samples from fayalite-bearing experiments, including experiments begun at pH 2 (upper three) and 4 (lower three) with all CO_2 levels explored in this work. Note the extremely similar Ångstrom measurements between experiments, highlighted grey for clarity: the peak measurements are often identical to several decimal places. These spectra all correspond to fayalite; no siderite or other Fe(II)-carbonate was identified via XRD.



Supplementary Figure 2: The typical signatures returned from Fourier transform infrared spectroscopy (FTIR) analysis of solid samples from fayalite-bearing experiments, including

experiments begun at pH 2 (upper three) and 4 (lower three) with all CO_2 levels explored in this work. Note the grey highlighted regions: these correspond to the central zones of absorption for siderite, whereby a strong absorption trough would be expected. These spectra, however, all correspond to fayalite; no siderite or other Fe(II)-carbonate was identified via FTIR.

Chapter 4

Columbia River Basalt as an Analogue for the Martian Crust in Experimental Recreations of Surface/Near-Surface Carbonation

1. Introduction

In this chapter, experiments that were run with powdered Columbia River Basalt (CRB) as a substrate are detailed and their results discussed at length in the context of forming carbonates under anoxic conditions. First discussed is why CRB was selected for use in experiments and its relevance to the Martian surface. Next discussed are the methods employed where they deviated from those written at length in Chapter 2 (Methods), which will not be repeated and may be found earlier in this thesis. The results of the experiments involving CRB are then described, interpreted, and discussed with regards to their carbonate-forming potential and any other interesting chemical observations that arose. Lastly, the key results of this discussion are summarised in the conclusions section that highlights the most important findings of this segment of the project.

1.1. Columbia River Basalt as a Martian analogue

In the previous chapter, pure fayalite (Fe_2SiO_4) and forsterite (Mg_2SiO_4) were used to simulate the geochemistry of the Martian surface for the simplicity of these minerals' composition in relation to the attempted synthesis of carbonates bearing Fe or Mg. As an advancement of this, Columbia River Basalt is here used as a more complete simulation of the Martian surface. Columbia River

Basalt (CRB) is a type of basalt from the Columbia River region of the American Northwest. Approximately 200,000 km^2 of basaltic lava were erupted here between 17 and 6 million years ago from great fissures (Hooper, 1982) leaving deposits that are in places more than 2.5 km thick. The CRB sequences are especially interesting to geologists given they are the youngest of the flood basalt provinces (Baksi et al., 1993), thus are better preserved, but also because they are deeply gouged by the Columbia-Snake river systems, exposing long, fresh stratigraphic sections for study.

CRB is one of the best approximate representations of the typical composition of the Martian crust. Missions across the Martian surface have identified *in situ* basalt, such as the pyroxene- and olivine-rich basalts studied by the Mars Exploration Rover *Spirit* at Gusev Crater (McSween, 2004; Morris et al., 2006) that likely originated from an undepleted mantle melt (McSween et al., 2006), and the basalt-based, olivine-, augite-, and plagioclase-rich sandstone in Gale Crater as seen by the Mars Science Laboratory *Curiosity* rover (Treiman et al., 2016; Edwards et al., 2017). Additionally, the Shergottite-Nakhlite-Chassignite (SNC) meteorite group are either basaltic or ultramafic cumulates that crystallised from basaltic melts (Bridges and Warren, 2006). As seen in Table 1, a typical flow from the CRB contains similar mineralogy, in similar abundances, to these basalts described *in situ* on Mars and Martian meteorites analysed on Earth (Wright et al., 1973; McCarthy et al., 1974; Gleason et al., 1997; McSween, 2004; Edwards et al., 2017). Basalt has been used as a representative of the Martian crust by numerous other experimental and modelling studies: for example, fine-grained, olivine-bearing basalt with plagioclase phenocrysts (Viles et al., 2010); basaltic glass from the Stapafjell Volcano, Iceland (Hausrath and Brantley, 2010); basalt from the Laki flow in Iceland (Keszthelyi et al., 2000); basalt from the Cerro Negro Volcano, Nicaragua (McCollom et al., 2013); basalt from the Deccan Traps, India (Wright et al., 2011); and Ordovician basalt from Helen's Bay, Northern Ireland (Parnell et al., 2014). CRB, however, has been the focus of numerous Mars analogue studies (e.g., Catling, 1999; Michalski et al., 2006; Thomson et al., 2014) and low temperature alteration experiments using CRB have previously produced smectites, iron oxides, and silicates (Hearne, 1990), all of which are relevant

to the Martian surface and found in abundance *via* spectroscopy (e.g., Bishop et al., 2008; Ehlmann et al., 2009). CRB has also been compared to several Martian meteorites (Baker et al., 2000) including Shergotty, Nakhla, and ALH 84001, and found to have particularly similar composition (see Table 1).

For a planet like Mars that hosts an extensive sedimentary record (e.g., (Malin and Edgett, 2000; McLennan et al., 2019), it is extrusive basalt from primary volcanic sources that forms the basis for many of the vast evaporite, conglomerate, sandstone, and mudstone sequences that comprise large swathes of the surface (e.g., Squyres and Knoll, 2005; Thompson et al., 2016), and apparently unaltered, *in situ* basalt that forms much of the remaining surface (Christensen et al., 2001; McSween et al., 2004). In addition to more closely approximating the average composition of the martian upper crust, the use of a differing substrate to the fayalite and forsterite of Chapter 3 provides a means of investigating the effect of primary mineralogy on dissolution rate, reaction progress, and mineral precipitation. Varying mineral type and abundance to match mineralogies constrained from Martian basalts yields a sense of how primary mineralogy and dissolution rates of specific minerals present in basalts influence the evolution of environmental chemistry, including total inorganic carbon levels available and total alkalinity. CRB is also known to contain a large glass component (e.g., (Schaef and McGrail, 2009), and understanding the effect this phase has on substrate dissolution and new mineral precipitation is of interest for a planet like Mars, which contains an abundance of glass owing to frequent meteorite bombardment (e.g., Marti et al., 1995) and/or volcanism (e.g., (Gabriel et al., 2018; Czarnecki et al., 2020).

Chemically, each of the separate basalt flows that comprise the CRB formation are distinct. Given these vast differences, its composition was gained from multiple pre-experimental analyses rather than assumed from published research, and is covered in the methods section of this chapter. The basalt itself originated from the Grande Ronde flow of the CRB, which comprises 87 vol. % of the CRB and covers parts of Washington, Idaho, and Oregon in the USA (Reidel et al., 2013). The particular samples came from Lawyer Canyon, Idaho, as first collected by Thomson

et al. (2014), and comprise reversed polarity Grande Ronde basalts that were considered more weathered than other similar units. It lies directly below a palaeosol followed by the basalt layer known as the Basalt of Icicle Flat (Bush et al., 2004), and is underlain by a saprolite.

2. Materials and methods

The methods employed for creating and executing the experiments, analysing the results, and modelling their implications, are outlined in Chapter 2 (methods) and will not be repeated here. Appendix 1 contains detailed descriptions of the set-ups of all individual experiments. To summarise, 6 sets of experiments, totalling 36 sub-experiments, were run for this section. Table 2 lists these six overarching sets, named by their date of inception. Individual experiments within these will henceforth be referred to by their characteristics for clarity. The experiments 190806, 190807, and 190808 are henceforth referred to collectively as the 1908 series.

2.1. The experiments

The experiments were run with finely ground CRB (powder-sized; <1-10 μm) and coarsely ground CRB (sieved to consistently sand-sized; ~100 μm) to investigate the effect, if any, of differing surface area on reaction rate. When analysed via X-ray diffraction, the composition of these two materials differed slightly. The crystalline material of the coarse CRB that was detectable by XRD consisted of ~95 % albite (the Na end-member plagioclase feldspar mineral) with the remaining ~5 % comprising anorthite (the Ca end member plagioclase feldspar), while the fine CRB consisted of roughly equal parts albite and anorthite, with minor augite (Ca-rich pyroxene) and diopside (Mg- and Ca-rich pyroxene). This difference in composition between grain sizes likely arises from the differing hardness of the minerals when the original rock sample was crushed: anorthite is 6 on the Mohs hardness scale while albite is slightly harder at 6-6.5. This is consistent with the coarser CRB sample containing mostly albite, which was more resistant to crushing.

Additionally, both samples contained a substantial amount of glass, yielding a broad scattering band between ~20-60 degrees 2-theta that could not be quantified via XRD. However, Schaef et al. (2010) obtained samples from within a similar region to the CRB sample used here, and estimated a 45.3 wt. % glass component. Schaef and McGrail (2009) measured the average composition of multiple flows within the CRB, including glass (Table 3). When evaluated with a Cross-Iddings-Pirrson-Washington (CIPW) normative mineralogy calculation (written by Kurt Hollocher, US), CRB including its glassy component is found to be predominantly plagioclase feldspar (47.86 wt.%; XRD analyses for this thesis found this was mostly albite), followed by quartz (13.75 wt.%; mostly from the glass component), with minor orthoclase feldspar, diopside, hypersthene, and hematite (for full table, see Table 4). A CIPW normative mineralogy calculation is limited in being based on many assumptions and only produces an idealised inventory of material composition. Thus, it must be used with caution. A common issue relevant to this study includes the calculation of erroneous oxidation states (e.g., magnetite versus hematite). This occurs when the calculation divides Fe between oxide phases and availability for silicate phases, and subsequently miscalculates the $Fe^{2+}Fe^{3+}$ ratio.

While a good approximation in being basaltic, the CRB has its own limitations as a Martian analogue in its composition being mostly plagioclase feldspar. The Martian surface is more pyroxene and olivine dominated (e.g., McLennan et al., 2019): selecting a more mafic material for an analogue, such as peridotite, would have been a truer approximation of the type of bedrock commonly encountered by Martian waters. However, with the experiments of Chapter 3 being olivine-bearing, such a substrate variant could have produced limited differences in results. Hence, the CRB reactant is considered here a useful analogue but with manageable limitations.

While a host of other elements, such as Na and Ca, are present in the CRB, only Fe, Si, and Mg were analysed by ICP-MS. This limited analysis resulted from a communication error that unfortunately limits the extent of the conclusions that can be drawn from this chapter.

Unlike the fayalite ± forsterite experiments of Chapter 3, no CRB experiments were run with 0.1 bar of CO_2, since from studying the results of Chapter 3, there was little difference between 0.1 and 0.5 bar experiments, and given limited time and funding, similar lack of reactions were assumed for CRB. As such, 190414 was run with only 0.5 and 1.0 bar CO_2. This ran for 85 days, intending to be the equivalent of the 190423 series for the fayalite-forsterite experiments of Chapter 3, which lasted for several months and permitted the majority of chemical reactivity to occur. 190812, the repeat of 190418, was the low rock:water ratio (1:1 and 1:10) equivalent of 190414 and also ran for several months at 72 days. These experiments only used 1.0 bar pCO_2 to investigate the effect of the maximum realistic amount of CO_2 on Mars that could be expected in the subsurface environments that low rock:water ratio conditions represent. Given additional time and funding, other levels of CO_2 would have been preferable, but given these limitations the maximum realistic pCO_2 for Mars was used. This was also the maximum pCO_2 used in the experiments of Chapter 3.

Experiments 190806, 190807, and 190808 form part of a series that repeats 190414 but with more rapid sample extraction over the course of 10 days to observe the rapid kinetics that occur at the inception of an experiment. 190806 is the only experiment in the CRB series to run with 0 bars of CO_2. This acts as an equivalent of the 190123 experiment of the fayalite-forsterite series, which used fayalite with 0 bar CO_2 as a control to observe the effects of reaction in fluids that did not contain CO_2, and is useful because this allows the effect of CRB added to water of moderate (pH 4) to high (pH 2) acidity to be observed. 190708 directly repeats the 0.5 bar CO_2 section of 190414, but run for ten days; 190808 repeats the 1.0 bar section.

All experiments were run with the same set-up to the Chapter 3 experiments: within in a sealed, anoxic glove box where atmospheric oxygen was kept at below 1 ppm. High rock:water ratio experiments used sealed beakers of 0.172 mL capacity, while low water-rock experiments used airtight syringes of 50 mL capacity. All experiments were prepared, run, and, where possible,

prepped for analysis within the glove box to minimise the effects of oxidation. Chapter 2 (Methods) outlines the experimental environment in detail.

A matter that has not been an issue for previous experiments but becomes relevant to discuss here is that carbonate was introduced to the system as sodium bicarbonate ($NaHCO_3$). Given that the main reactant in this chapter is albite (the Na-rich end member of plagioclase) it is worth considering whether the addition of sodium to solution as $NaHCO_3$ affected the results in any way, e.g., by reducing concentration gradients and thereby reducing dissolution. To produce the maximum pressure of carbon dioxide into the system (1.0 bar), 60.888 mL of 0.1 mmol/g sodium bicarbonate solution was added to a solution that totalled 172 mL. This was a total of 0.35 mmol within the solution. If 0.3444 g CRB were added to this solution, for coarse CRB at ~95 % albite ($NaAlSi_3O_8$) this is a total amount of Na within the mineral of 1.3 mmol. Thus the amount of Na in solution is considered only minor.

The analytical methods employed include X-ray diffraction (XRD), Fourier transform infrared spectroscopy (FT-IR), and scanning electron microscopy (SEM).

2.2. The model

To more broadly investigate a range of environmental parameters regarding solution chemistry evolution during water-rock interaction, a geochemical model was constructed in the software *The Geochemist's Workbench* (GWB), version 12 (Bethke, 2017), which uses thermodynamic data from the Lawrence Livermore National Laboratory database (Delany and Lundeen, 1991). In the *React* module, the model was created using the criteria in Table 5, with the components in Table 4 as calculated from Schaef and McGrail (2009) and the CIPW normative mineralogy calculation added as reactants with an identical rate constant to simulate their simultaneous release into solution. The rate constant used was 9.69×10^{-13} mol/cm^2/s as calculated from the Schaef and McGrail (2009) data. This was calculated from the experiments of Schaef and McGrail (2009) that were conducted under a range of temperatures (25, 40, 70, 90 °C), and pH (3, 4, 5, 7) and was used instead of the

rate constant used by Schaef and McGrail (2009) for their own experiments owing to the need to adjust this constant for temperature. For each experiment, the dissolution rate constant was given for Al, Na, Ca, Mg, Fe, and Si. To use a constant that was appropriate for this model, the following were selected: the Si rate (based on the CRB composition used here being >50 wt.% of the CRB); the 25 °C temperature (as used in the experiments described here); pH 5 (which was the rough median of pH experienced over these experiments); and, of these, there were two rate constants, one for the CRB flow top and one from the flow interior; an average was taken of the two. The dissolution rate constant under identical conditions but at pH 7 was also employed in the model (calculated as above but using pH 7, yielding 3.707×10^{-13} mol/cm^2/s) to investigate whether rendering this of higher pH would have an effect on the model, but in several tested scenarios (SiO_2 activity, siderite saturation, and pH) there was no to negligible change to the modelled results.

The pH 5 rate constant was applied to all the minerals listed in Table 4. The components listed in Table 4 were added as relative proportions that added to 10 g (which was used in modelling for the fayalite-forsterite experiments of Chapter 3, and kept here for consistency and comparability). Hematite can be added to GWB without oxygen by de-coupling the redox reaction for Fe, but not all of the CIPW-calculated components could be added, e.g. hypersthene, apatite, Na_2SO_4, titanite, and ilmenite. To compensate for this, the following changes were enacted: Na_2SO_4 was added as thenardite, which is its anhydrous form; apatite was added as hydroxyapatite; and hypersthene ($(Mg,Fe)Si_2O_6$) was added as quartz (SiO_2) as the closest match. The right-most column in Table 4 shows the components added, adjusted to their relative % against the components that could not be added. These components were then added to the model at proportions that totalled 10 g.

The models were run for the time it took to reach equilibrium, and pH was allowed to evolve naturally over their course from a starting position of 3.

3. Results

In this section, the solid and solution results from the 5 successful CRB experiments (28 sub-experiments) are described and summarised. First, a description of the results of each experiment is outlined and summarised. In the following section, the implications of these results are then discussed amongst the context of the Martian surface and subsurface environments.

3.1. Solution chemistry results

Over the course of each experiment, 10 solution samples were extracted and their elemental composition analysed via inductively coupled plasma mass spectrometry (ICP-MS). At the moment of sampling, the pH and Eh of the solution were measured prior to its acidification for storage before ICP-MS could be conducted. pH and Eh will be discussed and summarised first in this section. Then, the corresponding elemental composition in solution over the course of the experiments will be discussed and summarised.

3.1.1. pH

Figure 1 includes the pH measured over the course of 190414 and the 1908 series (190806, 190807, and 190808), divided into fine and coarse experiments to observe whether increased surface area alters reaction rate. The pH and Eh for experiment 190812 are found in Table 6 since, owing to the low rock:water ratio, samples could only be extracted once and were taken at the end of the experiment, and only for the 1:10 ratio experiments. This is because for the 1:1 experiments, only 1 mL of fluid was available, giving the experiment a muddy consistency and making it difficult to extract fluid of any measurable volume. Usually ~1.25 mL was extracted to ensure the total submersion of the pH and Eh probes, otherwise an accurate measurement could not be assured.

For 190414 fine and coarse begun at pH 2, the pH does not appreciably change from the experiments' start to end. The maximum change is of +0.6 for coarse CRB under pH 2 and 0.5 bar pCO_2. While there is a jump to pH 4.5 for fine CRB under pH 2 0.5, and 3.4 for fine CRB under pH 2 and 1.0 bar pCO_2, this returns to ~2 for the following datapoint and all thereafter; the

corresponding drop in Eh as seen in Figure 2 suggests this was not an anomaly with the pH probe but rather some transient change to the solution chemistry itself. This change was observed ~350 hours (14 days) into the experiment, which the 1908 series did not run for, thus its presence could not be tested as a recurring spike in other experiments. This is not considered a major issue as Eh was known to fluctuate in other experiments as anomalies that did not affect the long-term solution chemistry. The coarse 190414 did not observe such a change in any experiments, nor did the pH 4 experiments of the fine 190414 series.

For fine and coarse 190414 begun at pH 4, unlike at pH 2, there is a slight increase in pH for experiments begun under 0.5 bar pCO_2. This is best observed in the experiment run with fine CRB that began at pH 4 under 0.5 bars of CO_2, where pH climbs from 4 to 6 over the 85 days. A similar rise is observed for the coarse equivalent, which at maximum reaches pH 5.8. These increases were not observed for the pH 4 1.0 bar experiments, where the maximum increase was 0.5 pH with coarse CRB under pH 4 and 1.0 bar pCO_2.

The pH evolution for the 10-day 1908 series is far more varied. pH spikes up and down for all 12 experiments, with a maximum of +1.0 for the pH 2 experiments (in the case of fine CRB under pH 2 and 0.5 bar pCO_2) and +2.2 (in the case of fine CRB under pH 4 and 0 bar pCO_2). By the experiments' termination, however, similar to the longer-run 190414, there is little total change, with at maximum +0.9 for fine CRB under pH 4 and 0 bar pCO_2, and far less for all others both coarse or fine, pH 2 or 4. This suggests that, as with shorter equivalents of longer-run experiments within Chapter 3 (discussed at length in Appendix 2) such as the experiments named '180829' for '190423 Fo' or '180406' for '190423 Fa', the 1908 series reflect the initial stages of their longer-term equivalents.

The largest pH changes are seen in 190812 (Table 6). All previously discussed experiments occurred at a rock:water ratio of 1:500, but for 190812 two low rock:water ratios were used: 1:1 and 1:10. The 1:1 experiments contained too little fluid to be extracted, but sufficient sample could be extracted from the 1:10 rock:waterrock:water ratio experiments. For these 1:10 experiments, as

seen in Figure 1, maximum pH increase was +2.6 for coarse CRB under pH 4, from pH 4 to 6.6, while at minimum this was +1.6 for coarse CRB under pH 2. Unlike their high rock:water ratio equivalents, where pH changed at maximum +0.4 for both pH 2 and 4, pH was able to evolve to far higher levels where lower amounts of fluids could interact with the rocky substrate. It is interesting to note that unlike with higher rock:water ratio experiments, pH climbs by roughly the same amount — ~+2.2 — for both pH 2 and pH 4 experiments, whereby for high water-rock, the larger changes were confined to pH 4 experiments.

The summary from the pH results of the CRB experiments is that, for high water-rock experiments, pH changed only minimally, even for those lasting almost three months. This could reflect a limited amount of substrate dissolution to alter solution chemistry. However, for low rock:water ratio experiments the change in pH was far more pronounced and followed a clear increase by over 2 pH units for all 1:10 experiments. This may be due to the total budget of acidity in the waters remaining lower relative to the surface area of the mineral dissolving. Further information will be revealed by a closer look at the chemistry analysed by ICP-MS, discussed shortly.

3.1.2. Oxidation-reduction potential

The oxidation-reduction potential (ORP) of the solutions under examination here is likely dominated by variations in the oxidation and reduction state of Fe in solution, and is relevant to this study because the kinetics of the formation of Fe-carbonate is a particular focus of this thesis. ORP is defined as a measure of the tendency for a chemical species, such as Fe, to be reduced or oxidised by gaining or losing electrons, respectively, and is measured in volts. The more positive the measured ORP, the more oxidised the Fe in solution is compared to reduced Fe, while the reverse holds true for more negative ORP. Eh is partially dependent upon pH for most redox half-cell reactions, and this is a fact that has been repeatedly observed throughout the experiments conducted within this thesis.

In Figure 2, the ORP levels recorded over the course of experiments 190414 and the 1908 series are divided into separate diagrams for F (fine) and C (coarse) CRB used. The initial and final Eh measurements for 190812 are recorded in Table 6.

Reflecting the pH trends discussed in the previous section, at first glance ORP also changes little over the course of all the high rock:water ratio experiments in Figure 2. With increasing alkalinity the ORP becomes increasingly negative — this was a trend observed in the fayalite and forsterite experiments discussed in Chapter 3 and its extended discussion in Appendix 2, and is an implicit mirrored dependence essential to all redox reactions (see Equations 3.1.2). pH for 190414 and the 1908 series only changed slightly, and this is reflected in the only slight changes observed in their ORP trends.

For 190414, the maximum ORP variation is from 593.7 to 4.1 mV (fine CRB under pH 4 and 0.5 bar pCO_2), a change of 589.6 mV. This is unusual, because no corresponding increase in pH can be seen in Figure 1. The fact that the decrease of almost 600 mV for fine CRB under pH 4 and 0.5 bar pCO_2 ~200 hours in does not correspond to a similar change in pH suggests that this is an erroneous measurement: the ORP probe often took time to stabilise, and could jump from one stable measurement to another if disturbed. The different reading for this one datapoint in fine CRB under pH 4 at 0.5 bar pCO_2 could be explained by the ORP probe having not yet stabilised for this sample. It is possible this measurement was able to evade notice as erroneous owing to it being the first experiment sampled (fine CRB being sampled first over coarse, pH 2 over pH 4, and 0.5 bar pCO_2 over 1.0 bar pCO_2), as well as the first sample of the CRB series that was extracted (the first datapoint at 0 bar pCO_2 corresponding to the initial solution conditions prior to adding the reactant). Were such a measurement recorded at a later point in the CRB analyses, the anomaly from the pattern would have been detected and the probe allowed to sit for longer to stabilise. As such, the ORP measurement of 4.1 mV for fine CRB under pH 4 and 0.5 bar pCO_2 is here considered an error that does not accurately reflect the solution chemistry at this moment in the reaction.

The gradual increase in pH for fine CRB under pH 4 and 0.5 bar pCO_2 and coarse CRB under pH 4 and 0.5 bar pCO_2 is reflected in the gradual decrease in ORP, demonstrating as previously discussed that as the solution became more basic it also became more reducing. For solutions that displayed little change, such as the 1.0 series in both 190414 fine and coarse, there is little change in ORP from start to finish. This trend is reflected in the 1908 series, where little change occurs in both pH (Figure 1) and ORP (Figure 2). It is interesting that, while there is no appreciable start-to-finish trend, the ORP for the 1908 coarse series begins and ends lower than that for the 1908 fine series — at either side of ~450 mV compared to ~550 mV. The fact that, like the 1908 fine series, there is no appreciable change in ORP over the 10 days suggests the lower ORP for the 1908 coarse series is a function of low initial ORP. Why Eh would initially be lower for the same pH and same CO_2 levels as its 1908 fine equivalents is not immediately clear.

For the low rock:water ratio experiment of 190812, however, there is appreciable change observed in ORP from start to end (Table 6). For the 1:10 experiments whose solution could be extracted, ORP fell for all experiments but most notably in both pH 4 C and F, with a decline of 376.5 and 388.4 respectively. This follows their increasing pH trends that were higher for pH 4 experiments than pH 2. This again suggests that the low rock:water ratio experiments, in comparison to their high rock:water ratio equivalents, evolved further over the course of the experiment. This will be explored when the elemental chemistry data from ICP-MS is discussed in the following sections.

To conclude for both pH and ORP, little solution chemical change occurred as measurable through pH or ORP, with only minor trends noted for the pH 4 under 0.5 pCO_2 experiment (numbered 190414 with coarse and fine CRB), but otherwise for the shorter-term 1908 series, all pH 2 experiments, and the pH 4 at 1.0 bar pCO_2 190414 series, the solution chemistry did not appreciably alter. Without a closer look at the elemental composition of the solutions through time, these observations suggest little CRB dissolved into solution to alter the chemistry, excepting minor amounts in the 190414 at pH 4 and 0.5 bar pCO_2 series. Why these experiments in particular

experienced change must be a function of the CO_2 levels, since equivalent experiments also begun at pH 4 but with 1.0 bar pCO_2 did not show this change. Most likely, the acidity released by the additional dissolved CO_2 in the 1.0 bar experiments overpowered the ability of pH and solution chemistry to evolve. This can be interpreted quantitatively from the standpoint of mass balance and pH, and this is discussed and demonstrated at length using graphs depicting total dissolved inorganic carbon against total alkalinity in section 4.5, by calculating total alkalinity and total dissolved inorganic carbon across differing pH and pCO_2 levels. What such calculations and graphs show is that this effect is most likely due to relatively slow silicate dissolution rates, whereby the total alkalinity released is relatively small when compared to the total concentration of H^+. This, in turn, is an effect of higher concentrations of pCO_2.

The following sections outline the chemistry of solutions through time by analysis of their elemental composition — Fe, Si, and Mg — through ICP-MS.

3.1.3. Iron

Sampling was not begun for the 190414 coarse and fine experiments until ~350 hours into the experiments for the reason that approximately equal time periods were to be used in the sampling, and the aim of this experiment was to extract its ten samples over a period of several months. This is in contrast to the ~240 hour-long experiments of the 1908 series where samples were extracted every ~24 hours. Capturing the rapid kinetics and change that occurs at the experiments' beginnings where reactant is added to solution, the 1908 series' Fe concentrations as measured by ICP-MS in Figure 3 display a steady increase of Fe released to solution for experiments begun at pH 2. This can be seen for all three concentrations of CO_2: 0, 0.5, and 1.0 bar. The increase is on average from 0.1 to 0.3 mmol/kg for both fine and coarse and suggests an immediate dissolution of Fe from the CRB into solution that occurs only with the initial acidity of experiments begun at pH 2, as this Fe release is not seen for pH 4 experiments in the short-term 1908 series. Fe concentrations reach ~0.3 mmol/kg by 10 days into the pH 2 coarse and fine short-term experiments, and this is roughly the level observed between 350-2100 hours for the

long-term 190414 experiments. For both coarse and fine CRB material at an initial pH of 2, Fe concentrations remain between 0.2-0.3 mmol/kg with little observable trend of increase or decrease between the 85 days they ran for. This suggests that almost all of the dissolution of Fe from CRB occurred within the first ~250 hours of the experiment following the immediate addition of the reactant to the solution.

For experiments begun at pH 4, consistently less Fe is in solution than for pH 2 experiments. This is consistent with mineral dissolution occurring more effectively with the destructive effect of highly acidic solutions, which was also observed and discussed in Chapter 3 and its extended results in Appendix 2. Fe reaches a maximum of 0.8 mmol/kg 186 hours into the 1908 experiment coarse CRB under pH 4 and 0.5 bar pCO_2, but this is likely an error from the preparation or analysis of the sample, since the solution otherwise contains between 0.02-0.2 mmol/kg and does not show a steady rise or fall either side of the 186-hour datapoint. Aside from this probable anomaly, the highest Fe reaches in the pH 4 experiments is 0.3 mmol/kg in both coarse and fine CRB under pH 4 and 0.5 bar pCO_2, which are the experiments where Fe fluctuated the most wildly with little trend over their 10 day runs. Both rise to 0.2-0.3 mmol/kg between 186-210 hours in before Fe concentrations return to the negligible ~0.02 mmol/kg mark. This could reflect a precipitation — the removal of Fe from solution as a mineral. It is interesting to note that it is the pH 4 experiments begun at pH and 0.5 bar CO_2 that show limited Fe level variation when these were the experiments that also yielded the most pH and Eh activity change.

For the low water-rock 190812 experiment, as with pH and Eh, there is significantly larger variation in Fe concentrations compared to their high rock:water ratio equivalents. Far more Fe is released into solution for the pH 2 experiments than pH 4 (more than an order of magnitude, e.g., 0.1 compared to 2.5 mmol/kg), which is consistent with the high water-rock experiments. However, while there has been little observable difference between the fine and coarse experiments thus far despite their differing surface areas, 190812 Fe concentrations for the first

time suggest that more Fe is released into solution from the coarser material than the finer. There was no difference between the rate of release of Fe to solution for fine or coarse material.

To conclude for the Fe concentrations in solution, little Fe is released into solution for experiments begun at more neutral pH in comparison to more acidic pH, which agrees with the expected effect of increasing silicate dissolution rates as a function of decreasing pH. Under low rock:water ratio, higher concentrations of Fe are found in solution. This suggests environments that promote low concentrations of water compared to rock surface area, for example in the subsurface in pore spaces and interstitial zones, are more likely to see higher concentrations of Fe available in solution for the formation of new minerals. This is in line with the higher concentrations of pH reached for low water-rock experiments as well, and altogether suggests higher concentrations of reactivity where lower volumes of water compared to rock are found.

3.1.4. Silica

The graphs of Figure 4 display the concentrations of Si in mmol/kg for each of the high rock:water ratio CRB experiments. For the 85-day 190414 series, both for coarse and fine material, 0.5 and 1.0 bar of pCO_2, and whether begun at pH 2 or 4, there is little release of Si into solution. Si concentrations fluctuate between ~0.05-0.3 mmol/kg with little trend or variation between experiments, suggesting Si, like Fe, was only released in minor amounts from CRB when left for almost three months.

This trend is broadly seen again in the short-term 10-day 1908 series, where for 1.0 bar pCO_2 experiments ~0.5-0.3 mmol/kg Si remains level in solution from the experiments' beginning to termination for coarse, fine, pH 2, and pH 4 experiments. For all 0.5 bar experiments there is a precipitous decline in Si concentrations from the first hundred hours, where Si drops from ~0.6 mmol/kg to 0.3 mmol/kg for all experiments, suggesting the possible removal of Si from solution as a precipitate. This could be in the form of amorphous Si, which was identified in several of the fayalite-forsterite experiments, and is in this particular experiment supersaturated (as discussed at length in section 4.1). What is striking in the 1908 series is that the highest Si concentrations are

reached in the experiments that held no CO_2 at all, the 190806 series. In these, marked by dotted lines, CRB was reacted only with sulphuric acid, and this appears by far the most effective means of releasing Si into solution, with concentrations reaching almost 1.0 mmol/kg. This trend was not observed with Fe, which could mean either the non-stoichiometric release of Si into solution, or that more Si is present in the rock than Fe.

For the low water-rock experiments, Si concentrations are shown in Table 7 and, as for Fe, show elevated concentrations of Si released to solution compared to the experiments' high water-rock equivalents. This reaches at maximum 1.5 mmol/kg for coarse CRB under pH 4. It is interesting to note that the ratios of Fe to Si for all four experiments differ radically. For fine CRB under pH 2 there is ~1.5 mmol/kg more Fe in solution, while for fine CRB under pH 4 there is ~0.6 mmol/kg more Si; for coarse CRB under pH 2, there is 4.1 mmol/kg more Fe in solution, while for coarse CRB under pH 4 Fe and Si are almost equal. This suggests the non-stoichiometric release of these elements into solution where higher concentrations of Si enter solution with lower initial acidity and where larger grain size is used.

Plotting the stoichiometric ratio of Fe to Si in CRB against actual released concentrations of these elements is a means of examining whether dissolution occurred in bulk or was localised to specific species. Figure 5 displays the ratio of Fe to Si release for all CRB experiments. Since the exact amount of Fe and Si present in the original CRB used was not determined from pre-experimental analyses (for example, electron probe microscopy would have been sufficient), the average CRB composition determined by Schaef and McGrail (2009) in Table 3 is used. Here, Fe is present only as Fe_2O_3 (13.52 %) and Si as SiO_2 (52.795 %). Stoichiometrically, this is 5.4 % Fe and 17.6 % Si, or a ratio of 0.3. A line at 0.3 is added to the graphs of Figure 5 to distinguish stoichiometric release of Fe and Si.

As seen in Figure 5, for the longer-term experiment of 190414 (run for almost 2,100 hours) all experiments have above-stoichiometric release rates of Fe and Si, which corresponds to the favoured release of Si. This effect occurs both for coarse and fine CRB experiments. When run

only for 10 days (the 1908 series) stoichiometric release is maintained for all experiments with 0 bar pCO_2, with the experiment begun at pH 4 at 1.0 bar pCO_2 also remaining close to stoichiometric. As suggested earlier, higher concentrations of Si are entering solutions where initial acidity is higher, and within identical pH experiments, where pCO_2 is higher. Higher acidity and pCO_2, together with longer periods of time, encourage more aggressive dissolution through the availability of H^+, and it may be that particularly robust minerals such as the large glassy component of CRB only begins dissolution under these aggressive conditions.

3.1.5. Magnesium

Magnesium concentrations in solution as seen in Figure 6 vary very little across the course of all experiments, including those for the low rock:water ratio 190812 (Table 7). Mg concentrations remain below 0.03 mmol/kg for all high rock:water ratio experiments with little variation between material, initial pH, and CO_2. For low rock:water ratio the maximum is 0.3 mmol/kg. In all cases excepting fine CRB under pH 4, Mg is the element least present in solution; for fine CRB under pH 4 there are equal amounts Fe and Mg, with half as much Si.

3.1.6. Summary

To summarise the implications of Fe, Si, and Mg concentrations in solution as discussed in this section, experiments begun at pH 2 consistently release higher concentrations of material into solution compared to experiments begun at pH 4, and this occurs across all concentrations of dissolved CO_2 and both high and low rock:water ratio systems.

Overall, the experiments that released the highest elemental concentrations to solution began at low pH (2), used sand-sized reactants, and were conducted under low rock:water ratio (1:10). However, the presence of free elements within solution does not necessarily equate to the formation of new minerals. In the following section, the elemental concentrations discussed here are re-cast in terms of activity. As described in Chapter 2 (Methods), activity is a thermodynamic quantity and dimensionless measure of the effective concentration of a species within a solution. Ions in solution interact with other molecules and behave chemically as though they are at a lower

concentration than they are, or are measured, and this effective concentration, or the concentration that is available for a reaction, is called activity. As described in Chapter 2 section 5, the Debye-Hückel B-dot equation (Debye-Hückel, 1923), derived from the Helgeson-Kirkham-Flower model (Helgeson et al., 1981; Helgeson and Kirkham, 1974), was used to calculate the activity. This investigates the thermodynamic tendency of a mineral to remain in dissolved form or precipitate from solution. Ionic strength, in the absence of the total ionic component (only Fe^{2+}, SiO_2, and Mg^{2+} were measured) was estimated from the three measured elements alongside calculated inputs of Na^{2+}, HCO_3^-, and SO_4^{2-}. The contribution of other species cannot be measured, and only measuring Fe^{2+}, SiO_2, and Mg^{2+} is insufficient to draw estimations on the remaining characteristics of solution chemistries. This thesis acknowledges that the loss of this data renders the following sections severely hindered. The question of how other species may have contributed to the chemistry at this point is considered *via* a charge balance calculation. Seen in Table 10, the total negative and total positive species in moles are added together for one example experiment to produce a charge difference for this experiment of 1.52×10^{-2} moles. All solutions must be balanced overall in terms of charge, and the overall negative charge places a strong constraint that cations not measured, such as Ca^{2+}, K^+, Mn^{2+}, and Al^+. While the amount of moles of Fe^{2+}, Mg^{2+}, and SiO_2 in solution were extremely low, and thus it could be anticipated that these other such cations would also have a small effect on ionic strength, their effect on the overall charge balance of the solution is more difficult to assess and may have been significant.

3.1.7. Siderite

The first mineral to be discussed is the geologically-stable form of Fe(II)-carbonate, which is siderite ($FeCO_3$). In Figure 7, the saturation state of siderite (omega) is displayed, whereby if $\Omega = < 1$ dissolution is favoured, and if $\Omega = > 1$ precipitation is favoured. Ω reaches maximum 0.2 for 190414 fine CRB under pH 4 and 0.5 bar pCO_2 and 0.15 for the equivalent using a coarse substrate. For the short-term 1908 series, which represents the first 250 hours of 190414, there is no notable siderite saturation, and this agrees with the lack of reaction for this corresponding

period in 190414. The siderite saturation of the pH 4 and 0.5 bar pCO_2 series follows the rise in pH both the fine and coarse experiments that these parameters experienced (Figure 1), but does not match a rise in Fe (Figure 3). This suggests pH is the more dominant factor controlling siderite saturation state than Fe activity. This is a conclusion that was also observed in the fayalite-forsterite experiments of Chapter 3 and its appendix, Appendix 2, where experiments with higher pH but near-identical Fe concentrations to those of lower pH vastly exceeded their lower pH equivalents in siderite saturation. A means of demonstrating this is by examining the height and slope of the omega curves seen subsequently in this chapter (section 4.1), where this effect becomes more apparent when siderite saturation state is calculated through a combination of pH and the activity of Fe^{2+}.

For the low water-rock experiments, as seen in Table 8, siderite also reaches its highest saturation state in a pH 4 experiment, which contained coarse CRB. It is interesting that this experiment showed the second lowest Fe concentrations of the four low water-rock experiments (0.41 mmol/kg, Table 7) and the highest pH of 6.6, also the highest recorded pH of all the experiments discussed in this chapter. As with high water-rock experiments, it appears that pH is the dominant control on siderite saturation. Comparing between high and low rock:water ratio experiments, siderite is on average higher for low water-rock, reaching at maximum 0.8 compared to 0.2 mmol/kg for high. This suggests environments where a low ratio of water to rock is found are more conducive to the formation of siderite.

3.1.8. Amorphous silica

Silica is expected to precipitate alongside Fe(II)-carbonates because it is produced by aqueous CO_2 weathering of igneous rocks under anoxic conditions (Catling, 1999). As such, its presence in solution could be an indicator of important carbonate-related behaviours in solution. The results of amorphous silica saturation state in solution are shown in Figure 8.

For the low water-rock experiments, amorphous silica Ω also remains similar to the measured mmol/kg concentrations of Si in Table 7, with a maximum of 0.8. This is higher than

amorphous Si Ω reached for high water-rock experiments and suggests, as with siderite, that amorphous Si is more likely to be precipitated in higher amounts under low rock:water ratio.

3.1.9. Amorphous Fe-carbonate

The metastable Fe(II)-carbonate amorphous Fe-carbonate (AFC) reveals similarly low concentrations. These calculations were run using the calculations outlined in Appendix 3 for calculating $\Omega_{siderite}$, only rearranged for AFC:

$$\boldsymbol{\Omega = \frac{IAP}{K_{sp}} = \frac{\frac{a_{Fe2+} \times a_{CO32-}^{0.5}}{a_{H+}}}{K_{sp}}} \qquad \text{(eq. 3.1.8.1)}$$

However, K_{sp} for AFC does not exist, as AFC is not a mineral but an amorphous phase (Jiang and Tosca, 2019). Accordingly, Ω is represented as the IAP divided by the effective K_{sp} as calculated by Jiang and Tosca (2019) as $10^{-2.2}$. Table 9 lists several example Ω_{AFC} that were calculated using the formula of AFC as $Fe(CO_3)_{0.5}OH$ from Jiang and Tosca (2019), estimated to produce the highest Ω_{AFC} based on their similarly high $\Omega_{siderite}$ values. High rock:waterrock:water ratio experiments were included, namely samples extracted after 1,459 hours into experiment 190414 that was run with fine CRB under 0.5 bars pCO_2 and begun at pH 4. Low water-rock experiments as seen in Table 8, Ω_{AFC} are also included in Table 9 as a means of comparing Ω_{AFC} between high and low rock:waterrock:water ratios.

What is observed in Table 9 is that Ω_{AFC} for all those datapoints calculated by hand are extremely minute amounts, averaging 0.01 for the high rock:waterrock:water ratio datapoints and 1.00 for experiments run at low rock:waterrock:water ratio (1:1). It is apparent that, in line with the lack of reactivity suggested by limited pH change or elemental release, AFC activity in all CRB-bearing experiments is extremely low. An additional interesting observation is the difference between high and low rock:waterrock:water ratio experiments' Ω_{AFC}, whereby low rock:waterrock:water ratio experiments produced Ω_{AFC} on average two orders of magnitude higher

than that of high rock:waterrock:water experiments. While all Ω_{AFC} is significantly below the threshold for its precipitation as estimated by Jiang and Tosca (2019) as $10^{2.20}$, where less solute exists in contact with the mineral powder, AFC reaches higher saturation states.

To draw conclusions for how mineral saturation states vary across CRB experiments, it is firstly apparent across siderite, amorphous silica, and AFC that low rock:water ratio, either moderately, for amorphous Si, to significantly, for siderite and AFC, increases the supersaturation of these minerals. In real environmental systems, this translates to a heightened thermodynamic expectation for the formation of these minerals under conditions where rock and water coexist at ratios of 10 or less, rather than up to 500. Secondly, as pH increases the Ω of siderite vastly increases, a change which is not observed with increasing Fe, suggesting that environments where pH may reach more a more alkaline state are conducive for the formation of these Fe(II)-carbonates.

3.2. Solid sample results

In this section, the results of all solid material analyses are briefly summarised and their key conclusions discussed in relation to the ability of a CRB substrate to form carbonates under Mars-like conditions.

3.2.1. X-Ray diffraction

Seen in the XRD spectra of Figures 9, 10, 11, 12, and 13, no new minerals were identified when compared to the reference XRD spectra for fine and coarse CRB as seen in Figure 14. In all spectra, with key diagnostic peaks labelled, these correspond to plagioclase (Na-rich as albite, or Ca-rich as anorthite) or pyroxene (Al-rich as augite, or Mg/Ca-rich as diopside), which are the minerals that comprise the unaltered CRB. These figures were made using profile fitting and peak identification against a powder diffraction database and were background-corrected as outlined in Chapter 2 (Methods). Figure 14 also includes the XRD signature for pure siderite as extracted from the RRUFF Online Database (ID: R050262.1). The XRD employed in this study has a

detection limit of 1 %, which shows that the vast bulk of the CRB used in all experiments here remained unchanged during experimentation.

However, FT-IR enables slightly smaller amounts of materials to be detected, thus this technique was also used upon all solid samples to search for any newly precipitated mineral phases.

3.2.2. Fourier transform infrared spectroscopy

For all FT-IR spectra for the CRB-bearing experiments, as seen in Figure 15, Figure 16, Figure 17, Figure 18, and Figure 19, the CRB remained unchanged and no new precipitates were identified. For reference, the FT-IR spectra for both fine and coarse unreacted CRB can be seen in Figure 20 alongside the type spectra for pure siderite, taken from the RRUFF Online Database. Note the clear absorption bands may be distinguished at 800, 900, and 1100-1500 cm^{-1}, which together are diagnostic of siderite. These absorption bands are demarcated by light-grey columns in all experiments' FT-IR signatures for reference. In all experiments, no absorption troughs correspond to these regions. This suggests that at higher resolution than for XRD, neither siderite nor other new precipitates were formed from experiments using CRB as a substrate.

3.2.3. Scanning electron microscopy

The detection limits of both XRD and FT-IR mean small amounts of material could remain undetected. For these reasons a manual search of the solid samples was conducted via scanning electron microscopy (SEM) for all samples.

Figure 21 shows the fine and coarse CRB before experimentation at varying scales for reference. Note the average particle size for fine (a and b) is ~20 μm across, while for coarse (c and d) it is ~100 μm. The fine material in particular appears highly angular, with low sphericity, and larger particles are actually smaller particles that have clumped together. The coarse material, as observed in (c), is uniformly sized, sub-spherical in shape, and appears moderately sub-angular in comparison to the fine material As seen in a closer resolution in (d), the surface hosts smaller particles that are themselves highly angular, but the coarse CRB itself that attracts these shards

appears sub-angular to sub-rounded. With this morphology in mind, the reacted specimens will now be discussed.

Figure 22 shows SEM images of representative examples of the CRB experiments' solid samples following experimentation, with one fine (left column) and one coarse (right column) for 190414, 19086, 190807, 190808, and 190812. Differing scales are shown from one image to the next, but excepting the differences between the fine and coarse grains (namely scale), all appear similar to each other and unchanged from the unreacted CRB shown in Figure 21. The grains all appear angular (for fine) to sub-angular (for coarse); the fine material appears more commonly to contain smaller fines settled upon it (best exemplified in (a)) while the coarse material more commonly features a single mineral uncoated by finer particles (e.g., (d)). No new mineral growth was observed for any experiments under SEM. In Chapter 3 there were fibrous 'antler-like' growths determined to be a form of amorphous silica, and other precipitates aligned with respect to each other and several hundred nanometres at their longest axis were determined to be an additional growth. However, no such growths were observed here. In Chapter 3 for the fayalite-forsterite experiments, there were signs of erosion or scouring over the course of the experiments, all of which were run for periods shorter than the longer-format experiments discussed within this chapter such as 190414, yet no similar signs of acid scouring or material smoothening were observed in any post-reaction CRB solids. As seen in Figure 22, all solids retain their angularity and surface morphology as seen for the unreacted material in Figure 21. This strongly suggests a lack of significant reaction occurring in the solids of all CRB experiments, which by extension agrees with the XRD and FT-IR data suggesting no new, major phases formed as precipitates in any of the CRB-bearing experiments discussed in this chapter.

The implications of these results will now be discussed in the Discussion section, illustrated with geochemical modelling, and set within the context of the solution data to fully interpret the activity or lack thereof within the CRB experiments described within this chapter.

4. Discussion

Thus far, this chapter has discussed the motivation, set-up, and findings of a series of experiments that react a rock-type common on Mars (basalt: Grotzinger et al,. 2014; McLennan et al., 2019) under water-rich conditions that may have been prevalent earlier in the planet's history. In this section these findings will now be synthesised and contextualised within the wider question of how Fe(II)-carbonates may have formed on Mars.

The solution data for all experiments indicated limited change from initial conditions. This includes variation in pH, Eh, and elemental composition. For the low rock:water ratio experiment (190812) there was the highest concentrations of change: pH climbed the highest of all experiments under low water-rock conditions (1:10), while the highest dissolved concentrations of Fe, Si, and Mg were also reached under these conditions. Experiments begun at pH 4, predictably, experienced both higher relative amounts but also higher non-relative concentrations of pH rise compared to those begun at pH 2, which is expected behaviour given the initial higher pH. Experiments begun at pH 2, also predictably, yielded higher dissolved elemental compositions, which is expected given the more aggressive ability of acidic solutions in mineral dissolution compared to those closer to neutral. This has been observed in other studies chemically modelling carbonate formation on Mars (e.g., Niles et al., 2009).

4.1. Conditions conducive to Fe(II)-carbonate precipitation

Studying the effect of pH and dissolved elemental concentrations, the former more pronounced in pH 4 experiments and the latter in pH 2, highlighted that pH acts as the principal thermodynamic control on solution mineral saturation state compared to the activity of Fe. Specifically, slight increases in pH yielded significantly higher saturation states for the Fe(II)-carbonates siderite and AFC, while significantly higher dissolved Fe concentrations did not measurably affect either Fe(II)-carbonate's saturation state. This observation is best highlighted by Figure 23, which plots Fe^{2+} activity against pH. The light-grey lines represent saturation states for

siderite of, from left to right, 1 (beyond which siderite is thermodynamically expected to precipitate rather than dissolve), 100, and 400, the latter being the estimated critical supersaturation state of Tosca et al. (2018), which is a kinetic concept where a saturation state of 1 is insufficient to cross the nucleation threshold beyond which the atoms that comprise a mineral will begin to order, and in fact a 'critical supersaturation' is required that is in excess of 1. The heavy-grey line is the AFC-line of Jiang and Tosca (2019), as described in Chapter 3, below which AFC remains undersaturated and will not nucleate, and above which AFC is able to nucleate and precipitate. It is worth noting here that in these diagrams, both siderite and AFC remain undersaturated throughout the duration of the experiments — which agrees with all the datapoints of $\Omega_{siderite}$ and Ω_{AFC} calculated in Figure 7 and Table 9, and the AFC saturation states calculated by hand.

What is important to note about Figure 23 is the steepness of these supersaturation lines. Increasing Fe^{2+} activity only minorly advances a datapoint's proximity to these lines, while only a slight increase in pH — surpassing pH 5.5-6.5 depending on Fe^{2+} concentrations — permits an exceedance of the $\Omega_{siderite}$ line of 1. As already known from equilibrium carbonate chemistry, the more basic an environment's pH, the more likely Fe(II)-carbonates are to nucleate and precipitate. This was discussed in Chapter 1 (Introduction) where the Bjerrum plot of Section 2.1 shows the interdependencies of pH and the carbonate system. As the pH of a system increases, so too does the amount of HCO_3^- and CO_3^{2-} (with HCO_3^- declining after ~ pH 8), and these ions are free to react with available Fe^{2+} to form carbonates. By comparison, Fe^{2+} activity is relatively unimportant as an indicator for the likelihood of the formation of Fe(II)-carbonates.

A second factor to take note of in Figure 23 is that there are two diagrams, one per pCO_2 the experiments were conducted under. For 1.0 pCO_2 (right), the saturation state contours are shifted slightly to the left, which translates to lower pH and lower Fe^{2+} required for samples to exceed them. This is discussed in more detail in section 4.5.

4.2. Conditions conducive to the formation of Fe(II)-silicates

In an environment on Mars where Fe^{2+} is available to the system, the formation of Fe(II)-carbonates is not the only, nor the commonest, pathway for mineral formation. The Fe(II)-silicate greenalite ($Fe^{II}_3Si_2O_5(OH)_4$), a phyllosilicate that is the simplest stable form of the ferrous silicates likely to form on Mars, precipitates like siderite under anoxic conditions at circum-neutral pH (Niles et al., 2009; van Berk and Fu, 2011; Tosca et al., 2016). Greenalite has been previously modelled as a key competitor for available Fe^{2+} with carbonates, as well as being the primary alternate mineral to form where pCO_2 is not present in sufficient quantities to form a carbonate, which is defined by Catling (1999) as $\lesssim$0.1 bars. Greenalite has possibly been found on Mars, for example in situ within Gusev Crater (Wang et al., 2006) and possibly within the Nakhlite class of meteorites (Lee and Chatzitheodoridis, 2016), although its detection from orbit is hindered by its lack of unique spectra. This renders it indistinguishable from other Fe-bearing phyllosilicates or carbonates (Ehlmann et al., 2010), hindering further identification. It is also an indicator of reducing conditions, since where more Fe^{3+} is present than Fe^{2+}, ferric silicates such as nontronite may form instead (Chevrier et al., 2007). The concentration of dissolved CO_2 is the key factor in favouring whether siderite or greenalite forms. Siderite forms by the following reaction:

$$Fe^{2+} + CO_2 + H_2O = FeCO_3 + 2H^+ \qquad \text{(eq. 4.2.1.)}$$

while greenalite forms through:

$$3Fe^{2+} + 2SiO_2 + 5H_2O = Fe_2Si_2O_5(OH)_4 + 6H^+ \qquad \text{(eq. 4.2.2.)}$$

Note the lack of CO_2 is the determining factor. A study of the likelihood of greenalite forming within the same system as Fe(II)-carbonates has already been discussed at length by Jiang and Tosca (2019), who show that greenalite remained the dominant Fe(II)-bearing phase in their

experiments despite significant supersaturation with respect to AFC. This relationship is of interest to the experiments discussed within this chapter because the formation of clays as opposed to carbonates has commonly been discussed in the context of the Martian surface (e.g., (Ehlmann et al., 2012; Michalski et al., 2015; Peretyazhko et al., 2016; Gaudin et al., 2018). It has been postulated (Michalski et al., 2015) that the domination of Fe-rich clays on Mars in comparison to Mg-rich resulted in the opposite observation of larger deposits of surface-based Mg-rich carbonates (Ehlmann et al., 2008; Niles et al., 2013), whereby Fe was sequestered more readily into clays such as smectites than a less chemically-favoured formation pathway for carbonates. The observation of Mg-rich carbonates together with Fe-rich smectites in locations likely representing surface formation (Ehlmann et al., 2009; Bishop et al., 2013) is in contrast to the coeval presence of both Fe-carbonates and Fe-clays in the central peak of Leighton Crater (Michalski and Niles, 2010); a location that represents the deep subsurface. Clays are common precipitates from CRB reactants on Earth, including smectites such as nontronite, phyllosilicates such as kaolinite, and oxides such as hematite and other Fe-Ti oxides (Migoń and Lidmar-Bergström, 2002; Hobbs and Parrish, 2016; Baker and Neill, 2017); as it is possible the CRB-based experiments here could have formed clays, this investigation into the formation of greenalite — one of the simplest phyllosilicates capable of forming — is a means of testing simple clay formation under Mars-like conditions.

Figure 24**,** a solubility diagram for the Fe^{2+}-SiO_2-H_2O system, encompasses the dominant controls on greenalite, which are pH, the activity of SiO_2, and the activity of Fe^{2+}. In Figure 24, the apparent solubility of greenalite, as estimated by Tosca et al. (2016), is represented by the heavy grey line, beyond which greenalite is expected to precipitate. While for the fayalite-forsterite equivalent graph displayed in Chapter 3 there were multiple ascensions beyond this limit, for the CRB experiments on Figure 24, only those run under low rock:water ratios (marked by crosses) come close but do not exceed it. This suggests that greenalite did not precipitate in any of the experiments discussed in this chapter, which agrees with the solid sample analyses that do not suggest the formation of new precipitates in any samples. Additionally, amorphous silica

precipitation would have been indicated by any datapoints exceeding log $a_{SiO2(aq)}$ −2.2, which is to the right of both graphs and is not displayed because no datapoints approached this level of dissolved Si. This also suggests a lack of precipitated Si in solution.

Similarly to siderite, greenalite appears from Figure 24 to have remained distinctly undersaturated throughout all the CRB-bearing experiments. The lack of solution concentrations for Al, Na, and Ca has hindered a more comprehensive study of the formation of clay minerals, since these are common elemental constituents of many clays; assertive observations regarding the ability of clays to form during these CRB-based experiments cannot be made. The lack of greenalite saturation in Figure 24 could suggest that on Mars under the conditions explored here, the silicate greenalite would have been unlikely to form in significant quantities. However, this remains a hypothesis and must be taken as highly tenuous, given the lack of a complete elemental dataset from which to draw these conclusions. Considering the high likelihood of forming smectitic clays from CRB (Migoń and Lidmar-Bergström, 2002; Hobbs and Totman Parrish, 2016; Baker and Neill, 2017), it is plausible that with a more complete dataset, alternative conclusions would be reached.

4.3. Two hypotheses for variations in dissolution rate as a function of mineralogy

Neither Fe(II)-carbonates nor Fe(II)-silicates, nor any known mineral, precipitated over the course of all the CRB experiments documented in this chapter. This follows from data regarding the dissolution of the CRB, which also does not suggest significant dissolution of material from which new material could form.

There could be several reasons for the relative lack of reactivity in the CRB series when compared to the fayalite and forsterite experiments of Chapter 3, where up to 30 mmol/kg of Fe was released to solution (45 mmol/kg was seen but appears likely to be an anomaly as no other data point in the corresponding experiment, 180829, display such high concentrations) in comparison to the 0.4 mmol/kg maximum for the CRB-bearing experiments of this chapter.

Firstly, compared to the fayalite-forsterite series, the CRB used here appears to be relatively unreactive in comparison to olivine. An immediate caveat of such a statement is that there is not a complete picture of elemental composition in solution from which to draw inferences about dissolution or reactivity. Na, Ca, and/or K are several species known to have been abundant in the CRB studied in this thesis because the albite and anorthite that dominate its composition feature these elements, and the release rates of these elements to solution are wholly unknown here. While the composition of basalt across the Martian surface varies slightly (the reader is directed again to Table 1), the CRB as chosen for these experiments was deemed the most representative type of basalt based on its similar composition to those several basalts analysed across or from Mars by rovers or within meteorites, and is considered here to be broadly representative of a mineralogy common across the Martian surface. Multiple studies have investigated the dissolution of the basaltic components plagioclase and pyroxene (e.g., (Wollast and Chou, 1992; Oelkers and Schott, 1995). For albite, which dominated the CRB composition in this study, (Chen and El Goresy (2000) found the stoichiometric dissolution of albite occurred at 90 °C after several thousand hours (see also Nesbitt and Skinner, 2001), while at pH 2, (Kobayashi et al. (2001) found only the formation of reaction surfaces; these studies, along with much earlier research (Goldich, 1938) show that the dissolution of plagioclase is a slower process relative to the dissolution of other silicate minerals. Nesbitt and Skinner (2001) found that during the first stage of dissolution, Al and Na migrate to parts of the solid-solution interface low in their concentrations, releasing them into solution over a few hours to several days, a process occurring at faster rates with increasing temperature (Goosens et al., 1989). A variant of this process was observed solely with Al for anorthite (Oelkers and Schott, 1995), with anorthite comprising $\lesssim$5 % of the CRB. For albite, the reaction then proceeds far more slowly for the remaining mineral surface as the leached layer inhibits further dissolution (Nugent et al., 1998). Many researchers (e.g., Suzuki et al., 1996; Jordan et al., 1999; Nesbitt and Skinner, 2001) report this process as being accompanied by etch pits and steps marking sites of dissolution, or otherwise a 'roughening of the

surface' (Higgins, 1998) or 'non-uniform etching' (Inskeep et al., 1991). In addition, an amorphous gel likely of precipitated silica (Goosens et al., 1989) is sometimes observed at the leached site.

Such morphologic changes were not observed for any of the CRB solids analysed within this chapter. This suggests that the Na/Al leaching that marks the inception of dissolution had not begun for the material discussed here. Given the timescales often invoked for the inception of albite weathering (Nugent et al., 1998, reporting one month to 3.5 years), it is plausible the CRB experiments were not left to run for sufficiently lengthy periods of time for reaction activity to reach notable concentrations. Given the diverse composition of the basalt, any and all elements are important for understanding the leaching process during dissolution, but the Na and Al removal appears to be a common and useful indicator.

In addition to studies on albite, for basalt itself there are numerous studies both modelled and experimental detailing its dissolution (e.g., (Thorseth et al., 1992; Stevens and McKinley, 2000; Stefansson and Gislason, 2001). Common alteration products at low temperature typically include Mg-Fe smectites, amorphous Al hydroxide/ferrihydrite, and Al/Si minerals such as allophane or imogolite, while at higher temperatures or further along in the reaction progress, the reacted mineralogy comprises Ca/Na zeolites, Fe/Mg-rich clays, and calcite (e.g., Gislason and Arnórsson, 1993; Neuhoff, 1999; Stefansson and Gislason, 2001). The dissolution process for basaltic glass, which comprises roughly half the composition of CRB (Schaef et al., 2010), was summarised by (Oelkers and Gislason (2001) as (1) the rapid removal of univalent and divalent cations from the near surface; (2) Al-releasing exchange reactions between H^+ and Al in the glass structure itself; and (3) the slow detachment of partially liberated Si. These are molecular processes that could not be observed with the techniques deployed within this study, however, and the limited types of elements studied in solution renders confident assertions of a lack of divalent cations in solution as impossible to state. Specifically to Fe(II)-carbonates, carbonate formation has received particular interest in basaltic provinces for carbon capture storage (e.g., McGrail et al., 2006; Gislason et al., 2010) but even under high temperatures and pressures, formation is sparse and

tends not to be Fe(II)-bearing (e.g., Schaef et al., 2011), with CRB in particular showing poor Fe(II)-carbonatisation potential when under pure CO_2 and anoxic conditions (Schaef et al., 2010).

Gysi and Stefánsson (2011) numerically simulated CO_2 sequestration within basaltic glass at low temperature (25-90 °C) and high pressure relative to this thesis' work (30 bars). At 25 °C, pH was found to increase with reaction progress, as it does in this research, levelling off between pH 7.5 and 8. Additionally, in a follow-up study to their research, (Gysi and Stefánsson, 2012) experimentally reproduced their models at 40 °C and produced Ca-Mg-Fe-carbonates (predominantly calcite) and -clays following a sharp rise in pH from ~4.5 to 6. Their experiments ran for up to 6,420 hours (maximum in this study: 2,040). This pH rise and carbonate production was not observed in the experiments described here. While this could be a function of the lower concentrations of CO_2 employed, the fact that natural waters in contact with basaltic systems also commonly have similar pH (e.g., Gislason et al., 1996; Stefansson and Gislason, 2001; Neal and Stanger, 1983; Miller et al., 2016) suggests the experiments conducted here were not left to run for sufficient times to reflect the Martian subsurface/surface as expected during its earlier history. This earlier history was water-rich throughout the Noachian and perhaps as late as well into the Hesperian (Davis et al., 2019; Kite et al., 2019), which translates into a system where water may have been an active component for several 10^6 years, potentially as long as 10^7 years (using the Hartmann and Neukum, 2001, cratering chronology). However, these are not experimentally accessible timescales, and the experiments described in this chapter and the previous one show an initial phase of reactivity followed by substantial decay, which suggests that waiting longer would not necessarily produce different results.

Another factor to consider besides time is that of rock:waterrock:water ratio and other hydrological factors, such as fluid flow-through or the replenishment of fluids. Under natural systems, meteoric water flushes fresh species into solution in systems such as shallow aquifers, lakes, and other near-surface aqueous environments. This has the effect of removing advanced dissolved material from solution and concentrating them in certain settings, altering solution

chemistry and enabling novel reactions to occur. The experiments in this thesis all better simulate systems said to be 'closed' as opposed to 'open' like these, whereby once a species has been lost it is unable to be replenished. Closed systems are better represented by deep aquifers or ice-sealed lakes, and it could be that this lack of replenishment of further species to solution is a hindrance that directs the experiments from behaving like near-surface systems.

The relatively-slow dissolution rates of CRB in comparison to fayalite and forsterite can be explained by summarising surface area-normalised dissolution rates as a function of pH for major silicate minerals and glasses, whereby the dissolution rate of basaltic glass is a partial function of its SiO_2 concentration (Gislason and Oelkers, 2003) and forms one of the most significant processes of dissolution during its early phases (e.g., Humphris and Thompson, 1978; Lonker et al., 1993). Seen experimentally by Gíslason and Oelkers (2003), dissolution rates for basalt decrease significantly with increasing pH at acid conditions, whereby dissolution rates are minimised at near-neutral pH, then increase slower with increasing pH at basic conditions. This pH-dependent dissolution results in a strong decrease in overall dissolution rate as experiments such as the CRB-bearing types of this chapter progress, where pH was seen to slightly increase from acidic pH over their course.

To understand what factors promote carbonate formation, while taking into account the minerals present as initial substrates, alongside their characteristics such as dissolution rate, surface area, initial pH etc, a series of models were set up in GWB. These will now be discussed, and their data explored in a geochemical framework to elucidate what important components comprise the CRB and carbonate system in the absence of complete ICP-MS data to assist in the interpretation of experimental data.

4.4. Modelled conditions conductive to the formation of Fe(II)-carbonates and -silicates

As described earlier in the methods section, the geochemical modelling software GWB was employed to more broadly examine which conditions are most conducive to raising the saturation state of carbonates, and therefore their likelihood of forming.

Four models were run: (1) an open system with respect to CO_2 with high rock:water ratio (1:500), which simulates a lacustrine environment, for example, in contact with the atmosphere; (2) an open system with respect to CO_2 with low rock:water ratio (1:1), which simulates small amounts of water in contact with an atmosphere, e.g., the inter-dune playa environment that existed during the Noachian-Hesperian boundary in Meridiani Planum (Squyres et al., 2004); (3) a closed system with respect to CO_2 with high rock:water ratio (1:500), which simulates a water-rich environment out of contact with the atmosphere, e.g., an ice-covered lake; and (4) a closed system with respect to CO_2 with low rock:water ratio (1:1), which simulates a subsurface aquifer out of contact with the atmosphere. When run, models (1) and (3) produced almost identical results, thus are combined as open and closed high rock:water ratio.

What was consistently seen when the models were run was a propensity for the conditions promoting heightened Fe(II)-carbonate supersaturation to coincide with closed system, low rock:water ratio conditions. Seen in Figure 25, pH climbs to more than 8.5 for this scenario, in comparison to maximum 6.5 for low rock:water ratio but with a constant flux of CO_2; seen in Figure 26, Fe^{2+} activity climbs higher for the open system at low rock:water ratio than for the closed. Most telling are the concentrations of carbonate saturation: in Figure 27, after two years, AFC, calcite, magnesite, and siderite all become supersaturated for both low water-rock models, but consistently reach the highest $\Omega_{siderite}$ concentrations for low water rock within a closed system. Seen in Figure 28, the phyllosilicate greenalite, and the precursor for magnetite, $Fe(OH)_2$, only exceed the saturation point over the model's course for the closed system low rock:water ratio scenario.

An interesting observation worthy of closer inspection is the fact that, when seen in Figure 23, increasing the concentrations of dissolved CO_2 present in the system lowers the thresholds of pH and Fe^{2+} for siderite and/or AFC to precipitate. However, in practice this shift is likely negligible in effect. From this it may be derived that doubling the CO_2 available within a system from 0.5 bars to 1.0 bar, at least for the CRB substrate within this chapter, has little measurable effect on the likelihood of Fe(II)-carbonates to precipitate. While CO_2 itself is essential for the formation of any carbonate, which by definition is incorporated into its structure, Figure 23 (siderite saturation) suggests that this does not need to be significant in quantity, and that a system characterised by high concentrations of CO_2 is only slightly more likely to favour the formation of carbonates than one with lower CO_2. This agrees with the geochemical modelling study of Catling (1999), which found only ~0.1 bar pCO_2 was required for the precipitation of siderite under Mars-like conditions. Overall these data suggest the pCO_2 of a system is not the most dominant factor controlling carbonate formation under the environments studied here. This is, however, at odds with the conclusions within Chapter 3 (fayalite and forsterite), where pCO_2 was deemed the most significant parameter controlling Fe(II)-carbonate saturation on the basis of its control over dissolved inorganic carbon (DIC) concentrations in a solution and their interaction with the total alkalinity (TA) of the system. To discuss this, a DIC-TA diagram for a modelled reconstruction of the CRB experiments will now be explored.

4.5. Dissolved inorganic carbon and total alkalinity as constraints on the CO_2 system

As described in Chapter 1 section 6.2, differing systems may be plotted together in terms of their total alkalinity and DIC and estimated against $\Omega_{siderite}$ and Ω_{AFC}, which is a useful mechanism to understand which of the four modelled systems described above are most conducive to Fe(II)-carbonate formation. As DIC remains fixed for systems closed with respect to CO_2, e.g., aquifer environments or ice-covered lakes, as seen in Figure 29 (a) and (b), these systems produce a vertical line that, accordingly, surpasses AFC and siderite saturation thresholds more effectively than those

of open systems, where a rise in both DIC and total alkalinity produces diagonal trends that tend to run sub-parallel to supersaturation thresholds corresponding to nucleation. DIC increases with TA in the open systems because an increase in TA promotes CO_2 absorption through equilibrium carbonate chemistry. This effect is present for both low pCO_2 (left column at 0.1 bar) and high (right column at 1.0 bar). However, as the supersaturation states for siderite and AFC are steeper for 1.0 bar, therefore more readily exceeded even at low DIC, higher pCO_2 is demonstrably more conducive to the formation of both AFC and siderite. This is in comparison to experimental results obtained at 0.5 and 1.0 bar pCO_2, where the difference between 0.5 and 1.0 bar did not yield measurable change; between 0.1 and 1.0 bar, this difference becomes more important to Fe(II)-carbonate formation. It is also interesting to note that in discussing oxidation reduction potential in section 3.1.3, it was observed that increased dissolved CO_2 was possibly releasing sufficient acidity to overpower the ability of the solution chemistry to evolve to more basic pH; this is reflected in (c) and (d) of Figure 29, where pH for 1.0 bar CO_2 fails to reach the higher concentrations for 0.1 bar CO_2.

Figure 29 (c) and (d) mark pH trends over the four modelled pathways at high and low pCO_2. What is interesting to note is that the most elevated pH reached in these models, which is over pH 9 and 8 respectively for 0.1 and 1.0 bar systems, are reached under closed system, low rock:water ratio conditions. As seen experimentally and with the previous section's GWB models, alkaline pH is required for the formation of Fe(II)-carbonates, and higher pH environments on Earth as well as Mars appear to favour authigenic siderite formation (whether measured *in situ*, e.g., Neal and Stanger, 1983, or inferred from depth and olivine preservation, e.g., Michalski and Niles, 2010). Hence, while high rock:water ratio environments under closed systems with respect to CO_2 do enable both the supersaturation of AFC and siderite, the high pH achieved at low rock:water ratio under closed conditions appears to enable the coincidence of conditions most conducive to the formation of Fe(II)-carbonates. This is also seen clearly in (b), where at 1.0 bar pCO_2, $\Omega_{siderite}$ of 400 is exceeded, the only model where this condition is achieved. $\Omega_{siderite}$ 400 was

the estimated supersaturation state for siderite formation experimentally determined by Tosca et al. (2018). Low rock:water ratio, closed pCO_2 systems — such as aquifers in intermittent contact with CO_2-charged meteoric water — therefore appear to represent the type of environment where Fe(II)-carbonates may be best developed under anoxic conditions.

These results are consistent with the expectation, discussed at length earlier, that changes in alkalinity and/or DIC concentration will fundamentally control carbonate mineral saturation state (Zeebe and Wolf-Gladrow, 2001), whereby increases in in TA but fixed DIC promote carbonate precipitation. It is also in good agreement with the experimental and modelled results discussed in Chapter 3 regarding mono- or duo-mineralic systems, where plots featuring DIC and alkalinity for fayalite and forsterite yielded trends alike to those of Figure 29: where DIC was able to evolve further, $\Omega_{siderite}$ was hindered from reaching heightened states of saturation, while under conditions where this was not a constraint, the opposite was seen. This simulates CO_2-limited and CO_2-replenished environments, the former such as an aquifer or ice-covered lake severed from contact with atmospheric fluids, and the latter an equivalent body of water in frequent exchange with meteoric waters and fluid/species renewal.

Where the significant results of this chapter are found is in the vast difference in behaviour between the CRB-bearing experiments of this chapter, and the fayalite ± forsterite-bearing ones of Chapter 3. In Chapter 3, while no definitive Fe(II)-carbonate was identified, $\Omega_{siderite}$ reached supersaturation indicative of conditions conducive to its formation; no such saturation states were found in this chapter pertaining to CRB experiments. This appears to be a function of dissolution and reaction rate, alongside changes in the total alkalinity (TA) of a solution, as described in Figure 29.

4.6. The role of calcium

Finally, a note from the perspective of terrestrial weathering is a useful point of discussion given the high plagioclase component of Martian basalt. On Earth, plagioclase is the dominant mineral

that weather's in the upper crust, and its high Ca content releases significant amounts of this element for use in carbonate formation. Anorthite ($CaAl_2Si_2O_8$) is the Ca-rich endmember of plagioclase, while albite ($NAl_2Si_2O_8$) is the Na-rich opposite member. At moderately high temperatures (100 ºC), calcite is one of the first minerals to precipitate during the dissolution of anorthite-rich plagioclase (Al-hydroxide being the first; Munz et al., 2012), and multiple studies have found that dissolution rate increases with increasing anorthite content of the plagioclase (e.g. Stillings and Brantley, 1995). This composition is the opposite of the albite-dominated plagioclase used in this chapter, and could be a reason behind the slow dissolution and reaction rates seen here. Other experiments, such as the work of Hangx and Spiers (2009) at 200-300 ºC, showed that calcite was extremely difficult to produce from both albite and plagioclase, and that clays such as kaolinite and illite were more likely to form prior to carbonates, potentially sequestering the available Ca and preventing Ca-carbonate formation.

For the purpose of this study, it is important to note that the plagioclase composition on Mars is ~An_{60} on average, with significant variation (e.g., Taylor and McLennan, 2009; Milam et al., 2010), with anorthite being the more reactive plagioclase endmember. While it was beyond the scope of this study to run additional experiments solely investigating Ca-carbonate formation, and unfortunate that the full elemental analysis for this chapter was lost such that Ca studies could not be conducted, future work investigating the importance of Ca-carbonates on Mars would be an important addition to our understanding of basaltic weathering.

4.7. Modelling summary

The modelled CRB simulant dissolved and reacted over the course of the model, and in comparison to the experiments did yield supersaturated states for, in descending order of saturation state, AFC, siderite, magnesite, and calcite. This suggests that the lack of reactivity observed in this chapter was due to insufficient reaction times, as opposed to the inability of CRB to produce carbonates under up to 1.0 bar CO_2.

While the experiments of this chapter did not yield measurable precipitation in any form over their course, the higher saturation state for Fe(II)-carbonates for comparable low rock:water ratio, closed system experiments — the 1:10 rock:water ratio experiment 190812 — are in agreement with these modelled results that hold closed system, low water-rock environments as most effective for enabling carbonate supersaturation. The closed system matches the finite concentrations of CO_2 used in all experiments, which was added as sodium bicarbonate crystals and not as a steady influx of the gas within the glove box. An example of a closed system, low water-rock environment is the deep Martian subsurface: in the pore spaces between grains, small amounts of water are free to interact with a relatively large surface area of rock. Fe^{2+} concentrations from dissolved substrate rock are concentrated by the low volume of water, and alkalinity is able to increase owing to this water's interaction with the mafic geology. CO_2 enters the system by intermittent percolation through rock pore spaces as CO_2-charged meteoric water. As HCO_3^- and CO_3^{2-} ions, this CO_2 is able to react with the free Fe^{2+} (alongside Mg^{2+}, Ca^{2+}, and others) to form the AFC and siderite that were modelled to reach heightened states of supersaturation.

This research has posited slow dissolution rates as one possible hindrance to carbonate and clay formation on Mars, where both are limited, but given that at selected locations both these types of minerals can be found in relative abundance, some additional factor must be at work. This alternative or additional factor, tentatively suggested given the limited solution chemistry data that has so hindered analyses, could be that there is a control on the reactivity of silicate-forming minerals through initial substrate composition. A trend known in the wider literature is that plagioclase and glass-rich substrates tend to exhibit low dissolution rates, while olivine-rich substrates tend to exhibit much higher dissolution rates, which has indeed been replicated between this chapter and the olivine-bearing experiments of Chapter 3. One outcome of this observation could be that clay minerals are more likely to be formed from such glasses and plagioclases, while carbonates are more likely from the olivines. In fact, such a trend has been suggested on Mars: the Nili Fossae region where Mars' most widespread and densest carbonates are found is the most

olivine-rich on the planet (Ehlmann et al., 2008; Edwards and Ehlmann, 2015; Brown et al., 2020; Mandon et al., 2020) and the trend of olivine-carbonate has also been observed elsewhere (e.g., Wray et al., 2016). The rarity of clays and carbonates to be found contemporaneously also lends weight to this hypothesis (Ehlmann et al., 2012; Michalski et al., 2015), suggesting differing host mineralogy results in different secondary mineral formation under similarly aqueous conditions.

5. Conclusions

The leading rationale behind this thesis is to better understand the environmental conditions most conductive to the formation of carbonates in Mars' early history, particularly Fe(II)-carbonates. While this thesis' first results chapter (Chapter 3) discussed the effect of introducing simple, mono-minerallic material into solution (fayalite, fayalite and forsterite), this chapter specifically investigated the effect of introducing relatively complex material better simulating the Martian crust. Basalt, comprised of types of pyroxene and plagioclase, is likely the most common igneous rock found on Mars (e.g., McLennan et al., 2019), thus was selected as an important experimental variable.

What was discovered in this chapter over a series of 36 experiments where CRB was used as a reactant was that CRB did not fully dissolve over the course of the experiments, and, accordingly, no new minerals were detected as having formed in any measurable amounts. The CRB experiments were the same set-up as that run for the fayalite-forsterite experiments of Chapter 3, which did yield limited $\Omega_{siderite}$ concentrations over their course. The CRB discussed in this chapter, however, remained pristine when examined via SEM, free of dissolution pits, etching, or new growth, and XRD and FT-IR detected only CRB present in all solid masses. The solution chemistry over the course of the experiments by all measures showed little change from the starting conditions: pH, Eh, dissolved elemental concentrations, and the corresponding saturation states of relevant minerals, all remained similar to their starting concentrations with negligible activity.

When modelled to simulate CRB-bearing conditions that would be conducive to the formation of Fe(II)-carbonates, low water-rock simulations (1:1) yielded the highest saturation states for Fe(II)-carbonates in comparison with high (1:500), which is in agreement with the modelling of Chapter 3 that also observed this. The implication from such a result is that subsurface environments on Mars, where water and rock are present in near-equal measures as water flows through rock or grain pore space, will enable conditions better conducive to the formation of Fe(II)-carbonates through a combination of heightened pH, more concentrated concentrations of Fe^{2+} and CO_2, and where a system is open with respect to CO_2, cut off from constant replenishment in an open atmosphere, permit the rise of pH to overwhelm the inherent acidity introduced by CO_2. Reaction rates have also been determined in this chapter to be an important factor in the ability of both initial substrate dissolution and in the according subsequent precipitation. The CRB used in this chapter had a high silica content with a >45 % glass component (Schaef et al., 2010). While not all volcanic glasses are the same composition, and certainly interplanetary comparison must proceed with caution, glass is likely to be a common component of the Martian basaltic landscape: Mars' surface bears the scars of countless impact cratering events that will have produced shocked material and glassy substances such as tektites (Hildebrand et al., 1991), and this additional silica component is known to be in some cases very reactive: Nesbitt and Wilson (1992) observed that basaltic glass, alongside olivine, are the first phases to be altered during terrestrial and seafloor weathering. Despite its high glassy component, CRB remained unreactive relative to the fayalite-forsterite experiments of Chapter 3 despite olivine being known to be similar in levels of reactivity to glass with regards to common basaltic components (Nesbitt and Wilson, 1992). In the case of the experiments of Chapter 3, this olivine comprised the entire reacted substrate, as opposed to the ≤45 % glass component within the CRB used here in Chapter 4. It is worth noting that the dissolution rate of glasses varies strongly with Si content and thus high rates of reactivity are not a ubiquitous trait of glasses. This enhanced reactivity of some glasses has been attributed to a higher solubility and dissolution rate of the

glasses in comparison to crystalline rock (e.g., Gislason and Arnórsson, 1993), as well as its accordingly higher surface area (Sigurdsson and Ingimarsson, 1990), but the glass associated with CRB is a residual interstitial phase and thus high in Si content, rendering it less reactive than a pure volcanic glass. It is possible that the slow dissolution and reactivity rates observed in this chapter resulted from the nature of the CRB itself, whereby this less reactive glassy phase dominated the overall mineralogy of the samples deployed. The remaining material used in these experiments was crystalline basalt rock powder, which has a slower dissolution rate that may have rendered the reactivity of the CRB over the timescales observed here to be only minor.

This chapter suggests, as has been well documented, a clear influence of mineralogy on dissolution rate, which, in comparison to the relatively rapid dissolution rate of fayalite (e.g., (Wogelius and Walther, 1992; Daval et al., 2009, 2010), has been well documented as slow for CRB (Schaef and McGrail, 2009). The lack of observable reaction over timescales and conditions identical to those employed in Chapter 3 is likewise interesting, and the two together could suggest that this mineralogy on Mars is less conducive to the formation of new minerals — carbonates amongst others, as no products were formed in any CRB experiments. This more complex mineralogy has revealed more about of the role composition plays in influencing dissolution rate and reaction kinetics, and suggests that the basalt-dominated crust of the Martian surface could have been slow to react with carbonated fluids where such fluids were transient and, instead of carbonates, may have formed clays. Carbonates, on the other hand, could have been confined to more olivine-rich regions where higher dissolution rates maintained reducing, neutral-to-basic solution chemistries where the combination of high dissolved Fe^{2+}, high pCO_2, and high pH could combine to enable sufficient Fe(II)-carbonate saturation states to produce precipitates.

Overall, what this chapter has achieved is a more realistic view of the Martian surface and near-surface, where complex suites of interacting minerals within a host rock can be observed to interact with groundwater in a manner better representing the planet's geology. In comparison to the fayalite ± forsterite experiments of Chapter 3, here in Chapter 4 the increased complexity from

mono-minerallic powder to CRB revealed a corresponding step-ward increase in the complexity of element release to solution, which accordingly negatively influenced the ability of a solution to enable heightened saturation states of carbonates of any form. The key differences between the fayalite ± forsterite experiments of Chapter 3 and those bearing CRB of Chapter 4 are:

1) A lower dissolution rate for CRB than for fayalite and forsterite, corresponding to less free elemental material to engage in new reactions
2) Lower reaction activity for CRB than for fayalite and forsterite, owing to a reduced propensity for CRB to dissolve and react
3) No observable precipitation for CRB-bearing experiments in comparison to fayalite and forsterite, owing to both a lower dissolution rate and lower reaction activity, whereby CRB remained almost entirely unaltered despite in some cases two months of exposure to an aggressive sulphuric acid.

The most favourable environment for Fe(II)-carbonate formation appears to be the near-surface, where the system is closed with respect to CO_2 and where rock:water ratio is low. In such a subsurface environment, sheltered from the increasingly cool, irradiating, arid surface, temperatures may have risen higher than upon the surface: volcanism- or impact-related hydrothermalism, alongside a declining geothermal gradient, may individually or together produced conditions where temperatures were able to reach higher than the 25 ºC explored here. This consideration motivates the third and final research investigation of this thesis: how carbonates form under 75 ºC, from solutions bearing fayalite-forsterite or CRB, in comparison to at lower temperature.

6. Figures

	CRB	Gale Crater	Adirondack (Gusev Crater)	Shergotty	Nakhla	ALH 84001
SiO_2	47.09	51.4	45.4	51.36	48.24	50.30
Al_2O_3	12.35	10.7	10.9	7.06	1.45	1.38
FeO	17.65	17.7	15.2	19.41	20.64	18.40
MgO	4.38	11.8	12.8	9.28	12.47	26.10
CaO	8.84	5.6	7.49	10.00	15.08	1.77
Na_2O	2.43	3.0	2.79	1.29	0.42	0.132
K_2O	1.39	0.6	0.06	0.16	0.10	0.015
Ti_2O	3.65	1.2	0.46	0.87	0.29	0.220
P_2O_5	1.58	n/a	0.52	0.80	0.12	n/a
MnO	0.32	n/a	0.41	0.53	0.54	0.455
Cr_2O_3	n/a	n/a	0.60	0.20	0.42	1.19
Total	99.68	101.9	100.0	100.96	99.77	100.00

Table 1: Table comparing the composition in wt. % of one CRB flow (the Ice Harbor Dam 2 flow) as analysed by Wright et al. (1973), to the Adirondack class of igneous rocks in Gusev Crater (McSween et al., 2004), to basalts within Gale Crater (Edwards et al., 2017), and to three types of Martian meteorites. Data from Shergotty from McSween et al. (1985); Nakhla from McCarthy et al. (1974); ALH 84001 from Gleason et al. (1997). N/A: not analysed.

Experiment name	Number of sub-experiments	Duration (days)	Initial pH used	CO_2 used	Rock:water ratio	Material used
190414	8	85	2, 4	0.5, 1.0	1:500	Fine and coarse CRB
190418	8	85	2, 4	1.0	1:1, 1:10	Fine and coarse CRB
190806	4	10	2, 4	0	1:500	Fine and coarse CRB
190807	4	10	2, 4	0.5	1:500	Fine and coarse CRB
190808	4	10	2, 4	1.0	1:500	Fine and coarse CRB
190812	8	72	2, 4	1.0	1:1, 1:10	Fine and coarse CRB

Table 2: The parameters of each of the 36 sub-experiments used in the CRB section of this thesis.

Composition	Average wt. % in oxide
Na_2O	2.80
MgO	4.15
Al_2O_3	14.635
SiO_2	52.795
P_2O_5	0.405
SO_3	0.105
Cl^-	0.01
K_2O	0.95
CaO	8.125
TiO_2	2.095
V_2O_5	0.06
MnO	0.195
Fe_2O_3	13.52
ZnO	0.02
SrO	0.04
ZrO_2	0.025
BaO	0.055
Total	**99.79** (excluding values in red)

Table 3: The average composition, including glass, of multiple sections of CRB used by Schaef and McGrail (2009). Average taken from combined flow top and flow interior data. Data coloured red were unable to be inputted into the CIPW normative mineralogy calculation table.

Mineral	Wt.%	% added in GWB
Plagioclase feldspar	47.86	50.49
Quartz	13.75	23.09
Hematite (added as fayalite)	13.52	14.26
Hypersthene (added as quartz)	8.14	0
Orthoclase feldspar	5.61	5.91
Diopside	4.74	5.00
Titanite (not added)	4.60	0
Apatite (added as hydroxyapatite)	0.95	1.00
Ilmenite (not added)	0.43	0
Na_2SO_4 (added as thenardite)	0.20	0.21
Halite	0.02	0.02
Total	**99.82**	**99.98**

Table 4: The average mineral composition, including glass, of multiple sections of CRB used by Schaef and McGrail (2009). Average taken from combined flow top and flow interior data. Minerals were calculated by normalising the oxide composition based on data from Schaef and McGrail (2009) and inputting these into a CIPW normative mineralogy calculation by Kurt Hollacher.

Component	Value	Unit
H_2O	1	Free kg
H^+	3	
Fe^{2+}	0.1	mmol/kg
$SiO_{2(aq)}$	0.1	mmol/kg
Mg^{2+}	0.1	mmol/kg
Na^+	0.1	mmol/kg
Al^{3+}	0.1	mmol/kg
Ca^{2+}	0.1	mmol/kg
Mn^{2+}	0.1	mmol/kg
K^+	0.1	mmol/kg
HPO_4^{2-}	0.1	mmol/kg
Cl^-	0.1	mmol/kg
SO_4^{2-}	0.1	mmol/kg
$CO_{2(g)} \rightarrow HCO_3^-$	1	Fugacity
Temp	25	°C

Table 5: The components of the geochemical model seeking to reproduce conditions over a longer period of time than the experiments could be run.

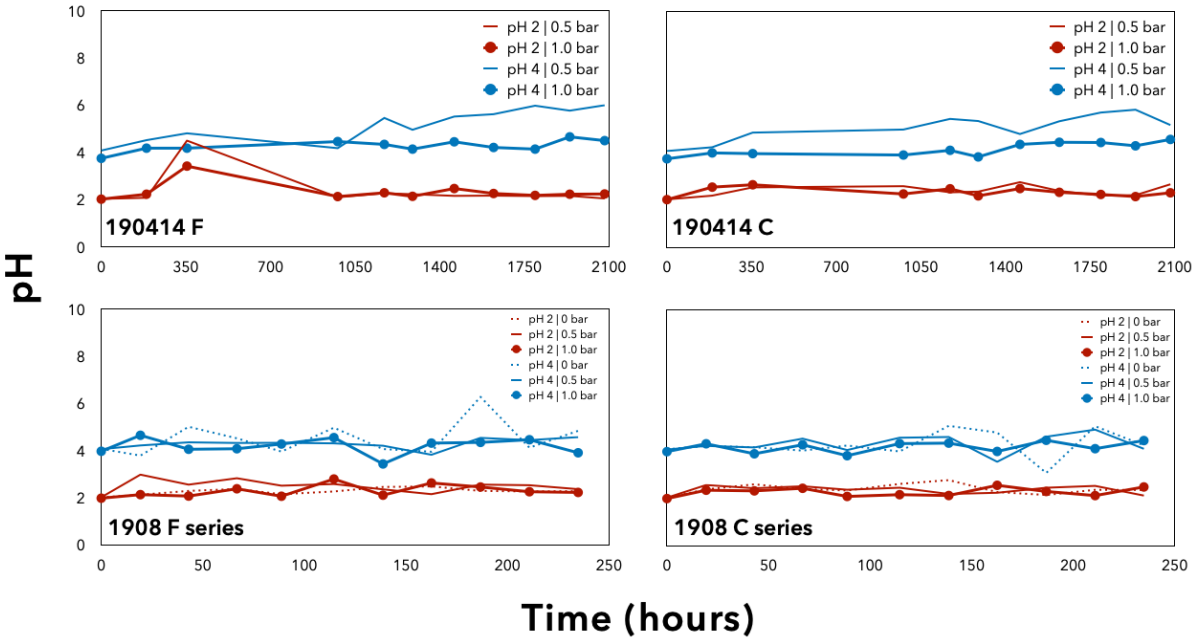


Figure 1: All CRB high rock:water ratio experiments' pH, where experiments are divided into fine (F) or coarse (C) material, and the 1908 series (190806 at 0 bar CO_2, 190807 at 0.5 bar, and 190808 at 1.0 bar) are displayed on the same graph. A legend for each graph displays which lines correspond to which experiments.

Experiment name	Initial pH	Initial ORP	Final pH	Final ORP
CRB F pH 2 1:1	2.055	369.2	Not taken	Not taken
CRB F pH 2 1:10	2.055	369.2	4.368	308.5
CRB F pH 4 1:1	3.998	545.0	Not taken	Not taken
CRB F pH 4 1:10	3.998	545.0	6.324	156.6
CRB C pH 2 1:1	2.055	369.2	Not taken	Not taken
CRB C pH 2 1:10	2.055	369.2	3.675	293.1
CRB C pH 4 1:1	3.998	545.0	Not taken	Not taken
CRB C pH 4 1:10	3.998	545.0	6.681	168.5

Table 6: The initial and final pH and Eh for the low rock:water ratio experiment 190812. The final pH and ORP for 1:1 rock:water ratio experiments could not be extracted owing to the total volume of fluid available (1 mL). ORP is measured in mV.

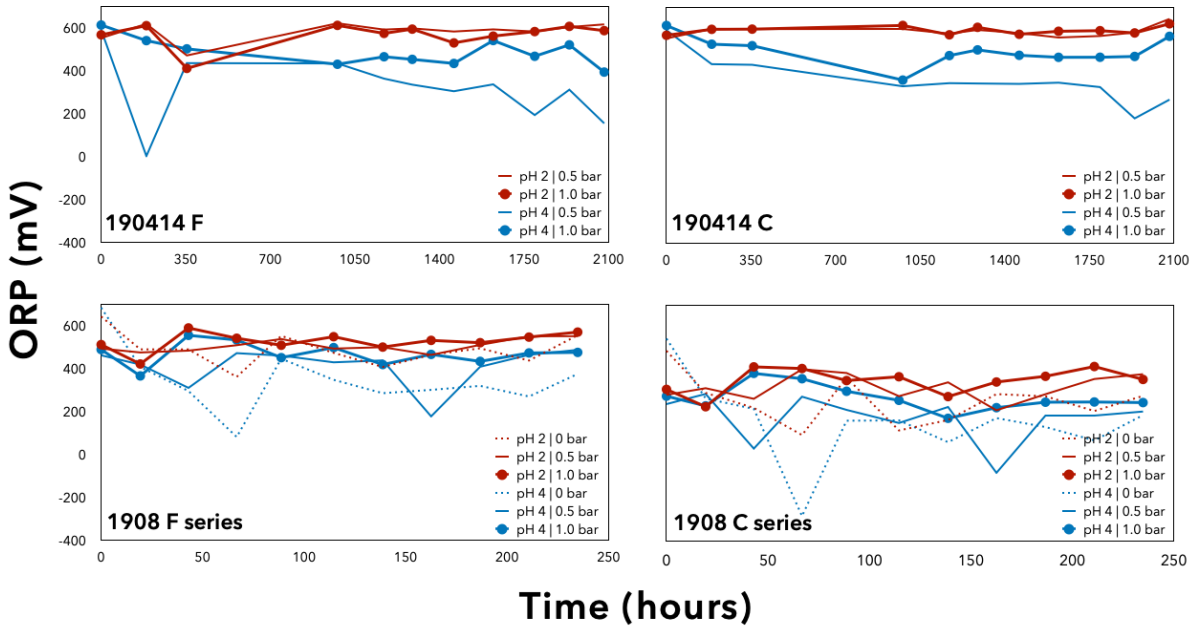


Figure 2: All CRB high rock:water ratio experiments' oxidation-reduction potential (ORP), where experiments are divided into fine (F) or coarse (C) material, and the 1908 series (190806 at 0 bar CO_2, 190807 at 0.5 bar, and 190808 at 1.0 bar) are displayed on the same graph. A legend for each graph displays which lines correspond to which experiments.

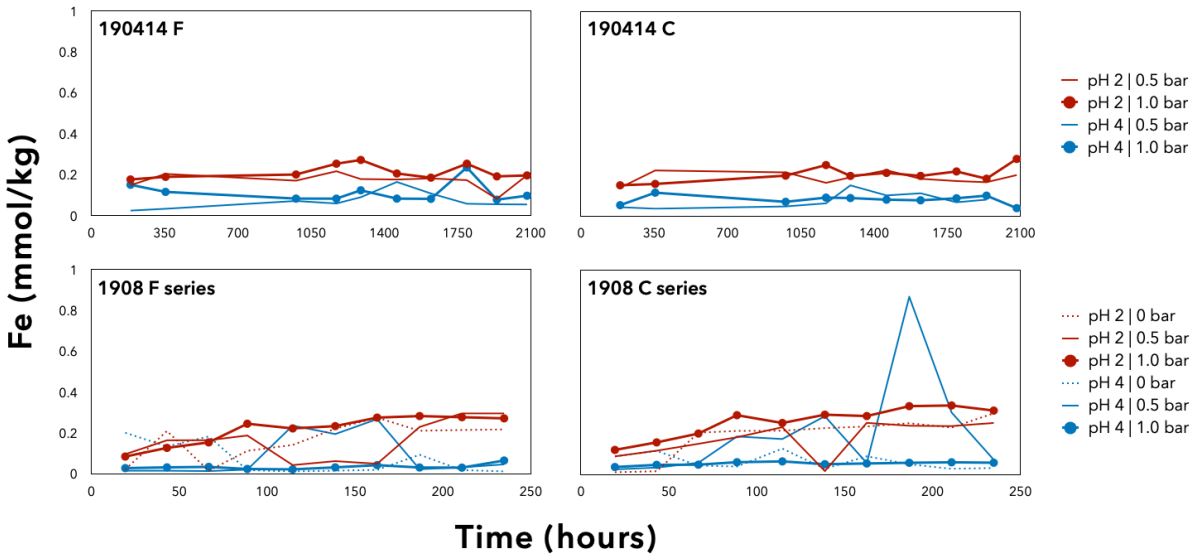


Figure 3: The Fe levels in mmol/kg for all high rock:water ratio CRB experiments, where experiments are divided into fine (F) or coarse (C) material, and the 1908 series (190806 at 0 bar CO_2, 190807 at 0.5 bar, and 190808 at 1.0 bar) are displayed on the same graph. A legend to the right of each row displays which lines correspond to which experiments on that row.

Experiment name	Fe	Si	Mg
CRB F pH 2 1:1	Not taken	Not taken	Not taken
CRB F pH 2 1:10	2.4694121	0.99501218	0.22672134
CRB F pH 4 1:1	Not taken	Not taken	Not taken
CRB F pH 4 1:10	0.14059394	0.71404845	0.1420447
CRB C pH 2 1:1	Not taken	Not taken	Not taken
CRB C pH 2 1:10	5.6583376	1.52508353	0.29156426
CRB C pH 4 1:1	Not taken	Not taken	Not taken
CRB C pH 4 1:10	0.41619397	0.45926067	0.11230317

Table 7: The final level of Fe, Si, and Mg in mmol/kg as detected by ICP-MS for the low rock:water ratio experiment 190812. Elemental data for 1:1 rock:water ratio experiments could not be extracted owing to the total volume of fluid available (1 mL).

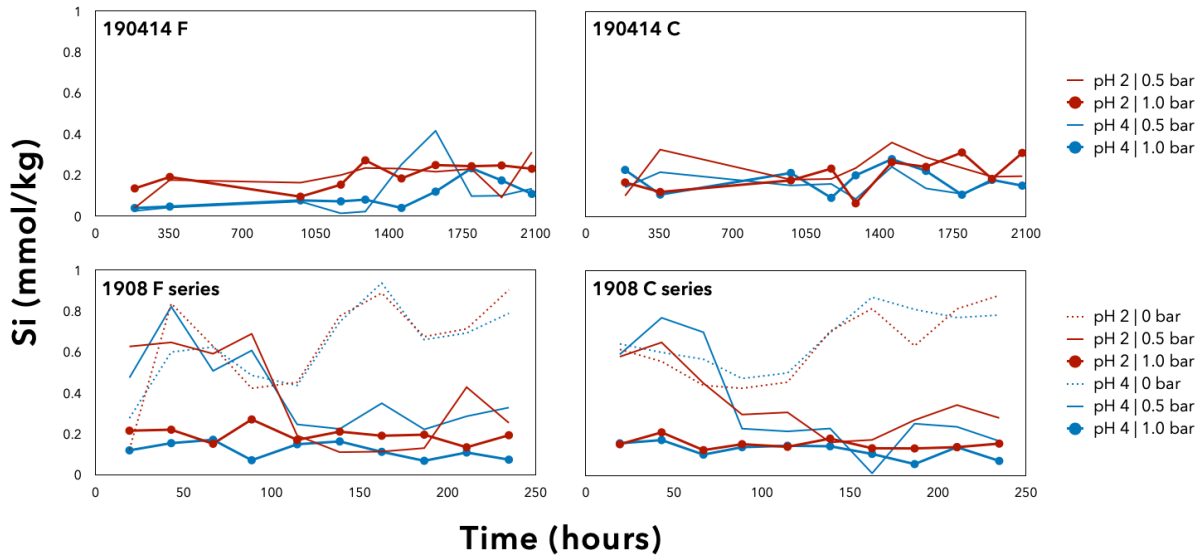


Figure 4: The Si levels in mmol/kg for all high rock:water ratio CRB experiments, where experiments are divided into fine (F) or coarse (C) material, and the 1908 series (190806 at 0 bar CO_2, 190807 at 0.5 bar, and 190808 at 1.0 bar) are displayed on the same graph. A legend to the right of each row displays which lines correspond to which experiments on that row.

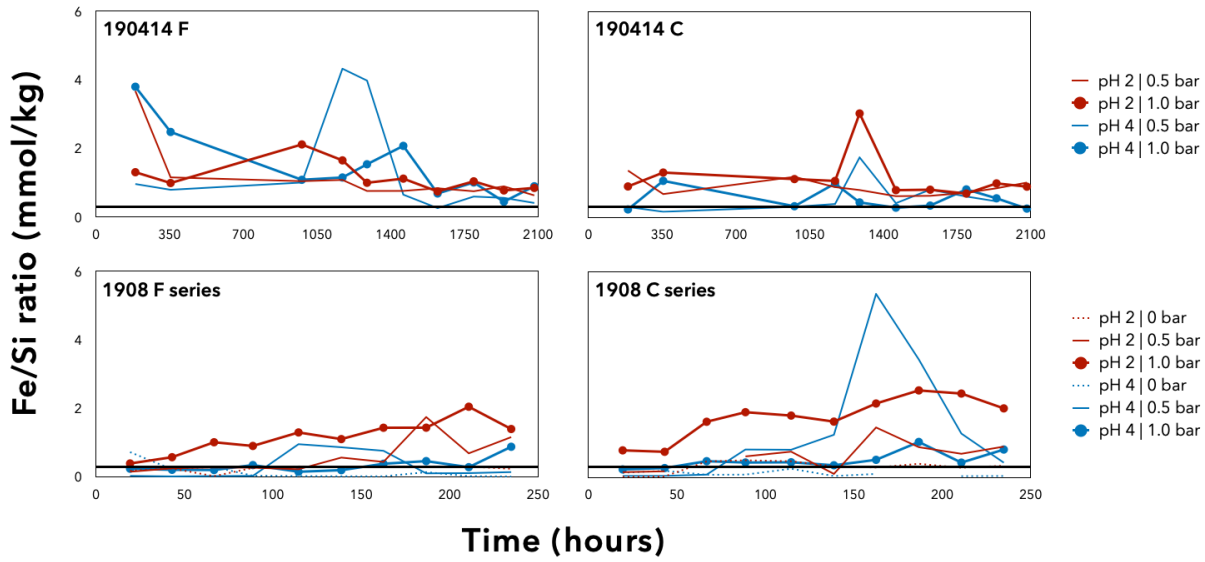


Figure 5: The elemental ratio of Fe to Si in solution, with the stoichiometric release reference line of 0.3 included on all.

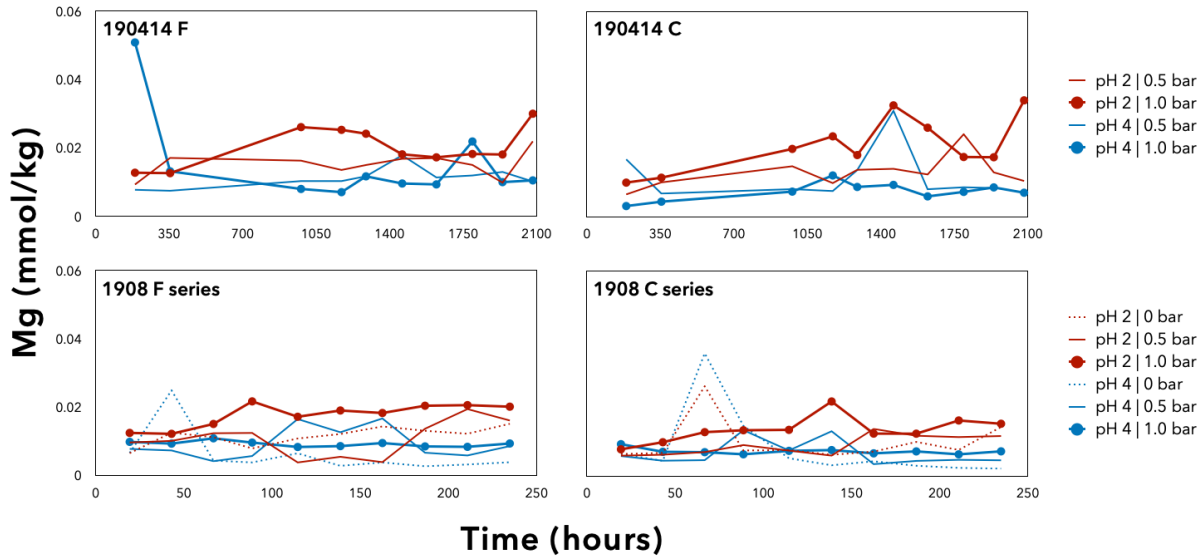


Figure 6: The Mg levels in mmol/kg for all high rock:water ratio CRB experiments, where experiments are divided into fine (F) or coarse (C) material, and the 1908 series (190806 at 0 bar CO_2, 190807 at 0.5 bar, and 190808 at 1.0 bar) are displayed on the same graph. A legend to the right of each row displays which lines correspond to which experiments on that row.

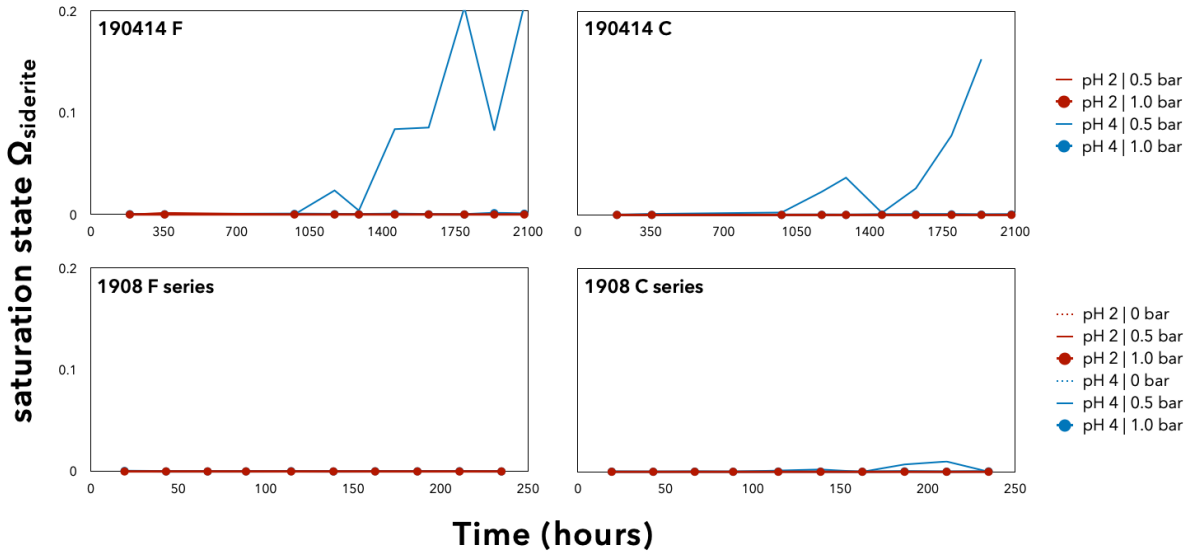


Figure 7: The saturation state (Ω) of siderite in solution for each of the high rock:water ratio experiments in this chapter. Experiments are divided into fine (F) or coarse (C) material, and the 1908 series (190806 at 0 bar CO_2, 190807 at 0.5 bar, and 190808 at 1.0 bar) are displayed on the same graph. A legend to the right of each row displays which lines correspond to which experiments on that row.

Experiment name	Siderite	Amorphous silica
CRB F pH 2 1:1	Not taken	Not taken
CRB F pH 2 1:10	0.0101	0.5248
CRB F pH 4 1:1	Not taken	Not taken
CRB F pH 4 1:10	0.3917	0.3745
CRB C pH 2 1:1	Not taken	Not taken
CRB C pH 2 1:10	0.0009	0.8107
CRB C pH 4 1:1	Not taken	Not taken
CRB C pH 4 1:10	24.0436	0.2404

Table 8: The final saturation state (Ω) of siderite, amorphous silica, and AFC as detected by ICP-MS for the low rock:water ratio experiment 190812. Elemental data for 1:1 rock:water ratio experiments could not be extracted owing to the total volume of fluid available (1 mL).

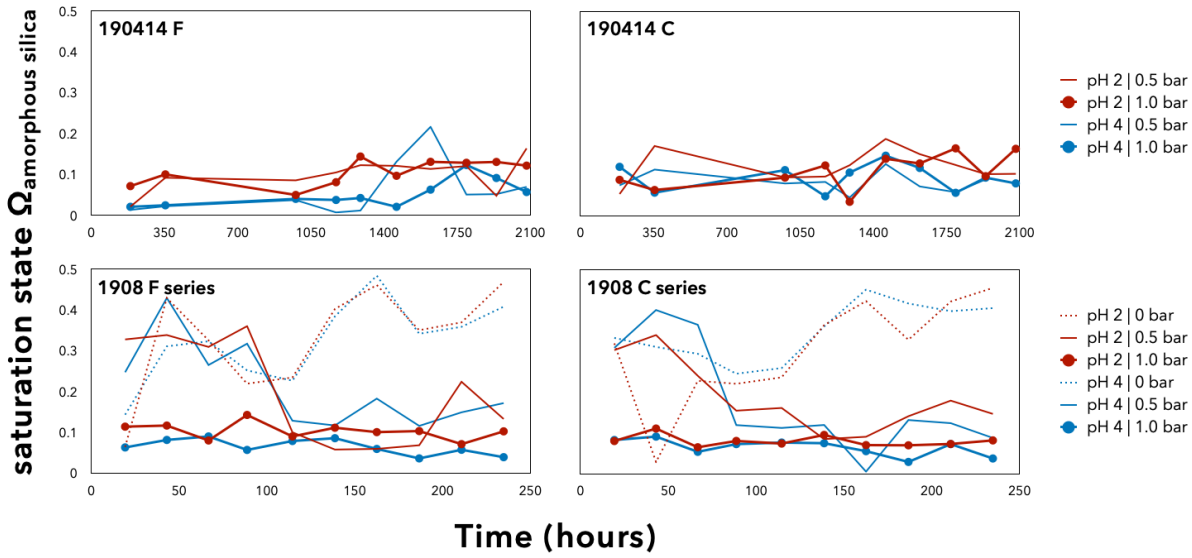


Figure 8: The saturation state (Ω) of amorphous Si in solution for each of the high rock:water ratio experiments in this chapter. Experiments are divided into fine (F) or coarse (C) material, and the 1908 series (190806 at 0 bar CO_2, 190807 at 0.5 bar, and 190808 at 1.0 bar) are displayed on the same graph. A legend to the right of each row displays which lines correspond to which experiments on that row.

Experiment and hours in	pH	aFe^{2+}	Ω_{AFC}
190414 F pH 4 0.5 bar: 1459.50	5.53	0.00010	3.58×10^{-5}
190414 F pH 4 0.5 bar: 1622.22	5.63	0.00007	3.75×10^{-5}
190414 F pH 4 0.5 bar: 1793.85	5.99	0.00004	1.06×10^{-4}
190414 F pH 4 0.5 bar: 1937.18	5.78	0.00003	3.86×10^{-5}
190414 F pH 4 0.5 bar: 2081.47	6.01	0.00003	1.10×10^{-4}
190812 F pH 2 1.0 bar: 1729.92	4.36	0.00116	3.07×10^{-6}
190812 F pH 4 1.0 bar: 1729.92	6.32	0.00007	1.46×10^{-3}
190812 C pH 2 1.0 bar: 1729.92	3.67	0.00259	2.85×10^{-7}
190812 C pH 4 1.0 bar: 1729.92	6.68	0.00022	2.37×10^{-2}

Table 9: Several example datapoints from experiments 190414 F (begun at pH 4 under 0.5 bar pCO_2) and 190812 F and C (begun under pH 2 and 4 and 1.0 bar pCO_2 that were selected for Ω_{AFC} calculation.

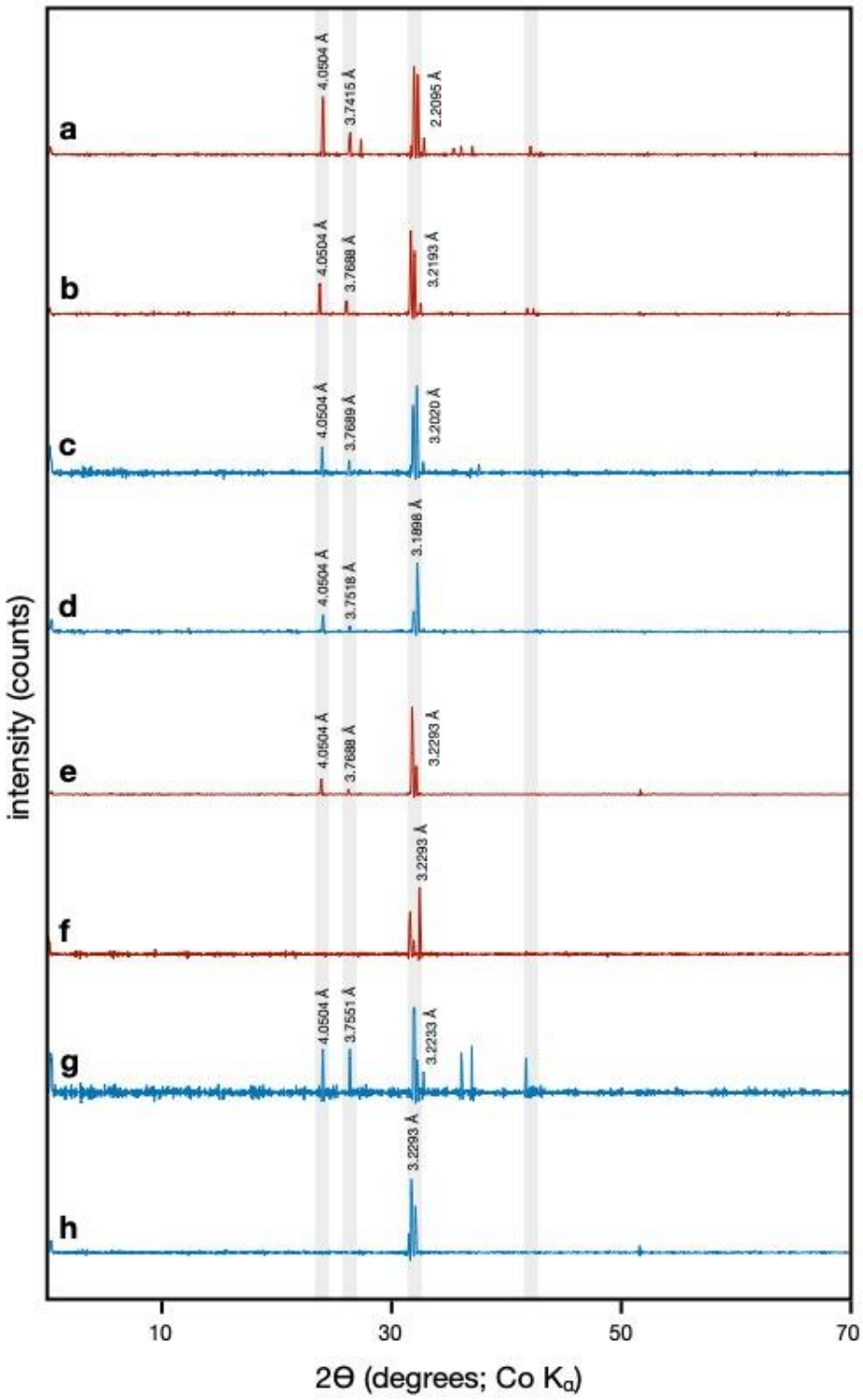


Figure 9: XRD signatures for the high rock:water ratio experiment 190414, in order: (a) pH 2 0.5 pCO_2 fine, (b) pH 2 0.5 pCO_2 coarse, (c) pH 4 0.5 pCO_2 fine, (d) pH 4 0.5 pCO_2 coarse; (e) pH 2 1.0 pCO_2 fine, (f) pH 2 1.0 pCO_2 coarse, (g) pH 4 1.0 pCO_2 fine, and (h) pH 4 1.0 pCO_2 coarse. Individual peaks are labelled for reference; where no peaks are labelled, none are sufficiently individually diagnostic. Shaded grey areas are key CRB peaks.

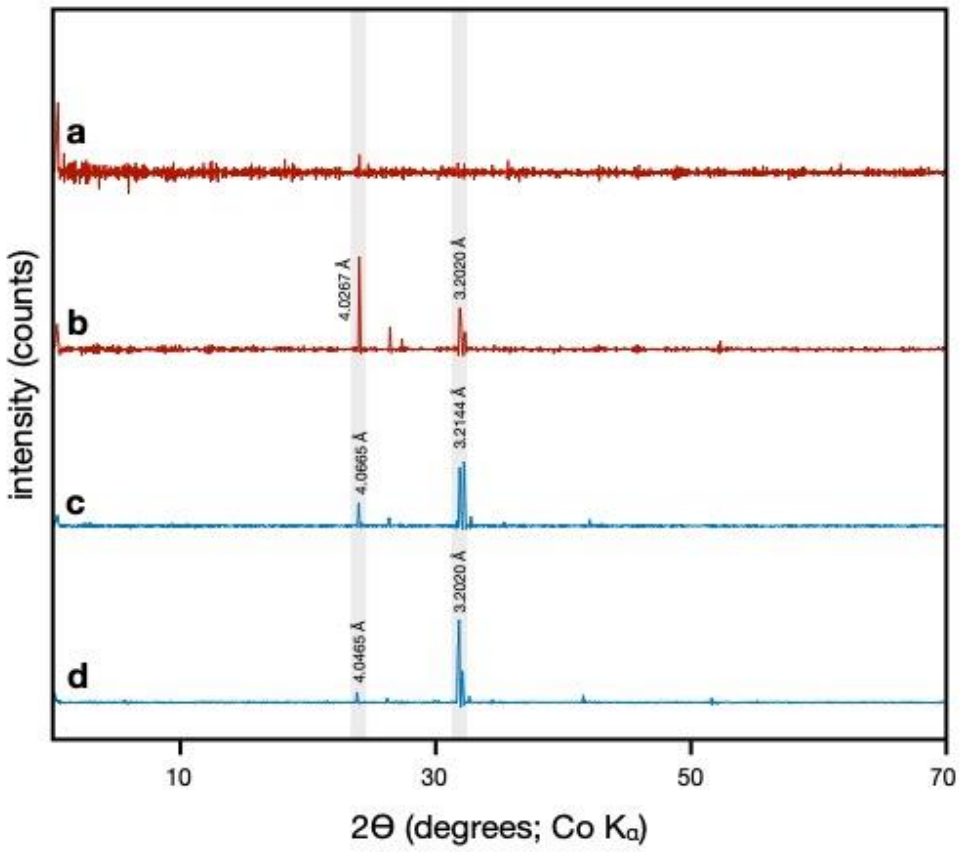


Figure 10: XRD signatures for the high rock:water ratio experiment 190806, which ran without CO_2. In order: (a) pH 2 fine, (b) pH 2 coarse, (c) pH 4 fine, and (d) pH 4 coarse, where F is fine and C is coarse. Individual peaks are labelled for reference; where no peaks are labelled, none are sufficiently individually diagnostic. Shaded grey areas are key CRB peaks.

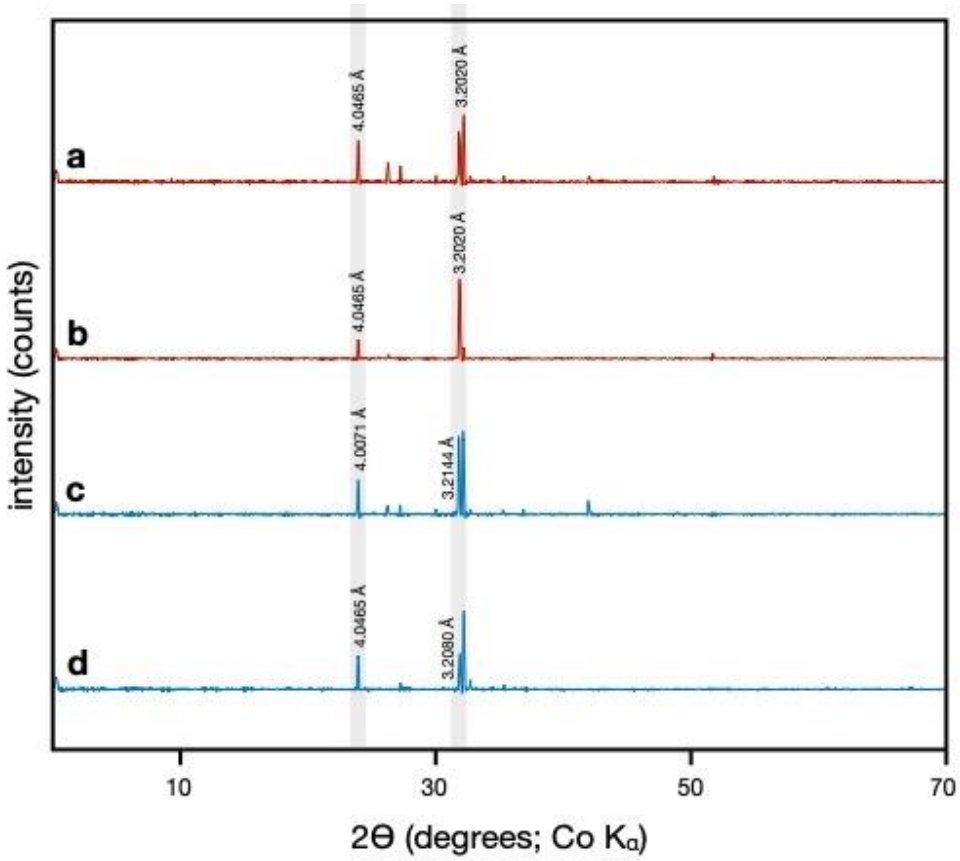


Figure 11: XRD signatures for the high rock:water ratio experiment 190807, which ran with 0.5 bars of CO_2. In order: (a) pH 2 pCO_2 0.5 fine, (b) pH 2 pCO_2 0.5 coarse, (c) pH 4 pCO_2 0.5 fine, and (d) pH 4 pCO_2 0.5 coarse. Individual peaks are labelled for reference; where no peaks are labelled, none are sufficiently individually diagnostic. Shaded grey areas are key CRB peaks.

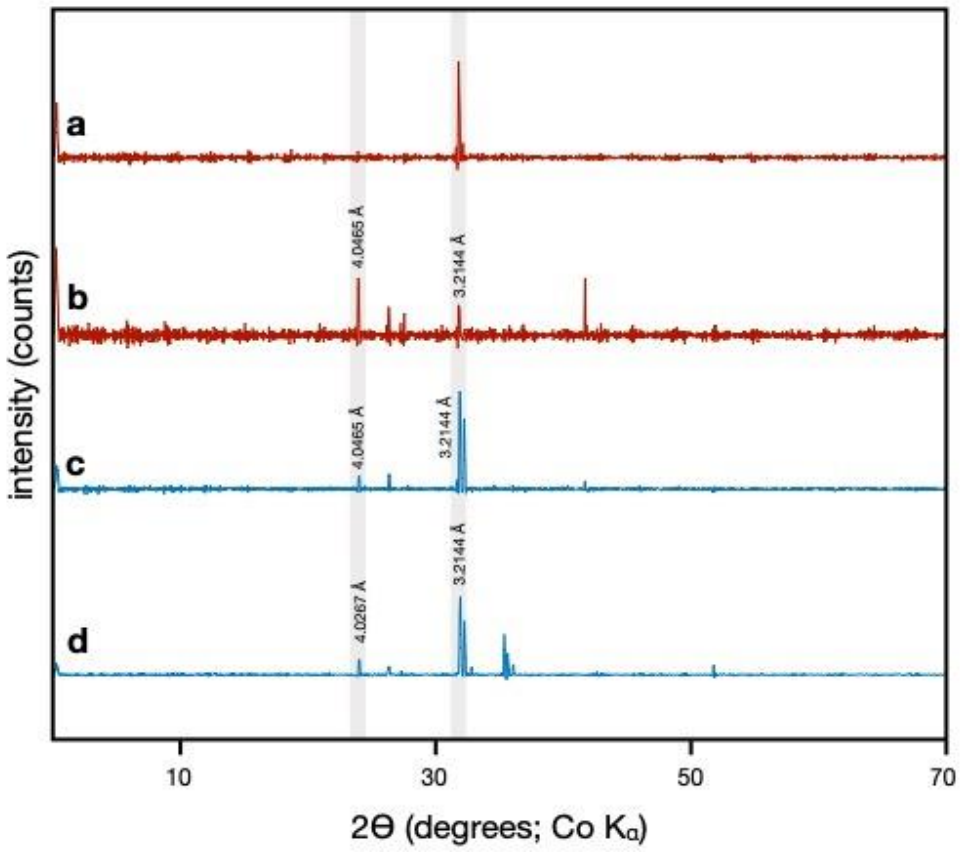


Figure 12: XRD signatures for the high rock:water ratio experiment 190808, which ran with 1.0 bar of CO_2. In order: (a) pH 2 pCO_2 1.0 bar fine, (b) pH 2 pCO_2 1.0 bar coarse, (c) pH 4 pCO_2 1.0 bar fine, and (d) pH 4 pCO_2 1.0 bar coarse. Individual peaks are labelled for reference; where no peaks are labelled, none are sufficiently individually diagnostic. Shaded grey areas are key CRB peaks.

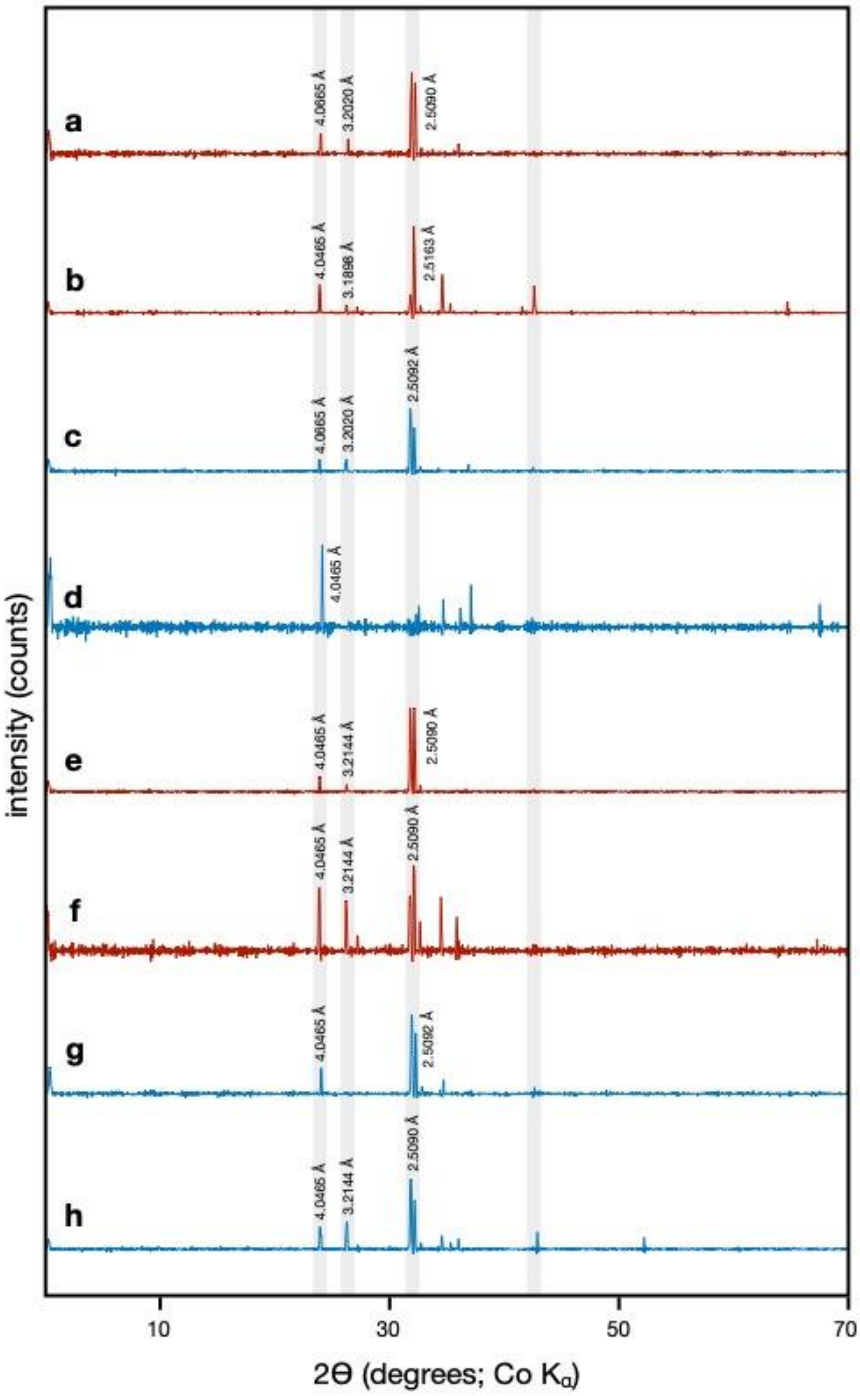


Figure 13: XRD signatures for the low rock:water ratio experiment 190812, which ran with 1.0 bar of CO_2. In order: (a) pH 2 1:1 fine, (b) pH 2 1:1 coarse, (c) pH 4 1:1 fine, (d) pH 4 1:1 coarse; (e) pH 2 1:10 fine, (f) pH 2 1:10 coarse, (g) pH 4 1:10 fine, and (h) pH 4 1:10 coarse. Individual peaks are labelled for reference; where no peaks are labelled, none are sufficiently individually diagnostic. Shaded grey areas are key CRB peaks.

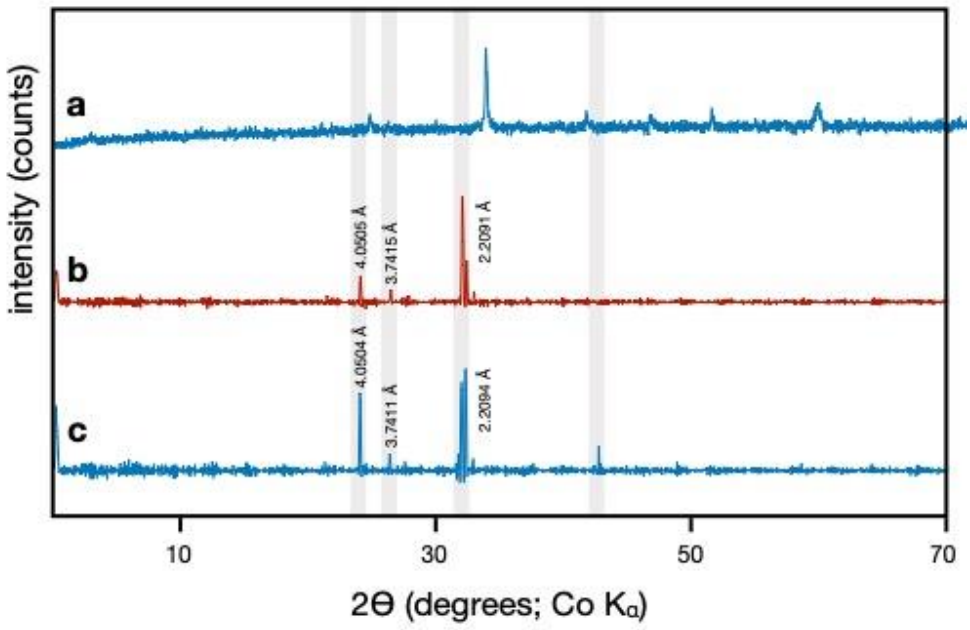


Figure 14: XRD signatures for (a) pure siderite, (b) fine CRB, and (c) coarse CRB. Individual peaks are labelled for reference; where no peaks are labelled, none are sufficiently individually diagnostic. Shaded grey areas are key CRB peaks.

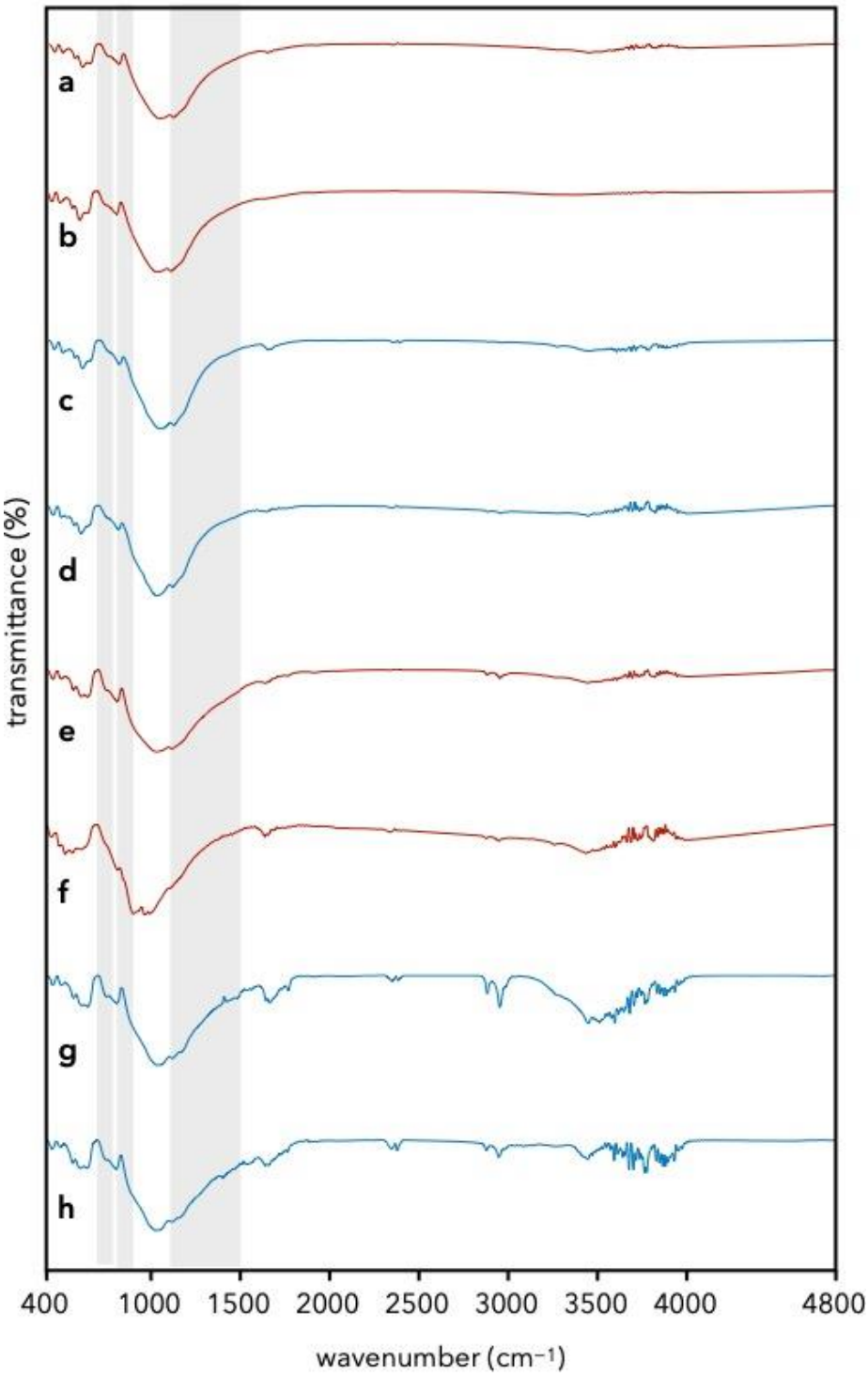


Figure 15: FT-IR signatures for the high rock:water ratio experiment 190414, in order: (a) pH 2 pCO_2 0.5 bar fine, (b) pH 2 pCO_2 0.5 bar coarse, (c) pH 4 pCO_2 0.5 bar fine, (d) pH 4 pCO_2 0.5 bar coarse; (e) pH 2 pCO_2 1.0 bar fine, (f) pH 2 pCO_2 1.0 bar coarse, (g) pH 4 pCO_2 1.0 bar fine, and (h) pH 4 pCO_2 1.0 bar coarse. Shaded grey regions correspond to absorption regions for siderite.

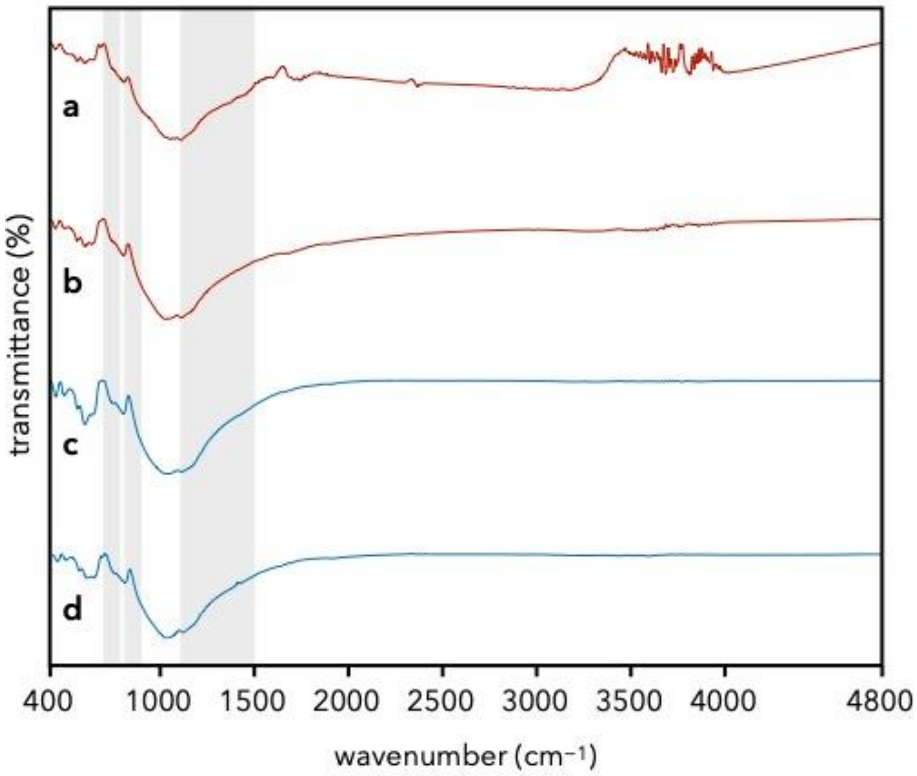


Figure 16: FT-IR signatures for the high rock:water ratio experiment 190806, which ran without CO_2. In order: (a) pH 2 fine, (b) pH 2 coarse, (c) pH 4 fine, and (d) pH 4 coarse. Shaded grey regions correspond to absorption regions for siderite.

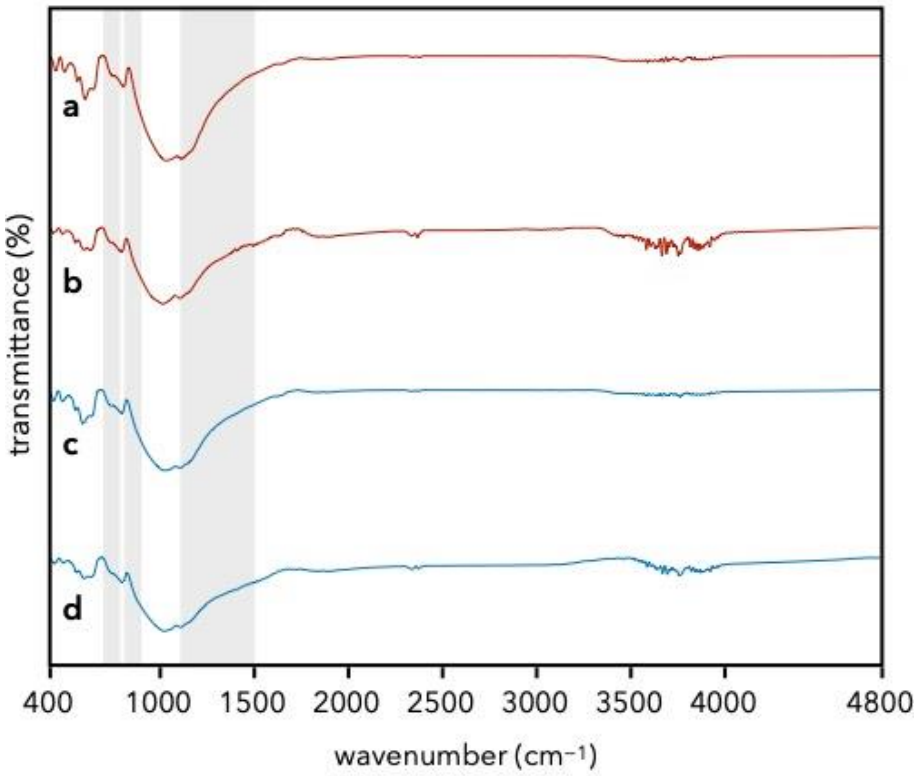


Figure 17: FT-IR signatures for the high rock:water ratio experiment 190807, which ran with 0.5 bars of CO_2. In order: (a) pH 2 pCO_2 0.5 bar fine, (b) pH 2 pCO_2 0.5 bar coarse, (c) pH 4 pCO_2 0.5 bar fine, and (d) pH 4 pCO_2 0.5 bar coarse. Shaded grey regions correspond to absorption regions for siderite.

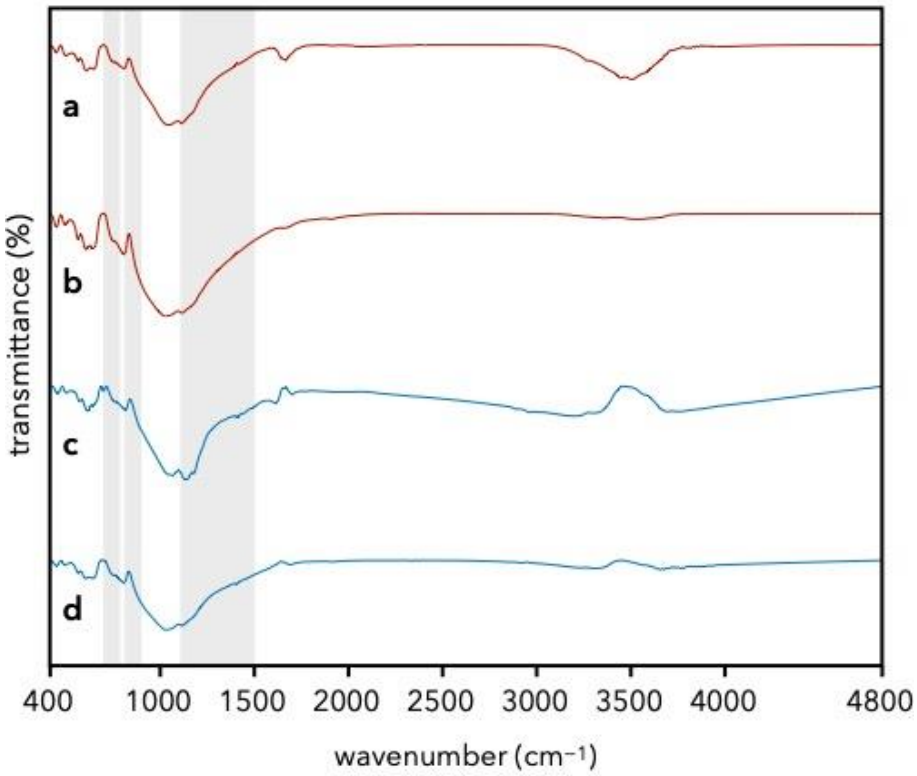


Figure 18: FT-IR signatures for the high rock:water ratio experiment 190808, which ran with 1.0 bar of CO_2. In order: (a) pH 2 pCO_2 1.0 bar fine, (b) pH 2 pCO_2 1.0 bar coarse, (c) pH 4 pCO_2 1.0 bar fine, and (d) pH 4 pCO_2 1.0 bar coarse. Shaded grey regions correspond to absorption regions for siderite.

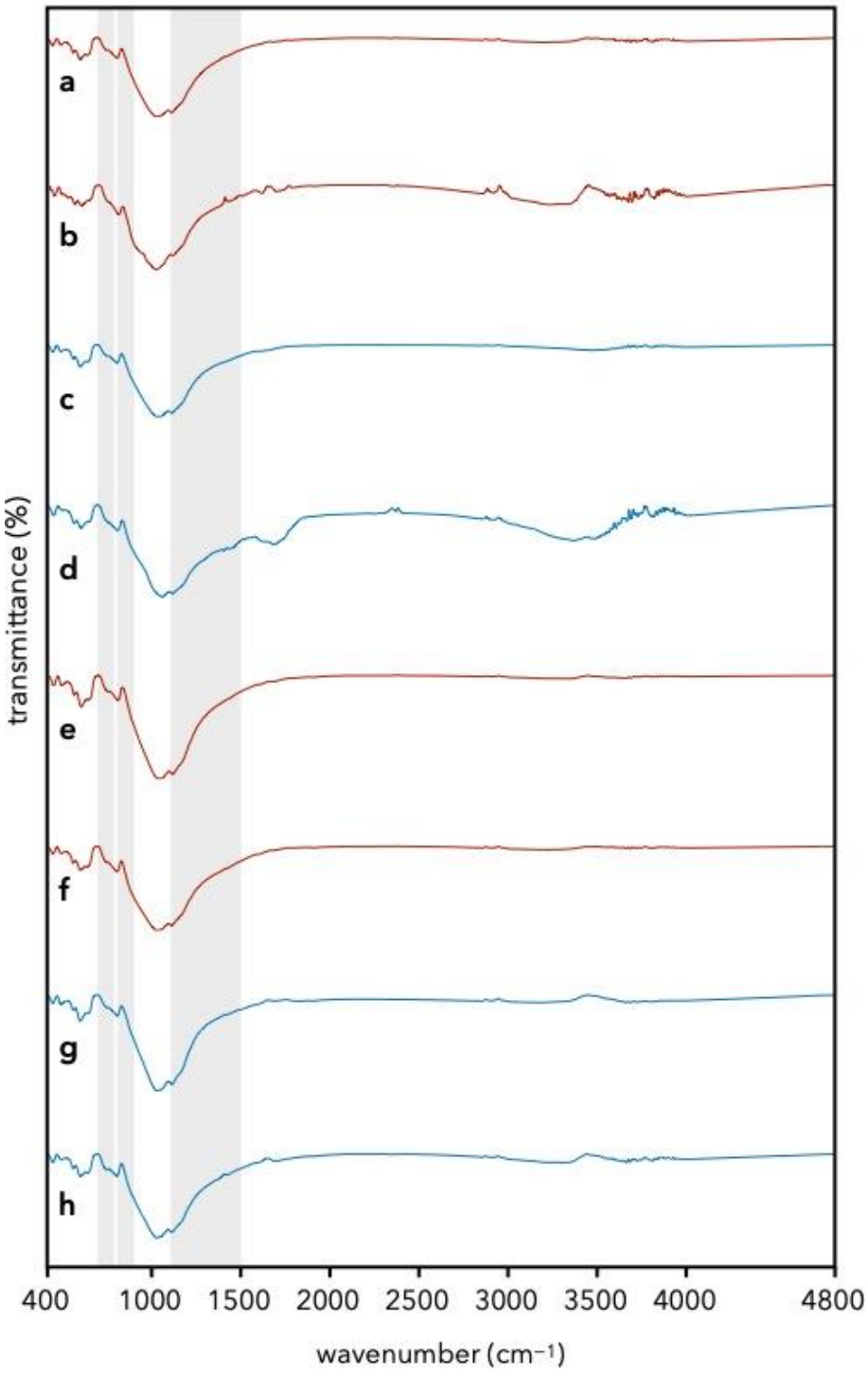


Figure 19: FT-IR signatures for the low rock:water ratio experiment 190812, which ran with 1.0 bar of CO_2. In order: (a) pH 2 1:1 fine, (b) pH 2 1:1 coarse, (c) pH 4 1:1 fine, (d) pH 4 1:1 coarse; (e) pH 2 1:10 fine, (f) pH 2 1:10 coarse, (g) pH 4 1:10 fine, and (h) pH 4 1:10 coarse. Shaded grey regions correspond to absorption regions for siderite.

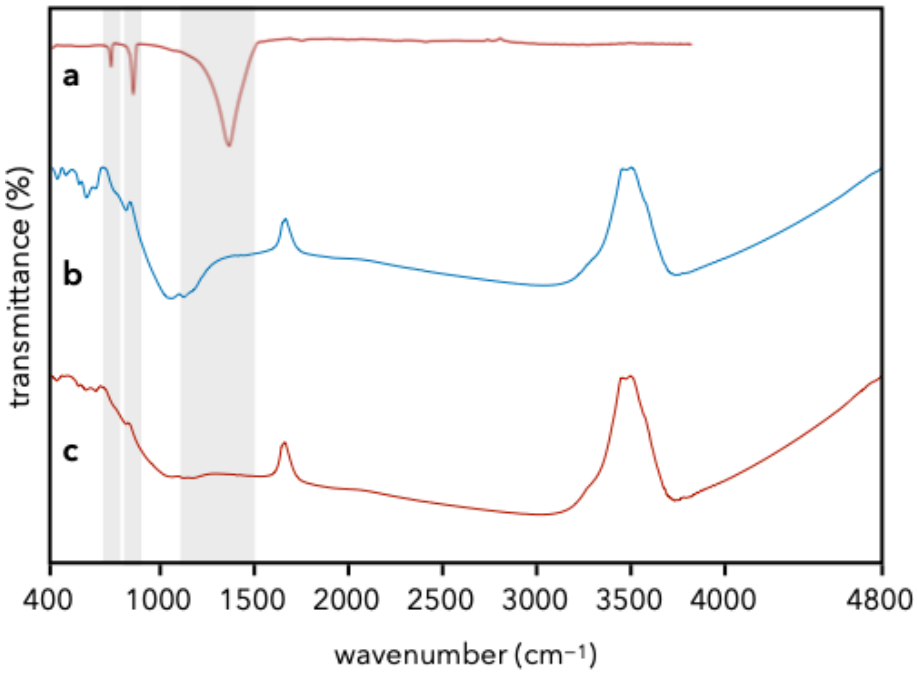


Figure 20: The FT-IR signatures for pure siderite (a) as taken from the RRUFF Online Database (ID: R050262.1); (b) fine CRB; and (c) coarse CRB.

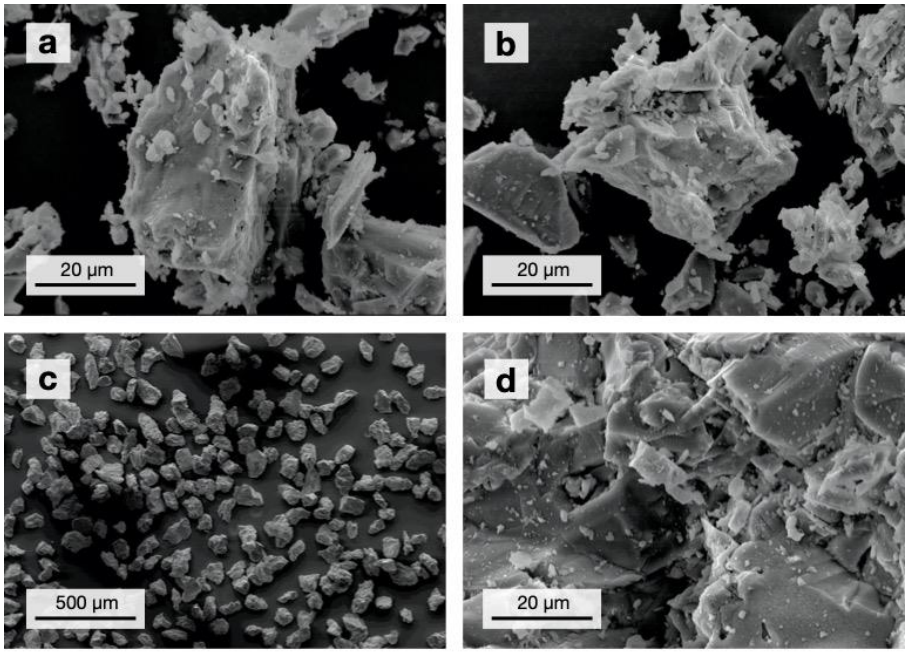


Figure 21: SEM images of the unreacted CRB used in all experiments discussed in this chapter. (a) and (b): Unreacted fine CRB; (c) and (d): Unreacted coarse CRB, where (c) demonstrates the uniformity of the coarse CRB grains and (d) the texture at high magnification.

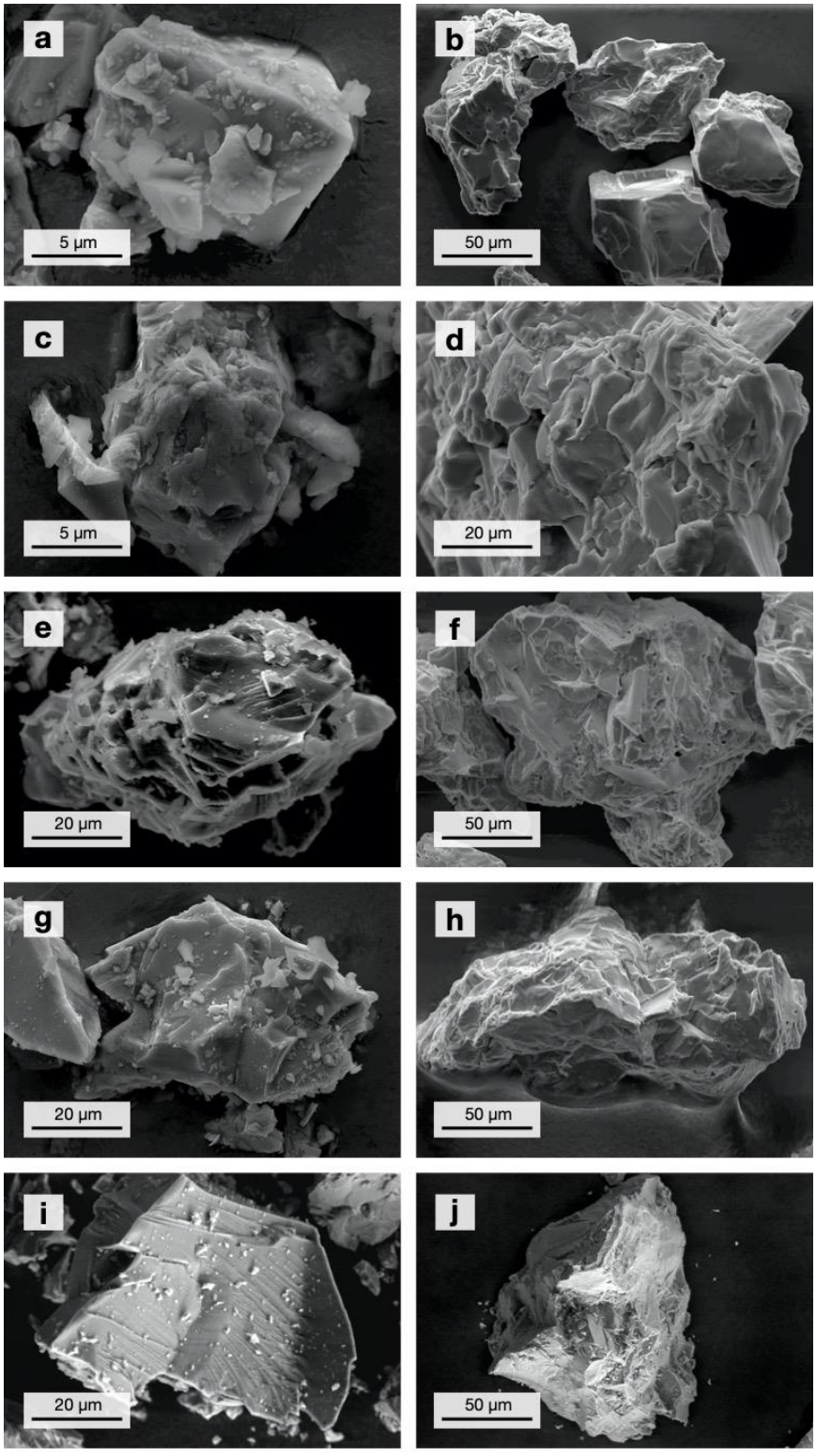


Figure 22: SEM images taken from all fine (lefthand column) and coarse (righthand column) CRB experiments. (a) 190414 F; (b) 190414 C; (c) 190806 F; (d) 190806 C; (e) 190807 F; (f) 190807 C; (g) 190808 F; (h) 190808 C; (i) 190812, F at low rock:water ratio; (j) 190812 C at low rock:water ratio.

Species	Moles/kg
H^+	2.95×10^{-6}
Fe^{2+}	3.30×10^{-4}
Mg^{2+}	3.58×10^{-5}
Na^+	1.77×10^{-2}
HCO_3^-	-2.77×10^{-3}
SO_4^{2-}	-1.15×10^{-4}
Charge difference	$\mathbf{1.52 \times 10^{-2}}$

Table 10: The number of moles of different charges for the species inputted into the extended Debye-Hückel equation calculation. Data taken from experiment 190414 F, begun at pH 4 and 0.5 bars of pCO_2, 1,459 hours in.

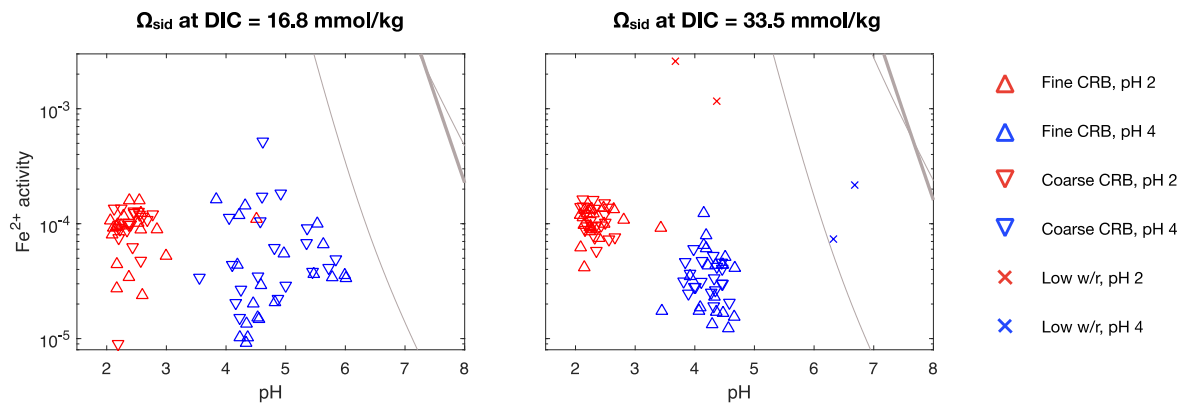


Figure 23: The saturation state of all extracted samples in terms of the Fe(II)-carbonates siderite and AFC, divided into two graphs depending upon 0.5 (DIC = 16.8 mmol/kg) or 1.0 (DIC = 33.5 mmol/kg) pCO_2 levels, and expressed in terms of Fe^{2+} activity and pH. The three light, grey lines on each represent the saturation state of siderite as 1, 100, or 400, while the heavy, grey line represents the 'AFC-line' of Jiang and Tosca (2019), beyond which AFC is expected to precipitate. Up-triangles are fine-grained CRB, down-triangles are coarse-grained CRB, and crosses are low water-rock experiments; red represents pH 2 experiments, while blue pH 4.

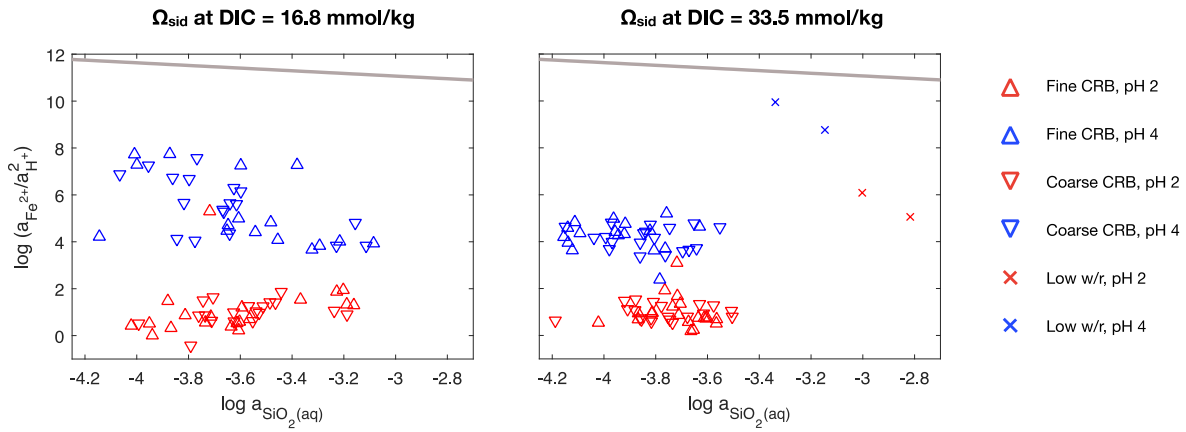


Figure 24: Solubility diagrams for greenalite, divided into two graphs depending upon 0.5 (DIC = 16.8 mmol/kg) or 1.0 (DIC = 33.5 mmol/kg) pCO_2 levels, involving the three principal factors controlling greenalite stability: the activities of Fe^{2+}, H^+, and $SiO_{2(aq)}$. All data are from solution samples extracted at 10 intervals across 20 experiments, or 4 samples extracted at their termination (low water-rock, in legend as "low w/r"), in separate graphs for CO_2 partial pressure. Datapoints in red correspond to experiments begun at pH 2; blue for pH 4. Upward-pointing triangles correspond to fine CRB experiments, while downward-pointing triangles are for coarse CRB, and cross-symbols for low rock:water ratio (1:10). Datapoints towards the top and the right generally correspond to increasingly later stages of an experiment. The heavy grey line is the greenalite saturation line of Tosca et al. (2016). Any datapoints exceeding this line are supersaturated with respect to greenalite.

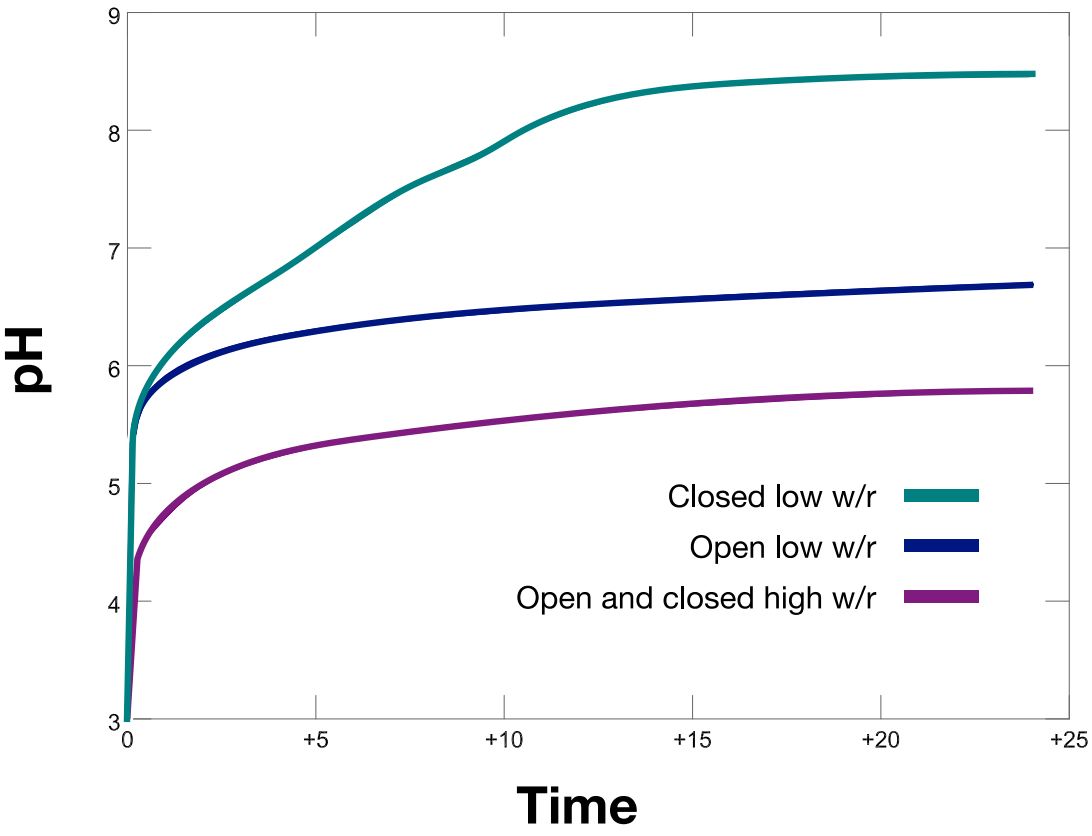


Figure 25: pH variation over three modelled conditions: closed system with low (1:1) rock:water ratio (teal); open system with low (1:1) rock:water ratio (navy); and both open and closed systems at high (1:500) rock:water ratio (violet). Model run over 24 months.

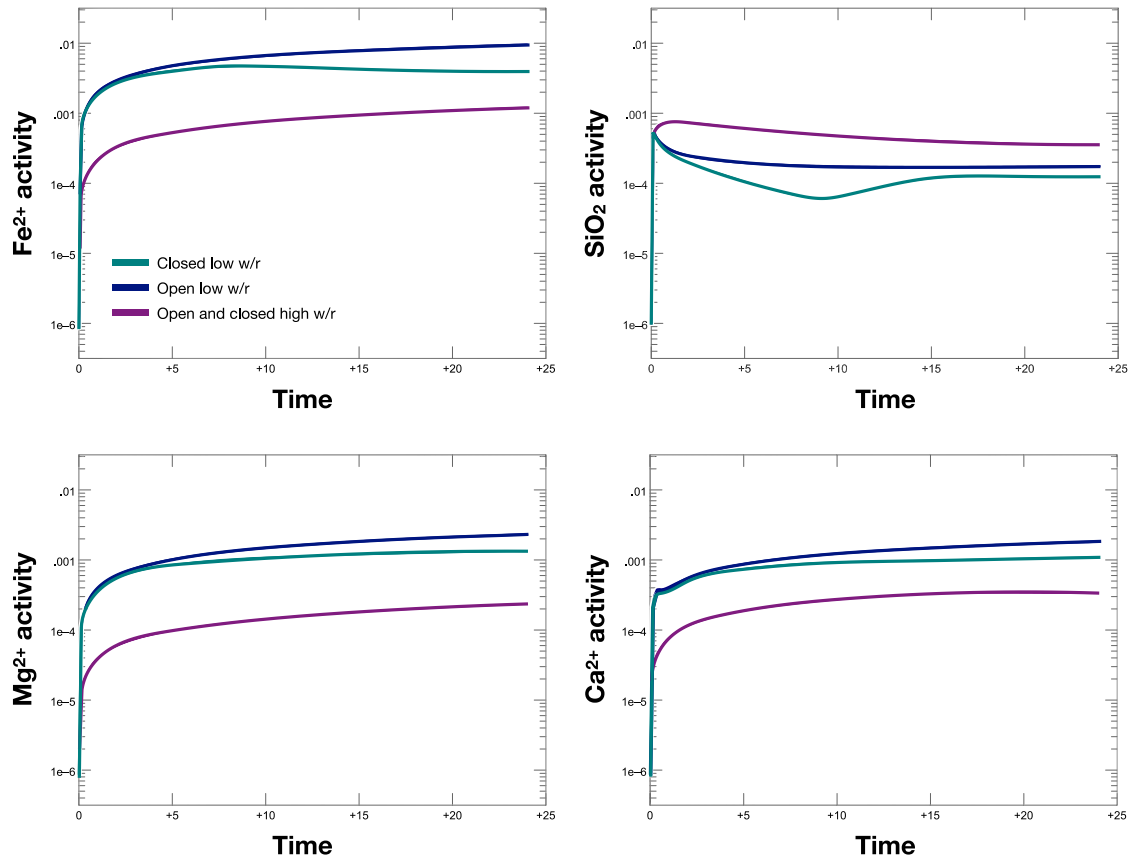


Figure 26: Activity for Fe^{2+}, SiO_2, Mg^{2+}, and Ca^{2+} over three modelled conditions: closed system with low (1:1) rock:water ratio (teal); open system with low (1:1) rock:water ratio (navy); and both open and closed systems at high (1:500) rock:water ratio (violet). Model run over 24 months. Note the identical axes.

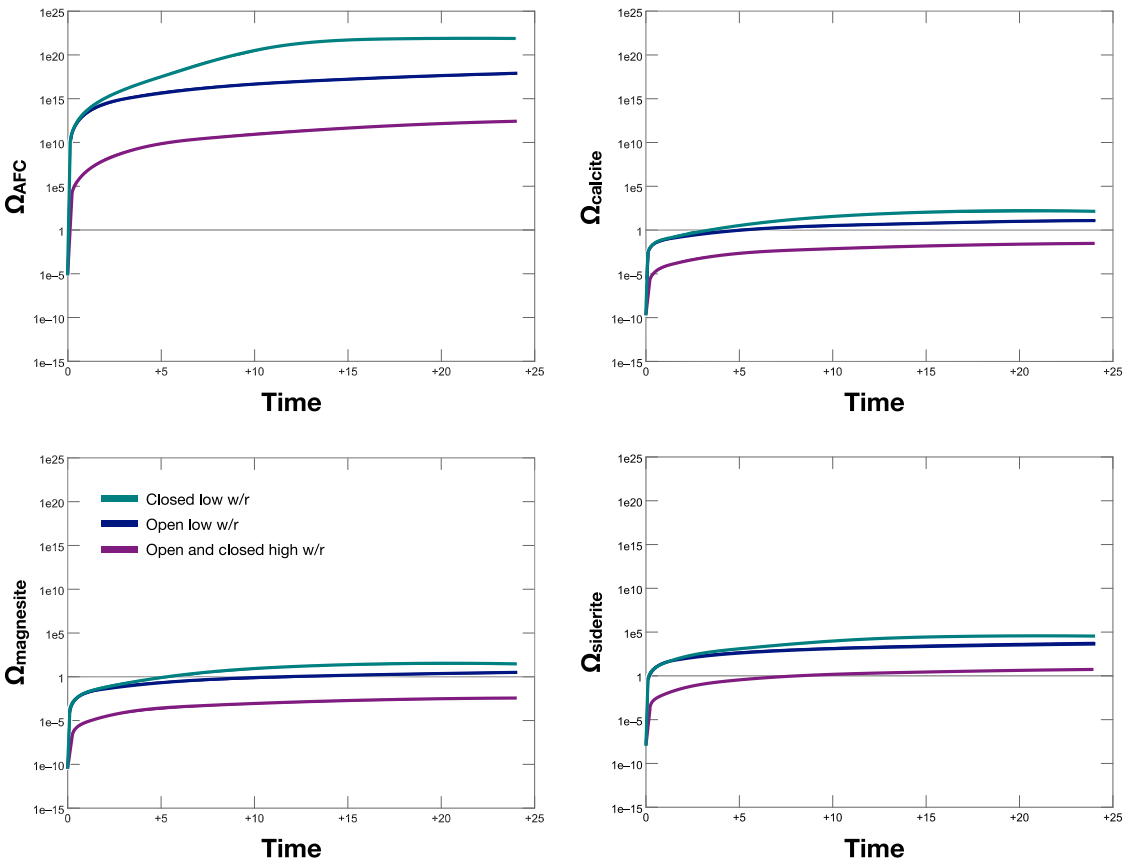


Figure 27: Mineral saturation state for the carbonates AFC, calcite, magnesite, and siderite over three modelled conditions: closed system with low (1:1) rock:water ratio (teal); open system with low (1:1) rock:water ratio (navy); and both open and closed systems at high (1:500) rock:water ratio (violet). Model run over 24 months. Note the identical axes.

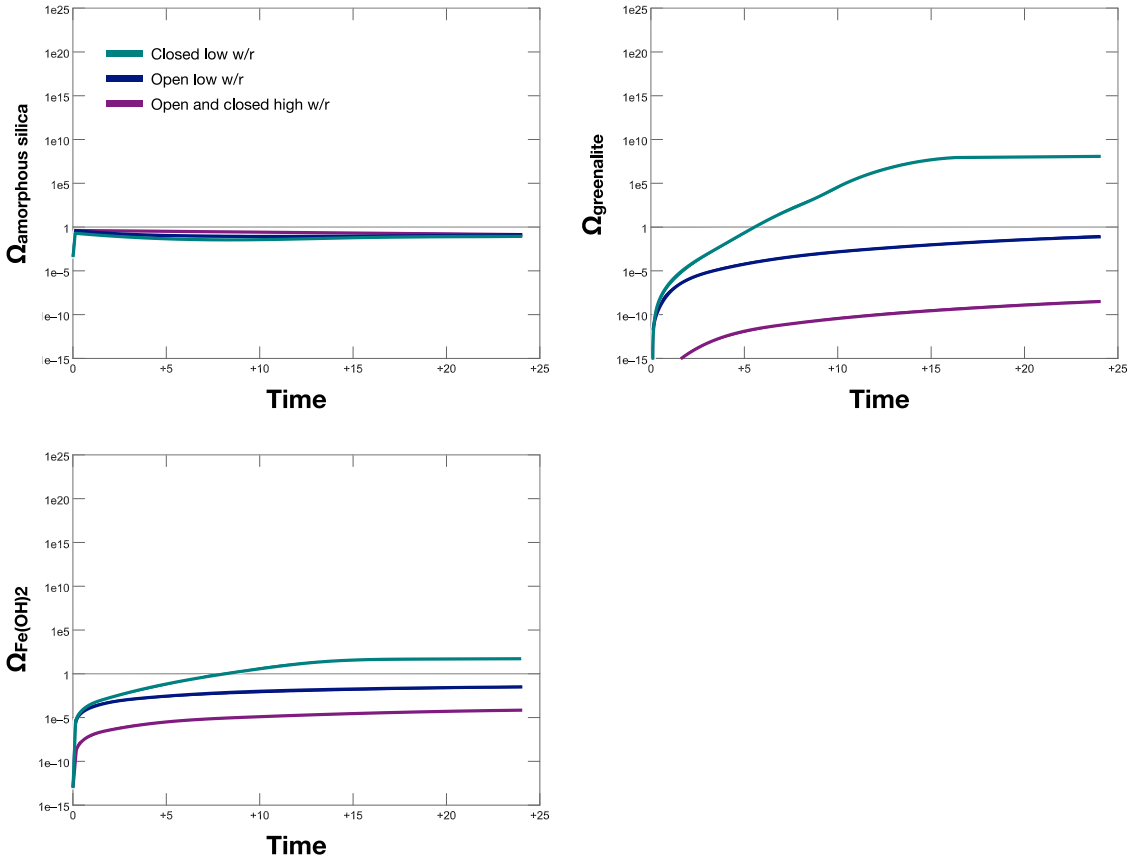


Figure 28: Mineral saturation state for relevant non-carbonates: amorphous silica, greenalite, and $Fe(OH)_2$ over three modelled conditions: closed system with low (1:1) rock:water ratio (teal); open system with low (1:1) rock:water ratio (navy); and both open and closed systems at high (1:500) rock:water ratio (violet). Model run over 24 months. Note the identical axes.

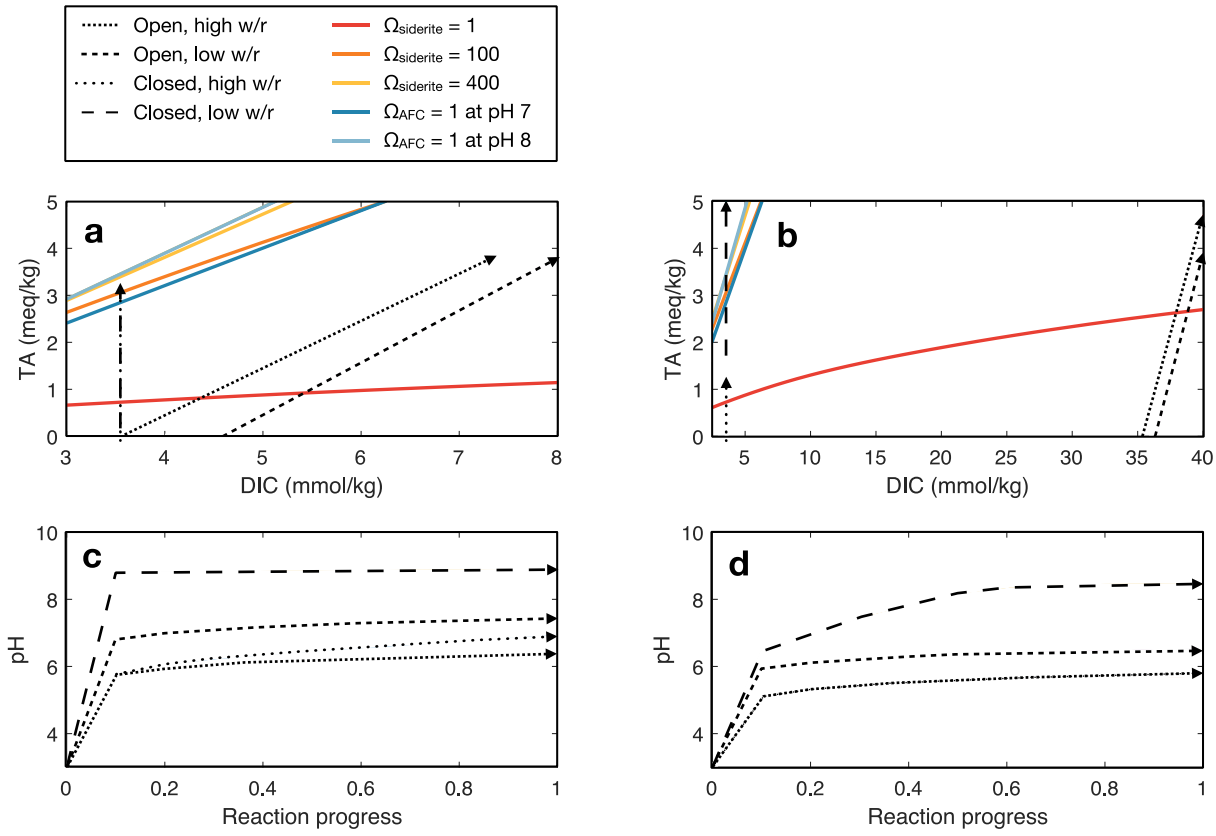


Figure 29: Results from four reaction path models of water-rock interaction at 25 °C: open-system with respect to CO_2 at high rock:waterrock:water ratio (tightly-dotted lines), open-system with respect to CO_2 at low rock:waterrock:water ratio (dashed lines), closed-system with respect to CO_2 at high rock:waterrock:water ratio (circular-dotted lines), and closed-system with respect to CO_2 at low rock:waterrock:water ratio (long dashed lines). Left column: models run with 0.1 bar CO_2; right column: models run with 1.0 bar CO_2. (a) and (b): siderite and AFC saturation state as a function of DIC and total alkalinity (TA). From bottom-up, red to yellow lines represent $\Omega_{siderite}$ of 1, 100, and 100,000; blue and pale blue lines represent an Ω_{AFC} saturation at pH 7 (lower) or 8 (higher). (c) and (d): pH variation over the course of the experiment (which corresponds closely to total alkalinity in this system). In order to illustrate the influence of water-rock interaction on the Fe(II)-carbonate system in DIC-TA space, these models were run under fixed Fe^{2+} concentration of 10 mmol/kg with CRB represented in components equivalent to the portions outlined in Table 4.

7. References

Baker, L.L., Agenbroad, D.J., Wood, S.A., 2000. Experimental hydrothermal alteration of a martian analog basalt: Implications for martian meteorites. Meteoritics & Planetary Science 35, 31–38. https://doi.org/10.1111/j.1945-5100.2000.tb01971.x

Baker, L.L., Neill, O.K., 2017. Geochemistry and mineralogy of a saprolite developed on Columbia River Basalt: Secondary clay formation, element leaching, and mass balance during weathering. American Mineralogist 102, 1632–1645. https://doi.org/10.2138/am-2017-5964

Baksi, A.K., Hoffman, K.A., McWilliams, M., 1993. Testing the accuracy of the geomagnetic polarity time-scale (GPTS) at 2–5 Ma, utilizing40Ar/39Ar incremental heating data on whole-rock basalts. Earth and Planetary Science Letters 118, 135–144. https://doi.org/10.1016/0012-821X(93)90164-5

Bethke, C.M., 2017. The Geochemist's Workbench, Version 12.0: GWB Essentials Guide. Champaign, Illinois, US.

Bishop, J.L., Dobrea, E.Z.N., McKeown, N.K., Parente, M., Ehlmann, B.L., Michalski, J.R., Milliken, R.E., Poulet, F., Swayze, G.A., Mustard, J.F., Murchie, S.L., Bibring, J.-P., 2008. Phyllosilicate Diversity and Past Aqueous Activity Revealed at Mawrth Vallis, Mars. Science 321, 830–833. https://doi.org/10.1126/science.1159699

Bishop, J.L., Perry, K.A., Darby Dyar, M., Bristow, T.F., Blake, D.F., Brown, A.J., Peel, S.E., 2013. Coordinated spectral and XRD analyses of magnesite-nontronite-forsterite mixtures and implications for carbonates on Mars: MAGNESITE-NONTRONITE-FORSTERITE MIXTURES. J. Geophys. Res. Planets 118, 635–650. https://doi.org/10.1002/jgre.20066

Bridges, J.C., Warren, P.H., 2006. The SNC meteorites: basaltic igneous processes on Mars. Journal of the Geological Society 163, 229–251. https://doi.org/10.1144/0016-764904-501

Brown, A.J., Viviano, C.E., Goudge, T.A., 2020. Olivine-Carbonate Mineralogy of the Jezero Crater Region. J. Geophys. Res. Planets 125. https://doi.org/10.1029/2019JE006011

Bush, J.H., Kauffman, J.D., Schmidt, K.L., Bird, J.S. and Stanford, L.R., 2004. *Geologic Map of the Craigmont Quadrangle, Lewis and Idaho Counties, Idaho*. Idaho Geological Survey, University of Idaho.

Catling, D.C., 1999. A chemical model for evaporites on early Mars: Possible sedimentary tracers of the early climate and implications for exploration. J. Geophys. Res. 104, 16453–16469. https://doi.org/10.1029/1998JE001020

Chen, M., El Goresy, A., 2000. The nature of maskelynite in shocked meteorites: not diaplectic glass but a glass quenched from shock-induced dense melt at high pressures. Earth and Planetary Science Letters 179, 489–502. https://doi.org/10.1016/S0012-821X(00)00130-8

Chevrier, V., Poulet, F., Bibring, J.-P., 2007. Early geochemical environment of Mars as determined from thermodynamics of phyllosilicates. Nature 448, 60–63. https://doi.org/10.1038/nature05961

Christensen, P.R., Bandfield, J.L., Hamilton, V.E., Ruff, S.W., Kieffer, H.H., Titus, T.N., Malin, M.C., Morris, R.V., Lane, M.D., Clark, R.L., Jakosky, B.M., Mellon, M.T., Pearl, J.C., Conrath, B.J., Smith, M.D., Clancy, R.T., Kuzmin, R.O., Roush, T., Mehall, G.L., Gorelick, N., Bender, K., Murray, K., Dason, S., Greene, E., Silverman, S., Greenfield, M., 2001. Mars Global Surveyor Thermal Emission Spectrometer experiment: Investigation description and surface science results. Journal of Geophysical Research: Planets 106, 23823–23871. https://doi.org/10.1029/2000JE001370

Czarnecki, S., Hardgrove, C., Gasda, P.J., Gabriel, T.S.J., Starr, M., Rice, M.S., Frydenvang, J., Wiens, R.C., Rapin, W., Nikiforov, S., Lisov, D., Litvak, M., Calef, F., Gengl, H., Newsom, H., Thompson, L., Nowicki, S., 2020. Identification and Description of a Silicic Volcaniclastic Layer in Gale Crater, Mars, Using Active Neutron Interrogation. J. Geophys. Res. Planets 125. https://doi.org/10.1029/2019JE006180

Daval, D., Martinez, I., Corvisier, J., Findling, N., Goffé, B., Guyot, F., 2009. Carbonation of Ca-bearing silicates, the case of wollastonite: Experimental investigations and kinetic modeling. Chemical Geology 265, 63–78. https://doi.org/10.1016/j.chemgeo.2009.01.022

Daval, D., Testemale, D., Recham, N., Tarascon, J.-M., Siebert, J., Martinez, I., Guyot, F., 2010. Fayalite (Fe2SiO4) dissolution kinetics determined by X-ray absorption spectroscopy. Chemical Geology 275, 161–175. https://doi.org/10.1016/j.chemgeo.2010.05.005

Davis, J.M., Gupta, S., Balme, M., Grindrod, P.M., Fawdon, P., Dickeson, Z.I., Williams, R.M.E., 2019. A Diverse Array of Fluvial Depositional Systems in Arabia Terra: Evidence for mid-Noachian to Early Hesperian Rivers on Mars. J. Geophys. Res. Planets 124, 1913–1934. https://doi.org/10.1029/2019JE005976

Debye, P., Hückel, E., 1923. De la theorie des electrolytes. I. abaissement du point de congelation et phenomenes associes. Physikalische Zeitschrift 24, 185–206.

Delany, J.M., Lundeen, S.R., 1991. The LLNL thermochemical data base--revised data and file format for the EQ3/6 package. Lawrence Livermore National Lab., CA (United States). Vancouver.

Edwards, C.S., Ehlmann, B.L., 2015. Carbon sequestration on Mars. Geology 43, 863–866. https://doi.org/10.1130/G36983.1

Edwards, P.H., Bridges, J.C., Wiens, R., Anderson, R., Dyar, D., Fisk, M., Thompson, L., Gasda, P., Filiberto, J., Schwenzer, S.P., Blaney, D., Hutchinson, I., 2017. Basalt-trachybasalt samples in Gale Crater, Mars. Meteorit Planet Sci. https://doi.org/10.1111/maps.12953

Ehlmann, B.L., Bish, D.L., Ruff, S.W., Mustard, J.F., 2012. Mineralogy and chemistry of altered Icelandic basalts: Application to clay mineral detection and understanding aqueous environments on Mars: CLAY MINERAL DETECTION, ICELANDIC BASALT. J. Geophys. Res. 117, n/a-n/a. https://doi.org/10.1029/2012JE004156

Ehlmann, B.L., Mustard, J.F., Murchie, S.L., 2010. Geologic setting of serpentine deposits on Mars: SERPENTINE ON MARS. Geophys. Res. Lett. 37, n/a-n/a. https://doi.org/10.1029/2010GL042596

Ehlmann, B.L., Mustard, J.F., Murchie, S.L., Poulet, F., Bishop, J.L., Brown, A.J., Calvin, W.M., Clark, R.N., Marais, D.J.D., Milliken, R.E., Roach, L.H., Roush, T.L., Swayze, G.A., Wray, J.J., 2008. Orbital Identification of Carbonate-Bearing Rocks on Mars. Science 322, 1828–1832. https://doi.org/10.1126/science.1164759

Ehlmann, B.L., Mustard, J.F., Swayze, G.A., Clark, R.N., Bishop, J.L., Poulet, F., Des Marais, D.J., Roach, L.H., Milliken, R.E., Wray, J.J., Barnouin-Jha, O., Murchie, S.L., 2009. Identification of hydrated silicate minerals on Mars using MRO-CRISM: Geologic context near Nili Fossae and implications for aqueous alteration. J. Geophys. Res. 114, E00D08. https://doi.org/10.1029/2009JE003339

Gabriel, T.S.J., Hardgrove, C., Czarnecki, S., Rampe, E.B., Rapin, W., Achilles, C.N., Sullivan, D., Nowicki, S., Thompson, L., Litvak, M., Mitrofanov, I., Downs, R.T., 2018. Water Abundance of Dunes in Gale Crater, Mars From Active Neutron Experiments and Implications for Amorphous Phases. Geophys. Res. Lett. 45. https://doi.org/10.1029/2018GL079045

Gaudin, A., Dehouck, E., Grauby, O., Mangold, N., 2018. Formation of clay minerals on Mars: Insights from long-term experimental weathering of olivine. Icarus 311, 210–223. https://doi.org/10.1016/j.icarus.2018.01.029

Gislason, S.R., Arnórsson, S., 1993. Dissolution of primary basaltic minerals in natural waters: saturation state and kinetics. Chemical Geology 105, 117–135. https://doi.org/10.1016/0009-2541(93)90122-Y

Gislason, S.R., Arnorsson, S., Armannsson, H., 1996. Chemical weathering of basalt in Southwest Iceland; effects of runoff, age of rocks and vegetative/glacial cover. American Journal of Science 296, 837–907. https://doi.org/10.2475/ajs.296.8.837

Gislason, S.R., Oelkers, E.H., 2003. Mechanism, rates, and consequences of basaltic glass dissolution: II. An experimental study of the dissolution rates of basaltic glass as a function of pH and temperature. Geochimica et Cosmochimica Acta 67, 3817–3832. https://doi.org/10.1016/S0016-7037(03)00176-5

Gislason, S.R., Wolff-Boenisch, D., Stefansson, A., Oelkers, E.H., Gunnlaugsson, E., Sigurdardottir, H., Sigfusson, B., Broecker, W.S., Matter, J.M., Stute, M., 2010. Mineral sequestration of carbon dioxide in basalt: A pre-injection overview of the CarbFix project. International Journal of Greenhouse Gas Control 4, 537–545. https://doi.org/10.1016/j.ijggc.2009.11.013

Gleason, J.D., Kring, D.A., Hill, D.H., Boynton, W.V., 1997. Petrography and bulk chemistry of Martian orthopyroxenite ALH84001: Implications for the origin of secondary carbonates. Geochimica et Cosmochimica Acta 61, 3503–3512. https://doi.org/10.1016/S0016-7037(97)00173-7

Goldich, S.S., 1938. A study in rock-weathering. *The Journal of Geology*, *46*(1), pp.17-58.

Goosens, H., De Leeuw, J.W., Irene, W., Rijpstra, C., Meyburg, G.J., Schenck, P.A., 1989. Lipids and their mode of occurrence in bacteria and sediments—I.A methodological study of the lipid composition of Acinetobacter calcoaceticus LMD 79-41. Organic Geochemistry 14, 15–25. https://doi.org/10.1016/0146-6380(89)90015-6

Gysi, A.P., Stefánsson, A., 2012. CO2-water–basalt interaction. Low temperature experiments and implications for CO2 sequestration into basalts. Geochimica et Cosmochimica Acta 81, 129–152. https://doi.org/10.1016/j.gca.2011.12.012

Gysi, A.P., Stefánsson, A., 2011. CO2–water–basalt interaction. Numerical simulation of low temperature CO2 sequestration into basalts. Geochimica et Cosmochimica Acta 75, 4728–4751. https://doi.org/10.1016/j.gca.2011.05.037

Hangx, S.J.T., Spiers, C.J., 2009. Reaction of plagioclase feldspars with CO2 under hydrothermal conditions. Chemical Geology 265, 88–98. https://doi.org/10.1016/j.chemgeo.2008.12.005

Hartmann, W.K., Neukum, G., 2001. Cratering Chronology and the Evolution of Mars, in: Chronology and Evolution of Mars, Space Sciences Series of ISSI. Springer, Dordrecht, pp. 165–194. https://doi.org/10.1007/978-94-017-1035-0_6

Hausrath, E.M., Brantley, S.L., 2010. Basalt and olivine dissolution under cold, salty, and acidic conditions: What can we learn about recent aqueous weathering on Mars? J. Geophys. Res. 115, E12001. https://doi.org/10.1029/2010JE003610

Hearne, P., 1990. 16. Geochemistry of Rock-Water Reactions in Basalt Aquifers of the Columbia River Plateau, in: Proceedings of a US Geological Survey Workshop on Environmental Geochemistry.

Helgeson, H.C., Kirkham, D.H., 1974. Theoretical prediction of the thermodynamic behavior of aqueous electrolytes at high pressures and temperatures; II, Debye-Huckel parameters for activity coefficients and relative partial molal properties. American Journal of Science 274, 1199–1261. https://doi.org/10.2475/ajs.274.10.1199

Helgeson, H.C., Kirkham, D.H., Flower, G., 1981. Theoretical prediction of the thermodynamic behavior of aqueous electrolytes by high pressures and temperatures; IV, Calculation of activity coefficients, osmotic coefficients, and apparent molal and standard and relative partial molal properties to 600 degrees C and 5kb. American Journal of Science 281, 1249–1516.

Higgins, S.R., 1998. In-Situ Observation of Oxide and Silicate Mineral Dissolution by Hydrothermal Scanning Force Microscopy: Initial Results for Hematite and Albite. Mineralogical Magazine 62A, 618–619. https://doi.org/10.1180/minmag.1998.62A.1.326

Hildebrand, A.R., Penfield, G.T., Kring, D.A., Pilkington, M., Camargo Z., A., Jacobsen, S.B., Boynton, W.V., 1991. Chicxulub Crater: A possible Cretaceous/Tertiary boundary impact

crater on the Yucatán Peninsula, Mexico. Geology 19, 867–871. https://doi.org/10.1130/0091-7613(1991)019<0867:CCAPCT>2.3.CO;2

Hobbs, K.M., Parrish, J.T., 2016. Miocene global change recorded in Columbia River basalt–hosted paleosols. Geological Society of America Bulletin 128, 1543–1554. https://doi.org/10.1130/B31437.1

Hooper, P.R., 1982. The Columbia River Basalts. Science 215, 1463–1468. https://doi.org/10.1126/science.215.4539.1463

Humphris, S.E., Thompson, G., 1978. Trace element mobility during hydrothermal alteration of oceanic basalts. Geochimica et Cosmochimica Acta 42, 127–136. https://doi.org/10.1016/0016-7037(78)90222-3

Inskeep, W.P., Nater, E.A., Bloom, P.R., Vandervoort, D.S., Erich, M.S., 1991. Characterization of laboratory weathered labradorite surfaces using X-ray photoelectron spectroscopy and transmission electron microscopy. Geochimica et Cosmochimica Acta 55, 787–800. https://doi.org/10.1016/0016-7037(91)90342-3

Jiang, C.Z., Tosca, N.J., 2019. Fe(II)-carbonate precipitation kinetics and the chemistry of anoxic ferruginous seawater. Earth and Planetary Science Letters 506, 231–242. https://doi.org/10.1016/j.epsl.2018.11.010

Jordan, G., Higgins, S.R., Eggleston, C.M., Swapp, S.M., Janney, D.E., Knauss, K.G., 1999. Acidic dissolution of plagioclase: in-situ observations by hydrothermal atomic force microscopy. Geochimica et Cosmochimica Acta 63, 3183–3191. https://doi.org/10.1016/S0016-7037(99)00225-2

Keszthelyi, L., McEwen, A.S., Thordarson, T., 2000. Terrestrial analogs and thermal models for Martian flood lavas. J. Geophys. Res. 105, 15027–15049. https://doi.org/10.1029/1999JE001191

Kite, E.S., Mayer, D.P., Wilson, S.A., Davis, J.M., Lucas, A.S., Stucky de Quay, G., 2019. Persistence of intense, climate-driven runoff late in Mars history. Sci. Adv. 5, eaav7710. https://doi.org/10.1126/sciadv.aav7710

Kobayashi, M., Sawada, A., Tani, Y., Soma, M., Tanaka, A., Honma, T., Seyama, H., Theng, B.K.G., 2001. Acid Dissolution of Olivines, Feldspars and Dunite. Water, Air, and Soil Pollution 130, 757–762. https://doi.org/10.1023/A:1013845804654

Lee, M.R., Chatzitheodoridis, E., 2016. Replacement of glass in the Nakhla meteorite by berthierine: Implications for understanding the origins of aluminum-rich phyllosilicates on Mars. Meteorit Planet Sci 51, 1643–1653. https://doi.org/10.1111/maps.12687

Lonker, S.W., Franzson, H., Kristmannsdottir, H., 1993. Mineral-fluid interactions in the Reykjanes and Svartsengi geothermal systems, Iceland. American Journal of Science 293, 605–670. https://doi.org/10.2475/ajs.293.7.605

Malin, M.C., Edgett, K.S., 2000. Sedimentary Rocks of Early Mars. Science 290, 1927–1937. https://doi.org/10.1126/science.290.5498.1927

Mandon, L., Quantin-Nataf, C., Thollot, P., Mangold, N., Lozac'h, L., Dromart, G., Beck, P., Dehouck, E., Breton, S., Millot, C., Volat, M., 2020. Refining the age, emplacement and alteration scenarios of the olivine-rich unit in the Nili Fossae region, Mars. Icarus 336, 113436. https://doi.org/10.1016/j.icarus.2019.113436

Marti, K., Kim, J., Thakur, A., McCoy, T., Keil, K., 1995. Signatures of the martian atmosphere in glass of the Zagami meteorite. Science 267, 1981–1984. https://doi.org/10.1126/science.7701319

McCarthy, T.S., Erlank, A.J., Willis, J.P., Ahrens, L.H., 1974. NEW CHEMICAL ANALYSES OF SIX ACHONDRITES AND ONE CHONDRITE. Meteoritics 9, 215–221. https://doi.org/10.1111/j.1945-5100.1974.tb00077.x

McCollom, T.M., Hynek, B.M., Rogers, K., Moskowitz, B., Berquó, T.S., 2013. Chemical and mineralogical trends during acid-sulfate alteration of pyroclastic basalt at Cerro Negro

volcano and implications for early Mars: ACID-SULFATE ALTERATION OF BASALT. J. Geophys. Res. Planets 118, 1719–1751. https://doi.org/10.1002/jgre.20114

McGrail, B.P., Schaef, H.T., Ho, A.M., Chien, Y.-J., Dooley, J.J., Davidson, C.L., 2006. Potential for carbon dioxide sequestration in flood basalts: SEQUESTRATION IN FLOOD BASALTS. J. Geophys. Res. 111, n/a-n/a. https://doi.org/10.1029/2005JB004169

McLennan, S.M., Grotzinger, J.P., Hurowitz, J.A., Tosca, N.J., 2019. The Sedimentary Cycle on Early Mars. Annu. Rev. Earth Planet. Sci. 47, 91–118. https://doi.org/10.1146/annurev-earth-053018-060332

McSween, H.Y., 2004. Basaltic Rocks Analyzed by the Spirit Rover in Gusev Crater. Science 305, 842–845. https://doi.org/10.1126/science.3050842

McSween, H.Y., Wyatt, M.B., Gellert, R., Bell, J.F., Morris, R.V., Herkenhoff, K.E., Crumpler, L.S., Milam, K.A., Stockstill, K.R., Tornabene, L.L., Arvidson, R.E., Bartlett, P., Blaney, D., Cabrol, N.A., Christensen, P.R., Clark, B.C., Crisp, J.A., Des Marais, D.J., Economou, T., Farmer, J.D., Farrand, W., Ghosh, A., Golombek, M., Gorevan, S., Greeley, R., Hamilton, V.E., Johnson, J.R., Joliff, B.L., Klingelhöfer, G., Knudson, A.T., McLennan, S., Ming, D., Moersch, J.E., Rieder, R., Ruff, S.W., Schröder, C., de Souza, P.A., Squyres, S.W., Wänke, H., Wang, A., Yen, A., Zipfel, J., 2006. Characterization and petrologic interpretation of olivine-rich basalts at Gusev Crater, Mars: OLIVINE-RICH BASALTS AT GUSEV CRATER, MARS. J. Geophys. Res. 111, n/a-n/a. https://doi.org/10.1029/2005JE002477

Michalski, J., Kraft, M., Sharp, T., Christensen, P., 2006. Effects of chemical weathering on infrared spectra of Columbia River Basalt and spectral interpretations of martian alteration. Earth and Planetary Science Letters 248, 822–829. https://doi.org/10.1016/j.epsl.2006.06.034

Michalski, J.R., Cuadros, J., Bishop, J.L., Darby Dyar, M., Dekov, V., Fiore, S., 2015. Constraints on the crystal-chemistry of Fe/Mg-rich smectitic clays on Mars and links to global

alteration trends. Earth and Planetary Science Letters 427, 215–225. https://doi.org/10.1016/j.epsl.2015.06.020

Michalski, J.R., Niles, P.B., 2010. Deep crustal carbonate rocks exposed by meteor impact on Mars. Nature Geosci 3, 751–755. https://doi.org/10.1038/ngeo971

Migoń, P., Lidmar-Bergström, K., 2002. Deep weathering through time in central and northwestern Europe: problems of dating and interpretation of geological record. CATENA 49, 25–40. https://doi.org/10.1016/S0341-8162(02)00015-2

Milam, K.A., McSween, H.Y., Moersch, J., Christensen, P.R., 2010. Distribution and variation of plagioclase compositions on Mars. J. Geophys. Res. 115, E09004. https://doi.org/10.1029/2009JE003495

Miller, H.M., Matter, J.M., Kelemen, P., Ellison, E.T., Conrad, M.E., Fierer, N., Ruchala, T., Tominaga, M., Templeton, A.S., 2016. Modern water/rock reactions in Oman hyperalkaline peridotite aquifers and implications for microbial habitability. Geochimica et Cosmochimica Acta 179, 217–241. https://doi.org/10.1016/j.gca.2016.01.033

Morris, R.V., Klingelhöfer, G., Schröder, C., Rodionov, D.S., Yen, A., Ming, D.W., de Souza, P.A., Fleischer, I., Wdowiak, T., Gellert, R., Bernhardt, B., Evlanov, E.N., Zubkov, B., Foh, J., Bonnes, U., Kankeleit, E., Gütlich, P., Renz, F., Squyres, S.W., Arvidson, R.E., 2006. Mössbauer mineralogy of rock, soil, and dust at Gusev crater, Mars: Spirit's journey through weakly altered olivine basalt on the plains and pervasively altered basalt in the Columbia Hills: MÖSSBAUER MINERALOGY AT GUSEV CRATER, MARS. J. Geophys. Res. 111, n/a-n/a. https://doi.org/10.1029/2005JE002584

Munz, I.A., Brandvoll, Ø., Haug, T.A., Iden, K., Smeets, R., Kihle, J., Johansen, H., 2012. Mechanisms and rates of plagioclase carbonation reactions. Geochimica et Cosmochimica Acta 77, 27–51. https://doi.org/10.1016/j.gca.2011.10.036

Neal, C., Stanger, G., 1983. Hydrogen generation from mantle source rocks in Oman. Earth and Planetary Science Letters 66, 315–320. https://doi.org/10.1016/0012-821X(83)90144-9

Nesbitt, H.W., Skinner, W.M., 2001. Early development of Al, Ca, and Na compositional gradients in labradorite leached in pH 2 HCl solutions. Geochimica et Cosmochimica Acta 65, 715–727. https://doi.org/10.1016/S0016-7037(00)00530-5

Neuhoff, P.S., 1999. Porosity evolution and mineral paragenesis during low-grade metamorphism of basaltic lavas at Teigarhorn, eastern Iceland. American Journal of Science 299, 467–501. https://doi.org/10.2475/ajs.299.6.467

Niles, P.B., Catling, D.C., Berger, G., Chassefière, E., Ehlmann, B.L., Michalski, J.R., Morris, R., Ruff, S.W., Sutter, B., 2013. Geochemistry of Carbonates on Mars: Implications for Climate History and Nature of Aqueous Environments. Space Sci Rev 174, 301–328. https://doi.org/10.1007/s11214-012-9940-y

Niles, P.B., Zolotov, M.Yu., Leshin, L.A., 2009. Insights into the formation of Fe- and Mg-rich aqueous solutions on early Mars provided by the ALH 84001 carbonates. Earth and Planetary Science Letters 286, 122–130. https://doi.org/10.1016/j.epsl.2009.06.039

Nugent, M.A., Brantley, S.L., Pantano, C.G., Maurice, P.A., 1998. The influence of natural mineral coatings on feldspar weathering. Nature 395, 588–591. https://doi.org/10.1038/26951

Oelkers, E.H., Gislason, S.R., 2001. The mechanism, rates and consequences of basaltic glass dissolution: I. An experimental study of the dissolution rates of basaltic glass as a function of aqueous Al, Si and oxalic acid concentration at 25°C and pH = 3 and 11. Geochimica et Cosmochimica Acta 65, 3671–3681. https://doi.org/10.1016/S0016-7037(01)00664-0

Oelkers, E.H., Schott, J., 1995. Experimental study of anorthite dissolution and the relative mechanism of feldspar hydrolysis. Geochimica et Cosmochimica Acta 59, 5039–5053. https://doi.org/10.1016/0016-7037(95)00326-6

Parnell, J., McMahon, S., Blamey, N.J.F., Hutchinson, I.B., Harris, L.V., Ingley, R., Edwards, H.G.M., Lynch, E., Feely, M., 2014. Detection of reduced carbon in a basalt analogue for martian nakhlite: a signpost to habitat on Mars. International Journal of Astrobiology 13, 124–131. https://doi.org/10.1017/S1473550413000360

Peretyazhko, T.S., Sutter, B., Morris, R.V., Agresti, D.G., Le, L., Ming, D.W., 2016. Fe/Mg smectite formation under acidic conditions on early Mars. Geochimica et Cosmochimica Acta 173, 37–49. https://doi.org/10.1016/j.gca.2015.10.012

Reidel, S.P., Camp, V.E., Tolan, T.L., Martin, B.S., Ross, M.E., Wolff, J.A. and Wells, R.E., 2013. The Columbia River flood basalt province: Stratigraphy, areal extent, volume, and physical volcanology. *The Columbia River flood basalt province: geological society of America special paper*, *497*, pp.1-43.

Schaef, H.T., McGrail, B.P., Owen, A.T., 2011. Basalt Reactivity Variability with Reservoir Depth in Supercritical CO2 and Aqueous Phases. Energy Procedia 4, 4977–4984. https://doi.org/10.1016/j.egypro.2011.02.468

Schaef, H.T., McGrail, B.P., Owen, A.T., 2010. Carbonate mineralization of volcanic province basalts. International Journal of Greenhouse Gas Control 4, 249–261. https://doi.org/10.1016/j.ijggc.2009.10.009

Schaef, T.H., McGrail, B.P., 2009. Dissolution of Columbia River Basalt under mildly acidic conditions as a function of temperature: Experimental results relevant to the geological sequestration of carbon dioxide. Applied Geochemistry 24, 980–987. https://doi.org/10.1016/j.apgeochem.2009.02.025

Sigurdsson, F., Ingimarsson, J., 1990. The permeability of Icelandic rocks. The Water and the Land. Reykjavik, National Energy Authority.

Squyres, S.W., Grotzinger, J.P., Arvidson, R.E., Bell, J.F., Calvin, W., Christensen, P.R., Clark, B.C., Crisp, J.A., Farrand, W.H., Herkenhoff, K.E., Johnson, J.R., Klingelhöfer, G., Knoll, A.H., McLennan, S.M., McSween, H.Y., Morris, R.V., Rice, J.W., Rieder, R., Soderblom, L.A., 2004. In Situ Evidence for an Ancient Aqueous Environment at Meridiani Planum, Mars. Science 306, 1709–1714. https://doi.org/10.1126/science.1104559

Squyres, S.W., Knoll, A.H., 2005. Sedimentary rocks at Meridiani Planum: Origin, diagenesis, and implications for life on Mars. Earth and Planetary Science Letters 240, 1–10. https://doi.org/10.1016/j.epsl.2005.09.038

Stefansson, A., Gislason, S.R., 2001. Chemical weathering of basalts, southwest Iceland: effect of rock crystallinity and secondary minerals on chemical fluxes to the ocean. American Journal of Science 301, 513–556. https://doi.org/10.2475/ajs.301.6.513

Stevens, T.O., McKinley, J.P., 2000. Abiotic Controls on H2 Production from Basalt−Water Reactions and Implications for Aquifer Biogeochemistry. Environ. Sci. Technol. 34, 826–831. https://doi.org/10.1021/es990583g

Stillings, L.L., Brantley, S.L., 1995. Feldspar dissolution at 25°C and pH 3: Reaction stoichiometry and the effect of cations. Geochimica et Cosmochimica Acta 59, 1483–1496. https://doi.org/10.1016/0016-7037(95)00057-7

Suzuki, M., Tagai, T., Hoshi, T., Tsukimura, K., 1996. Dissolution process and rate in feldspar: Effects of crystallographic orientation. Mineralogical Journal 18, 43–53. https://doi.org/10.2465/minerj.18.43

Taylor, S.R., McLennan, S.M., 2009. Planetary crusts: their composition, origin and evolution, Cambridge planetary science. Cambridge University Press, Cambridge, UK ; New York.

Thompson, L.M., Schmidt, M.E., Spray, J.G., Berger, J.A., Fairén, A.G., Campbell, J.L., Perrett, G.M., Boyd, N., Gellert, R., Pradler, I., VanBommel, S.J., 2016. Potassium-rich sandstones within the Gale impact crater, Mars: The APXS perspective: Potassium-Rich Sandstones on Mars. J. Geophys. Res. Planets 121, 1981–2003. https://doi.org/10.1002/2016JE005055

Thomson, B.J., Hurowitz, J.A., Baker, L.L., Bridges, N.T., Lennon, A.M., Paulsen, G., Zacny, K., 2014. The effects of weathering on the strength and chemistry of Columbia River Basalts and their implications for Mars Exploration Rover Rock Abrasion Tool (RAT) results.

Earth and Planetary Science Letters 400, 130–144. https://doi.org/10.1016/j.epsl.2014.05.012

Thorseth, I.H., Furnes, H., Heldal, M., 1992. The importance of microbiological activity in the alteration of natural basaltic glass. Geochimica et Cosmochimica Acta 56, 845–850. https://doi.org/10.1016/0016-7037(92)90104-Q

Tosca, N.J., Ahmed, I.A.M., Tutolo, B.M., Ashpitel, A., Hurowitz, J.A., 2018. Magnetite authigenesis and the warming of early Mars. Nature Geoscience 11, 635–639. https://doi.org/10.1038/s41561-018-0203-8

Tosca, N.J., Guggenheim, S., Pufahl, P.K., 2016. An authigenic origin for Precambrian greenalite: Implications for iron formation and the chemistry of ancient seawater. Geological Society of America Bulletin 128, 511–530. https://doi.org/10.1130/B31339.1

Treiman, A.H., Bish, D.L., Vaniman, D.T., Chipera, S.J., Blake, D.F., Ming, D.W., Morris, R.V., Bristow, T.F., Morrison, S.M., Baker, M.B., Rampe, E.B., Downs, R.T., Filiberto, J., Glazner, A.F., Gellert, R., Thompson, L.M., Schmidt, M.E., Le Deit, L., Wiens, R.C., McAdam, A.C., Achilles, C.N., Edgett, K.S., Farmer, J.D., Fendrich, K.V., Grotzinger, J.P., Gupta, S., Morookian, J.M., Newcombe, M.E., Rice, M.S., Spray, J.G., Stolper, E.M., Sumner, D.Y., Vasavada, A.R., Yen, A.S., 2016. Mineralogy, provenance, and diagenesis of a potassic basaltic sandstone on Mars: CheMin X-ray diffraction of the Windjana sample (Kimberley area, Gale Crater). J. Geophys. Res. Planets 121, 75–106. https://doi.org/10.1002/2015JE004932

van Berk, W., Fu, Y., 2011. Reproducing hydrogeochemical conditions triggering the formation of carbonate and phyllosilicate alteration mineral assemblages on Mars (Nili Fossae region). J. Geophys. Res. 116, E10006. https://doi.org/10.1029/2011JE003886

Viles, H., Ehlmann, B., Wilson, C.F., Cebula, T., Page, M., Bourke, M., 2010. Simulating weathering of basalt on Mars and Earth by thermal cycling: THERMAL WEATHERING

ON MARS AND EARTH. Geophys. Res. Lett. 37, n/a-n/a. https://doi.org/10.1029/2010GL043522

Wang, A., Korotev, R., Jolliff, B.L., Haskin, L., Crumpler, L., Farrand, W., Herkenhoff, K.E., de Souza, P.A., Kusak, A., Hurowitz, J.A., Tosca, N.J., 2006. Evidence of phyllosilicates in Wooly Patch, an altered rock encountered at West Spur, Columbia Hills, by the Spirit rover in Gusev crater, Mars. ournal of Geophysical Research: Planets 11.

Wogelius, R.A., Walther, J.V., 1992. Olivine dissolution kinetics at near-surface conditions. Chemical Geology 97, 101–112. https://doi.org/10.1016/0009-2541(92)90138-U

Wollast, R., Chou, L., 1992. Surface reactions during the early stages of weathering of albite. Geochimica et Cosmochimica Acta 56, 3113–3121. https://doi.org/10.1016/0016-7037(92)90292-Q

Wray, J.J., Murchie, S.L., Bishop, J.L., Ehlmann, B.L., Milliken, R.E., Wilhelm, M.B., Seelos, K.D., Chojnacki, M., 2016. Orbital evidence for more widespread carbonate-bearing rocks on Mars. Journal of Geophysical Research: Planets 121, 652–677. https://doi.org/10.1002/2015JE004972

Wright, R.J., Simms, L.A., Reynolds, M.A., Bogard, D.D., 1973. Depth variation of cosmogenic noble gases in the ~120-kg Keyes chondrite. J. Geophys. Res. 78, 1308–1318. https://doi.org/10.1029/JB078i008p01308

Wright, S.P., Christensen, P.R., Sharp, T.G., 2011. Laboratory thermal emission spectroscopy of shocked basalt from Lonar Crater, India, and implications for Mars orbital and sample data. J. Geophys. Res. 116, E09006. https://doi.org/10.1029/2010JE003785

Zeebe, R., Wolf-Gladrow, D., 2001. CO2 in Sewater: Equilibrium, Kinetics, Isotopes. Gulf Professional Publishing.

Chapter 5

Carbonation in Hot Martian Environments: Experimental Precipitation of Fe(II)-carbonates at 75 ºC

1. Introduction

In Chapter 3, the use of fayalite and later fayalite and forsterite was introduced as a proxy for the Martian surface in experiments seeking to reproduce the environmental conditions that once enabled carbonate formation. In Chapter 4, the complexity of this material was taken further, and experiments using albite- and quartz-rich Columbia River Basalt (CRB) powder were employed as a means of examining the additional effect of mineral dissolution upon carbonate formation.

For the third and final set of experiments discussed in this thesis, the fayalite, fayalite/forsterite, and CRB experiments were reproduced but conducted at 75 °C, rather than the 25 °C that characterised all previously run experiments. The reason for altering the temperature of the experiments was to observe what effect this has on the carbonate-forming process: Which carbonates are favoured, if any? How does the reactivity of the experiments vary in comparison with their 25 °C equivalents? How does initial substrate dissolution vary? How does pH vary? These questions are relevant to the surface and subsurface of Mars because it has not always been a cold, inactive world: once it was a planet cultivated by volcanism (Phillips et al., 2001; Werner, 2009), resurfaced by impact cratering (Nimmo et al., 2008; Werner, 2008), and with remnant subsurface heat from planetary formation (Parmentier and Zuber, 2007). Carbonates observed on

Mars have been dated as forming within the Noachian (given as ~4.0-3.7 Ga; Hartmann and Neukum, 2001) when potential high-temperature surface and subsurface environments are proposed to be more prevalent (e.g., Carr and Clow, 1981; Bullock and Moore, 2007; Bishop et al., 2008; Brown et al., 2010; Andrews-Hanna and Lewis, 2011; Goudge et al., 2012; Clifford and McCubbin, 2016; Davis et al., 2016). This has rendered such terrains of primary interest for missions to Mars, including the ESA ExoMars rover, which intends to explore Oxia Planum in Arabia Terra, and more pertinently NASA's *Perseverance* rover with the Mars 2020 mission, which intends to explore Jezero Crater of the Nili Fossae. Both of these locations sit within Noachian terrain (Tanaka et al., 2014), and Jezero hosts a possibly extensive carbonate sequence across deltas, alluvial fans, and other units within a crater basin (Bishop et al., 2008; Goudge et al., 2015; Brown et al., 2020; Horgan et al., 2020). As such, investigation is required into the role a heightened surface heat flux compared to today would have exerted upon the carbonate-forming potential of these environments that are both of immediate relevance to the planetary science community and accordingly our understanding of both our planetary neighbour and the operation of water-rich environments on other planets. This forms a major part of the motivation behind this chapter.

Research suggests that the most carbonate-rich outcrop on Mars, the Nili Fossae region (Ehlmann et al., 2008, 2009; Viviano et al., 2013; Edwards and Ehlmann, 2015) may have formed under such elevated temperatures (>75 ºC) around 3.82 ± 0.07 Ga (Mandon et al., 2020), adding this region to a wide range of locations on Mars where such mineralogy has been discussed (e.g., (Michalski and Niles, 2010; Morris et al., 2010). The region, rich in the magnesium carbonate magnesite as seen with the Compact Reconnaissance Imaging Spectrometer for Mars (CRISM), has been speculated to have formed by the aqueous alteration of olivine-rich rocks either by hydrothermal fluid intrusion or the percolation of near-surface water (Mustard et al., 2008; Ehlmann et al., 2008, 2009). These warm waters, heated from magmatic activity or impact crater formation (such as the Isidis basin; Ehlmann et al., 2011; Bultel et al., 2015), were likely neutral to alkaline based on the co-occurrence of clays alongside the carbonates (Ehlmann et al., 2008;

Viviano et al., 2013). These are conditions that have also been speculated as occurring in other zones corresponding to ancient Noachian terrain, often impact craters (e.g., (Michalski and Niles, 2010; Michalski et al., 2013, 2019; Wray et al., 2016). Such environments often contain non-carbonate minerals indicative of high temperatures such as serpentine (Poulet et al., 2008; Ehlmann et al., 2009); serpentine is also common alongside carbonates within Martian meteorites such as the Nakhlites (Mittlefehldt, 1994; Bridges et al., 2001; Halevy et al., 2011). This suggests at least some portion of the carbonates found on Mars formed under elevated temperatures, consistent with isolated outcrops that may have been uplifted from depths of up to 6 km (Michalski and Niles, 2010) and formed under the influence of a geothermal gradient. The consistent co-occurrence of Fe/Mg carbonates and phyllosilicates across such areas as Nili Fossae could suggest several co-occurring environmental conditions and/or mechanisms including low grade metamorphic or hydrothermal alteration in neutral to alkaline conditions (Bishop et al., 2008; Ehlmann et al., 2009), low rock:waterrock:water ratio serpentinisation (Brown et al., 2010; Klein et al., 2013), or carbonatization (Viviano et al., 2013). However, as was noted in the previous chapter, a negative correlation between carbonates and clays has also been noted by Ehlmann et al. (2012) and Michalski et al. (2015). There is clearly an important link — a correlation or anti-correlation — between the formation of clays and of carbonates on Mars, one that has been observed and noted but the mechanisms behind it not clearly discussed.

McSween (2004) suggested that at hydrothermal alteration temperatures of below ~350 °C, clays such as serpentine are favoured where low pCO_2 activity (0.1 bar) occurs. Higher pCO_2 activity, by comparison, tends to produce large amounts of carbonate as has been observed on Earth (e.g., Mora et al., 1996; Hänchen et al., 2008). The phyllosilicate greenalite ($Fe_3Si_2O_5(OH)_4$) has also been hypothesised to form under elevated temperatures (e.g., Tutolo et al., 2019; Rasmussen et al., 2020); what role such clays have to play in the formation of carbonates, whether as competitors, co-precipitates, or otherwise, remains an open topic of debate.

Thus, while there is a variety of geological evidence suggesting carbonate formation may have occurred at elevated temperatures, the scientific community's general understanding of the geochemical processes and products of anoxic aqueous alteration at elevated temperature are limited in their investigations. Previous work through modelling studies (e.g., Griffith and Shock, 1995; van Berk and Fu, 2011; van Berk et al., 2012) has researched this, but there are limited amounts of experimental constraints that research the kinetics driving the reactivity of these systems. This, alongside the role of phyllosilicate formation under such conditions, is the focus of this study.

1.1. Carbonate formation at hydrothermal temperatures

There is a substantial body of literature regarding the propensity for Mg-carbonates to form under conditions reflecting hydrothermal input (e.g., Graf and Goldsmith, 1956; Bischoff and Seyfried, 1978; Ludwig et al., 2006; Benezeth et al., 2013; Lafay et al., 2014) and this is relevant for discussion relating to Mars because Jezero Crater, within which the Mars 2020 rover will touchdown, is sited within the most Mg-carbonate-rich area on Mars (Edwards and Ehlmann, 2015). A discussion of Fe versus Mg carbonates, in addition, is also relevant because these are known to form under differing conditions, including low temperature, CO_2 saturated environments and low rock:waterrock:water ratio interactions for siderite, and water-rich hydrothermal settings or low temperature, CO_2 saturated environments for magnesite (e.g., Jimenez-Lopez and Romanek, 2004; Giammar et al., 2005; Saldi et al., 2009; Felmy et al., 2012; Qafoku et al., 2012). Therefore, the presence of either of these carbonates reflects such differing environments. Giammar et al. (2005) found that critical nucleation of magnesite occurred only at 95 °C and at 100 bar pCO_2, while Garcia et al. (2010) noted the complete conversion to magnesite of their olivine over eight weeks at 150 °C and 150 bars pCO_2. Additionally, Saldi et al. (2009) noted, consistent with earlier studies (Lippmann, 1973; Pokrovsky and Schott, 2000), that magnesite growth at ambient temperatures is limited by extremely slow step advancement rates, which are accelerated by increased salinity, CO_2

partial pressure, or temperature. The presence of Mg-carbonates on Mars has accordingly been widely attributed as representing localised hydrothermal conditions induced by impact, volcanism, or burial within the subsurface and heated by the planetary geotherm. This is despite the fact that Mg-carbonates do also form at low temperature: weathering of serpentinites (Oskierski et al., 2013) and precipitation from alkaline lakes (Thompson and Ferris, 1990) are alternate means of Mg-carbonate formation that have been well-documented. None of these are likely relevant on a large scale to Mars, however: while serpentine has been detected on Mars in association with magnesite (e.g., Ehlmann et al., 2008, 2010; Leask et al., 2018), only several sites have been confirmed (Lin et al., 2020).

Compared to Mg-carbonate formation at both low and high temperature, less is equivalently known about Fe-carbonate formation. While the earlier chapters of this thesis sought to address its low temperature formation, at high temperature there is only limited literature assessing this under conditions relevant to environments likely to occur at planetary surfaces and near-surfaces: Qafoku et al. (2012) were able to synthesise siderite at 35-80 °C over 85 days (the maximum conducted in this thesis), but this was under 90 bars pCO_2 (in contrast to the 1 bar used in this study — see below). Other studies, such as Kaszuba et al. (2005) synthesised siderite under 200 °C and 200 bar experiments. These >1 bar pressures are unrealistic amounts of surface of CO_2 either for the Martian surface or near-subsurface based on multiple corroborating lines of evidence including isotopic (Jakosky et al., 2018), geomorphologic (Kite et al., 2014; Warren et al., 2019), climatic modelling (Wordsworth et al., 2017), and others. Higher partial pressures of CO_2 may be obtained in some hydrothermal/magmatic systems that do not reflect equilibration with the atmosphere, but this chapter seeks to address the lack of lower pressure experimental data by investigating anoxic water-rock interaction at pCO_2 of no higher than 1 bar under temperatures above those characterising near-surface environments. Reactants of fayalite, fayalite/forsterite, and CRB are used, as in Chapters 3 and 4, but within solutions under hydrothermal conditions of 75 °C with at maximum 1.0 bar pCO_2. This is to investigate the ability of carbonates to form under

temperatures and CO_2 pressures relevant and realistic to both the Martian surface and near-subsurface (<10 km), and to assess to what degree the carbonates identified on Mars were formed under hydrothermal versus ambient conditions.

2. Materials and methods

2.1. The experiments

The experiments listed in Table 1 were conducted at 75 °C, all of which had been run under identical conditions but at 25 ºC in Chapter 3 (Kissick et al., 2021) and Chapter 4 (CRB at low temperature chapter), and discussed in Appendix 1: (1) fayalite-bearing for 10 days (equivalents to experiments 180313 and 180406 of Chapter 3); (2) fayalite- and forsterite-bearing in a 1:1 ratio mixture (as forsterite numbers for surface olivine on Mars tends to be ~30-60; Christensen et al., 2001; Brown et al., 2020; although it has been identified as up to ~77 from meteorites; Dreibus and Wanke, 1985) for 10 days (equivalent to experiment 180829 of Chapter 3); and (3) fine and coarse CRB-bearing for 10 days (equivalent to experiments 190807 and 190808). All were run at high (1:500) rock:water ratio. Two additional experiments were also set up investigating the effect of low rock:water ratio (1:1 and 1:10) on fayalite and fayalite/forsterite reaction at high temperature, but the experimental set-ups unfortunately failed due to a rupturing of the acrylic syringes used as reaction vessels at high temperature.

Experiment 191028 involved 8 sub-experiments of pure fayalite run at a 1:500 rock:water ratio under initial pHs of 2 and 4, and pCO_2 of 0, 0.1, 0.5, and 1.0 bars. The 0 bar experiments were a replication of the 180123 series as a control where no carbonates were anticipated to form due to the absence of CO_2.

Experiment 191107 involved 6 sub-experiments a 1:1 ratio mix of fayalite and forsterite run under a 1:500 rock:water ratio, with initial pHs of 2 and 4 and pCO_2 pressures of 0.1, 0.5, and 1.0 bar as a repeat of the three categories of CO_2 used in Chapter 3.

Experiment 191118 involved 12 sub-experiments that reacted both coarse and fine CRB at 1:500 rock:water ratios under initial pHs of 2 and 4 and pCO_2 of 0, 0.5, 1.0 bars. Experiment 191118 that used coarse CRB begun under pH 4 with no CO_2 present was terminated 7 days in owing to a pressure loss and subsequent evaporation that rendered the experimental setup entirely different and non-representative from its starting conditions. This was unable to be replicated due to time constraints. Unfortunately, the 0 bar pCO_2 experiments were misplaced between experimentation and analysis, whereby they disappeared from the lab during a several-month delay between sampling and analysis, and could not be studied for elemental composition.

Table 1 summarises the names and characteristics of the five categories of experiments run for this chapter, of which only the three successful ones will be discussed further. A total of 26 successful sub-experiments are described in this chapter (excluding the additional 8 that did not reach completion). These are outlined in Table 1.

Only 10-day experiments were run owing to time constraints.

The set-up of these experiments followed that previously documented in Chapter 2 (Methods); where not otherwise stated, the experimental set-up remained unchanged. pH and ORP were again measured at regular intervals following the extraction of a sample, and this was within several minutes of the sample being removed from the oven. Temperature was not measured at the same time. The samples were cooled to room temperature by the point of their dilution into a beaker containing nitric acid for storage; this vial was then transferred to a chiller for long-term storage prior to later analyses. The defining difference for the experiments discussed here was the use of a small oven kept at 75 °C within the glove box, into which all experiments were placed upon the addition of solid substrate to fluid. No orbital shaker was available for the experiments in this chapter owing to a lack of space or facilities within the oven; the beakers were instead shaken regularly and rigorously by hand once a day in between sampling. 'By hand' in this case refers to taking the flask by the lid and rigorously twisting the hand in a motion that shook

the contents thoroughly. As with all experiments prior, conditions were kept strictly anoxic. All experiments were sampled once per day for ten days without interruption.

2.2. The model

A reaction path model was set up using *The Geochemist's Workbench* (Bethke, 2017) in a recreation of that used in Chapter 4, thoroughly described in section 2.2 of this chapter with differences outlined below. For the fayalite-bearing model, pure fayalite was added, and its components of Fe^{2+} and SiO_2 available for reaction in the model; for forsterite, this included reactants of fayalite and forsterite in a 1:1 component, with Fe^{2+}, SiO_2, and Mg^{2+} available; for the CRB model, the reader is referred to Table 4 and Table 5 from Chapter 4 that show the percentage of mineral type added as reactants to represent the CRB, and also show the typical set-up for the ionic components of the reactants.

Several key differences were made to the model. As fayalite, fayalite and forsterite, and CRB were all used for this chapter, the mineralogy used in the Chapter 4 model was replaced with these three reactants, run individually. The dissolution rate constant used for fayalite and forsterite was 2.34×10^{-11} mol/cm^2/s (Bandstra and Brantley, 2008), and for CRB it was 3.975×10^{-12} mol/cm^2/s. This latter value was calculated from the experiments of Schaef and McGrail (2009) that were conducted under a range of temperatures (25, 40, 70, 90 °C), and pH (3, 4, 5, 7). For each experiment, the dissolution rate constant was given for Al, Na, Ca, Mg, Fe, and Si. To use a constant that was appropriate for this model, the following were selected: the Si rate (based on the CRB composition used here being >50 wt.% of the CRB); the 70 °C temperature (the closest match to that used in the experiments described here); pH 5 (which was the rough median of pH experienced experimentally over these experiments); and, of these, two rate constants were provided in the Schaaf and McGrail (2009) paper, one for CRB flow top (lava surface) and one from the flow interior; an average was taken of the two. This was calculated at 3.975×10^{-12} mol/cm^2/s.

The models were run for the time it took to reach equilibrium (2 years) and pH was allowed to evolve naturally over their course from a starting value of 3.

3. Results

In this section, the solid and solution results from the three successful CRB experiments (26 sub-experiments) are described and summarised. First a brief description of the results of each experiment is outlined with a summary at the end of each section, before discussing the implications of these results in the context of the Martian surface and subsurface environments in the discussion of section 4.

3.1. Solution chemistry results

As with the two previous data chapters, 10 solution samples were extracted at regular intervals (in this case once per day) and their elemental composition analysed via inductively coupled plasma mass spectrometry (ICP-MS).

3.1.1. pH

Figure 1 shows the pH measurements for all experiments conducted at 75 °C, with 191118 divided into fine and coarse CRB to observe whether changing surface area affects reaction rate. In summary, while several experiments could have benefited from a repeat run to ascertain whether their fluctuating trends are repeatable or anomalous, overall the values of pH reached in only 10 days — especially for the fayalite/forsterite and CRB pH 4 experiments — is striking. Comparative pH for fayalite/forsterite experiments run under 25 °C are roughly similar to slightly higher, e.g. for 190423 Fo, as discussed in Chapter 3, the pH of experiment pH 4 under pCO_2 1.0 bar is 6.4 at 257 hours in; for the equivalent in 191107 at 234 hours, this is 7.0. However, for the CRB experiments run at pH 4 pCO_2 1.0 bar under 25 °C, pH at 234 hours in is 3.9 for fine CRB

and 4.4 for coarse; for 191118, also at the terminal data extraction time of 234 hours, this is 5.3 and 6.3. This suggests heightened reactivity within experiments conducted at 75 °C.

3.1.2. Oxidation reduction potential (ORP)

In Figure 2, ORP amounts are displayed, which reflects the oxidation-reduction state of Fe, where the more positive is the more oxidising, and the more negative is more reducing.

Overall, ORP reflects an inverse trend to those observed for pH. From both, the following may be summarised:

- The fayalite/forsterite-bearing experiments behaved similarly to their lower temperature counterparts in Chapter 3, whereby pH rose more rapidly and to higher amounts than for experiments bearing solely fayalite
- Little reactivity occurred for experiments begun at pH 2 using CRB in experiments 191118
- At pH 4, CRB-bearing experiments experience higher amounts of pH and lower ORP, suggesting a level of reactivity for these experiments not observed for their 25 ºC counterparts.

3.1.3. Fe, Si, and Mg

Figure 3 displays the total concentrations of Fe in solution for each high-temperature experiment as measured via ICP-MS; Figure 4 displays the Si concentrations in solution across the high temperature experiments, as measured by ICP-MS; lastly magnesium, as seen in Figure 5 showing Mg concentrations in solution across the high temperature experiments, is a very minor component of the dissolved elemental solution composition.

To summarise, the key conclusions of elemental concentrations in solution at 75 ºC are:

- An increase in Fe concentrations compared to 25 ºC equivalents
- Experiments begun at pH 2 yield increased concentrations of Fe
- Experiments begun under higher bar of pCO_2 yield increased concentrations of Fe

- Higher concentrations of Si compared to Fe and Mg in CRB-bearing experiments reflect the initial Fe/Mg-poor composition of the CRB type reacted
- Low concentrations of Mg for CRB-bearing experiments reflect low concentrations of Mg in initial source material.

The next section discusses mineral saturation states as determined by the software GWB through inputting the pH and elemental concentrations.

3.1.4. Siderite

Figure 6 displays the calculated siderite supersaturation ($\Omega_{siderite}$) for each experiment, with the CRB-bearing experiment 191118 divided into fine (F) and coarse (C). What is immediately apparent for the four diagrams is how none of the experiments begun at pH 2 (in red) exceed an $\Omega_{siderite}$ of around 5, nor does the pH 4 experiment begun with 0.1 bar pCO_2. Only experiments begun under pH 4 with an initial pCO_2 of 0.5 or 1.0 in some cases reach heightened states of siderite supersaturation.

The repeated and consistent propensity for experiments begun at pH 4 to display the highest $\Omega_{siderite}$ suggests a dependence upon high pH in order for $\Omega_{siderite}$ to rise. This is in line with what was observed for the low temperature experiments of Chapters 3 and 4, where pH and CO_2 concentrations were linked to $\Omega_{siderite}$ supersaturation. The actual values of $\Omega_{siderite}$, however, are lower than the maximum recorded for fayalite-bearing low temperature experiments (Figure 6a: 1,625 $\Omega_{siderite}$) and fayalite/forsterite-bearing (Figure 6b: 3,605 $\Omega_{siderite}$), but these were both recorded after two months; only negligible $\Omega_{siderite}$ was ever recorded at ten days, which was the maximum length of experiment run for this chapter. For siderite, this shows that supersaturation is met far more rapidly when at high temperatures.

3.1.5. Amorphous silica

The trends in Figure 7 showing $\Omega_{amorphous\ silica}$ are very similar to the SiO_2 concentrations in Figure 4, both showing roughly level trends across fayalite and fayalite/forsterite experiments and a slight dip before a further rise for both the fine- and coarse-grained CRB experiments. More

SiO_2 dissolved into solution compared to Fe^{2+} (Figure 3), but this is not reflected in higher saturation states for amorphous silica compared to the Fe(II)-carbonate siderite as seen in Figure 6: amorphous silica saturation states remain modest across all experiments, peaking at 7.3 for the fayalite/forsterite experiment begun at pH 2 under 0.1 bar pCO_2. This may reflect the increasing solubility of silica polymorphs with increasing temperatures.

3.1.6. Magnesite

Magnesite supersaturation trends may be observed in Figure 8. No trend is recorded for the fayalite experiments of 191028 because this experiment did not bear significant quantities of Mg, being solely fayalite-bearing. For the fayalite/forsterite-bearing experiment 191107, $\Omega_{magnesite}$ can be seen to rise to similar amounts to those seen for siderite in Figure 6. Magnesite saturation appears dependent upon pH, more so than pCO_2 because even the pH 2 experiments under 1.0 pCO_2 do not show significant $\Omega_{magnesite}$ across both fayalite/forsterite- and CRB-bearing experiments.

3.1.7. Summary of saturation state calculations

To summarise the mineral saturation state data discussed above:

- $\Omega_{siderite}$ and $\Omega_{magnesite}$ are highly pH dependent and very sensitive to pH fluctuations
- $\Omega_{siderite}$ and $\Omega_{magnesite}$ are secondarily dependent upon pCO_2
- $\Omega_{siderite}$ is increased far more rapidly at 75 ºC than at 25 ºC
- Olivines are more reactive than the CRB, and accordingly tend to reach higher states of saturation for all minerals studied
- Sudden decreases in carbonate saturation states tend to follow pH decreases, but in some cases could represent precipitation.

3.2. Solid results

In this section, the results of all solid material analyses are briefly summarised and their key conclusions discussed in relation to the ability of carbonates to form under Mars-like conditions

at 75 ºC. The analytical methods covered include X-ray diffraction (XRD), Fourier transform infrared spectroscopy (FT-IR), and scanning electron microscopy (SEM).

3.2.1. X-Ray diffraction

Figure 9 contains the XRD spectra for the fayalite-bearing experiments of 191028. Noting the labelled dominant peaks, these peaks themselves correspond to those of the pure fayalite that was the starting material of the experiment. This suggests XRD is unable to detect any measurable change in the solids remaining following experimentation. Two peaks were unable to fit fayalite or any other known spectra confidently: this is at a d-spacing of 2.14 Angstroms for the experiments begun at pH 2 under pCO_2 0.5 and for the experiment begun under pH 4 and under pCO_2 1.0, which is a very slight peak. This does correspond to siderite, but the most intense powder diffraction peak of siderite, 2.76 angstroms, was absent, which more suggests the peaks could correspond to an alternative mineral.

In Figure 10, the XRD spectra for 191107 correspond to peaks for both fayalite and forsterite, which was the initial substrate of these experiments. However, for experiment pH 4 pCO_2 0.5 bar (e), there are two peaks labelled red. It was not possible to fit these to any known fayalite or forsterite spectra, but, while only minor, both form definitive small peaks.

In Figure 11 and Figure 12, as with the CRB-bearing experiments of Chapter 4, they suggest that there was little alteration to the CRB over the course of the experiments, and that any new precipitation was negligible.

In summary, a possible carbonate has been detected in an experiment via XRD: the fayalite/forsterite experiment 191107 pH 4 pCO_2 0.5 bar. The XRD is capable of detecting crystalline phases that comprise up to 5 wt.% of the sample. If this is indeed a carbonate phase, an absorption spectrum should also be visible via FT-IR, which is capable of detecting even finer amounts of new phases than XRD. The FT-IR spectra for all phases will now be investigated.

3.2.2. Fourier transform infrared (FT-IR) spectroscopy

In Figure 13 are the FT-IR spectra for the fayalite-bearing experiment 191028, where the shaded grey areas correspond to the absorption regions for siderite as seen in Chapter 4 Figure 14. For (d), which represents pH 2 at 1.0 bar, the entry shoulder into the larger zone at ~1200-1500 cm^{-1} is sharp and reflects a clear absorption. This absorption is centred at ~1100 cm^{-1} and enters into the main known absorption zone for siderite, which is between ~1100-1500 cm^{-1}. There is also an additional, smaller peak centred around 800 cm^{-1} that likewise corresponds to an absorption band for siderite. While there was no sign of siderite in the corresponding XRD signature for this experiment, FT-IR is capable of detecting more minute amounts of material, and the minor absorbed region in Figure 13 could suggest trace amounts of precipitate unable to be detected at the resolution of XRD.

A similar series of spectra are present in Figure 14, which corresponds to the fayalite/forsterite-bearing experiments of 191107. Here there are also low-gradient shoulders into the 1200-1500 cm^{-1} absorption zone that are ambiguous, but what is striking is a clear absorption peak at 1400 cm^{-1} for the experiment begun at pH 4 under 0.5 pCO_2 — the same experiment that yielded two possible peaks for siderite when observed via XRD. The presence of a sharp and previously-unseen absorption peak within the siderite absorption zone centred at ~1400 cm^{-1}, twinned with the possible siderite XRD match, together suggest more strongly that an Fe(II)-carbonate has precipitated within this experiment. Further analyses via SEM, where the physical morphology of a precipitate may be determined, will investigate this further.

Lastly, in the figures Figure 15 and Figure 16 are the spectra for the CRB-bearing experiment 191118 for fine and coarse CRB respectively. No absorption occurs across any of the regions for siderite for the fine experiments; however, for the coarse experiments, (b) and (c), corresponding to both experiments run under 0.5 pCO_2, there are minor absorption troughs within the siderite zone. There are some minor inversion features, particularly in (b) and (f), which

correspond to water absorbed within the FT-IR pellet that has been overly subtracted during the background correction calculation such that the absorption feature becomes an artificial rise.

In summary, the only experiment where a plausible Fe(II)-carbonate — or indeed, any possibly new mineral phase — was observed via FT-IR was for 191107, the fayalite/forsterite-bearing experiment run under 0.5 bars of CO_2 and begun at pH 4. As siderite was also deemed a possible match for two clear peaks that were unable to be matched with fayalite or forsterite via XRD, a clear morphologic investigation of the solid phase remaining after this experiment is necessitated. This next section covers such an investigation, and for the other experiments in this chapter, via SEM.

3.2.3. Scanning electron microscopy (SEM)

When analysed via SEM, two of the three high temperature groups of experiments revealed morphology not previously seen at low temperature. As seen in Figure 17, for the fayalite-bearing experiment series 191028, these included: butterfly-twinned, angular minerals 200 μm at their longest axis (a) that were aligned across fayalite surfaces (b); hexagonal plates ~5 μm in diameter and ~100 nm thick, often found interlocking and growing out of the fayalite (c), or as broken, loose faces; aligned nano-particles ~100 nm at their longest axis that morphologically resembled the platelets seen in Chapter 3, but which were far smaller (seen in the background of (d)); coral-like brachiating growths in parts widespread (d); string-like strands of growth often tangled, ~10 nm wide (seen in (d), in the centre); a single, rod-shaped object (d) that may have been contaminant or could be growth; antler-like spindly growths seen previously in Chapter 3 and tentatively identified as amorphous silica (e); and interlocking cuboids ~3 μm in diameter. All these growths were seen in experiments begun at pH 4, with the hexagons only observed under pH 4 pCO_2 0.5 bar and the cuboids under pH 4 pCO_2 1.0 bar, while the other phases were found throughout the pH 4 experiments.

For the fayalite/forsterite experiment 191107, the antler-like silica growths were observed again (Figure 18 (a)) alongside the coral-like growths (b), again all within experiments begun at pH

4. Additionally, the interlocking rhombs seen in the fayalite-bearing pH 4 pCO_2 1.0 bar experiment are in fayalite/forsterite pH 4 pCO_2 0.5 bar exquisitely developed: as seen in (c) and (d), these comprise individual rhombs ~3-5 μm across that form towers up to 20 μm high and coat whole fayalite grains. They are smooth-faced, angular, and were found closely clumped together or, on occasion, as isolated, smaller cuboids upon fayalite surfaces. When viewed up close, the boundaries between the rhombs contained dense growths of the stringy mineral (e), from which individual strings appear to fall loose, as well as the aligned nano-particles (f) seen in the fayalite-bearing 191028 as well as several low temperature experiments discussed in Chapter 3.

These rhombs are siderite: the classic morphology has been clearly observed and identified in several related studies (e.g., Jimenez-Lopez and Romanek, 2004; Romanek et al., 2009; Qafoku et al., 2012; Jiang and Tosca, 2019, 2020) and is the most common crystallisation morphology of siderite (Wenk and Bulakh, 2004). This is visual confirmation of the siderite that was detected by XRD and FT-IR for the fayalite/forsterite-bearing experiment 191107 pH 4 pCO_2 0.5 bar.

The remaining novel mineralogy could consist of Fe-silicates. Due to their lack of detection via XRD or FT-IR, confidence in assigning a mineral type to each cannot be assured; however, comparison to similar experimental studies yields some hints as to the minerals' type.

In Figure 18, Mg is also a consideration in addition to Fe and Si. The siderite-proximal material of (e) could be a form of smectite or perhaps needle aggregates of goethite.

4. Discussion

At 75 ºC, rhombs of the Fe(II)-carbonate siderite have formed and been positively identified as a solid precipitate after 10 days of reacting fayalite and forsterite under a pH of 4 and a pCO_2 of 0.5 bar. This was not clearly anticipated from solution chemistry: Fe^{2+} mmol/kg concentrations did not lower (Figure 3) and while a lone pH point lowered by more than 2.5 pH in a day, this trend reversed the following day. Siderite saturation states were also not immediately indicative of a

precipitate: in comparison to identical experiments run at 25 ºC, higher $\Omega_{siderite}$ was reached in experiment 190423 Fo (see Chapter 3) without producing a precipitate. It therefore appears that under high temperatures, a lower $\Omega_{siderite}$ must be exceeded for a precipitate to nucleate and form. It is important to note that growth rate of a precipitate will dictate how quickly solutions respond to a mineral forming; to observe a mineral and a supersaturated solution could suggest that nucleation indeed occurred but that growth was too slow to bring carbonate chemistry into equilibrium with siderite. This would be consistent with the only-short timescales the experiments were run under, and the very minor peaks suggesting, but not conclusive of, siderite observed under both XRD and FT-IR.

No magnesite was identified in any experiments, despite reaching identical supersaturation states to siderite. The reasons for this are not immediately clear. It could be that warmer, far more alkaline, high pCO_2 conditions are required to form magnesite, as seen in studies run at 200 ºC, pH 8.9, with 1 M $NaHCO_3$ (Lafay et al., 2014) where magnesite was found to outcompete clays likely to form under the same conditions such as serpentine. Magnesite has been well-documented to form from supersaturated aqueous solutions at high salinity, an increase in pCO_2, or an increase in temperature (Möller, 1989), but the $\Omega_{magnesite}$ of 20-100 in the Saldi et al. (2009) study suggests that the temperature in this study could be the limiting factor, in the same manner that higher saturation states for $\Omega_{siderite}$ at 25 ºC were reached than at 75 ºC yet did not produce a precipitate.

This discussion turns to the precipitation of siderite and leverages a series of tools to examine the controls on Fe(II)-carbonate nucleation and growth in anoxic water-rock systems examined here. First discussed is the activity of Fe^{2+} across all 75 ºC experiments set against pH, used as an alternate means of assessing saturation state. Following this are a series of models that simulate the experiments discussed above but across the time taken to reach equilibrium under varying rock:waterrock:water ratios and pCO_2 conditions. Finally, the dissolved inorganic carbon (DIC) amounts of each solution are calculated and plotted against the calculated total alkalinity

(TA), which as described in Chapters 3 and 4 are useful means of understanding saturation state from a standpoint that assesses other aspects of the carbonate system.

4.1. Carbonate activity

At the 75 ºC temperatures used in this chapter, the extended Debye-Hückel equation used for calculating ion activity coefficients must be adjusted in several ways. As a reminder, activity is calculated by the following:

$$a_i = \gamma_i c_i$$

(eq. 4.1.1)

where γ_i is activity coefficient and c_i is concentration. The activity coefficient itself is calculated by:

$$log\gamma_i = -\frac{Az_i^2\sqrt{\bar{I}}}{1 + B\mathring{a}_i\sqrt{\bar{I}}} + B_{dot}\bar{I}$$

(eq 4.1.2)

where A and B are the Debye-Hückel coefficients, z_i is the ith ion's valency, $\mathring{a}_i$ is mean distance of the closest approach of the ith ion (the ion size parameter), *B-dot* is a fitting parameter that is temperature-dependent, and $\bar{I}$ is the measured ionic strength of the solution. A and B are temperature-dependent and must be adjusted for 75 ºC. In the case of A, this is equal to:

$$A = 1.824928 \times 10^6 \rho_o^{\frac{1}{2}}(\epsilon T)^{-3/2}$$

(eq 4.1.3)

For B, this is:

$$B = 50.3(\epsilon T)^{-1/2}$$

(eq 4.1.4)

where p_O is the density of water, ε is the dielectric constant of water, and T is in Kelvin. At 75 ºC, ε is:

$$\varepsilon = 2727.586 + 0.6224107T - 466.9151lnT - 52000.87T$$

where T is Kelvin. When 75 ºC is inputted into the equations for A and B, this gives constants of 3.33×10^{-3} and 6×10^{-8}. These equations have been adapted from Helgeson et al. (1981).

Within the MatLab code itself used to plot activity, the solubility product (K_{sp}) was adjusted from $10^{-10.24}$ (Singer and Stumm, 1970) at 25 ºC to $10^{-11.5}$ as calculated by Bénézeth et al. (2009) for 75 ºC. The K_1 and K_2 constants were also adjusted to −6.192 and −9.89, respectively (He and Morse, 1993), which were the constants at 75 ºC obtained from experimental equilibrium carbonate chemistry as a function of temperature. As a reminder, K_1 and K_2 are the first and second dissociation constants for HCO_3^-, respectively.

In contrast to experiments run at 25 ºC, as seen in Figure 19 there are numerous datapoints that exceed the right-most line on each graph, which represents $\Omega_{siderite}$ of 400. These are almost all experiments begun at pH 4 (in blue), similarly to experiments conducted at 25 ºC; given the steepness of these siderite saturation state lines, pH is clearly a crucial factor in enabling these heightened saturation states, and only slight increases may lead to far higher omega values. The cluster of red datapoints in Figure 19 for the pCO_2 0.5 and 1.0 graphs represent experiment 191118, where pH — as at lower temperatures — did not evolve with a CRB substrate.

While the pH measurements themselves are slightly lower than the maximum reached at 25 ºC (~8.2), with none exceeding pH 8 at 75 ºC, the concentrations of Fe^{2+} activity are far higher at 75 ºC than from 25 ºC experiments, almost up to 50 mmol/kg in parts, in comparison to a maximum of ~0.01 (seen in Chapter 3 for fayalite and forsterite). This appears to account for the high number of datapoints across all three pCO_2 concentrations that exceed the saturation point

of siderite: higher Fe^{2+} activities, of the several orders of magnitude seen at 75 ºC, clearly enable a heightened propensity for siderite supersaturation.

Regarding the influence of pCO_2 amounts on siderite saturation, the higher the pCO_2, the lower the requirement for a high pH to reach high siderite saturation states. This reduced dependency results in more datapoints being able to exceed siderite saturation states, but the effect appears to be minor, with a reduction in pH requirement from pH 5.2 to 5.1 from pCO_2 0.5 to 1.0. pH and Fe^{2+} activity from Figure 19 appear to be more dominant controls on enhanced siderite saturation at high temperature.

Lastly, it is difficult to evaluate the effect of substrate itself upon siderite saturation, whether fayalite, fayalite and forsterite together, or CRB. This is because no CRB experiments were run at 0.1 bars, and only one of each type of substrate was run per one experiment. However, the lack of pH evolution for the pH 2, CRB experiments at 0.5 and 1.0 bar pCO_2 does follow the trends seen in Chapter 4 at 25 ºC, thus does not suggest an experimental or analytical error. Taking what limited data is available, as with lower temperature experiments there appears to be a heightened ability of forsterite-bearing experiments to reach the high pH required for high siderite saturation amounts, but — as seen in the 0.5 pCO_2 graph — experiments run with pure fayalite, coarse CRB, and, in the case of the 1.0 bar experiments, fine CRB, reach equally high siderite saturation states. This suggests that at the higher temperatures experimented with in this chapter, these materials are capable of dissolving into solution and potentially reacting with the carbonated fluids to produce novel minerals. This is in direct contrast to the lower temperature experiments of Chapters 3 and 4 where CRB was seen to be highly unreactive, and where almost exclusively jointly fayalite- and forsterite-bearing experiments exceeded the highest saturation states of siderite.

The 0.5 pCO_2 bar experiment begun at pH 4 that bore both fayalite and forsterite was the only high temperature set-up to produce a definite siderite precipitate. Analysis of Figure 19 for pCO_2 (middle panel) does show this experiment (blue squares) at supersaturated $\Omega_{siderite}$; however,

the equivalent experiment at 1.0 bar pCO_2 appears to show even higher, and the 0.1 bar equivalent is equal to or higher than for the 0.5 bar experiment. From siderite saturation state alone it is not immediately apparent why this experiment solely yielded a precipitate. Saturation state alone, however, is not an indicator of precipitation: as discussed earlier, it is plausible that the nucleation threshold had already been exceeded by this point, but mineral growth was insufficiently fast to produce measurable quantities. Therefore, while saturation state is a good indicator of the likelihood of precipitation, it is not a definitive tool, and is limited by other factors including nucleation threshold and mineral growth kinetics. In addition, with removal from solution by precipitation, saturation state and carbonate solution chemistry will have already responded to this change, thus the maximum saturation state of a precipitate-forming experiment will not be captured.

The following conclusions may be drawn from analysis of Figure 19 and its display of the relationship between pH and Fe^{2+} activity in enabling siderite saturation:

1) A relatively low pH is required to exceed the saturation state of 1 $\Omega_{siderite}$, far lower than the pH required for the same Ω at 25 ºC
2) Fe^{2+} concentrations are several orders of magnitude higher for all experiment datapoints at 75 ºC than at 25 ºC
3) pCO_2 has only a minor effect on siderite saturation state compared to pH
4) At high temperatures, all experiment substrates dissolved into solution and enabled >400 $\Omega_{siderite}$

Overall, the most useful information yielded by these graphs regarding the carbonate system under high rock:waterrock:water ratio, closed, anoxic conditions is that the conditions enabling significant siderite saturation are far wider in range at 75 ºC than at 25 ºC. Lower pH is required, with a lower effect of pCO_2 that translates to a lowered dependency of this gas' presence within a system, while the initial rock substrate itself can range in composition from pure olivine to 50:50 fayalite/forsterite to albite-dominated basalt. The naturally heightened reactivity of

systems of higher temperatures also results in higher elemental concentrations of cations into solution available for reaction with the carbonated fluids. The increased energy flux also reduces the timescales required for reactions, which could be important if the environmental conditions enabling siderite precipitation were transient (e.g., flash flooding of pore spaces, the formation of a crater lake). These factors all translate into a greater ease of formation of siderite at 75 ºC than at 25 ºC.

However, given that $\Omega_{siderite}$ appears equivalent or higher for experiments that did not yield a siderite precipitate as for the singular case that did, it is possible additional factors are at work affecting the ability of Fe(II)-carbonate to precipitate. The role of clays as competing sinks for free Fe^{2+} will now be investigated.

4.2. Greenalite formation

The phyllosilicate greenalite is amongst the simplest of the Fe-bearing clays. As has been discussed for previous chapters, assessing whether the experimental solutions exceeded its saturation state is a reasonable approximation for whether basic clay formation occurred, which has been known to act as a competing sink for available Fe^{2+} under anoxic, Mars-like conditions (e.g., Ehlmann et al., 2012). It is important to note that there is a lack of Al in greenalite, which is a common component in clays, thus to focus on greenalite does not enable a complete picture of clay formation on Mars. In Figure 20, all data points from the three high temperature experiments are plotted upon three graphs for pCO_2 concentrations, with the log of Fe^{2+} activity divided by H^+ activity on the y-axis and the log of the activity of SiO_2 on the x axis. Any data points that exceed the heavy grey line are said to be supersaturated with respect to greenalite, and this line was created using a K_{sp} of 18.4 for 75 ºC, which was calculated by taking the K_{sp}s between 25 ºC and 350 ºC from the GWB database (Delany and Lundeen, 1991), with values in turn extracted from Helgeson et al. (1978) and running a polynomial curve between the eight datapoints.

For previous chapters at low temperature, no CRB-bearing experiments exceeded this line (Chapter 4), but for fayalite and forsterite (Chapter 3), many did under all three pCO_2 amounts, whether pure fayalite or 50:50, begun at pH 2 or 4, although more data points exceeded the saturation line at high pCO_2. This was interpreted as clays such as greenalite being capable of forming under the experimental conditions studied, and was especially interesting given how on the corresponding plot for siderite, lines of saturation and even supersaturation was simultaneously exceeded, suggesting both clays and carbonates were capable of forming contemporaneously under the experimental conditions.

At high temperature, there are numerous datapoints that exceed the greenalite saturation line across all three pCO_2 amounts. Unlike the fayalite and forsterite equivalent graphs of Chapter 3, in Figure 20 pCO_2 does not appear to be a constraining factor, with experiments begun at both pH 2 and 4 regularly exceeding the saturation line for all three pCO_2 amounts. Experiments begun at pH 4 appear slightly more likely to exceed this line, and this appears to be a function of pH, with the pH 2 experiments bearing CRB (red triangles) all remaining well below the line. These did not evolve in pH and remained around pH 2-2.5; the fact that all other experiment types have at least some data points that exceed the line suggests this inability to evolve beyond an extremely acidic pH hinders greenalite precipitation under the experimental conditions.

Strikingly, unlike the CRB-bearing low temperature experiments of Chapter 4, in Figure 20 both fine and coarse CRB exceeds this line. As with siderite saturation in Figure 19, this is the first time CRB-bearing experiments have shown reactivity with regards to carbonate or clay saturation, which was not observed at low temperature. At 75 ºC in Figure 20, where CRB-bearing experiments were run at pCO_2 0.5 and 1.0 bars, both fine and coarse CRB when the experiment was begun at pH 4 exceed the greenalite saturation line. As with the carbonate saturation state in Figure 19, this suggests the substrate of CRB is more chemically reactive, and able to both release free ions into solution and for them to react to form new species. Only fayalite and forsterite displayed this kind of reactivity at 25 ºC; at 75 ºC, CRB also holds this function.

Overall, there is a notable increase in the ability of all solutions, excepting those that remained at low pH, to evolve to SiO_2 and Fe^{2+}/H^+ activity concentrations that surpass the saturation point of the clay greenalite. It is important to note at this stage that all experiments run in this chapter were continued for 10 days; this is in contrast to over 90 days maximum at low temperature, where pH and dissolved ionic content had several months to reach both the siderite and greenalite saturation states observed in Figure 19 and Figure 20. High temperature favours higher saturation states of both siderite and greenalite than ambient, 25 ºC temperatures, and at rates far more rapid.

To summarise, to enhance the saturation of greenalite, the following conditions appear favourable:

1) High pH, at least pH 4
2) Fayalite, forsterite, and CRB as initial substrates
3) More minorly, higher amounts of pCO_2.

Again to consider the single siderite precipitate of the 191107 experiment under 0.5 bar pCO_2, it is not apparent that greenalite saturation resulted in any relevant effect that sets this one particular experiment apart. The $\Omega_{greenalite}$ for the pH 4 0.5 bar experiment of 191107 (blue squares in the 0.5 bar graph) fall well within a range for both log SiO_2 activity and log Fe^{2+}/H^+ activity. Some other factor besides competition with clay formation, and something further than $\Omega_{siderite}$ acting in isolation, is at work to enable siderite precipitation within this one experiment.

Regarding both greenalite and siderite saturation, it is immediately apparent from both Figure 19 and Figure 20 that operating Mars simulation experiments under 75 ºC as opposed to 25 ºC enhances the saturation of both. However, all experiments were run under closed conditions (i.e., with a fixed pCO_2) and high rock:waterrock:water ratio (1 part rock for 500 parts water). To investigate how having an open system (constant replenishment of CO_2) and/or low rock:waterrock:water ratio (1:10) affects the ability of novel minerals to exceed their saturation states, several geochemical models were set up. This was also useful for enhancing the study of

the high rock:waterrock:water ratio, closed systems explored experimentally, since over 10 days these real-life experiments did not have time to reach equilibrium whereby their pH and elemental amounts in solution stabilised.

4.3. Modelled reaction pathways

This section discusses the series of models that were constructed in *The Geochemist's Workbench* (GWB; Bethke, 2017) to investigate multiple experimental conditions across the time taken for such conditions to reach equilibrium. The set-up of these models was described in full in Chapter 2 (Methods) with alterations specific to this chapter discussed in section 2.2. Both the compositions used in Chapter 3 (fayalite and fayalite/forsterite) and the CRB of Chapter 4 were used as initial reactants for the model, and four differing environmental scenarios modelled as used in previous chapters: 1) a system closed with respect to CO_2 (whereby CO_2 may leave the system and decreases over the course of the reaction) at low rock:waterrock:water ratio (1:10), simulating the vadose zone of aquifers in the sub-surface between grains; 2) a closed system at high rock:waterrock:water ratio (1:500), simulating such environments as ice-covered lakes (as has been suggested for within Gale Crater; Kling et al., 2018; or across parts of Arabia Terra; Warner et al., 2010); 3) an open system (whereby CO_2 is constantly replenished, as beneath an atmosphere) at low rock:waterrock:water ratio (1:10), simulating an environment such as the ephemeral, inter-dune playas of Meridiani Planum (e.g., Squyres et al., 2004); and 4) an open system at high rock:waterrock:water ratio (1:500), simulating open lakes on the surface of Mars such as those proposed for Gale Crater (e.g., Grotzinger et al., 2014; Hurowitz et al., 2017), McLaughlin Crater (e.g., Michalski et al., 2013, 2019), or Jezero Crater (Fassett and Head, 2005, 2008; Goudge et al., 2015, 2017; Horgan et al., 2020), and suggested as a formation mechanism for the Fe-Mg-Ca-rich carbonates identified in Gusev Crater (Ruff et al., 2014).

The purpose of these models is to recreate the experimental conditions explored in the results section but run to equilibrium, as well as explore other systems not run experimentally: the

open systems and the low rock:waterrock:water under closed conditions, which unfortunately failed to run.

First discussed in brief are each model run with the different substrates.

4.3.1. Fayalite model

Under fayalite-bearing systems, the model (Figures 21-24) suggests open systems are slightly more likely to form Fe(II)-carbonates than closed, while there is no discernible difference between high and low rock:waterrock:water ratio systems. What is immediately distinctive when the four reaction path models are run with pure fayalite is how very little difference in water chemistry is observed for the differing models. Both high rock:waterrock:water ratio systems take longer to reach equilibrium than the low rock:waterrock:water systems, which are almost instantaneous. In the case of siderite, it may be that only a minor change in pH has a correspondingly minor effect on $\Omega_{siderite}$, while the steady flux of CO_2 provides carbonate ions in sufficient quantities for siderite formation.

4.3.2. Fayalite and forsterite model

When fayalite and forsterite are run together in the model (Figures 25-28, the high saturation states of both siderite and greenalite (Figure 27 and Figure 28) reflect those observed experimentally in Figure 19 and Figure 20. This suggests good commonality between the model and reality, and is also interesting for furthering evidence that the two compete with each other, both being favoured under similar conditions.

More broadly, compared to the fayalite models the addition of forsterite causes the four environmental systems diverge. Seen in Figure 25, as for the pure fayalite system, the closed, low rock:waterrock:water ratio system also yields the highest pH and stabilises the most rapidly. In additional contrast to the pure fayalite system, where Fe^{2+} concentrations ascended and stabilised over the course of the model, as seen in Figure 26, Fe^{2+} plummets after around 5 % of the duration of the model — the exact frame where pH jumped to its highest before levelling off. At first glance this suggests precipitation; however, precipitation was not permitted in the model. As this ~5 %

of model duration was the time taken for the CO_2 to leave the system, it is possible there is some connection to the amount of HCO_3^- or CO_3^{2-} ions present in solution.

Combining this information on pH and elemental activity concentrations is helpful for discussing the trends of the two carbonates deemed by the model as likely to form: $\Omega_{siderite}$ and $\Omega_{magnesite}$, as seen in Figure 27. For both carbonates, all systems enable saturation and hence theoretical precipitation. While the experiments of this thesis observed an increased $\Omega_{siderite}$ broadly commensurate with increased pH (see Figure 1), the closed system at low rock:waterrock:water ratio in $\Omega_{siderite}$ (Figure 27) shows a lower saturation state than for the other three systems. This is a trend that appears reversed compared to the results of the previous, low-temperature chapters, where low rock:waterrock:water, high pH, closed systems yielded the greater saturation states of Fe(II)-carbonate. At high temperature, the open systems and those at high rock:waterrock:water ratio, where pH does not reach such high values, are more favourable to siderite saturation and hence possible precipitation.

In Figure 28, the clay greenalite for all systems reaches higher saturation points than for either of the carbonates. This is interesting because in studies observing the direct relationship between siderite and greenalite (Jiang and Tosca, 2019), both these species compete for available Fe^{2+} and so the phase that precipitates the fastest may use up the supply of Fe^{2+} available. This is greenalite at 25 ºC, but the formation of siderite in these experiments may suggest this is not the case with increasing temperature

4.3.3. CRB model

The CRB model (Figures 29-32) ran with a combination of minerals as outlined in Chapter 4. For high rock:waterrock:water ratio systems, there is little difference between the ability of siderite to form under these or the open low rock:waterrock:water ratio system. This suggests that in comparison to the low temperature models of previous chapters, but similarly to the fayalite/forsterite and fayalite models, siderite is capable of reaching relatively high supersaturation

under lacustrine conditions. This was not observed when models were run under 25 ºC (see Chapters 3 and 4) and is a direct function of this temperature increase.

Finally for greenalite, as seen in Figure 32 and also like the fayalite/forsterite models, this mineral reaches extremely high amounts of supersaturation, several orders of magnitude more than siderite for the same models, which implies that greenalite would be more likely to precipitate than siderite, hence outcompeting this carbonate for Fe^{2+} and reducing its chances of forming.

To summarise the findings of the three reactant models:

1) Siderite is capable of reaching high points of saturation under both open and closed systems
    a) This represents both aquifer and lacustrine systems
2) Under some conditions, closed, low rock:waterrock:water ratio systems representing subsurface aquifers are less likely to form siderite than other systems, owing to an inability of Fe^{2+} to dissolve into solution following rapid climbing pH that reduces the ability of the initial substrate to dissolve
3) The clay greenalite in all models exceeds the saturation state of siderite, suggesting that this clay is more likely to form than the carbonate under all simulated conditions
4) Amorphous silica and $Fe(OH)_2$ were in no model able to reach significant saturation states, suggesting these are not a significant component of any of the systems investigated
5) Magnesite was capable of forming in almost all models, with an inclination to reach higher amounts of supersaturation under low rock:waterrock:water ratio conditions except when run with pure fayalite, under which the ability of CO_2 to remain in contact with the system as open became the factor influencing $\Omega_{siderite}$
6) pH evolved to higher values the more types of minerals were present, and for closed systems, the latter reflecting the lack of carbonic acid within closed systems

Overall it may be concluded that, at 75 ºC, carbonates such as siderite and magnesite are capable of reaching supersaturation — hence being likely to precipitate — under open, closed, high rock:waterrock:water ratio, and low rock:waterrock:water ratio systems. In summary, this suggests that where hydrothermal temperatures at 75 ºC existed, siderite was capable of forming both, (i) below ground in low rock:waterrock:water ratio, closed system aquifers (discussed in Chapters 3 and 4) as has been observed on Mars (Michalski and Niles, 2010; Wray et al., 2016) and (ii) in high rock:waterrock:water ratio, open systems, e.g., lacustrine environments, as has been observed on Mars: within Jezero Crater (Horgan et al., 2020), on the outskirts of the Hesperia Planum volcanic province, within a delta that is directly overlain by once-molten lava (Shahrzad et al., 2019), and within the Columbia Hills of Gusev Crater, itself an island surrounded by volcanic flows (Squyres et al., 2004; Ruff et al., 2014).

There is good agreement between the models and the experiments where conditions overlapped (see Figures 1 (pH), 3 Fe^{2+}), 6 ($\Omega_{siderite}$), and 21-32 for the models), which were for high rock:waterrock:water, closed systems, and this has further elucidated the potentially carbonate-forming systems both upon Mars but also in other anoxic aqueous environments. While the model did not predict a precipitate, this was not built into its capability owing to the inability of GWB to distinguish between relevant phases common to such an environment or otherwise. The high saturation states of siderite and its increase across the course of both the high and low rock:waterrock:water system models under closed conditions was in good agreement with the experimental data whereby the closed system experiments under high rock:waterrock:water also reached high saturation of siderite. However, another modelled set of parameters useful for understanding the evolution of solution chemistry is a comparison between two components of the carbonate system: total alkalinity and dissolved inorganic carbon. Such an approach could be more successful in predicting a precipitate, which the above model was unable to do. Following trends in DIC and alkalinity, on the other hand, is a good means of assessing whether a system is

likely to deplete or increase both in pH and available carbon, both of which are relevant to the geochemistry studied here.

This will now be discussed to further understand the anoxic carbonate system at high temperatures, with this model operating as a tool to represent both natural and experimental systems and understand the key conditions that control Fe(II)-carbonate precipitation in open and closed environments.

4.4. Dissolved inorganic carbon vs total alkalinity

As discussed in previous chapters, the multiple variables that influence carbonate saturation state and precipitation in natural systems can be distilled to two fundamental parameters that describe the carbonate system: DIC and alkalinity. An evaluation of the reaction path modelling results indicates that water-rock interaction in open and closed systems and under a variety of conditions, results in only a finite number of trajectories in DIC-ALK space. These in turn illuminate the processes controlling carbonate saturation state and help constrain which natural systems are most likely to produce Fe(II)-carbonate and why. In Figure 33, the DIC vs total alkalinity (TA) of modelled experiments run with pure fayalite are shown. Of the four modelled conditions, in (a) and (b) of Figure 33 the $\Omega_{siderite}$ at 0.1 bar (a) and 1.0 bar (b) pCO_2 for the two closed system models run in tandem on trajectories that aim for the highest $\Omega_{siderite}$, in comparison to those run as open systems. This is because, with DIC remaining fixed by the nature of being a closed system in which CO_2 in any form is not replenished, the trajectories of the closed system models run vertical in the diagrams of Figure 33, since only TA may change. TA increases because the dissolution of silicate rocks, such as a fayalite, adds alkalinity to the system. Thus, as seen in Chapter 3 (fayalite and fayalite/forsterite at 25 ºC) and Chapter 4 (CRB at 25 ºC), closed systems where CO_2 is not replenished once depleted enable heightened states of $\Omega_{siderite}$ in comparison to open systems resembling contact with an atmosphere rich in pCO_2, whereby DIC increases alongside TA. This

trend holds at the 75 ºC temperatures the models in this chapter were run at, and is seen in Figures 34 and 35 for DIC-ALK for fayalite/forsterite and CRB substrates.

The inability to distinguish between the two closed systems — low rock:waterrock:water ratio (1:1) and high rock:waterrock:water ratio (1:500) — is important to discuss. In comparison to the 25 ºC models, where lower rock:waterrock:water ratios consistently enabled heightened $\Omega_{siderite}$ compared to the high rock:waterrock:water ratio system, at 75 ºC, this distinction between rock:waterrock:water ratio appears less important. The implication of this is that where temperatures are able to climb to these mildly hydrothermal amounts, rather than the more ambient 25 ºC, siderite formation is unconstrained, or less constrained, by rock:waterrock:water ratio.

4.5. The implications for carbonate and clay formation on the Martian surface

What the three DIC vs TA diagrams collectively appear to display is, at hydrothermal temperatures, the heightened ability for lacustrine environments to form siderite where Fe-bearing olivine occurs as the host rock. These would not be lakes that were wholly hydrothermal but a scenario where the lower portion of the lake could be at elevated temperatures owing to subsurface volcanic vents or the rise of superheated fluids in relation to nearby volcanism — an analogue environment on Earth is the Askja impact crater lake of Iceland, which, while not an impact crater, is a hydrothermal lake within basalt that is surrounded by far colder terrain (e.g., Cousins et al., 2013). Where Mg-bearing olivine or a more diverse suite of mineralogy forms the host rock, a lacustrine environment becomes less likely to yield siderite in significant quantities. These high rock:waterrock:water environments are more likely to be closed systems. This is a scenario that is harder to envisage in reality, where a closed but high rock:waterrock:water ratio environment could be an ice-covered lake (e.g., Kling et al., 2020); unlikely if such a lake was partially or wholly hydrothermal. An alternative could be high temperature springs: these would be considered open as well as high rock:waterrock:water ratio. However, as seen earlier for modelled conditions, high

rock:waterrock:water ratio, open system environments are not precluded from enabling heightened states of carbonate supersaturation. Combining the additional calculations discussed above — the Fe^{2+} activity/pH diagrams, the modelling, the DIC/TA diagrams — reveals a lowered dependence upon rock:waterrock:water ratio than was observed for ambient temperatures (Chapters 3 and 4). Meanwhile, the importance of closed vs open systems with respect to pCO_2 flux is also reduced in dependence, albeit with closed systems remaining as more conducive to higher carbonate saturation states, which was also seen at lower temperatures. This agrees with the information derived experimentally from reproducing closed, high rock:waterrock:water ratio conditions within the laboratory, where a siderite precipitate was identified when these experiments were conducted under 75 ºC. While closer analysis was unable to reveal the specifics of why this one experiment formed siderite — others reached higher pH, higher dissolved Fe^{2+} concentrations, and higher $\Omega_{siderite}$, under higher pCO_2 — a clear preference for these four characteristics of a solution to be at elevated amounts was observed. Higher temperature, in addition, clearly enabled siderite formation when compared to the non-activity of the earlier 25 ºC experiments.

The application of these data to the Martian surface permits insight into the formation of the carbonates that have been identified there. The Fe-Mg-rich carbonates of Jezero Crater in Nili Fossae, as well as the Fe-Mg-Ca-rich carbonates of Gusev Crater, could both have formed under the mechanism experimentally and computationally reproduced in this chapter: precipitation under anoxic, high rock:waterrock:water ratio (1:500), high pCO_2 ($\geq$0.5 bar), closed system conditions where pH may evolve to neutral-to-alkaline values and where Fe^{2+} is able to dissolve into solution from an olivine-rich substrate. It is salient to observe the lack of Mg-carbonate formation across all experiments, despite the presence of forsterite in some set ups. This suggests either one of two features of this system. Firstly, it could suggest that Mg-carbonate rich lithologies reflect water-rock interaction under oxic or UV photo-oxidised conditions, where Fe is immobilised by oxidation and is unable to act as an available cation for reactions. Alternatively, where Mg-

carbonates form on Mars, this could instead suggest initial substrates that are significantly Mg-rich and Fe-poor, such that the majority of cations that enter solution are Mg^{2+}.

While low rock:waterrock:water ratio conditions at 75 ºC were not able to be successfully produced as experiments for this research, geochemical modelling indicated that such environmental conditions are also conducive to Fe(II)-carbonate saturation. The regional carbonates of Nili Fossae are likely to have formed under such low rock:waterrock:water ratio conditions, possibly by the injection of hydrothermal fluids through an olivine host-rock (e.g., Ehlmann et al., 2008, 2009; Viviano et al., 2013). Under 75 ºC, siderite appears able to form even under open system conditions, along with aquifer conditions as at 25 ºC, when granted sufficiently high temperatures. This is an important observation that was also observed in the modelling: carbonates identified in Jezero Crater could be either detrital (Goudge et al., 2015) or lacustrine in origin (Horgan et al., 2020) and while they are dominated by Mg-rich phases, e.g., magnesite and hydromagnesite (Ehlmann et al., 2008; Bishop et al., 2013; Edwards and Ehlmann, 2015) as well as Fe- and Mg-rich olivine (Ehlmann et al., 2008; Salvatore et al., 2018), the presence of Fe-carbonates has been also indicated by minor absorption bands via spectroscopy (Horgan et al., 2020; Brown et al., 2020). At 25 ºC as determined by Chapters 3 and 4, siderite is not favoured in high rock:waterrock:water ratio, open to the atmosphere systems that the proposed lakes at Jezero (e.g., Fassett and Head, 2005; Schon et al., 2012; Goudge et al., 2012, 2015, 2017) or Gusev (Ruff et al., 2014) represent. However, the models at 75 ºC here indicate that siderite saturation, hence possible precipitation, becomes feasible at these higher temperatures. The Fe-carbonate components at Jezero and Gusev, if present, could have formed by the *in situ* alteration of olivine present in the surrounding volcanics (e.g., Ehlmann et al., 2008; Edwards and Ehlmann, 2015) at hydrothermal temperatures. Warm fluids, heated by nearby volcanism, or remaining from impact cratering, could have potentially provided a source of heating to enable these hydrothermal temperatures; however, supplying such a large amount of heat to a whole lake body is probably unfeasible across any significant length of time, and there is no evidence of such long-lived

volcanism in connection to Jezero Crater aside from adjacent lava fields and a known volcanic province. The temperature of such an impact-induced lake, or one proximal to volcanism, would be above-ambient, but it is unclear whether temperatures would be sufficient to support the level of hydrothermalism being discussed here across such a body of water.

What the modelling and experiments in this chapter have suggested is that at high temperatures, siderite and other Fe(II)-carbonates are also, as under high rock:waterrock:water ratio conditions, likely to form under low rock:waterrock:water ratio conditions. These may include within aquifers, where hydrothermal fluids migrate through host rock, or within shallow playa environments. Hydrothermal fluid migration has been suggested as the formation mechanism for the widespread Nili Fossae carbonates (e.g., Viviano et al., 2013), while for aquifers deeper within the crust, these would have been common where high geothermal gradients, pH gradients (with pH increasing with depth), and inter-pore space groundwater interacted together with meteorically- or volcanically-derived CO_2. Such environments may have produced the carbonates exposed as deep as 6 km below the surface in some impact craters (Michalski and Niles, 2010; Wray et al., 2016) or within ancient terrain exposing carbonates as part of weathering profiles across the Martian surface (Michalski et al., 2013; Bultel et al., 2019).

5. Conclusions

Chapters 3 and 4, with experiments conducted at low temperatures of 25 ºC, demonstrated that siderite and other Fe(II)-carbonates are more likely to precipitate upon Mars when under aquifer-type environments of low rock:waterrock:water ratio. These are conditions where limited amounts of CO_2 may enter the system and alter water pH. This agreed with observed mineralogy in some of the deepest impact craters upon Mars, where Fe(II)-carbonates that formed kilometres below the planet surface have been exposed by the excavating effects of impact cratering (Michalski and Niles, 2010; Wray et al., 2016), effectively explaining their localised formation within such aquifer-

bearing environments in a manner that removed the need for more generalised hypotheses for their absence elsewhere, such as low atmospheric pCO_2 (e.g., Chevrier et al., 2007; Bristow et al., 2017).

However, lacustrine environments at these ambient temperatures, whether open to the atmosphere (e.g., Grotzinger et al., 2014) or beneath a sealing cap of ice (Warner et al., 2010; Kling et al., 2020) did not permit heightened saturation states of such carbonates whether investigated experimentally or computationally. This left unexplained the Fe-bearing carbonates identified *in situ* in Gusev Crater by the *Spirit* rover (Morris et al., 2010; Ruff et al., 2014) and those of Jezero Crater (Horgan et al., 2020; Brown et al., 2020), which appear to be deltaic or otherwise lacustrine in nature, and to represent deposits that formed within standing bodies of water at high rock:waterrock:water ratios.

The research in this chapter, conducted at 75 ºC, presents experimental data that suggests the precipitation of siderite under such high rock:waterrock:water ratio conditions. Interconnected, rhombohedral crystals matching the morphology of siderite were identified via SEM, alongside XRD and FT-IR spectra also strongly favouring this carbonate as a precipitate. This experiment exceeded pH 7, while only displaying minor Fe^{2+} concentrations (at maximum 1.2 mmol/kg, in comparison to at highest 26.5 mmol/kg for all high-temperature experiments). This suggests pH is a critical factor in enabling siderite precipitation, alongside available pCO_2, as higher starting amounts of pCO_2 correlate to higher siderite saturation states. The siderite-bearing regions of Mars may, therefore, have hosted environments that reflected the following geochemical conditions during the period when siderite was formed:

1) High temperature (≥75 ºC), high pH (around ≥7);
2) Moderate amounts of pCO_2 (≥0.5 bars), only minimal Fe^{2+} (~ 1 mmol/kg) ;
3) Relatively high rock:waterrock:water ratios.

A standing body of water, as opposed to a sub-surface aquifer closed off from atmospheric CO_2 and with such higher rock:water ratios, could combine such conditions likely to form

authigenic siderite. An olivine-rich substrate would have been more conducive to the formation of siderite than that of basalt, since CRB-bearing experiments yielded far lower siderite saturation states. An ice-covered lake in an olivine-rich, volcanically active or recently impacted environment would fit all these criteria, and these are the characteristics of both Jezero Crater and the Columbia Hills of Gusev Crater, within which siderite has been identified and hypothesised as forming under lacustrine conditions.

Furthermore, modelling and other computational data implies Fe(II)-carbonates are also capable of reaching heightened states of supersaturation — a precursor for precipitation — under 1:1 rock:waterrock:water ratio conditions. This suggests that the aquifer-type environment that appeared to be responsible for the formation of the deep, exposed carbonates discussed in Chapters 3 and 4 could also have operated under high temperature conditions to form the siderite observed on Mars within deep impact craters. While further experimental work under low rock:waterrock:water conditions to validate these modelled data is recommended, the siderite saturation states reached within the models at high temperature exceed those both observed and modelled under low temperatures as recorded in Chapters 3 and 4, strongly suggesting that an increase in temperature has a positive effect upon the ability of siderite to precipitate under aquifer or other low rock:waterrock:water ratio-type environments that are anoxic.

The presence of siderite across the Martian surface, in quantities that surprised early geochemists when locally identified, may be explained through a combination of specific kinetic dependence and a rarity of environments conducive to its formation. This research has demonstrated for the first time the ability of siderite to form under hydrothermal temperatures at atmospherically realistic pressures of CO_2 for Mars, offering a geochemically derived explanation for its formation only within highly localised settings upon the visible Martian surface. Together with the data of Chapters 3 and 4, which strongly suggest siderite formation at ambient temperatures buried within the subsurface, the specific geography of siderite formation on Mars

can be explained through demonstrable aqueous chemistry. Such a hypothesis is directly testable *via* the planned 2021 landing of NASA's *Perseverance* rover upon the Jezero Crater delta.

6. Figures

Experiment name	Equivalent experiment at 25 °C	Duration (days)	Reactant	Initial pH	pCO_2 used	Rock:water ratio
191028	180313 and 180406	10	Fa	2, 4	0, 0.1, 0.5, 1.0	1:500
191107	180829	10	Fa:Fo (1:1)	2, 4	0.1, 0.5, 1.0	1:500
191118	190807 and 190808	10	CRB (f and c)	2, 4	0, 0.5, 1.0	1:500
191128	181004	(failed)	Fa	2, 4	1.0	1:1, 1:10
191129	181205	(failed)	Fa:Fo (1:1)	2, 4	1.0	1:1, 1:10

Table 1: List of the five experiments set up for this chapter. Note that the final two, 191128 and 191129, failed and were not completed.

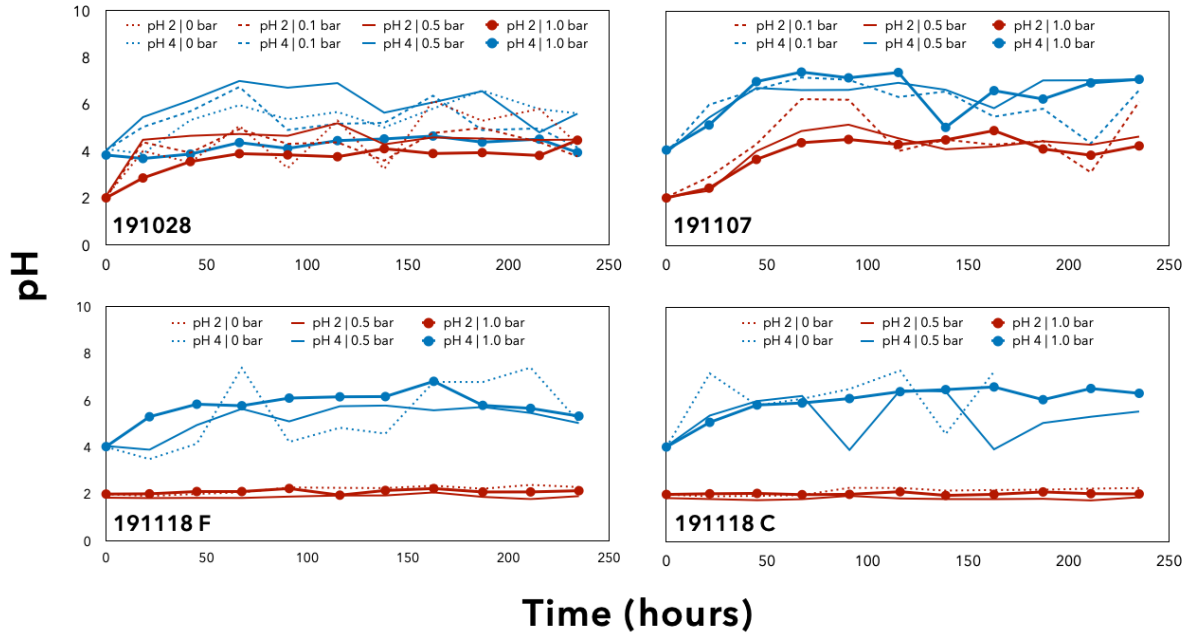


Figure 1: pH over time for each of the experiments successfully run at 75 °C, where the CRB experiment 191118 has been divided into fine and coarse. Differing legends are available for each graph. Note the same axes lengths.

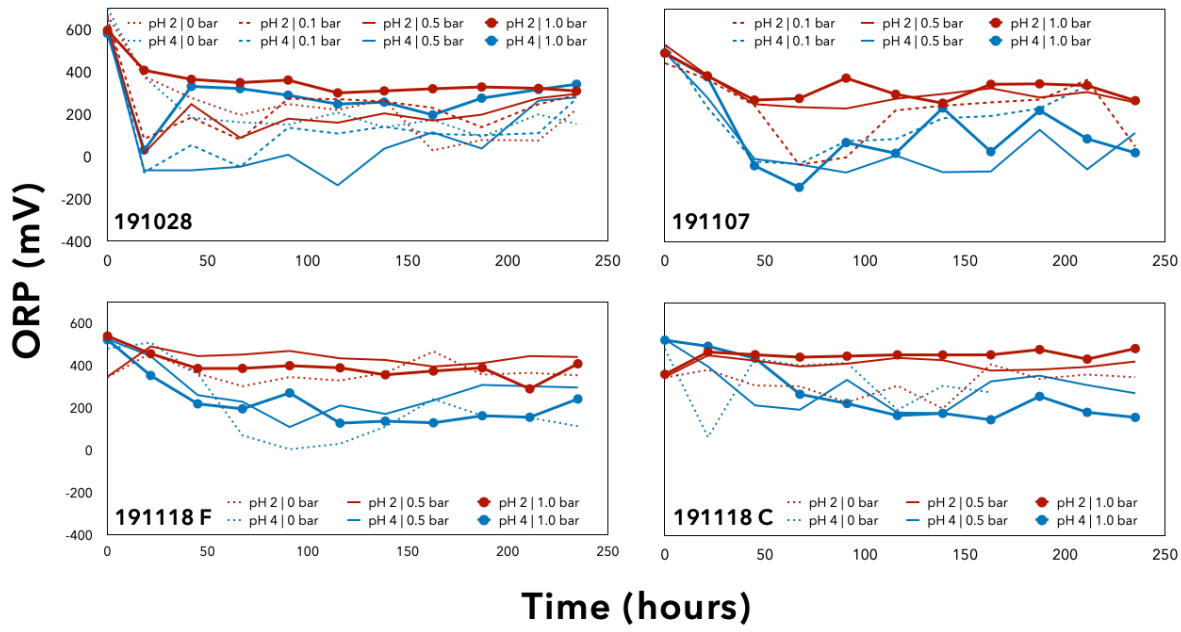


Figure 2: ORP measurements across the course of the 75 °C experiments conducted for this chapter. Note the identical axes but differing legends.

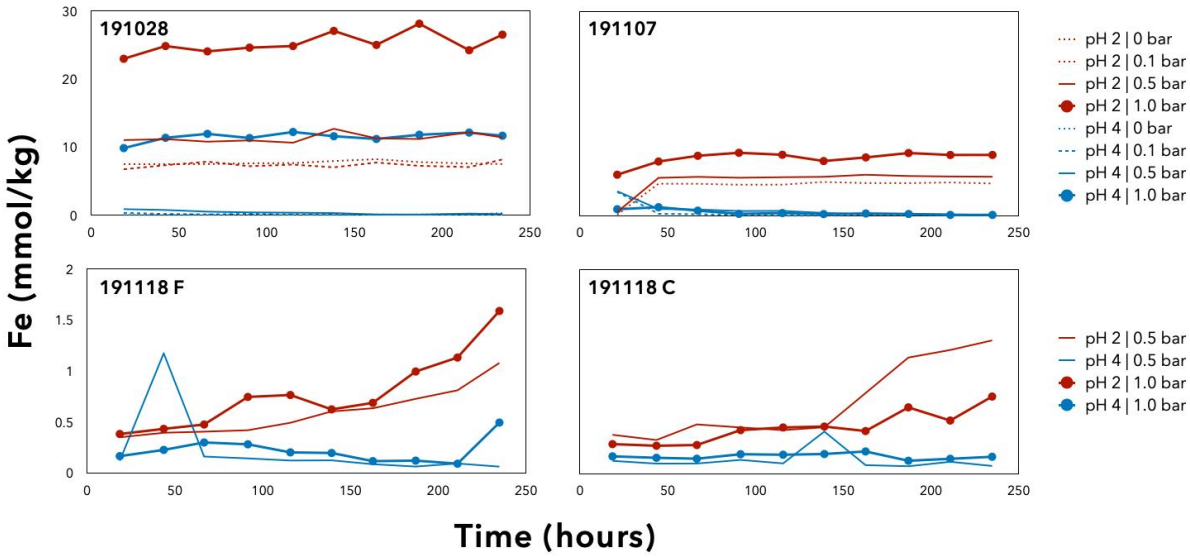


Figure 3: Levels of Fe in solution over time as determined by ICP-MS. The name of each experiment is listed in the top-left hand corner, with fayalite in the top-left, fayalite and forsterite in the top-right, and CRB fine grained in the bottom-left and CRB coarse grained in the bottom-right. Note the differing scales between the top and bottom, and the differing legends.

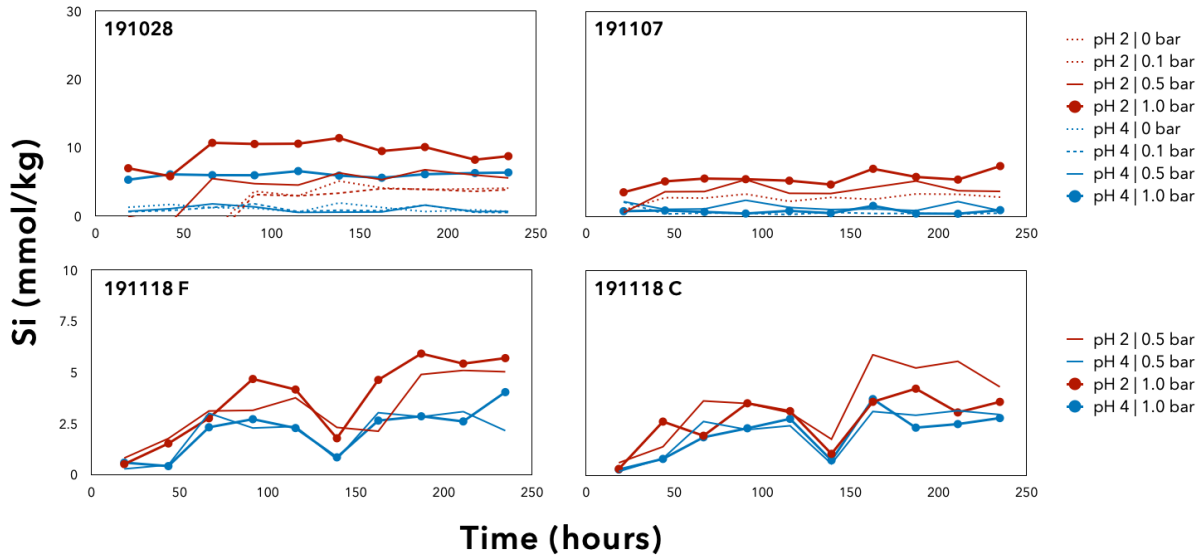


Figure 4: Levels of Si in solution over time as determined by ICP-MS. The name of each experiment is listed in the top-left hand corner, with fayalite in the top-left, fayalite and forsterite in the top-right, and CRB fine grained in the bottom-left and CRB coarse grained in the bottom-right. Note the differing scales between the top and bottom, and the differing legends.

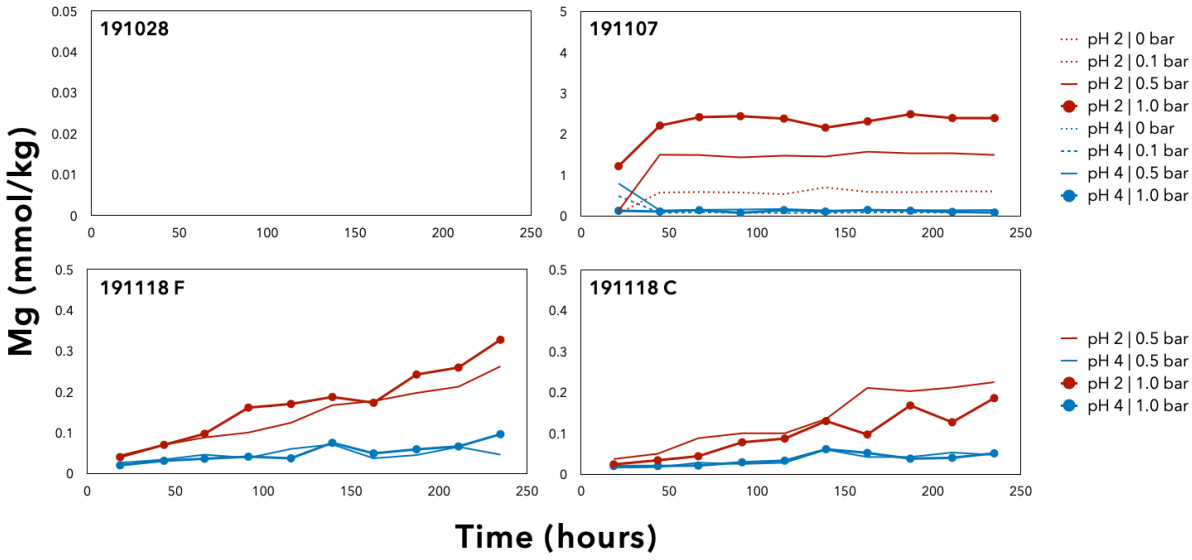


Figure 5: Levels of Mg in solution over time as determined by ICP-MS. The name of each experiment is listed in the top-left hand corner, with fayalite in the top-left, fayalite and forsterite in the top-right, and CRB fine grained in the bottom-left and CRB coarse grained in the bottom-right. Note the differing scales between the top and bottom, and the differing legends.

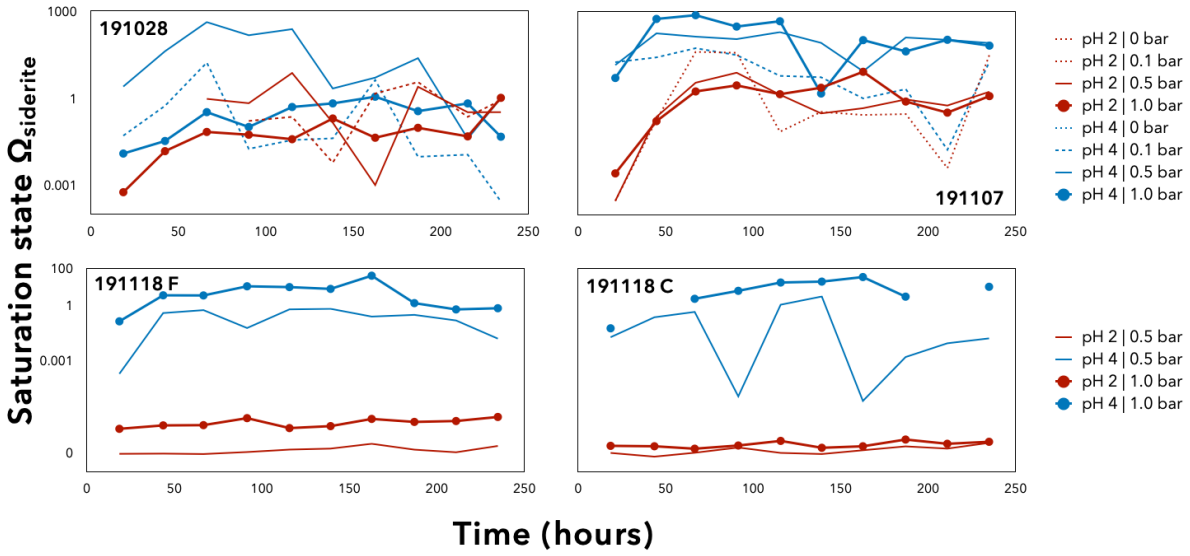


Figure 6: The saturation state (Ω) of siderite in solution for each of the experiments in this chapter. Note the logarithmic axes. The CRB experiments are divided into fine (F) or coarse (C) material. A legend to the right of each row displays which lines correspond to which experiments on that row.

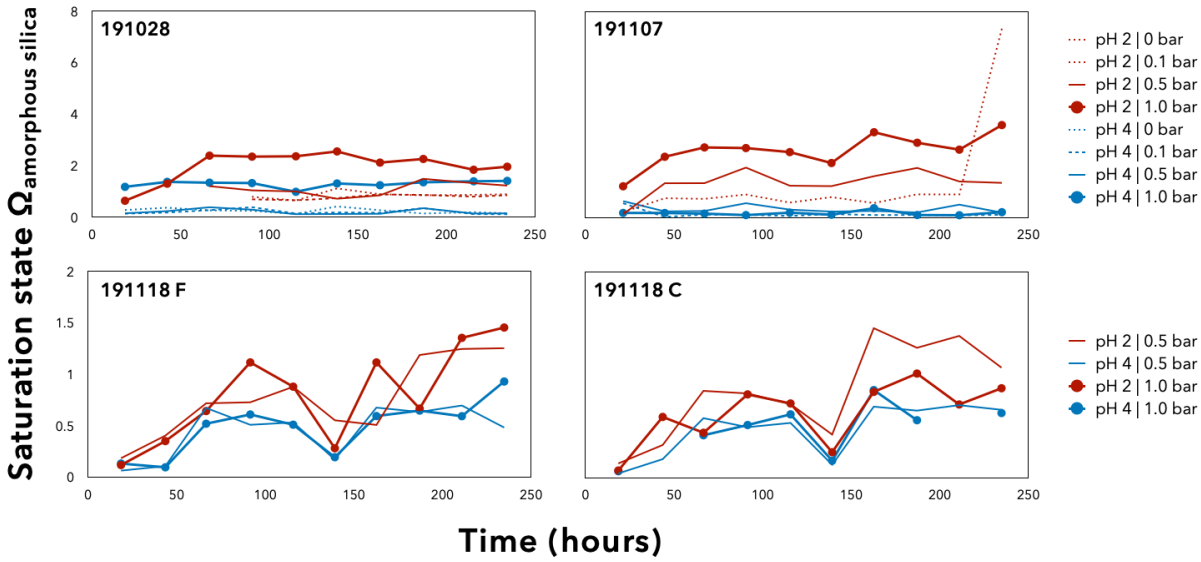


Figure 7: The saturation state (Ω) of amorphous silica in solution for each of the experiments in this chapter. The CRB experiments are divided into fine (F) or coarse (C) material. A legend to the right of each row displays which lines correspond to which experiments on that row.

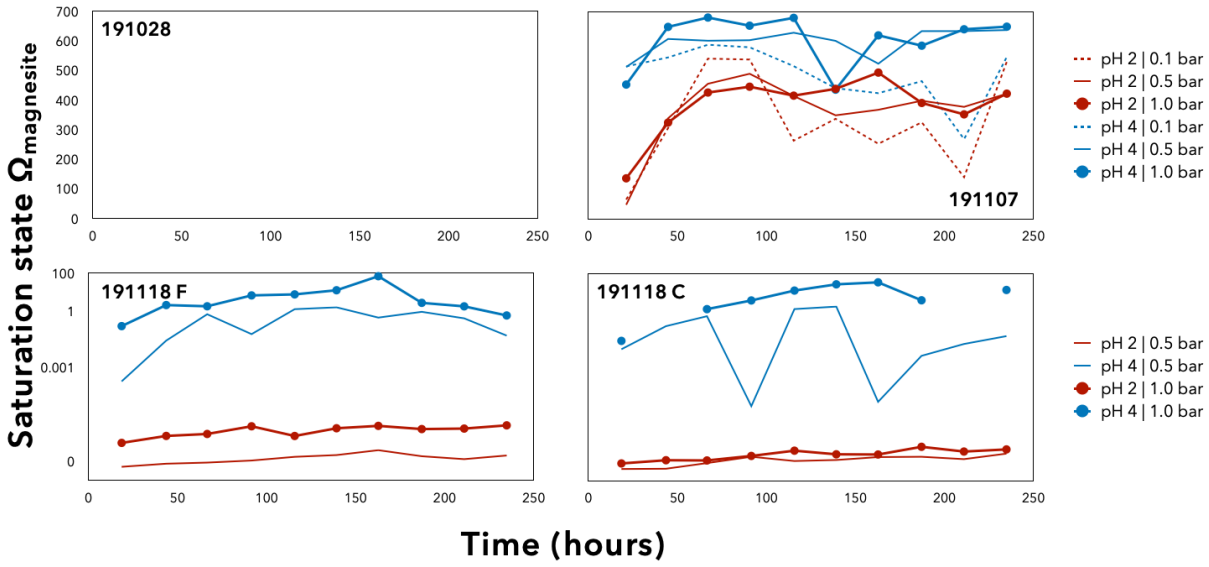


Figure 8: The saturation state (Ω) of magnesite in solution for each of the experiments in this chapter. Note the logarithmic axes. The CRB experiments are divided into fine (F) or coarse (C) material. A legend to the right of each row displays which lines correspond to which experiments on that row. There is no data displayed for 191028 because no magnesium was added to solution.

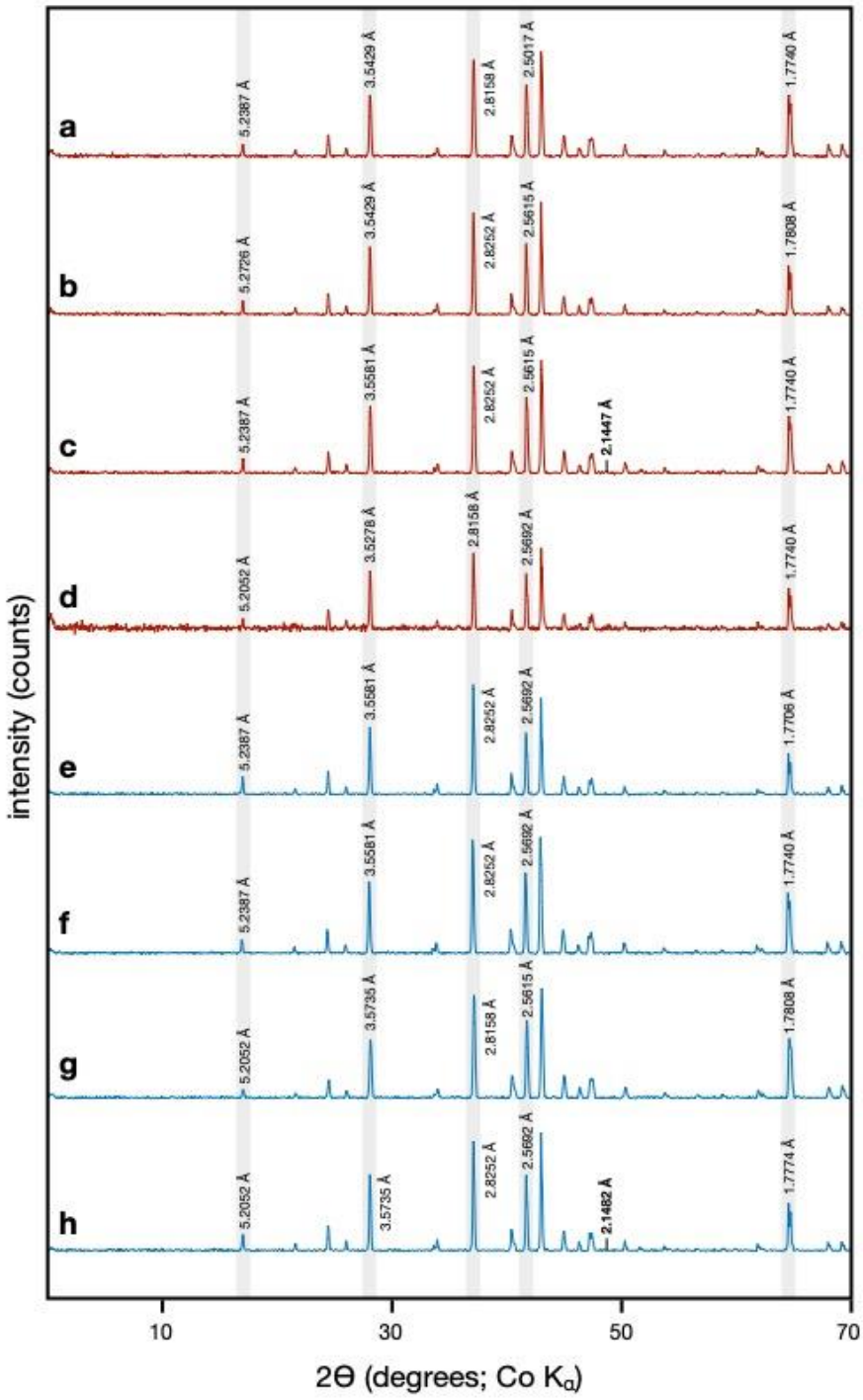


Figure 9: XRD signatures for 191028, which ran with 0, 0.5, or 1.0 bar of CO_2 with a substrate of Fa. In order: (a) pH 2 pCO_2 0 bar, (b) pH 4 pCO_2 0 bar, (c) pH 2 pCO_2 0.1 bar, (d) pH 4 pCO_2 0.1 bar, (e) pH 2 pCO_2 0.5 bar, (f) pH 4 pCO_2 0.5 bar, (g) pH 2 pCO_2 1.0 bar, and (h) pH 4 pCO_2 1.0 bar. Individual peaks are labelled for reference; where no peaks are labelled, none are sufficiently individually diagnostic. Shaded grey areas are key fayalite peaks. Peaks labels bolded were unable to be identified.

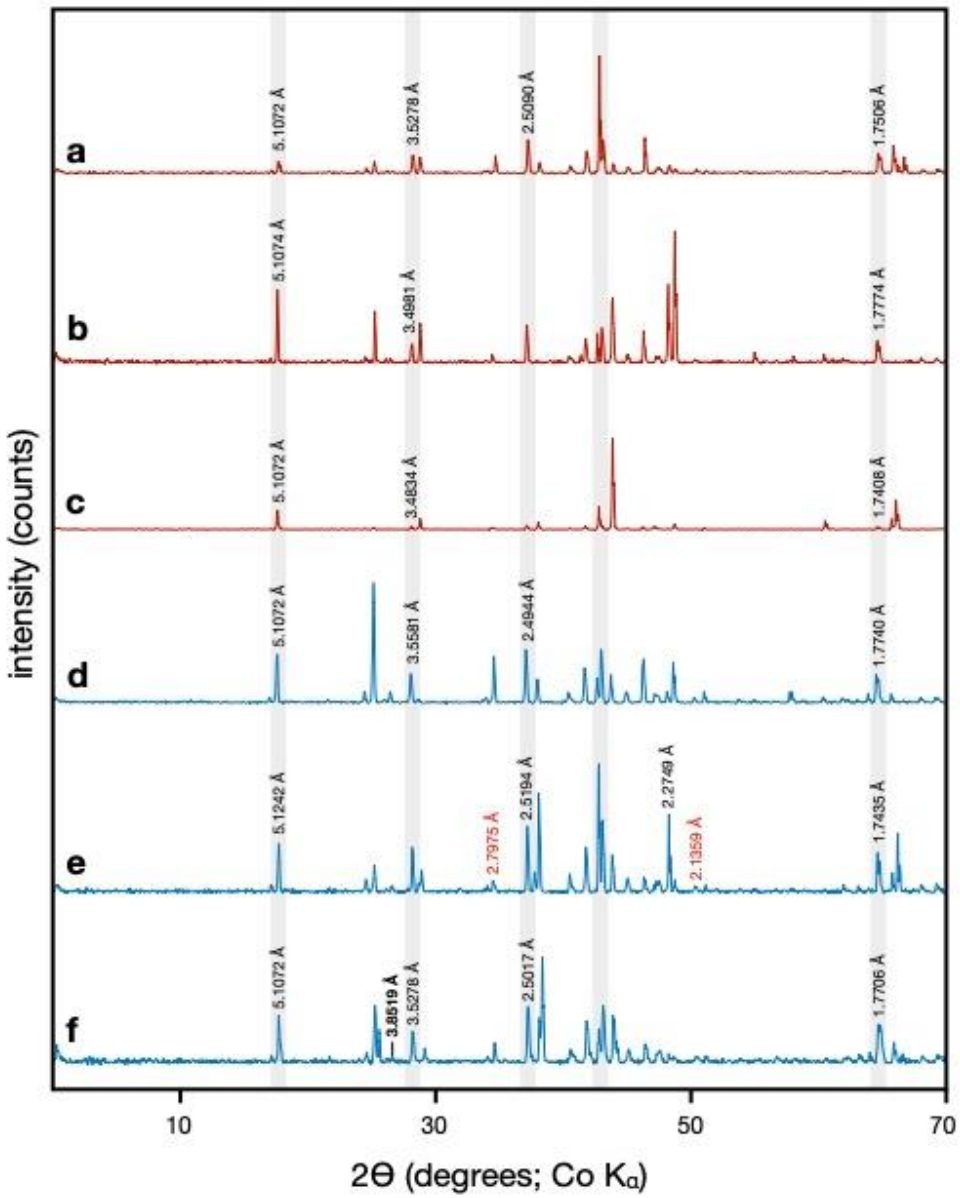


Figure 10: XRD signatures for 191107, which ran with 0.1, 0.5, or 1.0 bar of CO_2 with a substrate of Fa:Fo. In order: (a) pH 2 pCO_2 0.1 bar, (b) pH 4 pCO_2 1.0 bar, (c) pH 2 pCO_2 0.5 bar, (d) pH 4 pCO_2 0.5 bar, (e) pH 2 pCO_2 1.0 bar, and (f) pH 4 pCO_2 1.0 bar. Individual peaks are labelled for reference; where no peaks are labelled, none are sufficiently individually diagnostic. Shaded grey areas are key fayalite and forsterite peaks. Highlighted red are peaks that correspond to siderite. Peaks labels bolded were unable to be identified.

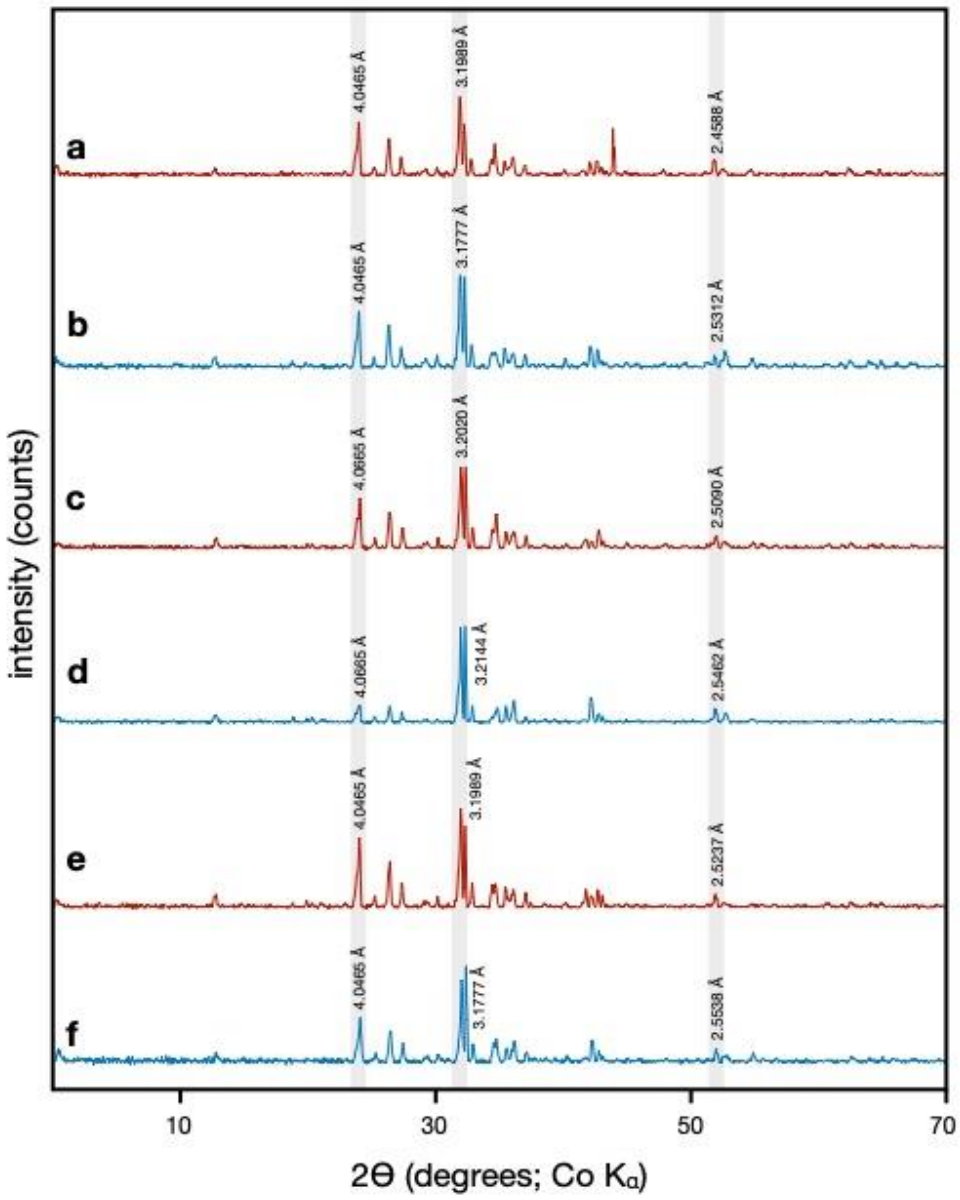


Figure 11: XRD signatures for 191118 F, which ran with 0, 0.5, or 1.0 bar of CO_2 with a substrate of CRB. In order: (a) pH 2 pCO_2 0 bar fine, (b) pH 4 pCO_2 0 bar fine, (c) pH 2 pCO_2 0.5 bar fine, (d) pH 4 pCO_2 0.5 bar fine, (e) pH 2 pCO_2 1.0 bar fine, and (f) pH 4 pCO_2 1.0 bar fine. Individual peaks are labelled for reference; where no peaks are labelled, none are sufficiently individually diagnostic. Shaded grey areas are key CRB peaks.

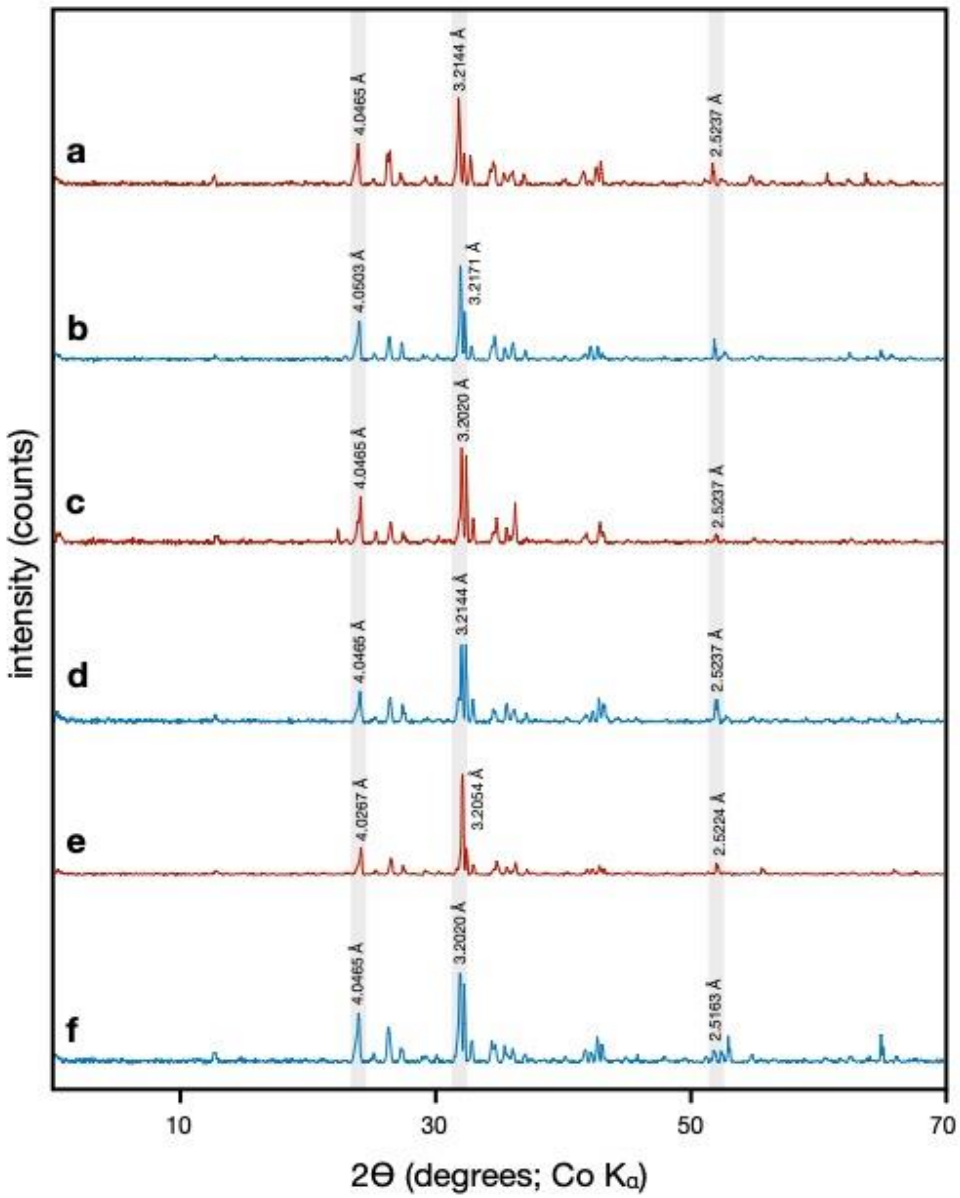


Figure 12: XRD signatures for 191118 C, which ran with 0, 0.5, or 1.0 bar of CO_2 with a substrate of CRB. In order: (a) pH 2 pCO_2 0 bar coarse, (b) pH 4 pCO_2 0 bar coarse, (c) pH 2 pCO_2 0.5 bar coarse, (d) 4 pCO_2 0.5 bar coarse, (e) pH 2 pCO_2 1.0 bar coarse, and (f) pH 4 pCO_2 1.0 bar coarse. Individual peaks are labelled for reference; where no peaks are labelled, none are sufficiently individually diagnostic. Shaded grey areas are key CRB peaks.

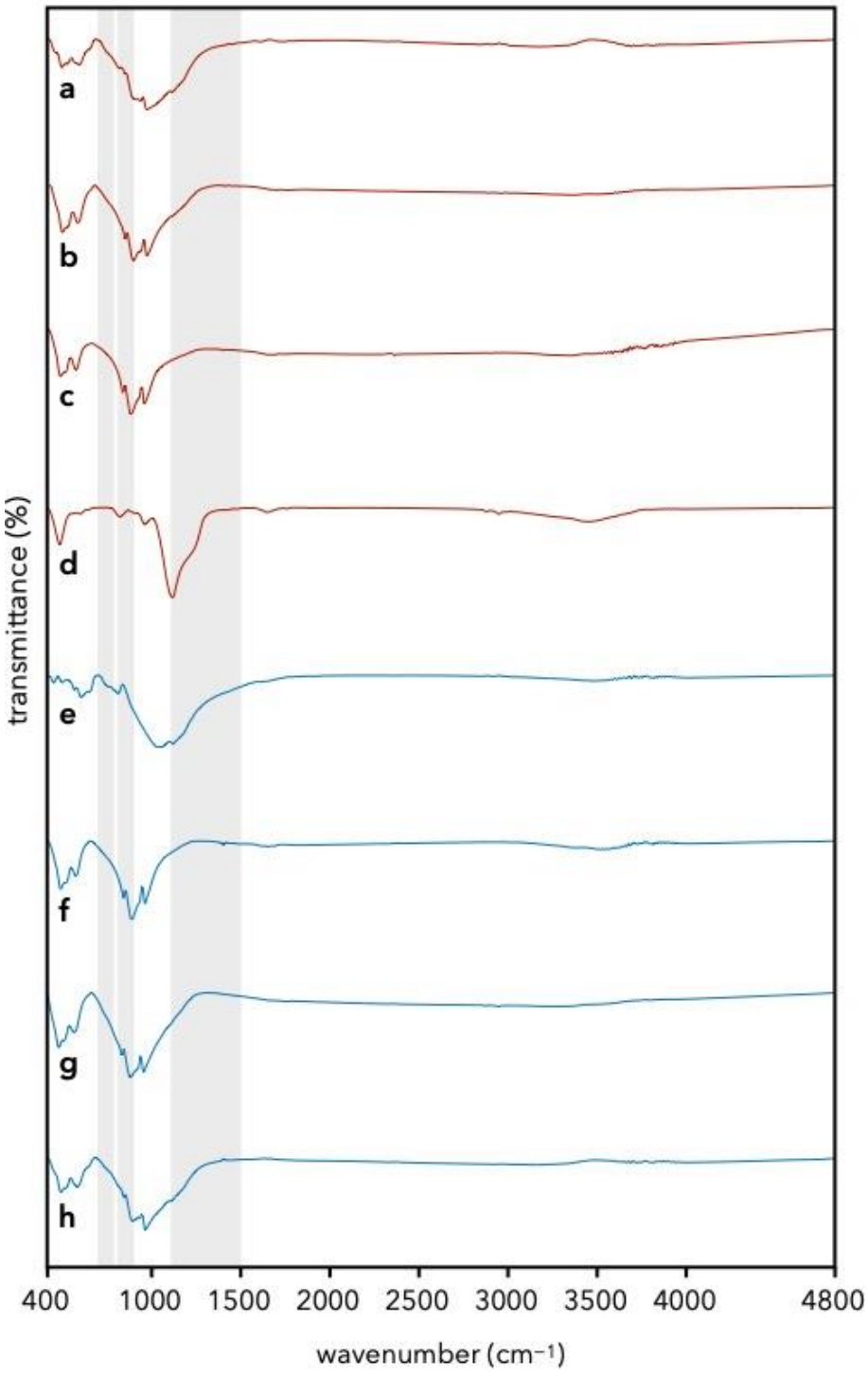


Figure 13: FT-IR signatures for the Fa-bearing experiment of 191028. In order: (a) pH 2 pCO_2 0 bar, (b) pH 4 pCO_2 0 bar, (c) pH 2 pCO_2 0.1 bar, (d) pH 4 pCO_2 0.1 bar, (e) pH 2 pCO_2 0.5 bar, (f) pH 4 pCO_2 0.5 bar, (g) pH 2 pCO_2 1.0 bar, and (h) pH 4 pCO_2 1.0 bar. Shaded grey regions correspond to absorption regions for siderite.

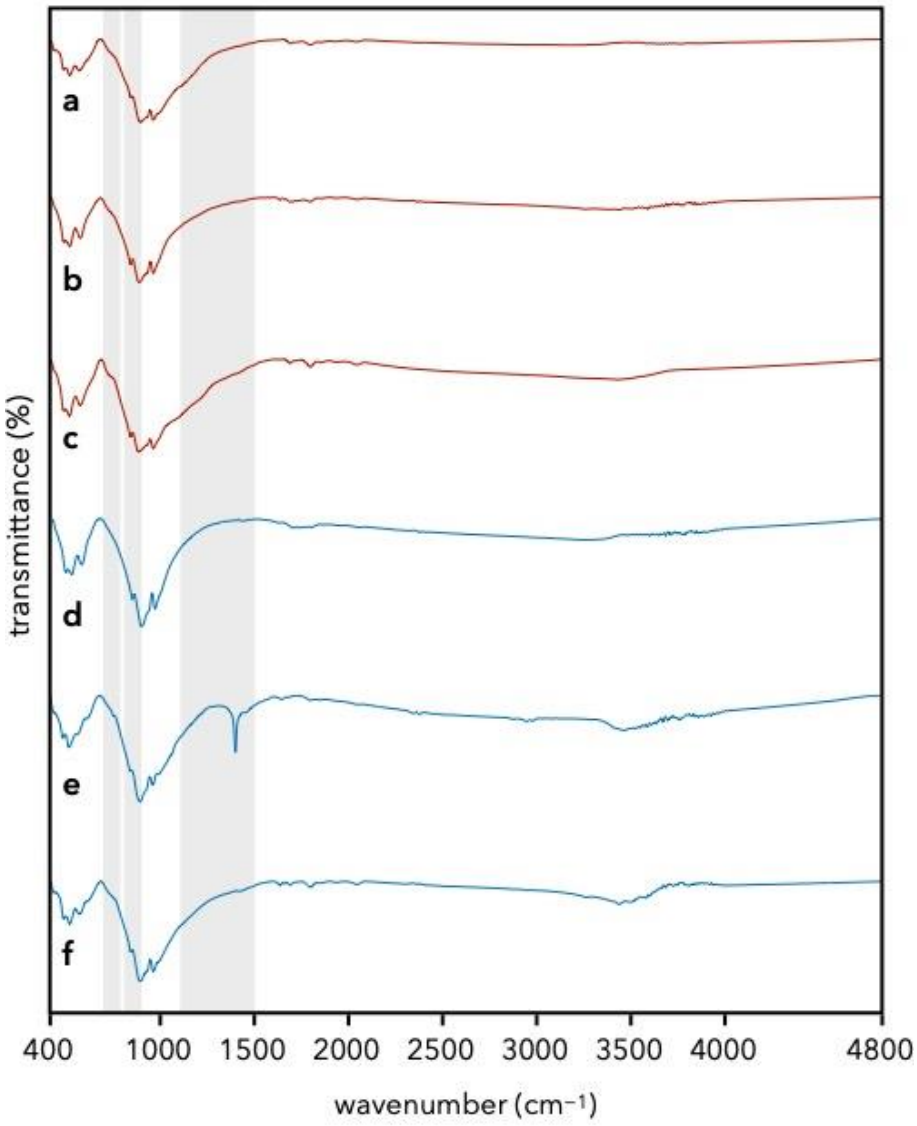


Figure 14: FT-IR signatures for the Fa:Fo-bearing experiment of 191107. In order: (a) pH 2 pCO_2 0.1 bar, (b) pH 4 pCO_2 1.0 bar, (c) pH 2 pCO_2 0.5 bar, (d) pH 4 pCO_2 0.5 bar, (e) pH 2 pCO_2 1.0 bar, and (f) pH 4 pCO_2 1.0 bar. Shaded grey regions correspond to absorption regions for siderite.

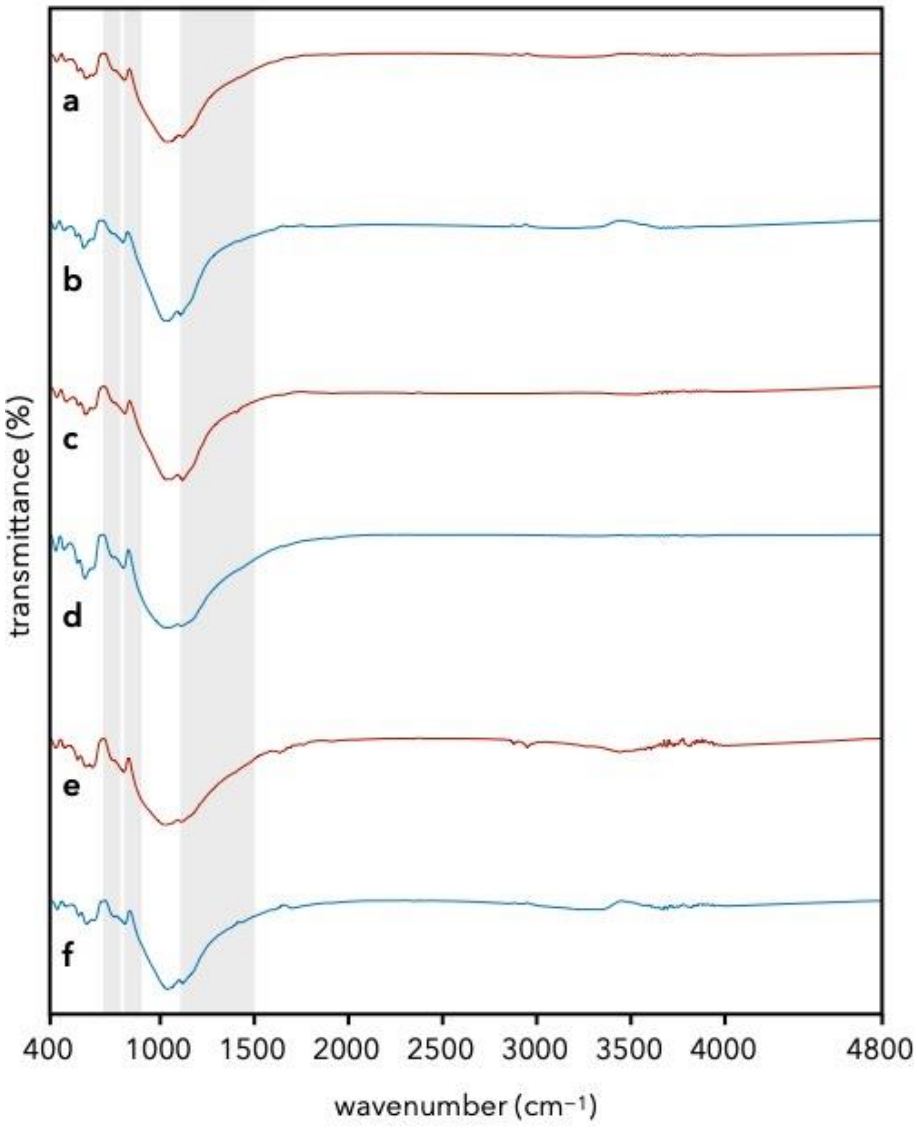


Figure 15: FT-IR signatures for the fine CRB-bearing experiment of 191118. In order: (a) pH 2 pCO_2 0 bar fine, (b) pH 4 pCO_2 0 bar fine, (c) pH 2 pCO_2 0.5 bar fine, (d) pH 4 pCO_2 0.5 bar fine, (e) pH 2 pCO_2 1.0 bar fine, and (f) pH 4 pCO_2 1.0 bar fine. Shaded grey regions correspond to absorption regions for siderite.

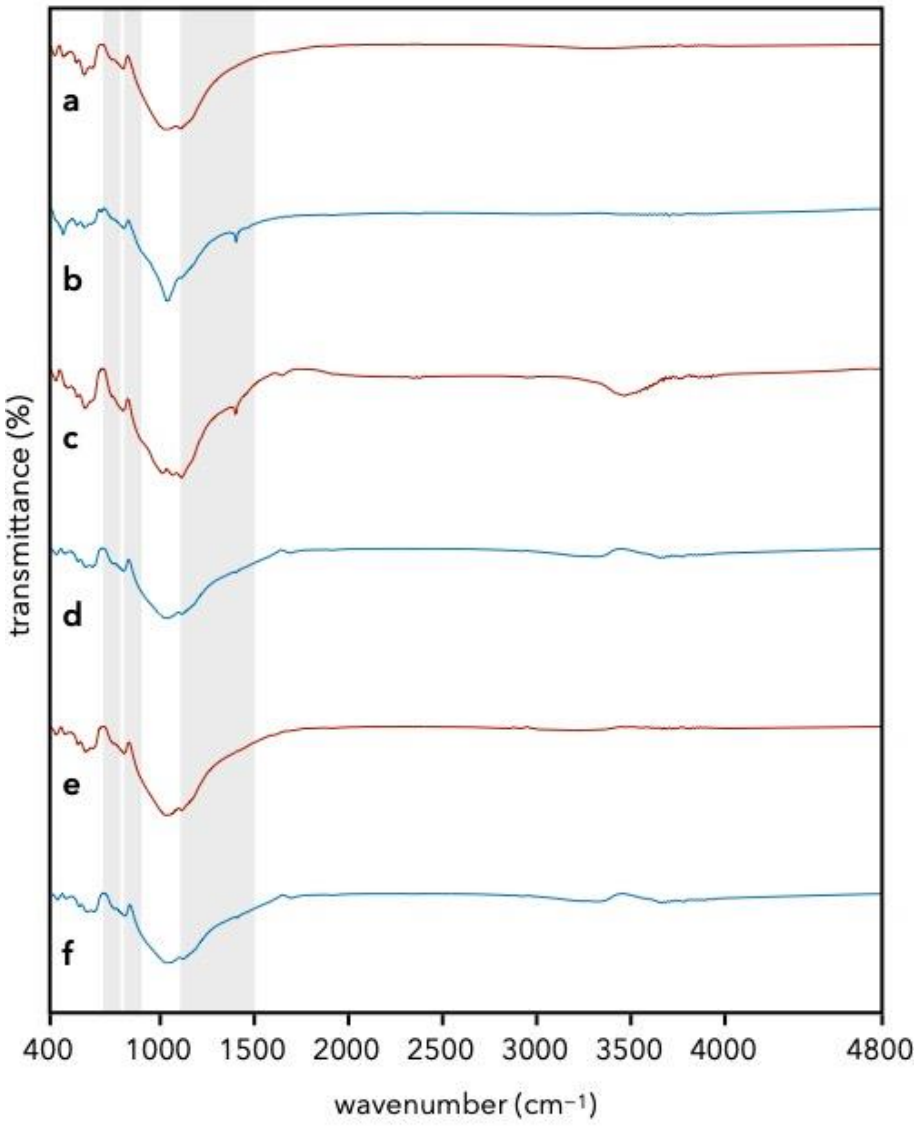


Figure 16: FT-IR signatures for the coarse CRB-bearing experiment of 191118. In order: (a) pH 2 pCO_2 0 bar coarse, (b) pH 4 pCO_2 0 bar coarse, (c) pH 2 pCO_2 0.5 bar coarse, (d) 4 pCO_2 0.5 bar coarse, (e) pH 2 pCO_2 1.0 bar coarse, and (f) pH 4 pCO_2 1.0 bar coarse. Shaded grey regions correspond to absorption regions for siderite.

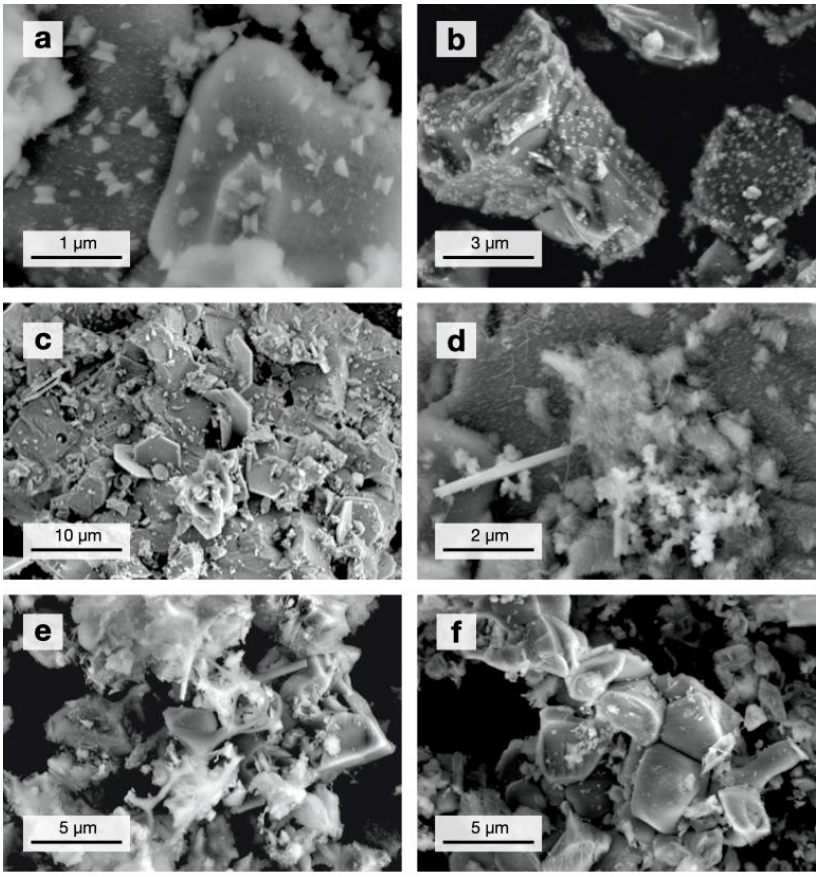


Figure 17: SEM images of fayalite reacted at 75 ºC. (a) Butterfly-twinned minerals up close from pH 4 0.1; (b) Butterfly-twinned minerals aligned along fayalite surface, also from 4 0.1; (c) Hexagon plates growing out of the surface of a fayalite grain in pH 4 0.5; (d) Coral-like growth, string-like growth, nano-metre scale aligned platelets, and a single rod-shaped growth, from 4 0.5; (e) Antler-like growths seen in low temperature experiments, from pH 4 1.0; (e) interlocking cuboid-shaped growths, also in 4 1.0.

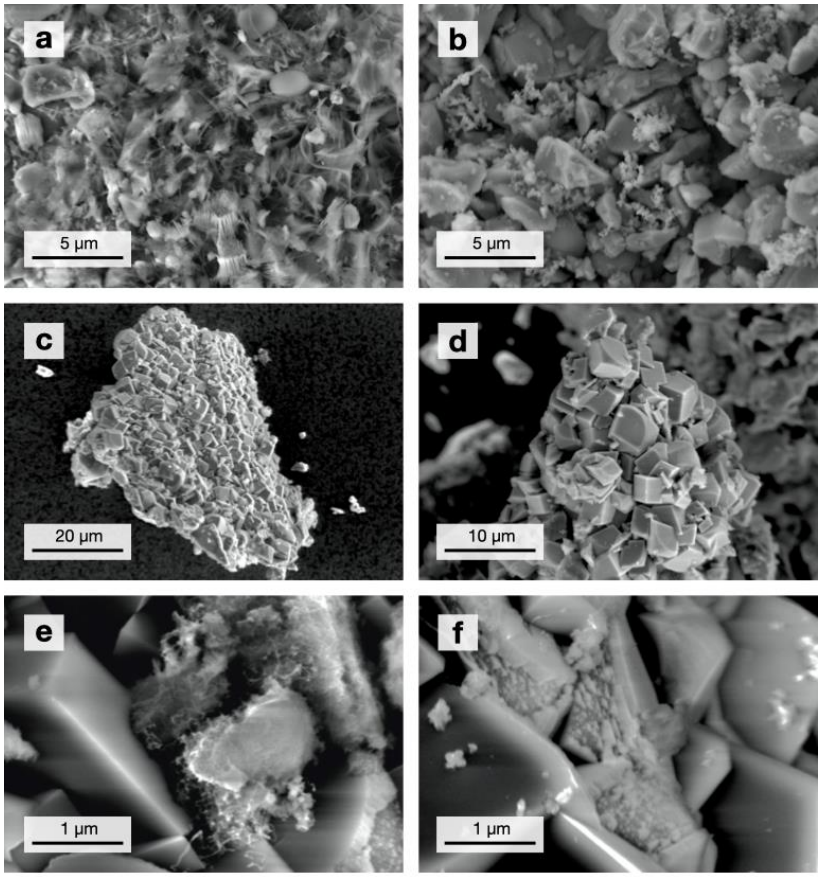


Figure 18: SEM images of fayalite and forsterite reacted at 75 ºC. (a) Antler-shaped growths seen here in pH 2 0.5, but present in most high temperature solids; (b) Coral-like growths on pH 4 1.0; (c) Interlocking rhombs growing upon the surface of fayalite in pH 4 0.5; (d) Close-up of rhombs in a tower in 4 0.5; (e) Close-up of rhombs reveals stringy mineral growth that loosens itself, seen in 4 0.5; (f) Close-up of rhombs also reveals aligned nano-scale platelets, seen in 4 0.5.

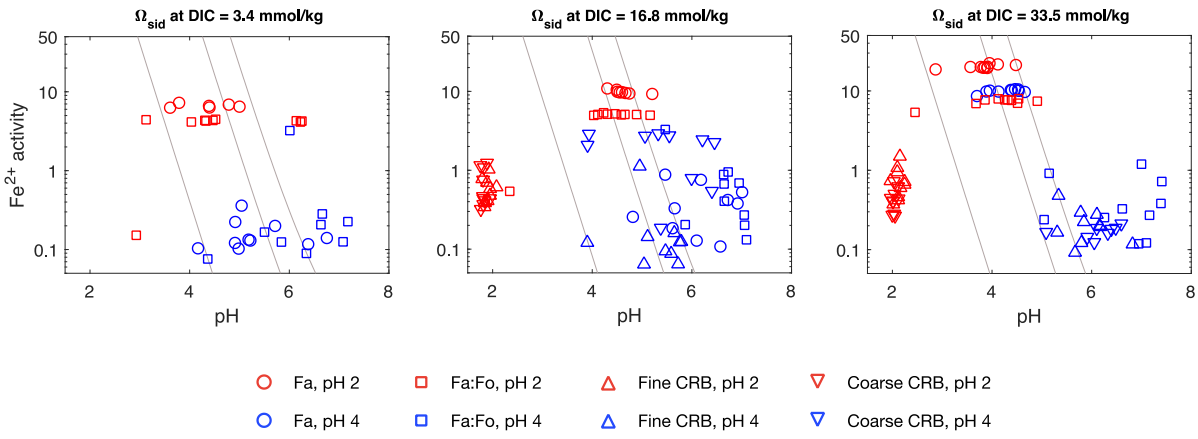


Figure 19: The saturation state of all extracted samples in terms of the Fe(II)-carbonate siderite, divided into three graphs depending upon 0.1 (DIC = 3.4 mmol/kg), 0.5 (DIC = 16.8 mmol/kg), or 1.0 (DIC = 33.5 mmol/kg) pCO_2 levels, and expressed in terms of Fe^{2+} activity and pH. The three light, grey lines on each represent the saturation state of siderite as 1, 100, or 400. The 'AFC-line' of Jiang and Tosca (2019) used in Chapters 3 and 4, is not included here because no thermodynamic data exists for AFC at temperatures of 75 ºC. Circles are fayalite-bearing experiments; squares are fayalite- and forsterite-bearing; up-triangles are fine-grained CRB; down-triangles are coarse-grained CRB; red represents pH 2 experiments, while blue pH 4.

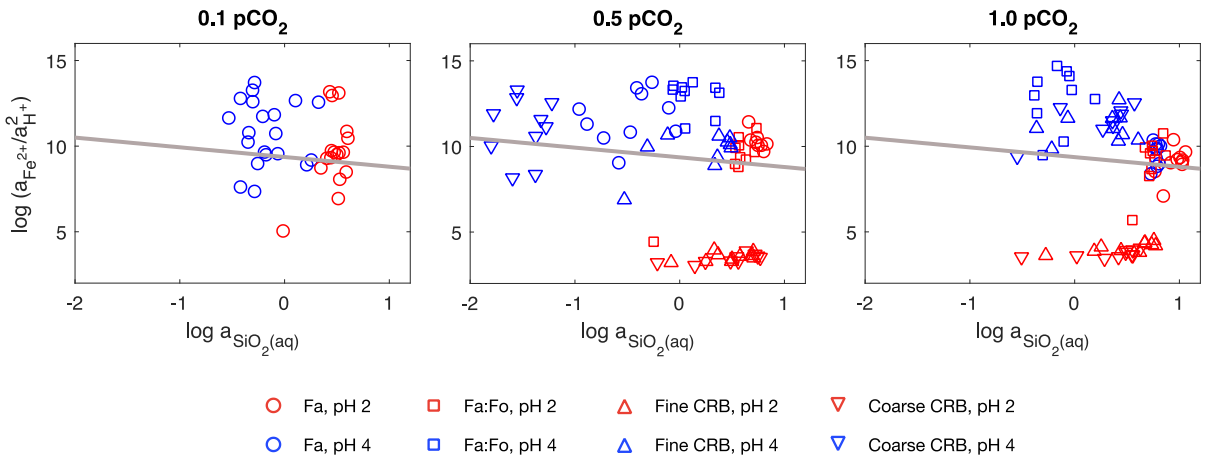


Figure 20: Solubility diagrams for greenalite, divided into three graphs depending upon 0.1 (DIC = 3.4 mmol/kg), 0.5 (DIC = 16.8 mmol/kg), or 1.0 (DIC = 33.5 mmol/kg) pCO_2 levels, involving the three principal factors controlling greenalite stability: the activities of Fe^{2+}, H^+, and $SiO_{2(aq)}$. Circles are fayalite-bearing experiments; squares are fayalite- and forsterite-bearing; up-triangles are fine-grained CRB; down-triangles are coarse-grained CRB; red represents pH 2 experiments, while blue pH 4. Datapoints towards the top and the right generally correspond to increasingly later stages of an experiment. The heavy grey line is the greenalite saturation line of Tosca et al. (2016). Any datapoints exceeding this line are considered supersaturated with respect to greenalite.

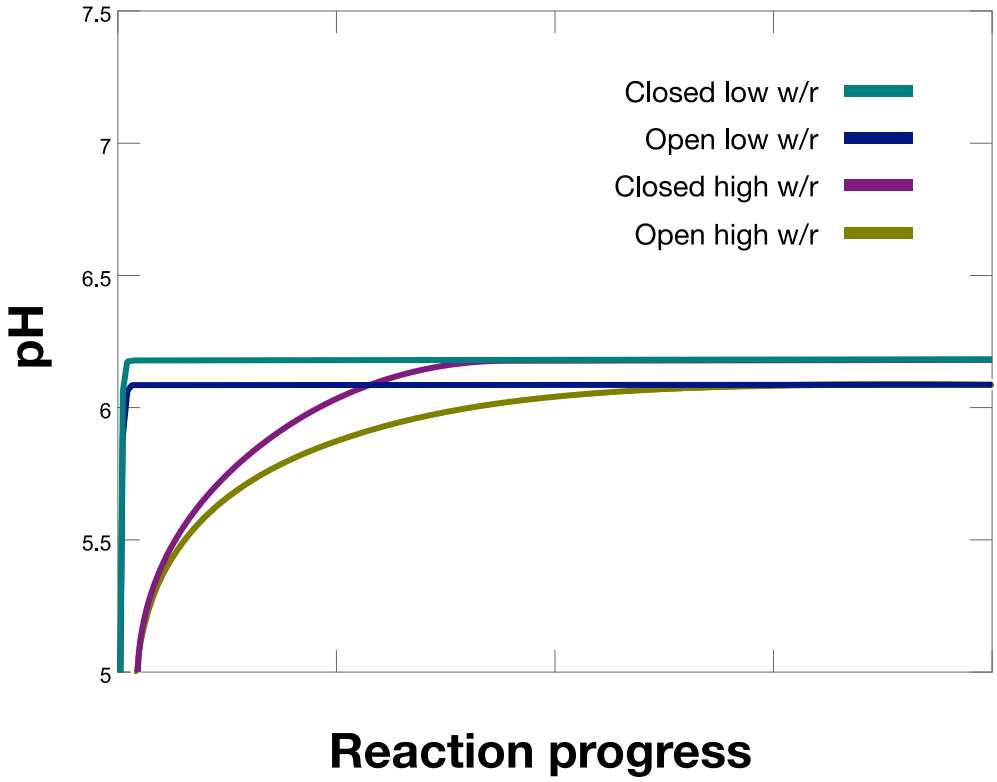


Figure 21: Modelled pH trends for the four modelled environments using fayalite as a substrate.

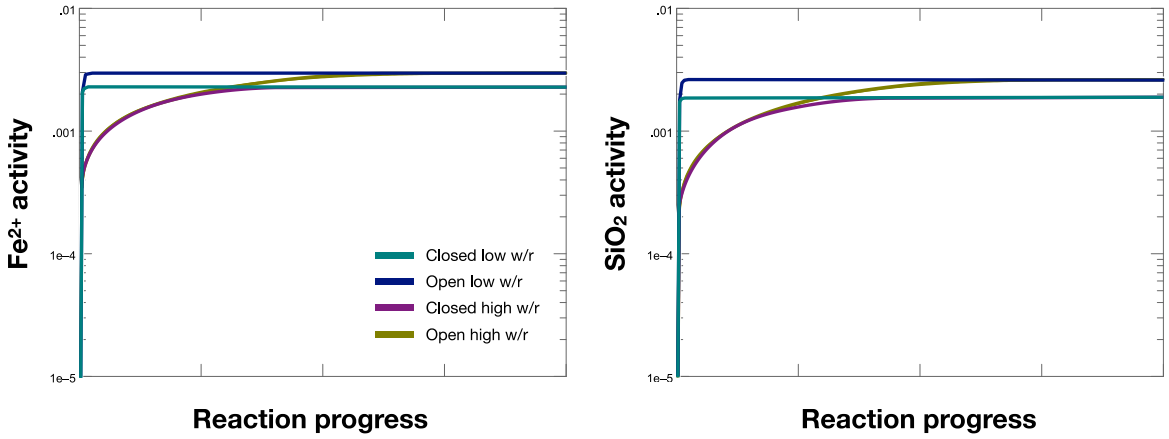


Figure 22: Modelled Fe^{2+} and SiO_2 activity for the four modelled environments using fayalite as a substrate.

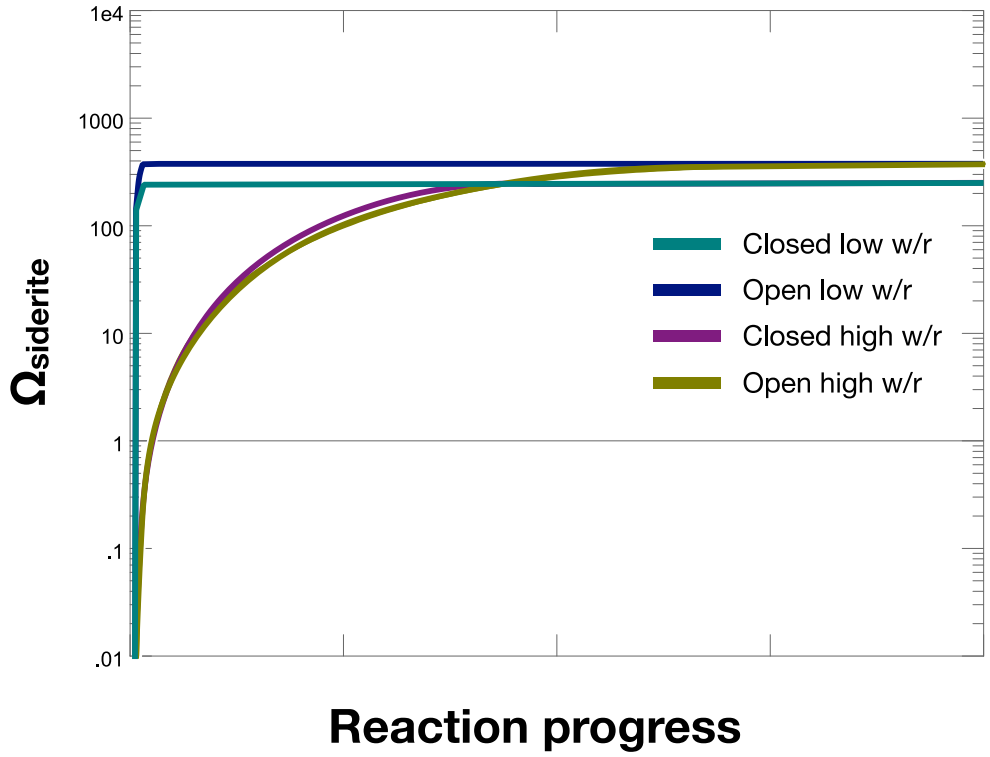


Figure 23: Modelled $\Omega_{siderite}$ for the four modelled environments using fayalite as a substrate.

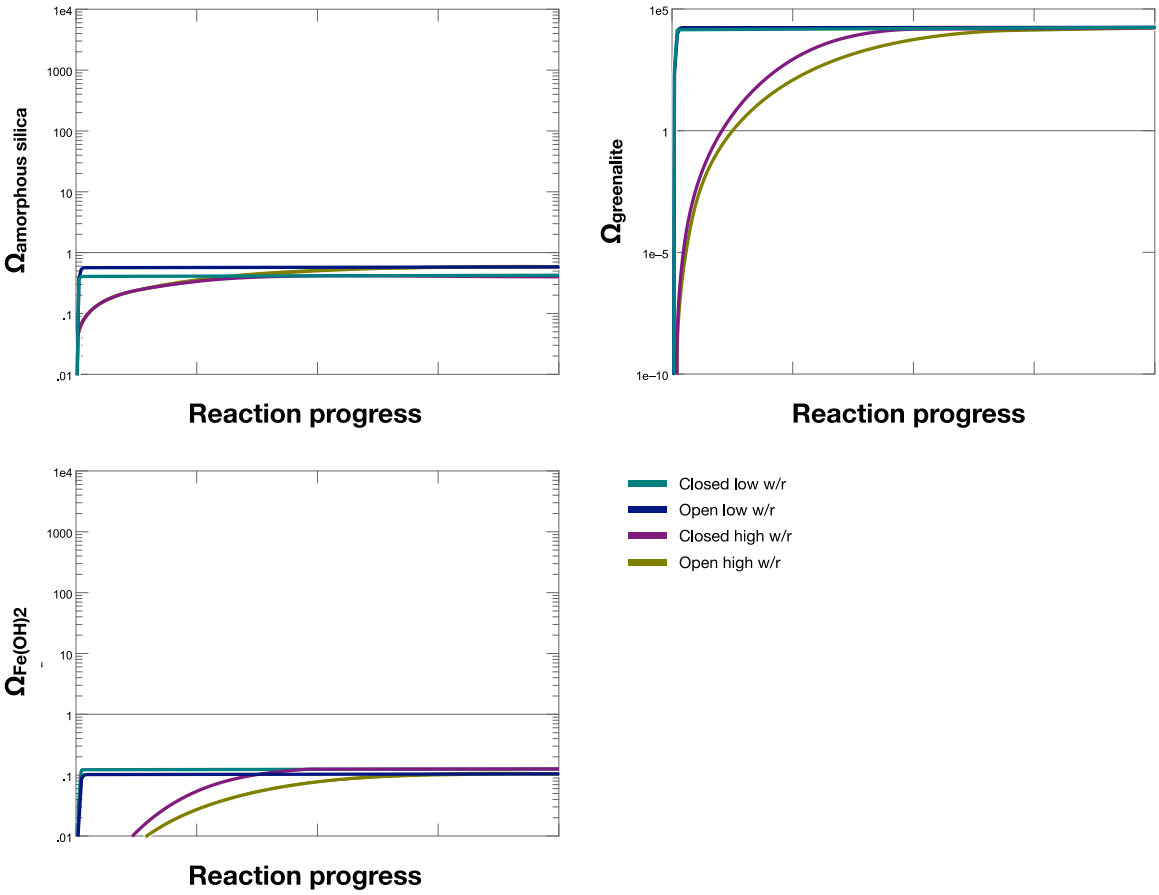


Figure 24: Modelled $\Omega_{amorphous_Si}$, $\Omega_{greenalite}$, and $\Omega_{Fe(OH)2}$ for the four modelled environments using fayalite as a substrate.

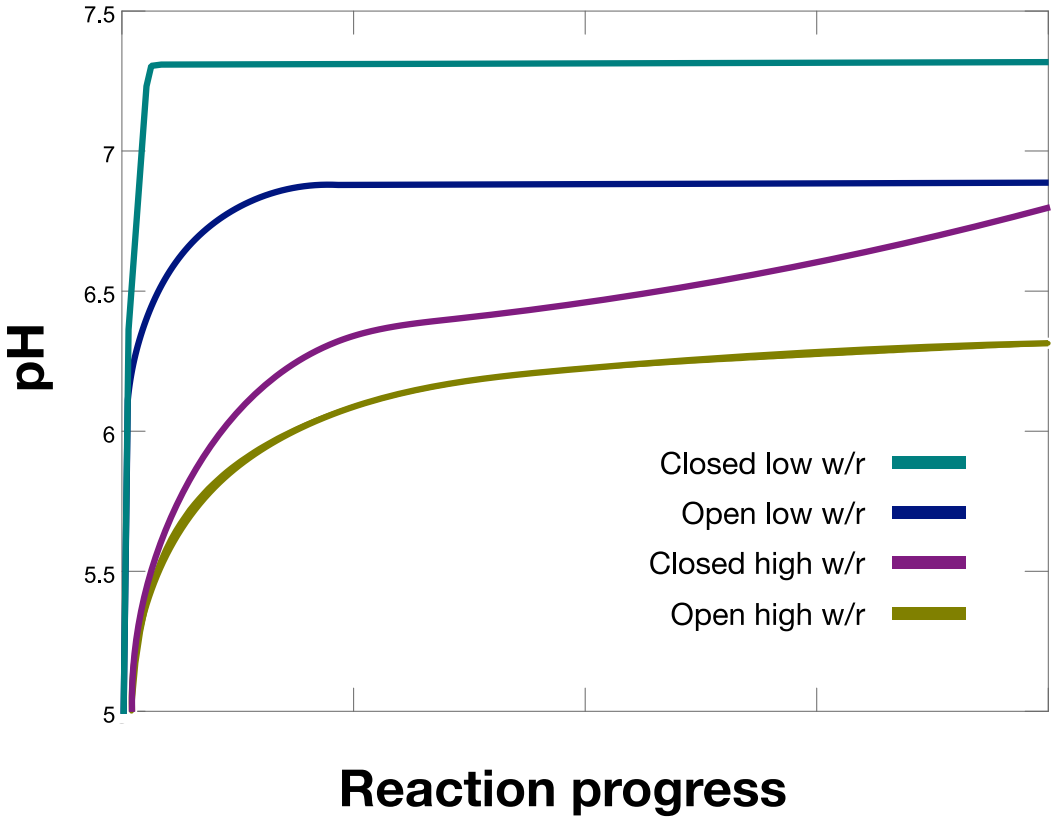


Figure 25: Modelled pH trends for the four modelled environments using forsterite as a substrate.

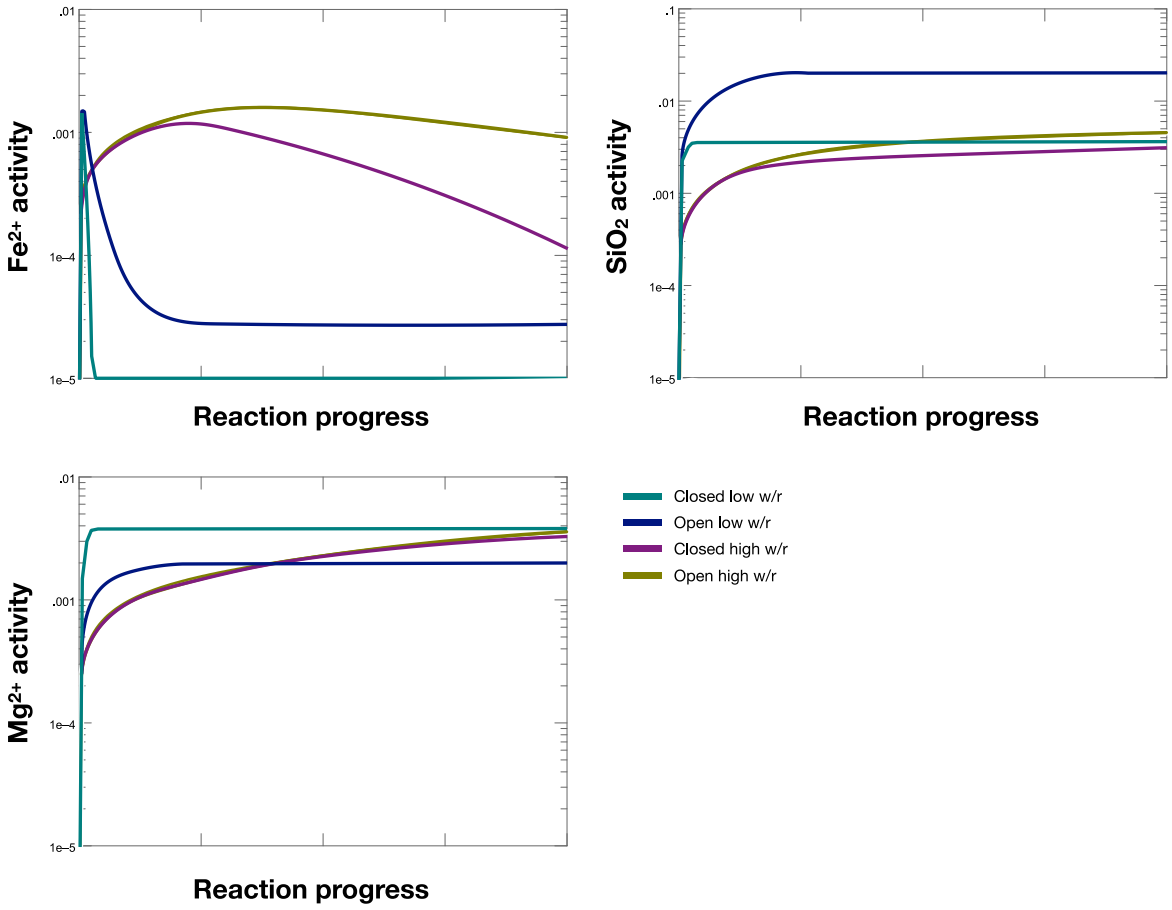


Figure 26: Modelled Fe^{2+}, SiO_2, and Mg^{2+} activity for the four modelled environments using forsterite as a substrate.

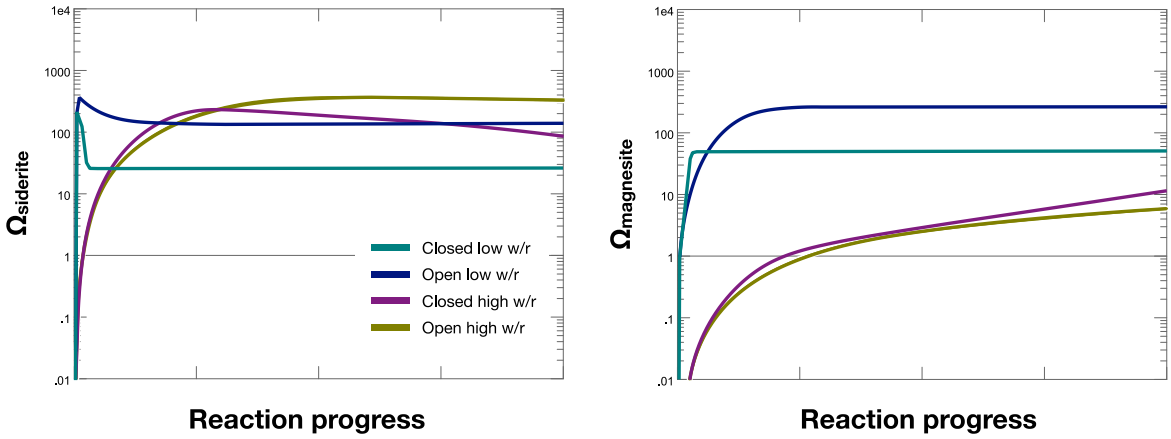


Figure 27: Modelled $\Omega_{siderite}$ and $\Omega_{magnesite}$ for the four modelled environments using forsterite as a substrate.

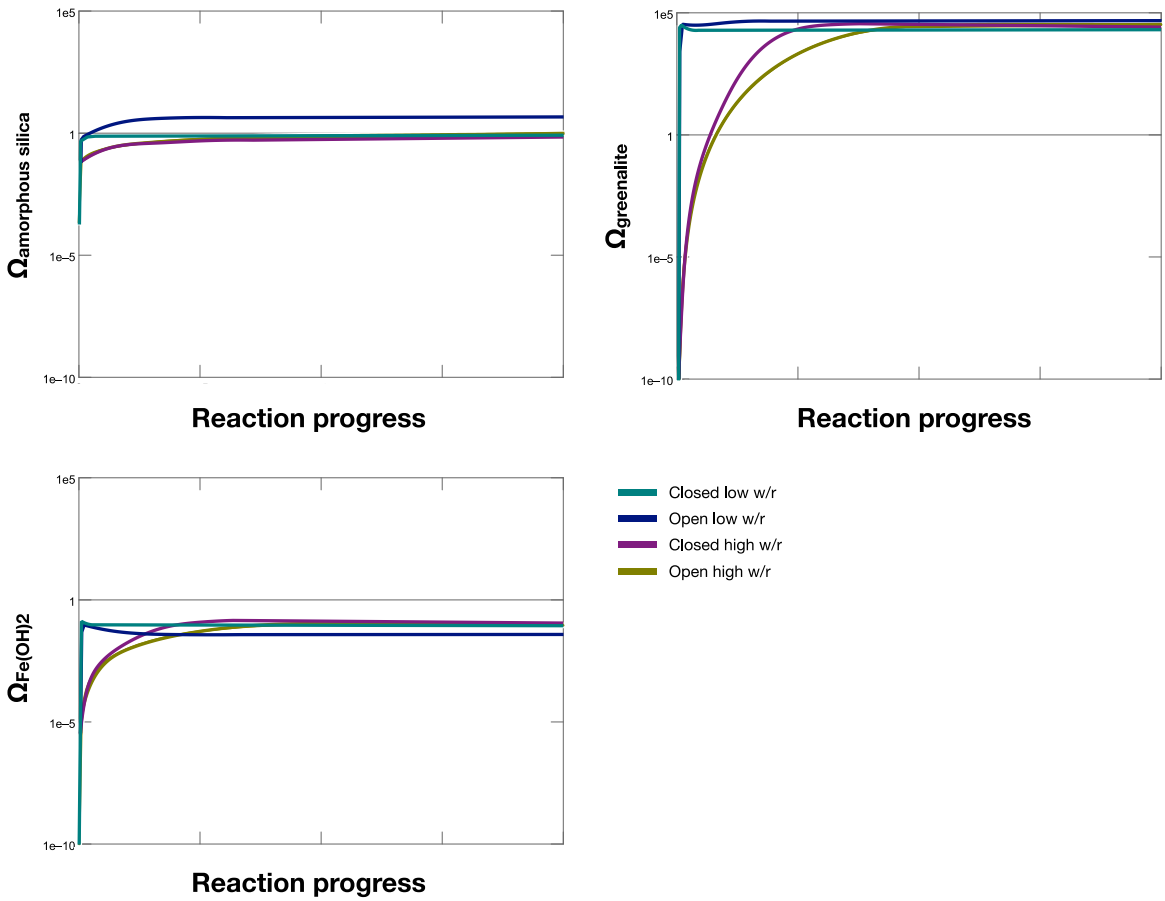


Figure 28: Modelled $\Omega_{amorphous_Si}$, $\Omega_{greenalite}$, and $\Omega_{Fe(OH)2}$ for the four modelled environments using forsterite as a substrate.

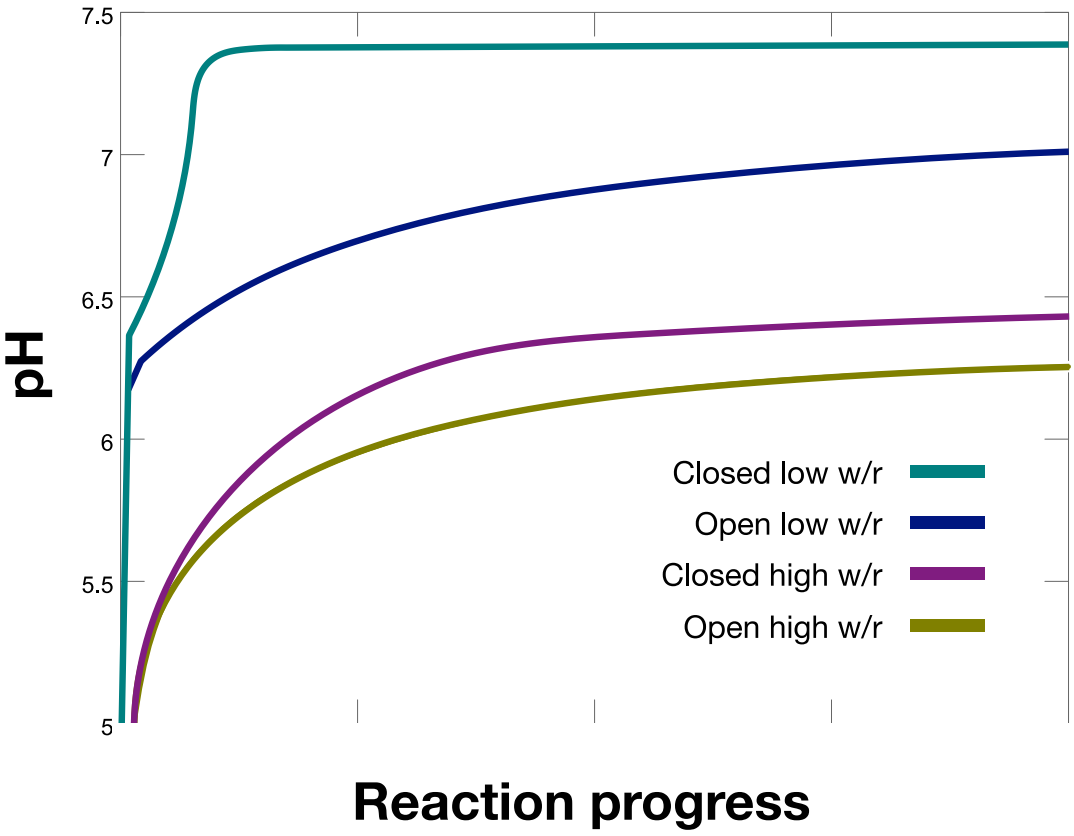


Figure 29: Modelled pH trends for the four modelled environments using CRB as a substrate.

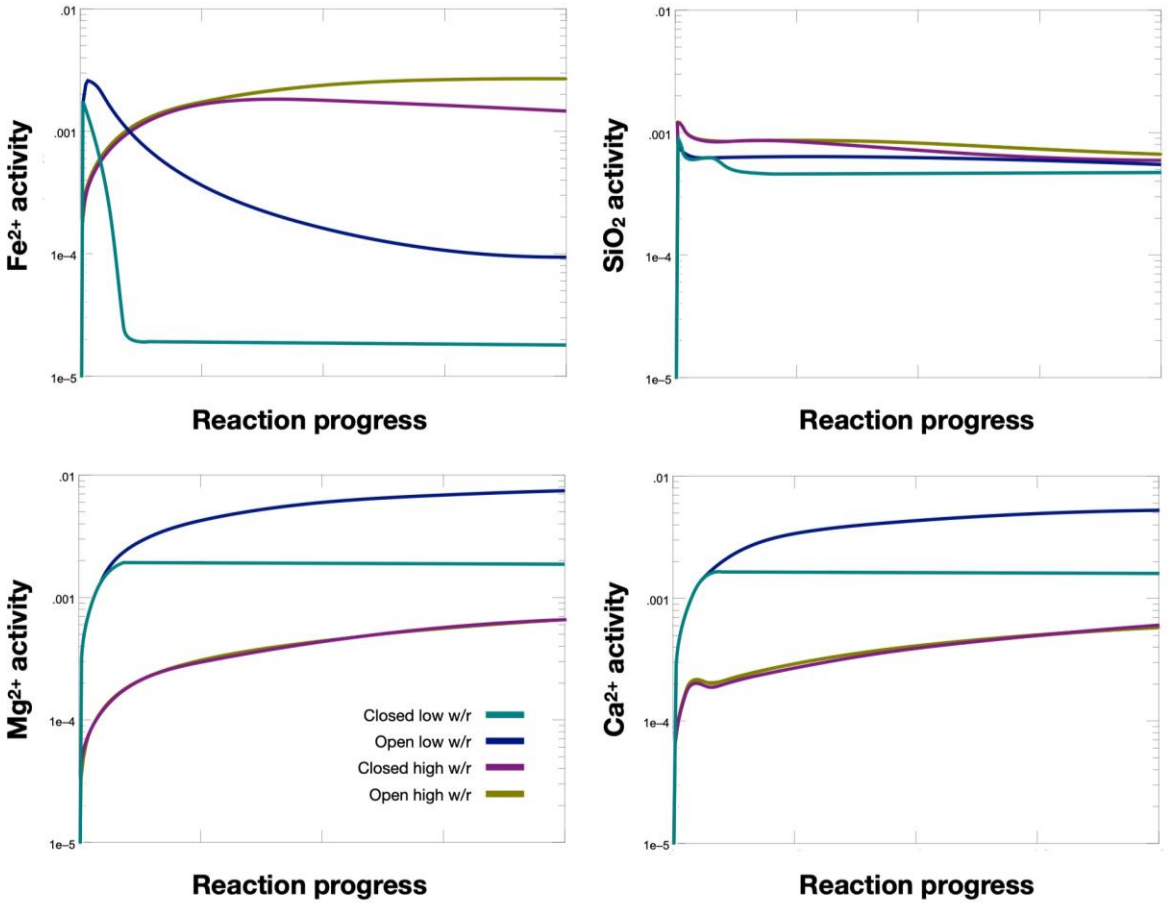


Figure 30: Modelled Fe^{2+}, SiO_2, Mg^{2+}, and Ca^{2+} activity for the four modelled environments using CRB as a substrate.

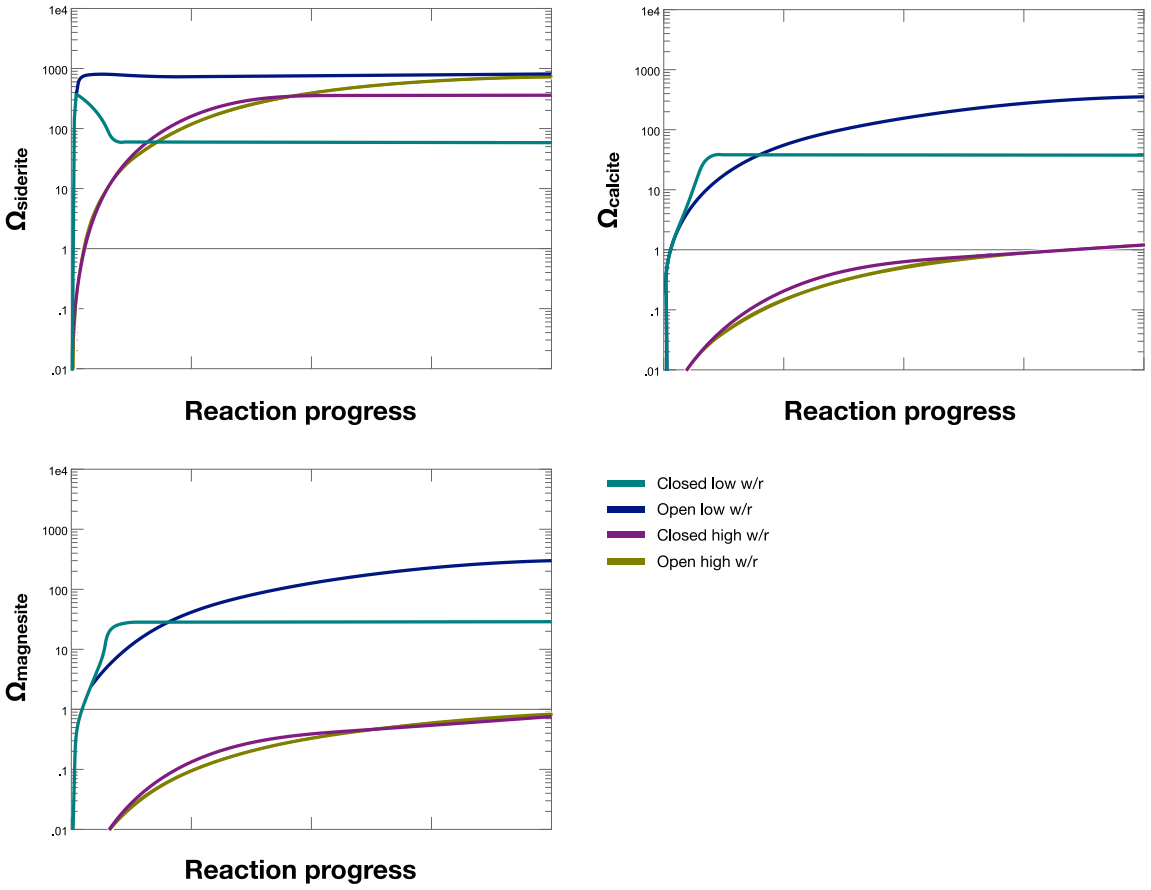


Figure 31: Modelled $\Omega_{siderite}$, $\Omega_{calcite}$, and $\Omega_{magnesite}$ for the four modelled environments using CRB as a substrate.

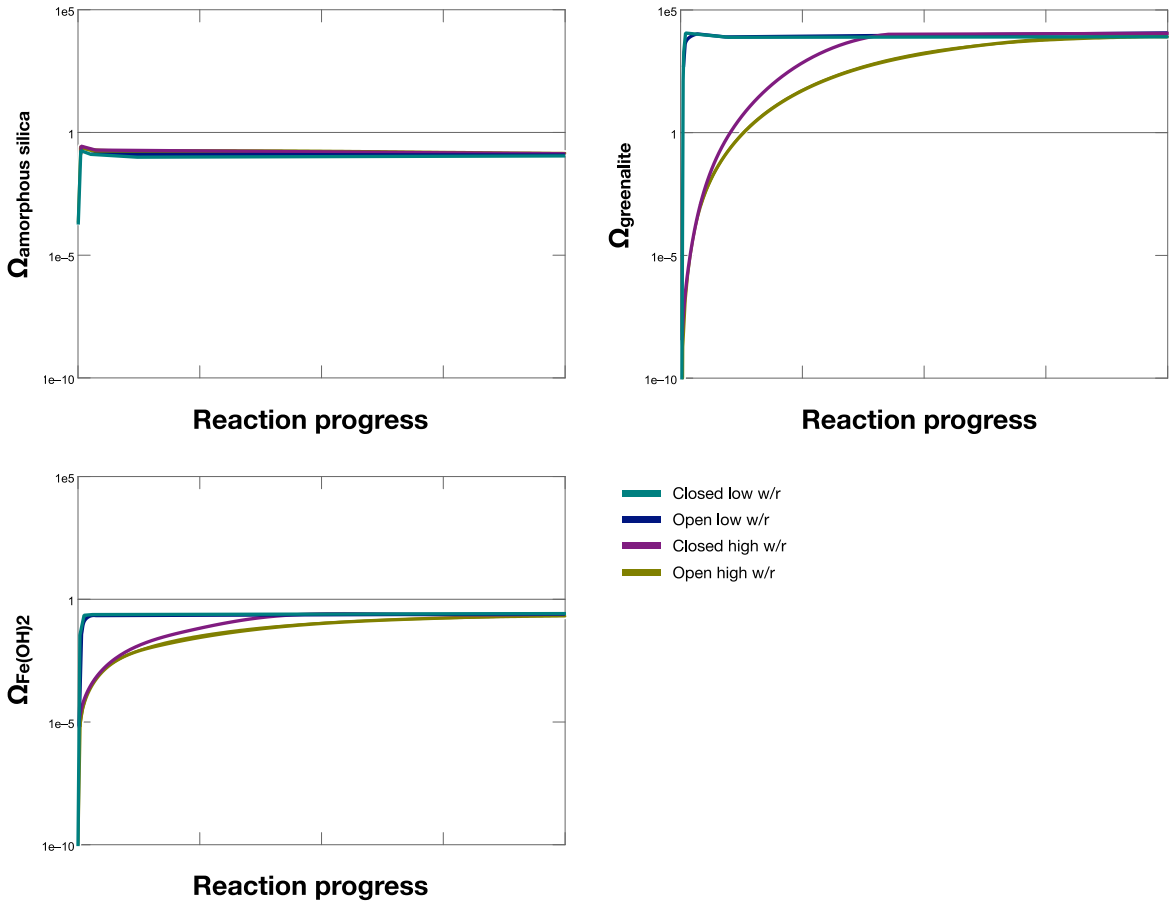


Figure 32: Modelled $\Omega_{amorphous_Si}$, $\Omega_{greenalite}$, and $\Omega_{Fe(OH)2}$ for the four modelled environments using CRB as a substrate.

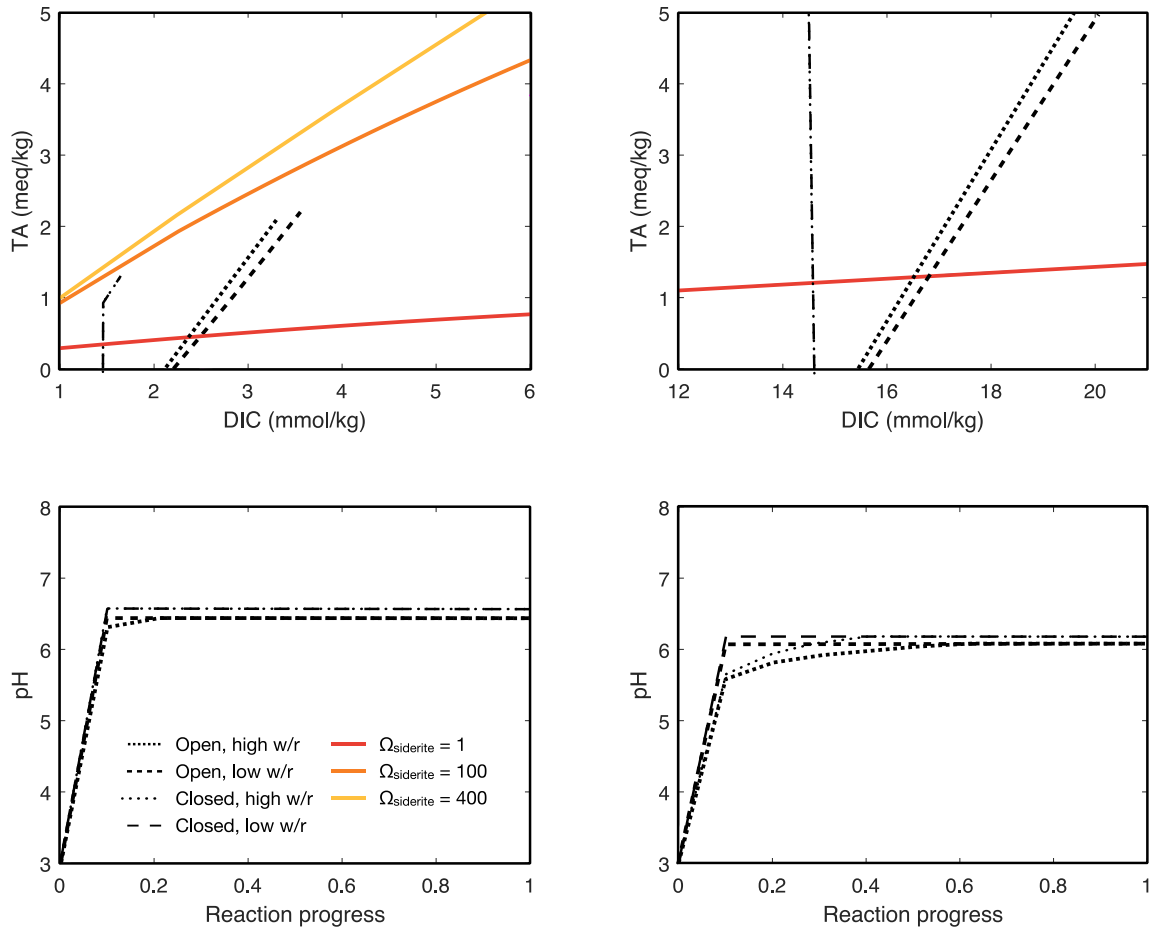


Figure 33: Results from four reaction path models of water-rock interaction at 75 °C with a substrate of fayalite: open-system with respect to CO_2 at high rock:waterrock:water ratio (tightly-dotted lines), open-system with respect to CO_2 at low rock:waterrock:water ratio (dashed lines), closed-system with respect to CO_2 at high rock:waterrock:water ratio (circular-dotted lines), and closed-system with respect to CO_2 at low rock:waterrock:water ratio (long dashed lines). Left column: models run with 0.1 bar CO_2; right column: models run with 1.0 bar CO_2. (a) and (b): siderite saturation state as a function of DIC and total alkalinity (TA). From bottom-up, red to yellow lines represent $\Omega_{siderite}$ of 1, 100, and 100,000. (c) and (d): pH variation over the course of the experiment (which corresponds closely to total alkalinity in this system). In order to illustrate the influence of water-rock interaction on the Fe(II)-carbonate system in DIC-TA space, these models were run under fixed Fe^{2+} concentration of 10 mmol/kg with fayalite as the sole reactant.

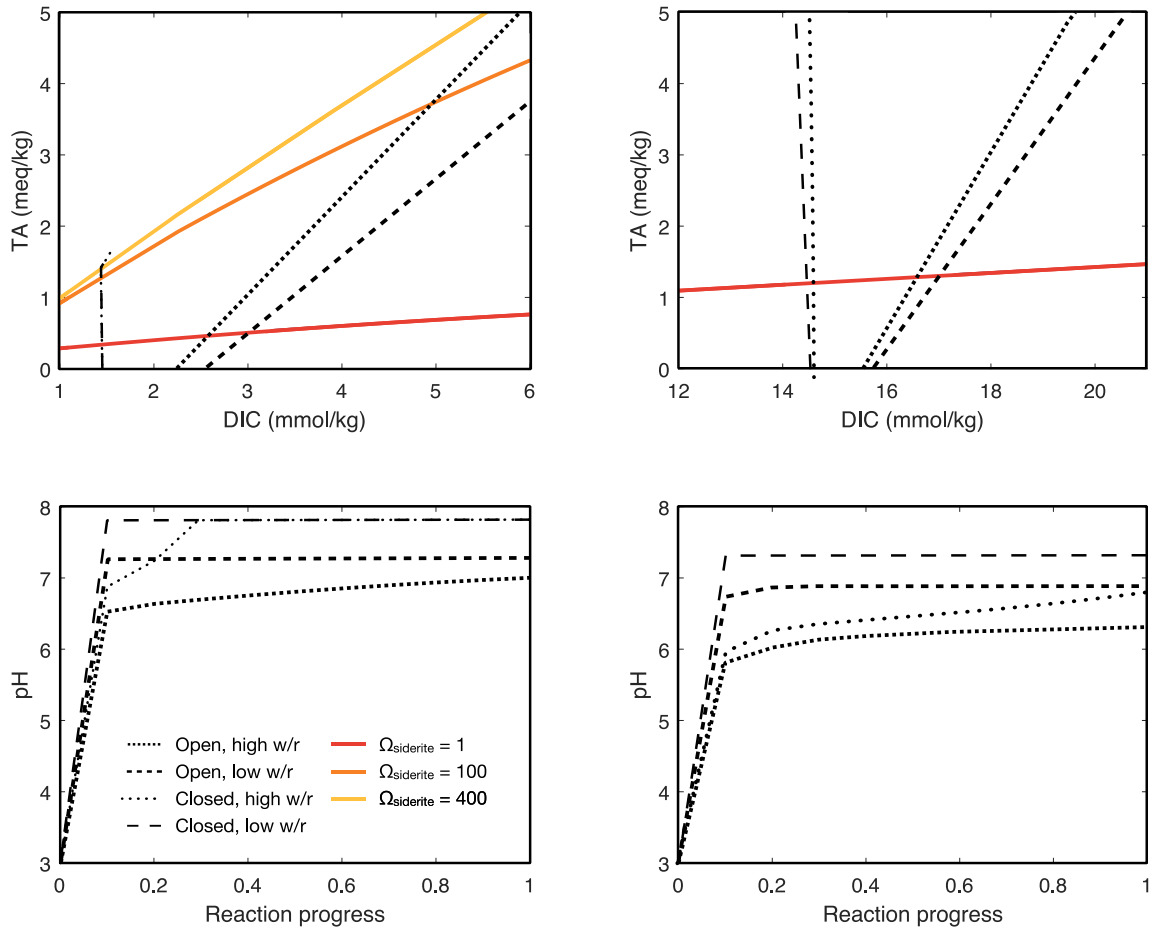


Figure 34: Results from four reaction path models of water-rock interaction at 75 ºC with a substrate of 1:1 fayalite and forsterite: open-system with respect to CO_2 at high rock:waterrock:water ratio (tightly-dotted lines), open-system with respect to CO_2 at low rock:waterrock:water ratio (dashed lines), closed-system with respect to CO_2 at high rock:waterrock:water ratio (circular-dotted lines), and closed-system with respect to CO_2 at low rock:waterrock:water ratio (long dashed lines). Left column: models run with 0.1 bar CO_2; right column: models run with 1.0 bar CO_2. (a) and (b): siderite saturation state as a function of DIC and total alkalinity (TA). From bottom-up, red to yellow lines represent $\Omega_{siderite}$ of 1, 100, and 100,000. (c) and (d): pH variation over the course of the experiment (which corresponds closely to total alkalinity in this system). In order to illustrate the influence of water-rock interaction on the Fe(II)-carbonate system in DIC-TA space, these models were run under fixed Fe^{2+} concentration of 10 mmol/kg.

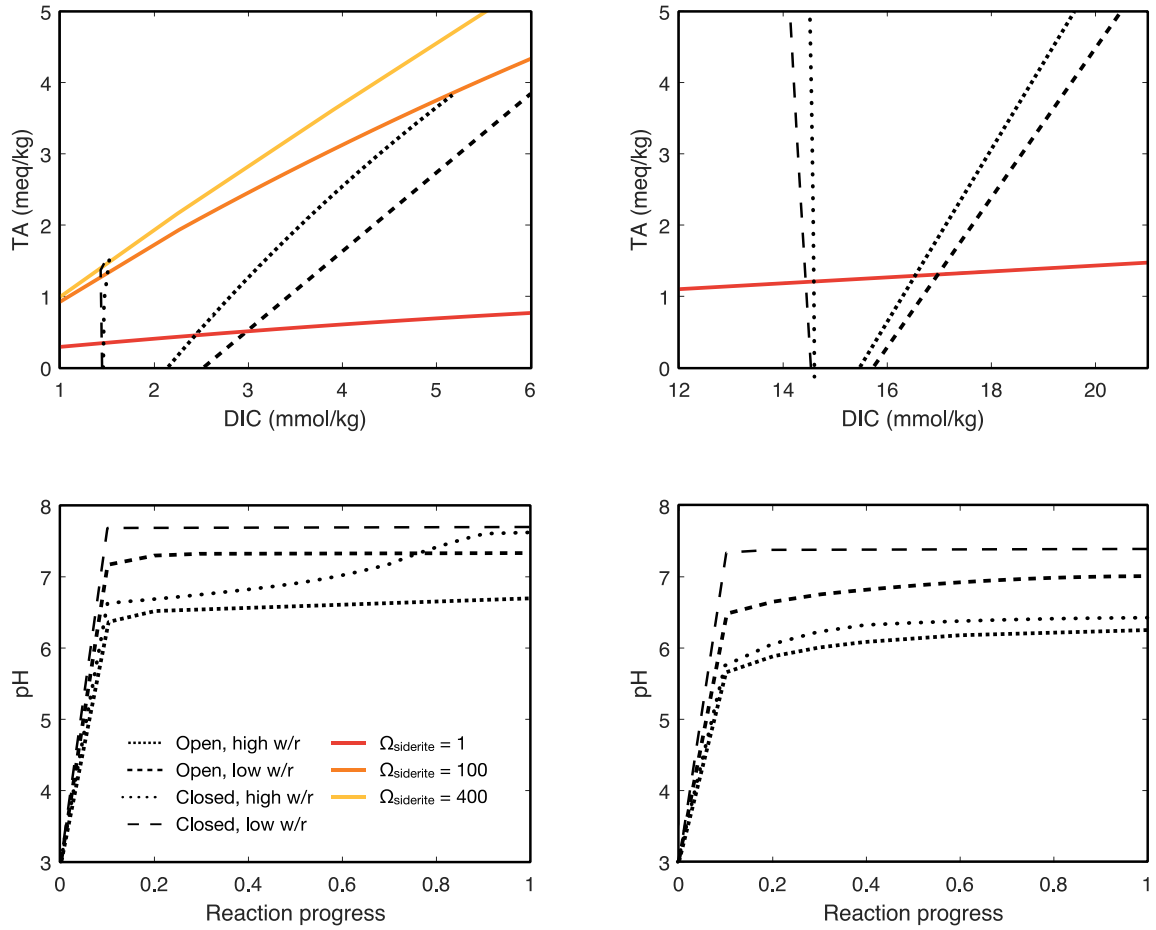


Figure 35: Results from four reaction path models of water-rock interaction at 75 ºC with the components that comprise CRB as a substrate: open-system with respect to CO2 at high rock:waterrock:water ratio (tightly-dotted lines), open-system with respect to CO2 at low rock:waterrock:water ratio (dashed lines), closed-system with respect to CO2 at high rock:waterrock:water ratio (circular-dotted lines), and closed-system with respect to CO2 at low rock:waterrock:water ratio (long dashed lines). Left column: models run with 0.1 bar CO2; right column: models run with 1.0 bar CO2. (a) and (b): siderite saturation state as a function of DIC and total alkalinity (TA). From bottom-up, red to yellow lines represent Ωsiderite of 1, 100, and 100,000. (c) and (d): pH variation over the course of the experiment (which corresponds closely to total alkalinity in this system). In order to illustrate the influence of water-rock interaction on

the Fe(II)-carbonate system in DIC-TA space, these models were run under fixed Fe2+ concentration of 10 mmol/kg.

7. References

Andrews-Hanna, J.C., Lewis, K.W., 2011. Early Mars hydrology: 2. Hydrological evolution in the Noachian and Hesperian epochs. J. Geophys. Res. 116, E02007. https://doi.org/10.1029/2010JE003709

Bandstra, J.Z., Brantley, S.L., 2008. Data Fitting Techniques with Applications to Mineral Dissolution Kinetics, in: Brantley, S.L., Kubicki, J.D., White, A.F. (Eds.), Kinetics of Water-Rock Interaction. Springer New York, New York, NY, pp. 211–257. https://doi.org/10.1007/978-0-387-73563-4_6

Bénézeth, P., Dandurand, J.L., Harrichoury, J.C., 2009. Solubility product of siderite (FeCO3) as a function of temperature (25–250 °C). Chemical Geology, CO2 geological storage: Integrating geochemical, hydrodynamical, mechanical and biological processes from the pore to the reservoir scale 265, 3–12. https://doi.org/10.1016/j.chemgeo.2009.03.015

Benezeth, P., Stefansson, A., Gautier, Q., Schott, J., 2013. Mineral Solubility and Aqueous Speciation Under Hydrothermal Conditions to 300 C - The Carbonate System as an Example. Reviews in Mineralogy and Geochemistry 76, 81–133. https://doi.org/10.2138/rmg.2013.76.4

Bischoff, J.L., Seyfried, W.E., 1978. Hydrothermal chemistry of seawater from 25 degrees to 350 degrees C. American Journal of Science 278, 838–860. https://doi.org/10.2475/ajs.278.6.838

Bishop, J.L., Dobrea, E.Z.N., McKeown, N.K., Parente, M., Ehlmann, B.L., Michalski, J.R., Milliken, R.E., Poulet, F., Swayze, G.A., Mustard, J.F., Murchie, S.L., Bibring, J.-P., 2008. Phyllosilicate Diversity and Past Aqueous Activity Revealed at Mawrth Vallis, Mars. Science 321, 830–833. https://doi.org/10.1126/science.1159699

Bridges, J.C., Catling, D.C., Saxton, J.M., Swindle, T.D., Lyon, I.C., Grady, M.M., 2001. Alteration Assemblages in Martian Meteorites: Implications for Near-Surface Processes. Space Science Reviews 96, 365–392. https://doi.org/10.1023/A:1011965826553

Bristow, T.F., Haberle, R.M., Blake, D.F., Marais, D.J.D., Eigenbrode, J.L., Fairén, A.G., Grotzinger, J.P., Stack, K.M., Mischna, M.A., Rampe, E.B., Siebach, K.L., Sutter, B., Vaniman, D.T., Vasavada, A.R., 2017. Low Hesperian PCO2 constrained from in situ mineralogical analysis at Gale Crater, Mars. PNAS 201616649. https://doi.org/10.1073/pnas.1616649114

Brown, A.J., Hook, S.J., Baldridge, A.M., Crowley, J.K., Bridges, N.T., Thomson, B.J., Marion, G.M., de Souza Filho, C.R., Bishop, J.L., 2010. Hydrothermal formation of Clay-Carbonate alteration assemblages in the Nili Fossae region of Mars. Earth and Planetary Science Letters 297, 174–182. https://doi.org/10.1016/j.epsl.2010.06.018

Brown, A.J., Viviano, C.E., Goudge, T.A., 2020. Olivine-Carbonate Mineralogy of the Jezero Crater Region. J. Geophys. Res. Planets 125. https://doi.org/10.1029/2019JE006011

Bullock, M.A., Moore, J.M., 2007. Atmospheric conditions on early Mars and the missing layered carbonates. Geophys. Res. Lett. 34, L19201. https://doi.org/10.1029/2007GL030688

Bultel, B., Quantin-Nataf, C., Andréani, M., Clénet, H., Lozac'h, L., 2015. Deep alteration between Hellas and Isidis Basins. Icarus 260, 141–160. https://doi.org/10.1016/j.icarus.2015.06.037

Carr, M.H., Clow, G.D., 1981. Martian channels and valleys: Their characteristics, distribution, and age. Icarus 48, 91–117. https://doi.org/10.1016/0019-1035(81)90156-1

Chevrier, V., Poulet, F., Bibring, J.-P., 2007. Early geochemical environment of Mars as determined from thermodynamics of phyllosilicates. Nature 448, 60–63. https://doi.org/10.1038/nature05961

Christensen, P.R., Bandfield, J.L., Hamilton, V.E., Ruff, S.W., Kieffer, H.H., Titus, T.N., Malin, M.C., Morris, R.V., Lane, M.D., Clark, R.L., Jakosky, B.M., Mellon, M.T., Pearl, J.C., Conrath, B.J., Smith, M.D., Clancy, R.T., Kuzmin, R.O., Roush, T., Mehall, G.L., Gorelick, N., Bender, K., Murray, K., Dason, S., Greene, E., Silverman, S., Greenfield, M., 2001. Mars Global Surveyor Thermal Emission Spectrometer experiment:

Investigation description and surface science results. Journal of Geophysical Research: Planets 106, 23823–23871. https://doi.org/10.1029/2000JE001370

Clifford, S.M., McCubbin, F.M., 2016. How Well Does the Present Surface Inventory of Water on Mars Constrain the Past? Presented at the Lunar and Planetary Science Conference, 21-25 Mar. 2016, United States.

Cousins, C.R., Crawford, I.A., Carrivick, J.L., Gunn, M., Harris, J., Kee, T.P., Karlsson, M., Carmody, L., Cockell, C., Herschy, B., Joy, K.H., 2013. Glaciovolcanic hydrothermal environments in Iceland and implications for their detection on Mars. Journal of Volcanology and Geothermal Research 256, 61–77. https://doi.org/10.1016/j.jvolgeores.2013.02.009

Davis, J.M., Balme, M., Grindrod, P.M., Williams, R.M.E., Gupta, S., 2016. Extensive Noachian fluvial systems in Arabia Terra: Implications for early Martian climate. Geology 44, 847–850. https://doi.org/10.1130/G38247.1

Delany, J.M., Lundeen, S.R., 1991. The LLNL thermochemical data base--revised data and file format for the EQ3/6 package. Lawrence Livermore National Lab., CA (United States). Vancouver.

Dreibus, G., Wanke, H., 1985. Mars, a Volatile-Rich Planet. Meteoritics 20, 367.

Edwards, C.S., Ehlmann, B.L., 2015. Carbon sequestration on Mars. Geology 43, 863–866. https://doi.org/10.1130/G36983.1

Ehlmann, B.L., Bish, D.L., Ruff, S.W., Mustard, J.F., 2012. Mineralogy and chemistry of altered Icelandic basalts: Application to clay mineral detection and understanding aqueous environments on Mars: CLAY MINERAL DETECTION, ICELANDIC BASALT. J. Geophys. Res. 117, n/a-n/a. https://doi.org/10.1029/2012JE004156

Ehlmann, B.L., Mustard, J.F., Clark, R.N., Swayze, G.A., Murchie, S.L., 2011. Evidence for low-grade metamorphism, hydrothermal alteration, and diagenesis on Mars from

phyllosilicate mineral assemblages. Clays Clay Miner. 59, 359–377. https://doi.org/10.1346/CCMN.2011.0590402

Ehlmann, B.L., Mustard, J.F., Murchie, S.L., 2010. Geologic setting of serpentine deposits on Mars: SERPENTINE ON MARS. Geophys. Res. Lett. 37, n/a-n/a. https://doi.org/10.1029/2010GL042596

Ehlmann, B.L., Mustard, J.F., Murchie, S.L., Poulet, F., Bishop, J.L., Brown, A.J., Calvin, W.M., Clark, R.N., Marais, D.J.D., Milliken, R.E., Roach, L.H., Roush, T.L., Swayze, G.A., Wray, J.J., 2008. Orbital Identification of Carbonate-Bearing Rocks on Mars. Science 322, 1828–1832. https://doi.org/10.1126/science.1164759

Ehlmann, B.L., Mustard, J.F., Swayze, G.A., Clark, R.N., Bishop, J.L., Poulet, F., Des Marais, D.J., Roach, L.H., Milliken, R.E., Wray, J.J., Barnouin-Jha, O., Murchie, S.L., 2009. Identification of hydrated silicate minerals on Mars using MRO-CRISM: Geologic context near Nili Fossae and implications for aqueous alteration. J. Geophys. Res. 114, E00D08. https://doi.org/10.1029/2009JE003339

Fassett, C.I., Head III, J.W., 2008. Valley network-fed, open-basin lakes on Mars: Distribution and implications for Noachian surface and subsurface hydrology. Icarus 198, 37–56. https://doi.org/10.1016/j.icarus.2008.06.016

Fassett, C.I., Head, J.W., 2005. Fluvial sedimentary deposits on Mars: Ancient deltas in a crater lake in the Nili Fossae region: FLUVIAL SEDIMENTARY DEPOSITS ON MARS. Geophys. Res. Lett. 32, n/a-n/a. https://doi.org/10.1029/2005GL023456

Felmy, A.R., Qafoku, O., Arey, B.W., Hu, J.Z., Hu, M., Todd Schaef, H., Ilton, E.S., Hess, N.J., Pearce, C.I., Feng, J., Rosso, K.M., 2012. Reaction of water-saturated supercritical CO2 with forsterite: Evidence for magnesite formation at low temperatures. Geochimica et Cosmochimica Acta 91, 271–282. https://doi.org/10.1016/j.gca.2012.05.026

Garcia, B., Beaumont, V., Perfetti, E., Rouchon, V., Blanchet, D., Oger, P., Dromart, G., Huc, A.-Y., Haeseler, F., 2010. Experiments and geochemical modelling of CO2 sequestration

by olivine: Potential, quantification. Applied Geochemistry 25, 1383–1396. https://doi.org/10.1016/j.apgeochem.2010.06.009

Giammar, D.E., Bruant, R.G., Peters, C.A., 2005. Forsterite dissolution and magnesite precipitation at conditions relevant for deep saline aquifer storage and sequestration of carbon dioxide. Chemical Geology 217, 257–276. https://doi.org/10.1016/j.chemgeo.2004.12.013

Goudge, T.A., Head, J.W., Mustard, J.F., Fassett, C.I., 2012. An analysis of open-basin lake deposits on Mars: Evidence for the nature of associated lacustrine deposits and post-lacustrine modification processes. Icarus 219, 211–229. https://doi.org/10.1016/j.icarus.2012.02.027

Goudge, T.A., Milliken, R.E., Head, J.W., Mustard, J.F., Fassett, C.I., 2017. Sedimentological evidence for a deltaic origin of the western fan deposit in Jezero crater, Mars and implications for future exploration. Earth and Planetary Science Letters 458, 357–365. https://doi.org/10.1016/j.epsl.2016.10.056

Goudge, T.A., Mustard, J.F., Head, J.W., Fassett, C.I., Wiseman, S.M., 2015. Assessing the mineralogy of the watershed and fan deposits of the Jezero crater paleolake system, Mars: Jezero Paleolake System Mineralogy. J. Geophys. Res. Planets 120, 775–808. https://doi.org/10.1002/2014JE004782

Graf, D.L., Goldsmith, J.R., 1956. Some Hydrothermal Syntheses of Dolomite and Protodolomite. The Journal of Geology 64, 173–186. https://doi.org/10.1086/626332

Griffith, L.L., Shock, E.L., 1995. A geochemical model for the formation of hydrothermal carbonates on Mars. Nature 377, 406–408. https://doi.org/10.1038/377406a0

Grotzinger, J.P., Sumner, D.Y., Kah, L.C., Stack, K., Gupta, S., Edgar, L., Rubin, D., Lewis, K., Schieber, J., Mangold, N., Milliken, R., Conrad, P.G., DesMarais, D., Farmer, J., Siebach, K., Calef, F., Hurowitz, J., McLennan, S.M., Ming, D., Vaniman, D., Crisp, J., Vasavada, A., Edgett, K.S., Malin, M., Blake, D., Gellert, R., Mahaffy, P., Wiens, R.C., Maurice, S.,

Grant, J.A., Wilson, S., Anderson, R.C., Beegle, L., Arvidson, R., Hallet, B., Sletten, R.S., Rice, M., Bell, J., Griffes, J., Ehlmann, B., Anderson, R.B., Bristow, T.F., Dietrich, W.E., Dromart, G., Eigenbrode, J., Fraeman, A., Hardgrove, C., Herkenhoff, K., Jandura, L., Kocurek, G., Lee, S., Leshin, L.A., Leveille, R., Limonadi, D., Maki, J., McCloskey, S., Meyer, M., Minitti, M., Newsom, H., Oehler, D., Okon, A., Palucis, M., Parker, T., Rowland, S., Schmidt, M., Squyres, S., Steele, A., Stolper, E., Summons, R., Treiman, A., Williams, R., Yingst, A., Team, M.S., 2014. A Habitable Fluvio-Lacustrine Environment at Yellowknife Bay, Gale Crater, Mars. Science 343, 1242777. https://doi.org/10.1126/science.1242777

Halevy, I., Fischer, W.W., Eiler, J.M., 2011. Carbonates in the Martian meteorite Allan Hills 84001 formed at 18 4 C in a near-surface aqueous environment. Proceedings of the National Academy of Sciences 108, 16895–16899. https://doi.org/10.1073/pnas.1109444108

Hänchen, M., Prigiobbe, V., Baciocchi, R., Mazzotti, M., 2008. Precipitation in the Mg-carbonate system—effects of temperature and CO2 pressure. Chemical Engineering Science 63, 1012–1028. https://doi.org/10.1016/j.ces.2007.09.052

Hartmann, W.K., Neukum, G., 2001. Cratering Chronology and the Evolution of Mars, in: Chronology and Evolution of Mars, Space Sciences Series of ISSI. Springer, Dordrecht, pp. 165–194. https://doi.org/10.1007/978-94-017-1035-0_6

He, S., Morse, J.W., 1993. The carbonic acid system and calcite solubility in aqueous Na-K-Ca-Mg-Cl-SO4 solutions from 0 to 90°C. Geochimica et Cosmochimica Acta 57, 3533–3554. https://doi.org/10.1016/0016-7037(93)90137-L

Helgeson, H.C., Kirkham, D.H., Flower, G., 1981. Theoretical prediction of the thermodynamic behavior of aqueous electrolytes by high pressures and temperatures; IV, Calculation of activity coefficients, osmotic coefficients, and apparent molal and standard and relative

partial molal properties to 600 degrees C and 5kb. American Journal of Science 281, 1249–1516.

Helgeson, S., Delany, L., Nesbitt, H., Bird, D., 1978. Summary and Critique of the Thermodynamic Properties of Rock Forming Minerals.

Horgan, B.H.N., Anderson, R.B., Dromart, G., Amador, E.S., Rice, M.S., 2020. The mineral diversity of Jezero crater: Evidence for possible lacustrine carbonates on Mars. Icarus 339, 113526. https://doi.org/10.1016/j.icarus.2019.113526

Hurowitz, J.A., Grotzinger, J.P., Fischer, W.W., McLennan, S.M., Milliken, R.E., Stein, N., Vasavada, A.R., Blake, D.F., Dehouck, E., Eigenbrode, J.L., Fairén, A.G., Frydenvang, J., Gellert, R., Grant, J.A., Gupta, S., Herkenhoff, K.E., Ming, D.W., Rampe, E.B., Schmidt, M.E., Siebach, K.L., Stack-Morgan, K., Sumner, D.Y., Wiens, R.C., 2017. Redox stratification of an ancient lake in Gale crater, Mars. Science 356, eaah6849. https://doi.org/10.1126/science.aah6849

Jakosky, B.M., Brain, D., Chaffin, M., Curry, S., Deighan, J., Grebowsky, J., Halekas, J., Leblanc, F., Lillis, R., Luhmann, J.G., Andersson, L., Andre, N., Andrews, D., Baird, D., Baker, D., Bell, J., Benna, M., Bhattacharyya, D., Bougher, S., Bowers, C., Chamberlin, P., Chaufray, J.-Y., Clarke, J., Collinson, G., Combi, M., Connerney, J., Connour, K., Correira, J., Crabb, K., Crary, F., Cravens, T., Crismani, M., Delory, G., Dewey, R., DiBraccio, G., Dong, C., Dong, Y., Dunn, P., Egan, H., Elrod, M., England, S., Eparvier, F., Ergun, R., Eriksson, A., Esman, T., Espley, J., Evans, S., Fallows, K., Fang, X., Fillingim, M., Flynn, C., Fogle, A., Fowler, C., Fox, J., Fujimoto, M., Garnier, P., Girazian, Z., Groeller, H., Gruesbeck, J., Hamil, O., Hanley, K.G., Hara, T., Harada, Y., Hermann, J., Holmberg, M., Holsclaw, G., Houston, S., Inui, S., Jain, S., Jolitz, R., Kotova, A., Kuroda, T., Larson, D., Lee, Y., Lee, C., Lefevre, F., Lentz, C., Lo, D., Lugo, R., Ma, Y.-J., Mahaffy, P., Marquette, M.L., Matsumoto, Y., Mayyasi, M., Mazelle, C., McClintock, W., McFadden, J., Medvedev, A., Mendillo, M., Meziane, K., Milby, Z.,

Mitchell, D., Modolo, R., Montmessin, F., Nagy, A., Nakagawa, H., Narvaez, C., Olsen, K., Pawlowski, D., Peterson, W., Rahmati, A., Roeten, K., Romanelli, N., Ruhunusiri, S., Russell, C., Sakai, S., Schneider, N., Seki, K., Sharrar, R., Shaver, S., Siskind, D.E., Slipski, M., Soobiah, Y., Steckiewicz, M., Stevens, M.H., Stewart, I., Stiepen, A., Stone, S., Tenishev, V., Terada, N., Terada, K., Thiemann, E., Tolson, R., Toth, G., Trovato, J., Vogt, M., Weber, T., Withers, P., Xu, S., Yelle, R., Yiğit, E., Zurek, R., 2018. Loss of the Martian atmosphere to space: Present-day loss rates determined from MAVEN observations and integrated loss through time. Icarus 315, 146–157. https://doi.org/10.1016/j.icarus.2018.05.030

Jiang, C.Z., Tosca, N.J., 2020. Growth kinetics of siderite at 298.15 K and 1 bar. Geochimica et Cosmochimica Acta 274, 97–117. https://doi.org/10.1016/j.gca.2020.01.047

Jiang, C.Z., Tosca, N.J., 2019. Fe(II)-carbonate precipitation kinetics and the chemistry of anoxic ferruginous seawater. Earth and Planetary Science Letters 506, 231–242. https://doi.org/10.1016/j.epsl.2018.11.010

Jimenez-Lopez, C., Romanek, C.S., 2004. Precipitation kinetics and carbon isotope partitioning of inorganic siderite at 25°C and 1 atm. Geochimica et Cosmochimica Acta 68, 557–571. https://doi.org/10.1016/S0016-7037(03)00460-5

Kaszuba, J.P., Janecky, D.R., Snow, M.G., 2005. Experimental evaluation of mixed fluid reactions between supercritical carbon dioxide and NaCl brine: Relevance to the integrity of a geologic carbon repository. Chemical Geology 217, 277–293. https://doi.org/10.1016/j.chemgeo.2004.12.014

Kissick, L.E., Mather, T.A. and Tosca, N.J., 2021. Unravelling surface and subsurface carbon sinks within the early Martian crust. *Earth and Planetary Science Letters*, *557*, p.116663.

Kite, E.S., Williams, J.-P., Lucas, A., Aharonson, O., 2014. Low palaeopressure of the martian atmosphere estimated from the size distribution of ancient craters. Nature Geoscience 7, 335–339. https://doi.org/10.1038/ngeo2137

Klein, F., Bach, W., McCollom, T.M., 2013. Compositional controls on hydrogen generation during serpentinization of ultramafic rocks. Lithos 178, 55–69. https://doi.org/10.1016/j.lithos.2013.03.008

Kling, A.M., Haberle, R.M., McKay, C.P., Bristow, T.F., Rivera-Hernández, F., 2020. Subsistence of ice-covered lakes during the Hesperian at Gale crater, Mars. Icarus 338, 113495. https://doi.org/10.1016/j.icarus.2019.113495

Lafay, R., Montes-Hernandez, G., Janots, E., Chiriac, R., Findling, N., Toche, F., 2014. Simultaneous precipitation of magnesite and lizardite from hydrothermal alteration of olivine under high-carbonate alkalinity. Chemical Geology 368, 63–75. https://doi.org/10.1016/j.chemgeo.2014.01.008

Leask, E.K., Ehlmann, B.L., Dundar, M.M., Murchie, S.L., Seelos, F.P., 2018. Challenges in the Search for Perchlorate and Other Hydrated Minerals With 2.1-μm Absorptions on Mars. Geophys. Res. Lett. 45. https://doi.org/10.1029/2018GL080077

Lin, C.Y., Turchyn, A.V., Krylov, A., Antler, G., 2020. The microbially driven formation of siderite in salt marsh sediments. Geobiology 18, 207–224. https://doi.org/10.1111/gbi.12371

Lippmann, F., 1973. Crystal Chemistry of Sedimentary Carbonate Minerals, in: Sedimentary Carbonate Minerals. Springer Berlin Heidelberg, Berlin, Heidelberg, pp. 5–96. https://doi.org/10.1007/978-3-642-65474-9_2

Ludwig, K.A., Kelley, D.S., Butterfield, D.A., Nelson, B.K., Früh-Green, G., 2006. Formation and evolution of carbonate chimneys at the Lost City Hydrothermal Field. Geochimica et Cosmochimica Acta 70, 3625–3645. https://doi.org/10.1016/j.gca.2006.04.016

Mandon, L., Quantin-Nataf, C., Thollot, P., Mangold, N., Lozac'h, L., Dromart, G., Beck, P., Dehouck, E., Breton, S., Millot, C., Volat, M., 2020. Refining the age, emplacement and alteration scenarios of the olivine-rich unit in the Nili Fossae region, Mars. Icarus 336, 113436. https://doi.org/10.1016/j.icarus.2019.113436

McSween, H.Y., 2004. Basaltic Rocks Analyzed by the Spirit Rover in Gusev Crater. Science 305, 842–845. https://doi.org/10.1126/science.3050842

Michalski, J.R., Cuadros, J., Bishop, J.L., Darby Dyar, M., Dekov, V., Fiore, S., 2015. Constraints on the crystal-chemistry of Fe/Mg-rich smectitic clays on Mars and links to global alteration trends. Earth and Planetary Science Letters 427, 215–225. https://doi.org/10.1016/j.epsl.2015.06.020

Michalski, J.R., Cuadros, J., Niles, P.B., Parnell, J., Deanne Rogers, A., Wright, S.P., 2013. Groundwater activity on Mars and implications for a deep biosphere. Nature Geoscience 6, 133–138. https://doi.org/10.1038/ngeo1706

Michalski, J.R., Glotch, T.D., Rogers, A.D., Niles, P.B., Cuadros, J., Ashley, J.W., Johnson, S.S., 2019. The Geology and Astrobiology of McLaughlin Crater, Mars: An Ancient Lacustrine Basin Containing Turbidites, Mudstones, and Serpentinites. J. Geophys. Res. Planets 124, 910–940. https://doi.org/10.1029/2018JE005796

Michalski, J.R., Niles, P.B., 2010. Deep crustal carbonate rocks exposed by meteor impact on Mars. Nature Geosci 3, 751–755. https://doi.org/10.1038/ngeo971

Mittlefehldt, D.W., 1994. ALH84001, a cumulate orthopyroxenite member of the martian meteorite clan. Meteoritics 29, 214–221. https://doi.org/10.1111/j.1945-5100.1994.tb00673.x

Möller, P., 1989. Minor and trace elements in magnesite. Geology 28, 173–195.

Mora, C.I., Driese, S.G., Colarusso, L.A., 1996. Middle to Late Paleozoic Atmospheric CO2 Levels from Soil Carbonate and Organic Matter. Science 271, 1105–1107. https://doi.org/10.1126/science.271.5252.1105

Morris, R.V., Ruff, S.W., Gellert, R., Ming, D.W., Arvidson, R.E., Clark, B.C., Golden, D.C., Siebach, K., Klingelhofer, G., Schroder, C., Fleischer, I., Yen, A.S., Squyres, S.W., 2010. Identification of Carbonate-Rich Outcrops on Mars by the Spirit Rover. Science 329, 421–424. https://doi.org/10.1126/science.1189667

Mustard, J.F., Murchie, S.L., Pelkey, S.M., Ehlmann, B.L., Milliken, R.E., Grant, J.A., Bibring, J.-P., Poulet, F., Bishop, J., Dobrea, E.N., Roach, L., Seelos, F., Arvidson, R.E., Wiseman, S., Green, R., Hash, C., Humm, D., Malaret, E., McGovern, J.A., Seelos, K., Clancy, T., Clark, R., Marais, D.D., Izenberg, N., Knudson, A., Langevin, Y., Martin, T., McGuire, P., Morris, R., Robinson, M., Roush, T., Smith, M., Swayze, G., Taylor, H., Titus, T., Wolff, M., 2008. Hydrated silicate minerals on Mars observed by the Mars Reconnaissance Orbiter CRISM instrument. Nature 454, 305–309. https://doi.org/10.1038/nature07097

Nimmo, F., Hart, S.D., Korycansky, D.G., Agnor, C.B., 2008. Implications of an impact origin for the martian hemispheric dichotomy. Nature 453, 1220–1223. https://doi.org/10.1038/nature07025

Parmentier, E.M., Zuber, M.T., 2007. Early evolution of Mars with mantle compositional stratification or hydrothermal crustal cooling. J. Geophys. Res. 112, E02007. https://doi.org/10.1029/2005JE002626

Phillips, R.J., Zuber, M., Solomon, S.C., Golombek, M.P., Jakosky, B.M., Banerdt, W.B., Smith, D.E., Williams, R.B., Hynek, B.M., Aharonson, O., Hauck, S.A., 2001. Ancient Geodynamics and Global-Scale Hydrology on Mars. Science 291, 2587–2591. https://doi.org/10.1126/science.1058701

Pokrovsky, O.S., Schott, J., 2000. Forsterite surface composition in aqueous solutions: a combined potentiometric, electrokinetic, and spectroscopic approach. Geochimica et Cosmochimica Acta 64, 3299–3312. https://doi.org/10.1016/S0016-7037(00)00435-X

Poulet, F., Mangold, N., Loizeau, D., Bibring, J.-P., Langevin, Y., Michalski, J., Gondet, B., 2008. Abundance of minerals in the phyllosilicate-rich units on Mars. A&A 487, L41–L44. https://doi.org/10.1051/0004-6361:200810150

Qafoku, O., Kovarik, L., Kukkadapu, R.K., Ilton, E.S., Arey, B.W., Tucek, J., Felmy, A.R., 2012. Fayalite dissolution and siderite formation in water-saturated supercritical CO2. Chemical Geology 332–333, 124–135. https://doi.org/10.1016/j.chemgeo.2012.09.028

Rasmussen, B., Muhling, J.R., Fischer, W.W., 2020. Greenalite Nanoparticles in Alkaline Vent Plumes as Templates for the Origin of Life. Astrobiology ast.2020.2270. https://doi.org/10.1089/ast.2020.2270

Romanek, C.S., Jiménez-López, C., Navarro, A.R., Sánchez-Román, M., Sahai, N., Coleman, M., 2009. Inorganic synthesis of Fe–Ca–Mg carbonates at low temperature. Geochimica et Cosmochimica Acta 73, 5361–5376. https://doi.org/10.1016/j.gca.2009.05.065

Ruff, S.W., Niles, P.B., Alfano, F., Clarke, A.B., 2014. Evidence for a Noachian-aged ephemeral lake in Gusev crater, Mars. Geology 42, 359–362. https://doi.org/10.1130/G35508.1

Saldi, G.D., Jordan, G., Schott, J., Oelkers, E.H., 2009. Magnesite growth rates as a function of temperature and saturation state. Geochimica et Cosmochimica Acta 73, 5646–5657. https://doi.org/10.1016/j.gca.2009.06.035

Salvatore, M.R., Goudge, T.A., Bramble, M.S., Edwards, C.S., Bandfield, J.L., Amador, E.S., Mustard, J.F., Christensen, P.R., 2018. Bulk mineralogy of the NE Syrtis and Jezero crater regions of Mars derived through thermal infrared spectral analyses. Icarus 301, 76–96. https://doi.org/10.1016/j.icarus.2017.09.019

Schaef, T.H., McGrail, B.P., 2009. Dissolution of Columbia River Basalt under mildly acidic conditions as a function of temperature: Experimental results relevant to the geological sequestration of carbon dioxide. Applied Geochemistry 24, 980–987. https://doi.org/10.1016/j.apgeochem.2009.02.025

Schon, S.C., Head, J.W., Fassett, C.I., 2012. An overfilled lacustrine system and progradational delta in Jezero crater, Mars: Implications for Noachian climate. Planetary and Space Science 67, 28–45. https://doi.org/10.1016/j.pss.2012.02.003

Shahrzad, S., Kinch, K.M., Goudge, T.A., Fassett, C.I., Needham, D.H., Quantin-Nataf, C., Knudsen, C.P., 2019. Crater Statistics on the Dark-Toned, Mafic Floor Unit in Jezero Crater, Mars. Geophys. Res. Lett. 46, 2408–2416. https://doi.org/10.1029/2018GL081402

Singer, P.C., Stumm, W., 1970. The Solubility of Ferrous Iron in Carbonate-Bearing Waters. Journal - American Water Works Association 62, 198–202. https://doi.org/10.1002/j.1551-8833.1970.tb03888.x

Squyres, S.W., 2004. The Spirit Rover's Athena Science Investigation at Gusev Crater, Mars. Science 305, 794–799. https://doi.org/10.1126/science.3050794

Squyres, S.W., Grotzinger, J.P., Arvidson, R.E., Bell, J.F., Calvin, W., Christensen, P.R., Clark, B.C., Crisp, J.A., Farrand, W.H., Herkenhoff, K.E., Johnson, J.R., Klingelhöfer, G., Knoll, A.H., McLennan, S.M., McSween, H.Y., Morris, R.V., Rice, J.W., Rieder, R., Soderblom, L.A., 2004. In Situ Evidence for an Ancient Aqueous Environment at Meridiani Planum, Mars. Science 306, 1709–1714. https://doi.org/10.1126/science.1104559

Tanaka, K.L., Robbins, S.J., Fortezzo, C.M., Skinner, J.A., Hare, T.M., 2014. The digital global geologic map of Mars: Chronostratigraphic ages, topographic and crater morphologic characteristics, and updated resurfacing history. Planetary and Space Science 95, 11–24. https://doi.org/10.1016/j.pss.2013.03.006

Thompson, J.B., Ferris, F.G., 1990. Cyanobacterial precipitation of gypsum, calcite, and magnesite from natural alkaline lake water. Geology 18, 995–998. https://doi.org/10.1130/0091-7613(1990)018<0995:CPOGCA>2.3.CO;2

Tutolo, B., Evans, B., Kuehner, S., 2019. Serpentine–Hisingerite Solid Solution in Altered Ferroan Peridotite and Olivine Gabbro. Minerals 9, 47. https://doi.org/10.3390/min9010047

van Berk, W., Fu, Y., 2011. Reproducing hydrogeochemical conditions triggering the formation of carbonate and phyllosilicate alteration mineral assemblages on Mars (Nili Fossae region). J. Geophys. Res. 116, E10006. https://doi.org/10.1029/2011JE003886

van Berk, W., Fu, Y., Ilger, J.-M., 2012. Reproducing early Martian atmospheric carbon dioxide partial pressure by modeling the formation of Mg-Fe-Ca carbonate identified in the Comanche rock outcrops on Mars: REPRODUCING EARLY MARTIAN pCO2. J. Geophys. Res. 117. https://doi.org/10.1029/2012JE004173

Viviano, C.E., Moersch, J.E., McSween, H.Y., 2013. Implications for early hydrothermal environments on Mars through the spectral evidence for carbonation and chloritization reactions in the Nili Fossae region: HYDROTHERMAL ENVIRONMENTS IN NILI FOSSAE. J. Geophys. Res. Planets 118, 1858–1872. https://doi.org/10.1002/jgre.20141

Warner, N., Gupta, S., Lin, S.-Y., Kim, J.-R., Muller, J.-P., Morley, J., 2010. Late Noachian to Hesperian climate change on Mars: Evidence of episodic warming from transient crater lakes near Ares Vallis. J. Geophys. Res. 115, E06013. https://doi.org/10.1029/2009JE003522

Warren, A.O., Kite, E.S., Williams, J. -P., Horgan, B., 2019. Through the Thick and Thin: New Constraints on Mars Paleopressure History 3.8 – 4 Ga from Small Exhumed Craters. J. Geophys. Res. Planets 124, 2793–2818. https://doi.org/10.1029/2019JE006178

Wenk, H.-R., Bulakh, A., 2004. Minerals.

Werner, S.C., 2009. The global martian volcanic evolutionary history. Icarus 201, 44–68. https://doi.org/10.1016/j.icarus.2008.12.019

Werner, S.C., 2008. The early martian evolution—Constraints from basin formation ages. Icarus 195, 45–60. https://doi.org/10.1016/j.icarus.2007.12.008

Wordsworth, R., Kalugina, Y., Lokshtanov, S., Vigasin, A., Ehlmann, B., Head, J., Sanders, C., Wang, H., 2017. Transient reducing greenhouse warming on early Mars. Geophys. Res. Lett. 44, 2016GL071766. https://doi.org/10.1002/2016GL071766

Wray, J.J., Murchie, S.L., Bishop, J.L., Ehlmann, B.L., Milliken, R.E., Wilhelm, M.B., Seelos, K.D., Chojnacki, M., 2016. Orbital evidence for more widespread carbonate-bearing rocks on Mars. Journal of Geophysical Research: Planets 121, 652–677. https://doi.org/10.1002/2015JE004972

Chapter 6

Conclusions

1. Overview

This thesis has discussed the following topics:

1) Fe(II)-carbonate precipitation at 25 ºC using olivine as a substrate;
2) Carbonate precipitation from Fa^{2+}, Mg^{2+}, and Ca^{2+} bearing material within a basaltic substrate at 25 ºC;
3) Carbonate precipitation at 75 ºC using olivine and basalt as substrates.

The key issues with these topics are that carbonate precipitation under anoxic conditions is poorly understood and has been the subject of much investigation (e.g., Jiminez-Lopez and Romanek, 2004; Romanek et al., 2009; Qafoku et al,. 2012; Sumner and Grotzinger, 1996; Tosca et al., 2018; Jiang and Tosca, 2019, 2020), and also how, specifically to Mars, there is an unresolved question of the fate of its ancient and likely CO_2-dominated atmosphere. Researching the formation mechanism of carbonates bearing cations relevant to Mars — Fe^{2+}, Mg^{2+}, and Ca^{2+} — addresses both of these issues by investigating a fundamental process relevant to aqueous, anoxic environments across both Earth and Mars, providing insight into the fate of a significant sink of Martian carbon but also the formational environment of such carbonates where they are found on Mars.

While the results outlined in this thesis have far-reaching applications for carbonate formation on early Earth (e.g., Jiang and Tosca, 2019), modern anoxic environments (e.g., Sengupta et al., 2020), and even wider afield to the study of exoplanetary atmospheres and surfaces (e.g., Wordsworth et al., 2017) this conclusions chapter concerns itself with the unresolved question of why carbonates, in particular Fe(II)-carbonates, are surficially rare within the ancient

Martian sedimentary record. This conclusion specifically looks towards this question before discussing the wider implications of Fe-, Ca-, and Mg-carbonate formation within the ancient Martian crust under the broader reach of aqueous, anoxic systems where free cations are able to mix with CO_2-charged waters at varying temperatures.

The overarching conclusions for this thesis are: (1) The kinetics of Fe(II)-carbonate formation at 25 ºC anoxic conditions necessitate an extremely high supersaturation state and the exceeding of a nucleation threshold higher than 100 $\Omega_{siderite}$; (2) Fe(II)-carbonates form most readily under low rock:water ratio, closed CO_2 systems where substantial alkalinity production, high pH, and a finite DIC pool permit crossing nucleation thresholds for Fe(II)-carbonate; (3) at 75 ºC, the kinetics of Fe(II)-carbonate formation require far lower saturation states for nucleation to occur, and under both low and high rock:waterrock:water ratio. Data indicate this process may be more kinetically favourable than Mg-carbonate production under the same conditions and (4) the subsurface of terrestrial planets in contact with high pCO_2 atmospheres, such as paleo-Mars, appear to be the environment where such conditions most conducive for Fe(II)-carbonate supersaturation are most likely to occur. The rarity of surface-based exposures of Fe(II)-carbonates on Mars may be due to their formation deep within the crust, with only large impact craters in the planet's oldest terrain gouging windows into this record, and revealing uplifted mineralogy rich in Fe(II)-carbonates.

This brief conclusions chapter summarises the key research findings of this thesis, beginning first with the mechanisms behind low and high temperature Fe(II)-carbonate formation before considering the environments most conductive to their formation. Lastly these results are then set within the context of the distribution of carbonates on Mars and their implications for the ancient Martian landscape.

2. The kinetics of Fe(II)-carbonate formation

Thermodynamically, exceeding an Omega value of 1 — that is, the conditions under which it becomes energetically favourable for a solid within solution to net precipitate — predicts the precipitation of a solid from solution. Although previous studies have focused on Fe(II)-carbonate precipitation as an isolated system, there are very few studies that examine this process in the context of water-rock interaction. The results presented in this thesis highlight that a significant supersaturation threshold is required for Fe(II)-carbonate formation in anoxic water-rock systems, which is in good quantitative agreement with previous studies that have focused on homogeneous precipitation from Fe(II)-carbonate solution (Tosca et al., 2018; Jiang and Tosca, 2019). Aligned, nano-scale platelets were found by scanning electron microscopy (SEM) in five individual experiments, the majority of which were found associated with fibrous structures likely to be amorphous silica, suggesting the silica from the fayalite reactants remained separate from the formation of these platelets. An Fe(II)-oxide or -carbonate is a possibility, especially as the morphology of the platelets when clumped together bore resemblance to the AFC of Jiang and Tosca (2019), and all but one platelet-producing experiment exceeded the AFC line.

In a similar series of kinetic calculations, the phyllosilicate greenalite ($Fe_3Si_2O_5(OH)_4$) also appears to be supersaturated under several experimental conditions, yet none of this mineral was identified as a precipitate in any experiments either.

The fact that no confirmed precipitate formed in any experiments conducted at 25 ºC, despite $\Omega_{siderite}$ exceeding 1000 for several datapoints, implies that there are strong kinetic controls upon Fe(II)-carbonate formation under anoxic, 25 ºC conditions. This was even under 1.0 bar of pCO_2, which is likely to have been the realistic maximum thickness of the Martian atmosphere (e.g., Jakosky et al., 2018; Warren et al., 2019) at its height in the Noachian (~4.0-3.7 Ga; Hartmann and Neukum, 2001).

Precipitates did form at 75 ºC (Chapter 5), but they cannot be extrapolated as relevant to or reflecting the general condition of the Martian surface. At lower temperature, however, the lack

of Fe(II)-carbonate precipitates under even 1.0 bar pCO_2 suggests that the limiting factor in carbonate formation at ambient temperatures on Mars is not the pCO_2 amounts themselves, but the intrinsically high supersaturation state required for nucleation. Several researchers have used geochemical modelling (Chevrier et al., 2007) or thermodynamic studies of surface mineralogy (Bristow et al., 2017) to suggest Noachian pCO_2 must have been at pressures insufficient to support liquid water (as low was 0.078 bars; Bristow et al., 2017) at the time standing bodies of water such as a lake or lakes existed in Gale Crater (Grotzinger et al., 2014). This line of reasoning postulates that either some alternative gas was responsible for the bulk of Mars' atmosphere (see Haberle et al., 2017, for summary); that Mars' atmospheres have always been highly transient and resulting from impact-induced steam and rock vapour (Segura et al., 2002); or that Mars was primarily cold and dry for all of its history, and that water-carved features existed under vast swathes of ice (e.g., Fastook and Head, 2015).

The hypotheses discussed above postulate either highly transient atmospheres, the presence of large amounts of other atmospheric components, or an atmosphere entirely insufficient to provide surficial warmth. A high pCO_2 atmosphere in itself is insufficient to warm the Martian surface (Ramirez et al., 2014, 2020; Wordsworth et al., 2017), with CH_4 and NH_3 gases (Sagan and Chyba, 1997) or the presence of CO_2 ice clouds (Forget and Pierrehumbert, 1997) having been proposed amongst other supplementary warming mechanisms to have supported a dominantly CO_2 atmosphere, thus the presence of other minor gases is a realistic and likely view of the ancient Martian atmosphere; however, proposing that the dominant atmospheric gas was a material other than CO_2 has little founding (e.g., Wadhwa, 2008; Haberle et al., 2017 for summary). Similarly, the effect of steam and rock vapour resulting from impact events was likely to be a partial contributor to the early Martian atmospheric inventory, but the extreme ends of these hypotheses that propose unrealistic amounts of such atmospheric components run counter to isotopic (e.g., Jakosky et al., 2018), geomorphologic (e.g., Davis et al., 2016; Kite et al., 2019; Warren et al., 2019),

and geochemical (e.g., (Ehlmann et al., 2008)) evidence that supports once-widespread liquid water across the Martian surface.

This thesis has proposed an alternative hypothesis for the composition of the early Martian atmosphere in relation to the lack of carbonates exposed on the surface. Here, a lack of pCO_2 is experimentally determined as not the limiting factor hindering widespread surface precipitation of carbonates on Mars. Rather, the key is for environments to be able to produce surplus alkalinity to dissolved inorganic carbon levels, and accordingly to surpass the nucleation threshold for an Fe(II)-carbonate.

3. Fe(II)-carbonate formation conditions

Over the 161 experiments conducted within this thesis, at a variety of rock:water ratios, pCO_2 concentrations, temperatures, initial pH, experiment duration, and initial reactants, constraints upon the formation of Fe(II)-carbonates under anoxic conditions were exacted. Rather than revealing pCO_2 as a determining factor, instead $\Omega_{siderite}$ was found to reach its highest concentrations under combined high pH, high Fe^{2+} activity, and high temperature, whereby slightly higher amounts of these had to be reached for all at lower pCO_2. At 75 ºC, an $\Omega_{siderite}$ of almost 700 was reached; for 25 ºC, the maximum was almost 4000. Since no measurable precipitate formed at 25 ºC but clear siderite rhombs precipitated at 75 ºC, this suggests the $\Omega_{siderite}$ threshold that must be exceeded for a precipitate to form is lower at high temperature. Alternatively, if the nucleation point was exceeded at lower pCO_2, precipitation rates must be far slower at low temperatures than at higher temperatures.

Where high Fe^{2+} activity and high pH coincided in the 25 ºC experiments, this was where the higher $\Omega_{siderite}$ occurred. The experiments that enabled pH and dissolved Fe concentrations to climb the highest were those conducted at low rock:water ratios. These are conditions that most likely represent aquifer environments on palaeo-Mars: phreatic zones within the pore spaces of

regolith and rock within the near-subsurface. These environments are well-constrained on Mars both from robotic missions (e.g., (Squyres et al., 2004; Tosca et al., 2008) and meteorites (Bridges, 2000; Bridges et al., 2019), and in the latter case have been known to bear carbonates formed in brines at temperatures as low as 18 ºC (Halevy et al., 2011).

Low water-rock environments appear to enable $\Omega_{siderite}$ to climb highest for several reasons. These results are consistent with the general expectation that changes in alkalinity and/or DIC concentration will fundamentally control carbonate mineral saturation state (Zeebe and Wolf-Gladrow, 2001). Among the most important processes that influence alkalinity during rock:waterrock:water interaction are the rock:waterrock:water ratio and initial pH. Both of these parameters control how rapidly silicate mineral dissolution provides alkalinity to the solution, the rate of which is maximised by low rock:waterrock:water ratios and relatively low initial pH. Accordingly, high $\Omega_{siderite}$ and eventual Fe(II)-carbonate precipitation can be thought of as functions of the ALK/DIC ratio, which in itself is most conductive to such precipitation under low rock:waterrock:water ratio and high pH. In addition, pCO_2 is also a significant parameter controlling Fe-carbonate saturation in that it controls how DIC concentrations evolve during water-rock interaction.

Additionally, geochemical modelling conducted in the three research chapters clearly outlined a low water-rock, closed system — that is, isolated from constant replenishment of CO_2 — as the environment where total alkalinity, alongside siderite and AFC saturation state, were able to reach the highest amounts. This was in contrast to open systems on Mars exposed to a constant supply of atmospheric CO_2, or those at high rock:waterrock:water ratio.

While no low rock:waterrock:water ratio experiments were successfully run for temperatures conducted at 75 ºC, a siderite precipitate was detected by three individual methods within high rock:waterrock:water experiments run for only 10 days. The high $\Omega_{siderite}$ seen in the low rock:waterrock:water ratio experiments conducted at 25 ºC had run for up to 85 days; the implication is clear that, given high rock:waterrock:water was at low temperature a relatively

unfavourable Fe(II)-carbonate-forming environment, at high temperatures (75 ºC) $\Omega_{siderite}$ is able to exceed the nucleation threshold for siderite even under high rock:waterrock:water conditions. Increasing temperature therefore appears to increase the saturation state for Fe(II)-carbonates even with factoring in the temperature dependence of saturation state calculations. Temperature increase also seems to reduce the specificity of their environment of formation. Such environments at high temperature could stretch to include surface hot springs and lakes proximal to active volcanism that reach hydrothermal temperatures with the injection of hot fluids.

Low rock:waterrock:water environments, by contrast, isolated from the surface as aquifers in the crust to depths where atmospheric CO_2 may still percolate down, have been identified within this thesis as the prime low temperature environment for forming Fe(II)-carbonates on Mars. The implications of such information in the light of the distribution of carbonates on Mars will now be summarised.

4. Implications for the distribution of carbonate minerals within the Martian crust

The experiments, geochemical modelling, and kinetic observations of this thesis conclude that at low temperature, low rock:water ratio environments — namely, aquifers — are those most conducive to the formation of Fe(II)-carbonates, and predicts that where such localities may be observed — whether on the surface or preserved within meteorites — such carbonates are most likely to be identified. At high temperature, as well as forming Fe(II)-carbonates within such low rock:waterrock:water ratio environments, systems of more plentiful water such as hydrothermal lakes or springs, for example, are predicted to enable such carbonates' formation. The spatial distribution of Fe(II)-carbonates on Mars, exposed within some of the deepest impact craters into ancient terrain and within crater lakes associated with remnant volcanism (Figure 1), matches these predictions:

(1) **Low temperature:** Fe(II)-carbonates within craters have sometimes been uplifted by as much as 6 km from within the crust (Michalski and Niles, 2010) and appear to represent the original, once-buried mineralogy as opposed to impact-induced hydrothermalism, metasomatism, or another, younger formation mechanism. This could suggest that the deep subsurface of Mars, dependent on hydrology permitting the flow of CO_2-charged aquifers (Harrison and Grimm, 2009; Michalski et al., 2013; Wray et al., 2016; Salese et al., 2019), could represent a vast, buried Fe(II)-carbonate reservoir exposed only rarely through these impact craters.

(2) **High temperature:** The rare *in situ* surface-based instances of Fe(II)-carbonates, for example as lacustrine sediments within the craters of Gusev and Jezero, are located within the vicinity of prominent volcanic complexes; few other candidate lakes display such mineralogy without this adjacent source of heat (Michalski and Niles, 2010; Morris et al., 2010; Goudge et al., 2015). These carbonate deposits, also Noachian in age, were able to form instead at high rock:waterrock:water ratio through the lowering of the $\Omega_{siderite}$ threshold accordant with the localised higher hydrothermal temperatures.

An implication of low temperature carbonate formation in particular would be a widespread, undiscovered sink of carbon buried within the planet's subsurface. This is because sufficiently warm (~25 ºC) intergranular spaces will have existed within the Martian crust at depths that varied through time and location with both local and geothermal temperature gradients. Rock pore spaces may have even been larger than those of Earth owing to frequent impact gardening breaking up the bedrock, which in addition to the planet's lower compacting gravitational force would enable pore spaces to exist at greater depths. Such an undiscovered carbon sink has indeed been predicted by mass balance calculations (Heard and Kite, 2020). Their research calculated that insufficient CO_2 can be lost via escape-to-space mechanisms to account for the estimated total loss through time: while oxygen escape rates from Mars could account for atmospheric CO_2 loss, this only works if CO_2 was the dominant source of the escaping oxygen. However, Heard and Kite

(2020) showed through H isotope ratios, O escape calculations, and by quantifying surface oxygen deposits that oxygen escape after 3.5 Ga must have been more commonly associated with the loss of H_2O, not CO_2. With an estimated ≥250 mbar of CO_2 having been lost to space in the last 3.5 Ga (Urata and Toon, 2013; Wordsworth, 2016; Haberle et al., 2017; Wordsworth et al., 2017), either this carbon had to have been removed from Mars by an unknown and unrealistically efficient mechanism, or remain somewhere upon the planet.

With only a few mbar of CO_2 estimated as being lost to space (Dong et al., 2018; Ramstad et al., 2018), the sink of carbon they propose as most viable is within the subsurface as carbonates, clathrates, or ices. Alternatively, this could be accounted for by CO_2 adsorbed on dust or carbonates (Kurahashi-Nakamura and Tajika, 2006; Niles et al., 2013; Jakosky, 2019). For the carbonate option, Heard and Kite (2020) acknowledge that insufficient deposits of surface carbonates have been identified to account for their missing sink (Edwards and Ehlmann, 2015; Jakosky and Edwards, 2018). Niles et al. (2013) calculated that with an overestimated crustal carbonate fraction of 0.5 wt. % within the upper 1 km of the Martian crust, ≤0.25 bar of CO_2 could be sequestered; via the mechanism proposed in this thesis — namely, carbonatisation of host rock within aquifers at depth — it is plausible that this could account for the missing carbon sink.

From these three lines of evidence — the necessity for an unaccounted-for carbon sink; the observation of Fe(II)-carbonates within uplifted strata; and the experimental and modelling campaign into Fe(II)-carbonate-producing conditions presented in this thesis — this work concludes that the relative scarcity of Fe(II)-carbonates on Mars's surface may be in part explained by the following two scenarios, low temperature and high temperature, both which would have occurred in the Noachian (~4.0-3.7 Ga; Hartmann and Neukum, 2001) when the planet was intermittently warm, wet (~1 Myr periods; Wordsworth et al., 2017), and CO_2-rich.

At low rock:waterrock:water, Fe(II)-carbonates formed within the subsurface at depths defined by the maximum at which CO_2-charged meteoric water could percolate through pore

space. There, in the CO_2-rich aquifers that occurred within the pore space of mineral grains or rock pore spaces, buffered to a basic pH after interaction within a mafic substrate, the CO_2 gas, now as HCO_3^- or CO_3^{2-} anions, reacted with the Fe^{2+} cations in solution. These Fe(II)-carbonates could have been AFC ($Fe(CO_3)_{0.5}OH$), chukanovite ($Fe_2(CO_3)(OH)_2$), or siderite ($Fe(CO)_3$), only the latter of which is sufficiently stable to persevere over geological timescales. This Fe(II)-carbonate was able to form over a region at least 6 km deep, possibly as deep as 10 km (Michalski et al., 2013) around the entirety of Mars. Later, and syn-depositionally, these rocks would occasionally be exposed at the surface: great impact events, producing craters gouging circles over ~20 km wide (Wray et al., 2016). The fact that only very large impact craters expose Fe(II)-carbonates suggests the depth at which the carbonates began forming could be as much as 6 km below the surface (Michalski and Niles, 2010), thus, only the largest impact craters will draw rocks from such depths to the surface. This produces the preferential impression that Fe(II)-carbonates only form rarely; in actuality, a substantial, geologically significant sink of carbon could be locked within the Martian subsurface as carbonate, which may account for the carbon deficiency seen in mass balance calculations. The rarity of the observations of carbonates themselves is consistent with this deep formation mechanism. Such a hypothesis could be tested with selected drilling campaigns on Mars or by quantifying the mass of carbon seen in the deepest impact craters where such a deposit could have been uplifted and exposed.

At high temperature the process of formation is more straightforward: in addition to the above process, Fe(II)-carbonates were also capable of precipitating authigenically from CO_2-charged waters within hydrothermal lakes and springs adjacent to volcanic complexes. Following this, the carbonates could be deposited as surface-based strata. Providing they escaped several billion years of destructive processes, such as burial by subsequent volcanic flows or dissolution by acidic fronts, such deposits remain readily identifiable upon the Martian surface today.

For Ca- and Mg-rich carbonates, while not the focus of this work and not specifically investigated, modelling and the use of materials bearing these elements (forsterite, Columbia River

Basalt) provided insights into their own relevance to the above process. For Ca-carbonates, these were found in modelling to become, like Fe-carbonates, a likely candidate for precipitation, but to a lesser degree; this could suggest that where CO_2 is present in a system, free Fe^{2+} was more likely to make use of this more effectively than the Ca^{2+}. The growth of calcite is quickly inhibited by the presence of impurities (Dromgoole and Walter, 1990), most effectively by Mg^{2+}, but also Fe^{2+}, which is known to be a strong calcite-precipitation inhibitor (Sumner and Grotzinger, 1996). This could also account for the far higher $\Omega_{magnesite}$ than $\Omega_{calcite}$ in most models. It is difficult to estimate the presence of Ca-carbonates on Mars owing to their signature being very similar to that of Fe-carbonate, but this modelling could suggest such signals are mostly related to Fe. For Mg-carbonates, the modelling indicated a near-identical pathway of formation to Fe-carbonates but only marginally reduced in saturation state. As no Mg precipitates formed in any experiments, this appears to be significant: the minor advance of Fe^{2+} over Mg^{2+} is sufficient for only Fe-carbonates to form under the conditions and timescales explored here. Unlike Ca-carbonates, however, Mg-carbonates are amongst the commonest type on Mars (e.g., Ehlmann et al. 2008). Their association with areas associated with warmth such as impact craters and volcanic provinces implies a formational link to hydrothermal temperatures; it is plausible that the 75 ºC waters employed here were of insufficient temperature for Mg-carbonate formation. The difficulty in forming Mg-carbonates within the research of this thesis is puzzling, and a dedicated research campaign equivalent to this thesis but into Mg-carbonate formation is recommended to focus on this issue.

5. Summary and final words

This thesis sought to understand the kinetic mechanisms and geologic reasons behind the scarcity of Fe(II)-carbonates on Mars. Over 161 experiments supplemented by geochemical modelling, across 3 data chapters, the conclusions of this thesis are as follows:

(1) Fe(II)-carbonates require heightened states of supersaturation prior to their formation;
(2) Such supersaturation is best met under low rock:water ratio, closed CO_2 system conditions, and expedited by higher temperatures;
(3) Aquifers in the Martian subsurface best represent these conditions;
(4) At 75 ºC, high rock:water ratio environments also become Fe(II)-carbonate-forming candidates;
(5) The lack of visible Fe(II)-carbonates on Mars does not necessarily reflect a lack of their existence, but potentially their formation predominantly below the surface under more favourable precipitation conditions;
(6) Mass balance calculations and the identification of Fe(II)-carbonates both from depth within uplifted impact craters and in open water settings associated with above-ambient temperatures supports these conclusions.

An experimental examination of the formation mechanism behind carbonates under anoxic, Mars-like conditions is highly timely given the impending arrival of NASA's *Perseverance* rover in 2021, which will explore the mineralogic diversity of Jezero Crater, Nili Fossae (Figure 1). Insight into the authigenic formation mechanism of Jezero's carbonates, which could include a larger proportion of Fe(II)-carbonates than first considered (e.g., Horgan et al., 2020), could offer broad constraints upon surface-based carbonate formation that may complement the work of this thesis. This is a direct means of testing the proposed high rock:waterrock:water ratio, hydrothermal, authigenic Fe(II)-carbonate formation mechanism proposed for the Jezero carbonates in Chapter 5.

It is, furthermore, possible that part of the spectroscopically investigated carbonate suite at Jezero could represent those uplifted from depth, similar to nearby Leighton Crater (Michalski and Niles, 2010) or the similarly sized McLaughlin Crater in Arabia Terra (Michalski et al., 2013).

Such *in situ* observations would enable refinement to the foundations of anoxic, Mars-relevant Fe(II)-carbonate formation as outlined in this thesis.

The *Perseverance* rover is part of a larger, planned series of missions that culminate in the return of Martian samples within the next decade. One of the four main goals of *Perseverance*'s mission is to cache samples that will be collected by subsequent missions and taken to an ascent vehicle to Earth. If samples of the Jezero carbonates were taken to Earthly laboratories, the hypotheses posited in this thesis — that they formed within a hydrothermal, open air, high rock:water ratio lacustrine environment — could be tested by the following:

1) **Clumped isotope analysis:** In line with the work of Halevy et al. (2011), who used this method to determine the formation temperature of carbonates within the ALH 84001 meteorite;
2) **Optical and Scanning Electron Microscopy:** To observe the morphology of the carbonate crystal structure and what likely formation environment this suggests, e.g., small crystals grown amidst host rock pore spaces compared to large, fanned crystals more suggestive of open space and abundant ion supply. Additionally, the composition and formation history of adjacent mineralogy would offer further information regarding environment (e.g., minerals suggesting reducing/oxidising, ambient/hydrothermal, water scarce/abundant conditions);
3) **Elemental analysis:** Using, e.g., Inductively Coupled Plasma Mass Spectrometry to determine the exact ion composition of the carbonates and whether this differed spatially such as in the case of the Gusev Crater carbonates (Morris et al., 2010);
4) **Stratigraphic analysis:** Observing the changing environments represented by up- and down-stratigraphic sections captured in other samples;
5) **X-Ray Diffraction:** To determine crystal composition as a means of cross-checking lower-resolution rover analytical techniques.

Such techniques, amongst others, could assist in determining the formation environment of the Jezero carbonates and therefore test the kinetic framework outlined in this thesis.

Lastly, while this thesis has sought in particular to investigate the Martian carbonates, the kinetics that drive mineral formation are bound by the universal laws of how physical matter interacts. Accordingly, where the conditions studied in this thesis operate on Earth — that is, anoxic, without the major influence of biology, within mafic geology, and under 0.1-1.0 bar pCO_2, — the formation mechanisms proposed in Chapter 3-5 would also operate. These conditions could exist in: anoxic environments such as swamps or buried within seafloors; in mafic aquifers such as the Samail Ophiolite in Oman; or in CO_2-charged volcanic lakes such as Askja in Iceland. A separate series of work that samples carbonates found in such environments and tests their formation means would be an excellent complementary study in preparation for actual carbonate samples returned from Mars.

6. Figures

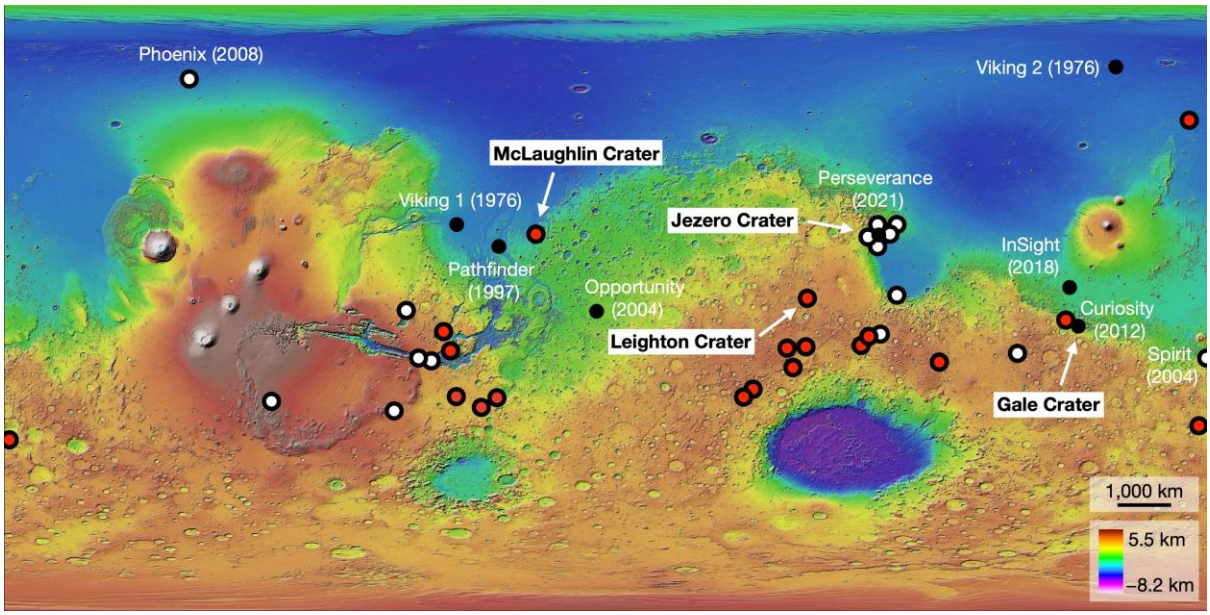


Figure 1: Mars Orbital Laser Altimeter (MOLA) map of Mars produced by the author, whereby colours correspond to topography. North is up. Circles correspond to the known sites bearing carbonates on Mars, including *in situ* from rovers and remotely from orbit-based spectroscopy. In red are Fe-bearing carbonates, while in white are carbonate signatures that do not bear Fe. Data compiled from Ehlmann et al., 2008; Boynton et al., 2009; Morris et al., 2010; Michalski and Niles, 2010; Carrozzo et al., 2013; Michalski et al., 2013; 2017; 2019; Gilmore et al., 2014; Carter et al., 2015; Edwards and Ehlmann, 2015; Jain and Chauhan, 2015; Wray et al., 2016; Turner et al., 2016; Viviano-Beck et al., 2017. Four oft-discussed impact craters in this thesis Jezero, Gale, Leighton, and McLaughlin, are noted for reference. Note also the dichotomy between blue (for lowland) and orange-red (for highland) between the north and south of this map of Mars.

7. References

Bridges, J., 2000. Evaporite mineral assemblages in the nakhlite (martian) meteorites. Earth and Planetary Science Letters 176, 267–279. https://doi.org/10.1016/S0012-821X(00)00019-4

Bridges, J.C., Hicks, L.J., Treiman, A.H., 2019. Carbonates on Mars, in: Volatiles in the Martian Crust. Elsevier, pp. 89–118. https://doi.org/10.1016/B978-0-12-804191-8.00005-2

Bristow, T.F., Haberle, R.M., Blake, D.F., Marais, D.J.D., Eigenbrode, J.L., Fairén, A.G., Grotzinger, J.P., Stack, K.M., Mischna, M.A., Rampe, E.B., Siebach, K.L., Sutter, B., Vaniman, D.T., Vasavada, A.R., 2017. Low Hesperian PCO2 constrained from in situ mineralogical analysis at Gale Crater, Mars. PNAS 201616649. https://doi.org/10.1073/pnas.1616649114

Chevrier, V., Poulet, F., Bibring, J.-P., 2007. Early geochemical environment of Mars as determined from thermodynamics of phyllosilicates. Nature 448, 60–63. https://doi.org/10.1038/nature05961

Davis, J.M., Balme, M., Grindrod, P.M., Williams, R.M.E., Gupta, S., 2016. Extensive Noachian fluvial systems in Arabia Terra: Implications for early Martian climate. Geology 44, 847–850. https://doi.org/10.1130/G38247.1

Dromgoole, E.L., Walter, L.M., 1990. Iron and manganese incorporation into calcite: Effects of growth kinetics, temperature and solution chemistry. Chemical Geology 81, 311–336. https://doi.org/10.1016/0009-2541(90)90053-A

Edwards, C.S., Ehlmann, B.L., 2015. Carbon sequestration on Mars. Geology 43, 863–866. https://doi.org/10.1130/G36983.1

Ehlmann, B.L., Mustard, J.F., Murchie, S.L., Poulet, F., Bishop, J.L., Brown, A.J., Calvin, W.M., Clark, R.N., Marais, D.J.D., Milliken, R.E., Roach, L.H., Roush, T.L., Swayze, G.A., Wray, J.J., 2008. Orbital Identification of Carbonate-Bearing Rocks on Mars. Science 322, 1828–1832. https://doi.org/10.1126/science.1164759

Fastook, J.L., Head, J.W., 2015. Glaciation in the Late Noachian Icy Highlands: Ice accumulation, distribution, flow rates, basal melting, and top-down melting rates and patterns. Planetary and Space Science 106, 82–98. https://doi.org/10.1016/j.pss.2014.11.028

Forget, F., Pierrehumbert, R., 1997. Warming Early Mars with Carbon Dioxide Clouds That Scatter Infrared Radiation. Science 278, 1273–1276. https://doi.org/10.1126/science.278.5341.1273

Goudge, T.A., Mustard, J.F., Head, J.W., Fassett, C.I., Wiseman, S.M., 2015. Assessing the mineralogy of the watershed and fan deposits of the Jezero crater paleolake system, Mars: Jezero Paleolake System Mineralogy. J. Geophys. Res. Planets 120, 775–808. https://doi.org/10.1002/2014JE004782

Grotzinger, J.P., Sumner, D.Y., Kah, L.C., Stack, K., Gupta, S., Edgar, L., Rubin, D., Lewis, K., Schieber, J., Mangold, N., Milliken, R., Conrad, P.G., DesMarais, D., Farmer, J., Siebach, K., Calef, F., Hurowitz, J., McLennan, S.M., Ming, D., Vaniman, D., Crisp, J., Vasavada, A., Edgett, K.S., Malin, M., Blake, D., Gellert, R., Mahaffy, P., Wiens, R.C., Maurice, S., Grant, J.A., Wilson, S., Anderson, R.C., Beegle, L., Arvidson, R., Hallet, B., Sletten, R.S., Rice, M., Bell, J., Griffes, J., Ehlmann, B., Anderson, R.B., Bristow, T.F., Dietrich, W.E., Dromart, G., Eigenbrode, J., Fraeman, A., Hardgrove, C., Herkenhoff, K., Jandura, L., Kocurek, G., Lee, S., Leshin, L.A., Leveille, R., Limonadi, D., Maki, J., McCloskey, S., Meyer, M., Minitti, M., Newsom, H., Oehler, D., Okon, A., Palucis, M., Parker, T., Rowland, S., Schmidt, M., Squyres, S., Steele, A., Stolper, E., Summons, R., Treiman, A., Williams, R., Yingst, A., Team, M.S., 2014. A Habitable Fluvio-Lacustrine Environment at Yellowknife Bay, Gale Crater, Mars. Science 343, 1242777. https://doi.org/10.1126/science.1242777

Haberle, R.M., Clancy, R.T., Forget, F., Smith, M.D., Zurek, R.W., 2017. The atmosphere and climate of Mars. Cambridge University Press.

Halevy, I., Fischer, W.W., Eiler, J.M., 2011. Carbonates in the Martian meteorite Allan Hills 84001 formed at 18 4 C in a near-surface aqueous environment. Proceedings of the National Academy of Sciences 108, 16895–16899. https://doi.org/10.1073/pnas.1109444108

Harrison, K.P., Grimm, R.E., 2009. Regionally compartmented groundwater flow on Mars. J. Geophys. Res. 114, E04004. https://doi.org/10.1029/2008JE003300

Hartmann, W.K., Neukum, G., 2001. Cratering Chronology and the Evolution of Mars, in: Chronology and Evolution of Mars, Space Sciences Series of ISSI. Springer, Dordrecht, pp. 165–194. https://doi.org/10.1007/978-94-017-1035-0_6

Heard, A.W., Kite, E.S., 2020. A probabilistic case for a large missing carbon sink on Mars after 3.5 billion years ago. Earth and Planetary Science Letters 531, 116001. https://doi.org/10.1016/j.epsl.2019.116001

Horgan, B.H.N., Anderson, R.B., Dromart, G., Amador, E.S., Rice, M.S., 2020. The mineral diversity of Jezero crater: Evidence for possible lacustrine carbonates on Mars. Icarus 339, 113526. https://doi.org/10.1016/j.icarus.2019.113526

Jakosky, B.M., 2019. The CO2 inventory on Mars. Planetary and Space Science 175, 52–59. https://doi.org/10.1016/j.pss.2019.06.002

Jakosky, B.M., Brain, D., Chaffin, M., Curry, S., Deighan, J., Grebowsky, J., Halekas, J., Leblanc, F., Lillis, R., Luhmann, J.G., Andersson, L., Andre, N., Andrews, D., Baird, D., Baker, D., Bell, J., Benna, M., Bhattacharyya, D., Bougher, S., Bowers, C., Chamberlin, P., Chaufray, J.-Y., Clarke, J., Collinson, G., Combi, M., Connerney, J., Connour, K., Correira, J., Crabb, K., Crary, F., Cravens, T., Crismani, M., Delory, G., Dewey, R., DiBraccio, G., Dong, C., Dong, Y., Dunn, P., Egan, H., Elrod, M., England, S., Eparvier, F., Ergun, R., Eriksson, A., Esman, T., Espley, J., Evans, S., Fallows, K., Fang, X., Fillingim, M., Flynn, C., Fogle, A., Fowler, C., Fox, J., Fujimoto, M., Garnier, P., Girazian, Z., Groeller, H., Gruesbeck, J., Hamil, O., Hanley, K.G., Hara, T., Harada, Y.,

Hermann, J., Holmberg, M., Holsclaw, G., Houston, S., Inui, S., Jain, S., Jolitz, R., Kotova, A., Kuroda, T., Larson, D., Lee, Y., Lee, C., Lefevre, F., Lentz, C., Lo, D., Lugo, R., Ma, Y.-J., Mahaffy, P., Marquette, M.L., Matsumoto, Y., Mayyasi, M., Mazelle, C., McClintock, W., McFadden, J., Medvedev, A., Mendillo, M., Meziane, K., Milby, Z., Mitchell, D., Modolo, R., Montmessin, F., Nagy, A., Nakagawa, H., Narvaez, C., Olsen, K., Pawlowski, D., Peterson, W., Rahmati, A., Roeten, K., Romanelli, N., Ruhunusiri, S., Russell, C., Sakai, S., Schneider, N., Seki, K., Sharrar, R., Shaver, S., Siskind, D.E., Slipski, M., Soobiah, Y., Steckiewicz, M., Stevens, M.H., Stewart, I., Stiepen, A., Stone, S., Tenishev, V., Terada, N., Terada, K., Thiemann, E., Tolson, R., Toth, G., Trovato, J., Vogt, M., Weber, T., Withers, P., Xu, S., Yelle, R., Yiğit, E., Zurek, R., 2018. Loss of the Martian atmosphere to space: Present-day loss rates determined from MAVEN observations and integrated loss through time. Icarus 315, 146–157. https://doi.org/10.1016/j.icarus.2018.05.030

Jakosky, B.M., Edwards, C.S., 2018. Inventory of CO2 available for terraforming Mars. Nat Astron 2, 634–639. https://doi.org/10.1038/s41550-018-0529-6

Jiang, C.Z., Tosca, N.J., 2020. Growth kinetics of siderite at 298.15 K and 1 bar. Geochimica et Cosmochimica Acta 274, 97–117. https://doi.org/10.1016/j.gca.2020.01.047

Jiang, C.Z., Tosca, N.J., 2019. Fe(II)-carbonate precipitation kinetics and the chemistry of anoxic ferruginous seawater. Earth and Planetary Science Letters 506, 231–242. https://doi.org/10.1016/j.epsl.2018.11.010

Jimenez-Lopez, C. and Romanek, C.S., 2004. Precipitation kinetics and carbon isotope partitioning of inorganic siderite at 25 C and 1 atm. *Geochimica et Cosmochimica Acta*, *68*(3), pp.557-571.

Kite, E.S., Mayer, D.P., Wilson, S.A., Davis, J.M., Lucas, A.S., Stucky de Quay, G., 2019. Persistence of intense, climate-driven runoff late in Mars history. Sci. Adv. 5, eaav7710. https://doi.org/10.1126/sciadv.aav7710

Kurahashi-Nakamura, T., Tajika, E., 2006. Atmospheric collapse and transport of carbon dioxide into the subsurface on early Mars: TRANSPORT OF CO $_2$ IN EARLY MARS. Geophys. Res. Lett. 33, n/a-n/a. https://doi.org/10.1029/2006GL027170

Michalski, J.R., Cuadros, J., Niles, P.B., Parnell, J., Deanne Rogers, A., Wright, S.P., 2013. Groundwater activity on Mars and implications for a deep biosphere. Nature Geoscience 6, 133–138. https://doi.org/10.1038/ngeo1706

Michalski, J.R., Niles, P.B., 2010. Deep crustal carbonate rocks exposed by meteor impact on Mars. Nature Geosci 3, 751–755. https://doi.org/10.1038/ngeo971

Morris, R.V., Ruff, S.W., Gellert, R., Ming, D.W., Arvidson, R.E., Clark, B.C., Golden, D.C., Siebach, K., Klingelhofer, G., Schroder, C., Fleischer, I., Yen, A.S., Squyres, S.W., 2010. Identification of Carbonate-Rich Outcrops on Mars by the Spirit Rover. Science 329, 421–424. https://doi.org/10.1126/science.1189667

Niles, P.B., Catling, D.C., Berger, G., Chassefière, E., Ehlmann, B.L., Michalski, J.R., Morris, R., Ruff, S.W., Sutter, B., 2013. Geochemistry of Carbonates on Mars: Implications for Climate History and Nature of Aqueous Environments. Space Sci Rev 174, 301–328. https://doi.org/10.1007/s11214-012-9940-y

Qafoku, O., Kovarik, L., Kukkadapu, R.K., Ilton, E.S., Arey, B.W., Tucek, J. and Felmy, A.R., 2012. Fayalite dissolution and siderite formation in water-saturated supercritical CO2. *Chemical Geology*, *332*, pp.124-135.

Ramirez, R.M., Craddock, R.A., Usui, T., 2020. Climate Simulations of Early Mars With Estimated Precipitation, Runoff, and Erosion Rates. J. Geophys. Res. Planets 125. https://doi.org/10.1029/2019JE006160

Ramirez, R.M., Kopparapu, R., Zugger, M.E., Robinson, T.D., Freedman, R., Kasting, J.F., 2014. Warming early Mars with CO2 and H2. Nature Geosci 7, 59–63. https://doi.org/10.1038/ngeo2000

Romanek, C.S., Jiménez-López, C., Navarro, A.R., Sánchez-Román, M., Sahai, N. and Coleman, M., 2009. Inorganic synthesis of Fe–Ca–Mg carbonates at low temperature. *Geochimica et Cosmochimica Acta*, *73*(18), pp.5361-5376.

Sagan, C., Chyba, C., 1997. The Early Faint Sun Paradox: Organic Shielding of Ultraviolet-Labile Greenhouse Gases. Science 276, 1217–1221. https://doi.org/10.1126/science.276.5316.1217

Salese, F., Pondrelli, M., Neeseman, A., Schmidt, G., Ori, G.G., 2019. Geological Evidence of Planet-Wide Groundwater System on Mars. J. Geophys. Res. Planets 124, 374–395. https://doi.org/10.1029/2018JE005802

Segura, T.L., Toon, O., Colaprete, A., Zahnle, K., 2002. Environmental Effects of Large Impacts on Mars. Science 298, 1977–1980. https://doi.org/10.1126/science.1073586

Sengupta, R., Tosca, N.J. and Robinson, S.A., 2020. Geochemical controls on the elemental composition of siderite: Implications for palaeo-environmental reconstructions. *Geochimica et Cosmochimica Acta*, *271*, pp.1-15.

Squyres, S.W., Grotzinger, J.P., Arvidson, R.E., Bell, J.F., Calvin, W., Christensen, P.R., Clark, B.C., Crisp, J.A., Farrand, W.H., Herkenhoff, K.E., Johnson, J.R., Klingelhöfer, G., Knoll, A.H., McLennan, S.M., McSween, H.Y., Morris, R.V., Rice, J.W., Rieder, R., Soderblom, L.A., 2004. In Situ Evidence for an Ancient Aqueous Environment at Meridiani Planum, Mars. Science 306, 1709–1714. https://doi.org/10.1126/science.1104559

Sumner, D.Y., Grotzinger, J.P., 1996. Were kinetics of Archean calcium carbonate precipitation related to oxygen concentration? Geology 24, 119–122. https://doi.org/10.1130/0091-7613(1996)024<0119:WKOACC>2.3.CO;2

Tosca, N.J., Ahmed, I.A.M., Tutolo, B.M., Ashpitel, A., Hurowitz, J.A., 2018. Magnetite authigenesis and the warming of early Mars. Nature Geoscience 11, 635–639. https://doi.org/10.1038/s41561-018-0203-8

Tosca, N.J., Knoll, A.H., McLennan, S.M., 2008. Water Activity and the Challenge for Life on Early Mars. Science 320, 1204–1207. https://doi.org/10.1126/science.1155432

Urata, R.A., Toon, O.B., 2013. Simulations of the martian hydrologic cycle with a general circulation model: Implications for the ancient martian climate. Icarus 226, 229–250. https://doi.org/10.1016/j.icarus.2013.05.014

Wadhwa, M., 2008. Redox Conditions on Small Bodies, the Moon and Mars. Reviews in Mineralogy and Geochemistry 68, 493–510. https://doi.org/10.2138/rmg.2008.68.17

Warren, A.O., Kite, E.S., Williams, J. -P., Horgan, B., 2019. Through the Thick and Thin: New Constraints on Mars Paleopressure History 3.8 – 4 Ga from Small Exhumed Craters. J. Geophys. Res. Planets 124, 2793–2818. https://doi.org/10.1029/2019JE006178

Wordsworth, R., Kalugina, Y., Lokshtanov, S., Vigasin, A., Ehlmann, B., Head, J., Sanders, C., Wang, H., 2017. Transient reducing greenhouse warming on early Mars. Geophys. Res. Lett. 44, 2016GL071766. https://doi.org/10.1002/2016GL071766

Wordsworth, R.D., 2016. The Climate of Early Mars. Annu. Rev. Earth Planet. Sci. 44, 381–408. https://doi.org/10.1146/annurev-earth-060115-012355

Wray, J.J., Murchie, S.L., Bishop, J.L., Ehlmann, B.L., Milliken, R.E., Wilhelm, M.B., Seelos, K.D., Chojnacki, M., 2016. Orbital evidence for more widespread carbonate-bearing rocks on Mars. Journal of Geophysical Research: Planets 121, 652–677. https://doi.org/10.1002/2015JE004972

Zeebe, R., Wolf-Gladrow, D., 2001. CO2 in Sewater: Equilibrium, Kinetics, Isotopes. Gulf Professional Publishing.

Appendix 1

Descriptions of All Experiments

A total of 155 individual experiments were performed over the course of this project, 134 of which were considered successful (that is, yielded data used in papers and thesis chapters). Each will now be described to reproducible detail within several distinct categories. Each experiment's title corresponds to the date at which it was begun.

1. Fayalite/forsterite

1.1. Fayalite: non-CO_2

In this subset of experiments, no CO_2 was added to solutions to observe the effect of both rock:water ratio and pH variation upon a substrate of pure synthetic fayalite. This set-up was devised to act as a control in anticipation of more complex mineralogy expected to form with the addition of CO_2, thereby enabling CO_2-dependent and non-dependent minerals to be distinguished.

1.1.1. 170906

An experiment not discussed elsewhere in this thesis is 170906, the first set-up, all data for which was discarded with the entry of an unacceptable level of oxygen into the glove box (>300 ppm), thereby voiding the experiment. 170906 ran for 28 days and comprised five sub-experiments (A-E), each sampled daily and their pH and Eh noted. 0.5 g of synthetic fayalite was added to 125 mL of deoxygenated DI water at pH at intervals of 2, 3, 4, 5, and 6. The set-up was not reproduced for any subsequent experiments: Teflon beakers with screw-caps were each placed on a magnetic stirrer bar and, to stir the experiments and keep their reactants in constant overturn within the

solution, Teflon-wrapped magnetic stirrers were added to each beaker. These proved difficult to align on magnetic bar, however: some stirrers only ticked at intervals, while others would not move at all. The fayalite also coated these magnets (despite being non-magnetic itself), making both cleaning the equipment and retrieving solids at the end of the experiment difficult. With the leak of atmospheric oxygen into the glove box, all samples were disposed of and the experiment prematurely terminated. At this stage only a limited amount of synthetic fayalite had been produced, thus there was a time interval of several months before sufficient material was prepared and a new experimental set-up devised, after which began further experiments in 2018.

1.1.2. 180123

This first successful experiment comprises of six sub-experiments, two begun at pH 2, 4, and 6, and of those each with a rock:water ratio of either 1:100 or 1:500. The set-up was as follows: cylindrical Nalgene beakers of 125 mL capacity were attached to an orbital shaker that rotated at 230 rpm. For the three at low rock:water ratio, 50 mL of DI water calibrated to pH 2, 4, or 6 was added to 0.5 g of fayalite. For the three at high rock:water ratio, 125 mL of DI water calibrated to pH 2, 4, or 6 was added to 0.25 g of fayalite. 10 samples at 500 μL were extracted from each sub-experiment over 8 days. As there were no gases dissolved within solution, beakers were opened to the glove box air with each sampling set, a pH and Eh probe placed inside the beaker, and the sample extracted via syringe.

1.1.3. 180203

While 180123 was monitored at 1 hour, 6 hours, and at 1 day intervals thereafter, significant pH and Eh change occurred within the first 24 hours. As such 180203 is a direct repeat of 180123 but sampled on the hour, every hour, for the first ten hours of experimentation, after which time the experiment was terminated to prevent more than 10% of the solution being removed and significantly altering the rock:water ratio.

1.1.4. 180310

This experiment is a direct repeat of 180203, again over 10 hours, to assess the reproducibility of the results of the previous two experiments. Its solution samples were not analysed via ICP-OES due to duding constraints and the similarity of the data to the previous experiment.

1.2. Fayalite ± forsterite: CO_2, short term

The following experiments all had CO_2 dissolved within their fluids via the addition of bicarbonate of soda by the methods described in the section above. All employed the orbital shaker at 230 rpm, as every experiment henceforth described does. Square Nalgene beakers of 0.172 mL capacity were used for CO_2-bearing experiments due to their ability to maintain a gas-tight seal when capped with butyl-rubber, through which a syringe could be injected without opening during sampling and thereby losing dissolved CO_2. A rock:water ratio of 1:500 was maintained between 0.3444 g of fayalite ± forsterite and 0.172 mL of fluid, which was calibrated to pH 2 or 4 with dissolved levels of CO_2 at 0.1, 0.5, or 1.0 bars.

1.2.1. 180313

This experiment lasted for 13 days, during which ten samples at 500 µL were extracted. Only fayalite was used.

1.2.2. 180406

This experiment is a repeat of 180313 but lasting for 17 days: it was sampled daily for the first nine samples, then left for one week to determine if pH and Eh change persisted for a longer duration than previously run.

1.2.3. 180612

In the first experiments to use forsterite in addition to fayalite, the rock:water ratio was reduced to 1:250 by adding 0.3444 g of both fayalite and forsterite to 0.172 mL of solution. This solution, as with previous CO_2-bearing experiments, comprised of 6 sub-experiments, 3 each at

pH 2 and 4, and of those 2 at 0.1, 0.5, and 1.0 bars of CO_2. The experiment was sampled daily for 9 days then left to run for 15, when it was terminated.

1.2.4. 180829

180829 is a direct repeat of 180612 when the pH in this experiment unexpectedly dipped in the case of sub-experiment pH 2 1.0 bar. This did not follow any pattern previously seen in experiments either CO_2-bearing or not, and a repeat was run to determine whether this was a product of the forsterite addition or due to some mistake. As this phenomenon was not observed in either this repeat or two longer-runs of identical experiments (180628 and 181029 Fo), but was seen again in the non-Fo-bearing 181029 Fa, a hypothesis for why the pH dropped is perhaps the starter pH was unstable when noted down, and suddenly dropped when the solution was disturbed during its transfer to the experiment beaker. To prevent this happening again after its recurrence in 181029 Fa, greater care was subsequently taken to ensure the pH measurement was stable before transferring the solution to its beaker. As the pH did not drop in the case of 180612, 180829 was run for fewer days than 180612, at 12 days.

1.3. Fayalite ± forsterite: CO_2, long term

This category of experiments follows an identical set-up to the previous, excepting that its experiments were left to run for up to 80 days to understand whether pH and Eh continued to change over time.

1.3.1. 180628

This experiment used both forsterite and fayalite to a rock:water ratio of 1:250, and as before there were 6 sub-experiments. The experiment was sampled 10 times during its 61-day duration.

1.3.2. 181029 Fa

Given the interesting results of 180628, a long-term experiment using only fayalite was set up to determine whether the results of 180628 were due to the long duration time or the addition

of forsterite, or both. This experiment was set up simultaneously with 181029 Fo; to fit both experiments upon the single orbital shaker, an acrylic rack was attached with zip-ties to the shaker, into which the 12 sub-experiments could all be placed. However, the sample holes in the rack were circular, not square like the beakers that had been employed for all CO_2 experiments. The butyl-rubber caps used atop the square bottles fit very well to the cylindrical Nalgene beakers last used in the non-CO_2 experiments, and so given the time constraints of the thesis timeline and the ability of the sealed cylindrical beakers to hold water, they appeared as capable of maintaining a gas-tight seal as the square beakers. This experiment ran for 80 days. The rock:water ratio of this experiment was 1:500.

1.3.3. 181029 Fo

This experiment is a repeat of 180628, only run for 80 days not 60. It ran simultaneously with 181029 Fa as described in the paragraph previously, and was run with the intention of testing the reproducibility of the interesting results of 180628. The rock:water ratio of this experiment was 1:250.

1.3.4. 190423 Fa

This experiment is a direct repeat of 181029 Fa, which, like 180612, experienced an anomalous drop in pH for sub-experiment pH 2 1.0 bar. Though experienced twice, this instance remains considered an anomaly based on both its rarity compared to near-identical experimental set-ups, but also because the drop in pH does not make sense from an understanding of the kinetic evolution of the experiment. 181029 Fa is an important experiment in understanding whether the duration of time running or the addition of forsterite is central to the results of 180628, and thus, though cumbersome, its 80 day repeat is vital to the integrity of this thesis. As the source of the anomaly could have been due to the use of cylindrical beakers instead of the square ones as employed for all other CO2-bearing experiments, for 190423 Fa and its twin 190423 Fo, square beakers were used by more-economically placing the twelve beakers within the orbital shaker,

which were all found to fit without the use of the acrylic rack used in the 181029 experiments. The rock:water ratio of this experiment was 1:500.

1.3.5. 190423 Fo

The results of 181029 Fo did not yield the same as those of 180628. This may have been due to the use of the possibly less airtight cylindrical beakers, and this in this repeat, as with 180423 Fa, square beakers were used. The two twin experiments were run simultaneously upon the one orbital shaker by fitting them close together. Their square shapes also prevented randomly oriented rattling within the circular holders of the 181029 experiments, which might have promoted their hypothesised gas loss and their wildly-fluctuating pH and Eh measurements. 190423 Fo, like 190423 Fa, was run for 80 days. The rock:water ratio of this experiment was 1:500.

1.4. Fayalite ± forsterite: CO_2, low rock:water ratio

In this category of experiments, gas-tight 50 mL Luer-Lock syringes were used to contain the experiments to eliminate headspace, which would involve too much rocky substrate for such low rock:water ratios if the regular square beakers were used. For 1:1 ratios, 1 g fayalite (or 0.5 × 2 Fa and Fo) were added to 1 mL solution at pH 2 or 4; for 1:10 ratios, this was 10 mL. CO_2 levels were kept fixed at 1.0 bar. The experiments had too little solution to sample, but at their termination a small amount was sampled from the high water-rock experiments for pH and Eh measurements, then stored for ICP-OES analysis. No fluid could be recovered from the 1:1 experiments as the substrate had taken on a mudlike consistency.

1.4.1. 181004

4 sub-experiments were run simultaneously: 2 at pH 2, 2 at pH 4, each with one at 1:1 and 1:10 water rock-ratios. The substrate was pure fayalite. The experiments ran for 60 days.

1.4.2. 181205

4 sub-experiments were run simultaneously: 2 at pH 2, 2 at pH 4, each with one at 1:1 and 1:10 water rock-ratios. The substrate was 50:50 fayalite and forsterite. The experiments ran for 60 days.

1.5. Fayalite ± forsterite: CO_2, high Fa-Fo ratio

In an effort to estimate the effect of increasing quantities of forsterite in the system, these experiments were run with ratios of 1:9 fayalite to forsterite. For a rock:water ratio of 1:250 in the square beakers of 0.172 mL capacity, this equated to a total of 0.3444 g substrate, 0.0688 g as fayalite and 0.6199 as forsterite.

1.5.1. 190121

This experiment lasted 80 days and comprised six experiments, with 3 at 0.1, 0.5, and 1.0 bar CO_2 under pH 2, and the same for pH 4.

2. Columbia River Basalt

2.1. CRB: CO_2, long term

Chapter 4 forms the second part of this research and uses a different substrate—Columbia River Basalt (CRB)—to simulate the more complex interactions between differing minerals under Mars-like conditions. These experiments used the 0.172 mL square Nalgene bottles set upon the orbital shaker at 230 rpm, and each comprised 4 sub-experiments. The 0.1 bar CO_2 experiments were discontinued for the CRB experiments because none of the previous experiments with up to 1.0 bar CO_2 had precipitated even nanoscopic amounts of carbonate minerals. Given the time, funding, materials, and energy expended upon the set-up and sampling of experiments, these limited resources were better employed by discontinuing this additional CO_2 category and instead focusing on the effect of particulate surface area. CRB was sourced from a previous research

project of the author's adviser's, and came pre-sieved into two distinct sizes as discussed in Chapter 2.

2.1.1. 190414

Fine and coarse CRB sediment was used in this experiment. 4 beakers, 2 at pH 2 and 2 at pH 4, contained either 0.5 or 1.0 bar of CO_2 and were filled with 0.172 mL solution to eliminate beaker headspace. 0.172 g of fine or coarse CRB was added to produce a rock:water ratio of 1:1000. As with all CO_2-hearing experiments, the beakers were not opened until experiment termination and were sampled via a butyl-rubber cap. The experiment was sampled over a duration of 85 days before ending.

2.2. CRB: CO_2, low rock:water ratio

These experiments, as above comprising both fine- and coarse-grained CRB, were set at low rock:water ratios of 1:1 and 1:10. They were set up with the same equipment in the low rock:water ratio: 50 mL Luer-Lock syringes that could be compressed to hold only the volume of the solution within them. Unlike previous low water-rock experiments, a method was devised at this point to attach the syringes to a lid designed to fit atop the orbital shaker already containing running experiments. The 8 syringes of 190418 F and C were zip-tied to a sheet of cardboard punctured with holes through which string could be threaded to tie the makeshift rack to the rotating shaker. This way particulates suspended within the syringe solutions could be continually shaken, disturbing fresh sediment and exposing it to solution, potentially catalysing any reactions occurring.

2.2.1. 190418

8 sub-experiments were run together, all with 1.0 bar CO_2 dissolved within them. The substrate used was 1 g of fine- and coarse-grained CRB. Of the 4, 2 were begun at pH 2 and 2 at pH 4, and within these were 1:1 and 1:10 rock:water ratios. This experiment was run for 85 days and was not sampled due to the low fluid levels, and although a sample was anticipated to be

collected from sub-experiments at higher rock:water ratios (1:10), a failure of the vacuum pumping system meant that no fluids were obtained.

2.2.2. 190812

Due to a fault with the vacuum pumping system, no solids were able to be obtained from either 190418, nor solution samples and pH/Eh measurements upon termination. For this reason the four experiments were directly repeated for the same duration of time (85 days).

2.3. CRB: CO_2, short term

Three experiments were set up to more closely examine the earliest days of CRB experimentation, since, like with fayalite and forsterite experiments, the majority of change appeared to occur within the first week. The three experiments thus described all occurred over a ten-day range under identical conditions, but for the levels of CO_2 used.

2.3.1. 190806

This experiment used no CO_2 and involved four sub-experiments: fine CRB at pH 2; coarse CRB at pH 2; fine CRB at pH 4; and coarse CRB at pH 4. The experiment lasted for ten days and ran in an orbital shaker parallel to 190807 (begun a day later) and 190808 (begun two days later).

2.3.2. 190807

This experiment used 0.5 bars of CO_2 for all four sub-experiments within. The four sub-experiments followed the same pattern as 190806 and included: fine CRB at pH 2; coarse CRB at pH 2; fine CRB at pH 4; and coarse CRB at pH 4. The experiment lasted for ten days and ran in an orbital shaker parallel to 190806 (begun a day earlier) and 190808 (begun a day later).

2.3.3. 190808

This experiment used 1.0 bars of CO_2 for all four sub-experiments within. The four sub-experiments followed the same pattern as 190806 and included: fine CRB at pH 2; coarse CRB at

pH 2; fine CRB at pH 4; and coarse CRB at pH 4. The experiment lasted for ten days and ran in an orbital shaker parallel to 190806 (begun two days earlier) and 190807 (begun a day earlier).

3. Heated experiments at 75 °C

Chapter 5 of this thesis discusses experiments conducted at 75 °C that are repeats of those run at room temperature (25 °C). These experiments followed the same set-up as those previously: 0.172 L Nalgene bottles were foil-wrapped to prevent oxidation and sealed with septum caps through which a syringe could be incised to sample the solution within. These beakers were stored inside a furnace that contained the capacity for 9 such bottles simultaneously, or 8 50 mL capacity syringes used as previously for low rock:water ratio experiments. Fayalite, forsterite, fine CRB, and coarse CRB were used from the previous experiments, and the sampling procedure followed the same as previously. During sampling, each bottle was removed from the furnace for the duration of sample extraction, then immediately returned to prevent unnecessary cooling.

3.1. Fayalite at 75 °C

These experiments recreate those bearing pure fayalite, and were conducted over short (10 day) time periods. Longer timescales (2-3 months) were desired, but incompatible with the time scale of this project.

3.1.1. 191028

This comprises of eight sub-experiments, four each begun at pH 2 and 4, and of those one with 0 bars of CO_2, 0.1, 0.5, and 1.0. The set-up was as follows: cylindrical Nalgene beakers of 125 mL capacity were placed within a glovebox-housed furnace at 75 °C. No orbital shaker could be used as with previous experiments for this reason. 0.172 L of DI water, the capacity of the Nalgene bottles, was calibrated to pH 2 or 4 and was added to 0.344 g of fayalite (1:500 rock:water

ratio). 10 samples at <1.72 mL were extracted from each sub-experiment over 10 days to capture the rapid precipitation kinetics that occur over this period. All beakers, even that with no dissolved CO_2, remained sealed from the start of experiment to its termination. All samples were extracted via syringe.

3.2. Fayalite + forsterite at 75 °C

These experiments used both fayalite and forsterite in a 1:1 ratio as seen in previous low temperature equivalent experiments.

3.2.1. 191107

This experiment ran for 10 days and comprised six sub-experiments, three begun at pH 2, three at pH 4, and within those, one each at 0.1, 0.5, and 1.0 bars of dissolved CO_2.

3.3. CRB at 75 °C

These experiments used both fine and coarse CRB in separate sub-experiments as seen in their previous low temperature equivalents.

3.3.1. 191118

This experiment ran for 10 days and comprised eight sub-experiments, four of fine CRB and four of coarse. Within these, two began at pH 2, two at pH 4, and within those, one each at 0.5 and 1.0 bars of dissolved CO_2. This experiment ran for 10 days.

3.4. Low water-rock at 75 °C

These experiments were conducted within 50 mL capacity syringes to remain airtight, and hosted either 1:1 or 1:10 rock:water ratio experiments using both fayalite ± forsterite, and fine/coarse CRB. Unfortunately, all syringes ruptured and the experiments were lost; the methods are included

here for completeness. Due to time constraints these were unable to be repeated within the time frame of the project.

3.4.1. 191128

This experiment used pure fayalite. It comprised four sub-experiments, two begun at pH 2, two at pH 4, and within those, one each at 1:1 and 1:10 rock:water ratio (2 g of fayalite for 2 or 20 mL of solution). All contained 1.0 bar of dissolved CO_2.

3.4.2. 191129

This experiment is identical to the previous, but contained 1 g fayalite and 1 g forsterite for each sub-experiment.

4. Conclusions

This appendix has detailed each of the 155 individual experiments run across the course of this project. This includes those that were unsuccessful (170906), behaved anomalously (e.g., 180310, 180612, 191023 Fa, 191029 Fo), were unable to be analysed owing to analytical failure (190418), or were structurally compromised (191128, 191129).

These experiments form the backbone of this research and are referenced heavily across Chapters 3, 4, 5, and synthesised in Chapter 6.

Appendix 2

Expanded Analytical Results for Chapter 3

1. Introduction

In this chapter, the pH and Eh variation during experimentation for each experiment are described in detail. The results of every analysis conducted on both the liquid and solid components of terminated experiments are also described in full detail. This includes inductively-coupled plasma optical emission spectrometry (ICP-OES) for liquid, and X-Ray diffractometry (XRD), Fourier transform infrared spectroscopy (FT-IR), scanning electron microscopy (SEM), and Brunauer-Emmett-Teller analysis (BET) for solid. The reader is referred to Appendix 1 for in-depth descriptions of each experiment's set-up.

2. pH and Eh during experimentation

In this section, the changes in conditions during runs of experiments are closely examined and described visually in graphs with corresponding text to explain these changes. pH and Eh are covered in this section.

2.1. pH

pH is a measure of how acidic or basic a solution is, usually on a scale of 0 to 14, where 0 is most acidic and 14 is most basic. Specifically, pH is equal to $-\log_{10} c$, c being hydrogen ion concentration in moles per litre.

pH was measured at intervals over the course of all experiments to monitor the availability of H^+ and/or OH^- ions in solution, which is important for understanding the switch in iron chemistry from ferrous to ferric. This in turn affects which minerals are capable of forming, and is vital when used in conjunction with ICP-OES data of element concentration, as it can yield data about which minerals are kinetically stable at these conditions and therefore capable of forming.

2.1.1. 180123

Experiment 180123 lasted for 193 hours (8 days, 1 hour). As seen in Figure 1 (180123), all sub-experiments excepting pH 6 high w/r show an immediate climb over the first day. For experiments begun at pH 2 and 4 this is a climb of around 4 pH; for sub-experiment pH 6 low w/r it is 2 pH. The high pH 6 experiment drops within the first hour to pH 4.4 before climbing steadily. All experiments appear to stabilise by 193 hours, with high pH 2 in particular showing a smooth curve that levels off then begins to fall.

It is interesting that pH 2 and 6 experiments are distinctly apart and both level at pHs that do not overlap, but pH 4 experiments overlap with those of 6. For low pH 4, this reaches the same pH as both pH 6 experiments, while high pH 4 is far less stable than all others and fluctuates up and down by ~0.5 pH.

The low w/r experiments of pH 2 and 6 stabilise ~24 hours earlier, though low pH 4 follows the same trend as the high w/r experiments and stabilises after 24 hours. This relative stability is different for all sub-experiments. While low pH 2 reaches pH 6 and from there steadily climbs to 6.5 over the next ~170 hours, low pH 4 deviates by only ~0.1 pH between 24 and 193 hours, and low pH 6 steadily drops from 8.6 to 8.2 during this time. For their high w/r equivalents, high pH 2 also shows a gradual climb from pH 5 at 48 hours to 5.9 at 173 hours, before dropping to 5.7. High pH 4, as discussed, is less stable than other sub-experiments, and high pH 6 like low pH 6 seems to show a gradual decline after 24 hours from a maximum of 8.2 at 73 hours.

2.1.2. 180203

Experiment 180203, as seen in Figure 1 (180203) is an exact repeat of 180123 but sampled on the hour, every hour, for its first 10 hours before termination. This allows for a comparison to be made with the first hours of 180123, for datapoints recorded both 1 and 7 hours in. Table 1 shows the difference in recorded measurements taken at 1 hour for experiments 180123 and 180203 and finds there is a minimum 0.013 and a maximum 0.933 pH value between the two identically set up experiments. This is an average of 0.239. For measurements taken 7 hours in, Table 2 shows this and finds a minimum 0.092 and a maximum 1.699 pH difference, with an average of 0.637.

Interestingly, 180203 also agrees with 180123 in that low pH 2 and 6 show a far-steeper pH rise over the 12 hours of the experiment than low pH 4. High pH 2, likewise, shows the same lag in pH rise in both 180123 and 180203, and high pH 6 even shows the same drop 1 hour in before climbing high, within 0.234 of a pH difference.

This is excellent consistency between experiments and suggests that even with the removal of ~10% of experimental liquids for analysis, as with 180203 by 12 hours, the experiment continues to function sufficiently similarly to as it would have if left undisturbed (180123 had only ~2% of its liquids removed by 12 hours in).

This experiment was also conducted to view that sudden leap in pH between 0-12 hours in 180123 in higher resolution, and 180203 showed that this leap occurs steadily over that time, rising faster for the low w/r experiments and climbing more steadily for the high sub-experiments, particularly in the cases of high pH 2 and 4, which show a very smooth, slow ascent.

2.1.3. 180310

For the purposes of understanding how many repeats of identical experiments needed to be run — how common anomalous results would be — experiment 180310 was conducted as a repeat of the 10 hour 180203, which is in turn a repeat of 180203 with no CO_2 present. The pH

for experiment 180310 is not included in Figure 1 as no further analysis was conducted on this experiment, due to lack of resources and given the experiment's anomalous nature.

180310 was invaluable in teaching that the confidence assumed from the 180203 repeat must be far more restrained, and that the most critical of experiments must be repeated at least three times to most vigilantly ensure the reliability and repeatability of the results.

180310 does not follow the trends of 180203 or 180123's first 10 hours. The initial pHs for each sub-experiment are missing due to a loss of unsaved data from a computer shutdown, but given the high pH measurements for all low w/r sub-experiments and for high pH 6 for 1 hour in, which are far higher than for the two previous experiments, it is possible the starter pHs were higher. This may have contributed to the anomalous pH trends. Additionally, the sampling procedure itself was relatively new, and sampling six experiments on the hour often took more than an hour and a half, pushing back sampling time for the next hour. This also could have produced the anomalous results as samples were extracted at different times.

Table 3 and Table 4 compare the measurements between 180203 and 180310 at 1 hour and 7 hours and find significant differences in measurements taken at the same time during supposedly identical experiments. This is as high as a 3.8 pH difference, although some values are as small as the differences between 180123 and 180203, such as for high pH 2 across both measurements. The differences were greater for measurements taken after 1 hour, again suggesting the lost initial pH of each experiment may have deviated from that of 180123 and 180310.

From this experiment, the following lessons were learned:

1. Save work vigilantly after each collected datapoint, and back up all spreadsheets
2. Ensure initial pH of each experiment is precisely 2, 4, or 6
3. Practice the sampling procedure until × 6 experiments may be sampled within half an hour
4. For vital experiments, e.g., those that produce results sufficiently significant for publication, the experiment must be completed at least three times to ensure its repeatability and reliability

2.1.4. 180313

Experiment 180313 was the first to involve dissolved CO_2 in solution. pH 6 experiments were discontinued as these were deemed too neutral a starter to produce siderite. Rock:water ratio was maintained at 'high' (1:250) and 'low' discontinued due to the limited resources of equipment, sampling time, and analysis funds, and because the difference between high and low rock:water ratios in the previous experiments was not deemed sufficiently significant to warrant further study at this time.

The graphs following and including 180313 features only red (pH 2) and blue (pH 4) lines, with their weight determined by the levels of CO_2 included in the experiment. For 0.1 bar this is dashed; for 0.5 this is a narrow line; and for 1 bar this is a thicker line.

180313 ran for 310 hours (12.9 days). Please note the change in x axis for this experiment's graph in Figure 1 to 400 hours. The graph shows red and blue lines clearly separated, with main pH difference resulting from starter pH rather than dissolved CO_2 levels. Similarly to 180123, there appears to be a lag in the first 24 hours before pH begins to climb; this is shared by all 180313 sub-experiments. Unlike 180123, experiments begun at pH 4 do not climb as high in pH for 180313, instead keeping consistently ~0.8-1.2 pH above pH 2 experiments and straddling either side of pH 6. For 180123, pH 4 experiments reached pHs of 7 and higher, which is not observed in 180313. All experiments continue to rise in pH until the experiments' termination, with a possible levelling off after 12 days in.

2.1.5. 180406

Experiment 180406 is a direct repeat of 180313, as this was the first time CO_2 had been used in an experiment, but 180406 was left to run for 407 hours (17 days). The two experiments show excellent similarity, as seen in Figure 1, though experiments pH 4 0.5 and 1.0 notably climb faster than previously observed, jumping from pH 4 to ~5.5 within 24 hours. A lag for pH 2 0.5 occurs that is not observed in 180313. There is also a slight decoupling of pH 4 1.0 from the other pH 4 experiments: after ~110 hours, pH 4 1.0 rises less-steeply in pH and appears to level off, as

all sub-experiments do, by the experiment's termination 0.5 pH lower than the other pH sub-experiments.

2.1.6. 180612

Up until 180612, all experiments were run with pure fayalite (Fe_2SiO_4). 180612 used half fayalite, half forsterite (Mg_2SiO_4) and lasted for 356 hours (14.8 days). Many of the sub-experiments in 180612 behaved strangely compared to previous experiments. Most strikingly, pH 2 1.0 did not rise in pH but dropped immediately to 1.1 and continued to fall over the experiment's duration. This is both at odds with all other observed experiments set up with these conditions, and also with the kinetically-predicted experimental pathway, whereby ions released into low pH solutions react with H^+ ions to relatively enrich a solution with OH^-, therefore increasing pH.

Other sub-experiments also differed from the expected norm of its predecessors. pH 4 0.1 was very unstable, with pH fluctuating by ~1.3 pH with every other reading. Sub-Experiment pH 4 0.5 behaved erratically for the first 40 hours, dropping to pH 2.9 before climbing to 5.4, where it followed the same pH trend as pH 4 1.0 for the remainder of the experiment. pH 4 0.5 and 1.0 both show similar trends to previous experiments. pH 2 0.5's pH climbs steadily along this same trend but remaining consistently ~3.5 pH lower, but pH 2 0.1 erratically jumps to a high pH within the first 24 hours, following a trend broadly similar to those of previous experiments.

To understand whether the experiment's differing results originated from the addition of forsterite, or whether an unknown factor was at hand, the experiment was repeated, as will now be described.

2.1.7. 180628

Experiment 180628 was the first to run for 60 days, which later all experiments adopted. The decision to continue it beyond the duration of 180612's length was as a direct result of 180628 not following the unusual pattern of 180612 but instead better emulating the trends of prior experiments. Keen to see whether the steady upward trend in pH would continue when left for

longer than two weeks, 180628 was sampled intermittently over a period of 1,459 hours (60.8 days).

All sub-experiments display an upward trend in pH; for all except pH 2 0.5, this trend increases rapidly after the first 24 hours, as seen in previous experiments. There are several notably anomalous datapoints that deviate from this trend: a spike from pH 4.8 to 6.8 for 2 1.0; a decline from 5.7 to 4.2 for 2 0.1; and, most notably of all, a drop from 7.4 to 3.1 for 4 1.0. This last point is important to understand because it could be an anomalous datapoint or represent the start of a new trend that could not be observed due to the termination of the experiment. For this reason, experiments were later set up that lasted for 80 days, and the drop in pH at 60 days was not observed again — most likely this was an anomaly.

Despite these specifics, the six sub-experiments follow the trend of those previously: a sharp rise in pH over the first ~48 hours, before steadily rising and continuing to rise over the course of the experiment. Sub-experiments begun at pH 2 and 4 are distinctly separated, as has been observed in previous experiments such as 180313 and 180406, though the pH gap between them is slightly larger at 0.5-1, rather than ~0.5 for 180313 and 180406. This experiment strongly suggested that the results of 180612 were anomalous and did not represent the typical run of a forsterite-bearing experiment. To be sure, however, a repeat of 180628 was later conducted (181029 Fo). A repeat of 180612 in length was also held, to ascertain that the faster removal of solution samples in 180612 was not responsible for the differing trends between it and 180628. The results of this experiment, 180829, will now be discussed.

2.1.8. 180829

This experiment ran for 282 hours (11.8 days) and was a direct repeat of 180612. It ran with fayalite and forsterite. While there is a clearly anomalous datapoint at 41 hours when 4 1.0 drops from 4.9 to 2.5 before climbing to 5.6, the trend for all six sub-experiments is the same gentle rise in pH after an initial spike around 48 hours in. Experiments begun at pH 2 or 4 again

show a distinct difference in pH, and for most of the experiment appear as near-parallel lines, though with some erratic pH jumps for 2 0.1.

This again suggests that the results of 180612 were anomalous and do not reflect the standard reaction path for experiments of fayalite and forsterite substrates.

2.1.9. 181004

Due to the extremely small amounts of fluids available for sampling during these low water/rock ratio experiments, pH was measured for all samples at their beginning, and only for experiments containing 20 mL (water/rock ratio of 1:10). This is because the 2 mL solution added to 2 g of fayalite for the low water/rock ratio experiments (1:1) combined with the fayalite to form a kind of slurry.

Table 5 displays the pH recorded for 181004. While little may be inferred from this beyond speculation, the final pH measurements for 2 1:10 and 4 1:10 are consistent with final pH measurements taken from regular, non-low water/rock ratio experiments. Lowering the water/rock ratio does not appear to have a significant effect on pH change over time in these experiments.

2.1.10 181029 Fa

This experiment was the first of ones run for 2000 hours (~80 days), which were designed to see whether the gradual upward trend observed to the end of 1500-day experiments continued. 181029 Fa was run simultaneously with 181029 Fo, with both experiments sampled within hours and sharing the same orbital shaker. 1801029 Fa is the pure fayalite (hence Fa) equivalent of 180628, but run for longer, while the Fo equivalent is designed as a repeat for 180628, only run for slightly longer. Running repeated experiments for longer also has the possibility of determining the effect (if any) of removing solution samples on the reaction itself.

181029 Fa does not behave in line with previous experiments. Like the pH 2 0.1 sub-experiment of 180612, this sub-experiment also remains at extremely low pH throughout the duration of the experiment, reaching a high of 2.47 at 190 hours in (~8 days), and a low of 2.26 at

1,920 hours in (80 days). While not as low as the experiment within 180612, nonetheless 2 0.1 behaves anomalously when all other experiments with these conditions (excepting its equivalent in 180612) show a rise of ~3-4 pH.

The other five sub-experiments in 181029 Fa are unstable, with pH fluctuations between 4-7, with the initial starter pH having apparently little effect on these trends. Unlike 180628, where experiments begun at pH 2 and 4 keep separate by ~1-2 pH, there is no such distinction in 181029 Fa.

Another anomalous point shared by both the 181029 experiments is a spike at 835 hours in (~35 days). For 1801029 Fa 2 0.1 and 2 0.5 this is an increase of 1.78 and 1.08 pH respectively, while for 4 0.5 it is a decrease of 1.67. The fact that this anomaly is shared by 181029 Fo at the same time shows that this was likely due to a sampling error on the day. Possibly the pH probe had not been thoroughly cleaned; or the solution sample sizes were too small for the probe to stabilise; perhaps the KCl solution the probe is stored in was running low, and solid K crystals contaminated the probe for these experiments.

The overall trend of the 181029 Fa experiment also does not agree with those previously. While difficult to tell because each datapoint varies so greatly even within sub-experiments, the overall trend does not seem to climb gradually upwards in pH as it has previously. Given these overall anomalous results, both 181029 Fa and Fo were repeated as 190423 Fa and 190423 Fo subsequently.

2.1.11. 181029 Fo

This experiment is identical in length, set-up, and sampling times to 181029 Fa, only 50:50 fayalite and forsterite was used. This experiment serves as a longer repeat of 180628, and was designed to be a means of testing the reliability and repeatability of this experiment, since its results proved to be very important in drawing this section's conclusions.

Unlike in 181029 Fa, sub-experiment 2 1.0 behaved as expected in 181029 Fo, climbing rapidly by 3.258 pH to reach 5.304 within the first 93 hours (the earliest sampling time) before

stabilising, fluctuating only by 0.489 pH until the experiment's termination. This is a trend followed closely by all other sub-experiments: excepting the anomalous dip in pH at ~912 hours in, which was also shared by 181029 Fa and ascribed to a sampling error, the stability of the pH trend across all sub-experiments is remarkably uniform. Interestingly, the gradual pH rise reported in experiments 190313, 180406, 180628, and 180829 is not observed. Given the highly anomalous twin experiment 181029 Fa, this lack of rise in 181029 Fo was deemed worthy of further investigation as well, which is why experiment 190423 Fo was created as an identical repeat of 181029 Fo.

2.1.12. 191205

As with the low water/rock ratio experiment 181004, pH could only be measured for high (1:10) w/r ratio sub-experiments. The results of this are presented in Table 6. What is very interesting is how pH for 2 1:10 is significantly lower than for its equivalent in 181004: 5.385, 0.97 pH in difference. Yet, for 4 1:10, the pH at the end of the experiment yields the highest value yet climbed to in a CO_2-bearing experiment, of 7.915. This experiment used 50:50 Fo and Fa, rather than pure Fa in 181004.

2.1.13. 190121

This experiment was the first to employ high ratios of Fo to Fa, and uses 90:10, meaning this experiment was dominated by forsterite. Over a running time of 1,941 hours (~81 days), the experiment performed in line with previous sets, particularly showing resemblance to the neatly-separated pH 2 and 4 lines of 180313. What is interesting, however, is that the upward trend in pH across all sub-experiments is consistently slightly higher for 190121. As with previous experiments, the same sharper rise within the first 48 hours is observed, but pH continues to climb at a steeper rate than previously observed in any experiments, and by the experiment's termination shows no sign of levelling off.

2.1.14. 190423 Fa

The experiment 180423 Fa is a repeat of 181029 Fa: pure fayalite-bearing, left to run for 85 days. Unlike 181029 Fa, pH behaved akin to previous pure-Fa experiments including 180313 and 180406: sub-experiments begun at pHs 2 and 4 remain distinct in their pH pathways, with pH 4 sub-experiments remaining consistently ~0.5-1 pH higher than their pH 2 counterparts. Also like previous pure-Fa experiments, the pH trends within starter pH sub-experiments are moderately affected by levels of dissolved CO_2, with only minor increases of ~0.1 for sub-experiments with greater dissolved levels of CO_2. However, whether 0.1, 0.5, or 1.0 bars within pH 2 or 4, the trends for pH do intersect and intertwine across the experiment's course, though the aforementioned distinction between pH 2 and 4 sub-experiments remains withheld.

There is an anomalous drop in pH for 2 1.0 at 1578 hours (~65 days) in, from pH 6.531 to 4.358, but this is recovered by the next sampling interval, returning to follow the same gradual upward trend at 6.979. A slight decline for 4 0.1 also occurs at this time; it is possible the discrepancy can be explained by an incorrectly-calibrated pH probe, or perhaps the probe was poorly cleaned for 2 1.0, and this contamination was carried to 4 0.1 (the sub-experiment subsequently sampled after 2 1.0).

The overall pH increases over the course of all sub-experiments are some of the largest seen in this category of experiments. For 2 0.1, 0.5, and 1.0, the final pH measurements are 6.731, 6.875, and 7.015; for 4 0.1, 0.5, and 1.0, these are 7.555, 7.498, and 7.665. Figure 1 plots final pH against time to facilitate this comparison, and is discussed in more detail in the Conclusions section of the pH discussion.

2.1.15. 190423 Fo

The pH trend for 190423 Fo follows that, broadly, of its Fa counterpart. After an immediate climb over the first 237 hours (10 days) to pHs of 5.6-58 for pH 2 sub-experiments (excepting 2 0.1, which climbed until 762 hours in (31 days) before stabilising) and pHs 6.3-6.8 for pH 4, the sub-experiments' pH increase becomes far smaller between sampling intervals. From

237 hours until the experiment's termination at 2061 hours (85 days), pH only climbs at most 1.786 for 4 1.0; most change occurs within those first 237 hours and likely within a far narrower window; such a climb has been observed in shorter-lived, pure-Fa experiments such as 180829, where pH jumped then broadly stabilised by 41 hours in.

pH climbs to the highest levels observed for all Fa- or Fa/Fo-bearing experiments: for 4 1.0, this is 8.192. As pH has shown for all experiments to gradually continue to increase right up to termination, the length for which this experiment was run — over 85 days — may have contributed to this measurement.

2.1.16. pH Conclusions

From this section's extensive description and discussion of each experiment's pH trends, several overarching conclusions may be drawn. These are the following observations:

- Sub-experiments begun at pH 2 and 4 commonly remain distinct, almost parallel, in their pH pathways, with pH 4 sub-experiments consistently reaching between 0.5-2 pH higher than their pH 2 counterparts
- There is a pH spike at the very beginning of the experiment, normally a jump of around pH 2, within the first ~250 hours but often far faster where sampling rates are more rapid
- pH continues to climb more gradually after this spike across the remaining course of the experiment, frequently between 1-2 pH over ~1500 hours (62 days)
- There are no routine causes of deviation from this trend: any sudden drops or rises in pH are isolated to particular samples from particular sub-experiments, which are neither repeated nor continued, suggesting these discrepancies are due to some sampling irregularity that does not reflect the experiment itself
- pH stabilises on average between 5-7 for pH 2 sub-experiments and 6-8 for pH 4 sub-experiments
- The rate of change between pH 2 and 4 sub-experiments is not significantly different

- Experiments 180612 and 181029 Fa behave anomalously in that the pH for sub-experiments 2 1.0, and in the case of 180612 also 2 0.5, remains at or falls to extremely low pH that is not kinetically predicted for such experiments, and this is a pathway that is not repeated in other, similarly set-up experiments
- 181029 Fo also behaved anomalously in that pH, as for 181029 Fa, plateaued for all sub-experiments after an initial rise, which does not reflect the gradual rise trend observed in all other sets of experiments
- pH climbed significantly higher without the presence of CO_2 in experiment 180123, without the acidic effect of carbonic acid hindering pH rise. However, where CO2 is introduced, the higher the levels of CO_2, the higher pH climbs

The diagram in Figure 2 plots the final pH of each sub-experiment (excluding non-CO_2-bearing experiments) against the time of sampling (i.e. the end of the experiment). Different symbols correspond to different experiments (see the legend), while the darker the blue or red colour, the higher the levels of dissolved CO_2 (again see the legend). While there is a distinct dichotomy in experiment length, with categories of ~200-600 and ~1400-2000 hours, there is a slight but notable increase in pH with experimental length. This is a key conclusion to be drawn from this section: that pH gradually increases with time across CO_2-bearing experiments. The diagram also demonstrates how pH climbs higher for experiments begun at higher initial pH: the topmost datapoints are generally blue for pH 4, whereas lower datapoints tend to be red for pH 2 experiments. Anomalous datapoints previously discussed can be clearly seen: the pH 2 1.0 experiments of 180612 and 181029 Fa, and the unusual and unrepeated drop in pH for 4 1.0 of 180628 that prompted the repeat of this experiment in 181029 Fo and 190423 Fo. Another intriguing observation from Figure 1 is how Fo-bearing experiments tend to reach higher pH. This includes both the open and coloured downward-pointing triangles (181029 Fo and 190423 Fo respectively), the coloured diamonds (181205), and coloured circles (190121; the open diamonds representing 180612 will not be discussed here).

These conclusions are used in Chapter 3 to understand the chemical pathways followed during these experiments and the implications of these for the chemistry upon the surface of Mars.

2.2. Eh

Eh is a measure of the oxidation-reduction potential (ORP) of a solution, and is measured in millivolts (mV). The higher a measurement, the more oxidising a solution is, with measurements typically ranging between 600 to −600 mV.

Eh was measured at intervals over the course of all experiments to monitor the availability of Fe^{2+} and/or Fe^{3+} ions in solution, which is important for understanding the switch in iron chemistry from ferrous to ferric. This in turn affects which minerals are capable of forming. Critically, a switch to Eh dominated by Fe^{3+} ions could indicate an unnoticed oxygen leak into the experiments, which would void the experiment.

Eh from every experiment conducted in the Fa-Fo remit of this thesis, from the first successfully completed one, 180123, to the final one, 190423 Fo, are visualised in Figure 3. Low rock:water ratio experiments 181004 and 181205 are not shown because, owing to the small amounts of available fluids, Eh was measured only twice during experimentation. These measurements are recorded in tables associated with the experiments. Lines are shown in red for experiments begun at pH 2; blue for pH 4, and, for 180123, 180203, and 180310 where this was a parameter, green for pH 6. In 180123, 180203, and 180310 where no CO_2 was added and rock:water ratio was the parameter explored alongside pH, these experiments show solid lines for high rock:water ratio and dashed for low. For all other experiments, the weight of the line denotes CO_2 pressure in bars. For the thickest line, this is 1 bar; for the lighter line, this is 0.5 bar; for the dashed line, this is 0.1 bar.

Please note the change in x-axis length. This varies from 12 hours to 2000 hours (80 days). The y-axis remains the same for all graphs at between 0 and 10 pH. The nomenclature used for describing each sub-experiment will use the starter pH and the additional defining parameter, e.g.,

an experiment begun at pH 2 at a low water-rock (w/r) ratio will be referred to as low pH 2, while an experiment begun at pH 4 with 0.1 bars of CO_2 will be referred to as pH 4 0.1, etc.

2.2.1. 180123

Experiments begun at pH 2 jump within the first hour from −65.5 to 552 mV before rapidly falling, but for all other experiments they begin at low Eh and remain there for the duration of the experiment. All experiments appear to stabilise in Eh after ~47 hours in, and do not significantly deviate from between ~−200 to ~−400. This suggests that all change occurs within the first ~two days of the experiment before a stability is reached.

2.2.2. 180203

Fascinatingly, this experiment, which is a repeat of 180123 but sampled on the hour for the first 10 hours, shows exactly the patterns described above but contracted within the experiment's 10 hour run time.

For instance, the Eh of 2 high w/r remains high throughout the experiment's duration, agreeing with 180123, where it drops only after 24 hours in. 2 low w/r declines in Eh gradually over the experiment, in line with the drop observed from 6 to 24 hours in 180123. The remaining experiments at pH 4 and 6 closely follow the trends of 180123, beginning within −200 to −250 mV and gradually declining, as occurs within the first 24 hours of 180123. This is excellent repeatability between these experiments, and agrees with the matching pH data for the two experiments, which also showed very close agreement.

2.2.3. 180310

This experiment was not analysed further.

2.2.4. 180313

The Eh trend of 180313, and indeed all those subsequently, does not follow that of the three earliest experiments. These three did not contain dissolved CO_2, whereas all subsequently did. Clearly this has a measurable affect on the trend of Eh across an experiment, which will now be discussed.

Broadly, three steps in Eh change appear to occur for 180313. The first occurs 22 hours in, when all sub-experiments show a rise in Eh of ~100-120 mV. This is followed by a sharp decline at the next sampling point, where all sub-experiments excepting 2 0.5 drop to almost identical points (~150). It should be noted that the sub-experiment 2 0.1 has missing data, and so only appears on the graph two data points in. Between 22 and 189 hours in, a period of stability is observed where experiments fluctuate either side of 200 mV: 2 0.5 fluctuates particularly during this period, while its equivalent at pH 4 deviates from this trend by steadily dropping in mV from 140 hours; perhaps under these conditions, the 0.5 bar CO_2 caused these sub-experiments to oscillate either side of some stability boundary; observing whether subsequent experiments show similar trends will be interesting.

At ~200 hours in, this period of stability ends and there is another drop in mV experienced by all six experiments, a fall of ~400-500 mV to ~−300. From here the mV appears to stabilise again, but this experiment only ran for 310 hours; later experiments that ran for longer will tell whether this trend continued.

It is interesting that these steps in mV drops do not have corresponding activity within pH measurements taken at the same time. While the rise ~24 hours in could be connected to the rise in pH at the same time, the gradual rise in pH following this spike in activity shows no disturbance that could reflect what has happened with the Eh. As no minerals were revealed to have grown from the pure fayalite used, when analysed with solid sample techniques, the loss of certain elements from solution can also not explain this Eh change. Further experimental analysis may shed light on this issue.

2.2.5. 180406

Immediately looking at the graph of Eh for 180406, it is clear the trends are less ordered and defined than for 180313. However, the same three-step trend does broadly appear: there is a sharp rise 24 hours in (in this case for pH 2 experiments; it is a decline for pH 4 of almost the same magnitude); there is a period of relative stability between 47 and 167 hours in, albeit much

less confined than for 180313 and with clearly-lower mV values for pH 4 experiments. pH 4 experiments also drop to the third level slightly faster than pH 2 ones. Lastly, the drop to ~−200 to 300 is observed for all sub-experiments excepting 2 0.1 and 0.5, and 2 1.0 stabilises at a notably higher Eh than the pH 4 sub-experiments: at −212 mV, 80 mV above its equivalent at pH 4.

The Eh of 180406 reaches greater extremes at both ends than its twin, 180313, of which it was a direct repeat. The highest mV reached is from 2 0.5 at 24.5 hours in, of 583.2 mV, while for 180313 this value is 418.1 with sub-experiment 2 1.0 at roughly the same hours in. The causes of these discrepancies compared to 180313 are not immediately apparent: neither experiments produced new solid material that could alter solution chemistry. pH differences for 180406 are slightly wider compared to those of 180313, where pH is very closely confined between experiments. These slight pH deviations could be responsible for the more-wildly oscillating pHs recorded during 180406.

2.2.6. 180612

From the analysis of pH change during 180612, it has been established that 180612 did not follow the conventional pathway as expected of such an experiment. This is clearly reflected in Eh variation over the course of the experiment.

Most notably different from previous experiments is the rise and stabilisation of 2 1.0 . Where all other experiments follow a rise followed by a drop, or sometimes a steady drop, with 180612 this jumps from 250 to 526 mV within the first 18 hours, and from there remains stable until the experiment's termination. Similarly, 2 0.5 followed a similar trend to its 1.0 bar counterpart, but instead of falling into pH ~1, only climbed extremely slowly over the course of the experiment. This sub-experiment shares the same Eh measurements as 2 1.0 after 40 hours, suggesting that highly acidic pH is a cause for elevated Eh. This is very interesting because the corresponding pH for experiment 2 1.0 records a drop in pH at 18 hours in before remaining almost level until the experiment's termination, mirroring the anomalous Eh pathway. This shows that pH and Eh are intimately linked and that each reflects the change of the other.

Sub-experiment 2 0.1 also remains at elevated Eh but less significantly so than the other pH 2 experiments. It reaches at maximum 427 mV and possibly stabilises by the experiment's end.

The pH 4 experiments, in contrast, remain closely linked throughout the duration of the experiment. Despite initial deviation within the first 89 hours, after this the three sub-experiments almost lie atop each other's Eh measurements until 208 hours, where they divide to almost equal increments apart by order of CO2 level.

The three-step variation observed in 180313 and 180406 is not observed, but as this experiment was deemed anomalous for several reasons, its further peculiarities will not be discussed.

2.2.7. 180628

In 180628, an overall decrease in Eh through time before levelling off is observed, with several key anomalies. The first is for sub-experiment 4 1.0. This experiment behaves in line with its fellow pH 4 experiments until the last datapoint, where Eh shoots up to 344 mV. Intriguingly, the pH for this sub-experiment showed a draconian drop from 7.4 to 3.1 pH. Previous experiments have already established the link between Eh and pH, which explains why both pH and Eh datapoint mirror each other in their anomalousness for 4 1.0. Where this dual anomaly is particularly interesting is that it discounts the idea of the pH measurement alone being anomalous. During its previous discussion, a possible explanation for this value was posited to be experimental error: a contaminated pH probe, an incorrect measurement, etc. Yet with an equally anomalous datapoint for Eh, and with the well-established link between Eh and pH, the pH measurement at 1461 hours for 4 1.0 appears to be the true value.

Additional comments to make about this graph are how distinct the pH 2 and 4 experiments are. While the two are distinct from the experiment's beginning, it is only after 185 hours that the two truly diverge, with an Eh difference of 477.2 mV at maximum in the case of 4 0.1. Interestingly, for pH 4 experiments Eh rises again, which does not correlate with any corresponding variations in pH as the graphs in Figure 1 are smooth lines. No minerals were found

to have precipitated from these solutions, either, so variation in Eh does not correspond with the removal of key species from solution.

Overall, the Eh trends for 180628 suggest a gradual decline, one that is steeper for pH 4 experiments and that responds to extremely anomalously acidic solutions. Interestingly, the drop in Eh at 306 hours in displayed most acutely in the pH 4 experiments mirrors the drop also experienced around this time in experiments 180313, 180406, and even the non-anomalous pH 4 sub-experiments of 180612.

2.2.8. 180829

As with all CO_2-bearing experiments, the exception being the anomalous 180612, the Eh measurements for 180829 begin high; in all cases but for 2 0.1 and 1.0, this is almost at 600 mV. While all six sub-experiments show a general decline in Eh throughout the experiment, it is remarkable how similar their trends are. pH 4 experiments generally trend lower than their pH 2 counterparts, though pH 2 0.5 notably intersects these lines at 18.6 and 208.1 hours in.

It is interesting that the step-like drop observed ~200 hours in for 180313, 180406, the pH 4 sub-experiments of 180612, and 180628 is not observed within 180829. There are no anomalous pH trends, though perhaps it could be argued that the initial rise in pH commonly observed in other experiments is slightly shallower in 180829: by 180829's termination, the maximum pH of all sub-experiments reached is 6.8 whereas it is 7.4 for 180628. Given the link between pH and Eh already established by previous experiments' analyses, this is one explanation for the more gentle Eh trends than previously observed.

A familiar trend is emerging amongst the experiments at this point: elevated initial Eh, followed by a decline over the experiment's duration.

2.2.9. 181004

As for the discussion of low water/rock ratio experiments in the previous section on pH, Eh data was only extracted from sub-experiments within 181004 bearing 20 mL of fluid at a w/r ratio of 1:10. The results, where extracted, are displayed in Table 7.

Following trends of previous experiments, the final Eh between pH 2 and 4 experiments is distinct and pH 2 is elevated, in this case by a difference of exactly 68 mV. Neither Eh measurement is extreme, but falls well within documented final Eh measurements, though it is interesting that 181205's final Eh measurements are somewhat higher than previously documented for typical purely Fa-bearing experiments: no comparison may be made to the anomalous 181029 Fa, but 180313 and 180406 both on average show Eh as falling into the −200 to −400 range, certainly for pH 4 experiments.

2.2.10. 181029 Fa

Experiment 181029 Fa showed the same anomaly as 180612 in that the pH of sub-experiment 2 1.0 remained low throughout the duration of the experiment. The pH for the rest of the sub-experiments remained disordered and irregular, with no distinction between pH 2 and 4 experiments. Earlier it was discussed at length that this experiment was likely to be anomalous and not reflect the typical reaction pathway of fayalite-bearing solutions for extended periods.

The Eh trends reflect this. For 2 1.0, Eh remains anomalously high; there is by now a clear correlation between high Eh and low pH, and vice versa. For the remaining experiments, Eh is as unstable as their corresponding pH measurements and is highly unstable, fluctuating from 112.1 to at maximum 439.2 mV for sub-experiment 4 1.0. There is no distinction between pH 2 and 4 experiments, which is a trend observed even in the anomalous 180612, and Eh even begins to climb within the final half of the experiment, which does not agree with any previous experiment.

Overall the trends for Eh observed in 181029 Fa agree with the decision reached by its pH results: that this experiment is anomalous and should be repeated to fully understand the experimental pathway under these conditions.

2.2.11. 181029 Fo

While the pH results of 181029 Fo showed the unusual trend of stabilising within the first ~94 hours (~4 days) and not rising further, the experiment did not appear to behave as anomalously as its Fa (pure fayalite) counterpart, with pH 2 and 4 experiments remaining distinctly

separated in pH measurements, excepting an established sampling anomaly ~933 hours (~39 days) in.

The Eh measurements reflect this. They follow previous experiments' results in several ways: they all begin at high mV, between 479 and 329; they all show a steep drop in mV within the first ~933 hours; and pH 2 and 4 experiments remain distinctly separated in mV. Where they act unusually is that, instead of contouring to fall in mV, the Eh measurements of 181029 Fo consistently rise after their initial drop. At closer look, it is possible that this is a trend that is broadly consistent with the Eh measurements of 180628 and 180829, both also Fa-Fo-bearing experiments, which both also show relatively little decline in Eh over the latter two-thirds of the experiment. The slight bow of Eh measurements between 190 and 836 hours in for sub-experiments at pH 4 imitates that which occurs for pH 4 experiments in 180628, between 185 to 767 hours, but to a lesser magnitude. Eh for 180628 and 180829, the only previous non-anomalous Fo-bearing experiments, is maintained for most of the experiment within the same range — ~500 to 0 mV — as 181029 Fo. Thus, the Eh for 181029 Fo may reflect wider trends in Fo-bearing experiments: the lesser ability of forsterite to modulate the influx of reducing fluids during its dissolution across the course of the experiment. This is a striking departure from the pure-fayalite experiments of 180313 and 180406 (discounting 181029 Fa for its anomalousness), where Eh commonly falls below −300 mV.

2.2.12. 181205

As with pH for low rock:water ratio experiments, and as discussed earlier in this section for 181004, Table 8 displays the Eh measurements taken where they were able. These Eh measurements taken at the end of sub-experiments 2 1:10 and 4 1:10 broadly align with the known patterns of previous experiments. The Eh for pH 4 settles distinctly lower than for pH 2, and both fall within the modest zone of between 150 to −100 mV, where all the final Eh measurements of the likewise-Fo-bearing 180628 all within (excepting 180628 4 1.0, which, while not erroneous as discussed, is certainly anomalous).

2.2.13. 190121

190121 was the first time a high forsterite to fayalite ratio was employed, and its Eh graph reflects previous Fo-bearing experiments for several reasons: firstly, pH 2 and 4 experiments are mostly distinctly separated, though 4 0.1 and 2 0.1 in particular overlap with experiments of differing start pH. Secondly, the Eh trend overall for all sub-experiments is one of gradual decline but not at so steep an incline as for pure-Fa-bearing experiments. And thirdly, several sub-experiments show a slight increase in Eh similarly to 181029 Fo: 2 0.1 at 720 hours from 45.9 to 308.9; and 2 0.5 from 131.4 to 444.3 mV at 1580 hours in.

2.2.14. 190423 Fa

For experiment 190423 Fa, an overall trend of decline from high mV to low is observed across the experiment's 2060 hours run-time. For pH 4 sub-experiments, the decline begins earlier and is steeper, with Eh falling at maximum from 463.9 to −44.4 mV within the first 237 hours, while the maximum decline in this time amongst the pH 2 sub-experiments is from 486.4 to 291.1 mV for 2 1.0.

Much like a reverse of its pH trend, Eh roughly levels off after 762 hours (32 days), fluctuating up and down for all sub-experiments until the experiment's termination, but remaining on average around the −100 mV mark for pH 4 and 0 mV for pH 2 sub-experiments. While less clear-cut than previous pure-Fa experiments such as 180313, sub-experiments begun at pH 2 in general display higher levels of Eh than for those of pH 4, although this is more obvious with the neat parallel trends observed in 180829, 181029 Fo, and to an extent 190423 Fo. It is possible the addition of forsterite has some stabilising effect on the fluctuation of Eh, as these Fo-bearing experiments seem less prone to the rapid inclines and declines in E between samples as seen in 180313, 180406, and 190423 Fa (the anomalous 180612 and 181029 Fa will not be discussed here).

The Eh of the experiments reach within a region reflected in previous Fa-bearing experiments, between −200 and 0 mV; a drop on average of ~400 mV over the course of the experiment.

2.2.15. 190423 Fo

From beginning at high and dispersed mVs of between 486.4-550.7 for pH 2 sub-experiments and 271.5-463.9 for pH 4, by 190423 Fo's termination after 2060 hours, the Eh trends for all six sub-experiments have strikingly converged to within 27.3 mV of each other: between −96.6 mV for 2 1.0 and −123.9 mV for 4 0.5, a trend that has not been observed in any previous experiments. This may reflect the closeness of the final pH values across all sub-experiments, although the still-maintained distinction between pH 2 and 4 sub-experiments remains apparent, and this closeness in pH is also observed for 190423 Fa, where the convergence in Eh is not.

The steady overall decline, in contrast to the sudden drop followed by stability experienced by Fa-bearing experiments such as 180313, 180406, and 190423 Fa, agrees with the Eh trends of Fo-bearing experiments. 180628 (aside from its pH 4 sub-experiments), 180829 and 190121 all display the steady decline shown in 190423 Fo (due to loss of significant amounts of fluid in 181029 Fo, and the resulting unusual pH trend, this experiment will not be discussed).

The low Eh recorded appears to trend with this experiment's increase in pH: as one declines, the other increases. The continuing decline of Eh here suggests the experiment has yet to reach stability, and that reaction was still occurring by the experiment's termination at a slow and steady rate.

2.2.16. Eh conclusions

The following conclusions may be drawn from this discussion and description of Eh results across fayalite- and fayalite-forsterite-bearing experiments:

- Except in anomalous sub-experiments where pH dropped or remained low, below pH 2, Eh begins high, generally ~500-300 mV, and drops over the course of the experiment to ~100-−200 mV
- For forsteritic experiments, Eh between pH 2 and pH 4 sub-experiments remains reasonably distinct, with pH 4 sub-experiments showing generally lower Eh than their pH 2 equivalents by a difference of up to ~100 mV

- Eh generally reflects an inverse pattern of pH: where pH rises, Eh tends to fall, and where pH fluctuates, so does Eh
- At its lowest, Eh reaches −329.3 mV for 4 0.1 in 180406
- At its highest, Eh reaches 583.2 mV for 2 0.5, also in 180406

Overall, the trends in Eh translate to a gradual onset of more reducing conditions, consistent with the rise in pH from the conversion of dissolved CO_2(aq) to carbonic acid, and subsequently to HCO_3^- and then to CO_3^{2-}. Understanding the oxidation-reduction potential of the solutions during experimentation will be of importance in understanding the ability of the solutions to seed Fe(II)-carbonates, and how such solute conditions affect reactions upon the solids contained within them.

2.3. pH and Eh comparison

In Figure 4, pH is plotted against Eh (in V) to assess the relationship, if any, between these two critical parameters that were constantly monitored throughout experimental duration. At once a relationship is clear: an overarching trend follows that as pH increases, Eh decreases. This trend follows a roughly straight line, plotted as two ellipses in Figure 4: one for the main trend, and the smaller for a secondary cluster outside of this that encompasses most of experiments 180313, all of 180406, and 4 1.0 from 180612. Within both these ellipses there is a reasonable distinction between experiments begun at pH 2 (in red) and those at pH 4 (blue), whereby pH 4 experiments in blue trend towards high pH and show a smaller spread of Eh measurements: between 344.4 and −328.2 mV, a difference of 672.6, whereas for pH 2 experiments the maximum is 543.8 mV and the minimum −254.6, a difference of 798.4 mV. As such the upper end of the ellipse is dominated by red, for pH 2 experiments, and its lower end is mostly blue for pH 4.

For the smaller ellipse, it is interesting that the first two CO_2-bearing experiments to be conducted — 180313 and 180406 make up this island. The same experimental set-up was used for these two as for all the others (excepting the anomalous 181029 Fa and Fo pair), and the

experiments' duration were within the normal range for short-term (~200-500 hour) set-ups. As pH lies in the average range that would otherwise fall well within the main ellipse, it is possible that for these earliest experiments the Eh probe was incorrectly calibrated, but as the same bottle of ZoBell's Solution was used for all experiments, and the probes are calibrated prior to each sampling — which may occur at intervals of days or weeks — the recurring offset from the main trend seems too consistent for such an explanation. Further thought is given to this matte ring the following paragraphs.

Several individual anomalous datapoints do not fall into the major or minor ellipses, and unlike those within the minor ellipse, these tend to be from a variety of experiments and sub-experiments within them. The top-leftmost datapoint belongs to 180612 2 1.0, which was an anomalous sub-experiment that dropped to as low as pH 1.014 in a pathway that did not follow the well-document pH rise for such experimental conditions. Other datapoint outside of the two ellipses include 2 0.5 and 4 0.5 from 180612, which also behaved unusually as discussed earlier, along with 2 1.0 from 181029 Fa (likewise an anomalous experiment that saw pH remain consistently low for 2 1.0), 4 1.0 from 180628 (where pH inexplicably plummeted from 7.429 to 3.145 after 1461 hours running), and 2 0.5 from 190121. This last one is a surprise: 190121 was an unusual experiment in being the first and only to employ a fayalite-forsterite ratio of 1:9, but the pH pathway as explored earlier behaves as expected — it is only for 2 0.5 and 2 1.0 at the last sampling point (1941 hours) that deviation from a typical Eh pathway occurs. A possible explanation for this is slow Eh stabilisation time: sometimes where too little fluid is drawn for a probe to make a confident measurement, Eh in particular is prone to stabilise over a time period of as much as 30 minutes or more. This is rare, and Eh usually does eventually stabilise, but in such cases such stability may be reached so slowly that an incorrect measurement may be recorded under belief that it is stable, only for Eh to continue to drop/rise were the probe to be left in solution for longer.

This could also be an explanation for why experiments 180313 and 180406 consistently display such distinctly low Eh measurements: as these were the first two CO_2-bearing experiments to be sampled, the person sampling would have been unaccustomed to such idiosyncrasies of the instruments used, and so would have been unaware that on occasion longer time is required for the probe to reach stability.

As for the datapoints within the major ellipsis itself, the top-leftmost are dominated by both up- and downward-pointing open triangles: those representing 181029 Fa and Fo respectively. These were known to produce anomalously acidic and oxidising solutions, which were not found to be reproducible when repeats of such starter conditions were run (e.g., 180628, 180829, 180423 Fa, 180423 Fo). The bottom-right of the ellipse, by contrast, is dominated by both up- and downward-pointing coloured triangles: those representing the direct repeats of the 181029 series, 180423 Fa and Fo. These two experiments ran in line with trends by this point anticipated for Fa and Fa-Fo-bearing experiments: a sharp rise in pH and sharp decrease in Eh over the first ~200 hours, followed by a steady pH rise and steady Eh decline over the remainder of the experiments. As the 190423 series were the longest experiments run in the fayalite-forsterite series discussed in this chapter, and as pH has been established to continually climb, and Eh continually fall, over an experiment's course, it is perhaps no surprise to find this bottom-leftmost segment of the ellipse dominated by these two experiments. In many ways the 190423 pair summarise the pH and Eh trends discussed in this chapter, exemplifying anomalous experiments and validating those of which 190423 repeat.

The pH-Eh graph of Figure 4 is therefore an excellent summary figure for this pH-Eh discussion, and is a good representation of the overall results discussed within this chapter.

3. Solution chemistry: ICP-OES

In this section, the changes in solution chemistry during experiments are closely examined and described visually in graphs with corresponding text to explain these changes. Solution chemistry was analysed via ICP-OES, and the change in saturation of the elements Fe, Si, and, where used, Mg in mmol/kg is here described.

Following discussion of the raw ICP-OES elemental data, corresponding mineralogical data is then discussed. This involves using the mmol/kg data for Fe, Si, and Mg, in conjunction with the corresponding pH measured for the sample, to produce a kinetically modelled prediction of the types and amounts of minerals that — kinetically — should be present. The process of creating these estimations uses the software Geochemist's Workbench and was outlined in the Methods chapter.

3.1. Iron

Fe was the most important element to measure in solution because all experiments contained Fe in the form of fayalite. An increase in Fe corresponds to the release of Fe into solution, which in these experiments originates from the dissolution of fayalite. The presence of Fe through this dissolution is vital if new minerals are to be formed, which was one of the primary objectives of this thesis: to observe the conditions under which siderite, iron carbonate, is commonly documented as forming. An increase in dissolved Fe, therefore, corresponds to the ability of a solution to produce new minerals. Its absence suggests the fayalite was unable to dissolve (for reasons that will be discussed when this instance arises), and that new minerals were not capable of forming.

In this section, the dissolved Fe trends for all fayalite- and, where applicable, forsterite-bearing experiments are displayed in the graphs of Figure 5. This is excepting the low water/rock ratio experiments of 181004 and 181205, where such minute levels of liquids were involved that

sampling was not possible. Results from the beginning and termination of their experiments are displayed within the tables Table 9 and Table 10.

For the graphs in Figure 5, please note the same y axis for all graphs from 0 to 50 mmol/kg, but the differing x axis to account for experiments conducted over lengths varying from 10 to 2000 hours. Following the symbology of the pH and Eh graphs, lines are shown in red for experiments begun at pH 2; blue for pH 4, and, for 180123 and 180203 where this was a parameter, green for pH 6. In 180123, 180203, and 180310 where no CO_2 was added and rock:water ratio was the parameter explored alongside pH, these experiments show solid lines for high rock:water ratio and dashed for low. For all other experiments, the weight of the line denotes CO_2 pressure in bars. For the thickest line, this is 1 bar; for the lighter line, this is 0.5 bar; for the dashed line, this is 0.1 bar.

The nomenclature used for describing each sub-experiment follows the previous section by using the starter pH and the additional defining parameter, e.g., an experiment begun at pH 2 at a low water-rock (w/r) ratio will be referred to as low pH 2, while an experiment begun at pH 4 with 0.1 bars of CO_2 will be referred to as pH 4 0.1, etc. Unless otherwise stated, all experiments were run with fayalite (Fe_2SiO_4).

As discussed earlier, experiment 180310 was not analysed via ICP-OES due to funding limitations.

3.1.1. 180123

The Fe released into solution during experiment 180123 follows a simple trend. For pH 2 sub-experiments, samples were first extracted at the experiment's beginning and thus display 0 mmol/kg Fe in solution, as do all sub-experiments, but this rapidly changes: within the first 6 hours, Fe begins to enter solution in both pH 2 sub-experiments at low and high w/r, of a faster rate for low at 9.87 mmol/kg for 6.7 hours in rather than 4.51 mmol/kg for high. Both level off to almost-identical values at ~10 mmol/kg, and remain stable throughout the course of the

experiment. For sub-experiments begun at pH 4 and 6, the amounts of dissolved Fe are below an order of magnitude smaller, and most probably represent background levels.

This is likely very strongly linked to pH. At acidic pH, minerals may more readily dissolve due to the higher concentrations of protons (H^+ ions) in solution, which more readily break down material and enable them to interact within solution. At lower pH, even to pH 4, this effect is here demonstrably reduced, and at pH 6 — almost neutral, almost pure water — this effect is negligent. It was due to this that experiments begun at pH 6 were discontinued when the parameter of CO_2 was introduced, as under standard conditions no measurable change could occur at this pH.

3.1.2. 180203

180203, the ten-hour repeat of 180123, mirrors the results of 180123 but in higher resolution. Again the sub-experiments begun at pH 4 and 6 show excruciatingly minute levels of are in solution, enough to be background levels; again sub-experiment pH w low w/r ratio releases Fe into solution faster than 2 high w/r, though both may be seen climbing. As Fe levels did not stabilise within 180123 until 24 hours in, this continued rise in Fe levels for both pH 2 experiments is expected and agrees with the strong correlation between pH and Eh between the two experiments. As with 180123, conclusions to be drawn from 180203 are that experiments run at pH 2 are sufficiently acidic to release Fe into solution, while those at pH 4 and higher are an order of magnitude less capable.

3.1.3. 180313

Experiment 180313 was the first to run with the presence of CO_2. CO_2 reacts when dissolved in water to form HCO_3^-, which from there may form carbonic acid (H_2CO_3), which is weakly dissociating. This may be one explanation for why sub-experiments run at pH 4 in 180313 do reveal detectable levels of dissolved Fe in solution when analysed. Corroborating this is how the more dissolved CO_2 within a pH 4 experiment, roughly higher the levels of dissolved Fe: for pH 4 0.1 at 309 hours in, this is 0.85 mmol/kg; for 0.5 it is 1.95 mmol/kg; and for 1.0 it is 1.75 mmol/kg. This pattern continues for pH 2 experiments, whereas for 180123 all three pH 2

experiments levelled off at ~1 mmol/kg: pH 2 0.1 climbs nearly parallel to its 0.5 and 1.0 bar counterparts, remaining ~3-4 mmol/kg lower and reaching at maximum 13.3 mmol/kg 287 hours in. pH 2 0.5 and 1.0 closely follow each other, excepting an anomaly for 0.5 at 44 hours in (which does not correlate with its corresponding pH or Eh measurements, so may be an analytical error).

It is interesting that for experiments containing 0.5 bar CO_2 and above, both at pH 2 and 4, little variation is observed in dissolved Fe between 0.5 and 1.0 bar, whereas for 0.1 bar dissolved Fe content is notably lower. This may be due to some threshold being crossed through release of carbonic acid that enables sufficient Fa dissolution, which is not crossed in the case of only 0.1 bar CO_2.

All six sub-experiments gradually rise in dissolved Fe levels over the course of the experiment, in line with rising pH as discussed earlier. This may be due to the increasing production of carbonic acid, which in turn enables the further dissolution of fayalite, which may react with available H^+ ions to reduce acidity, steadily increasing pH, as has been observed.

3.1.4. 180406

As this experiment is a direct repeat of 180406, the dissolved Fe content is anticipated to be very similar. Several broad trends may be immediately observed: the distinction between pH 2 and 4 experiments; the similar order of magnitude (pH 2 experiments stabilising ~ 13-14 mmol/kg, pH 4 ~1-4 mmol/kg). In detail, there are minor deviations from 180313, including the lack of obvious upward trend begun in the final hours of 180313.

3.1.5. 180612

In the first experiment run with Fo and Fa together there were several discrepancies in measured pH and Eh that, in comparison with more recent experiments, strongly suggested this experiment was anomalous. A description of its elemental solution analysis will be given, but little weight offered to its implications, as this experiment is not reflective of overall trends for Fo-bearing experiments.

Dissolved Fe levels are far higher for pH 2 sub-experiments in 180612 than for previous experiments, and like with previous experiments there is a distinction between 2 0.1, and 2 0.5 and 1.0, the latter two which closely mirror one another.

A missing datapoint for 2 0.1 is due to a loss of data pertaining to the relative ratio of sample weight per storage acid weight during shipment for ICP-OES analysis (whereby ~1.5 mL of sample is added to 15 mL of 4% nitric acid to prevent the precipitation of solids between sampling and analysis).

Aside from a jump from 7.68 mmol/kg to 20.37 mmol/kg for 2 0.1 over the last 155 hours of the experiment, the sub-experiments appear to have levelled off by the experiment's end.

3.1.6. 180628

Experiment 180628 forms one of the main bases for the discussion of Chapter 3, thus its data will now be discussed in detail.

pH 4 sub-experiments of 180628 behave similarly to those previous: with very little deviation above background Fe levels, although with a slight distinction between 0.1 and the higher CO_2 0.5 and 1.0 sub-experiments, which contain ~0.2-0.8 mmol/kg more Fe than for 0.1.

For pH 2, the three sub-experiments are distinct and aligned so that the higher the dissolved CO_2 levels, the higher the dissolved Fe levels. The three lines remain broadly parallel, rising and falling in tandem, reaching their maxima at 668 hours in (~28 days) for 0.5 and 1.0, with 0.1 lagging behind at 767 hours (32 days). After this maxima the three sub-experiments either gradually fall (for 1.0) or level off (for 0.5 and 0.1), but either way an overall equilibrium appears to be reached by the experiment's termination after 1461 hours (60 days). The upward trend in the final hours of 180313 could be reflected in that aforementioned peak that terminates ~668 hours in, as the climb for 2 1.0 begins 305 hours in; similar to 213 hours in for the climb of 180313.

Overall, the trends of 180628 suggest relatively stable levels of activity that continue throughout the duration of the experiments, and which follow trends in pH stability as seen in Figure 5.

3.1.7. 180829

180829, which is 180628 but sampled more regularly at the experiment's start and over a shorter period to produce higher resolution at this critical period, follows several trends observed in 180628. First, for pH 2 experiments, the three are distinctly separated by CO_2, with higher levels of CO_2 corresponding to higher dissolved levels of Fe. Secondly, for pH 4 experiments, these remain at dissolved Fe levels an order of magnitude lower than for pH 2, on the order of 0.04-1.50 mmol/kg, compared to ~7-21 mmol/kg. Thirdly, excepting an anomalous spike at 208 hours in, from 20.1 mmol/kg to 45.2 mmol/kg for 2 1.0 (which does not correspond to any significant pH trend, nor other experiments, so is likely an anomaly), the sub-experiments appear to trend gradually upwards through time. This is particularly notable for 2 and 4 1.0, and agrees with the observed rise in Fe up to ~600 hours in observed for 180628, and the rise observed in 180612 until ~150 hours in. This suggests that experiments reach stability after this period, at least 500 hours (~3 weeks) in.

This experiment follows 180628 and 180612 by suggesting that the presence of Fo enables more Fe to be released, despite its overall decrease in presence by halving the total amount of Fa and replacing this half with Fo (Mg_2SiO_4). The presence of Mg, therefore, appears to act as a catalyst for the dissolution of Fe.

3.1.8. 181004

There were insufficient fluid levels for regular sampling in the low rock:water ratio experiment of 181004: two sub-experiments contained 20 mL while the other two contained only 2 mL. As such, only fluid from the very end of the two high rock:water ratio (1:10) experiments was extracted, and are displayed in Table 9. For pH 2 1:10, the amount of Fe in solution after 1464 hours (61 days) was 8.6283 mmol/kg, while for pH 4 1:10 it was 0.1207 mmol/kg. These are both within the typical range for terminated experiments of such starter pHs, where those within pH 2 average between 8-25 mmol/kg, and for pH 4 this is between ~0-2 mmol/kg. While for pH 2

1:10, this measurement is at the lower end of average, the pH of the analysed solution was not especially high, at 6.355.

Overall, the use of low rock:water ratio at 1:10 did not significantly affect the release of Fe into solution in comparison with experiments conducted at the far-higher rock:water ratio of 1:500 for the vast majority of experiments.

3.1.9. 181029 Fa

181029 Fa, as has been discussed earlier concerning the experiment's pH and Eh, does not reflect the typical experimental pathway of long-term fayalite-bearing experiments.

In this light, it is interesting to note the reversal of a usual trend in the pH 2 sub-experiments: where usually the higher the dissolved levels of CO_2, the higher the levels of dissolved Fe, in 181029 Fa it is the reverse: the highest levels of dissolved Fe are reached by 2 0.1. Though only miniscule Fe levels were detected in pH 4 sub-experiments, the highest reaching 0.23 mmol/kg (interesting, also for the 0.1 bar sub-experiment), these overall follow the more conventional trend of more CO_2, more Fe, although with anomalies as mentioned.

The pH 2 experiments remain level throughout their duration, and, in the case of the anomalous 2 1.0, remain at lower levels than usual for their starter pH amongst both Fa and Fa-Fo experiments. This may reflect the exceptionally low pH recorded for this experiment, which remained ~1 after falling rapidly from 2. While experiments begun at pH 4 consistently show significantly lower levels of Fe, 2 1.0 of 181029 Fa is evidence that this link is not directly proportional to pH, and that pH can become too low to inhibit fa dissolution and therefore levels of Fe in solution.

It is important to remember, however, that Fa alone appears to yield less dissolved Fe than Fa-Fo experiments, thus the trends for pH 0.1 and 0.1, which showed pH behaving as expected, imitate the trends of their equivalent sub-experiments in 180313 and 180406.

3.1.10. 181029 Fo

181029 Fo performed more for less in line with the previous, long-lived, Fo-bearing experiment 180628. It is interesting that the spike in dissolved Fe at 934 hours in (39 days) also corresponded to a spike in pH across both 181029 Fo and Fa; on closer inspection, this spike is manifested less strikingly at the same time in the dissolved fe graph of 181029 Fa. Due to both these experiments running at the same time, they were sampled at the same time, and it seems unlikely that both were to yield unusual and unrepeated deviations from experimental trend, thus this anomaly has been attributed to some kind of cross-contaminated error amongst the sampling equipment, affecting both experiments simultaneously.

After the anomaly, the pH 2 experiments settle at a higher level of dissolved Fe, greater in magnitude for the 0.5 and 1.0 experiments. It is consistent with previous experiments that the 0.1 sub-experiment becomes disconnected from the more-closely mirroring 0.5 and 1.0 sub-experiments. The settling of Fe to this new, higher level after the anomaly is consistent with dissolved fe remaining in solution after the anomaly, i.e. not crystallising out of solution to form new minerals. This is consistent with the results of corresponding solid analyses on this experiment, which did not find any new solids amongst the Fa and Fo, even down to nanoscopic levels.

Like 180628, the dissolved levels of Fe of 181029 Fo remain level outside of the anomaly, indicating that no further dissolution of Fa/Fo takes place following the early stage of the experiment (~500 hours, as seen in higher reolsution by such shorter experiments as 180829). The lack of any lowering of Fe also suggests no minerals are forming from Fe precipitating from solution, which is in line with solid analyses.

3.1.11. 181205

Table 10 displays the ICP-OES results of Fe, Si, and Mg levels at the termination of 181205, which ran with both fayalite and forsterite. Unusually low levels of Fe are present for the

pH 4 experiment, almost an order of magnitude below expected and lower than both the Si and Mg levels. This could be from the removal of Fe by the precipitation of an Fe-bearing mineral.

3.1.12. 190121

Fe levels for 19021, as seen in Figure 5, follow the trend of a clear dichotomy between experiments begun at pH 2 and pH 4, reflecting the enhanced dissolutive ability of acidic solutions.

3.1.13. 190423 Fa

Both for 190423 Fa and Fo, the levels of Fe remain steady in solution across the course of more than 2000 hours. Other, shorter experiments record a steady rise at the start of the experiment, but this is not present in 190423 Fa or Fo because the first sample was taken over 150 hours in – a point by which some experiments had already been terminated. As such this initial rise was lost owing to the far lengthier timescale between each sampling point. These two experiments ran for the longest duration of any and both consistently show neither a rise nor fall in Fe, suggesting there is little change either by further dissolution or precipitation, even when the experiment is left to run for several months. As with previous similar experiments such as 180406, though far-shorter, there is a clear distinction between pH 2 and pH 4 experiments, which reflects the ease of Fe to dissolve during mineral dissolution into solution at pH 2 rather than pH 4, where the heightened alkalinity impedes rapid dissolution.

3.1.14. 190423 Fo

Similarly to 190423 Fo, Fe does not appear to be added or removed from the system even over three months of experimentation. The distinction between pH 2 and pH 4 experiments is again highly distinct, excepting an anomaly for pH 2 0.1 that is resolved by the next datapoint, suggesting it was an analytical error. S with previous experiments, 2 0.1 shows a slightly lesser ability to dissolve Fe into solution – this is possibly a function of the lack of CO_2 to form carbonic acid, which may enhance the dissolution process. The lack of change of Fe over time does not suggest any major precipitate of a new mineral.

3.1.15. Conclusions

The following conclusions may be drawn from this section's analysis of dissolved Fe levels in Fa and Fa-Fo-bearing experiments:

- Within the first hour of experimentation, Fe begins dissolving into solution from the initial substrate, and quickly levels off
- Fo-bearing experiments enable higher amounts of dissolved Fe to enter solution
- Dissolved Fe generally remains relatively level across experiments, though higher-resolution shorter experiments show a gradual rise for the first ~500 hours, after which very little change occurs
- The higher the dissolved CO_2 levels, generally the higher the dissolved Fe levels
- Fe levels do not decline, suggesting none is being removed from solution by precipitation
- Dissolved Fe is strongly linked to pH: at pH 4, very little Fe is able to get into solution. However, too low a pH and this does not allow Fe to reach as high levels either
- Lowering the rock:water ratio by more than a magnitude, from 1:500 to 1:10, had little notable effect on the release of Fe into solution except for a possible slight decrease in the ability of Fe to dissolve into solution at an initial pH of 2

Overarching trends show that Fe dissolution is highest when pH is highest, and within this, where dissolved CO_2 saturation is highest. Once Fe is released into solution it tends to remain there, excepting a lowering with 180628 where pH reached its highest, which suggests possible precipitation as pH becomes more basic. The general lack of Fe decline, however, argues that Fe did not precipitate in any experiments, excepting 180628, where possible small amounts (from 24.6 to 19.9 = a loss of 4.7 mmol/mg) may have precipitated for sub-experiment 2 1.0. This could, however, be an anomaly. Thus, studies of dissolved levels of Fe strongly suggest an absence of mineral precipitation with Fe under these conditions, excepting where conditions reach the very

basic pH of 7.9 as in the case of 180628 2 1.0. As pH reached higher levels in subsequent experiments (181205, 190423 Fa and Fo), and this drop was not observed again, it is perhaps more likely this was an anomaly owing to analytical error. In the case of 180628, solid samples from this sub-experiment will as a result of the analysis here be searched extremely vigorously to determine whether this precipitation occurred, and if so what mineral form was taken.

The study of dissolved Fe in solution has proved an extremely useful tool for predicting the outcome of experiments regarding the precipitation of solid minerals, which is this research's overarching objective. While the solid analyses discussed subsequently will describe for certain, the level Fe amounts displayed in these graphs strongly argue against precipitation of any significant amount of minerals, suggesting that these conditions have not been inductive to the formation of the iron carbonate siderite.

3.2. Silica

Si is found within the structure of fayalite and forsterite, and while not incorporated into siderite, its presence or absence in solution is indicative of the dissolution of either fayalite or forsterite. This thereby represents the release of other elements into solution (Fe, Mg) that may be available for the precipitation of new minerals. Silica is also interesting in itself as amorphous silica has been found on Mars in conjunction with iron oxides such as magnetite, and is therefore a diagnostic species representing certain conditions. An increase in dissolved Si, therefore, corresponds to the ability of a solution to produce new minerals. Its absence suggests the fayalite was unable to dissolve (for reasons that will be discussed when this instance arises), and that new minerals were not capable of forming.

In this section, the dissolved Si trends for all fayalite- and, where applicable, forsterite-bearing experiments are displayed in the graphs of Figure 6. This is excepting the low water/rock ratio experiments of 181004 and 181012, where such minute levels of liquids were involved that

sampling was no possible. Results from the beginning and termination of their experiments are displayed in Table 9 and Table 10.

For the graphs in Figure 6, please note the same y axis for all graphs from 0 to 50 mmol/kg, but the differing x axis to account for experiments conducted over lengths varying from 10 to 2000 hours. Following the symbology of the pH and Eh graphs, lines are shown in red for experiments begun at pH 2; blue for pH 4, and, for 180123 and 180203 where this was a parameter, green for pH 6. In 180123, 180203, and 180310 where no CO_2 was added and rock:water ratio was the parameter explored alongside pH, these experiments show solid lines for high rock:water ratio and dashed for low. For all other experiments, the weight of the line denotes CO_2 pressure in bars. For the thickest line, this is 1 bar; for the lighter line, this is 0.5 bar; for the dashed line, this is 0.1 bar.

The nomenclature used for describing each sub-experiment follows the previous section by using the starter pH and the additional defining parameter, e.g., an experiment begun at pH 2 at a low water-rock (w/r) ratio will be referred to as low pH 2, while an experiment begun at pH 4 with 0.1 bars of CO_2 will be referred to as pH 4 0.1, etc. Unless otherwise stated, all experiments were run with fayalite (Fe_2SiO_4).

Experiment 180310 was not analysed via ICP-OES due to funding limitations.

3.2.1. 180123

In comparison to the trend of dissolved Fe in Figure 5 for 180123, Si closely follows that overall trend but for its lowering in magnitude. The pH 2 sub-experiments both consistently hold an order of magnitude more Si in solution than for both pH 4 and 6 sub-experiments, with both low and high w/r pH 2 holding level between ~ 9.5-10.5 mmol/kg up to the experiment's termination at 193 hours.

As with Fe levels, dissolved Si levels for low pH 2 briefly outnumber those for high pH 2, but the two quickly reach identical Si levels, settling to 10.0±0.2 mmol/kg after the first 24 hours.

For pH 4 and 6 sub-experiments, Si levels are so low as to be considered background levels, and no observable trend may be detected.

3.2.2. 180123

180203 is a repeat of 180123 in its first 10 hours, and follows trends observed in both the experiment's Fe levels but also, interestingly, its pH.

Acting as a higher resolution version of the first 10 hours of 180123, the faster ability of low pH 2 to release Si in solution is mirrored here as it was for Fe, and rises steadily within the first 4 hours before reaching steady state at ~10.6 mmol/kg. High pH 2 can be seen climbing steadily at a lower incline, agreeing with the observation of 180123 that Si reaches steady state beyond the length of 180203.

Sub-experiments at pH 4 and 6, as for 180123, show negligible activity. pH 6 Is levels are below the limit of detection.

3.2.3. 180313

As with Fe trends, for CO_2-bearing experiments such as 180313 there is a clear deviation from the non-CO_2-bearing experiments previously. For pH 2 sub-experiments, Si rise is steeper and at higher levels; by the end of 180123, high pH 2 (the same w/r ratio as used henceforth) was at 3.9 mmol/kg Si, whereas for 2 1.0 at this same time, Si levels are at 7.2 mmol/kg.

Similarly to Fe levels, there is a clear distinction between sub-experiments under 0.1 bar CO_2 and 0.5 and 1.0, with this distinction most clearest with pH 2, where 2 0.1 terminates with 5.3 mmol/kg Si, and 0.5 and 1.0 at 6.7 and 7.2 mmol/mg respectively.

pH 4 experiments show a slight rise through time, implying Si now represents real concentrations and no longer just background levels. This rise is slightly higher the higher the levels of dissolved CO_2, with pH 4 1.0 containing 0.8 mmol/kg Si by the experiment's termination but 4 0.1 only 0.4 mmol/kg.

The slight rise in Si over time through all experiments suggests fayalite dissolution was ongoing by the experiment's end. This, along with the experiment's continued rise in pH, prompted further experiments with identical set-ups but run for longer periods of time.

3.2.4. 180406

As a direct repeat of 180406, the levels of Si were expected to be similar, and this is broadly observed. pH 2 sub-experiments remain consistently above those at pH 4; Si levels remain either steady or at a low climb after stabilising within their first few hours of the experiment; sub-experiments with lower levels of dissolved CO_2 tend to lag with lower levels of dissolved Si than for those with higher levels of CO_2; and the overall magnitude of dissolved Si falls below 10 mmol/kg for pH 2 and at maximum 1.7 mmol/kg for pH 4, which is also consistent with 180313.

A slight decrease in Si levels for the pH 4 sub-experiments at 261 hours in mirrors a similar decrease seen with Fe levels, and this may correspond to a slight increase in Si levels in the pH 2 sub-experiments. This slight anomaly may be due to sampling equipment contamination, as subsequent searches via solid analyses did not detect any measurable precipitation that may have lowered or increased Si levels across all experiments. This could also be due to an ICP-OES analytical error. Regardless, the overall trend of the experiment is not affected, as by the next sampling point Si for pH 4 sub-experiments has increased to previous levels, while for pH 2 it had decreased to previous levels, this further suggests analytical error rather than the addition or removal of Si from solution, as such variations appear to propagate to subsequent samples (as seen with 181029 Fa).

3.2.5. 180612

Si trends are very unusual for 180612, which has been discussed previously as an anomalous experiment. Hence, little weight will be given to the results discussed here, but they will be described nonetheless.

pH for sub-experiment 2 1.0 and to a lesser extent 2 0.5 were highly anomalous and dropped to very low levels that were not kinetically anticipated, and this is reflected in the dissolved

Si levels over the course of the experiment. Both rise sharply over the first ~200 hours of the experiment before climbing less steeply in the case of 2 1.0 or possibly levelling off with 0.5, reaching at maximum 26.6 and 21.5 mmol/kg respectively — by far the highest levels yet observed.

The remaining experiments behave more normally, in line with their pH behaving as expected during experimentation. pH 2 0.1 reaches levels similar to those of its counterpart in 180406, despite 180612 containing 50:50 Fa-Fo, and does not climb after reaching ~4.2 mmol/kg 63 hours in. The pH 4 sub-experiments behave in line with those of previous CO_2-bearing experiments: the higher the levels of dissolved CO_2, the higher those of Si. These levels are at their highest yet, with 1.9 mmol/kg reached for 4 1.0 by the experiment's end after 355 hours, 0.8 mmol/kg for 4 0.5, and 0.6 mmol/kg for 0.1. As these high levels are no observed in any successive experiments that also bear forsterite, this may be due to the overall anomalousness of this experiment that is reflected in the heavily fluctuating pH and Eh levels discussed in sections prior.

3.2.6. 180628

While broad trends are visible in the dissolved Si levels of 180628 in comparison to previously experiments, they are less constrained and with more variety. For sub-experiments begun at pH 2, it is unusual that 0.1 and 0.5 display near-identical values for most of the experiment, when previously it is 0.5 and 1.0 that show closer kinship. It is likewise unusual for Si levels to lower through time rather than steadily increase or level off, as which occurs for 2 1.0. While pH trends for this experiment do fluctuate more than previously, they overall follow a trend and climb to some of the highest pH levels observed across any experiment previous or later. Given that Si levels increase for the furthermost datapoint, where pH unexpected plummeted to 3.1 at 1461 hours in, it is possible that pH climbed so highly for this sub-experiment that it allowed Si to be taken from solution. Amorphous Si would be difficult to detect in conventional solid analysis methods, as it would not display the crystal structure that would make it visible by XRD. With the fall in Si relatively small — from maximum 10.8 mmol/kg at 306 hours in to minimum 5.4 mmol/kg at 1273 hours — any minerals produced would be minute in quantity, which would

make them difficult to physically observe via SEM too. FT-IR is one possibility. However, such amorphous Si would appear in FT-IR, and none has been found.

It is worth considering that the precipitated solids may have been redissolved back to solution: with the sharp pH decrease 1273 hours in, Si levels once more rose. Perhaps the precipitation was temporary and, with the increase in pH, amorphous silica was no longer stable.

That the decrease in pH for 2 1.0 enabled higher levels of Si in solution must equate to a direct correlation between decrease in pH and increase in Si. Such low pH levels as for 2 1.0 have never been seen before or since, and neither have such high levels of Si. This is interesting because, as discussed earlier for dissolved Fe, with Fe there appeared an ideal pH level whereby Fe would most readily dissolve into solution, somewhere higher than 2 but lower than 4. This does not appear the case for Si; rather, Si appears to most readily dissolve into solution when at pH 1.

As for sub-experiments begun at pH 4, these follow the established trend of slowly rising through time but only at minute levels: in the case of 4 1.0, Si levels increased from 0.3 mmol/kg at the sub-experiment's beginning and rose to 0.7 mmol/kg by its termination. The pH 4 sub-experiments also remain generally separated by levels of CO_2, i.e. the higher the levels of CO_2, the higher the levels of dissolved Si. This agrees with previous experimental trends.

3.2.7. 180829

As a repeat of the anomalous 180612, 180829 more closely imitates the first ~300 hours of 180628 and shows these in higher resolution. Sub-experiments pH 2 are separated by CO_2 levels, with higher levels of CO_2 corresponding to higher levels of Si; Si remains within the range of 180628 at ~5-12 mmol/kg; and the sub-experiments gradually trend upward. There is an anomaly at 208 hours in for sub-experiment 2 1.0, where Si jumps from 10.6 mmol/kg at 185 hours to 26.2 mmol/kg. This is reflected across Fe and Mg levels as well, and as it does not correspond to any particular change in pH or Eh, nor is it shared by any of its other sub-experiments, has been attributed to an ICP-OES analytical error or possible contamination during the sampling procedure itself.

Levels of dissolved Si remain extremely low for pH 4 sub-experiments, barely rising above background detection levels, but there is a slight increase in Si with increased CO_2, and a slight upward trend: for 4 0.1 this increase is small, from 0.1 mmol/kg at the experiment's beginning to 0.4 mmol/kg at its end, but more notable for 4 1.0, from 0.1 mmol/kg to 0.7 mmol/kg.

Overall, the trends are in line with that observed in 180628 and further corroborate the anomalousness of 180612. Fo-bearing experiments such as 180628 and 180829 show greater deviation between pH-same sub-experiments than seen in purely Fa-bearing experiments. They also enable greater levels of Si to enter into solution as a whole. This mirrors what has been observed and discussed regarding levels of dissolved Fe.

3.2.8. 181004

As discussed earlier for Fe levels in 181004, this experiment was conducted at low rock:water ratios of 1:1 and 1:10, where the 1:1 experiments contained too little solution for any sampling, and the 1:10 for a single sample to be extracted at the experiments' termination. Please observe Table 9 for the measurements discussed here. For pH 2 1:10, dissolved Si levels were 2.025 mmol/kg after 1464 hours (61 days), and 0.454 mmol/kg for 4 1:10. For pH 4 this is within the typical range of dissolved Si levels for pH 4 sub-experiments, but the levels of Si in the pH 2 sub-experiment of 181004, like its Fe levels, are slightly lower than expected. The usual range for Si levels in pH 2 sub-experiments, as seen in Table 9, is between ~6-10 mmol/kg. Si appears slightly inhibited from release into solution in low rock:water ratio experiments begun at pH 2.

3.2.9. 181029 Fa

This experiment behaved unusually regarding pH and Eh measurements, and this is reflected in the solution sampling data. As discussed earlier regarding its Fe levels, for Si, these levels do not agree with previous purely Fa-bearing experiments in that there is a reversal in correlation between CO_2 levels and Si levels. Previously, the higher the dissolved CO_2 content the higher the levels of dissolved Si, but for pH 2 sub-experiments in 181029 Fa this is reversed. By the experiment's termination after 1920 hours, 2 1.0 has 3.5 mmol/kg dissolved Si in solution,

while for 2 0.1 this is 4.5 mmol/kg. There is also no trend for 0.5 and 1.0: aside from a slight anomaly at 933 hours in shared by all sub-experiments, Si levels remain steady.

For pH 4 sub-experiments, Si levels remain barely above detection for the entirely of the experiment, reaching at maximum 0.5 mmol/kg for 4 0.1 experiment 500 hours in. As for pH 2, the lower the CO_2, the higher the levels of dissolved Si. This extremely low level for all pH 4 sub-experiments may be attributable to pH the unusually low and unstable pH levels for these sub-experiments.

Overall, the anomalousness of 2 1.0 is clearly reflected by its depressed Si values, and it is interesting to note that Si did not reach extremely high levels such as for 180612's sub-experiment 2 1.0. In the latter case, pH plummeted to ~1, whereas for this experiment in 181029 Fa, while pH did not climb as expected, pH did not fall below 2, reaching at lowest 2.2 at 1919 hours in. Dissolved Si levels in 181029 Fa, therefore, better reflect the earliest hours of previous purely Fa-bearing experiments such as 180313 and 180406, where pH has yet to climb — only this condition remained throughout the duration of the experiment.

3.2.10. 181029 Fo

This experiment is a direct repeat of 180628, thus is expected to show similar trends. Broadly this is observed: pH 2 and 4 sub-experiments remain distinct throughout the course of the experiment, and each remains within the limits expected by now based on previous experiments: for pH 2 this is between ~5-10 mmol/kg, while for pH 4 it is 0.1 to 0.2 mmol/kg. As with 180628, there is little change in Si levels, even after the experiment's beginning (although take care to note that the first sample was taken ~100 hours in, well past the point of notable change observed in 180829 until ~50 hours in).

As has been discussed at length previously, there is a jump in Si for pH 2 experiments at 933 hours in and a corresponding dip for pH 4, which propagates through the experiment.

The relatively low levels of Si shown in this graph are perhaps surprising given the slightly higher levels first observed at the beginning of pH 2 experiments in 180628, but while the graph

profiles differ — showing gradual decline and levelling for 180628, and remaining level for 181029 Fo before acclimatising to an anomaly — the range of Si is similar, and indeed both experiments end with very similar Si levels. This is, respectively for 180628 and 181029 Fo, 4.2 mmol/kg and 4.7 mmol/kg for 2 0.1; 3.9 mmol/kg and 4.7 mmol/kg for 2 0.5; 7.8 mmol/kg and 6.4 mmol/kg for 2 1.0; 0.3 mmol/kg and 0.1 mmol/kg for 4 0.1; 0.5 mmol/kg and 0.1 mmol/kg for 4 0.5; and 0.7 mmol/kg and 0.1 mmol/kg for 4. 1.0.

Overall, the trends between differing Fo-bearing experiments appear to broadly align, excepting the anomalous 190612. Broadly they show a slightly higher release in Si than for purely Fa-bearing experiments, and they appear to reach steady state by the experiment's terminations.

3.2.11. 181205

As with previous experiments both low and high water/rock ratio, there is a strong dichotomy in dissolved Si between pH 2 and pH 4 sub-experiments in 181205 that is reflected across Fe and Mg as well, for reasons that have already been discussed. Slightly higher levels of Si are found for pH 2 than for 181004, while for pH 4 slightly lower – while the trend is only minor, it is possible that Si precipitated out of solution more efficiently for 181004 owing to the slightly higher pH achieved.

3.2.12. 190121

Dissolved Si levels for 190121, as seen in Figure 6, follow the trend of a dichotomy between pH 2 and pH 4 experiments, and release similar levels of Si into solution as previous experiments at <10 mmol/kg. This is despite this experiment beginning with a ratio of 9:1 Fo:Fa, suggesting that Si is released into solution at roughly similar levels for Fo as for Fa.

3.2.13. 190423 Fa

Reflecting the trends for Fe, Si release varies very little throughout the course of all sub-experiments within 190423 Fa. This is again owing to the slow pace of the sampling across the >2000 days of experiment running time, thus the rapid changes that were observed at the start of shorter-term experiments were not observed here. The levels of Si released are slightly lower than

that of previous, similar experiments such as 180313 – for example, 6.45 mmol/kg of Si was recorded at 213 hours in for 180313, while at 237 hours for 190423 Fa this was 4.53 mmol/kg – however, the general flat trend is consistent even over the far-lengthier timescale.

3.2.14. 190423 Fo

The Si levels for 190423 Fo are almost identical to those of its non-forsterite-bearing equivalent 190423 Fa. For example, for the final recorded datapoint, for Fo 2 1.0, 3.977 mmol/kg was recorded, while for the same sub-experiment in Fa this was 3.85 mmol/kg. While there were slight pH differences between the two (Figure 1), for the release of Si (and Fe) into solution, there appears to be little change between a 100 % fayalitic substrate or 50:50 fayalite/forsterite.

As with Fe, for sub-experiment 2 0.1 there is a slight anomaly at 1406 hours in, but considering this corrects itself by the following datapoint, this is likely to be an analytical error.

3.2.15. Conclusions

The following overarching conclusions may be drawn from this section analysing Si:

- Slightly less Si is released to solution than Fe, in line with fayalite being comprised by ~2/3 Fe
- The lower the pH, the higher the Si levels released into solution
- Si levels rarely fall, suggesting no new minerals (likely amorphous silica) are being precipitated. One instance (190628) reached very high pH, which may have caused some precipitation before a subsequent rise in pH again rose Si levels back, perhaps implying redissolution of recently precipitated Si
- Si remains constant throughout the experiments, climbing at a steady gradient for the first ~300 hours before levelling
- This steady levelling does not suggest any lasting precipitation
- Si appears slightly inhibited from release into solution in low rock:water ratio experiments begun at pH 2 – this may reflect a precipitate of amorphous silica.

The study of dissolved Si in solution, as with Fe, also clearly hints at the fate of solid samples prior to their analysis, in this case also suggesting a lack of precipitation of new minerals excepting a slight amount of silica – possibly amorphous silica – being precipitated from solution in pH 2 experiments. The last element analysed via ICP-OES will now be discussed: magnesium, in whichever experiments it was present within.

3.3. Magnesium

Mg is found within the structure of forsterite, and while not incorporated into siderite, its presence or absence in solution is indicative of the dissolution of forsterite. The possibility of forming Mg carbonates (such as magnesite, hydromagnesite, dolerite, or ankerite) is considered, but these are unlikely due to the higher temperatures required. More important for this study is how Mg in solution, as with Fe and Si, represents the release of elements into solution that may be available for the precipitation of new minerals. An increase in dissolved Mg is here important because it corresponds to the ability of a solution to produce new minerals. Its absence suggests the forsterite was unable to dissolve (for reasons that will be discussed when this instance arises), and that new minerals were not capable of forming.

In this section, the dissolved Mg trends for all forsterite-bearing experiments are displayed in the graphs of Figure 7. This is excepting the low water/rock ratio experiments of 181004 and 181012, where such minute levels of liquids were involved that sampling was no possible. Results from the termination of their experiments are displayed within the tables Table 9 and Table 10.

For the graphs in Figure 7, please note the same y axis for all graphs from 0 to 50 mmol/kg, but the differing x axis to account for experiments conducted over lengths varying from 10 to 2000 hours. Following the symbology of the pH and Eh graphs, lines are shown in red for experiments begun at pH 2; blue for pH 4, and, for 180123 and 180203 where this was a parameter, green for pH 6. In 180123 and 180203 where no CO_2 was added and rock:water ratio was the parameter explored alongside pH, these experiments show solid lines for high rock:water ratio and

dashed for low. For all other experiments, the weight of the line denotes CO_2 pressure in bars. For the thickest line, this is 1 bar; for the lighter line, this is 0.5 bar; for the dashed line, this is 0.1 bar.

The nomenclature used for describing each sub-experiment follows the previous section by using the starter pH and the additional defining parameter, e.g., an experiment begun at pH 2 at a low water-rock (w/r) ratio will be referred to as low pH 2, while an experiment begun at pH 4 with 0.1 bars of CO_2 will be referred to as pH 4 0.1, etc.

The graphs representing non-Mg-bearing experiments have been left blank intentionally to facilitate comparison between other experimental parameters or analyses, such as Eh or pH.

3.3.1. 180123

Left blank due to no Mg (forsterite) present.

3.3.2. 180203

Left blank due to no Mg (forsterite) present.

3.3.3. 180313

Left blank due to no Mg (forsterite) present.

3.3.4. 180406

Left blank due to no Mg (forsterite) present.

3.3.5. 180612

The first experiment to use forsterite to supplement the fayalite was 180612, and, as has been discussed, was anomalous. Its Mg levels closely follow those of Si, rising to 30.0 mmol/kg at maximum for 2 1.0 at 355 hours in; for Si this was 26.7 mmol/kg; for Fe 28.9 mmol/kg. As with Si, Mg appears closely linked with pH, and appears to more readily enter solution as pH remains low. pH did not change significantly across 180612 2 1.0, therefore the increasing Si is cumulative and suggests that Mg, like with Si, is being continuously released into solution, whereas for 2 0.1 and the pH 4 experiments, that either remain level or show a minute rise, Mg was released within the first few hours and has remained unchanged since.

The lack of any decrease in Mg across any sub-experiment does not suggest the precipitation of any new minerals.

3.3.6. 180628

Unlike the Si levels for 180628, dissolved Mg remains steady across all sub-experiments. There is a minor peak of 6.1 mmol/kg at 668 hours in for 2 1.0 — only 1.3 mmol/kg above the Mg levels at which this sub-experiment terminates, which is 4.8 mmol/kg at 1461 hours — but overall there is none of the reduction of dissolved Mg as was seen for Si. This does not indicate the precipitation of any Mg-bearing species.

Where 2 0.5 and, to a greater extent, 2 1.0 of 180612 displayed continuously low, anomalous pH, these sub-experiments functioned normally for 180628, in line with trends that have since been confirmed with 180829 and 181029 Fo. Accordingly, 2 0.5 and 2 1.0 for 180628 fall within a range reflected by 180829 and 181029 Fo. This is ~5-7 mmol/kg; less than observed for Si and Fe levels. Mg is a significantly lighter element than these, but its lesser presence in solution could also reflect a reluctance to dissolve from forsterite.

The sub-experiment with the highest levels of dissolved Mg is 2 1.0, not surprising given pH 2 experiments' continued ability to yield higher levels of dissolved elements, due to the ability of H^+ protons to oxidise available elements and release them into solution. The higher the CO_2 in solution also appears to promote Mg dissolution as with previous experiments and elements.

For pH 4 sub-experiments, these levels remain very low, as appears common when looking to the trends of other Fo-bearing experiments (180829 and 181029 Fo, for example). At maximum, Mg in solution is 0.28 mmol/kg at 767 hours in for sub-experiment 4 1.0. The more CO_2 in the sub-experiment, overall the higher the levels of Mg, but given how minute the quantities are the differences are a matter of 0.1s.

Overall the trend of dissolved Mg better resembles Fe dissolution trends for 180628 than for Si, suggesting that, like Fe, Mg does not readily precipitate from solutions of these conditions.

3.3.7. 180829

180829's dissolved Mg data behaves much as 180628's does: pH 2 and 4 sub-experiments are distinct, with pH 4's being an order of magnitude lower ~0.1-0.2 mmol/kg in comparison to ~3-6 mmol/kg for pH 2; sub-experiments within the same pH align with higher levels of dissolved Mg where there is more dissolved CO_2; and there is little change over the course of the experiment, with only the slightest rise from beginning to end (e.g., 2 1.0 from 3.4 mmol/kg at 17 hours in to 5.1 mmol/kg at 282). The anomaly 208 hours in for 2 1.0 has already been discussed and is likely a sampling or analytical error, perhaps due to an imperfect recording of the ratio of sample to storage nitric acid.

The trends of 180829, which is a repeat of the anomalous 180612, suggest that Mg is realised into solution within the first few hours and there remains stable, neither precipitating new minerals nor dissolving further forsterite, as Mg levels remain stable. As with 180628, which is this experiment but run over 1500 hours rather than 400, these stable conditions suggest that Mg does not form Mars-relevant minerals under such conditions, at least at these timescales.

3.3.8. 181004

Although no Mg was included in 181004, which was purely Fa-bearing, the two samples extracted from this low rock:water ratio experiment were analysed via ICP-OES for Mg out of interest to observe what levels would be detected as background where no Mg was intended to be present. Most interestingly, Mg levels were detectable, and between the pH 2 and pH 4 sub-experiments, the standard ratio of ~1 to 0.1 between pH 2 and pH 4 sub-experiments was maintained. For sub-experiment 181004 pH 2 1:10, Mg levels are 0.101 mmol/kg. This is an order of magnitude lower than for Mg-bearing pH 2 sub-experiments such as 181029 Fo (results between 1.849-3.444 mmol/kg). However, it is within the same magnitude of Mg-bearing pH sub-experiments: for example with 181029 Fo, pH 4 sub-experiments contain between 0.072-0.586 mmol/kg. Mg levels for 181004 pH 4 1:10 are only just above detection at 0.035 mmol/kg, but again this is in the same region of Mg-bearing pH 4 sub-experiments.

This raises an interesting question as to whether such amounts — ~0.1 mmol/kg for pH 2, ~0.01 for pH 4 — should be deducted from all experiments' ICP-OES measurements and taken as background levels. If this were so, pH 2 and pH 4 levels would be expected to be identical; as the pH 2 to pH 4 elemental levels for Mg in this experiment mirror those for both Fe and Si, but also Fe, Si, and Mg levels for other experiments, it appears more likely that minute amounts of Mg are contained within the pure synthetic fayalite used in all these experiments, and this has been released into solution alongside Fe and Si. While this can be considered contamination, the release of minute amounts of Mg does not affect measurements of Fe or Si, and so these Mg levels for a pure-Fa experiment can be taken as an interesting means of testing the true purity of the fayalite synthesised for these experiments.

3.3.9. 181029 Fa

Left blank due to no Mg (forsterite) present.

3.3.10. 181029 Fo

Compared to Mg levels within 180628 and 180829, those of 181029 Fo appear subdued, but it is only the pH 2 sub-experiments that display this; pH 4 contain as little dissolved Mg as they have generally, and for Fe and Si as well. 2 1.0 in particular displays lower levels of Mg than similar experiments, reaching maximum 4.9 mmol/kg at 933 hours in (at the point of the anomaly previously mentioned that drives up concentrations in pH 2 and down in pH 4 sub-experiments), compared to 5.9 mmol/kg at the same time for the equivalent sub-experiment in 189628. Even despite the 933 hour anomaly, this is still lower than levels for previous Fo-bearing experiments, and may be due to pH remanning constant, rather than climbing as with 180628: as pH climbed higher, further amounts of Mg could be released into solution, which would grow cumulatively greater throughout the course of the experiment. As pH for 181029 Fo remained roughly constant, this would not enable the release of further Mg to solution, which may account for the stable, lower amounts observed for all sub-experiments across 181029 Fo.

The general trends, however, reflect those seen of previous Fo-bearing experiments: a release of Mg within the first few hours that neither increases or decreases even across almost 2000 hours of experimentation. Mg does not appear to precipitate as new minerals under these conditions.

3.3.11. 181205

As with observed Fe and Si for 181205, the difference in Mg levels between the pH 2 and pH 4 sub-experiments is an order of magnitude (Table 10). This reflects the differences in released as seen in high rock:water ratio experiments as well as within 181004.

3.3.12. 190121

Higher levels of dissolved Mg are observed for experiment 190121 in comparison with previous Mg-bearing, which is owing to the 9:1 ratio of Fo to Fa. There are localised rises in Mg levels, such as ~250 hours in for 2 1.0, which could reflect a major dissolutive episode or a sampling/analytical anomaly.

3.3.13. 190423 Fa

Left blank due to no Mg (forsterite) present.

3.3.14. 190423 Fo

190423 Fo shows unusually low levels of Mg in solution compared to all other Mg-bearing experiments. While the overall trend is in line with Fe and Si for 190423 Fo, including the slight anomaly at 2 0.1 that disappears by the following sampling point, these low releases of Mg could suggest a lessening of dissolution that extended throughout the experiment. The trend across all six sub-experiments for 190423 Fo is flat: for example, from the first recorded measurement of Mg in 2 1.0 (1.54 mmol/kg) to its final 2061 hours later (1.43 mmol/kg) this is actually a slight lowering but only by a minute amount. This could suggest a slight precipitation, but if so it would be so minute as to be virtually undetectable by XRD or FT-IR. Alternatively, the low levels for both 190423 Fa and Fo across all sub-experiments could be due to the switching of analytical methods: owing to an inability to continue with use of facilities at the Scottish Universities

Environmental Research Centre, East Kilbride, in-house ICP mass spectrometry (ICP-MS) was instead used using a PerkinElmer NexION 350D mass spectrometer.

3.3.15. Conclusions

The key conclusions to be drawn from this section's analysis of dissolved Mg in solution over time are as follows:

- Lower initial experimental pH yields higher levels of dissolved Mg in solution
- Mg levels do not decrease over time, suggesting no precipitation as new minerals
- Where pH is anomalously low, as in the case of 180612 2 1.0, Mg levels rise far higher than otherwise seen — the lower the pH, the higher the level of Mg dissolution
- In 181004 where no forsterite was added, minute amounts of Mg were still identified in solution at levels that differed between pH 2 and pH 4 sub-experiments, suggesting the Mg was released from the fayalite itself into solution. This suggests the synthesised fayalite is not pure Fe_2SiO_4 on a microscopic level, but this discovery has no further bearing on the validity of the experiments undertaken.

The absence of decline in dissolved Mg levels suggests an absence of precipitation, which means these conditions do not yield new, Mg-bearing minerals on the surface of Mars. Further analysis of the experiments' solids will enlighten this.

3.4. Siderite

The combination of Fe, Si, and (where applicable) Mg data from a particular sample, together with pH measured from the same sample, may be inputted into the software Geochemist's Workbench to produce kinetically derived estimations of the amount and type of minerals that should have formed under those pH and mmol/kg levels.

In this section, graphs describing the flux of kinetically-predicted siderite levels will be first discussed, followed by additional minerals studied including amorphous silica, fayalite, forsterite, greenalite, $Fe(OH)_2$, and magnesite. The units for describing levels of siderite are $\Omega_{siderite}$, which equates to saturation state, where anything above 0 denotes precipitation from a mineral-saturated solution. An undersaturated solution permits a mineral to remain within solution, hence not permitting a precipitate and producing 0 solids from solution. The exact amount of siderite that saturation state accounts for may be calculated in grams (g) and is later discussed.

Figure 8 shows 12 graphs corresponding to each CO_2-bearing experiment (thus containing the capacity to form siderite), with the experiment name in the top left-hand side of the graph, e.g., 180313. Following the convention of previous figures, the y axis remains the same for all graphs while the y axis differs according to each experiment's length. The legend (top righthand side of graph 180313) is the same for each subsequent graph. Each graph will now be briefly described.

3.4.1. 180123

No CO_2 was included in this experiment, and so siderite levels remained at 0 throughout.

3.4.2. 180203

No CO_2 was included in this experiment, and so siderite levels remained at 0 throughout.

3.4.3. 180313

For 180313, siderite levels remain virtually 0 for all pH 2 sub-experiments until the last ~100 hours, with levels rising to at maximum 14.9 $\Omega_{siderite}$ for 2 1.0. For pH 4 sub-experiments, $\Omega_{siderite}$ levels climb slightly higher: reaching at maximum 78.3 $\Omega_{siderite}$ for 4 1.0. There is a definite correlation, within pH, where the higher the levels of dissolved CO_2, the higher the $\Omega_{siderite}$ of siderite. This agrees with other analyses of these experiments, where higher levels of CO_2 would also produce higher levels of dissolved Fe. This in turn is partially responsible for enabling siderite, which has Fe in its chemical formula ($FeCO_3$), thus without the presence of dissolved Fe in solution, siderite may not form.

Siderite $\Omega_{siderite}$ levels increase over the course of the experiment for both pH 2 and 4 sub-experiments, which is in line with a gradual increase in pH over the experiments.

The maximum $\Omega_{siderite}$ reached — 78.3 for 4 1.0 — translates to siderite being supersaturated within the solution by a factor of 78.3. To be above 0 equals a likely precipitate forming, but to be over 70 times saturated with respect to the solution strongly suggests that a precipitate ought to be forming. A lowering of siderite levels, such as observed for 4 0.5 at 287 hours in from 64.1 to 35.5 at 309 hours in could suggest a removal of siderite from solution (i.e. as a precipitate). The solid residue of 4 0.5 is discussed in the following sections.

3.4.4. 180406

180406 was a repeat of 180313 but lasting 407 rather than 309 hours. Its pH 2 sub-experiments follow the same trend as 180313: pH 2 sub-experiments show level saturation states for siderite than pH 4, but within pH 2, the higher the levels of dissolved CO_2, generally the higher the saturation state of siderite. This reaches at maximum 72.7 for 4 0.5, and it is unusual that for pH 4 sub-experiments, this path of 'higher CO_2 levels = higher $\Omega_{siderite}$' does not hold true in this case.

There is a prominent anomaly for 4 0.5 at 238 hours in where $\Omega_{siderite}$ jumps from 3.7 to 155.9, before falling to 0 (below detection). This is very likely an analytical artefact: neither pH nor dissolved Fe levels for this sampling point behave strangely, and nor do any other sub-experiments within 180406 to suggest this commonly occurs at this time.

3.4.5. 180612

Despite the addition of Mg to 180612 in comparison with 180313 and 180406, the trends of siderite saturation state for 180612 follow those of previous experiments and at the same order of magnitude. Sub-experiments begun at pH 2 show significantly lower levels of $\Omega_{siderite}$ than their equivalents at pH 4; $\Omega_{siderite}$ levels do not exceed 100, reaching maximum 91.8 (the highest so far) for 4 1.0, as with all previous maximum $\Omega_{siderite}$ levels; and all sub-experiments increase in $\Omega_{siderite}$ levels over the course of the experiment, likely linked to the gradual rise in pH. Interestingly, pH

levels for 2 0.5 and 1.0 remained extremely low (2 and under) for the duration of the experiment, and their $\Omega_{siderite}$ levels are their lowest so far for these categories across the experiments. This strongly suggests a causal link between pH and resulting $\Omega_{siderite}$ levels, particularly as Fe levels remain roughly stable.

3.4.6. 180628

180628, also Mg-bearing was the first experiment run for over 500 hours, terminating after 1461 hours (~2 months). Ignoring the immediate, overall trends for now, and zooming in on the first 400 hours, reveals a trend much as has been already observed for experiments lasting 400 hours and under. This includes the well-observed propensity for $\Omega_{siderite}$ levels in pH 2 sub-experiments to remain far lower than within their pH 4 counterparts, and for higher levels of CO_2 to yield higher levels of $\Omega_{siderite}$. Additionally, the order of magnitude at which $\Omega_{siderite}$ levels for pH 4 sub-experiments climb (maximum 106.6 at 392 hours in for 4 1.0) is of the same order for this time in previous experiments (91.8 for 4 1.0 at 355 hours in for 180612, also Mg-bearing).

After ~600 hours, the experiment deviates from this established path of gradual increase in $\Omega_{siderite}$ levels with time. At 767 hours in all sub-experiments increase sharply in $\Omega_{siderite}$ levels, and the greater the levels of CO_2 the higher this increase is, at maximum 179.9 for 4 1.0 from 134.8 at 667 hours to 314.7 at 767 hours in. This is significant as the first time pH 2 sub-experiments reached $\Omega_{siderite}$ levels greater than 10: in the case of 2 1.0, at this point $\Omega_{siderite}$ levels are at 65.9. By the next sampling point at 954 hours, however, 4 1.0 has dipped to below the levels of 667 hours, to 93.5, while 4 0.5, 2 1.0, and 2 0.5 have mostly remained level. Only 2 and 4 0.1 continue to increase, casting into disarray the established trend of the highest levels of CO_2, within pH 4 then 2, dictating the amount of $\Omega_{siderite}$. This instability remains by the next sampling point at 1272 hours in, where both 2 and 4 1.0 bar CO_2 sub-experiments soar to 818.4 and 582.1, respectively. For 2 1.0 especially, this is an extreme departure, but for both sub-experiments these levels of $\Omega_{siderite}$ have not been observed in previous experiments. 2 and 4 0.5 continue to climb at a trend comparable to within the first 600 hours, while 2 and 4 0.1 dip once more to levels between 4-12,

also returning to their levels within the first ~600 hours. Finally, at the last sampling point at 1461 hours in, 2 1.0 continues to climb but at a shallower incline, reaching 903.6 at maximum, while 4 1.0 plummets to 0.0000175. This is due to pH for 4 1.0 plummeting itself from 7.4 to 3.1. Though such a drop has never observed before or since, the drop is not likely an artefact of the pH measurement as the anomaly is also reflected in Eh measurements, which likewise show a corresponding increase (pH and Eh commonly display an inverse trend). This is from −44 to 344.4 — as significant an increase as the pH was a fall. As Fe levels for 4 1.0 180628 remain level, it is this drop in pH that is responsible for the drop in $\Omega_{siderite}$ levels for the final datapoint in this sub-experiment. While difficult to understand the cause of this drop, as it was not observed in any other experiments continued for this length of time, the anomaly further strengthens the link between pH and $\Omega_{siderite}$ levels: without high levels of pH, siderite is unable to form within solution, and hence possibly form a precipitate.

Overall, experiment 180628 shows how experiments may deviate from an apparently set trend when left for long enough, and it was this that prompted the switch from shorter experiments to those lasting 1500 days and longer. Very roughly, $\Omega_{siderite}$ levels increase over time, with some drops that coincide with decreases in pH. 180628 is significant for reaching the highest $\Omega_{siderite}$ levels observed, at maximum 903.6 for 2 1.0, in contrast to previous experiments where 4 1.0 has displayed the highest $\Omega_{siderite}$ levels. This is likely because over time, pH 2 experiments had sufficient time to climb to pH levels sufficient to enable the presence of siderite within solution, whereas previous experiments did not extend for long enough to allow this steady increase in pH to reach such levels. This suggests a lag in which pH 2 experiments are capable of producing siderite within solution, but only after time enough for pH to climb. The fact that dissolved Fe levels are consistently almost an order of magnitude lower for pH 4 sub-experiments than for 2 suggests that pH is the predominant factor controlling $\Omega_{siderite}$ levels. The sudden jump in $\Omega_{siderite}$ levels for pH 2 sub-experiments after time, to higher levels than pH 4 sub-experiments, may reflect pH levels in pH 2 su-experiments reaching sufficient siderite-forming levels and having higher

levels of dissolved Fe than pH 4 sub-experiments, enabling $\Omega_{siderite}$ levels to overtake those of pH 4 sub-experiments'. Further experiments will shed further light on this, but if so it would imply dissolved Fe levels do play a part in $\Omega_{siderite}$ levels.

3.4.7. 180829

180829, a repeat of 180612 that does not display the anomalously low pH trends for sub-experiments 2 0.5 and 1.0, behaves similarly to all sub-experiments of 180612 excepting 2 0.5 and 2 1.0. For these two, given pH was able to climb and permit higher $\Omega_{siderite}$ levels, these two sub-experiments' $\Omega_{siderite}$ levels climb far higher and better resemble their 180313 and 180406 counterparts. The pH 2 sub-experiments of 180829 reach at maximum 6.9 $\Omega_{siderite}$ for 2 0.5. The pH 4 sub-experiments display the well-established trend of higher dissolved CO_2 levels displaying higher levels of $\Omega_{siderite}$, reaching at maximum 116.1 at 281 hours in for 4 1.0 after climbing steadily through time. It is clear that $\Omega_{siderite}$ levels increase over time in tandem with the rise in pH over time, and are less directly affected by dissolved Fe levels, which, as seen for 180829, rise before stabilising early on in the experiment. As with previous experiments, $\Omega_{siderite}$ levels only begin to rise after the first ~150 hours in. This lag appears related to the slow climb of pH before it reaches sufficient levels at which siderite may form within solution.

3.4.8. 181004

Table 11 shows the end levels of $\Omega_{siderite}$ for 181004, which was low rock:water ratio. Diverging from the trend commonly seen in Figure 8, the experiment begun at pH 2 shows far higher levels of siderite than for pH 4, more than three times. This could be owing to fayalite's heightened ability to dissolve under the acidic pH, as well as how pH was able to climb to the high pH of 6.3 by the experiment's end. This is in contrast with the pH 4 experiment which, while the higher pH of 7.3 was recorded by its end, did not permit similarly high levels of Fe or Si to dissolve into solution.

3.4.9. 181029 Fa

$\Omega_{siderite}$ levels remain low and fluctuating for the entirely of this experiment, because much like 180612, pH behaved very erratically for all sub-experiments. This, as was discussed earlier, was likely down to an instability of a trialled orbital shaker set-up that disturbed the beakers. The maximum $\Omega_{siderite}$ reached was 5.7 for 4 0.5 at 1656 hours in and this is strongly linked to how low and unstable pH remained throughout the experiment's 1919 hours. Given the anomalousness of this experiment, little more bearing will be given to these $\Omega_{siderite}$ levels.

3.4.10. 181029 Fo

This experiment ran under the same trialled orbital shaker set-up as 181029 Fa, thus was also subject to an instability of pH likely due to fluid loss from beaker instability upon the shaker. Like 181029 Fa, the maximum $\Omega_{siderite}$ level reached was significantly lower than that reached in 180628, of which 181029 Fo was a direct repeat. This was 40.7 for 4 1.0 at 190 hours in, which is in itself anomalous as generally higher $\Omega_{siderite}$ levels are found as the experiment continues and pH rise, which enables higher $\Omega_{siderite}$ levels. $\Omega_{siderite}$ levels actually overall decline over the course of the experiment, which has not been observed before and does not make sense in accordance with the pathways of previous experiments.

Due to both 181029 experiments showing these anomalous trends, these experiments were repeated and the anomalies found to be isolated to these experiments, and not a product of the true reaction pathway.

3.4.11. 181205

As seen in Table 12, unlike its fayalite-bearing low rock:water ratio equivalent experiment 181004, 181205 follows the main trend of $\Omega_{siderite}$ levels as seen in Figure 8 by the pH 4 sub-experiment yielding higher $\Omega_{siderite}$ levels. Owing possibly due to the lower pH observed by the termination of the pH 2 experiment (5.3), $\Omega_{siderite}$ is far lower than its equivalent in 181004. While $\Omega_{siderite}$ for pH 4 181205 is also lower than its fayalite-bearing equivalent, the relative difference

between 181205 pH 2 and 4 likely is owed to the pH difference (7.9 for 4), while the lower $\Omega_{siderite}$ for 181205 4 compared to 181004 4 could reflect the lower Fe levels released in 181205.

3.4.12. 190121

190121 follows the general trend of increasing $\Omega_{siderite}$ levels for higher CO_2, superimposed upon the trend of high $\Omega_{siderite}$ levels corresponding to high pH. While higher $\Omega_{siderite}$ levels were reached than all previous experiments excepting 180628, this was lesser than 180628 and appears to be a function of both lower pH and lower Fe levels. Both of these factors have significant control on $\Omega_{siderite}$ levels.

3.4.13. 190423 Fa

$\Omega_{siderite}$ reaches its highest levels yet for 190423 Fa owing to a combination of high pH and high dissolved Fe. While dissolved Fe levels reach lower heights than, for example, for 190121, the high pHs of up to 7.6 permit $\Omega_{siderite}$ of up to almost 2000. The clear up and down trend, especially for pH 2 and 4 1.0 in its final three datapoints, clearly follows pH, suggesting this is the dominant control on $\Omega_{siderite}$.

3.4.14. 190423 Fo

Further to the observations of 190423 Fa, for the forsterite-bearing equivalent the pH-dependent trend is even more striking. While dissolved Fe levels remain broadly constant (see Figure 5), $\Omega_{siderite}$ fluctuates in extremes of 500 or me from one datapoint to the next for 4 1.0, and the change can be correlated to changes in pH, which also fluctuates significantly for ths experiment: for example, from 7.6, 7.3, 7.7, 7.5, and 8.1 for its final datapoints. $\Omega_{siderite}$ accordingly jumps or falls with pH, which strongly affirms pH as the dominant control on $\Omega_{siderite}$ in these experiments. 4 1.0 reaches the highest $\Omega_{siderite}$ observed in all experiments at over 3500, and correspondingly has the highest pH observed in all experiments at 8.1.

3.4.15. Conclusions

Several overarching conclusions may be drawn from describing the graphs of Figure 8. They are as follows:

- pH is the strongest control on $\Omega_{siderite}$ levels, where the higher the pH, the higher the $\Omega_{siderite}$
- Dissolved Fe levels appear to have a significant secondary control on $\Omega_{siderite}$ levels
- pH 2 sub-experiments can reach siderite-forming levels of pH when left to run for sufficient time for pH to grow higher
- When pH reaches sufficiently high levels to enable siderite formation, solutions with greater amounts of dissolved Fe enable higher $\Omega_{siderite}$ levels
- A lag time for $\Omega_{siderite}$ levels to begin to climb is likely related to the slow climb of pH, since $\Omega_{siderite}$ and pH appear intricately linked
- Wherever $\Omega_{siderite}$ levels reach above 0, a solid precipitate ought, based on our kinetic understanding of the system, to have formed, and for all experiments barring the 181029 Fa/Fo anomalies, 0 is exceeded, in some cases by almost a factor of 4000

The combination of dissolved Fe with pH yielded $\Omega_{siderite}$ levels for the graphs in this section, and this data is invaluable in drawing the conclusions of the research in Chapter 3. By understanding the ability of siderite to form in solution, and its abundance within that solution, the ease at which siderite ought — kinetically — to precipitate may be deduced. In conjunction with solid sample analyses, this prediction of siderite precipitation may be tested. For any experiment that yielded $\Omega_{siderite}$ levels of above 0, a solid precipitate kinetically ought to have formed, and the presence or absence of such a precipitate is the crux of this research.

3.5. Amorphous silica

An additional mineral to reach supersaturation (i.e. implying a precipitate) was amorphous silica. Amorphous silica is a form of silicon dioxide (SiO_2) in non-crystalline form that often appears gel-like and cannot be identified via XRD or FT-IR due to its lack of a crystalline structure.

A broad discussion of the Ω_{silica} will now be discussed based on the trends within the graphs of Figure 9.

Aside from the anomalous 180612, and an anomalous datapoint in 180829, Ω_{silica} generally remains constant across the course of an experiment for all pHs and dissolved CO_2. One exception is for 180628, where Ω_{silica} can be seen to decline for 2 0.5 and 2.10. This corresponds with a slight decline in dissolved Si levels (Figure 6) while pH remains constant (e.g., 6.404 to 6.427 corresponds to 5.388 and 7.803 mmol/kg of Si respectively for 2 1.0). The level pH but changing Si levels suggests, unlike $\Omega_{siderite}$, that dissolved Si is the dominant control over Ω_{silica} rather than change in pH. This is reflected in the constant levels for Ω_{silica} for 190423 Fa and Fo, where pH increases to maximum 8.

Overall the following conclusions maybe gathered from a study of Figure 9:

- Amorphous silica saturation is strongly controlled by dissolved Si levels
- pH variation has a negligible effect on Ω_{silica}
- Ω_{silica} remains broadly constant over the course of all non-anomalous experiments: this is consistent with their dissolved Si levels in mmol/kg
- Ω_{silica} is higher for experiments begun at pH 2, likely owing to the heightened release of Si into solution under acidic conditions
- There is very little Ω_{silica} difference between dissolved CO_2 levels, and where there is, this reflects dissolved Si levels.

3.6. ICP-OES conclusions

The study of relative abundances of elements released into solution has proved extremely valuable in understanding the evolution of solid substrate break-down and dissolution over the course of the experiment, and the subsequent trends of elemental release. However, Ω is only an estimate of actual mineral precipitation based on kinetic theory and calculation, and does not directly reflect the actual solution chemistry. To understand whether precipitates formed as kinetically expected,

a thorough survey of the solid material at the end of each experiment must be conducted. The next section of this appendix will cover all solid sample analyses.

4. Solid results

In this section, the results of all the analytical techniques employed to study the solid substrates used in experiments will here be discussed. This includes X-ray Diffractometry (XRD), Scanning Electron Microscopy (SEM) including EDS, and Fourier Transform Infrared spectroscopy (FT-IR). Each technique will be discussed in turn, and graphs/images relating to each experiment and sub-experiment within discussed. Overarching conclusions will be drawn for each section, which form the basis of information used for Chapter 3, which discusses scientific conclusions drawn from the research. This section, however, is primarily descriptive, with only initial explanations offered to understand the results discussed.

4.1. X-Ray Diffractometry

X-Ray diffractometry, or X-Ray crystallography (XRD) is an analytical technique that uses X-ray beams to understand the molecular structure of a mineral. It works by releasing X-rays upon a sample, then recording the pattern and intensity of x-rays that are diffracted upon contact with the sample. The diffraction pattern corresponds to specific molecular structures that, in turn, correspond to a specific mineral or element structure. Thus, the returned diffraction pattern may be though too as a diagnostic 'fingerprint' or signature of a particular mineral or element, which makes XRD extremely valuable in mineralogy as a high precision analytical technique.

In this thesis, XRD was used to analyse solid samples from every experiment due to this extreme precision. The instrument at the University of Oxford used in this study, a PANalytical Empyrean Series 2 powder X-Ray diffractometer, uses a Co Kα source, was operated at 40 kV and 40 mA, and was scanned between 5-65 2Ø. This section describes the signatures returned by XRD

analysis and what minerals these signatures correspond to as identified by this built-in mineral database within the PANalytical instrument. Key diagnostic peaks are noted on the corresponding figures, and to emphasise similarity between sub-experiment signatures, pale grey vertical boxes highlight certain recurring peaks across the signatures. Lone peaks that stand outside of the dominant signatures are labelled with their peak (Ångstrom) number and are discussed.

4.1.1. 180123

The graphs of all 6 sub-experiments for 180123 (Figure 10) correspond to fayalite — the sole mineral that was present in the experiment. 5 key diagnostic peaks for fayalite are highlighted in pale grey, with their corresponding peak numbers attached. These peak numbers are identical often to three decimal places, but slight, sub-decimal place variation is normal and acceptable in peak diagnosis.

2 distinct regions of the graphs sometimes display peaks that do not correspond to fayalite. These are the 6.1160/6.2293 peak — barely visible — of low pH 2 and high pH 6, and the ~3.3 peak for low pH 2, 4, and 6, and high pH 2. In both peak's cases, the peaks are so small that any mineral presence must be extremely small. In such cases it is helpful to cross-correlate with FT-IR and SEM, which may pick things up in higher resolution.

4.1.2. 180203

The graphs of all 6 sub-experiments in Figure 11 for 180203 correspond to fayalite — the sole mineral that was present in the experiment. 5 key diagnostic peaks for fayalite are highlighted in pale grey, with their corresponding peak numbers attached.

The two peaks found in 180123 sub-experiments that do not correspond to fayalite are also present in 180203 sub-experiments, which — as a direct repeat of 180203 but run only for 10 hours — shows that these non-fayalitic components formed rapidly. The presence of the peaks in different sub-experiments to 180123 suggests the minerals may be forming in all sub-experiments but in such low quantities as to lie below detection limit, or to be within the 0.01 g sample that

was analysed. Only one sub-experiment — high pH 4 — displays the peak at 6, while low pH 4 (again), high pH 2 (again), and high pH 4 all display the 3.3 peak.

An additional unidentifiable peak at 1.7002 was identified for low pH 6. As pH 6 experiments showed very little activity, including pH change, Eh change, or release of elements into solution, this peak is attributed to either contamination of the very small sample size or to an analytical anomaly.

4.1.3. 180310

Due to time and funding constraints, and the well-constrained analysis of solids from the identical experiments 180123 and 180203, XRD analysis was not conducted for this experiment.

4.1.4. 180313

The graphs of all 6 sub-experiments in Figure 12 for 180313 again correspond to fayalite — the sole mineral present in the experiment. 5 key diagnostic peaks for fayalite are highlighted in pale grey, with their corresponding peak numbers attached.

The two peaks found in the 180123 and 180203 experiments that do not correspond to fayalite are also present: the 6 peak for 2 0.5 and 4 0.1, and the 3.3 peak for all but 4 0.5. As with the two earlier experiments analysed, these peaks probably represent minute amounts in all experiments and only appear in some due to it being present in sufficient quantities to enable detection, or to its presence in a sample size that is itself +0.03% of a sub-experiment's total solids.

An additional peak at 4.6596 appears in 2 0.1.

4.1.5. 180406

The graphs of all 6 sub-experiments in Figure 13 for 180406 again correspond to fayalite. 5 key diagnostic peaks for fayalite are highlighted in pale grey, with their corresponding peak numbers attached.

The 3.3 peak returns for 2 0.1, 2 1.0, and 4 0.1, likely for reasons discussed earlier. The 6 peak is not present, nor the 4.6596 for 2 0.1 previously. In 4 1.0 there is a new peak at 1.7620,

straddling the far larger 1.7781 that represents the signature for fayalite. It is possible that this very minor peak is part of the fayalite peak distribution, but otherwise, for a lone peak and very minor at that, this peak could be due to contamination of the sample.

4.1.6. 180612

All 6 sub-experiments for 180612 remain pure fayalite and forsterite, with no unidentified peaks. While the graphs in Figure 14 each appear distinct from the others, this is due to the differing ratios of fayalite and forsterite, of which were randomly included in the sample. For sub-experiment 2 1.0, insufficient amounts of solid sample were present for the XRD to ascribe to one mineral (only two peaks overall were identified). The lack of solids from this experiment was due to a leakage within the vacuum pump system to extract solids from solution at the experiment's termination — a significant amount of solution, and with it suspended sediment, was lost. However, given the anomalous nature of this experiment, and the continuous Fa/Fo results of the surrounding sub-experiments, the lack of data is here acceptable.

4.1.7. 180628

The graphs of all 6 sub-experiments in Figure 15 for 180628 correspond to a combination of fayalite and forsterite — the two minerals present in the experiment. Given that the relative ratios of fayalite to forsterite are entirely random, the sample of ~0.01 g scooped from a total of 3.344 g, the relative ratio of fayalite to forsterite peaks across sub-experiments is variable, hence the variation between sub-experiments regarding peak intensity. What is critical, however, is the absolute position of the peaks. Most notably, forsterite displays a strong peak at 5.1327 and this is reflected in all six 180628 sub-experiments to varying degrees, being strongest in 2 0.5, which is consistent with each sample having random ratios of fayalite to forsterite in the sample selected for XRD. A prominent peak for fayalite is at 1.7785, which again may be found to varying intensity in all six sub-experiments of 180628.

The 6 anomalous peak appears again, in 4 1.0, as 6.009. The 6 peak anomalies are not as well constrained as the 3.3 peak, which could suggest this supposed mineral signature is an artefact

of the sampling procedure mistakenly taken up at roughly this position. The 3.3 peak returns for 2 0.1 and 4 0.5, as 3.3424 and 3.3776 respectively, showing this peak's enduring constraint across multiple experiments, and suggesting in comparison to the 6 peak that this may be a real presence — albeit as contamination, as has been discussed.

4.1.8. 180829

The sub-experiments of 180829 as seen in Figure 16 consistently show fayalite and forsterite, with all peaks accounted for by these two minerals. The solids in solution therefore did not react to form any new minerals. Similarly to 180612 — also a Fa/Fo-bearing experiment that showed only Fa/Fo in XRD — the different sub-experiments' XRD diffractograms differ slightly in peak intensity, but the peaks themselves always lie in the same positions. This can be seen by following the grey lines down and noting the broadly-similar Ångstrom values for the different peaks.

4.1.9. 181004

The graphs of all 4 sub-experiments for 181004 in Figure 17 correspond to fayalite — the sole mineral present in the experiment. 5 key diagnostic peaks for fayalite are highlighted in pale grey, with their corresponding peak numbers attached.

The 3.3 peak occurs in high pH 4 as 3.4057, while several new peaks are seen in low pH 2: 3.5042, 2.7951, 2.5376, and 3.3424.

4.1.10. 181029 Fa

This is a very unusual experiment for remaining unstable in pH and Eh during experimentation, in particular with the pH 2 sub-experiments, where pH remained exceptionally and anomalously low. However, the pH 2 experiments in Figure 18 show XRD diffractograms broadly consistent with those of previous Fa-bearing experiments, excepting 2 1.0, where too-little sediment for analysis was available, owing — as with the equivalent in 180612 — to a leakage during the filtering phase. Two anomalous peaks in 2 0.1 are 3.3734 and 2.9571.

It is the pH 4 sub-experiments that here display unusual activity. Both 4 0.1 and 0.5 have more anomalous peaks than previously seen in diffractograms for this research, and of the possible mineral fits detected by the built-in database of the XRD, two types of iron carbonate were discoverable as possible fits to satisfy several of the anomalous peaks. This was chukanovite ($Fe_2(CO_3)(OH)_2$, metastable with respect to siderite, for 4 0.1 and siderite for 4 0.5. The peaks for which these minerals satisfy are highlighted in red.

Given that the fayalitic signature remains dominant for the diffractograms of 4 0.1 and 0.5, any chukanovitic or sideritic component must be very minor and may evade visual observation in SEM. FT-IR, however, is higher resolution than XRD, but the characteristic peaks for these Fe(II) carbonate minerals are not visible in the FT-IR spectra for these two sub-experiments. Equally, the amounts of carbonate material could be so minute they were only present in the small sample used for these XRD samples. In which case the data cannot be reproducible, and in the absence of confirmation the carbonate seen in sub-experiments 4 0.1 and 4 0.5 of 181029 Fa remain inconclusive and not taken as definitive evidence of fayalitic carbonation under the applied experimental conditions.

4.1.11. 181029 Fo

Like 181029 Fa, the experiment 181029 Fo in Figure 19 was anomalous and was repeated as 180423 Fo, which followed trends in pH, Eh, and dissolved elemental levels, that correlated well with similar experiments. Thus 181029 Fo is given little bearing, as it is possible a new experimental set-up technique, applied both to 181029 Fa and Fo, allowed steady fluid and CO_2 leakage that altered experimental conditions beyond value.

For sub-experiment 2 0.1, insufficient solid sample was extracted from the filtration that occurred at the experiment's termination, possibly owing to a leak within the vacuum pump apparatus that allowed solid-bearing fluids to escape the mechanism without passing through the filter paper. For 2 0.5 so little sample was available that the diffractogram is diminished, with few peaks identified by the in-XRD database. The signature, nevertheless, matches that of fayalite and

forsterite in combination. Sub-experiment 2 1.0 yielded sufficient solid material for a thorough diffractogram, and its signature also reflects that of Fa/Fo with one anomalous peak at 6.0009.

The pH 4 sub-experiments also display Fa/Fo in varying ratios, and show several anomalous peaks: 3.7035, 3.3344, and 3.1324 for 4 0.1; 1.6862 for 4 0.5; and 6.2314 for 4 1.0.

4.1.12. 181205

The graphs of all 4 sub-experiments for 181205 in Figure 20 correspond to a combination of fayalite and forsterite — the two minerals present in the experiment. Given that the relative ratios of fayalite to forsterite are entirely random, the sample of ~0.01 g scooped from a total of 2 g, the relative ratio of fayalite to forsterite peaks across sub-experiments is variable, hence the variation between sub-experiments regarding peak intensity.

The 6 peak anomaly appears in low pH 2 as 6.1893. As this is now a common feature of the XRD graphs, its presence appears to represent something that has occurred in most if not all experiments and so does not have significant bearing on the overarching conclusions of the XRD study.

Several additional non-fayalitic or -forsteritic peaks are also present in low pH 2, as with this sub-experiment in the pure fayalite low w/r experiment 181004: these are 4.6577, 4.1801, and 3.3690. Of these, none were shared by the 181004 equivalent, except possibly a peak at 3.5042, but in XRD diffractograms the 0.2 difference in position may equate these as two distinct minerals.

All 4 181205 sub-experiments show the 3.3 anomaly. In low pH 4, the only other non-Fa or -Fo peak is 3.1397, but both high w/r ratio experiments show no other anomalous peaks besides at 3.3.

4.1.13. 190121

Experiment 190121 in Figure 21 was the first to use high forsterite to fayalite ratios — 9:1 — and this is clearly reflected in the XRD diffractogram where the dominating signature is that of forsterite. All 6 sub-experiments display a particularly dominant peak at ~5.1; 2 0.1 also holds a

dominant peak at 1.8793 that represents fayalite. Few anomalous peaks were detected: 2.8321 in 2 0.1, and 3.2232 for 4 0.5.

4.1.14. 190423 Fa

The peaks across Figure 22 all correspond to fayalite.

4.1.15. 190423 Fo

The peaks across Figure 23 all correspond to fayalite and forsterite.

4.1.16. Conclusions

Several overarching conclusions may be drawn from this study of XRD signatures, which forms part of the basis of the conclusions of Chapter 3. While different experiments contained differing isolated peaks, these were so minor as to be considered contamination, artefacts of the XRD process, or oxidation products from the brief exposure to air during transfer from the glove box to the XRD. These peaks aside, the initial substrate for the experiments — fayalite or a fayalite-forsterite mix — remains intact and without the presence of other minerals anticipated to form under experimental conditions (e.g., siderite). Most simply put, the experiments began with fayalite or fayalite/forsterite, and ended with fayalite or fayalite/forsterite.

While the in-XRD database presented chukanovite and siderite as possible resolutions for several peaks within sub-experiments 4 0.1 and 4 0.5 of 181029 Fa, several other possible resolutions were a match, including fayalite and forsterite. As such carbonates were not detected in other solid-phase analyses — including the higher-resolution technique FT-IR — their presence cannot be substantiated, thus this is not considered evidence of Fe(II)-carbonate formation in these experiments.

As the XRD employed in this study had a detection limit of 1 %, if other minerals had formed, they would be in extremely small amounts. The vast majority of the fayalite or fayalite/forsterite — if not all — remained unaltered by the experiment. This means that the experimental conditions explored here are not conducive for the formation of siderite or other carbonates when applied to the context of Mars.

4.2. Fourier Transform Infra-Red Spectroscopy

Fourier Transform Infra-Red (FT-IR) spectroscopy is the highest-resolution technique used in this thesis, and is used to obtain an infrared spectrum of absorption for the solid samples collected during experimentation.

FT-IR analyses were acquired in the transmission mode of an in-house PerkinElmer Frontier mid-IR spectrometer using powdered samples. Measurements were collected by combining ~0.001 g of sample with ~0.2 g optically-transparent KBr powder (a sample to KBr ratio of ~1:200). The KBr powder and sample were ground together and compressed into pellets at 7 tonnes and analysed within 15 minutes of exposure to air. Collected measurements were analysed over 400 to 4000 cm^{-1} at 1 cm^{-1} resolution, and the detector used was a deuterated triglycine sulphate with a KBr window and beam-splitter.

In this section the trends within each experiment's FT-IR spectra will be discussed, and overarching conclusions drawn that will be used in support of the data interpretation of Chapter 3. The primary objective of using FT-IR was to search for nanoscopic levels of siderite that may have been overlooked by the lower-resolution XRD.

Figure 24 (a) is adapted from the RRUFF Online Database (ID: R050262.1) as the type signature for pure siderite in FT-IR, and is here included as a reference for the signature expected, where siderite to be present. Note the clear absorption bands that may be distinguished at 800, 900, and 1100-1500 cm^{-1}, which together are diagnostic of siderite. These absorption bands are demarcated by light-grey columns in all experiments' FT-IR signatures for reference.

In Figure 24 (b), the FT-IR signatures for pure fayalite and (c) for pure forsterite are displayed as reference for the pre-experimental signature of these materials. Note the especially prominent absorption at 500, 600, and 900 cm^{-1} for fayalite and 550, 650, and 900 cm^{-1} for forsterite. The inversion features in (b) and (c) correspond to absorbed water in the KBr pellets during FT-IR analysis, which during background subtraction and noise removal of the spectra

have become incorrectly inverted. This does not affect the validity of the spectra themselves since these inversions only affect the water absorption regions. The FT-IR signatures of post-experimental solids may be compared to these references to observe any precipitates.

4.2.1. 180123

No CO_2 was dissolved within the waters of 180123; this experiment was designed to understand the changes that occur when fayalite is reacted with acidic water. As such, siderite is not anticipated in this experiment, but other minerals — e.g., magnetite — could form. No precipitates were identified in XRD, and nor were any in FT-IR, as can be seen in Figure 25, which shows all six sub-experiments in order of low rock:water ratio pH 2, pH 4, pH 6, then high rock:water ratio pH 2, pH 4, and pH 6. Comparisons with Figure 24 (b) show all sub-experiments' solids closely match this initial signature.

No precipitates were found within the FT-IR signature for all 180123 sub-experiments, which agrees with XRD results.

4.2.2. 180203

The FT-IR signatures for this experiment, seen in Figure 26 match those of 180123, of which 180203 is a repeat that lasted 12 hours. No new minerals have precipitated and the FT-IR signatures for all sub-experiments match that of pure fayalite.

4.2.3. 180313

For the first experiment to use dissolved CO2, the FT-IR spectra displayed in Figure 27 are ordered pH 2 0.1 bar, 0.5, 1.0, pH 4 0.1, 0.5, and 1.0. No absorption within the three bands diagnostic for siderite (marked in light-grey) are seen. This is consistent with XRD results and suggests no iron carbonate formed within these experiments.

4.2.4. 180406

As seen in Figure 28, no absorption takes place within the bands for siderite diagnosis, suggesting this mineral did not form in any of the experiments within 180406. The spectra for 2

0.5 and 1.0, however, deviate from the trends thus far seen: notably, the main absorption, which usually centres around 900 cm^{-1}, is shifted to centre around 1100 cm^{-1} for both 2 0.5 and 1.0.

4.2.5. 180612

As with previous experiments, the spectra for 180612, as seen in Figure 29, show their main absorptions centred at ~500 cm^{-1} and 900 cm^{-1}, with no troughs centred for any of the three diagnostic for siderite. This is consistent with XRD results that did not indicate the precipitation of any new minerals. As both fayalite and forsterite were present in these experiments, the spectra for 180612 — and others bearing forsterite — deviate slightly from the pure fayalite spectra previously seen.

4.2.6. 180628

In Figure 30, absorption is again centred at ~500 and 900 cm^{-1}, with an additional minor absorption at ~1100 cm^{-1} for 2 0.5 and 2 1.0. No absorption occurs in any of the three bands diagnostic for siderite, suggesting that no new minerals formed. This is consistent with XRD results for these experiments.

4.2.7. 180829

The FT-IR spectra for 180829, as seen in Figure 31, show absorption mostly at ~500 and 900 cm^{-1} as has been seen previously. Three experiments — 2 0.1, 2 0.5, and 4 0.5, show a very minor absorption centred at ~1450 cm^{-1}. The lack of absorption within any of the three bands diagnostic of siderite suggests this did not form, agreeing with XRD results for these experiments.

4.2.8. 181004

181004 was the first low rock:water ratio experiment used, which contained pure fayalite. As seen in Figure 32, absorption centres at ~500 and 900 cm^{-1} for the four sub-experiments, which in order down are 1:1 rock:water ratio pH 2, 1:10 rock:water ratio pH 2, 1:1 rock:water ratio pH 4, and 1:10 rock:water ratio pH 4. Minor absorption appears in all sub-experiments at 1250 cm^{-1}, within the largest band for siderite absorption, but the absence of absorption in the two other

diagnostic regions (marked light-grey) and the extremely minor absorption within this largest band does not suggest the diagnosis of siderite.

4.2.9. 181029 Fa

181029 Fa returns to the earlier layout of pH 2 0.1, 0.5, 1.0, pH4 0.1, 0.5, and 1.0 bar experiments, as seen in Figure 33. For 2 1.0, unfortunately so little solids were extracted from this experiment due to a fault with the vacuum pump that no FT-IR spectra could be obtained. For the remaining five, the typical main absorptions at ~500 and 900 cm^{-1} may be discerned, as well as a minor absorption at ~1400 cm^{-1} for all five, strongest for 4 0.1. No trace of any corresponding new mineral was found in XRD or by SEM.

No siderite was identified in any of the sub-experiments of 181029 Fa.

4.2.10. 181029 Fo

As seen in Figure 34, the main absorption for all sub-experiments are at ~500 and 900 cm^{-1} like all previous experiments, but a weaker absorption at 1400 cm^{-1} may be discerned for all sub-experiments excepting 2 0.5. This is strongest for 2 0.1. This does not match the largest absorption for siderite, which centres at 1250 cm^{-1}, nor is absorption found for either of the other two bands (marked light-grey). Siderite was not formed in this experiment, which is consistent with XRD results.

4.2.11. 181205

In Figure 35, the four spectra represent experiments 1:1 rock:water ratio pH 2, 1:10 pH 2, 1:1 pH 4, and 1:10 pH 4. The familiar absorption at ~500 and 900 cm^{-1}. No minor peaks can be discerned in the 1100-1500 cm^{-1} band, nor in either of the other two bands diagnostic of siderite. This mineral did not form in any of the sub-experiments of 181205, consistent with XRD results.

4.2.12. 190121

In this experiment, 90 % forsterite and 10 % fayalite was used, meaning the dominant spectra in Figure 36 represents forsterite. This explains the far shallower absorption centred at 900 cm^{-1}. No absorption is seen at any of the diagnostic bands for siderite, excepting a minor

absorption for 4 0.5 at 1400 cm^{-1}. This is consistent with XRD results and suggests this mineral did not form in experiment 190121.

4.2.13. 190423 Fa

190423 Fa contained only fayalite, as seen in Figure 37, although there are minor absorptions in the siderite grey zone for 2 0.5, 2 1.0, and 4 0.5. These do not bear any similarity to the siderite peak in Figure 24, nor were any Fe(II)-carbonate minerals identified by any other means, suggesting that this could be a H_2O absorption peak like the distinctive absorption troughs beyond 2000 cm^{-1}. No new minerals were identified via FT-IR for 190423 Fa.

4.2.14. 190423 Fo

In Figure 38, the forsterite and fayalite mix of its primary substrate continues to hold for all six sub-experiments. No new minerals were identified and there are no unexplained absorption troughs in any of the spectra in Figure 38.

4.2.15. Conclusions

The following overarching conclusions may be taken from this section discussing the FT-IR signatures of all fayalite (± forsterite)-bearing experiments. These conclusions form part of the basis of the discussion in Chapter 3:

- No siderite was identified in any of the experiments' FT-IR spectra. As FT-IR was the highest resolution technique employed in this study, this suggests no siderite formed even in nanoscopic quantities under the conditions explored here
- The dominant absorptions for the samples were at ~500 and 900 cm^{-1}, which is the same as the spectra for fayalite (or 50:50 fayalite/forsterite)
- The samples were unaltered from their fayalite/forsterite pre-experiment mineralogy

As FT-IR was the highest resolution technique used to identify crystals, the lack of identified siderite strongly favours this mineral having not formed under the experimental conditions explored here. However, some precursor mineral phases to siderite may bear carbon

but are amorphous, and as such are invisible to both XRD and FT-IR, which rely on crystallography. Amorphous iron carbonate (AFC) is a possible carbon-bearing phase that may form before rapidly transforming to siderite (Jiang and Tosca, 2019). Thus, to assess whether this phase formed in the experiments' solids, Scanning Electron Microscopy is now employed to search for non-crystalline mineral phases.

4.3. Scanning Electron Microscopy

The last solid-phase analytical method to be employed upon the samples discussed in this thesis was Scanning Electron Microscopy. A Scanning Electron Microscope (or Scanning Electron Microscopy; SEM) is a high resolution microscope that uses a focused beam of electrons to produce an image up to nanometres in resolution. In this thesis, the detector used was an Everhart-Thornley Detector (ETD), which uses the intensity of detected electrons excited by the initial electron beam to produce a view of sample topography, and samples were analysed upon carbon-rich adhesive paper attached to aluminium stubs, which were prepared within the glove box to prevent oxidation. To prevent charging, samples were gold-coated to produce a gold layer 9 nm thick. SEM is used in this thesis to search for micro-crystalline structures diagnostic of particular minerals — for example, rhombs for siderite; glassy, conoidal fracturing for forsterite; porous, 'fluffy' textures for fayalite — at a resolution of up to ~5 μm. While all samples were analysed with XRD and FT-IR, only selected ones were imaged with an SEM as a means of calibrating the accuracy of these higher-resolution techniques by manually searching for the diagnostic mineral structures of siderite or other carbonate phases (e.g., chukanovite and amorphous Fe-carbonate, which are crystallographically transparent as they do not have a crystal structure).

In this section, SEM images taken of a sample of selected sub-experiment will be discussed regarding their morphology. This includes the shape of the individual grains, their texture, their porosity, their size, their interaction with other grains, and any other notable features or characteristics. Given the number of experiments and sub-experiment discussed within this

chapter, only selected experiments will be discussed but this is deemed a representative sample after extensive scanning of the samples under the SEM.

4.3.1. Unreacted fayalite and forsterite

Unreacted fayalite and forsterite were first observed to gain a thorough understanding of the starting morphology before addition to CO_2- or non-CO_2-bearing fluids. Grain size was typically ~10-200 μm for both, and individual particles could be easily discerned against the visually-black carbon background.

For fayalite, morphology typically consists of a porous, granular, sometimes wispy texture as seen in Figure 39 (a) and (b), where larger grains are coated in parts by finer material of the same composition. The grains appear angular and irregularly-shaped with no obvious axes, and are often studded with small depressions that are likely pores created by the escape of air during synthesis under high temperature. In Figure 39 (b), a spongey, vermicular texture can be seen.

For forsterite, morphology typically consists of a smooth, uniform, glassy, concoidally-fractured texture (Figure 39 (c) and (d)), and is highly angular. This is consistent with the type of forsterite purchased, which was gem-grade peridot, formed by the volcanic eruption of molten material into air, where it is quickly quenched to a green glass. When analysed via EDS, small quantities of Fe are present (~5 wt %) agreeing with XRD detection.

With this understanding, the SEM images of post-experiment solids can now be compared to these pre-experiment images, and be assessed for mineral precipitation/dissolution over the course of experimentation.

4.3.2. 180123

Experiment 180123 was selected for SEM analysis as a non-CO_2-bearing, short-duration experiment involving pure fayalite. In Figure 40 (a) and (b), two typical textures from this experiment, also observed in the similar experiment 180203, can be seen. In both images a knobbly texture is visible that appears to be the product of dissolution. Particularly in (b), parts of the surface appear to have been removed from the outside in to generate the smoother, better-rounded

surface than seen in Figure 39 (a) and (b). While difficult to discern, no new mineral growth is apparent upon these surfaces. Instead, the texture is dominated by the scouring and smoothening of the existing fayalite. This could be due to acid-scouring, which 'eats' in at a mineral surface, and could account for the smoother, rounder texture than seen in the unreacted fayalite.

No new minerals were identified via SEM for the solids of the non-CO_2-bearing experiments 180123 and 180203. This agrees with XRD and FT-IR data for the same samples.

4.3.3. 180313

The solids from Experiment 180313, the first to use CO_2-bearing fluids, also shows no evidence of new mineral precipitation. In Figure 40 (c), the effect of acid-scouring is particularly pronounced and has weathered the fayalite grain's surface into parallel grooves; this effect was found across all sub-experiments within 180313. In (d), these grooves can be seen more like ridges that taper away from the grain where the grain has been weathered from its edges inwards. In both c and d, smaller grains can be seen settled atop the larger one. These do not appear attached and are fines that adhered to the larger grain. Other grains appear entirely unaltered, and are discussed in the next section.

No new minerals were identified via SEM for the solids of the CO_2-bearing experiment 180313, consistent with XRD and FT-IR for these samples. A repeat of this experiment, 180406, is now discussed to highlight the morphology of the non-acid-scoured grains, which were observed in both experiments.

4.3.4. 180406

This experiment, a repeat of 180313, showed the same acid-scoured texture across some grains, as well as (as in 180313) others that appeared entirely unaltered. In (e) and (f) of Figure 40, two similarly-sized grains at ~10 μm across at their longest axis. Both show finer grains settled upon their surfaces, but otherwise appear barely altered from the unreacted fayalite of Figure 39, though they are possibly smoother in texture. This suggests some fayalite particulates were barely

affected under the experimental conditions of 180313 and 180406, which bore CO_2 in solution up to 1.0 bar.

No new minerals were identified via SEM for the solids of 180406, consistent with XRD and FT-IR analyses of the same samples.

4.3.5. 180628

For the forsterite-bearing experiments of 180612, 180628, and 180829, little change was observed to the forsterite grains when observed in all these experiments. The image in Figure 40 (g), a ~60 μm across forsterite grain from experiment 180628, sub-experiment 4 1.0, exemplifies this when compared to the unreacted forsterite of Figure 39 (c) and (d). The smooth, glassy texture remains, with the prominent lines trending northwest-southeast being conoidal fracturing of this glass. Fayalite grains (h) assume the same texture as for the Fa-bearing experiments of 180313 and 180406.

No new minerals were identified after thorough searching of all sub-experiments within 180612, 180628, and 180829 via SEM. This is consistent with their XRD and FT-IR spectra.

4.3.6. 181004

181004 was the first low water-to-rock ratio experiment (1:1 or 1:10), and reacted solely fayalite for a period of ~2 months. Despite this difference to previous experiments, the post-experiment fayalite when analysed via SEM shows no difference from higher rock:water ratio experiments. For grains ~10 μm across in Figure 40 (i), the same blocky, sub-angular to angular shape appears for all grains, and no material appeared to deviate from this trend to suggest the precipitation of any new minerals. This is also true for larger grains such as the ~15 μm across one in Figure 40 (j). The large grain shown is representative of the jumbled, interconnected, blocky appearance of larger grains that appear as an amalgamation of smaller ones, which are in actuality loosely connected smaller grains of the finer material.

No new minerals were identified in the sub-experiments of 181004 when analysed via SEM. This is consistent with their spectra from XRD and FT-IR.

4.3.7. 181029 Fa and 181029 Fo

These were two experiments that behaved anomalously, where pH remained unusually low in a manner that was only reflected in the similarly-behaved 180612 and unrepresentative of the overall trends of similar experiments. The grains in Figure 40 (k) and (l) are representative of the typical material found when these experiments were analysed via SEM. Despite the difference in experimental pathways, the solids are similar to the typical fayalite and forsterite grains of other experiments, such as seen in Figure 40 (i). The material is blocky, in the case of fayalite, and highly angular, in the case of fayalite, and no new minerals were identified after extensive searching. This is consistent with XRD and FT-IR analyses for both of these experiments.

4.3.8. 190121

This experiment was dominated by forsterite (a forsterite-fayalite ratio of 9:1), yet again the grains when analysed via SEM showed no dissimilarity from all previous experiments. No new minerals were formed, and forsterite grains remained highly angular, glassy, and without the growth of new minerals, as seen in both Figure 40 (m) and (n), which represent typical material found. For Figure 40 (m), the conoidal fracturing typical of glassy materials is clearly visible even at scales of ~500 nm apart. At a larger scales, the ~250 nm grain in Figure 40 (n) shows fine dust having settled upon it, which up close appear as the smaller particle atop the background of Figure 40 (m).

No new minerals were found within the solids from experiment 190121 when analysed via SEM. This is consistent with its XRD and FT-IR analyses.

4.3.9. 190423 Fa and 190423 Fo

The first time possible new minerals were identified via SEM was in the experiments 190423 Fa and 190423 Fo. Both 190423 Fa and Fo were repeats of the 181029 Fa and 181029 Fo experiments, which ran for two months with pure fayalite (Fa) and 50:50 fayalite/forsterite (Fo). 181029 Fa was the first long-duration pure fayalite experiment, while 181029 Fo was a repeat of

180628. As both 181029 experiments behaved unusually, these were repeated as 190423 Fa and Fo, respectively, and ran for approximately 80 days.

Possible new minerals were found in solids from all sub-experiments of 190423 Fo, and 4 1.0 of 190423 Fa. These possible new minerals are displayed in Figure 41, and display striking antler-like structures ~100 nm thick that brachiate to follow the edges of knobby protrusions upon minerals. They appear exclusively upon fayalite grains; however, as the structures were only found in the forsterite-bearing experiment and not its pure fayalite equivalent, this does not preclude a formation origin from forsterite material; further analytical methods cover this. The 'antlers' have sharply-defined edges as triangular branches as seen in Figure 41 (a) that appear to have grown around the edges of minerals. While sometimes they can be followed as unbroken threads, as in (a), sometimes the branches appear broken into smaller pieces (Figure 41 (b)) or form more complex shapes, such as the skeleton of a cube or pyramid in the same image. The branches can be traced for a length of at least 20 μm in places, as in Figure 41 (c), where the mineral is not associated on any host substrate, suggesting they form weakly upon a host mineral and are fragile and able to be broken off and transported with minimal force. At higher magnification (Figure 41 (d)), the sharp edges are still clearly present. The origin of the threads is possibly from the mineral itself: following the stalks to the right of Figure 41 (e) and they possibly grow from this background mineral, where the threads appear to emerge from the edge of a mineral face so closely that it could be a dissolution pattern rather than precipitation. The threads often follow the outline of mineral protrusions, or their sharply curving shapes suggest formation then separation from around an initial host mineral. This suggests they formed in interstitial mineral spaces.

Several other interesting mineral structures were identified in 190423 Fo. Closely associated with the antler-like structures were extremely acid-scoured surfaces of the same fundamental texture seen in Figure 40 (c) and (d), but seen three-dimensionally and far more dissolved. In Figure 41 (f) is an exceptional example of this texture, where the mineral has been dissolved into flake-like filaments not just on the surface as previously seen in other experiments

(e.g., Figure 40 (c), (d)), but right through the mineral to the extent that the mineral is barely a coherent structure. These highly flaked minerals are often associated with the antlers, as can be seen in Figure 41 (f) to the upper right. Another good example of the flaky texture is seen in Figure 41 (g), where fibres are as fine as <100 nm. Figure 41 (h) provides context for these high-resolution features in a grain ~25 μm across, where both the antler and flaky textures are found adjacent to one another.

Additionally, unusually spherical structures were also only found within the 190423 Fo experiments. The particular specimen shown in Figure 41 (i) was found in the sub-experiment pH 2 0.5 bar CO_2 and is ~750 nm in diameter. The crenulated, vermicular texture on its surface at the nanometre scale is owing to its gold-coating. This sphere could be new mineral growth as it does not appear flaked or scoured, and lies atop the surrounding mineral upon which it is associated.

Other possible new minerals were found as minute lines of aligned, platy minerals upon grains of fayalite in the 190423 Fo pH 4 experiments. These can be seen up close in Figure 41 (j) aligned in a north-north-west to south-south-east direction, each ~200 nm long and ~20 nm across, brighter than the background mineral, but with the same crenulated, vermicular texture just about discernible at this resolution. In Figure 41 (k) these platy minerals are contextualised at lower resolution and can be clearly seen across the face of this fayalite grain. A larger forsterite grain in Figure 41 (l) does not show these aligned plates; they were only found on fayalite grains.

Lastly, additional dissolution patterns were identified only in the pH 4 sub-experiments of 190423 Fo. Seen in Figure 41 (m), these are discrete, circular pits in fayalite grains ~50-100 nm across upon grains affected at their peripheries by the fibrous flaking texture observed in Figure 41 (f) and (g). The bright, rod-shaped lamellae upon this mineral face could be pieces of these flakes having cleaved loose, as unlike the aligned plates of Figure 41 (j) they are randomly oriented and sized, with those larger appearing closer to the flaky texture towards the image's top. Other unusual dissolution textures only seen in the pH 4 sub-experiments of 190423 Fo are the bright, aligned, barb-like needles seen in Figure 41 (e) that follow the same orientation as the flaky texture

seen in the bottom-right-hand corner, suggesting a common erosional origin; and a spongey, non-aligned texture seen adjacent in Figure 41 (n) closely associated with the 'antlers' that can be seen in the context image of Figure 41 (o) as grading into both the flaky and the barb-like texture of Figure 41 (m), suggesting again that this is dissolution of original fayalitic material rather than precipitation of a new mineral. This texture can also be seen in Figure 41 (a), again closely associated with the new mineral growth of the 'antlers'.

Overall, these dissolution (flaky, barb-like, circular pits, and spongey textures) and precipitation (antlers, aligned plates) features were all identified within, upon, or associated with fayalite — by comparison, the forsterite grains appeared as relatively unaltered as all previous experiments. This is exemplified in Figure 41 (p), where a smooth, glassy forsterite grain is adjacent to a similarly sized fayalite grain, upon which the antlers, flakes, and aligned plates are all clearly visible. The absence of such features in fayalite grains from previous experiments but within a forsterite-bearing set-up suggests the forsterite, while not the source of the new minerals, is intrinsic to their formation, as well as to the formation of the dissolution features. An overarching interpretation of the images from 190423 Fo, as well as all other experiments, will now be discussed.

4.3.10. Conclusions

From experiment 180123, through to 190423 Fa — experiments encompassing both fayalite and forsterite, from 12 hours to over 80 days, with rock:water ratios from 1:1 to 1:250, and with CO_2 levels ranging from 0 to 1.0 bars — no trace of new mineral precipitates, or of mineral dissolution, was identified. This agreed with the XRD and FT-IR results for these experiments that showed unreacted starter material still present with no additional minerals having formed. Under the SEM, these experiments showed fayalite that still displayed the knobbly, lumpy, rounded texture observed when unreacted; for forsterite, the same glassy, concoidally-fractured, highly angular material was also present as it had been seen when unreacted. A vermicular, crenulated texture was found the nanometre-scale for all grains whether reacted or unreacted,

fayalite or forsterite, and this is likely an artefact of the heavy gold coating (10 nm) deposited upon all samples to prevent charging.

Only one experiment showed signs of possible precipitate. Experiment 190423 Fo was the longest running experiment (>80 days), contained both fayalite and forsterite, and involved dissolved CO_2 up to 1.0 bar in solutions with initial pHs of 2 and 4. Upon the fayalite grains within all sub-experiments of this experiment, long, brittle threads ~100 nm across were found, which apparently formed between minerals before being dislodged. Also upon fayalite grains but solely within pH 4 sub-experiments, platy minerals that are likely newly precipitated were found coating the fayalite in aligned patterns. This suggests that experiment 190423 Fo exceeded some saturation limit in all sub-experiments to produce the antler-like threads, and that pH 4 sub-experiments exceeded an additional threshold beyond which an additional mineral could precipitate. Neither of these two minerals have been found in the solids of any other experiment, consistent with the extremely alkaline pH reached in all 190423 Fo sub-experiments, particularly those begun at pH 4.

Given no new minerals were identified in XRD or FT-IR for these solids, they may be non-crystalline. This would include amorphous silica — which according to all ICP-OES analyses is sufficiently saturated to form a precipitate — and amorphous Fe-carbonate (AFC), which is a short-lived precursor to chukanovite or siderite.

EDS (Energy Dispersive X-Ray Spectroscopy) can reveal the composition of objects within an SEM. This is a technique that is vital if the mineralogy of the new precipitates is to be understood, and is discussed in Chapter 3.

4.4. Brunauer-Emmett-Teller Analysis

Brunauer-Emmett-Teller Analysis (BET) is a means of determining particulate average surface area through the adsorption of gas molecules (in this case nitrogen) onto a solid surface. It was employed in this study for use during geochemical modelling.

The BET-surface area of fayalite and forsterite used in all experiments were measured using a Micromeritics TriStar II Plus surface area and porosity analyser with N_2 gas as adsorptive at a bath temperature of −195.850 °C. This was conducted at the Surface Analysis Facility, Department of Chemistry, University of Oxford.

The results were an average surface area of 0.2956 m^2/g for fayalite and 0.0554 m^2/g for forsterite. These values are used in Chapter 3, which discusses geochemical modelling from the experimental results.

5. Geochemical modelling

Detailed results for the geochemical modelling component of this research are here outlined in detail. Table 13 displays again the model parameters first outlined in Chapter 2 (Methods).

5.1. pH

In Figure 42, the evolution of pH is explored across five differing conditions. In blue are the conditions set as 'original' in the model (see Table 13 for full list), which include high rock:water ratio (1:500), high surface area (1000 cm^2/g), high dissolved CO_2 (1.0 bar), and fixed (non-varying) CO_2 levels. Over 30 years, the pH of a solution containing fayalite and forsterite under these conditions can be seen to stabilise at 7.2. Higher pH is reached under conditions where is in an open system (pH 8.2) and where only 0.1 bar of CO_2 is present (pH 7.8). This increase is due to a reduction in acidity in the form of carbonic acid. Lowering the rock:water ratio also has the effect of slightly increasing pH, to 7.4: with more reactant to consume protons within less solution, the solution reaches elevated levels of alkalinity. Decreasing particle surface area decreases the pH achieved by equilibrium (pH 7.1, reached after 250 years), likely due to the reduced area for reactant-solution reaction, which also accounts for this far-lengthier time required for equilibrium to be reached. In Figure 43, it is also apparent that initial reactants of fayalite and forsterite struggle

to dissolve in solution at low surface area compared to models run at high surface area, explaining both the lengthy experimentation period and less complete pathway, reflected both in its lower pH but also lower element and mineral saturation states, as will now be discussed.

5.2. Element concentration in solution

The three graphs in **Figure 44** display the concentration of Fe^{2+}, $SiO_{2(aq)}$, and Mg^{2+} in mmol/kg over the course of the 30-year model. The high alkalinity achieved in both models run with both 0.1 bar closed CO_2 and 1.0 bar open CO_2 experiments produces correspondingly low concentration of all three elements in comparison to conditions of fixed and high CO_2 levels, while a low rock:water ratio enhances them. While all three of these conditions show elevated and rapid reactant dissolution in **Figure 43**, in the case of low rock:water ratio, this model's pH does not climb as high, permitting further dissolution at these more acidic conditions.

5.3. Species saturation state

Lastly, the evolution of several relevant species' saturation states (Ω) over time is modelled in Figure 45. These are AFC, siderite, greenalite, and $Fe(OH)_2$, the latter which is a precursor to magnetite and is known to compete with siderite for free Fe^{2+} (Tosca et al., 2018). Following trends for high pH, modelled conditions with either lower CO_2 than 1.0 bar or open CO_2 levels, where CO_2 almost instantly leaves the system, enabled elevated AFC saturation states relative to higher CO_2 conditions. This is consistent with our experimental results also yielding elevated saturation states for these species when in high pH solutions. In contrast, siderite saturation states fall below those under lower CO_2 conditions, which may reflect siderite's greater dependence on high CO_2: as noted in Figure_AFC_supersaturation, solutions are better able to reach elevated siderite saturation states where higher bars of CO_2 are present. Lowering rock:water ratio enhances both AFC and siderite saturation more effectively and rapidly than altering any other parameter. This

could be due to increased levels of dissolved rock per level of solute, reflected in Figure 44, hence increasing the likelihood of element interaction to form species.

Greenalite reaches the most heightened states of supersaturation of the four discussed species. This reflects our experimental results, where the greenalite line of Figure_greenalite_supersaturation was exceeded more readily than the AFC saturation line of Figure_AFC_supersaturation (25 datapoints for AFC to 83 for greenalite), and is a function of the 6^{th} order of dependence between greenalite saturation state and pH.

$Fe(OH)_2$, a precursor to magnetite, competes as greenalite does with siderite for Fe^{2+}. Under all modelled conditions the saturation state of $Fe(OH)_2$ does not exceed that of AFC, siderite, or greenalite under the same modelled conditions.

5.4. Summary of model

This model feeds into the main findings of Chapter 3, namely that low water-rock environments are more conducive to the formation of Fe(II)-carbonates.

6. Conclusions

In this chapter, a thorough description of the results from each of the both syn- and post-experimental analyses conducted for fayalite/forsterite experiments has been provided. For syn-experimental analyses, this included pH and Eh measurements from the inception to the termination of an experiment, while for post-experimental analyses, this was divided into two categories: 1) analysis of liquid samples, which included ICP-OES analysis of the Fe, Si, and, where applicable, Mg content of fluids extracted at intervals during the experiments; and 2) analysis of solids extracted following experiment termination. This included XRD, FT-IR, SEM, EDS, and BET analyses.

The main reason for employing so many varying techniques was to assess the precipitation or theoretical likelihood of precipitation of the iron carbonate siderite. For ICP-OES, siderite was super-saturated with respect to the solution for many of the ICP-OES samples. However, of the solid experimental samples analysed, siderite was not found in any, even by the suite of analytical techniques employed at varying resolution by various crystallographic and non-crystallographic means. This is the main conclusion of this chapter. The results of this chapter are given in brief in Chapter 3 to justify this discussion, and have here been laid out in their entirety for the reader to fully understand the discussion therein.

7. Figures and tables

All of the figures and tables discussed in this appendix are now displayed in order of their appearance, beginning overleaf.

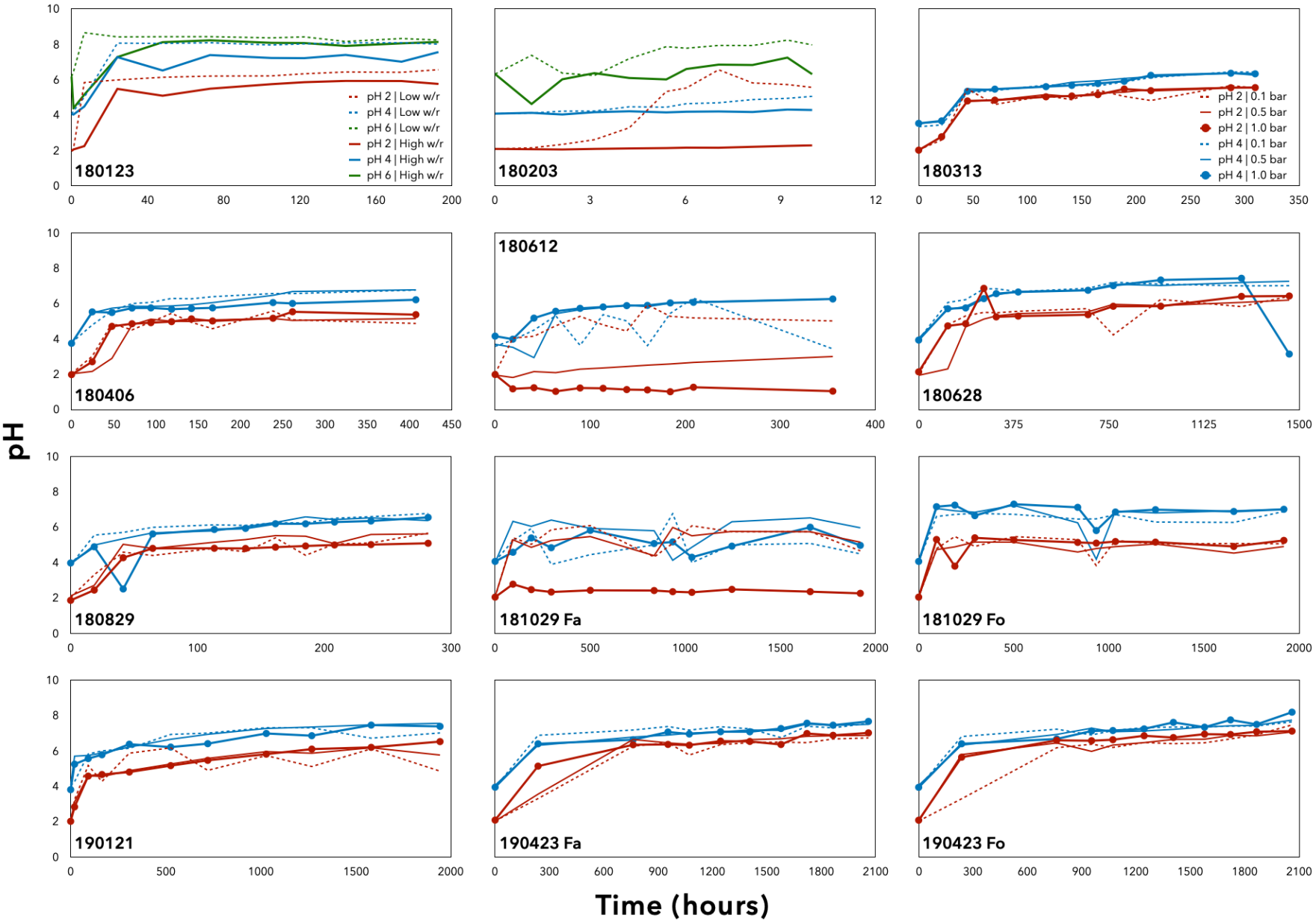

pH
Time (hours)
180123
180203
180313
180406
180612
180628
180829
181029 Fa
181029 Fo
190121
190423 Fa
190423 Fo
pH 2 | Low w/r
pH 4 | Low w/r
pH 6 | Low w/r
pH 2 | High w/r
pH 4 | High w/r
pH 6 | High w/r
pH 2 | 0.1 bar
pH 2 | 0.5 bar
pH 2 | 1.0 bar
pH 4 | 0.1 bar
pH 4 | 0.5 bar
pH 4 | 1.0 bar

Figure 1 (previous page): All pH measurements for fayalite- ± forsterite-bearing experiments, where experiments begun at pH 2 are coloured red, coloured blue for pH 4, and green for pH 6. Heavy lines with circles for datapoints signify 1.0 bars of dissolved CO_2, moderately-heavy is 0.5 bar, and dashed is 0.1 bar. For experiments 180123 and 180203, heavy lines denote high rock:water ratio while lighter lines are low, as indicated in the respective legends.

Sub-experiment	180123 value (1 hour)	180203 value (1 hour)	Difference
Low pH 2	2.101	2.152	0.051
Low pH 4	4.232	4.120	0.112
Low pH 6	6.452	7.385	0.933
High pH 2	2.060	2.073	0.013
High pH 4	4.035	4.131	0.096
High pH 6	4.396	4.630	0.234

Table 1: The difference in recorded measurements from two identically set up experiments, 180123 and 180203. These measurements were taken 1 hour into the experiment.

Sub-experiment	180123 value (7 hours)	180203 value (7 hours)	Difference
Low pH 2	5.844	6.565	0.721
Low pH 4	5.013	4.700	0.313
Low pH 6	8.662	7.941	0.721
High pH 2	2.250	2.158	0.092
High pH 4	4.489	4.209	0.280
High pH 6	5.158	6.857	1.699

Table 2: The difference in recorded measurements from two identically set up experiments, 180123 and 180203. These measurements were taken 7 hours into the experiment.

Sub-experiment	180203 value (1 hour)	180310 value (1 hour)	Difference
Low pH 2	2.152	5.986	3.834
Low pH 4	4.120	7.959	3.839
Low pH 6	7.385	8.277	0.892
High pH 2	2.073	2.409	0.336
High pH 4	4.131	5.211	1.080
High pH 6	4.630	8.137	3.507

Table 3: The difference in recorded measurements from two identically set up experiments, 180203 and 180310. These measurements were taken 1 hour into the experiment.

Sub-experiment	180203 value (7 hours)	180310 value (7 hours)	Difference
Low pH 2	5.844	5.785	0.059
Low pH 4	5.013	7.982	2.969
Low pH 6	8.662	8.120	0.542
High pH 2	2.250	2.73	0.480
High pH 4	4.489	7.283	2.794
High pH 6	5.158	7.714	2.556

Table 4: The difference in recorded measurements from two identically set up experiments, 180203 and 180310. These measurements were taken 7 hours into the experiment.

Sub-experiment	Starting pH	Final pH
Low pH 2	1.802	Not taken
High pH 2	2.08	6.355
Low pH 4	3.991	Not taken
High pH 4	3.940	7.394

Table 5: The measurements of pH taken from experiment 181004, which involved low water/rock ratios of 1:1 and 1:10. pH was unable to be taken for 1:1 sub-experiments at their termination.

Sub-experiment	Starting pH	Final pH
Low pH 2	2.520	Not taken
High pH 2	2.520	5.383
Low pH 4	3.789	Not taken
High pH 4	3.789	7.915

Table 6: The measurements of pH taken from experiment 181205, which involved low water/rock ratios of 1:1 and 1:10. pH was unable to be taken for 1:1 sub-experiments at their termination.

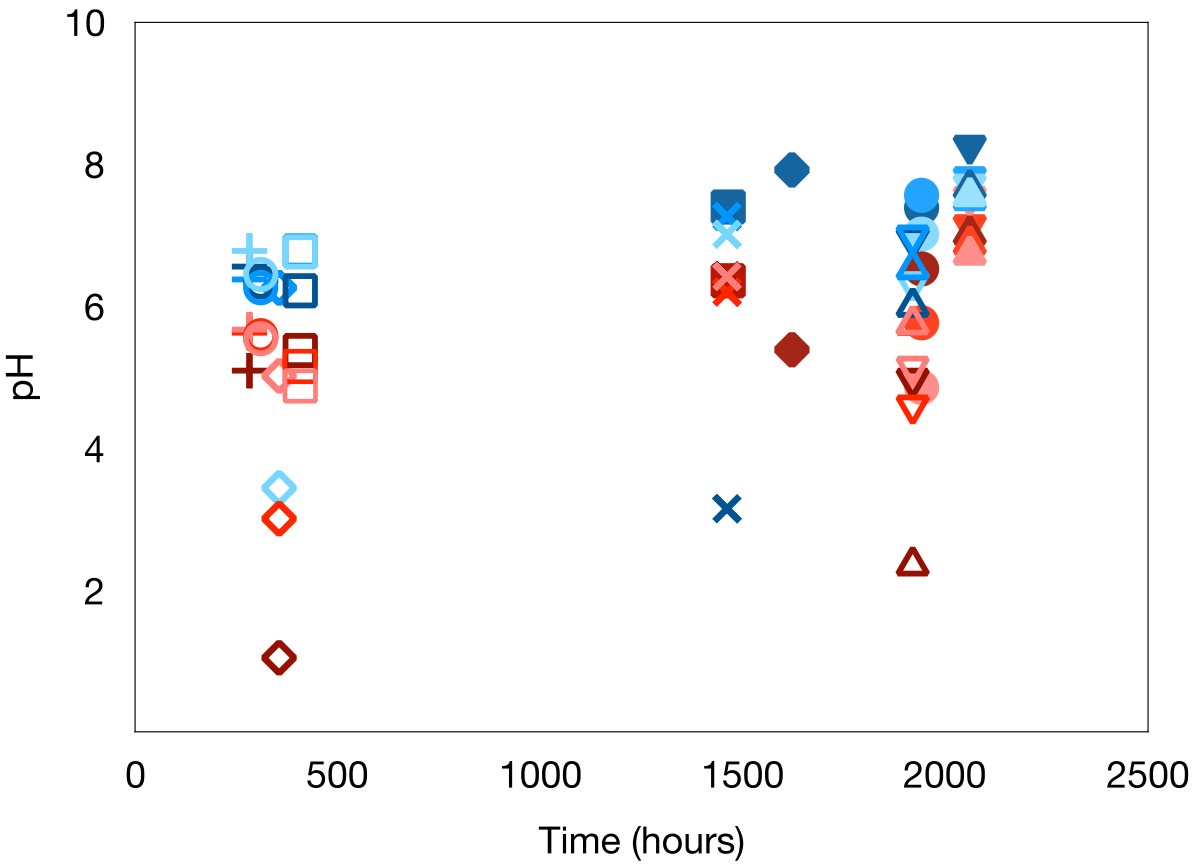


Figure 2: The final recorded pH of all experiments bearing fayalite ± forsterite, set against the length of time run for. By colour, from palest red to darkest, this represents 0.1, 0.5, and 1.0 CO_2 begun at pH 2, while pale to dark blue represent CO_2 levels of 0.1, 0.5, and 1.0 begun at pH 4. The differing symbols correspond to differing experiments: plus for 190313, circle for 190403, diamond for 180612, cross for 180628, square for 180829, filled-in square for 181004, upward triangle for 181029 Fa, downward triangle for 181029 Fo, filled-in diamond for 181205, filled-in circle for 190121, filled-in upward triangle for 190423 Fa, filled-in downward triangle for 190423 Fo.

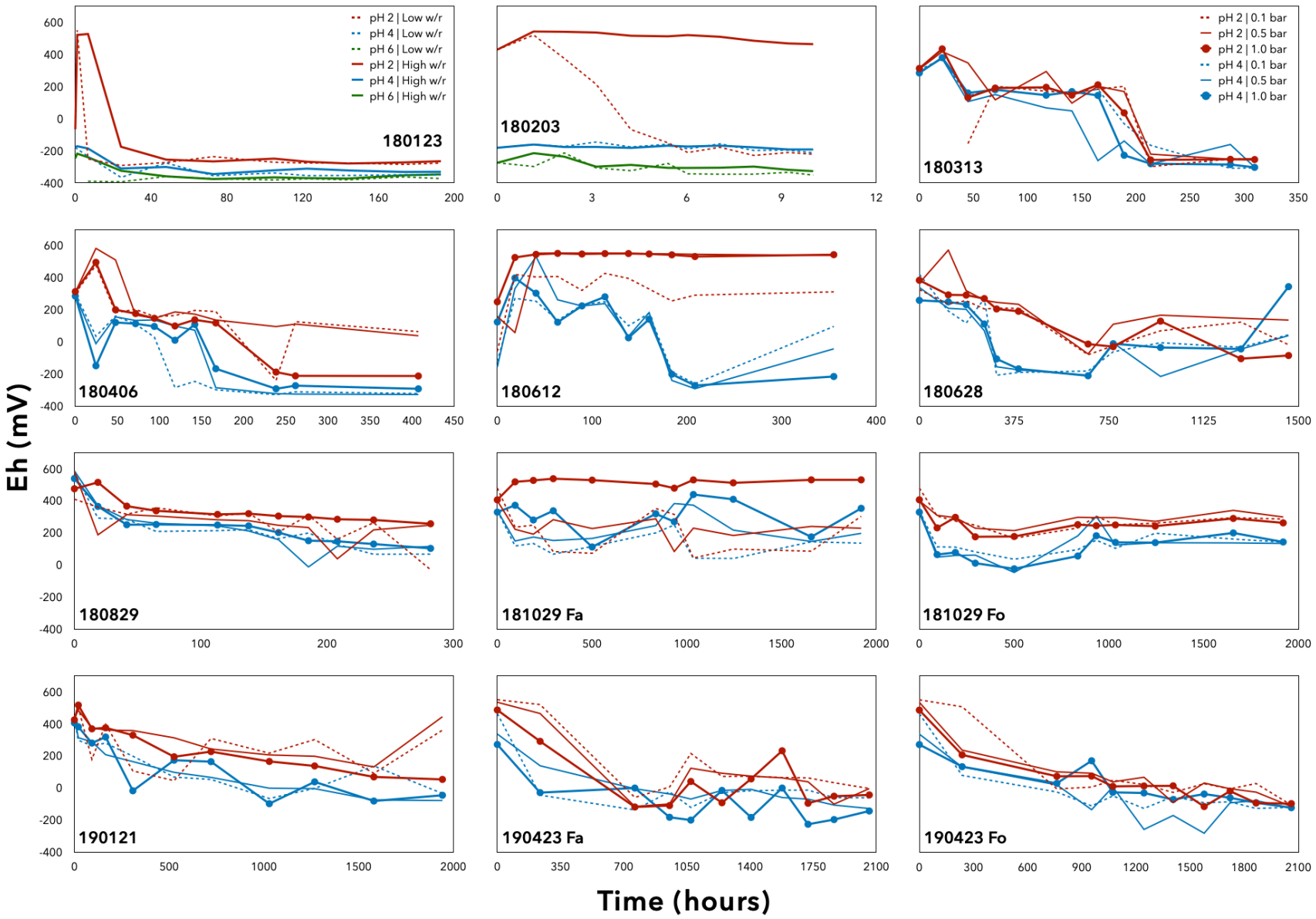

pH 2 | Low w/r
pH 4 | Low w/r
pH 6 | Low w/r
pH 2 | High w/r
pH 4 | High w/r
pH 6 | High w/r
180123
180203
pH 2 | 0.1 bar
pH 2 | 0.5 bar
pH 2 | 1.0 bar
pH 4 | 0.1 bar
pH 4 | 0.5 bar
pH 4 | 1.0 bar
180313
180406
180612
180628
180829
181029 Fa
181029 Fo
190121
190423 Fa
190423 Fo
Eh (mV)
Time (hours)

Figure 3 (previous page): All Eh measurements for fayalite- ± forsterite-bearing experiments, where experiments begun at pH 2 are coloured red, coloured blue for pH 4, and green for pH 6. Heavy lines with circles for datapoints signify 1.0 bars of dissolved CO_2, moderately-heavy is 0.5 bar, and dashed is 0.1 bar. For experiments 180123 and 180203, heavy lines denote high rock:water ratio while lighter lines are low, as indicated in the respective legends.

Sub-experiment	Starting Eh	Final Eh
Low pH 2	537.8	Not taken
High pH 2	537.8	60.4
Low pH 4	524.8	Not taken
High pH 4	524.8	−7.6

Table 7: The measurements of Eh taken from experiment 181004, which involved low water/rock ratios of 1:1 and 1:10. Eh was unable to be taken for 1:1 sub-experiments at their termination.

Sub-experiment	Starting Eh	Final Eh
Low pH 2	338.0	Not taken
High pH 2	338.0	112.3
Low pH 4	398.0	Not taken
High pH 4	398.0	−62.5

Table 8: The measurements of Eh taken from experiment 181205, which involved low water/rock ratios of 1:1 and 1:10. Eh was unable to be taken for 1:1 sub-experiments at their termination.

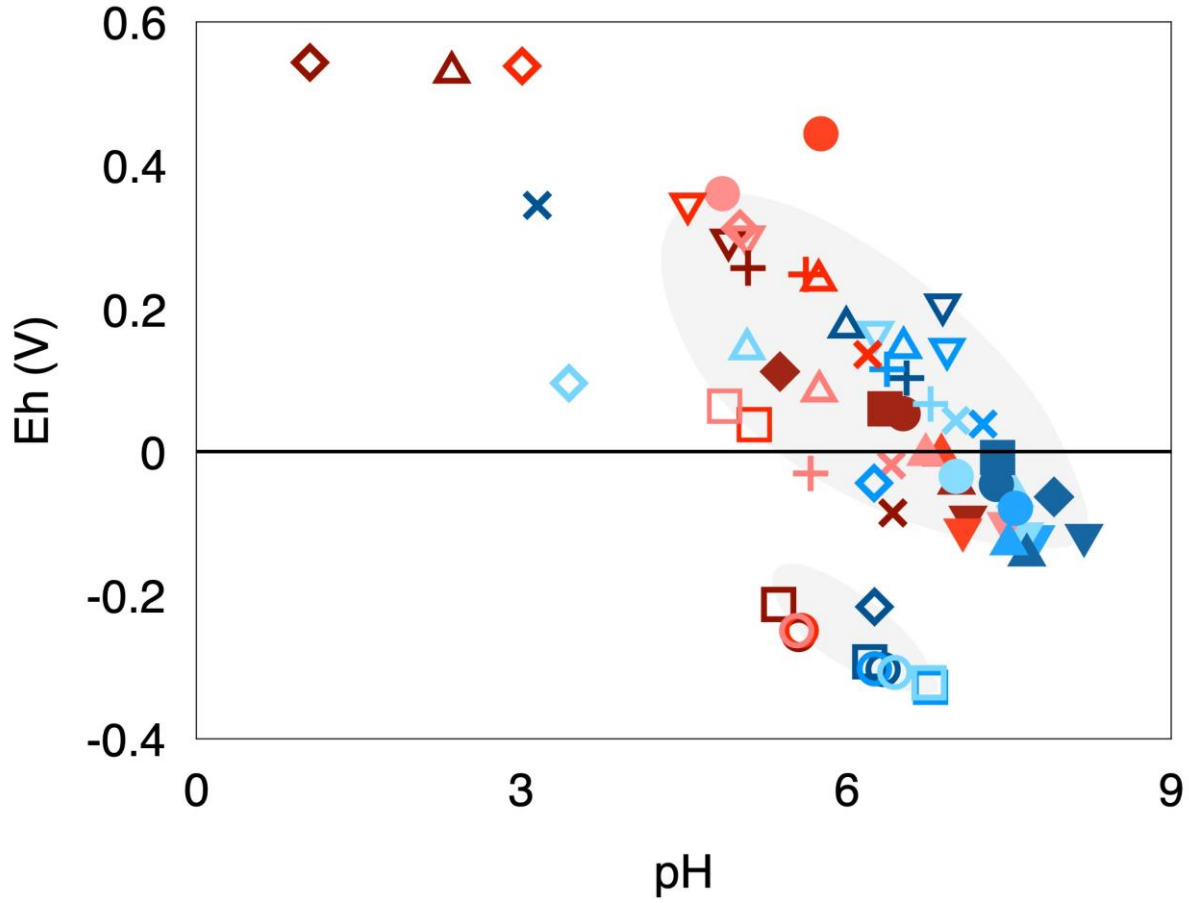


Figure 4: The final recorded pH and Eh for all experiments bearing fayalite ± forsterite. The ellipses represent clusters of main trends. By colour, from palest red to darkest, this represents 0.1, 0.5, and 1.0 CO_2 begun at pH 2, while pale to dark blue represent CO_2 levels of 0.1, 0.5, and 1.0 begun at pH 4. The differing symbols correspond to differing experiments: plus for 190313, circle for 190403, diamond for 180612, cross for 180628, square for 180829, filled-in square for 181004, upward triangle for 181029 Fa, downward triangle for 181029 Fo, filled-in diamond for 181205, filled-in circle for 190121, filled-in upward triangle for 190423 Fa, filled-in downward triangle for 190423 Fo.

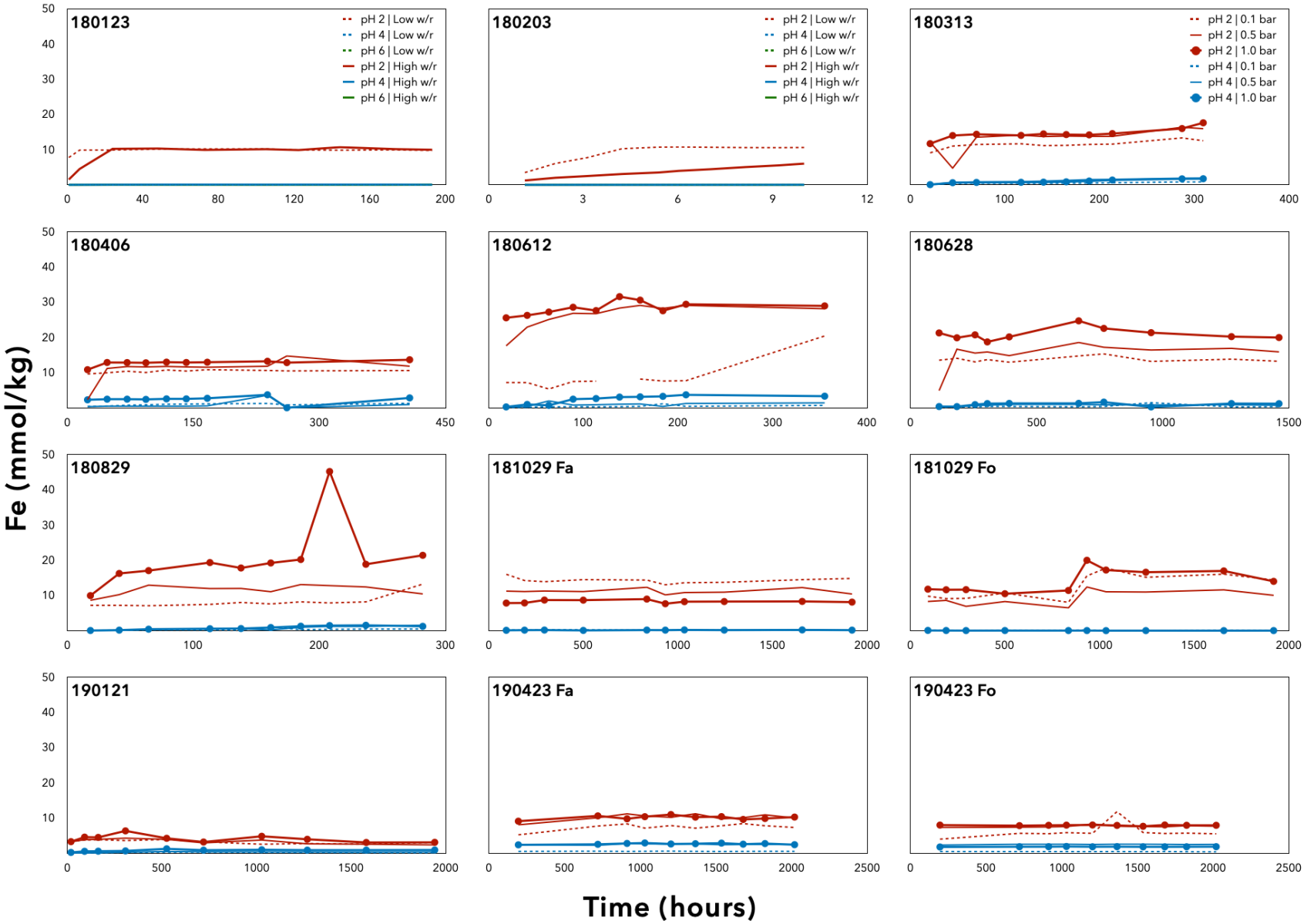

180123
180203
180313
180406
180612
180628
180829
181029 Fa
181029 Fo
190121
190423 Fa
190423 Fo
pH 2 | Low w/r
pH 4 | Low w/r
pH 6 | Low w/r
pH 2 | High w/r
pH 4 | High w/r
pH 6 | High w/r
pH 2 | 0.1 bar
pH 2 | 0.5 bar
pH 2 | 1.0 bar
pH 4 | 0.1 bar
pH 4 | 0.5 bar
pH 4 | 1.0 bar
Fe (mmol/kg)
Time (hours)

Figure 5 (previous page): All Fe measurements for fayalite- ± forsterite-bearing experiments, where experiments begun at pH 2 are coloured red, coloured blue for pH 4, and green for pH 6. Heavy lines with circles for datapoints signify 1.0 bars of dissolved CO_2, moderately-heavy is 0.5 bar, and dashed is 0.1 bar. For experiments 180123 and 180203, heavy lines denote high rock:water ratio while lighter lines are low, as indicated in the respective legends.

Sub-experiment	Final Fe (mol/kg)	Final Si (mol/kg)
Low pH 2	Not taken	Not taken
High pH 2	0.008628	0.002026
Low pH 4	Not taken	Not taken
High pH 4	0.000121	0.000455

Table 9: The measurements of Fe and Si taken from experiment 181004, which involved low water/rock ratios of 1:1 and 1:10. Solution data was unable to be taken for 1:1 sub-experiments at their termination due to their minute amounts.

Sub-experiment	Final Fe (mol/kg)	Final Si (mol/kg)	Final Mg (mol/kg)
Low pH 2	Not taken	Not taken	Not taken
High pH 2	0.007012	0.003813	0.006601
Low pH 4	Not taken	Not taken	Not taken
High pH 4	0.000077	0.000386	0.000857

Table 10: The measurements of Fe, Si, and Mg taken from experiment 181205, which involved low water/rock ratios of 1:1 and 1:10. Solution data was unable to be extracted for low rock:water ratio experiments owing to the minute amount of fluids available.

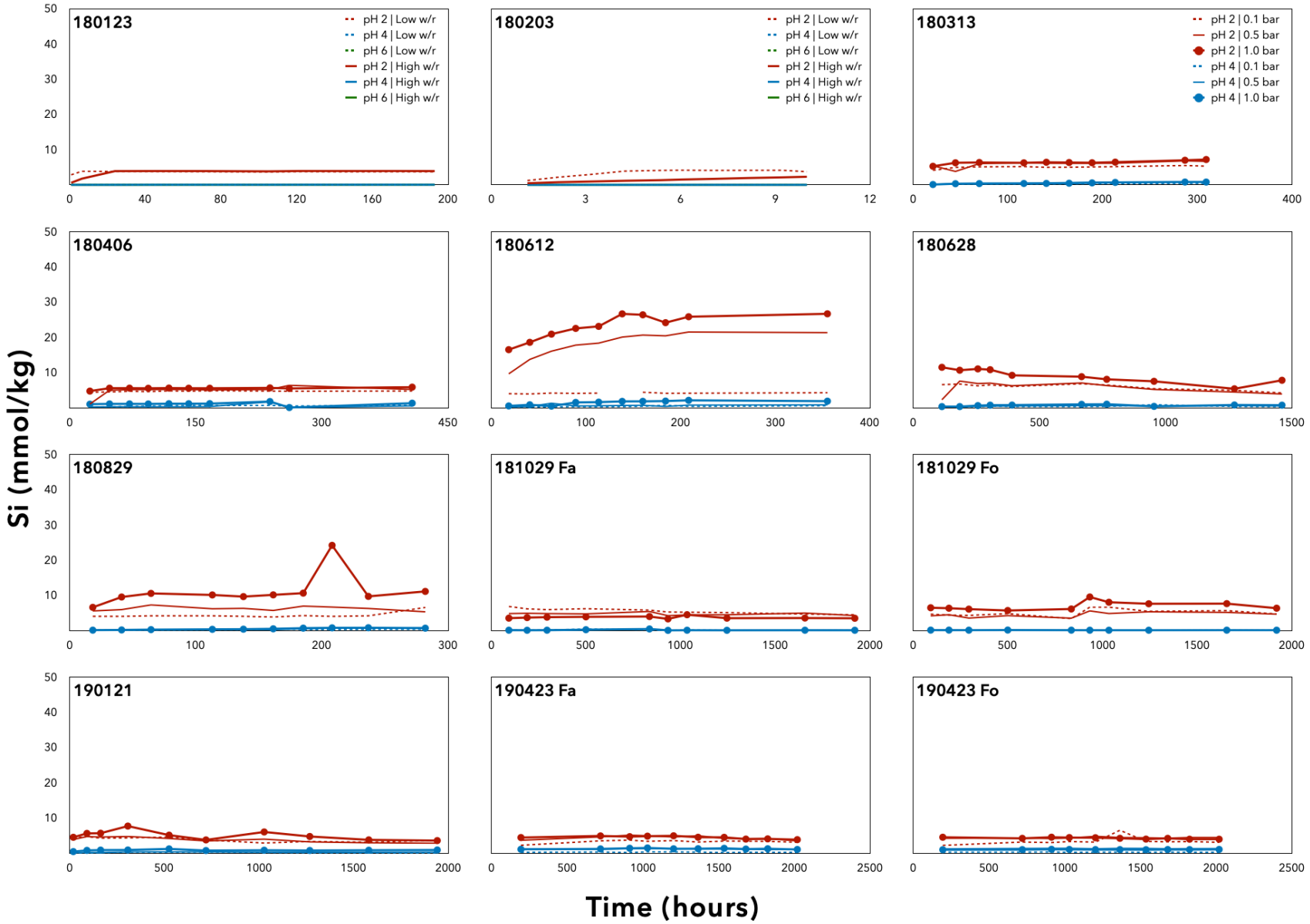

180123
pH 2 | Low w/r
pH 4 | Low w/r
pH 6 | Low w/r
pH 2 | High w/r
pH 4 | High w/r
pH 6 | High w/r
180203
180313
pH 2 | 0.1 bar
pH 2 | 0.5 bar
pH 2 | 1.0 bar
pH 4 | 0.1 bar
pH 4 | 0.5 bar
pH 4 | 1.0 bar
180406
180612
180628
180829
181029 Fa
181029 Fo
190121
190423 Fa
190423 Fo
Si (mmol/kg)
Time (hours)

Figure 6 (previous page): All Si measurements for fayalite- ± forsterite-bearing experiments, where experiments begun at pH 2 are coloured red, coloured blue for pH 4, and green for pH 6. Heavy lines with circles for datapoints signify 1.0 bars of dissolved CO_2, moderately-heavy is 0.5 bar, and dashed is 0.1 bar. For experiments 180123 and 180203, heavy lines denote high rock:water ratio while lighter lines are low, as indicated in the respective legends.

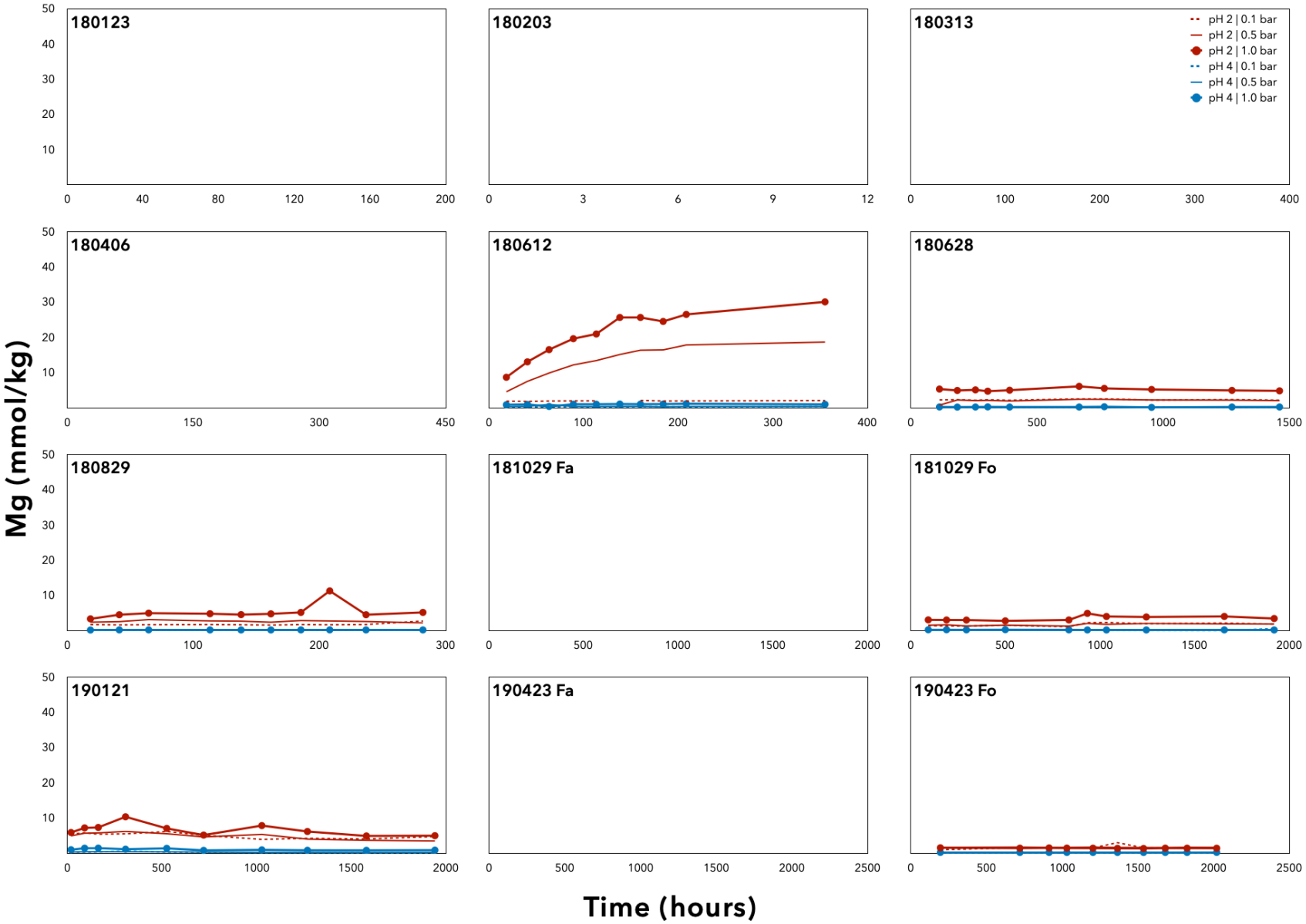

180123
180203
180313
180406
180612
180628
180829
181029 Fa
181029 Fo
190121
190423 Fa
190423 Fo
pH 2 | 0.1 bar
pH 2 | 0.5 bar
pH 2 | 1.0 bar
pH 4 | 0.1 bar
pH 4 | 0.5 bar
pH 4 | 1.0 bar
Mg (mmol/kg)
Time (hours)

Figure 7 (previous page): All Mg measurements for fayalite- ± forsterite-bearing experiments, where experiments begun at pH 2 are coloured red, coloured blue for pH 4, and green for pH 6. Heavy lines with circles for datapoints signify 1.0 bars of dissolved CO_2, moderately-heavy is 0.5 bar, and dashed is 0.1 bar. For experiments 180123 and 180203, heavy lines denote high rock:water ratio while lighter lines are low, as indicated in the respective legends.

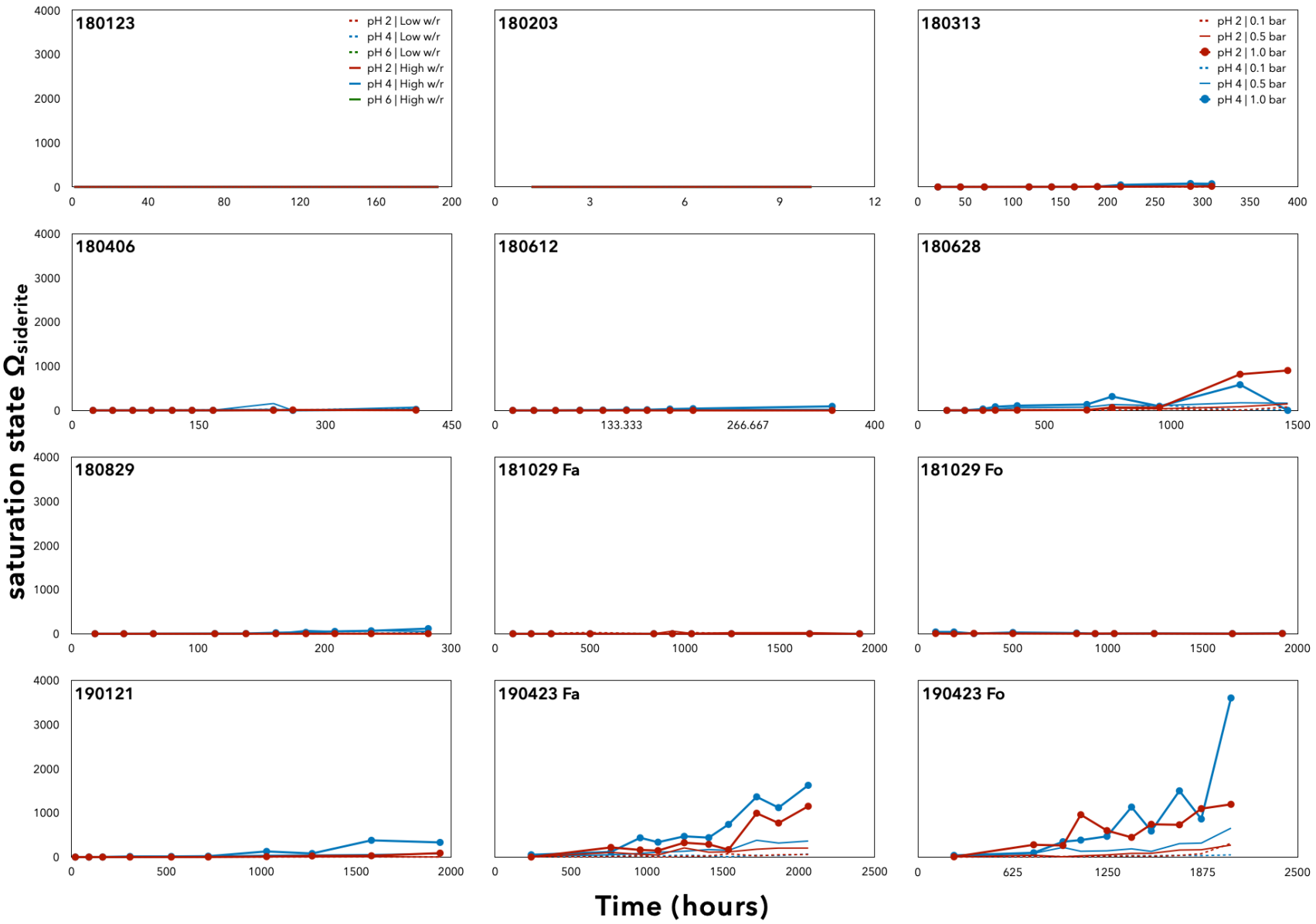

180123
180203
180313
180406
180612
180628
180829
181029 Fa
181029 Fo
190121
190423 Fa
190423 Fo
pH 2 | Low w/r
pH 4 | Low w/r
pH 6 | Low w/r
pH 2 | High w/r
pH 4 | High w/r
pH 6 | High w/r
pH 2 | 0.1 bar
pH 2 | 0.5 bar
pH 2 | 1.0 bar
pH 4 | 0.1 bar
pH 4 | 0.5 bar
pH 4 | 1.0 bar
saturation state Ωsiderite
Time (hours)

Figure 8 (previous page): All omega measurements for siderite as calculated from Fe and Si measurements by ICP-OES/MS for fayalite- ± forsterite-bearing experiments, where experiments begun at pH 2 are coloured red, coloured blue for pH 4, and green for pH 6. Heavy lines with circles for datapoints signify 1.0 bars of dissolved CO_2, moderately-heavy is 0.5 bar, and dashed is 0.1 bar. For experiments 180123 and 180203, heavy lines denote high rock:water ratio while lighter lines are low, as indicated in the respective legends. Note the differing x axes but identical y axes.

Sub-experiment	Siderite (Ω)	Amorphous silica (Ω)
Low pH 2	Not taken	Not taken
High pH 2	383.7072455	1.066596121
Low pH 4	Not taken	Not taken
High pH 4	122.4616199	0.259417936

Table 11: Siderite and amorphous silica saturation states as calculated from measurements of Fe and Si taken from experiment 181004, which involved low water/rock ratios of 1:1 and 1:10. Solution data was unable to be taken for 1:1 sub-experiments at their termination due to their minute amounts.

Sub-experiment	Siderite (Ω)	Amorphous silica (Ω)
Low pH 2	Not taken	Not taken
High pH 2	2.426051412	2.025816015
Low pH 4	Not taken	Not taken
High pH 4	92.74702759	0.198061471

Table 12: Siderite and amorphous silica saturation states as calculated from measurements of Fe and Si from experiment 181205, which involved low water/rock ratios of 1:1 and 1:10. Solution data was unable to be extracted for low rock:water ratio experiments owing to the minute amount of fluids available.

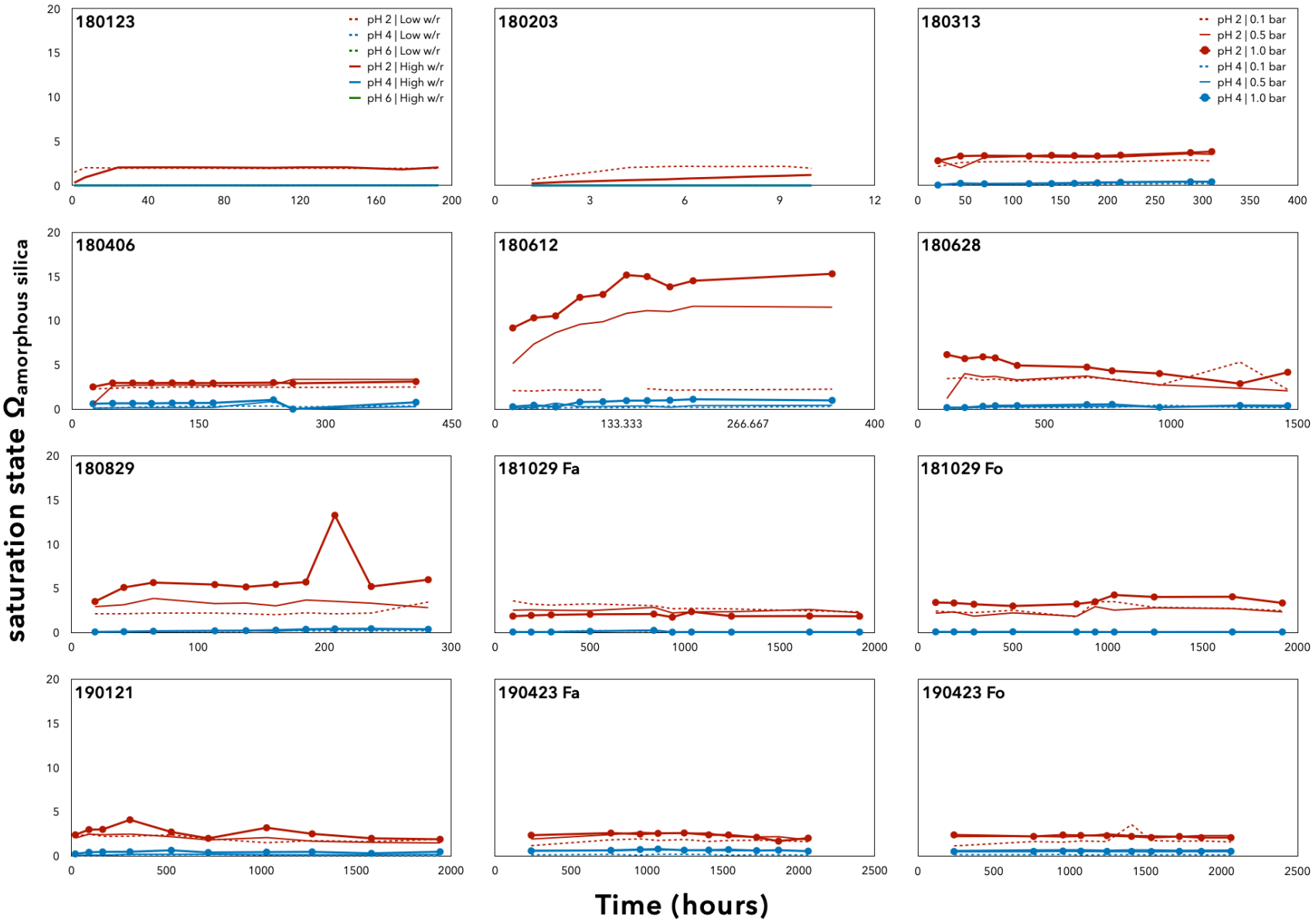

180123
pH 2 | Low w/r
pH 4 | Low w/r
pH 6 | Low w/r
pH 2 | High w/r
pH 4 | High w/r
pH 6 | High w/r
180203
180313
pH 2 | 0.1 bar
pH 2 | 0.5 bar
pH 2 | 1.0 bar
pH 4 | 0.1 bar
pH 4 | 0.5 bar
pH 4 | 1.0 bar
180406
180612
180628
180829
181029 Fa
181029 Fo
190121
190423 Fa
190423 Fo
saturation state Ωamorphous silica
Time (hours)

Figure 9 (previous page): All omega measurements for amorphous as calculated from Fe and Si measurements by ICP-OES/MS for fayalite- ± forsterite-bearing experiments, where experiments begun at pH 2 are coloured red, coloured blue for pH 4, and green for pH 6. Heavy lines with circles for datapoints signify 1.0 bars of dissolved CO_2, moderately-heavy is 0.5 bar, and dashed is 0.1 bar. For experiments 180123 and 180203, heavy lines denote high rock:water ratio while lighter lines are low, as indicated in the respective legends. Note the differing x axes but identical y axes.

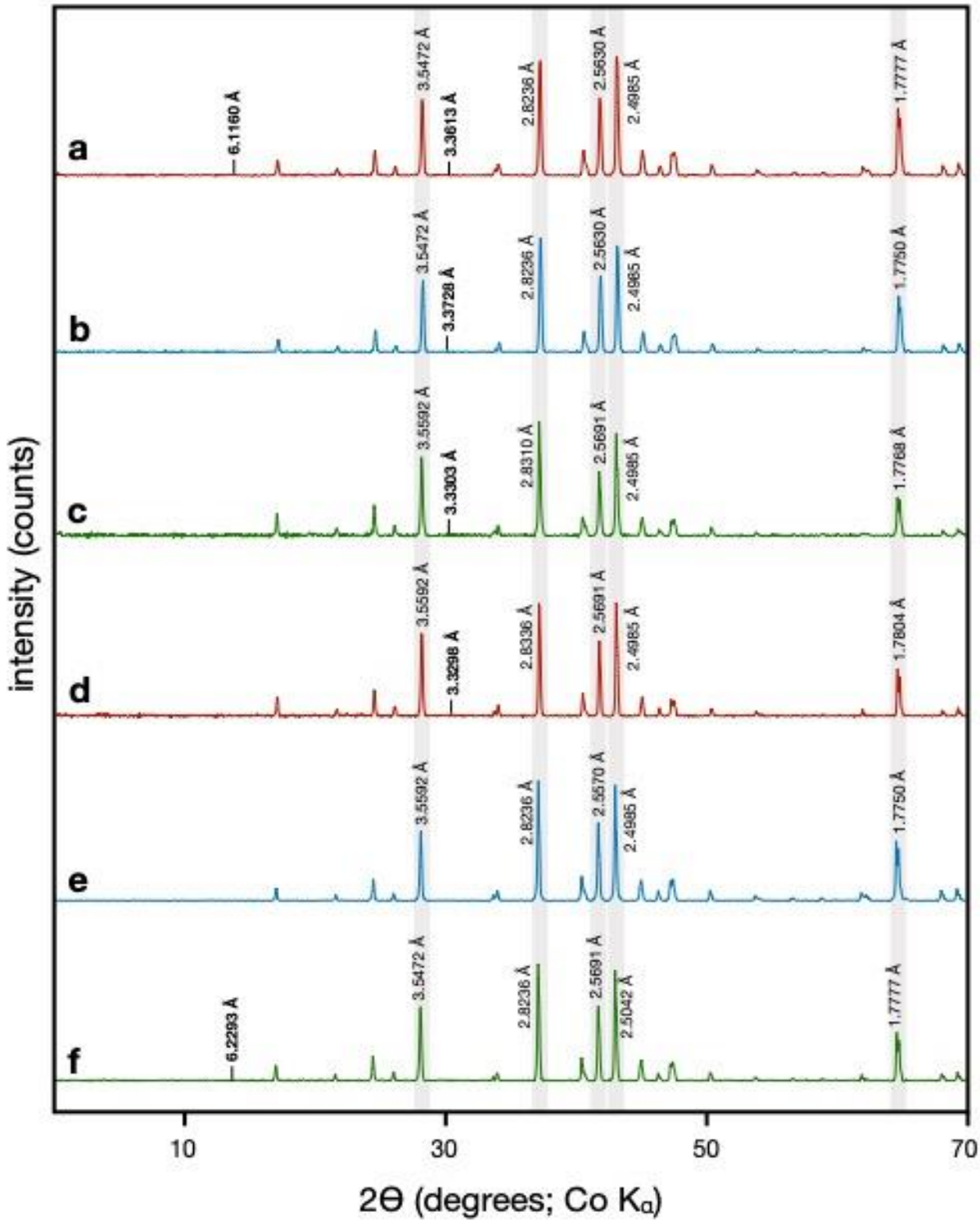


Figure 10: The XRD spectra for the non-CO_2-bearing solids of 180123. From top to bottom: pH 2 low water-rock; pH 4 low-water rock; pH 6 low water-rock; pH 2 high water-rock; pH 4 high-water rock; and pH 6 high water-rock. Anomalous peaks that were not identified as belonging to any one mineral spectra are labelled and bolded.

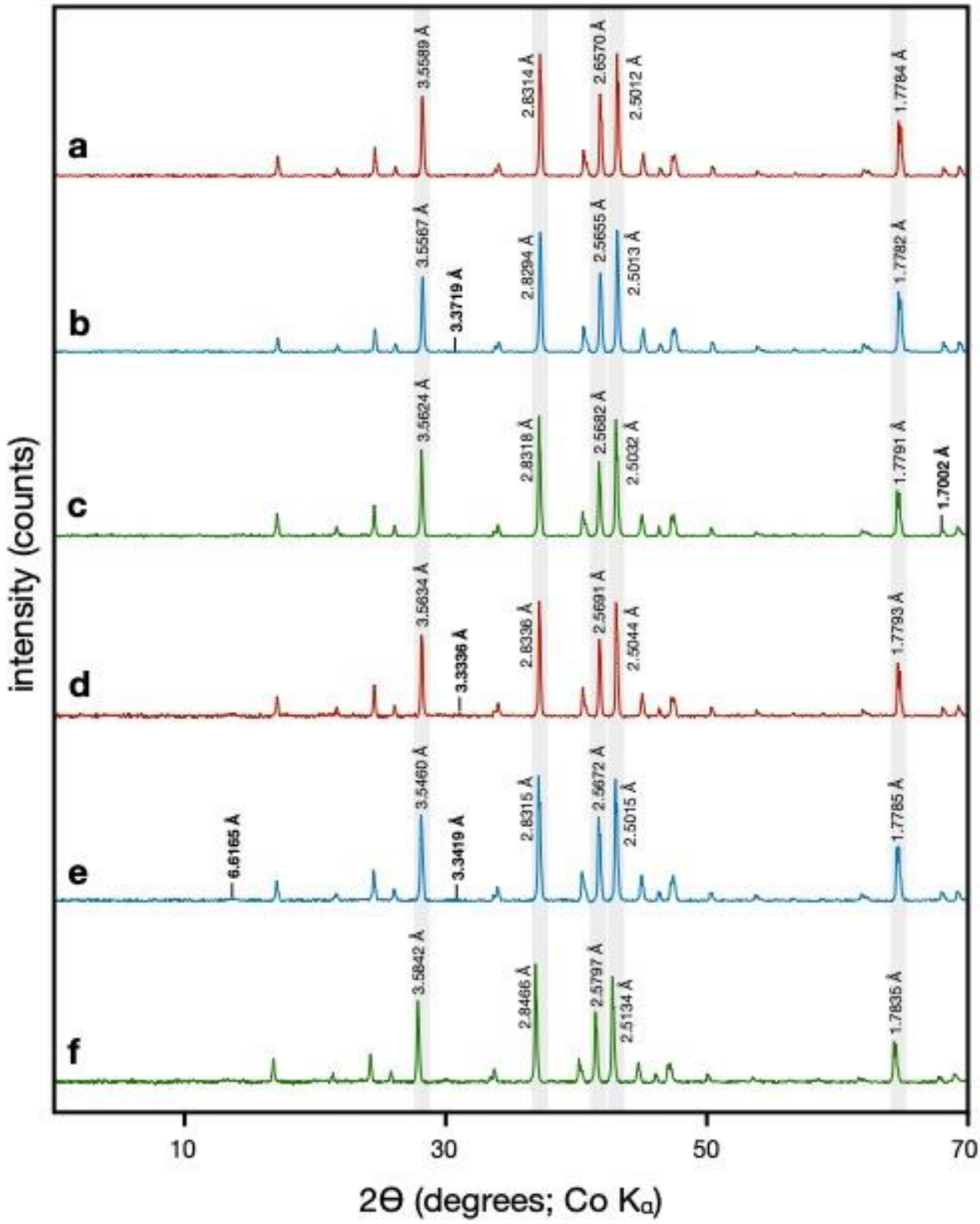


Figure 11: The XRD spectra for the non-CO_2-bearing solids of 180203. From top to bottom: pH 2 low water-rock; pH 4 low-water rock; pH 6 low water-rock; pH 2 high water-rock; pH 4 high-water rock; and pH 6 high water-rock. Anomalous peaks that were not identified as belonging to any one mineral spectra are labelled and bolded.

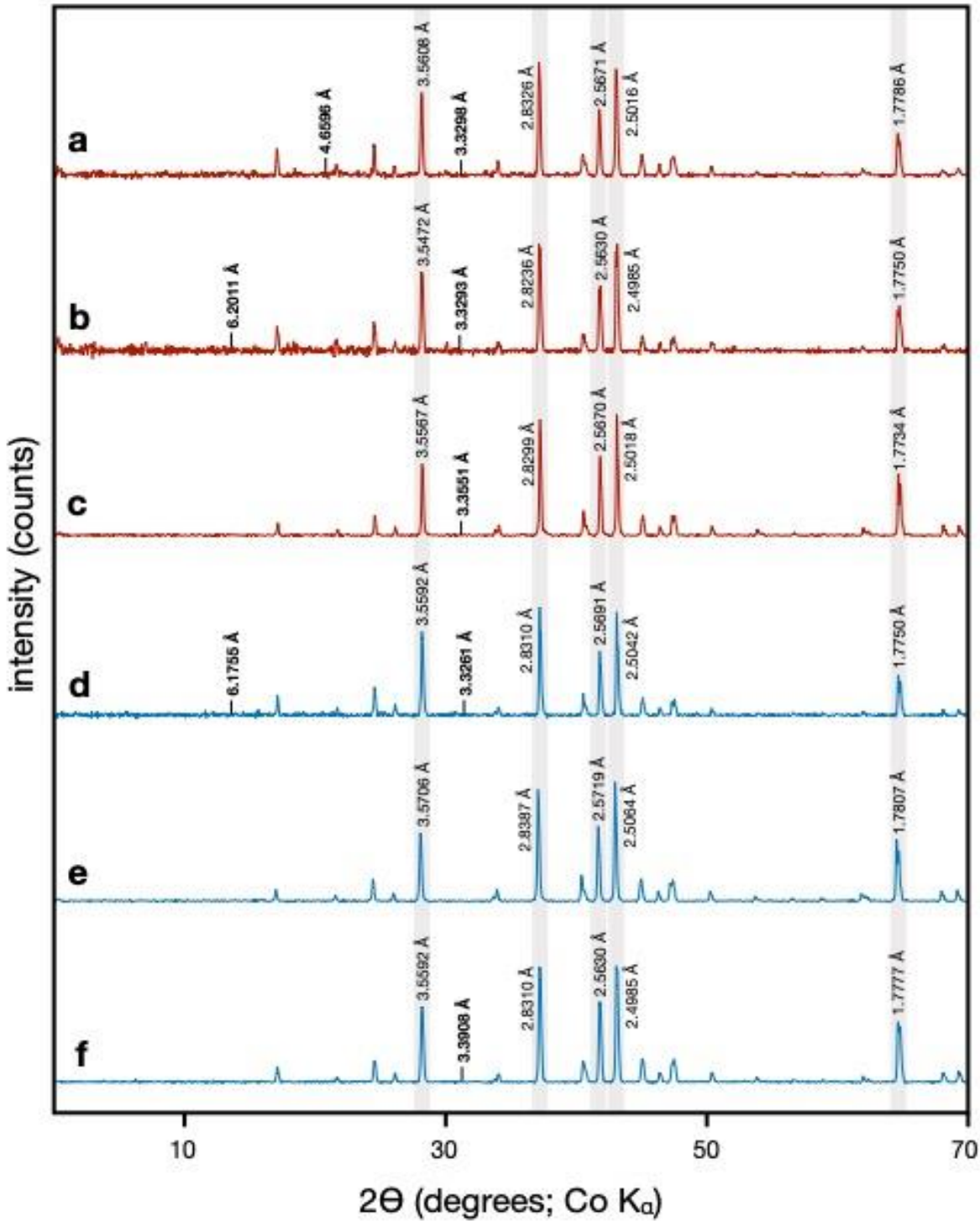


Figure 12: The XRD spectra for the solids of 180313. From top to bottom: pH 2 CO_2 0.1 bar; pH 2 CO_2 0.5 bar; pH 2 CO_2 1.0 bar; pH 4 CO_2 0.1 bar; pH 4 CO_2 0.5 bar; pH 4 CO_2 1.0 bar. Anomalous peaks that were not identified as belonging to any one mineral spectra are labelled and bolded.

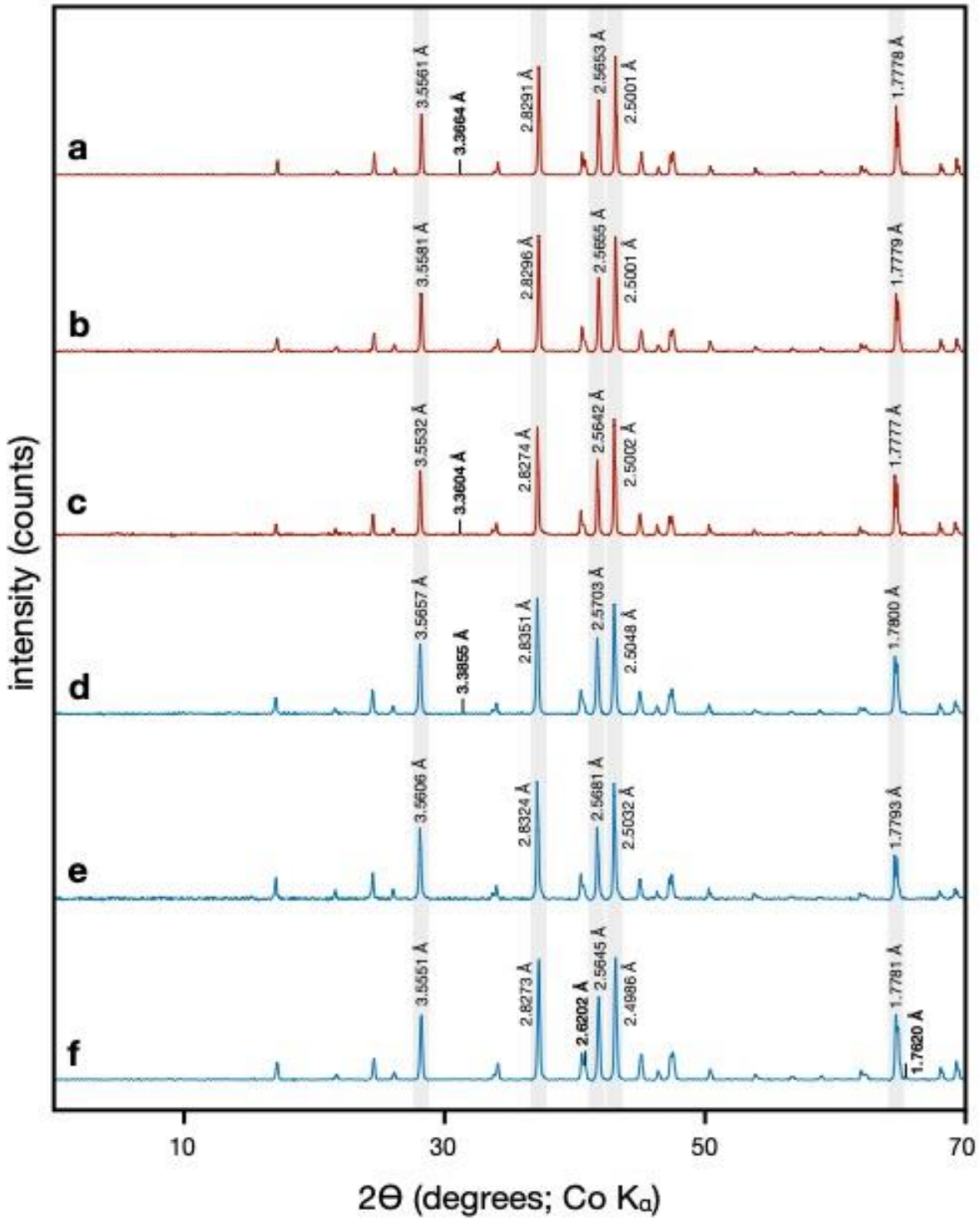


Figure 13: The XRD spectra for the solids of 180406. From top to bottom: pH 2 CO2 0.1 bar; pH 2 CO2 0.5 bar; pH 2 CO2 1.0 bar; pH 4 CO2 0.1 bar; pH 4 CO2 0.5 bar; pH 4 CO2 1.0 bar. Anomalous peaks that were not identified as belonging to any one mineral spectra are labelled and bolded.

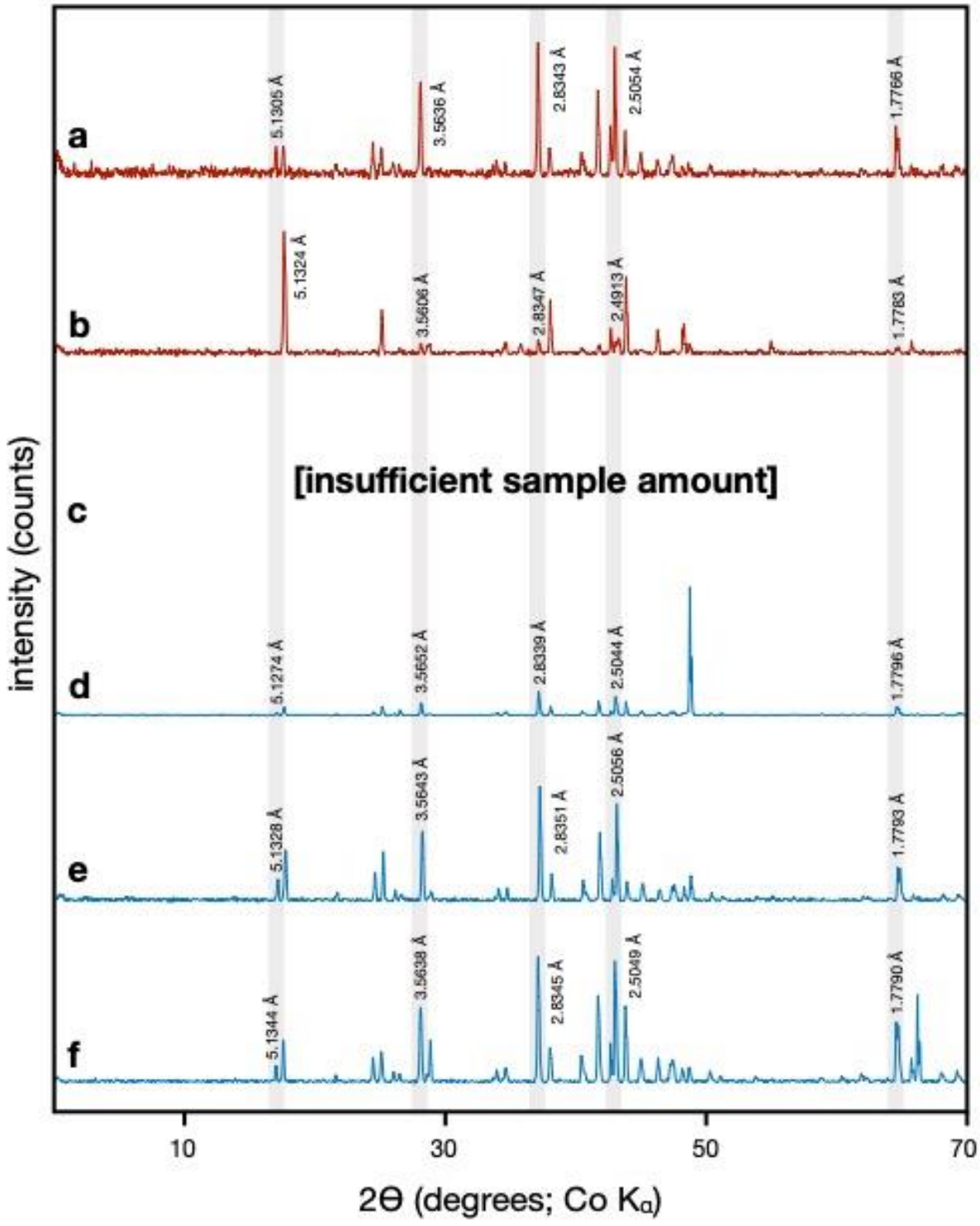


Figure 14: The XRD spectra for the solids of 180612. From top to bottom: pH 2 CO2 0.1 bar; pH 2 CO2 0.5 bar; pH 2 CO2 1.0 bar; pH 4 CO2 0.1 bar; pH 4 CO2 0.5 bar; pH 4 CO2 1.0 bar. Anomalous peaks that were not identified as belonging to any one mineral spectra are labelled and bolded.

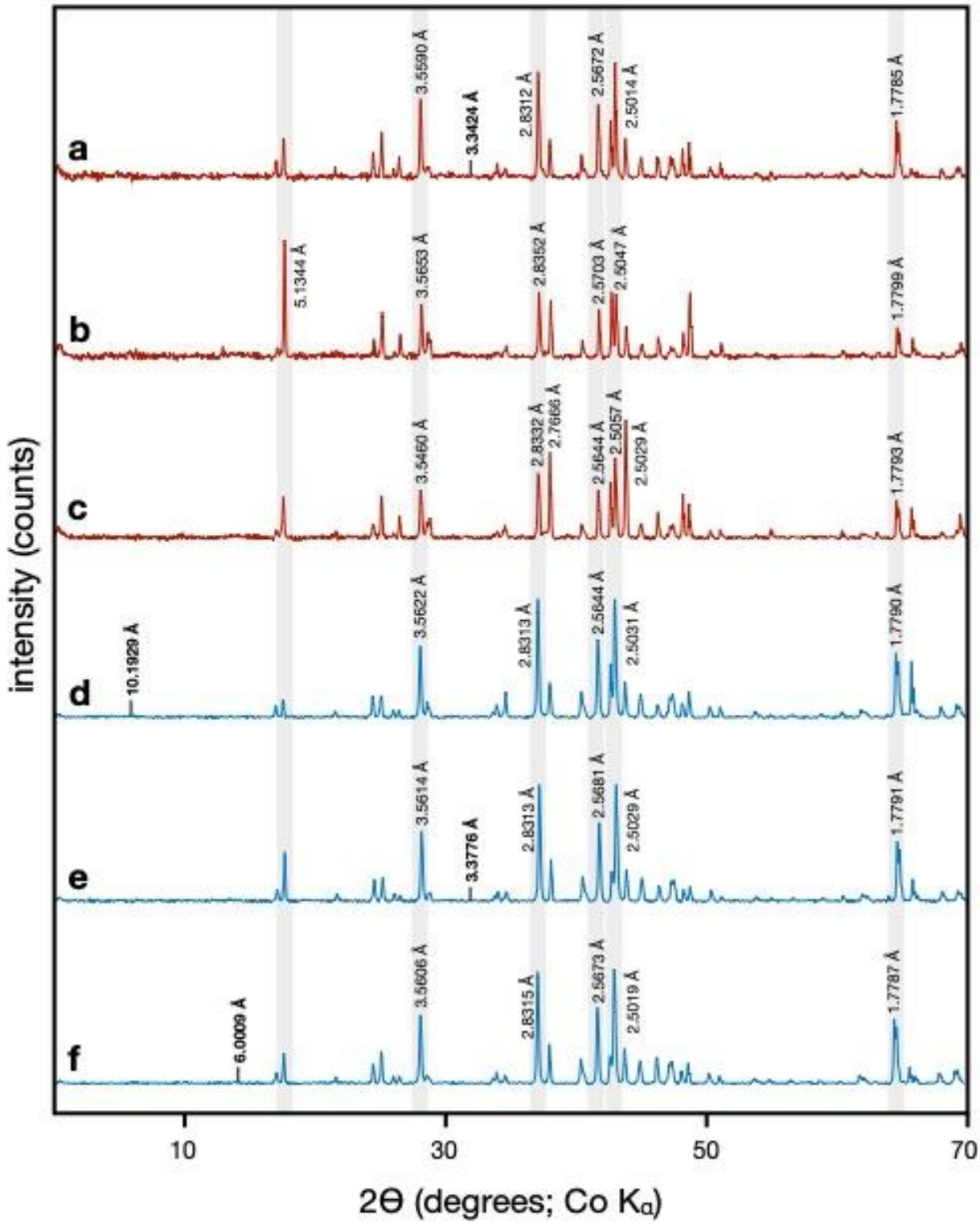


Figure 15: The XRD spectra for the solids of 180628. From top to bottom: pH 2 CO2 0.1 bar; pH 2 CO2 0.5 bar; pH 2 CO2 1.0 bar; pH 4 CO2 0.1 bar; pH 4 CO2 0.5 bar; pH 4 CO2 1.0 bar. Anomalous peaks that were not identified as belonging to any one mineral spectra are labelled and bolded.

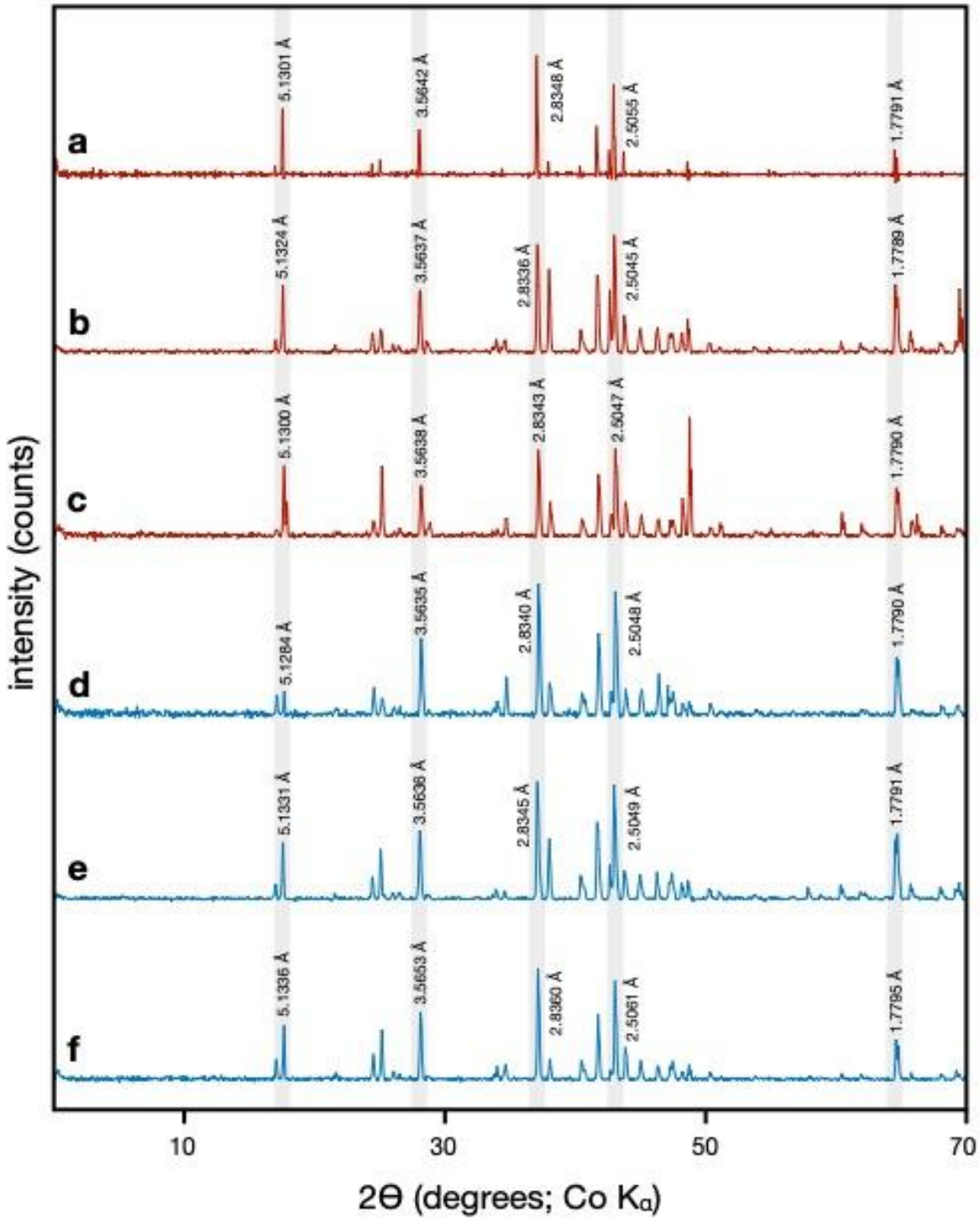


Figure 16: The XRD spectra for the solids of 180829. From top to bottom: pH 2 CO2 0.1 bar; pH 2 CO2 0.5 bar; pH 2 CO2 1.0 bar; pH 4 CO2 0.1 bar; pH 4 CO2 0.5 bar; pH 4 CO2 1.0 bar. Anomalous peaks that were not identified as belonging to any one mineral spectra are labelled and bolded.

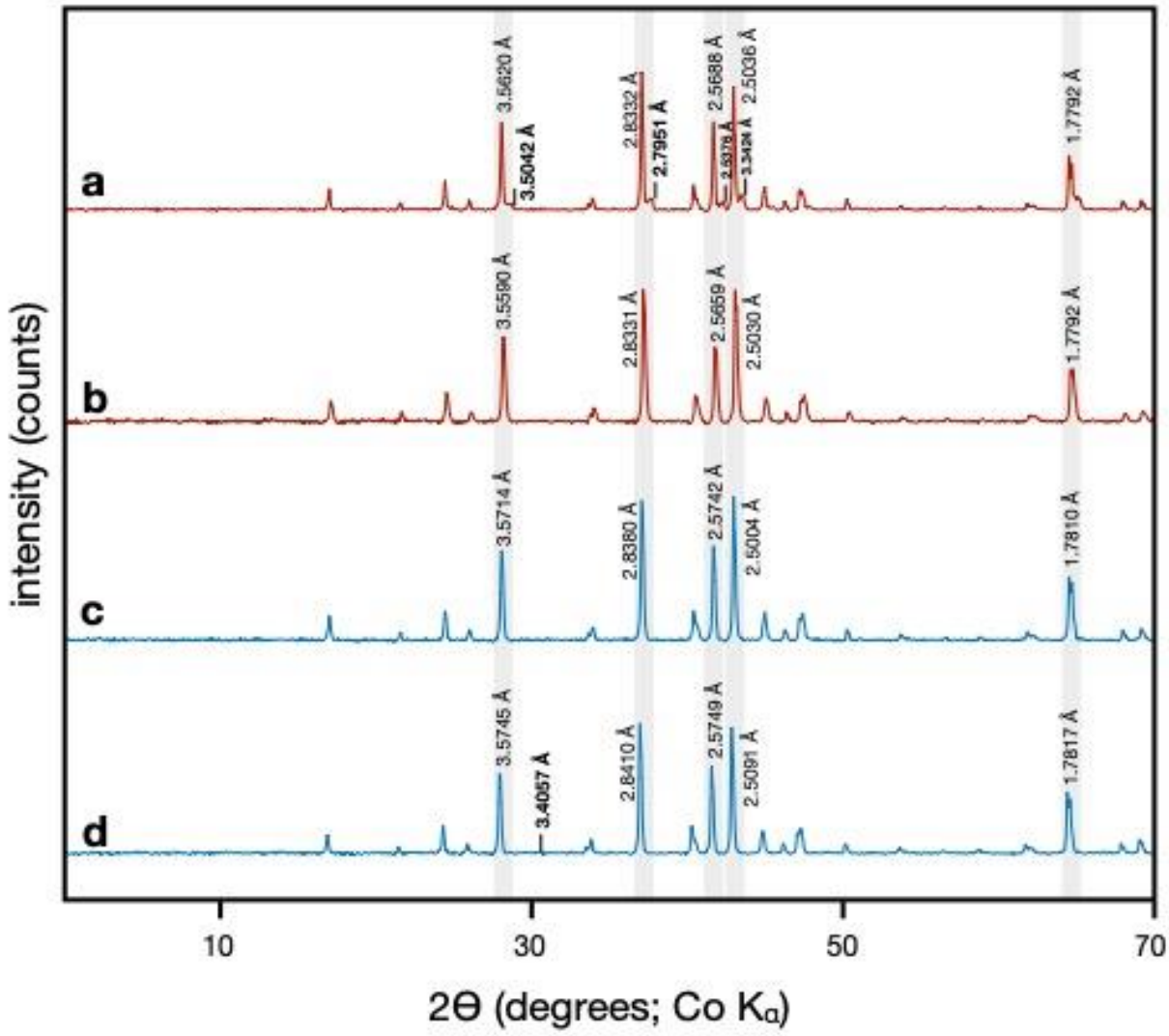


Figure 17: The XRD spectra for the solids of 181004. From top to bottom: pH 2 low rock:water ratio; pH 2 high rock:water ratio; pH 4 low rock:water ratio; and pH 4 high rock:water ratio. Anomalous peaks that were not identified as belonging to any one mineral spectra are labelled and bolded.

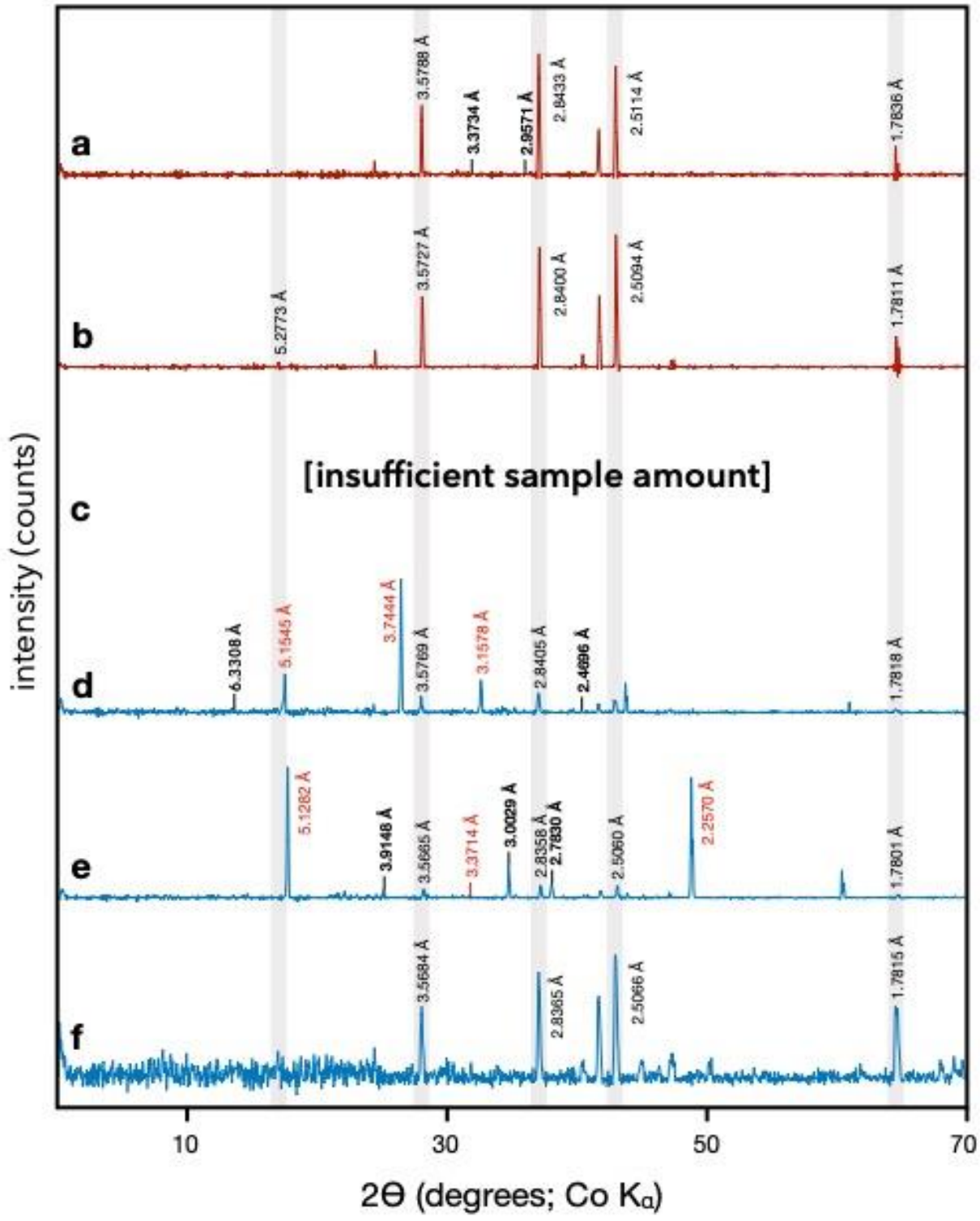


Figure 18: The XRD spectra for the solids of 181029 Fa. From top to bottom: pH 2 CO2 0.1 bar; pH 2 CO2 0.5 bar; pH 2 CO2 1.0 bar; pH 4 CO2 0.1 bar; pH 4 CO2 0.5 bar; pH 4 CO2 1.0 bar. Anomalous peaks that were not identified as belonging to any one mineral spectra are labelled and bolded. Peaks corresponding to siderite are highlighted red.

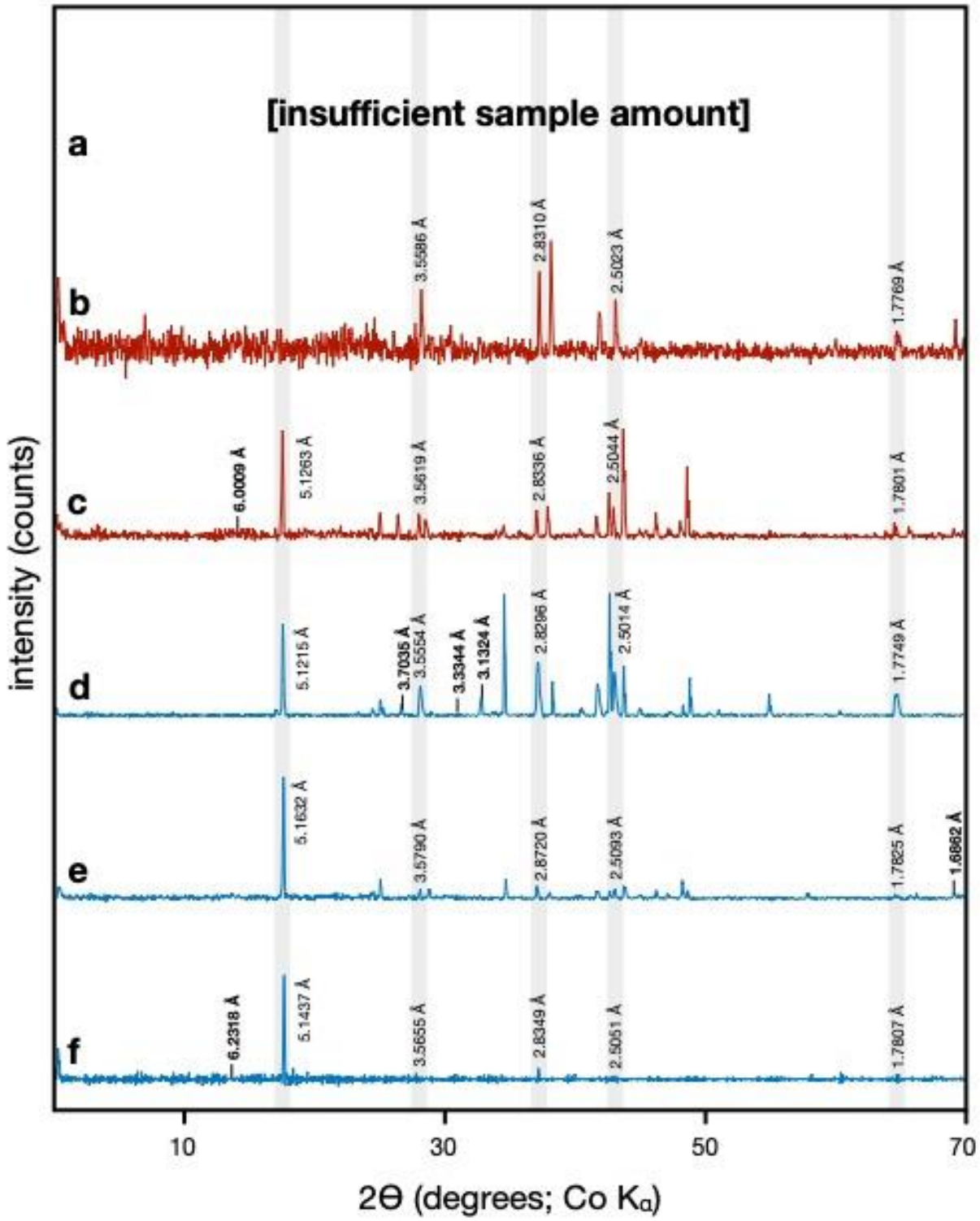


Figure 19: The XRD spectra for the solids of 181029 Fo. From top to bottom: pH 2 CO2 0.1 bar; pH 2 CO2 0.5 bar; pH 2 CO2 1.0 bar; pH 4 CO2 0.1 bar; pH 4 CO2 0.5 bar; pH 4 CO2 1.0 bar. Anomalous peaks that were not identified as belonging to any one mineral spectra are labelled and bolded.

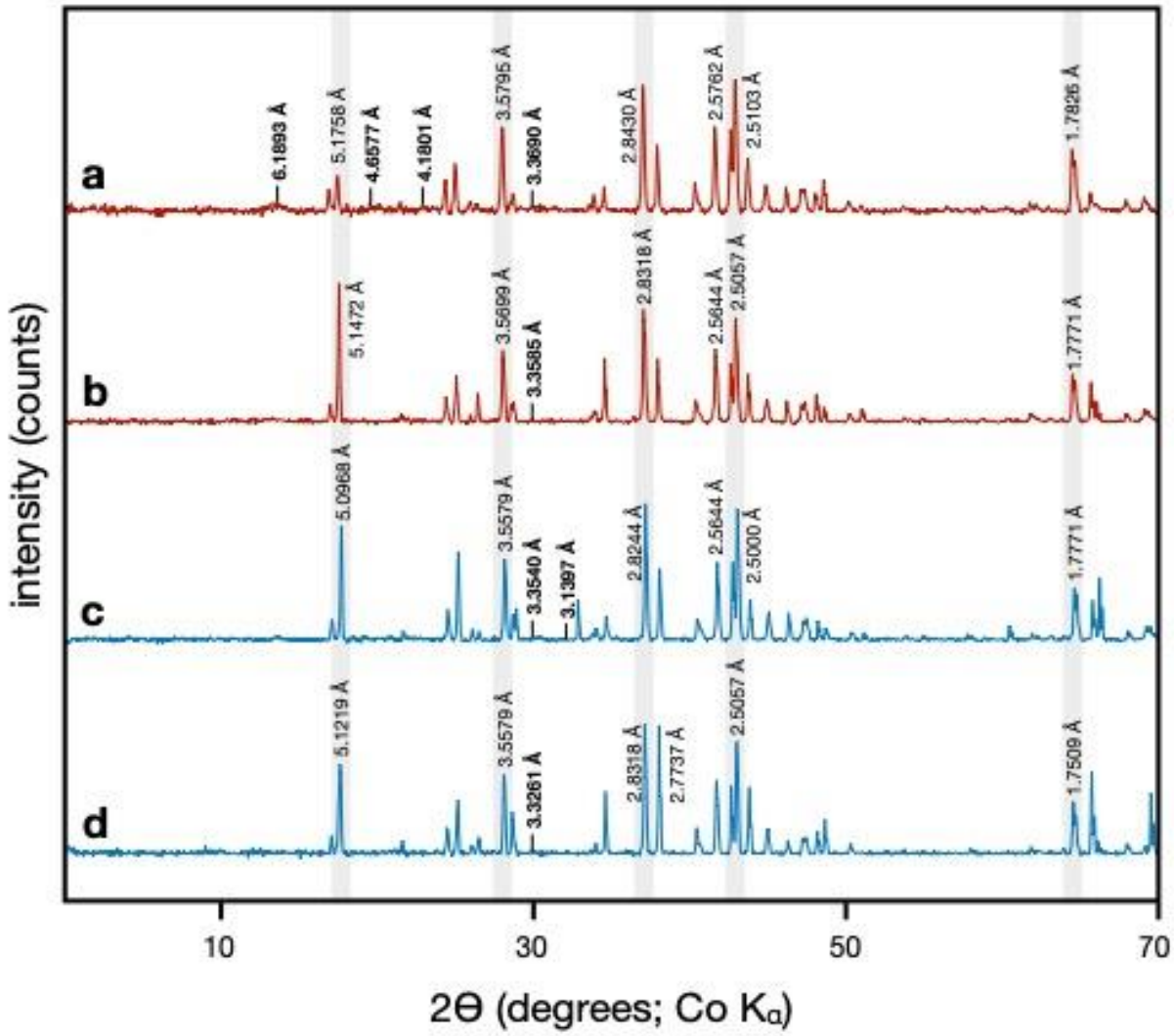


Figure 20: The XRD spectra for the solids of 181205. From top to bottom: pH 2 low rock:water ratio; pH 2 high rock:water ratio; pH 4 low rock:water ratio; and pH 4 high rock:water ratio. Anomalous peaks that were not identified as belonging to any one mineral spectra are labelled and bolded.

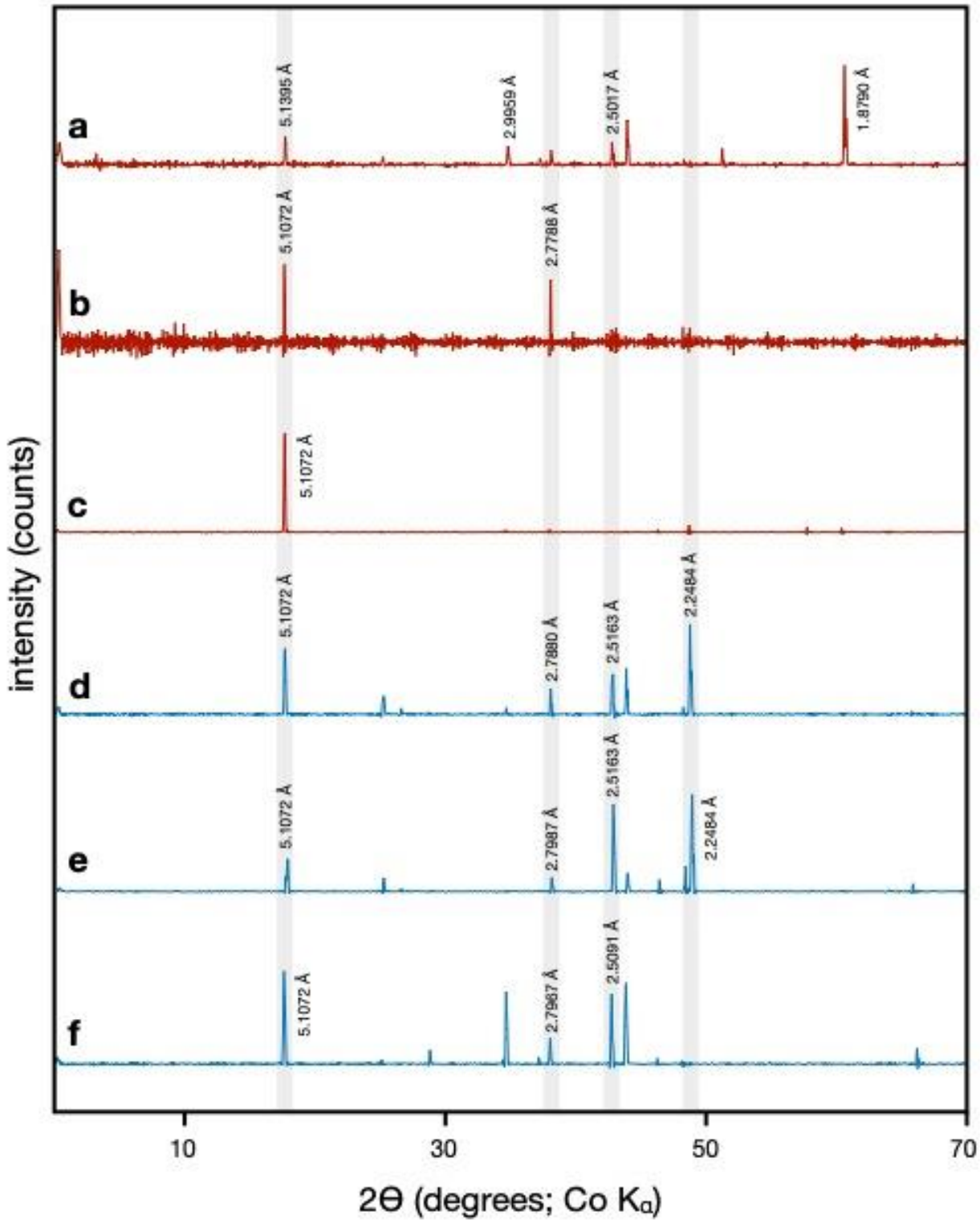


Figure 21: The XRD spectra for the solids of 190121. From top to bottom: pH 2 CO2 0.1 bar; pH 2 CO2 0.5 bar; pH 2 CO2 1.0 bar; pH 4 CO2 0.1 bar; pH 4 CO2 0.5 bar; pH 4 CO2 1.0 bar. Anomalous peaks that were not identified as belonging to any one mineral spectra are labelled and bolded.

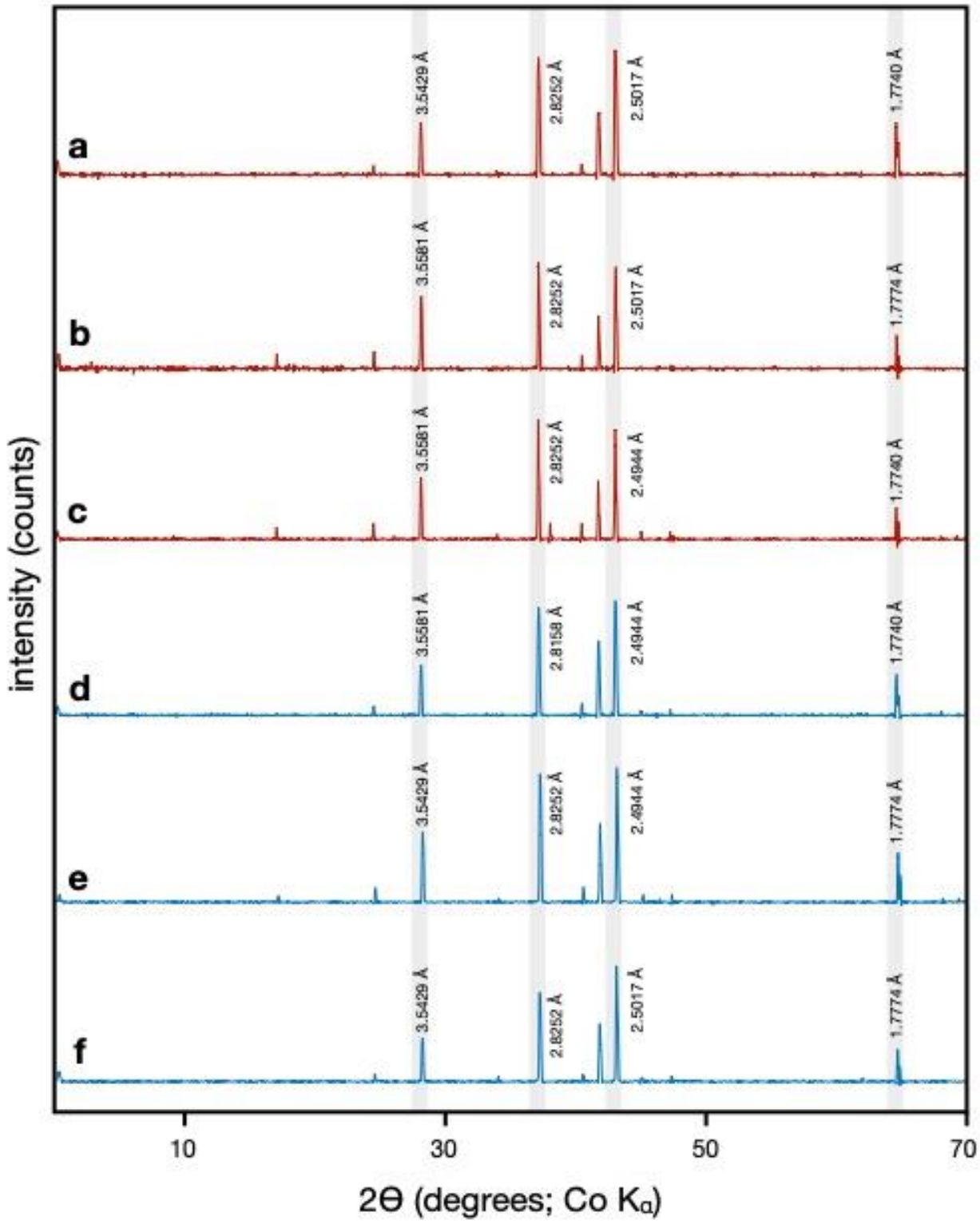


Figure 22: The XRD spectra for the solids of 190423 Fa. From top to bottom: pH 2 CO2 0.1 bar; pH 2 CO2 0.5 bar; pH 2 CO2 1.0 bar; pH 4 CO2 0.1 bar; pH 4 CO2 0.5 bar; pH 4 CO2 1.0 bar. Anomalous peaks that were not identified as belonging to any one mineral spectra are labelled and bolded.

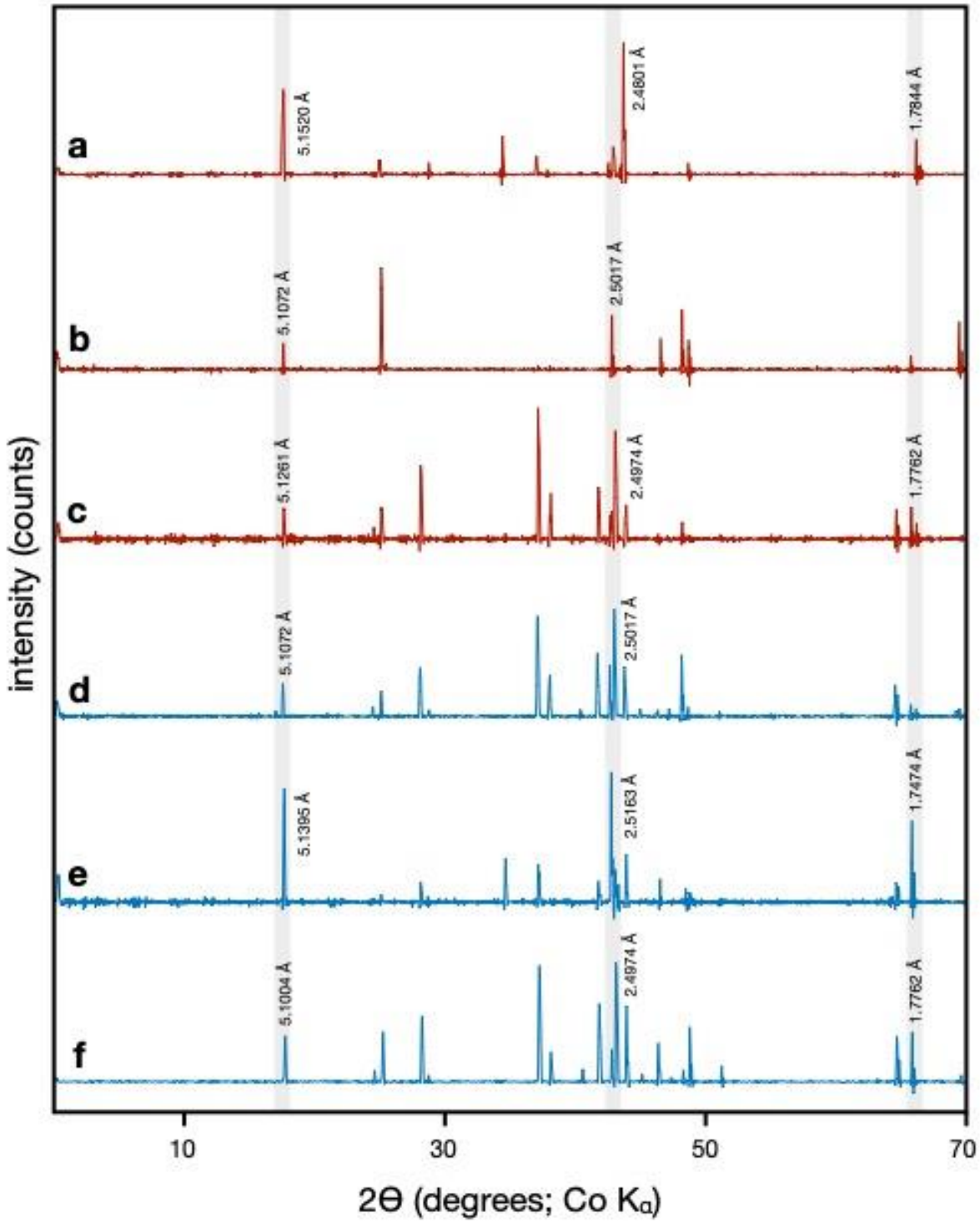


Figure 23: The XRD spectra for the solids of 190423 Fo. From top to bottom: pH 2 CO2 0.1 bar; pH 2 CO2 0.5 bar; pH 2 CO2 1.0 bar; pH 4 CO2 0.1 bar; pH 4 CO2 0.5 bar; pH 4 CO2 1.0 bar. Anomalous peaks that were not identified as belonging to any one mineral spectra are labelled and bolded.

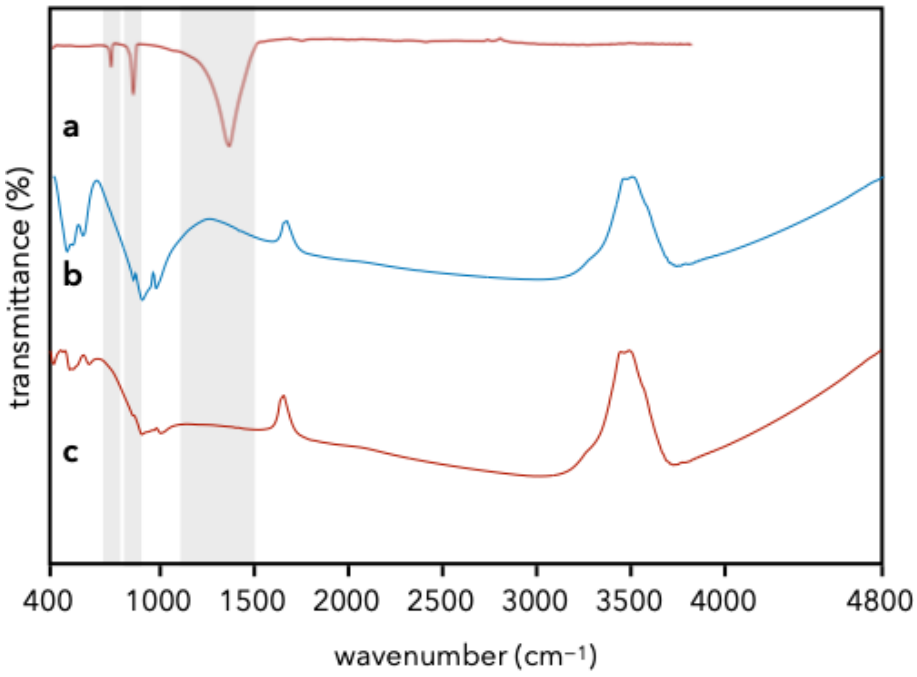


Figure 24: The FT-IR spectra for pure siderite (a), pure fayalite (b), and pure forsterite (c). The pale grey bars mark the key absorption zones that are diagnostic of siderite.

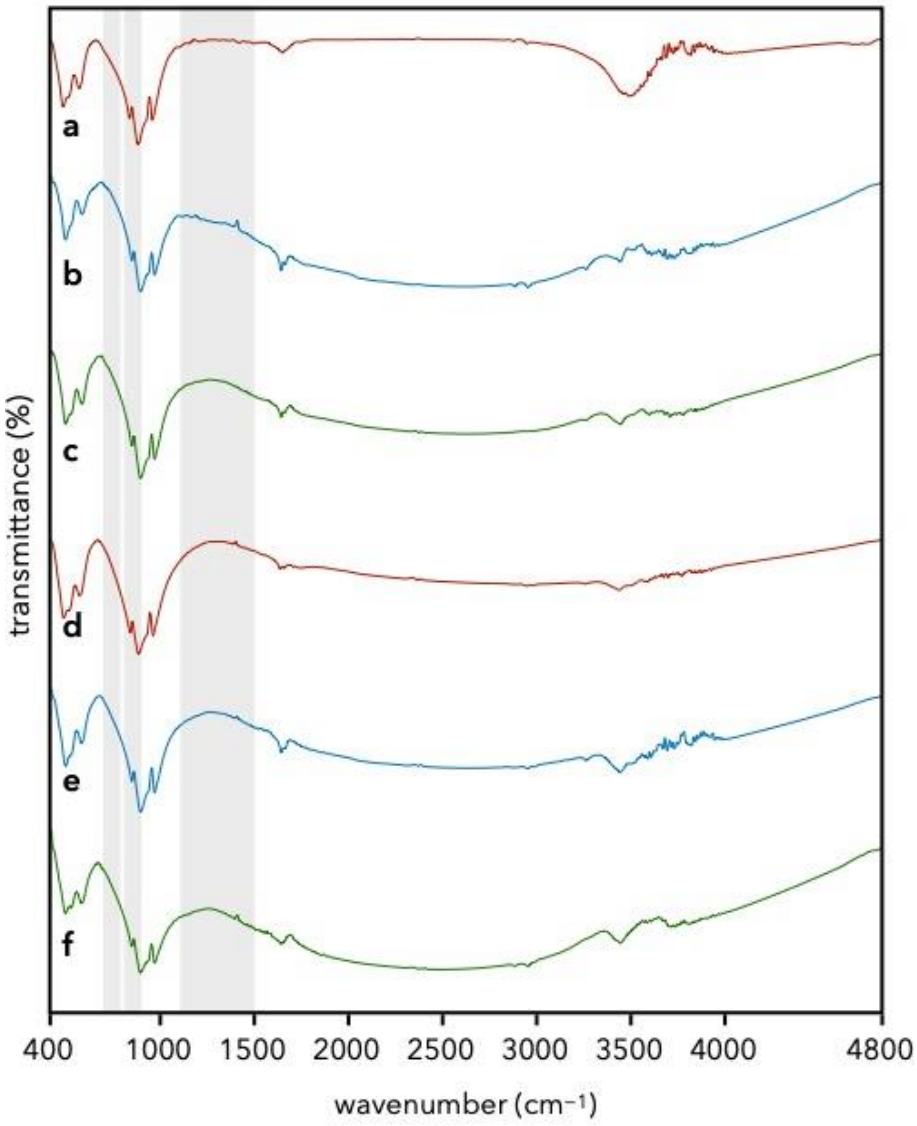


Figure 25: The FT-IR spectra for 180123. From top to bottom: pH 2 low water-rock; pH 4 low-water rock; pH 6 low water-rock; pH 2 high water-rock; pH 4 high-water rock; and pH 6 high water-rock. The pale grey bars mark the key absorption zones that are diagnostic of siderite.

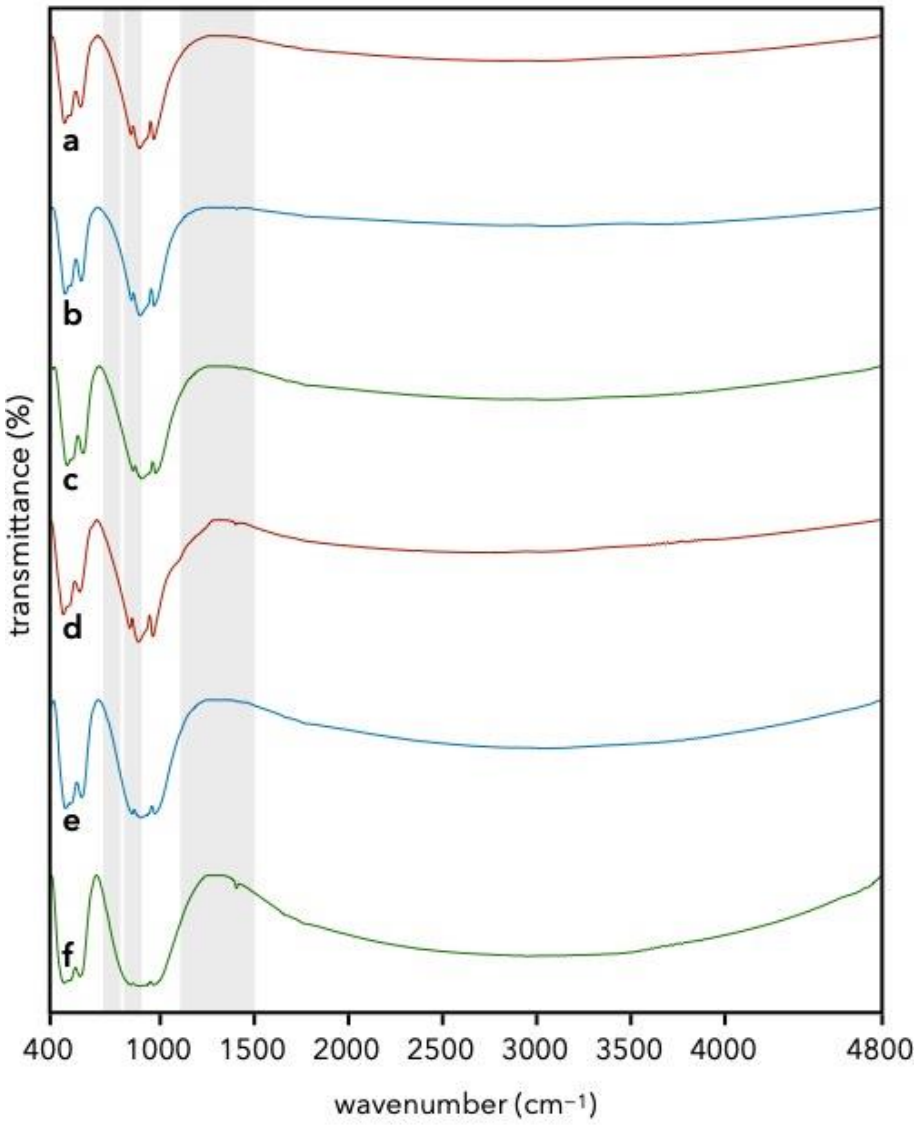


Figure 26: The FT-IR spectra for 180203. From top to bottom: pH 2 low water-rock; pH 4 low-water rock; pH 6 low water-rock; pH 2 high water-rock; pH 4 high-water rock; and pH 6 high water-rock. The pale grey bars mark the key absorption zones that are diagnostic of siderite.

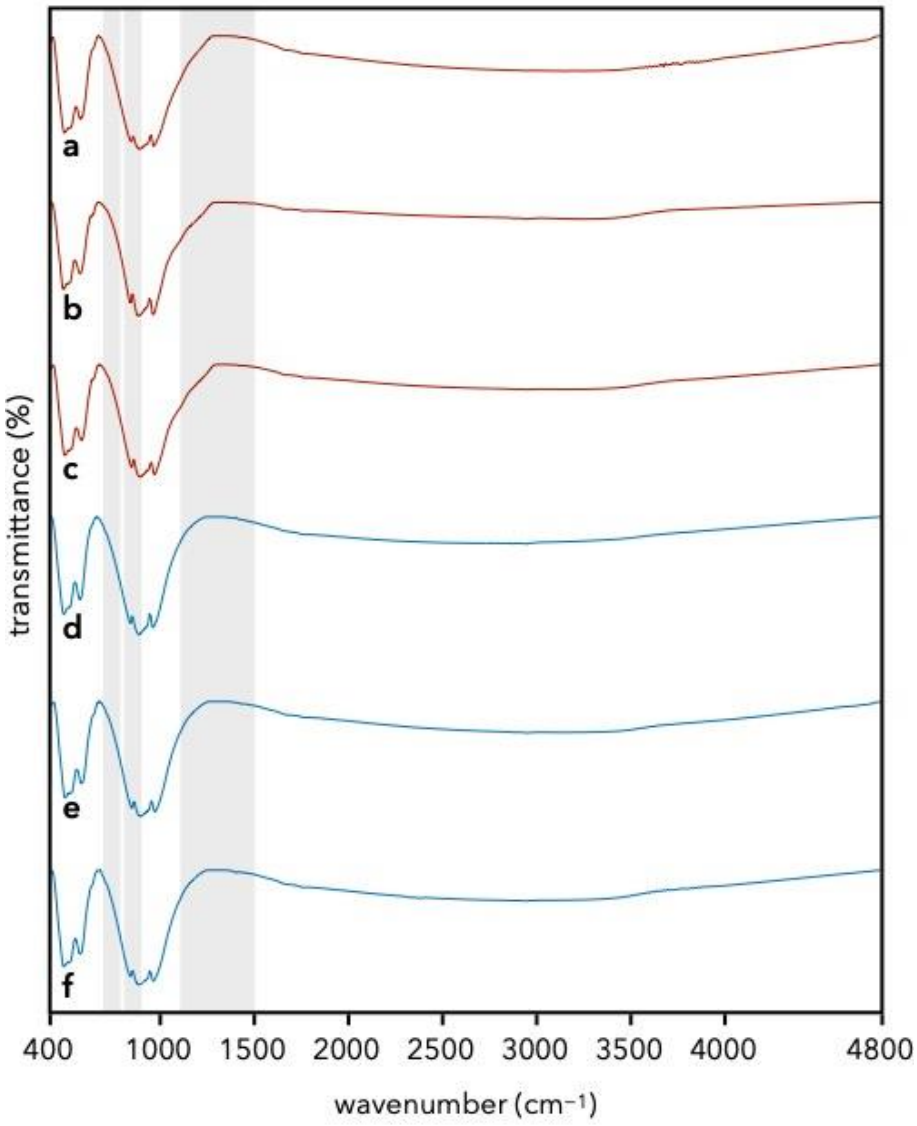


Figure 27: The FT-IR spectra for 180313. From top to bottom: pH 2 CO_2 0.1 bar; pH 2 CO_2 0.5 bar; pH 2 CO_2 1.0 bar; pH 4 CO_2 0.1 bar; pH 4 CO_2 0.5 bar; pH 4 CO_2 1.0 bar. The pale grey bars mark the key absorption zones that are diagnostic of siderite.

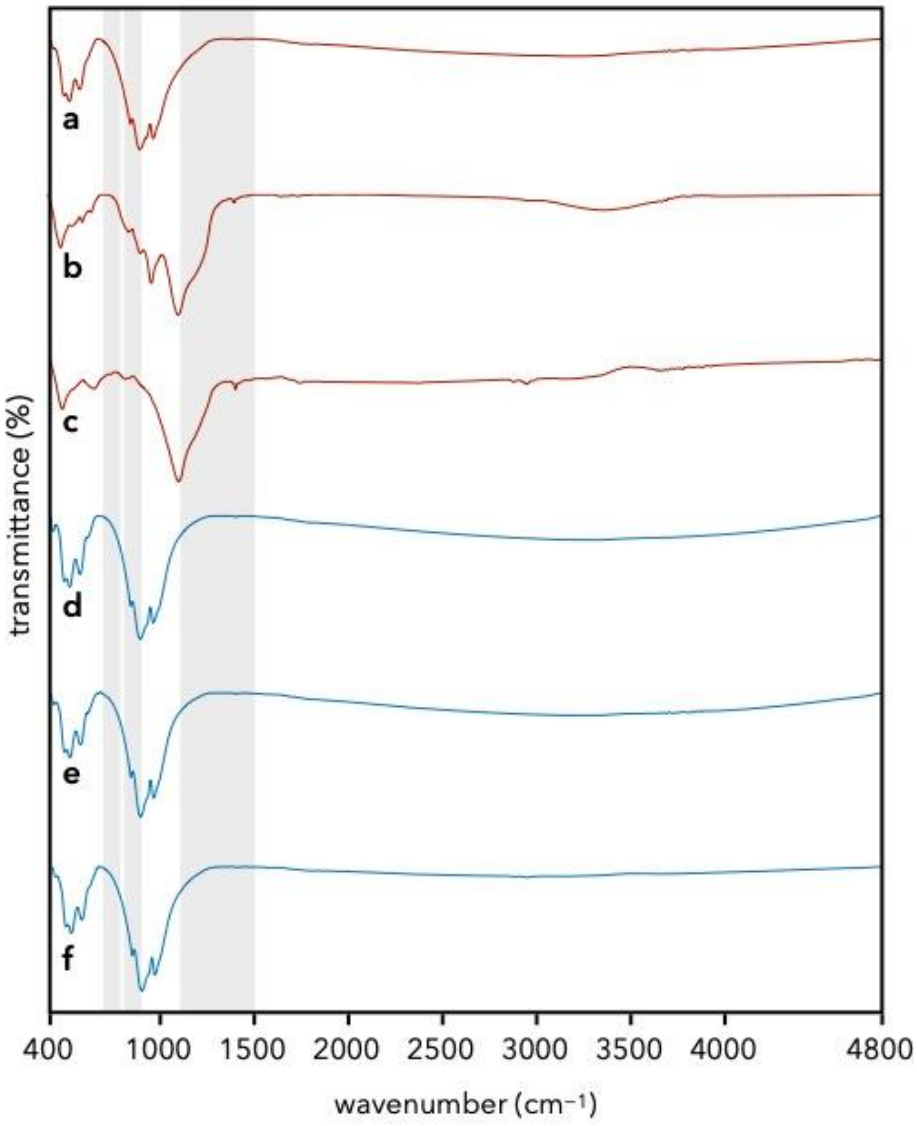


Figure 28: The FT-IR spectra for 180406. From top to bottom: pH 2 CO_2 0.1 bar; pH 2 CO_2 0.5 bar; pH 2 CO_2 1.0 bar; pH 4 CO_2 0.1 bar; pH 4 CO_2 0.5 bar; pH 4 CO_2 1.0 bar. The pale grey bars mark the key absorption zones that are diagnostic of siderite.

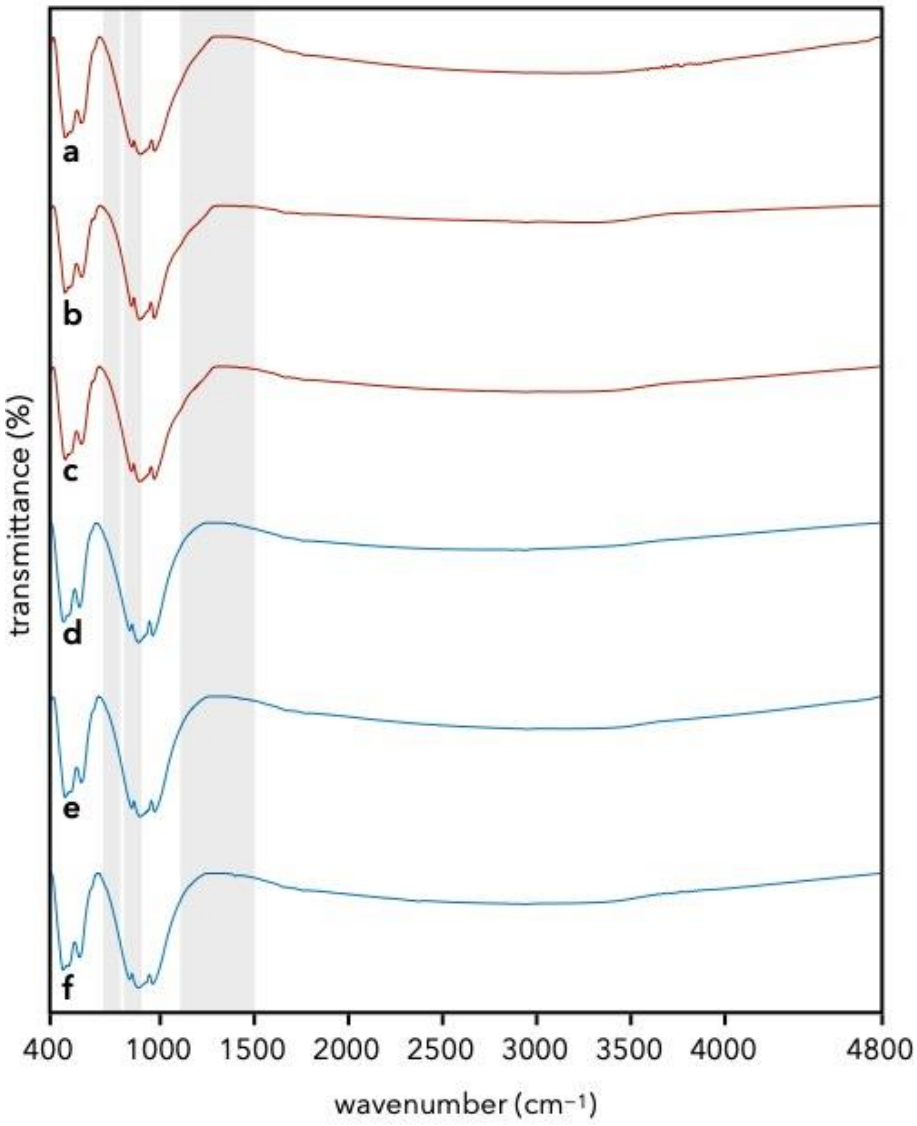


Figure 29: The FT-IR spectra for 180612. From top to bottom: pH 2 CO_2 0.1 bar; pH 2 CO_2 0.5 bar; pH 2 CO_2 1.0 bar; pH 4 CO_2 0.1 bar; pH 4 CO_2 0.5 bar; pH 4 CO_2 1.0 bar. The pale grey bars mark the key absorption zones that are diagnostic of siderite.

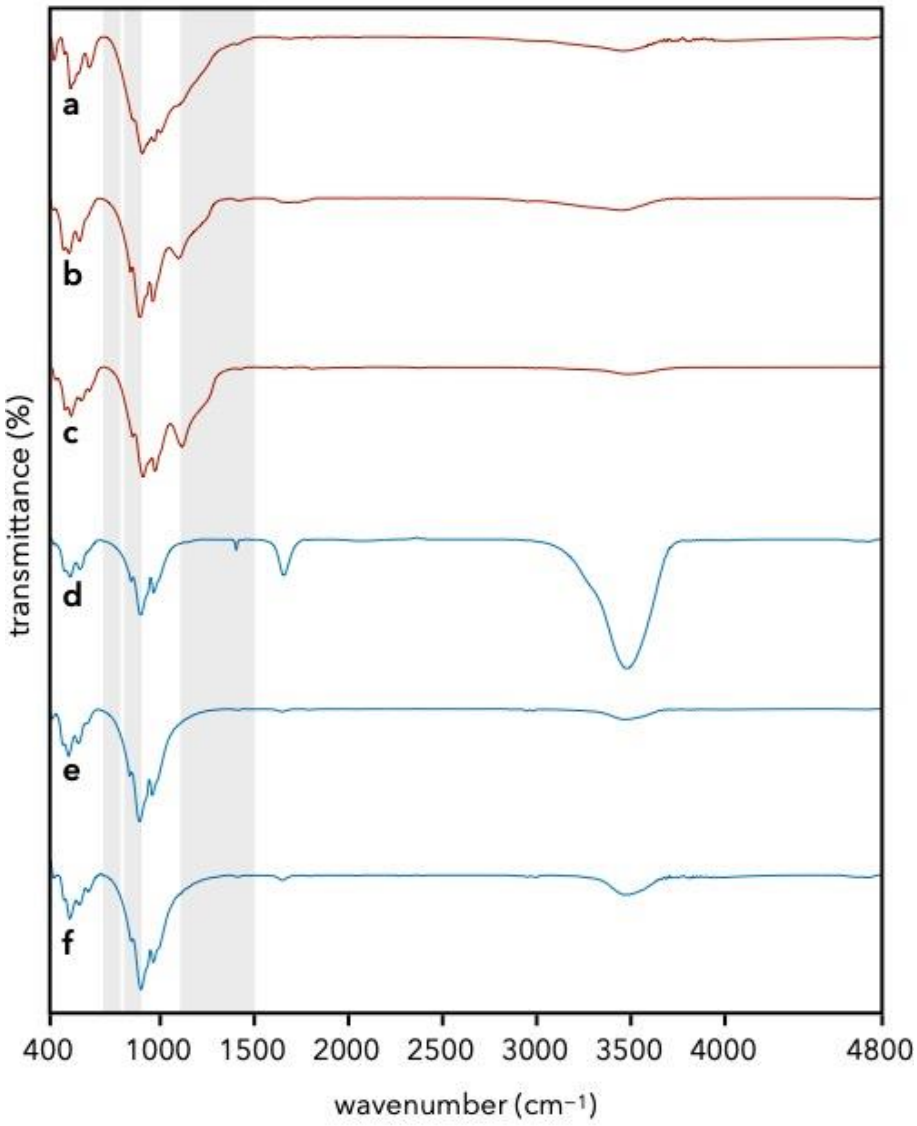


Figure 30: The FT-IR spectra for 180628. From top to bottom: pH 2 CO_2 0.1 bar; pH 2 CO_2 0.5 bar; pH 2 CO_2 1.0 bar; pH 4 CO_2 0.1 bar; pH 4 CO_2 0.5 bar; pH 4 CO_2 1.0 bar. The pale grey bars mark the key absorption zones that are diagnostic of siderite.

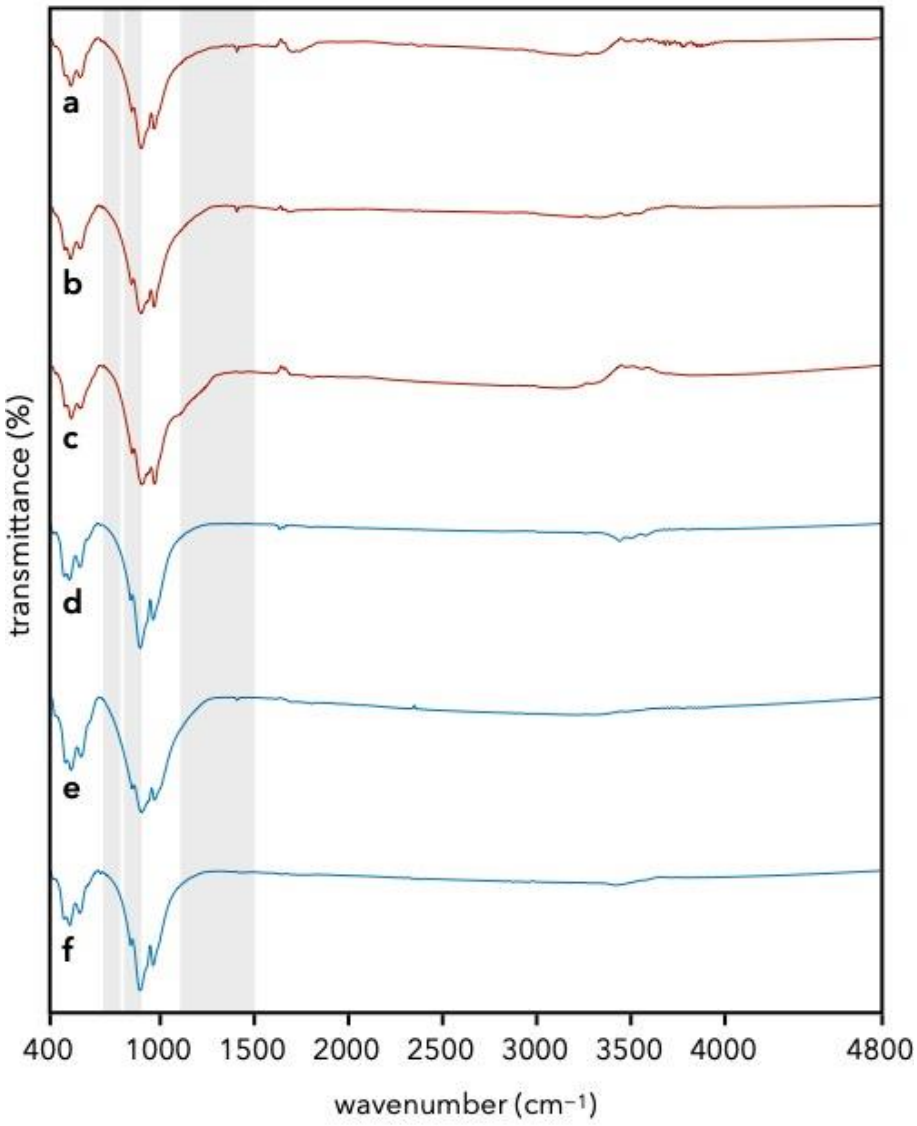


Figure 31: The FT-IR spectra for 180829. From top to bottom: pH 2 CO_2 0.1 bar; pH 2 CO_2 0.5 bar; pH 2 CO_2 1.0 bar; pH 4 CO_2 0.1 bar; pH 4 CO_2 0.5 bar; pH 4 CO_2 1.0 bar. The pale grey bars mark the key absorption zones that are diagnostic of siderite.

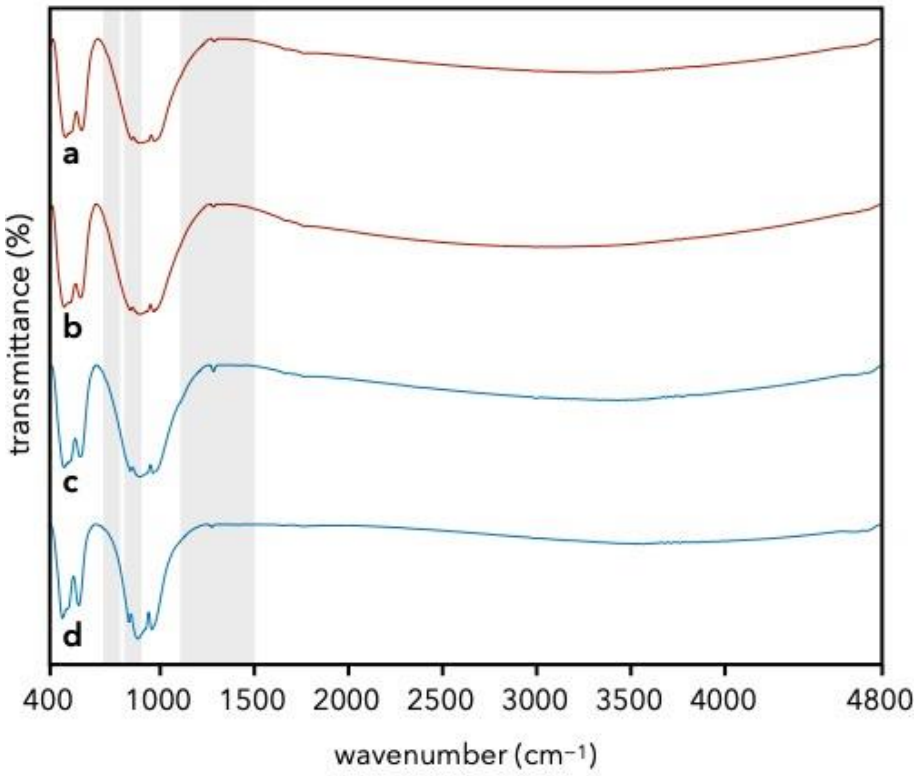


Figure 32: The FT-IR spectra for 181004 From top to bottom: pH 2 low rock:water ratio; pH 2 high rock:water ratio; pH 4 low rock:water ratio; and pH 4 high rock:water ratio. The pale grey bars mark the key absorption zones that are diagnostic of siderite.

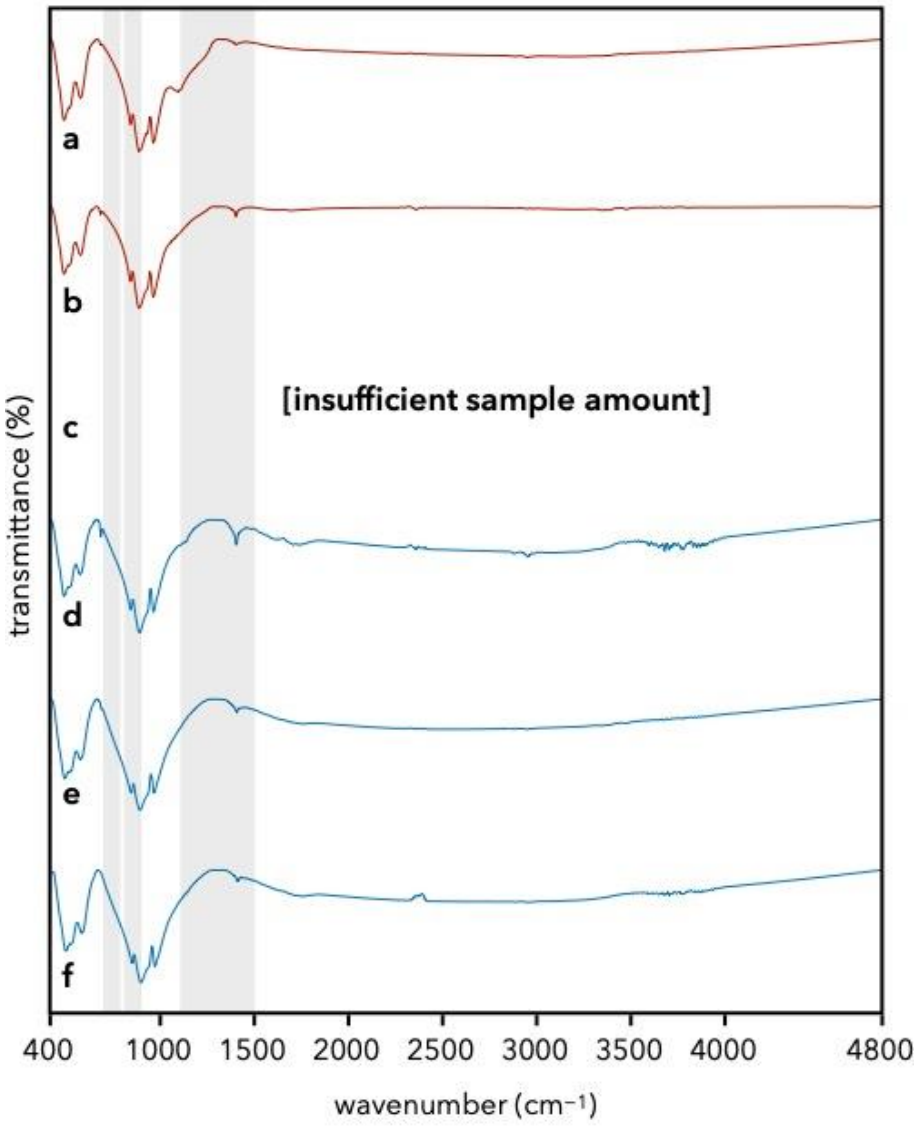


Figure 33: The FT-IR spectra for 181029 Fa. From top to bottom: pH 2 CO_2 0.1 bar; pH 2 CO_2 0.5 bar; pH 2 CO_2 1.0 bar (insufficient amount); pH 4 CO_2 0.1 bar; pH 4 CO_2 0.5 bar; pH 4 CO_2 1.0 bar. The pale grey bars mark the key absorption zones that are diagnostic of siderite.

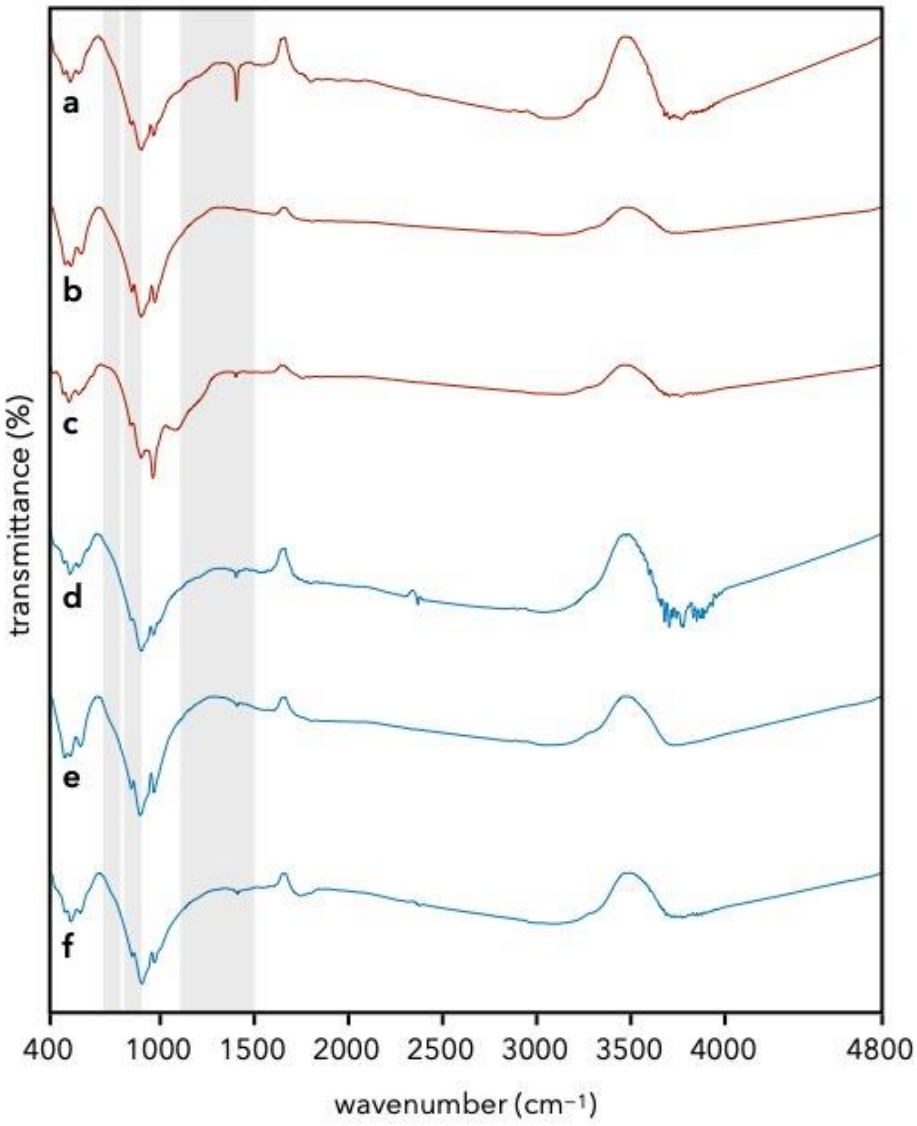


Figure 34: The FT-IR spectra for 181029 Fo. From top to bottom: pH 2 CO_2 0.1 bar; pH 2 CO_2 0.5 bar; pH 2 CO_2 1.0 bar; pH 4 CO_2 0.1 bar; pH 4 CO_2 0.5 bar; pH 4 CO_2 1.0 bar. The pale grey bars mark the key absorption zones that are diagnostic of siderite.

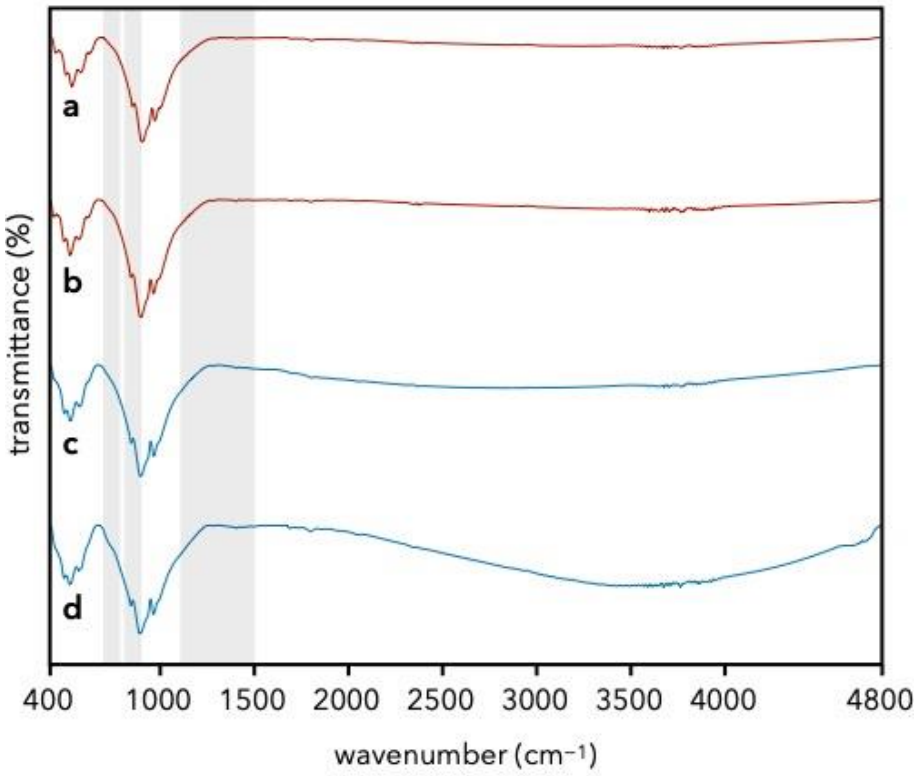


Figure 35: The FT-IR spectra for 181205. From top to bottom: pH 2 low rock:water ratio; pH 2 high rock:water ratio; pH 4 low rock:water ratio; and pH 4 high rock:water ratio. The pale grey bars mark the key absorption zones that are diagnostic of siderite.

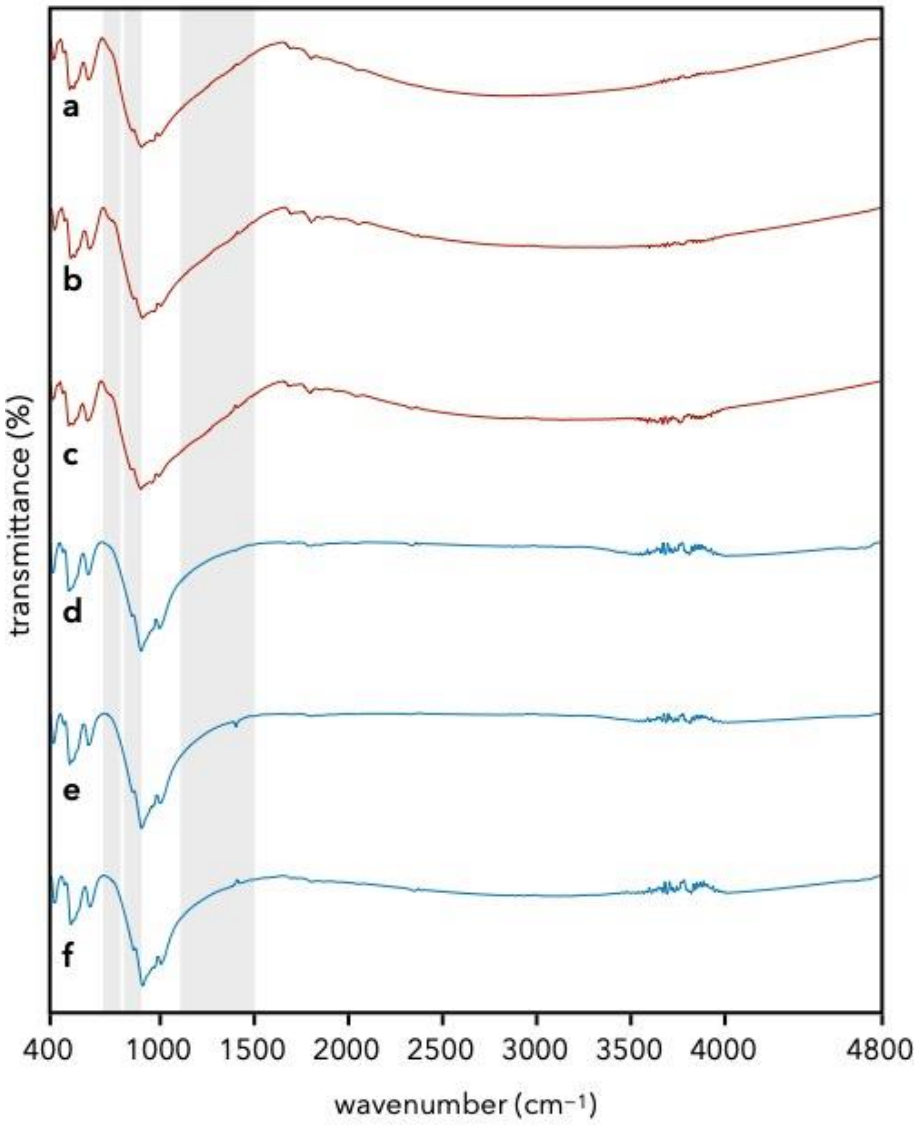


Figure 36: The FT-IR spectra for 190121. From top to bottom: pH 2 CO_2 0.1 bar; pH 2 CO_2 0.5 bar; pH 2 CO_2 1.0 bar; pH 4 CO_2 0.1 bar; pH 4 CO_2 0.5 bar; pH 4 CO_2 1.0 bar. The pale grey bars mark the key absorption zones that are diagnostic of siderite.

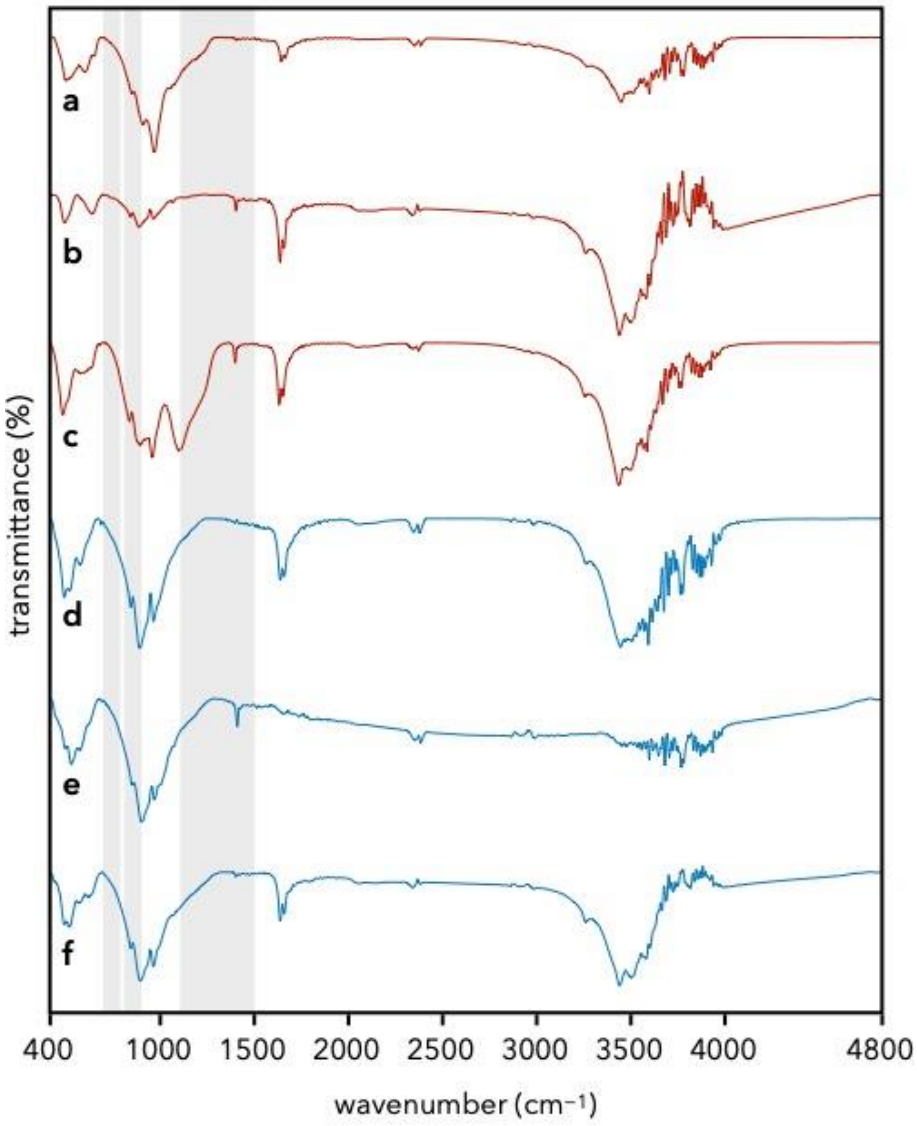


Figure 37: The FT-IR spectra for 190423 Fa. From top to bottom: pH 2 CO_2 0.1 bar; pH 2 CO_2 0.5 bar; pH 2 CO_2 1.0 bar; pH 4 CO_2 0.1 bar; pH 4 CO_2 0.5 bar; pH 4 CO_2 1.0 bar. The pale grey bars mark the key absorption zones that are diagnostic of siderite.

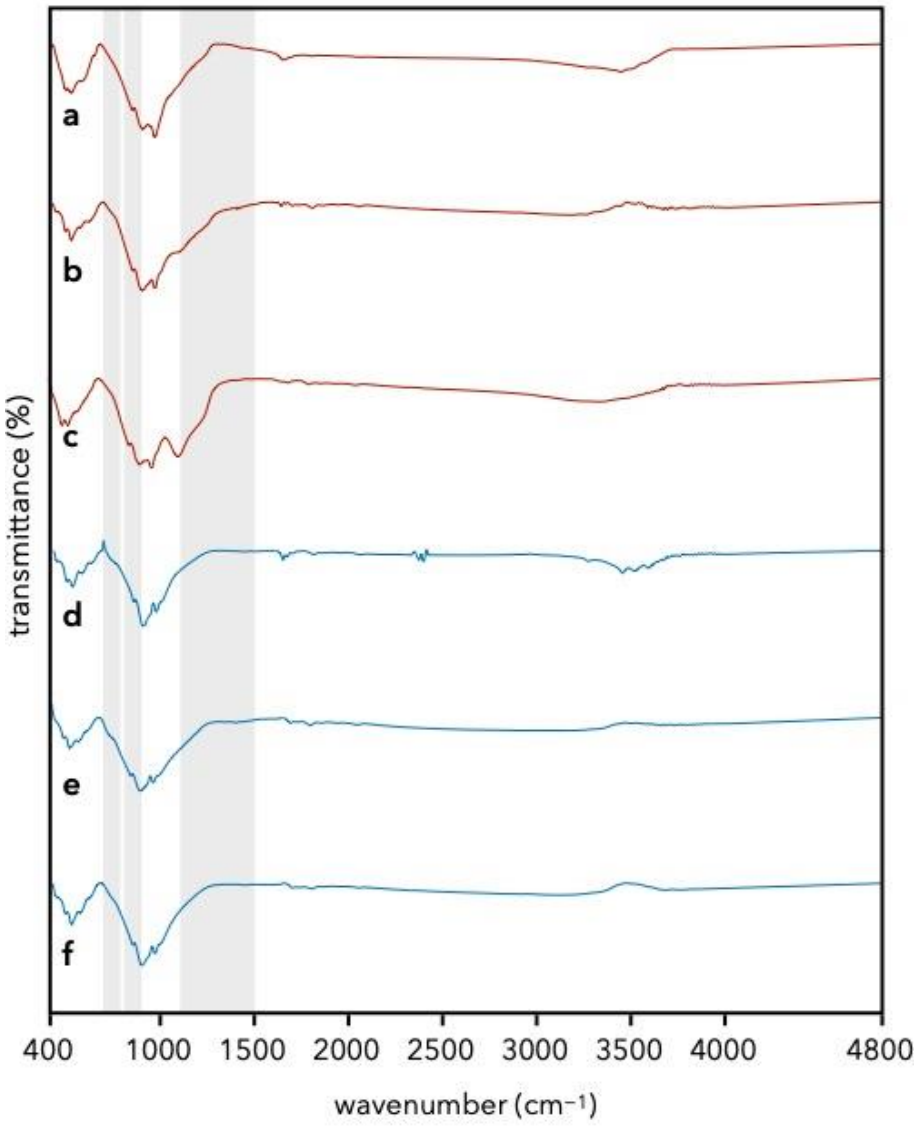


Figure 38: The FT-IR spectra for 190423 Fo. From top to bottom: pH 2 CO_2 0.1 bar; pH 2 CO_2 0.5 bar; pH 2 CO_2 1.0 bar; pH 4 CO_2 0.1 bar; pH 4 CO_2 0.5 bar; pH 4 CO_2 1.0 bar. The pale grey bars mark the key absorption zones that are diagnostic of siderite.

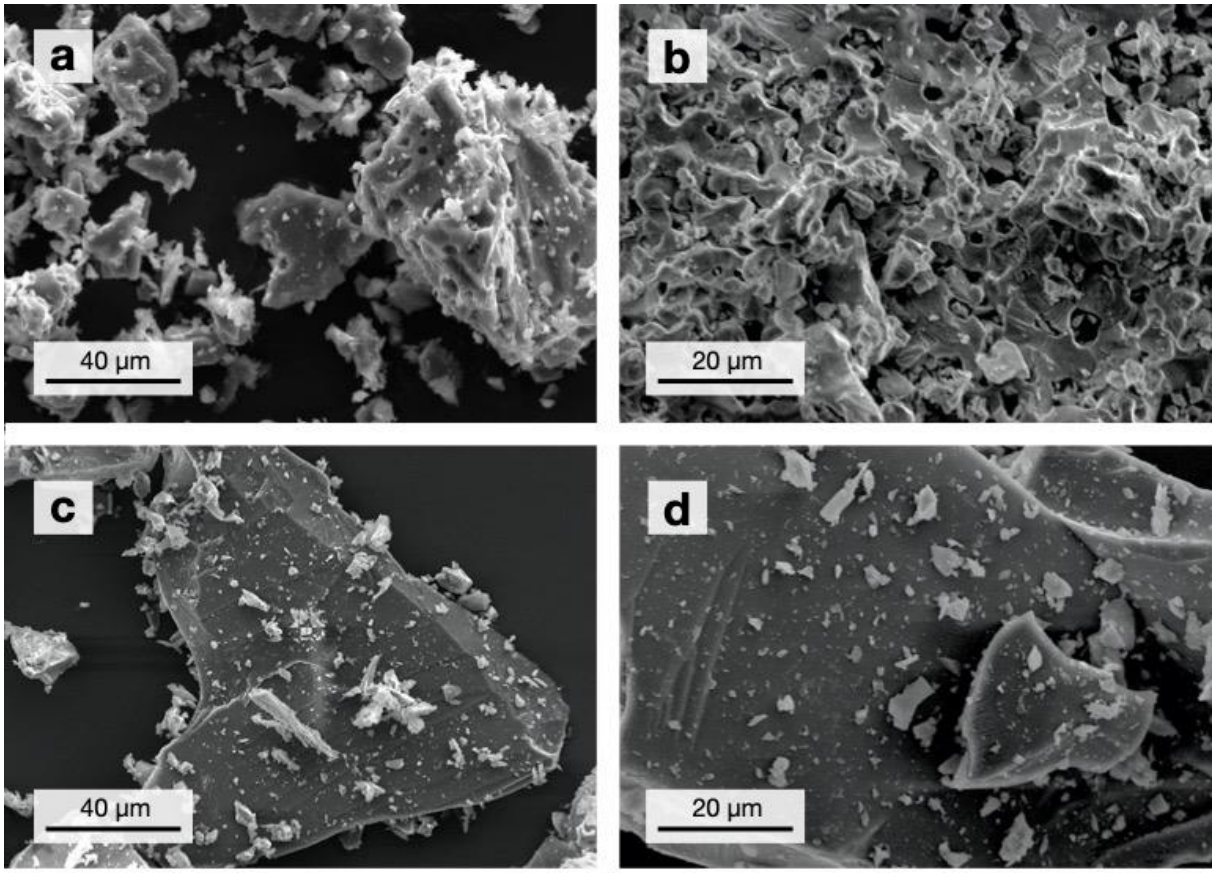


Figure 39: SEM images of: (a) and (b) synthetic fayalite; (c) and (d) natural forsterite.

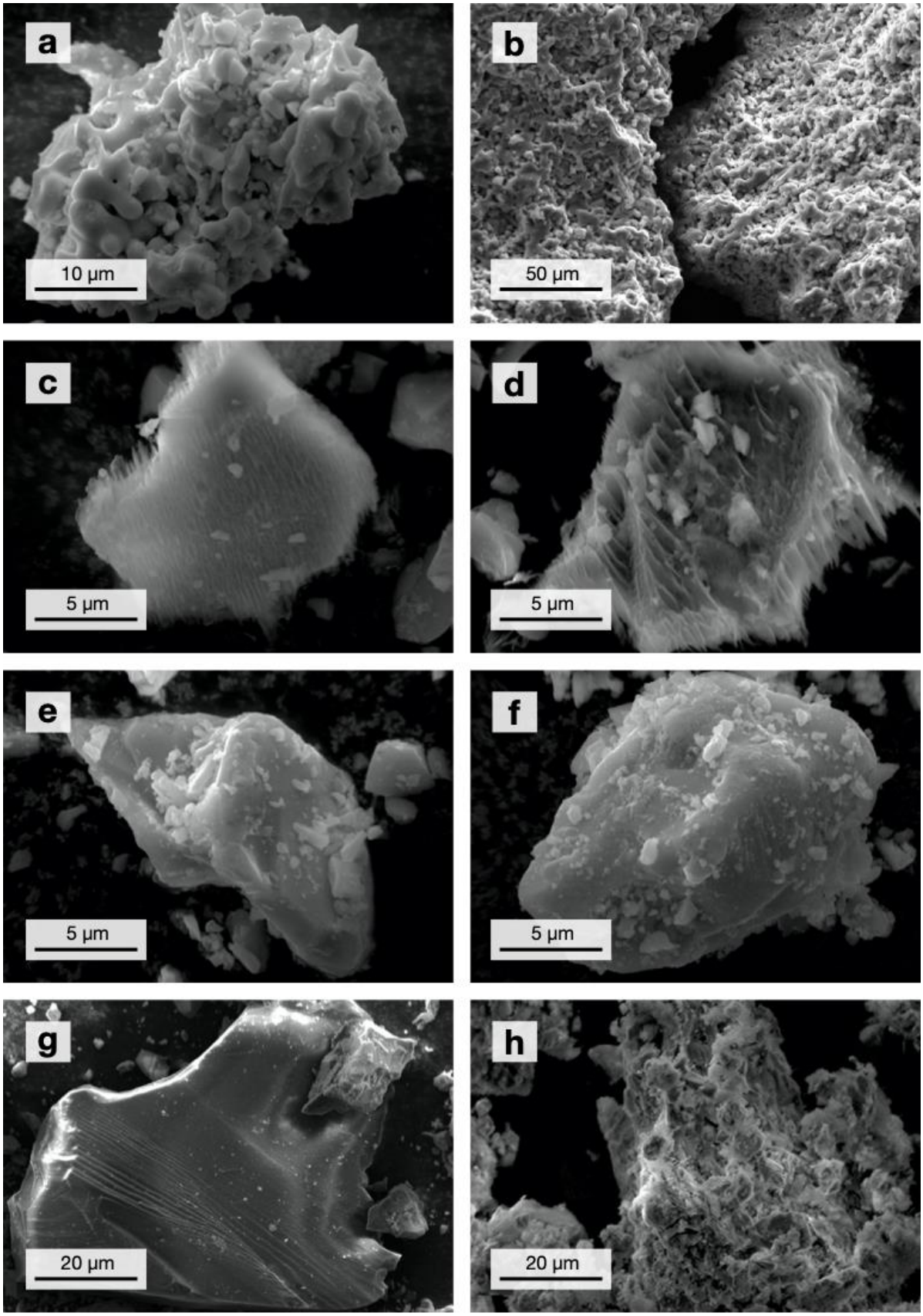


Figure 40: (a) and (b): Fayalite texture for 180123; (c) and (d): Fayalite texture for 180313; (e) and (f): Fayalite texture for 180403; (g) and (h): Forsterite and fayalite textures for 180628.

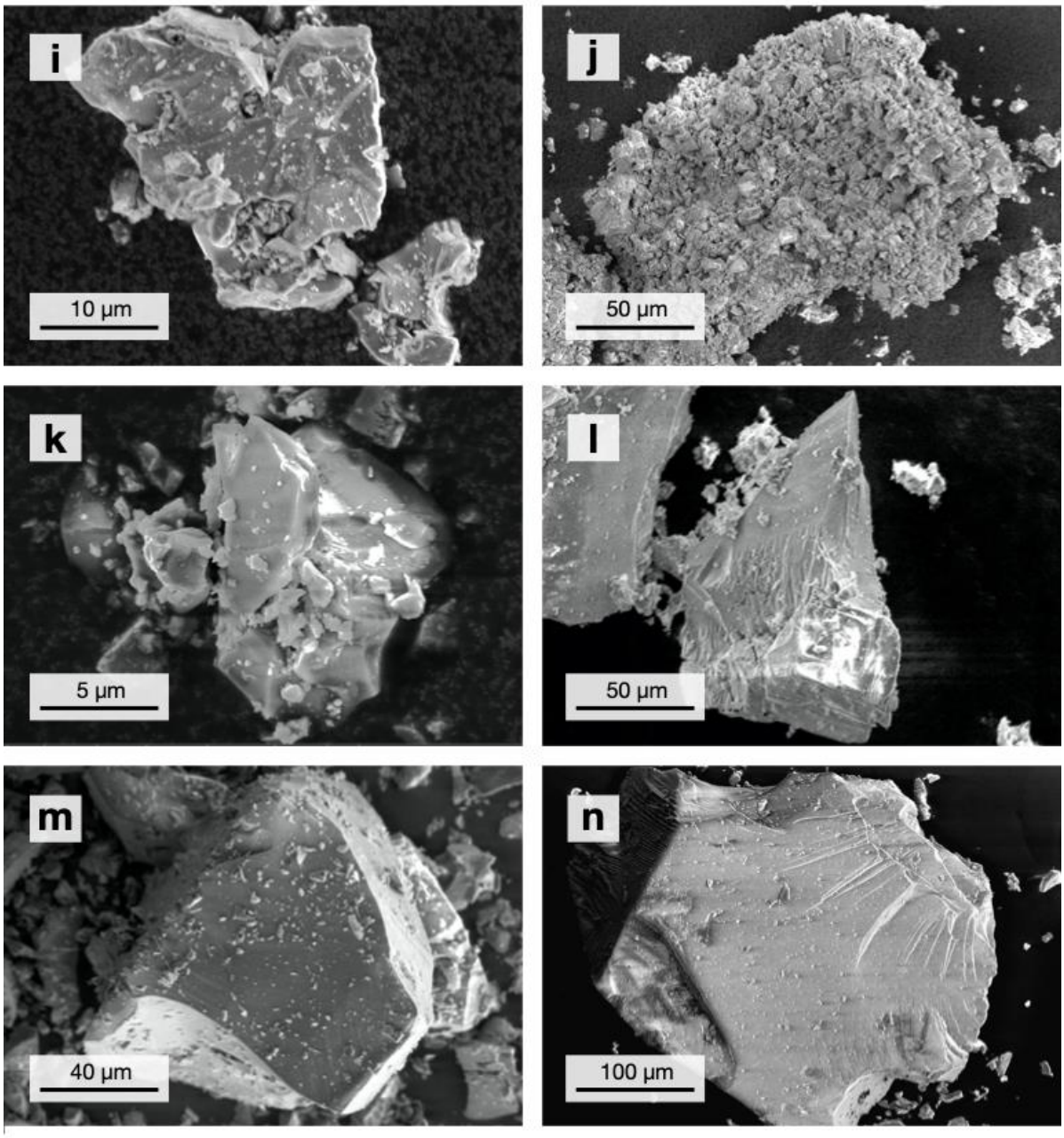


Figure 40 (continued): (i) and (j): Fayalite texture for 181004; (k) and (l): Forsterite and fayalite textures for 181029 Fa and Fo; (m) and (n): Forsterite and fayalite textures for 190121.

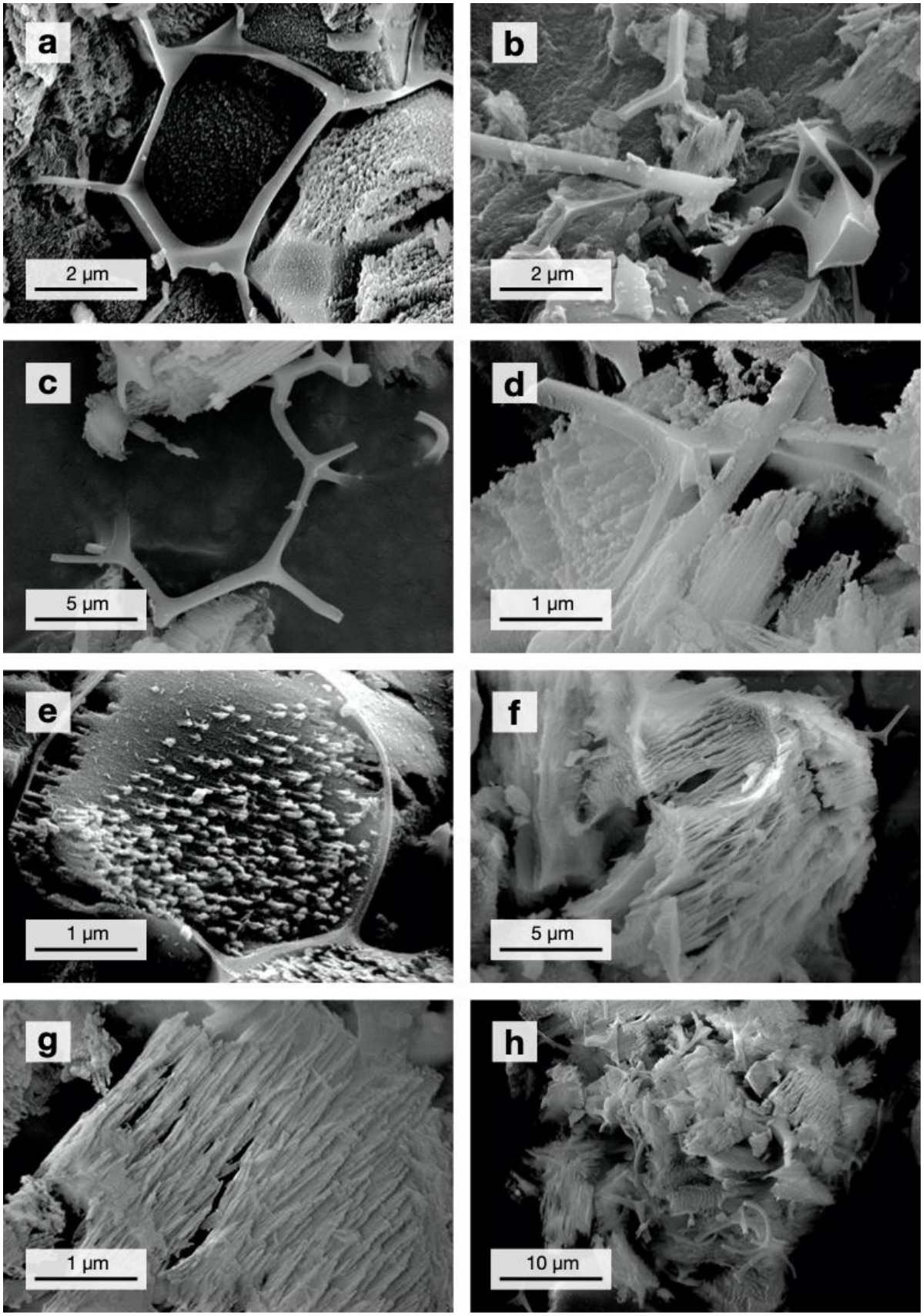


Figure 41: (a)-(d): Spindly, brittle 'antlers' that appear to have precipitated around mineral boundaries and fallen loose; (e)-(h): unusual dissolution patterns and their context.

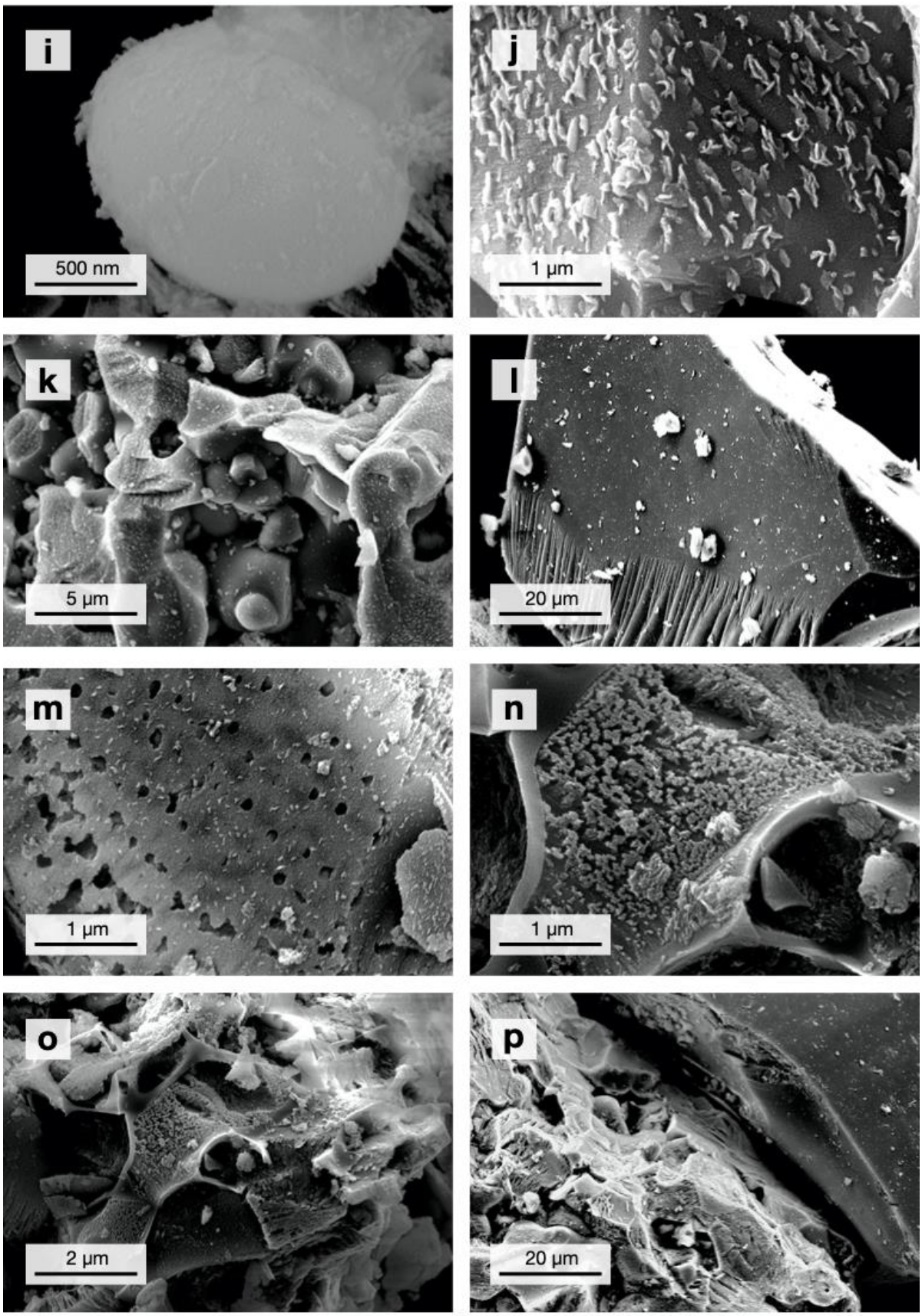


Figure 41 (continued): (i): Spherical precipitate; (j)-(k): aligned nano-scale particles; (l): unaltered forsterite grain; (m)-(p): unusual dissolution patterns and their context.

Parameter	Unit
H_2O	1 kg
H^+	Charge balance
Fe^{2+}	0.1 mmol/kg
SiO_2	0.1 mmol/kg
Mg^{2+}	0.1 mmol/kg
Cl^-	1.0 mmol/kg
SO_4^{2-}	1.0 mmol/kg
$CO_{2(g)}$ to HCO_3^-	1 fugacity
Time	30 years (all systems reach equilibrium)
Temp	25 °C
Reactant times	2 (1:500)
Fayalite	5 g
Forsterite	5 g
Surface area	1000 cm^2/g
Rate constant	2.34 e−11
$CO_{2(g)}$	Fixed

Table 13: Table of the original conditions used in each modelling run, where conditions deviated only to investigate a specific parameter; for example, CO_2 fugacity changed from 1.0 to 0.1 bar to investigate the effect of varying atmospheric CO_2.

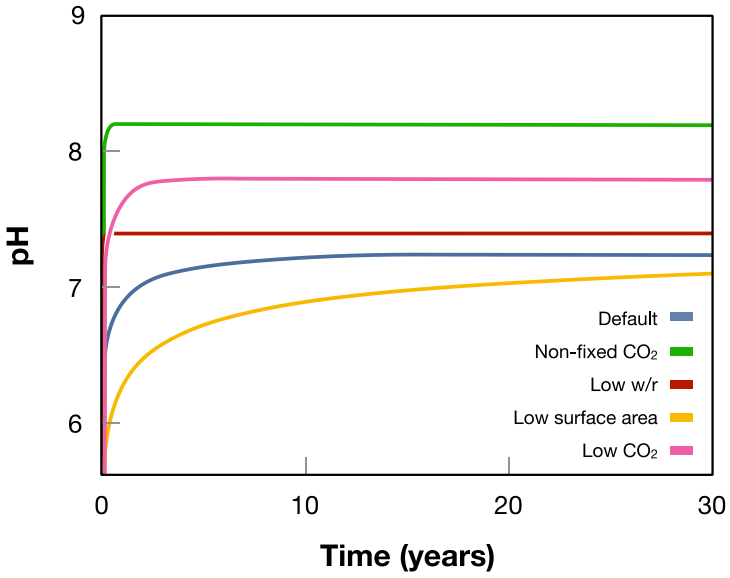


Figure 42: pH over 30 years for models constructed under differing parameters. Original (blue): conditions outlined in **Table 13**. Non-fixed CO_2: CO_2 allowed to leave a closed system. Low w/r: rock:water ratio of 1:1. Low surface area: surface area of 100 cm^2/g. Low CO_2: CO_2 levels at 0.1 bar.

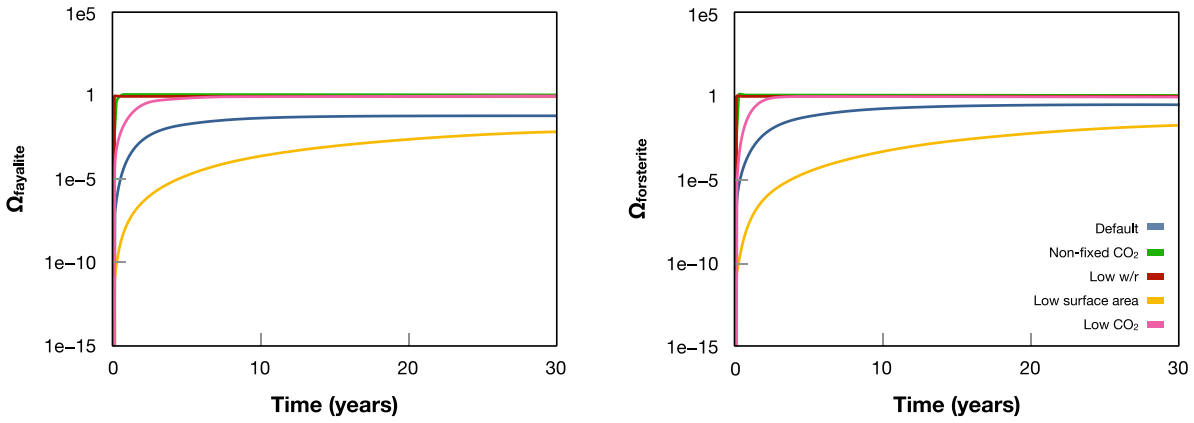


Figure 43: The increasing dissolution of fayalite (left) and forsterite (right) over 30 years under differing conditions. Note that under lower rock:water ratio, lower dissolved CO_2, and non-fixed CO_2 levels, fayalite and forsterite reach complete dissolution over this time. Models run with low particle surface area stabilised at the same level as the high surface area conditions after ~250 years.

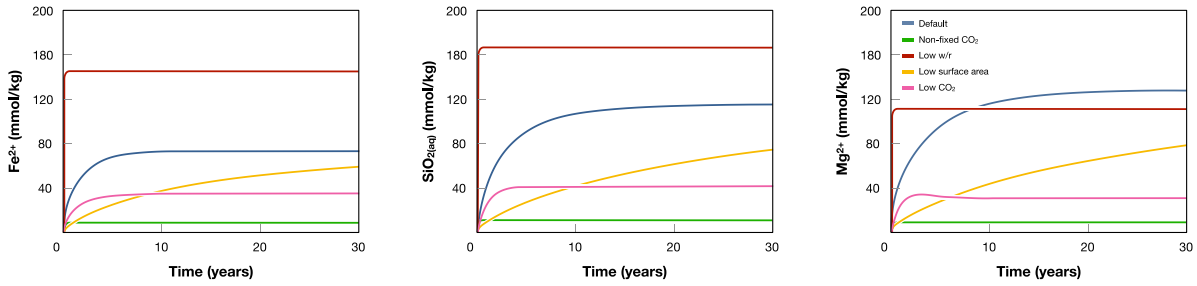


Figure 44: Levels of Fe^{2+}, $SiO_{2(aq)}$, and Mg^{2+} in solution over a 30-year model, measured in mmol/kg. Models run with low particle surface area stabilised at the same level as the high surface area conditions after ~250 years.

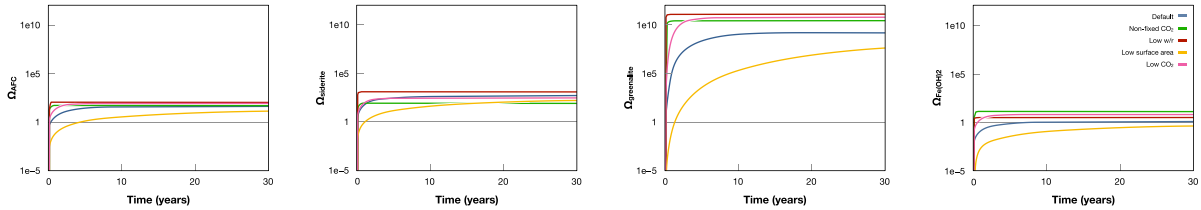


Figure 45: The saturation state (Ω) of amorphous Fe(II)-carbonate (AFC), siderite, greenalite, and $Fe(OH)_2$ over a 30-year model. Models run with low particle surface area stabilised at the same level as the high particle surface area conditions after ~250 years.

Appendix 3

Equations to Calculate aCO_3^{2-}

To calculate the activity of CO_3^{2-}, the following equations may be rearranged and calculated.

The equation describing siderite ($FeCO_3$) equilibria in aqueous solution is:

$$FeCO_3 = Fe^{2+} + CO_3^{2-} \quad \text{(eq. 1)}$$

The K_{sp} (solubility product, which defines activities at equilibrium) for siderite is $10^{-10.24}$ (Singer and Stumm, 1970), and can be expressed as:

$$\boldsymbol{K_{sp} = a_{Fe} \times a_{CO_3^{2-}} = 10^{-10.24}} \quad \text{(eq. 2)}$$

Adjusting this in terms of the ratio (denoted by Ω) between K_{sp} and the product of the activities present regardless of equilibrium state (or the Ion Activity Product; IAP) gives:

$$\boldsymbol{\Omega = \frac{IAP}{K_{sp}} = \frac{a_{Fe^{2+}} \times a_{CO_3^{2-}}}{K_{sp}}} \quad \text{(eq. 3)}$$

This equation may now be rearranged in terms of the desired activity to be calculated:

$$\boldsymbol{a_{Fe^{2+}} = \frac{\Omega \times K_{sp}}{a_{CO_3^{2-}}}} \quad \text{(eq. 4)}$$

To calculate the activity of Fe, which is inputted in Figure 2, the activity of CO_3^{2-} must first be calculated. This is achieved through use of the following equations outlined in Zeebe and Wolf-Gladrow (2001):

$$\boldsymbol{CO_2conc = pCO_2 \times K_H} \quad \text{(eq. 5)}$$

where pCO_2 is the level of CO_2 used in the experiment, and K_H is Henry's constant (3.4 E−2). Once the concentration of CO_2 (CO_2conc) has been determined, the dissolved inorganic carbon (DIC) concentration of the solution can be calculated:

$$\boldsymbol{DIC = CO_2conc \times \left(1 + \left(\frac{k_1}{Hconc}\right) + \left(\frac{k_1 \times k_2}{Hconc^2}\right)\right)} \quad \text{(eq. 6)}$$

where k_1 is the first dissociation constant of carbonic acid given as 5 mol kg^{-1} (He and Morse, 1993), k_2 is the second dissociation constant of carbonic acid given as $10^{-10.12}$ mol kg^{-1} (He and Morse, 1993), *Hconc* is 10^{-pH} (inputted variable from our experiments) divided by the ion activity coefficient for H^+ (0.8180 as calculated through the b-dot equation; Jiang and Tosca, 2019). This value requires an ionic strength, which describes the electrostatic force an ion is subjected to from neighbouring charged species. This was estimated by accounting for soluble compounds and complexes that reduce the concentration of charged species, producing the 'true ionic strength' as opposed to the stoichiometric ionic strength.

Inputting DIC into the following equation allows the concentration of CO_3^{2-} to be calculated:

$$\boldsymbol{CO_3conc = \frac{DIC}{\left(1 + \left(\frac{Hconc}{k_1}\right) + \left(\frac{Hconc^2}{k_1 \times k_2}\right)\right)}} \quad \text{(eq. 7)}$$

The activity of CO_3^{2-} can then be calculated:

$$a_{CO_3^{2-}} = \gamma_{CO_3^{2-}} \times CO_3 conc \quad \text{(eq. 8)}$$

where the activity coefficient of CO_3^{2-} is 0.3058 (b-dot equation calculation from Jiang and Tosca, 2019). As above, this was estimated by accounting for soluble compounds and complexes that reduce the concentration of charged species to represent the 'true ionic strength' as opposed to the stoichiometric ionic strength. The activity of CO_3^{2-} can then be inputted into the equation in the paper:

$$a_{Fe^{2+}} = \frac{\Omega \times K_{sp}}{a_{CO_3^{2-}}} \quad \text{(eq. 9)}$$